Organisation and dynamics of an amphiphilic block copolymer at the air/water interface

Brian R. Rochford

Organisation and Dynamics of an Amphiphilic Block Copolymer at the Air/Water Interface

September 1995

Brian R. Rochford

Collingwood College

University of Durham

Supervisor

Professor R.W. Richards

A thesis submitted to the University of Durham in partial fulfilment of the regulations for the Degree of Doctor of Philosophy

ORGANISATION AND DYNAMICS OF AN AMPHIPHILIC BLOCK COPOLYMER AT THE AIR/WATER INTERFACE

BRIAN R. ROCHFORD PhD THESIS, SEPTEMBER 1995

ABSTRACT

This thesis describes the techniques of anionic polymerisation and characterisation used in the synthesis of poly(methyl methacrylate)/poly(ethylene oxide) diblock copolymers, the various surface techniques used to examine the interfacial properties of these copolymers spread on water, and the dynamics of these copolymers in solution. The surface techniques used were surface pressure-concentration isotherm studies, neutron reflectivity, surface quasi-elastic light scattering, and ellipsometry. The thermodynamics of micellization and dynamic properties of the copolymer solutions were investigated using light scattering.

The diblock copolymers had a target composition of 50:50 mole ratio and M_w = 50000. In addition, several copolymers had one or both blocks fully deuterated which was necessary for the neutron reflectivity studies where contrast variation was required to apply the kinematic approximation.

Surface pressure isotherms give thermodynamic information about the behaviour of polymer segments at the interface. It has been possible to interpret this behaviour by using neutron reflectivity to obtain information concerning the thickness and distribution of the PMMA and PEO blocks, and water at the interface.

The trends in layer thickness have been supported by the ellipsometric measurements and interpretation of the viscoelastic SQELS data has allowed conclusions about the hydrodynamics of the polymer chains at various surface concentrations.

ACKNOWLEDGEMENTS

I would like to thank everybody who has helped me during my time at Durham. Firstly, I would like to acknowledge the help and advice of my supervisor, Dr Randal Richards, over the past three years. The experimental investigations described in this thesis would not have been possible without something to investigate, I am therefore grateful to Tom Kiff for advice on the synthesis of the diblock copolymers. For the characterisation of these copolymers I would like to thank Gordon Forrest for the GPC data, and Dr Alan Kenwright and Mrs J. Say for the NMR data. For help with the Neutron Reflectivity experiments and data analysis I would like to thank Drs Jeff Penfold, John Webster and David Bucknall of the Rutherford-Appleton Laboratory. The Surface Quasi-Elastic Light scattering experiments proved successful due to the efforts of Dr Mark Taylor who improved the experimental setup. Ellipsometry measurements at the Cavendish Laboratory, Cambridge, were possible due to Drs Richard Jones, Adrian Rennie and in particular Joe Keddie.

Financial support for this work was provided by the ESPRC for the first two years and the third year was partially funded by the IRC.

I would like to thank everyone I have encountered while studying in Durham for the good times. In particular I would like to mention such people as Richard *'captain birdseye'* Towns, Donald *'five bellies'* Davison, Ian *'five strands'* Reynolds (wee-man), Carl *'Hull'* Redshaw, Gary *'fish finger'* McGeorge, Steve *'big lad'* Carss, Abdullah *'spiros'* Ahmed, and Michael *'tee-total'* Jeshcke (pecky).

DEDICATION

I would like to dedicate this work to my family and friends and all who have helped me over the past three years.

Declaration

All work contained in this thesis is, unless stated otherwise, the sole work of the author and has been carried out in the laboratories of the Interdisciplinary Research Centre in Polymer Science and Technology (University of Durham), the Rutherford Appleton Laboratory (Didcot, Oxfordshire) and at the Cavendish Laboratory (University of Cambridge) and remains the copyright of the author. No quotation from it should be published without the prior written consent of the author and information derived from it should be acknowledged. No work contained in this thesis has previously been submitted for any other qualification

CONTENTS

Preface -Glossary of Terms

Wherever appropriate standard SI units have been used to quote physical properties in this thesis. However, for some of the techniques described in this thesis it is usual to quote physical properties in non-SI units. Layer thickness, for example is normally quoted in Ångstroms, Å. Where these non-SI units are used the following list shows their relationship to the standard SI equivalents.

$1Å = 10^{-10}m$

$1\mu l = 10^{-6}l = 10^{-9}m^3$

$1\mu m = 10^{-6}m$

$1nm = 10^{-9}m$

$1\mu s = 10^{-6}s$

$1eV = 1.6020x10^{-19}J = 1.6020x10^{-}19m^2\ kg\ s^{-2}$

The following list gives brief definitions of the symbols used in the text and also an indication of the technique which they are relevant to in paranthesis

a -monomer length (surface pressure theory)

A -molecular area or area available per segment of polymer molecule (surface pressure theory)

A_0 -molecular area in the close packed state, or limiting area per molecule

A -amplitude factor (SQELS correlation function expression)

A_2 -second virial coefficient (polymer solution theory)

$A_{2,2}$ -two dimensional second virial coefficient (surface pressure theory)

b -atomic coherent scattering length (neutron reflectivity)

B -instrumental background (SQELS correlation function expression)

β -standard deviation of the instrumental function in the frequency domain (SQELS correlation function expression)

β -instrumental line broadening term (SQELS correlation function expression)

β -the phase shift of the multiply reflected wave inside the film as it traverses from one interface to the other (ellipsometry)

cmc -critical micelle concentration

cmt -critical micelle temperature

C -concentration (polymer solution theory)

C* -initial chain overlap concentration, concentration of transition from dilute to semi-dilute solution behaviour

C** -concentration of transition from semi-dilute to concentrated solution behaviour

d -dimensionality (scaling theory)

d -film thickness (optical theory)

d -physical density (neutron reflectivity)

d_k -thickness of the kth layer (ellipsometry)

D -distance between grafting points (neutron reflectivity theory)

D -diffusion coefficient (polymer solution theory)

D_0 -diffusion coefficient at infinite dilution (polymer solution theory)

$D(\omega)$ -Lamb-Levich dispersion expression (SQELS)

ΔG^0 -standard Gibbs energy (micellization)

ΔH^0 -standard enthalpy (micellization)

ΔS^0 -standard entropy (micellization)

ΔG^E -excess Gibbs energy (surface pressure theory)

ΔH^E -excess enthalpy (surface pressure theory)

ΔS^E -excess entropy (surface pressure theory)

Δ -phase difference of x and y electric vibrations (ellipsometry)

$\delta\Delta$ -change in phase difference (ellipsometry)

$\delta\theta$ -deviation from specular angle (SQELS)

$\delta\psi$ -change in amplitude attenuation (ellipsometry)

$\Delta\rho$ -scattering length density between two bulk media (neutron reflectivity)

E -total amplitude of scattered light (ellipsometry)

ε_0 -surface dilational elastic modulus (SQELS)

ε' -surface dilational viscosity (SQELS)

$f(\tau)$ -time dependence of the correlation function expected from waves of a selected q value (SQELS)

φ -volume fraction (neutron reflectivity)

φ^* -polymer volume fraction of transition from dilute to semi-dilute regime (two dimensional scaling theory)

φ^{**} -polymer volume fraction of transition from semi-dilute to concentrated regime (two dimensional scaling theory)

g -gravitational acceleration = $9.81 m/s^2$

$g(\tau)$ -correlation function in time domain (SQELS)

$G(\tau)$ -measured auto-correlation function (SQELS)

$G^*(\omega)$ -dynamic modulus (SQELS)

$G'(\omega)$ -storage modulus (SQELS)

$G''(\omega)$ -loss modulus (SQELS)

Ge -the equilibrium elastic modulus at infinite relaxation time ($\omega \rightarrow 0$) (SQELS)

G -amplitude of relaxation process (SQELS)

G_ε -dilational amplitude of relaxation process (SQELS)

γ -surface tension (surface pressure theory)

γ -surface tension modulus (SQELS)

γ_0 -transverse shear modulus (SQELS)

γ' -transverse shear viscosity (SQELS)

γ^* -complex strain (SQELS)

Γ -damping constant (SQELS)

Γ_C -capillary wave damping (SQELS mode coupling theory)

Γ_D -longitudinal wave damping (SQELS mode coupling theory)

Γ -surface concentration (two dimensional scaling theory)

Γ^* -surface concentration of transition from dilute to semi-dilute regime (two dimensional scaling theory)

Γ^{**} -surface concentration of transition from semi-dilute to concentrated regime (two dimensional scaling theory)

Γ_a -apparent surface concentration (neutron reflectivity)

Γ_s -spread amount of material (neutron reflectivity)

h(Q) -modifying form factor in kinematic expressions for neutron reflectivity

h'(Q) -modifying form factor in kinematic expressions for neutron reflectivity

η -solvent viscosity (micellization)

η -dynamic viscosity (SQELS)

I -intensity of incident radiation (neutron reflectivity)

I_r -intensity of reference beam (SQELS)

I_s -intensity of scattered light (SQELS)

$\mathbf{k_0}$ -neutron wave vector outside medium

$\mathbf{k_1}$ -neutron wave vector inside medium

$\mathbf{K}$ -scattering vector

K_B -Boltzmann constant

λ -radiation wavelength (optical or neutron reflectivity)

Λ -wavelength of capillary wave (SQELS)

m -association number (micellization)

M_m -molecular weight of scattering species or monomer unit (neutron reflectivity)

M_n -number average molecular weight

M_w -weight average molecular weight

nrw -null reflecting water

$n_i(Q)$ -Fourier transform of the distributions of number density of each interfacial component

N -degree of polymerisation

N -atomic number density (neutron reflectivity)

N_{av} -Avogadro's Number = 6.022×10^{23}

ν -the kinematic viscosity ($=\eta/\rho$)

ν -critical scaling exponent (scaling theory)

ν_θ -theta condition value of scaling exponent (scaling theory)

ω -measure of flexibility or unfolding of polymer chain (surface pressure theory)

ω_0 -measure of flexibility with zero cohesion

ω -complex capillary ripplon frequency (SQELS)

ω_0 -propagation frequency (SQELS)

$P(\omega)$ -Bouchiat and Meunier power spectrum (SQELS)

π -surface pressure

q -interfacial wavenumber, component of the scattering vector parallel to the liquid surface (SQELS)

Q -scattering vector normal to the interface (neutron reflectivity)

Q_c -critical value below which total reflection takes place (neutron reflectivity)

R -the gas constant = 8.314 J K^{-1} mol^{-1}

R -reflected component of radiation (neutron reflectivity)

Re -Reynolds number

R_g -radius of gyration of polymer coil (neutron reflectivity)

R_h -hydrodynamic radius (polymer solution theory)

R_p -complex reflection coefficient (ellipsometry)

R_s -complex reflection coefficient (ellipsometry)

$r_{i,j}$ -Fresnel coefficient for reflection between layers i and j (ellipsometry and neutron reflectivity)

ρ -physical density, mass per unit volume

ρ -scattering length density (neutron reflectivity)

$\rho(Q)$ -one dimensional Fourier transform of $\rho(z)$

$\rho(z)$ -mean scattering length density at level z in the interface

σ -standard deviation in the rate of change of the scattering length density (kinematic theory of neutron reflectivity)

σ_a -adsorption cross-section (neutron reflectivity)

$\langle\sigma\rangle$ -mean square roughness (neutron reflectivity)

σ^* -reduced surface density (surface pressure and neutron reflectivity)

σ -surface density (surface pressure and neutron reflectivity)

σ_{01} $-1/\pi R_g^2$ (surface pressure and neutron reflectivity)

t -time

T -absolute temperature

T -transmitted component of radiation (neutron reflectivity)

τ -mean width of the interface (neutron reflectivity)

τ -reduced temperature (surface pressure theory)

τ_ε -dilational relaxation time (SQELS)

θ -temperature of theta or Flory condition behaviour (surface pressure theory)

θ -angle of radiation incidence (neutron reflectivity, ellipsometry, SQELS)

θ_c -critical angle of total reflection (optical and neutron reflectivity)

θ -scattering angle (light scattering)

W -interchain cohesion

ψ -amplitude attenuation (ellipsometry)

ψ_θ -scaling exponent (scaling theory)

z -co-ordination number of the monomer units in the chain

ζ -interfacial disturbance from the mean plane for a two dimensional wave (SQELS)

ζ -width parameter of tanh profile (neutron reflectivity)

CHAPTER 1 - INTRODUCTION

1.1 Spread Monolayers

1.1.1 Examination of Interfacial Monolayers Using Classical Methods

Investigations of monolayers at fluid-fluid interfaces have mainly been confined to the interface between air and an aqueous subphase. To a lesser extent organic solvents and liquid metals have been used instead of water. Several techniques exist for characterisation of these systems which rely on measurement of surface pressure, surface viscosity, surface shear modulus values or surface potential. The most widely used method is to measure surface pressure as a function of surface area.

1.1.1.1 Surface Pressure Measurements

In a bulk solution molecules are subject to equal attractive forces. When molecules are present at a surface or interface these forces are unequal which has the effect of pulling some of the molecules into the subphase. This phenomenon is referred to as surface tension which is defined as the work required to expand the surface isothermally by unit area (Newton-metres per metre squared). The ability of surface active molecules to accumulate at the interface allows expansion of the interface which lowers the surface tension. This reduction in surface tension is known as the surface pressure, π

$$\pi = \gamma_{sub} - \gamma_{film} \qquad (1.1)$$

where γ_{sub} and γ_{film} are the surface tensions of the subphase and film respectively. Surface pressure readings are measured using either a paper or metal Wilhelmy plate attached to a microbalance. This microbalance contains a force transducer which measures the force required to keep the plate in a stationary vertical position. A plot of surface pressure as a function of area is called a surface pressure isotherm. The word isotherm is used because the measurement is taken at constant temperature. The simplicity of this technique has made it a standard method of characterising these two-dimensional systems. The

drawback of this technique is the limited understanding of how these isotherms relate to the surface organisation of the interfacial material.

Outline of a surface pressure measurement

Surfactants consisting of polar head groups and hydrocarbon chains are an example of a typical material investigated at the air/water interface. The polar head groups are submerged in the aqueous subphase and the forces affecting them are ionic and proportional to $1/r^2$, where r is the intermolecular separation. The forces between the hydrocarbon chains are van der Waal's interactions and the forces are proportional to between $1/r^6$ and $1/r^{12}$. The interactions in the subphase are therefore of a longer range than those at the interface. The surface pressure isotherm consists of three characteristic regions (figure 1.1). After deposition onto the aqueous subphase the surface area is at a maximum and the molecules act as a two-dimensional film described by the equation

$$\pi A = K_B T \qquad (1.2)$$

where A is the molecular area, K_B the Boltzmann constant and T the thermodynamic temperature. On compression of the film the surface pressure increases due to ordering of the molecules and it acts as a two-dimensional liquid. Further compression of the monolayer causes higher increases in surface pressure as more ordering of the molecules occurs and the monolayer behaves as a quasi-solid. The surface pressure here increases steeply and has an approximately linear relationship with the molecular area.

1.1.1.2 Theory of Surface Pressure Effects from Spread Polymeric Monolayers

The development of quantitative theories describing polymeric monolayers in terms of molecular interactions at the interface was pioneered by Crisp[1,2]. Many early investigations were made of polymeric monolayers at interfaces and various equations of state for linear polymers were presented in order to explain the surface pressure isotherms[3,4]. Singer[4] derived an equation using the theory of polymer solutions

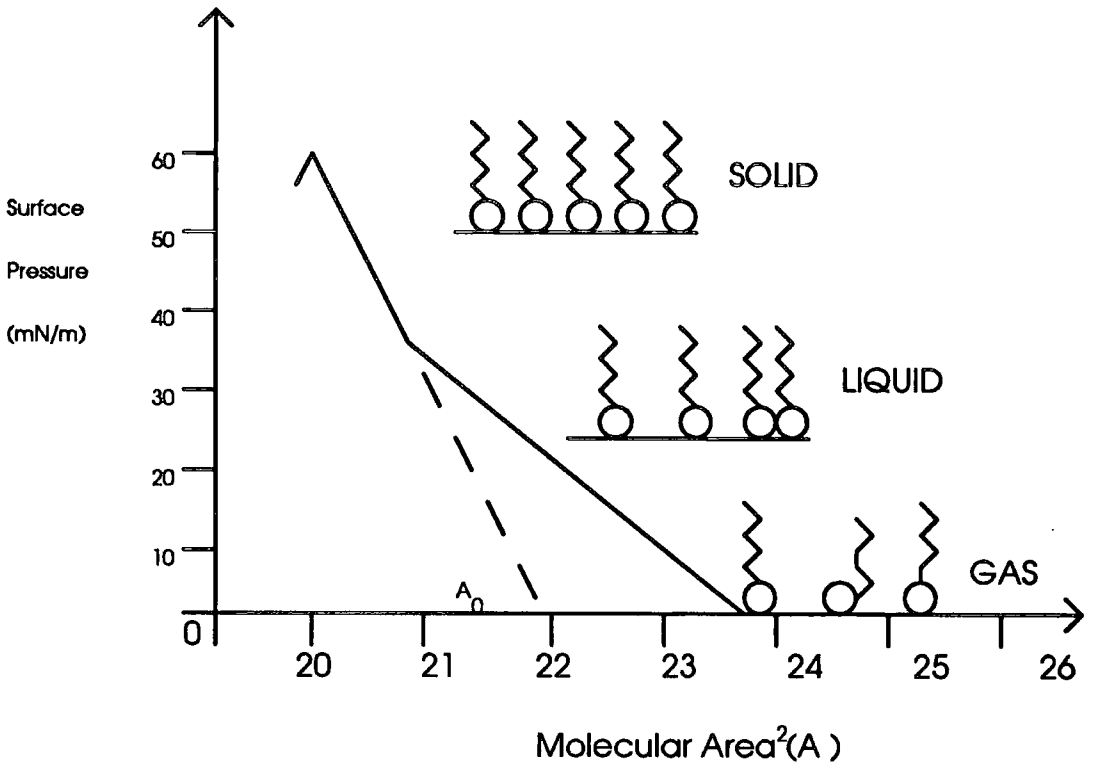

Figure 1.1 Typical surface pressure isotherm for a surfactant

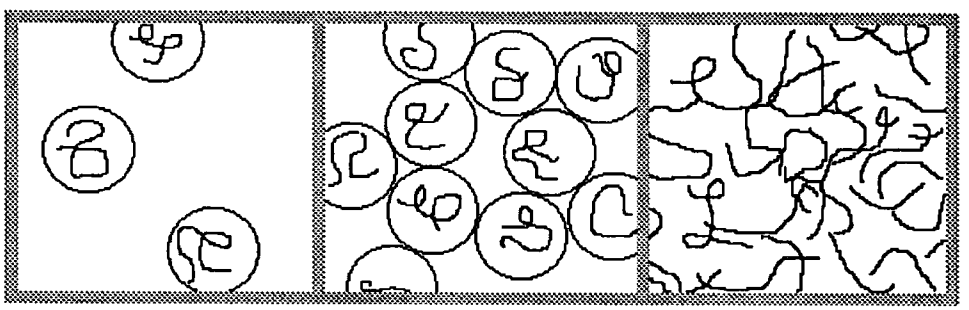

Figure 1.2 Crossover between dilute and semi-dilute solutions

developed by Huggins[5] and assuming a two-dimensional lattice model for strong cohesive forces where the surface pressure was less than that for a random coil.

Singer's equation is

$$\pi = \frac{Nk_BT}{A_0}\left[\ln\left(\frac{A}{A-A_0}\right)+\left(\frac{N-1}{N}\right)\frac{z}{2}\ln\left(1-\frac{2A_0}{zA}\right)\right] \qquad (1.3)$$

where A is the area available per segment of polymer molecule, A_0 the corresponding area in the close-packed state, K_B the Boltzmann constant, T the absolute temperature, z the co-ordination number of the monomer units in the chain and N is the degree of polymerisation.

Davies and Llopis[6] defined a quantity $\omega = z - 2$ as a measure of flexibility or unfolding which depended upon the cohesive forces between segments. When z = 2 the chain is rigid and equation 1.3 reduces to

$$\pi = \frac{Nk_BT}{A_0}\ln\left(\frac{A}{A-A_0}\right) \qquad (1.4)$$

When z = 4 the chain is fully flexible and

$$\omega = \omega_0 \exp(-W/K_BT) \qquad (1.5)$$

where ω_0 is the flexibility with zero cohesion and W is the interchain cohesion from Van der Waal's forces between polymer segments. Singer's approach makes no allowance for entropic effects on the chain flexibility at the interface. The equation of state formulated by Matuura and Motomura[7] used a two-dimensional lattice model for polymeric monolayers similar to Singer's original approach. In their calculation of the equation of state they took into account both the entropic constraints of the limited available area as well as the enthalpic effects of the area dependent number of intersegmental contacts on the lattice.

1.1.1.3 Scaling Laws

A. Scaling Theory in Three Dimensions

The scaling theories developed by P.G. de Gennes[6] have shown the fundamental distinction between dilute and more concentrated polymer solutions. Figure 1.2 shows a schematic of polymer molecules at various solution concentrations. In dilute polymer solutions the coils are separate while in semi-dilute solutions the coils begin to be densely packed. The threshold where coils begin to be densely packed is called the chain overlap concentration C*. For a very good solvent then

$$C^* \cong N/R_g^3 = a^{-3}N^{1-3\nu} \tag{1.6}$$

where R_g is the radius of gyration, N is the degree of polymerisation, a is the monomer length and ν is the critical exponent. The corresponding threshold Φ^* may be defined in terms of the polymer fraction Φ

$$\Phi^* \sim N^{-4/5} \tag{1.7}$$

(i) Dilute Regime

In dilute solutions $C < C^*$ and the system consists of separate coils behaving essentially as 'hard spheres' of radius ~ R_g. This implies the following equation of state for the osmotic pressure

$$\pi/T = C^2/N + A_2C_2^2 + \ldots \tag{1.8}$$

and the N dependence of the second virial coefficient A_2 is

$$A_2 \cong R_g^2N^{-2} \sim N^{-1/5} \tag{1.9}$$

(ii) Semidilute Regime

In the semidilute regime the coils overlap but the polymer fraction Φ is still low

$$\Phi^* < \Phi < \Phi^{**} \tag{1.10}$$

where Φ^{**} represents the polymer fraction where the transition to concentrated solution behaviour occurs. The chain overlaps make it necessary to include an excluded volume interaction term. This scaling law for the osmotic pressure is

$$\frac{\pi}{T} = \frac{C}{N} f_{\pi}\left(\frac{CR_g^3}{N}\right) = \frac{C}{N} f_{\pi}\left(\frac{C}{C^*}\right) \tag{1.11}$$

where the function $f_{\pi}(x)$ is a dimensionless function. To eliminate all dependence on N, the function $f_{\pi}(x)$ must behave as a simple power of x such that

$$\lim_{x\to\infty} f(x) = \text{constant } x^m = \text{constant } (\Phi/\Phi^*)^m = \text{constant } \Phi^m N^{4m/5} \tag{1.12}$$

In terms of Φ and N, this gives

$$\frac{a^3\pi}{T} = const.\Phi^{m+1} N^{(4m/5)-1} \tag{1.13}$$

Since the thermodynamic properties are independent of N, then m must equal 5/4 which gives

$$\frac{a^3\pi}{T} = const.\Phi^{9/4} \tag{1.14}$$

It should be noted that this differs from the mean field prediction where $\pi \sim \Phi^2$.

B. Scaling Theory in Two Dimensions

The scaling theories proposed by de Gennes for polymer chains in three dimensions were expressed as a general dimensional dependence by Daoud and Jannink[9]. By envisaging a two dimensional 'solution' for polymer monolayers then the distinction between dilute and more concentrated films may be made.

(i) Dilute Regime

In the dilute regime the concentration of polymer is low and the virial expansion

$$\pi/\Gamma RT = (1/M_n + A_{2,2}\Gamma + ...) \tag{1.15}$$

is valid, where R is the gas constant, T the absolute temperature, M_n the number average molecular weight of the polymer, $A_{2,2}$ the second virial coefficient at the two-dimensional

space, and Γ is the surface concentration. It is possible to determine the value of M_n from the intercept of the plot of $\pi/\Gamma RT$ versus Γ, and the slope of the plot gives $A_{2,2}$. For any dimensionality the second virial coefficient may be expressed as

$$A_{2,d} \sim N^{\nu d} \tau^{d(\nu-\nu_\theta)/\psi_\theta} \tag{1.16}$$

where τ is the reduced temperature. The exponent ν is the critical exponent of the excluded volume, ν_θ is the tricritical exponent of the excluded volume and ψ_θ is the tricritical exponent of the crossover concentration. The values of these exponents have been predicted by many theoretical models. For d = 2 the ε-expansion renormalization-group calculations predicted $\nu = 0.77$[10], $\nu_\theta = 0.505$[11], and $\psi_\theta = 0.60$[12]. Substitution of these values into equation (1.16) gives

$$A_{2,2} \sim N^{1.54}\tau^{0.88} \tag{1.17}$$

In an attempt to predict the value of the ν exponent other theoretical methods have been used. The use of mean field theory has predicted that in the good solvent regime, ν=0.75. For short chains, self avoiding walk calculations[13] have suggested a similar value (N < 18) while Monte Carlo simulations[14] predict ν=0.7503±0.004. The predicted values of ν_θ, the value of ν in the θ condition, are much more diverse. For the mean field prediction ν_θ = 2/3 but this considers only ternary interactions. Ideal random walk treatment gives a collapsed chain value of 1/2 while Monte Carlo simulations have yielded values between 0.51[15] and 0.59[16]. Predictions of 0.55 and 0.59 have been obtained by transfer matrix[17] and real space normalisation methods[18].

(ii) Semidilute Regime

The polymer concentration C* where polymer chains begin to overlap is the transition from dilute to semidilute regimes, concentrations above C* being in the semidilute regime. The crossover polymer concentration C* can be expressed as a function of molecular weight and temperature

$$C^* \sim N / R_{g,d}{}^d \sim N^{1-\nu d} \tau^{-d(\nu-\nu_\theta)/\psi_\theta} \quad (1.18)$$

and $$R_{g,d} \sim N^{\nu} \tau^{(\nu-\nu_\theta)/\psi_\theta} \quad (1.19)$$

$R_{g,d}$ being the radius of gyration of polymer in a dimensional space of d. Substituting the values of the exponents used in equation (1.17) into (1.18) then

$$\Gamma^* \sim N^{-0.54} \tau^{-0.88} \quad (1.20)$$

des Cloizeaux[15] obtained an osmotic pressure expression

$$\pi / T \sim C^{\nu d(\nu d-1)} \tau^{(\nu-\nu_\theta) d/\psi_t^{(\nu d-1)}} \quad (1.21)$$

By substituting the values of the exponents used in equation (1.17) then

$$\pi/T \sim \Gamma^{2.85} \tau^{1.64} \quad (1.22)$$

(iii) Concentrated Regime

The crossover C** between the semidilute and concentrated regimes is defined as a function of reduced temperature, τ

$$C^{**} \sim \tau^{(\nu_\theta d-1)/\psi_\theta} \quad (1.23)$$

For concentrations above C** there is chain overlap but the θ condition holds. The concentrated regime corresponds to the semidilute regime at the θ point and the osmotic pressure π is defined as

$$\pi / T \sim C^{\nu_\theta d/(\nu_\theta d-1)} \quad (1.24)$$

For d = 2 then

$$\Gamma^{**} \sim \tau^{0.0167} \quad (1.25)$$

and

$$\pi/T \sim \Gamma^{101} \quad (1.26)$$

Attempts to confirm these power laws experimentally have not proved successful[19-21]. Meaningful A_{22} measurements have to be performed in the dilute regime, where the

molecules behave as individual objects, but extremely low surface pressures corresponding to low surface concentrations are subject to large error.

1.1.2 Non-Contact Methods

Classical techniques such as surface pressure measurements are very precise for studying monolayers but unfortunately they perturb the thermodynamic equilibrium. They are also slow which inhibits investigation of dynamic processes. Techniques such as X-ray fluorescence microscopy, X-ray reflectometry, ellipsometry, surface quasi-elastic light scattering and neutron reflectometry have the advantage that they are non-perturbative. The latter three of these non-pertubative techniques are of interest in the context of the work presented in this thesis.

1.2 Review of Techniques used to Investigate Spread Monolayers

1.2.1 Surface Pressure Measurements

The intriguing properties of oils spread on water have been recorded since the eighteenth century B.C, when ancient Babylonians attributed supernatural significance to their multi-coloured patterns. The last two centuries have established a scientific basis for these observations. Benjamin Franklin made one of the earliest observations of wave damping by oil on water in 1765 when he spread oil onto a pond at Clapham common. He observed that one teaspoon full of oil had a calming influence over half an acre of water. Modern studies of monolayer systems began when Irving Langmuir published his studies of fatty acids, alcohols and esters spread on water[22]. A co-worker of Langmuir was Katherine Blodgett who devised a technique of lifting monolayers onto solid glass substrates for further investigation. This technique is commonly referred to as the Langmuir-Blodgett technique (L-B technique).

The pioneering efforts of Langmuir and Blodgett have led to a wide variety of work regarding the study of monolayers and L-B films[23]. Experimental apparatus has improved greatly with advances in techniques of preparation and lifting of L-B films and also of overall trough design.

Polymeric films are an example of spread monolayers studied. Initial studies centred on macromolecular films consisting of cellulose derivatives[24] and polyesters[25]. Some synthetic polymers can be spread as monolayers and have been studied systematically since the early investigations of Crisp[1,2].

The behaviour of a 2-D monolayer system is analogous with three dimensional phases allowing it to be described in terms of gaseous, liquid or solid behaviour. Decreasing the molecular area produces changes in surface pressure, the rate of change depending on the interactions between the molecules in the film. For gaseous behaviour the molecules

are far apart and no surface pressure is noticeable. On compression of the film the molecules feel some influence from each other as they are pushed closer together and the surface pressure increases due to a transition from gaseous to liquid behaviour. This liquid film behaviour is of two types, expanded and condensed. Expanded films characteristically have an initial rise in surface pressure at larger areas per molecule than for condensed films. The rate of increase in surface pressure is also usually much less for expanded films than condensed films. Further compression of the film forces the molecules very close together until further compression is impossible. At this point the film is very stiff and a rapid rise in the surface pressure occurs until a point where the film collapses. At the collapse point the surface pressure drops of suddenly due to the molecules being pushed out of the two-dimensional layer.

For surfactants these phase changes may be rationalised in terms of the orientation of the molecules and intermolecular distances. However, the behaviour of monolayers composed of polymeric material is less straightforward. A common method to infer the packing of molecules at the air/water interface is to calculate the limiting area per molecule by extrapolating the initial slope of the liquid region to zero surface pressure. This method does not give any information concerning the statistical distributions of chain configurations as observed in three dimensional polymer solutions. Shuler and Zisman[26] rationalised the measured behaviour of polymer films with their structure. Their work involved a combination of surface pressure measurements and physically induced wave damping techniques to argue for the existence of two distinct conformations of poly(ethylene oxide) associated with the presence of bound water molecules along the chain, which depended on the degree of chain compression. Many polymeric films have been studied and classified as either liquid expanded or liquid condensed. Examples of liquid expanded films are poly(2-vinyl pyridine)[27], poly(vinyl

acetate)[2,28-32], poly(ethylene oxide)[33], poly(propylene oxide) and poly(vinyl alkyl ethers)[34]. Examples of liquid condensed films are poly(vinyl benzoate)[35] and poly(methyl methacrylate)[36,37]. Poly(alkyl acrylates) and poly(alkyl methacrylates) are examples of systematic trends occurring in a homologous series of polymers. Here an increase in expanded behaviour is noticed on increasing the alkyl group size from methyl to butyl[1,2].

New theoretical approaches to the interpretation of experimental results by Daoud and Jannink[9] have seen an increased interest in the study of polymer films. These approaches predicted that polymer films may exist in three regions of behaviour depending on the surface concentration. In the dilute regime, where the surface concentration is less than a critical Γ^* value then the relationship between surface pressure and surface concentration scales according to an exponent y ($\pi \sim \Gamma^y$). In the semi-dilute regime ($\Gamma^* < \Gamma < \Gamma^{**}$) the exponent y is expressed as a function of ν where $y = 2\nu/(2\nu-1)$. Above Γ^{**} a concentrated regime is predicted and an exponential dependence to the power of 101 holds ($\pi/T \sim \Gamma^{101}$). This dependence has never been observed experimentally which is attributed to looping out of the molecules and collapse of the monolayer.

The ν exponent gives an indication of the thermodynamics of the interaction between polymer segments and the subphase. For good 2-D solvent conditions it has been predicted theoretically that $\nu = 0.77$. There are a variety of predictions for the theta state ν_θ varying from 0.505 to 0.59, compared to a collapse value of 0.5. A value of 0.56 for the theta state has general agreement. Ober and Vilanove[38] attempted to apply these scaling laws in a study of poly(vinyl acetate). The work of Vilanove and Rondelez[39] applied scaling laws to the characterisation of the thermodynamics of polymer films at high surface concentrations. The results of their work was to extract values of ν governing the relationship between the degree of polymerisation and radius of gyration.

For poly(methyl methacrylate), ν was equal to 0.56 while for poly(vinyl acetate) the value of ν was 0.79. This value of $\nu = 0.79$ is characteristic of that predicted for good, excluded volume behaviour, while $\nu = 0.56$ describes a two dimensional theta state.

Kawaguchi et al[15,40] determined the theta temperature for monolayers of poly(methyl methacrylate) by using the equation of state in the dilute regime. They plotted $\pi/\Gamma RT$ versus Γ at $\Gamma<\Gamma^*$ and observed the initial slope at different temperatures. From this they extracted the molecular weight by extrapolating to zero concentration and the two dimensional second virial coefficient from the slope (which was zero at 18.2°C). Temperatures above the theta temperature produced values of $\nu = 0.77$ and at the theta temperature $\nu = 0.51$ was obtained which was close to the lowest previous theoretical prediction of $\nu = 0.505$.

Vilanove et al[41] were unable to observe a theta state for poly(methyl acrylates). This contradicted the previous work especially since they found good solution conditions independent of temperature between 5 and 30°C. This paper also reconsidered observations of the behaviour of poly(methyl methacrylates). They previously obtained a ν value of 0.56, but later experiments produced a ν value of 0.53 over a temperature range from 1 to 35°C.

Investigations of lower molecular weight PMMA samples by Vilanove et al[43] produced a higher ν value of 0.57. This difference was thought to be due to scaling predictions relying on the basis of infinite dilution. Another consideration was that different stereotactic sequences in previous samples may have led to erroneous results. The difference in syndiotactic and isotactic PMMA at surfaces has long been realised[36,37]. At the air/water interface syndiotactic PMMA exists as a liquid condensed film while the isotactic polymer forms a liquid expanded film. Differences in the stereotactic sequences in separate samples may therefore have a profound effect on the properties of the films.

1.2.1.2 Charged Monolayers

Although the existence of charge effects in ionised monomolecular films has been known for a long time, Davies and Rideal[43] were the first to make systematic studies. They used the Gouy-Chapman model of the double layer for the first time and calculated the surface potential of the monolayer. This surface potential allowed them to derive the surface pressure increment due to the repulsive interaction between charges of like sign. It was noted that the total surface pressure π is the sum of the electrical term π_e plus the contribution of the corresponding neutral film which was described by a van der Waals-type of equation of state. It was therefore possible to obtain π_0 independently and deduce the π_e term from $\pi_e = \pi - \pi_0$. Studies of charged monolayers have been confined mainly to surfactants such as fatty acids[44,45] due to fully ionised poly-electrolyte molecules usually being water soluble and unable to form stable films. Attempts to avoid these difficulties involved using polyampholytes where the ionic dissociation can be controlled by altering the pH of the substrate[46]. Statistical copolymers[47] having varying numbers of ionizable groups along the chain were obtained by altering the proportions of charged and neutral monomer units. However, in all cases the polymer chain conformation changed with the amount of linear charge density present. This was thought to give spurious increases in the surface pressure of the monolayer therefore obscuring the effect of intermolecular interactions. Bringuier et al[48] studied monolayers of diblock copolymers composed of one neutral poly(methyl methacrylate) block and one charged poly(vinyl-4-pyridinium bromide) block. For the dilute regime, where the chains do not overlap and the van der Waals intermolecular interaction is weak, it was found that there was a significant electrical contribution π_e to the total surface pressure π. When the subphase consisted of salt free water then π_e increased linearly with the partial molar concentration of charged monomers but was independent of the chain length of the

polyelectrolyte sequence. It was also shown that π_e decreased with increasing salt concentration and tended to zero above about 0.1M potassium chloride.

1.2.2 Neutron Reflectometry

Fermi and coworkers[49] were the first to observe the total reflection of slow neutrons. Neutron reflection was not applied to practical applications until neutron guide technology, which utilised total external reflection, allowed its potential use to be realised. Neutron reflection experiments were advanced by the observation of interference of reflected neutrons from magnetised metal films using the IN11 instrument on the high flux reactor of the Institut Langevin, Grenoble, France[50].

A dedicated spectrometer was needed if neutron reflection was to be optimised for surface analysis experiments. The commissioning of the pulsed spallation neutron source ISIS at the Rutherford Appleton Laboratory, Oxfordshire, allowed the CRISP reflectometer, operating as a time of flight, fixed angle reflectometer, to be attached. The CRISP instrument has been used to investigate a large range of interfacial systems, the results of which have been greatly publicised[51].

Neutron reflectometry has been used to study a wide variety of interfacial systems. The systems studied to the greatest extent include

(i) solid and liquid surfaces,

(ii) solid-solid, liquid-solid and liquid-liquid interfaces,

(iii) magnetic films,

(iv) conducting films,

(v) semi-conducting films

(vi) biological membranes.

The study of solid surfaces has included using the neutron reflectometry technique to characterise silicon oxide layers of varying thicknesses on a crystalline silicon substrate,

Langmuir-Blodgett films and a number of thin magnetic films, studied using spin polarised neutrons. These films include a structural study of docosanoic acid Langmuir-Blodgett films and the fatty acid salts with cadmium[52], and an absolute determination of the superconducting penetration length in niobium was carried out[53]

Solid polymer surfaces have also been the subject of much work. Solution cast films have been studied[54] and the surface organisation of such a film of a diblock copolymer has been reported[55]. Russell et al[56] have investigated the polymer-polymer interface by observing the interdiffusion of two layers of polymer molecules, one layer composed of deuterated molecules, the other being protonated. One sample consisted of a bilayer having deuterated polystyrene on top of protonated polystyrene, the protonated material being deposited on an optical flat of fused silica. The other sample used was composed of a deuterated/protonated bilayer of polyimide on fused silica. As well as measuring the segment density profile for the specimen the aim was to follow its evolution after being annealed. Higgins et al[57] have investigated both immiscible and miscible polymer pairs[58,59]. Surface segregation effects have been measured by Jones et al[60,61] for blends of deuterated and hydrogenous polystyrene.

Neutron reflectometry has been applied to the surface chemistry of surfactants which have everday and industrial importance. Thomas et al[62,63,66-72] have provided a major contribution to this field, studying the adsorption of several surfactants at the air/solution interface. The adsorption of both[62] decyltrimethylammonium bromide (DTAB) and mixtures of DTAB and sodium decanoate were studied at the air/solution interface. The structure of tetramethylammonium dodecylsulphate[63] solution at the air/water interface was also investigated. Richardson et al[64,65] have studied spread monolayers of docosanoic acid and pentadecanoic acid on water. Application of the Kinematic Approximation to neutron reflection data has become prominent in recent studies of

surfactant layers[66-72] at the air/water interface. Three surfactant layers[66,67], sodium dodecyl sulphate, tetradecyltrimethylammonium bromide and triethylene glycol monododecyl ether adsorbed from solution were studied. It was possible to obtain the mean centre to centre separation between the distribution of a hydrophobic chain of a surfactant at the air/water interface and the aqueous surface. Further analysis of the data for tetradecyltrimethylammonium bromide[68] adsorbed from solution at the air/water interface allowed Gaussian distribution profiles to be drawn for the number density distributions of the chain and head groups of the surfactant, while it was possible to apply a hyperbolic tangent profile to the water in the layer. A recent study has determined the structure of dodecyltrimethylammonium bromide[69] (C_{12}TAB) adsorbed at the air/water interface for three surface concentrations. A comparison of the structure was then made with other C_nTABs having different alkyl chain lengths in the range C_{12} to C_{18}. Simister et al[70] have used neutron reflectivity to study a mixed surfactant system of ammonium perfluorooctanoate and ammonium decanoate adsorbed at the air/water interface.

The type of experiments conducted on surfactants at the air/water interface have also been applied to studies of polymer monolayers and solutions. Rennie et al[71,72] have studied both the adsorption of poly(ethylene oxide) at the solution-quartz interface and the air/water interface. Lee et al[73,74] have investigated poly(dimethylsiloxane) (PDMS) adsorbed from toluene at the surface of the solution. A volume fraction profile of PDMS at the surface of the solution was then made. Soluble block copolymers adsorbed from solution on solid interfaces have also been studied. Cosgrove et al[75] studied the conformation of both a polystyrene/poly(2-vinylpyridine) block copolymer and the homopolymer polystyrene adsorbed on mica from solution. Russell et al[76] reported results for a polystyrene/poly(methylmethacrylate) diblock copolymer adsorbed from

CCl_4 at a quartz wall. Adsorption at the liquid/liquid interface[77] has been studied for two fatty acids and a triblock copolymer of poly(ethylene oxide)/poly(propylene oxide)/poly(ethylene oxide). The measurements were made by depositing a layer of n-hexane, a few microns thick, on the surface of water, thereby allowing transmission of the neutron beam.

A variety of polymers may be spread as monolayers at the air/water interface yielding information such as molecular interactions and phase equilibria which are simpler systems to understand than bulk solutions. Recent work has investigated insoluble polymers spread as monolayers at the air/water interface. Studies of homopolymers give an insight into theoretical models for understanding polymer molecules in two dimensions. Two homopolymers studied by neutron reflection have been poly(methyl methacrylate)[78] (PMMA) and PDMS[79] spread on water. Hodge et al[80] used neutron reflectivity to study spread monolayers of derivatives of alternating styrene-maleic anhydride copolymers at the air/water interface. Kent et al[81] studied PDMS-PS diblock copolymers spread as monolayers on the surface of ethyl benzoate. The concentration profile and free energy of the submerged PS blocks were reported. The system was considered to be a tethered chain system, the PS block being soluble in the solvent but anchored to the surface by the PDMS block. This thesis describes the use of neutron reflectivity to investigate an MMA/EO diblock copolymer spread as a monolayer at the air/water interface and work concerning these investigations has been published[82,83].

1.2.3 Ellipsometry

Ellipsometry is a quick, non-destructive and nonperturbative optical method for the study of in situ thin films[84]. The technique is best suited to thick films (>1000Å) but has been applied to ultrathin films such as Langmuir-Blodgett monolayers on solid substrates (LB films) and to a lesser extent Langmuir monolayers on aqueous subphases[85-89]. For

films having thicknesses greater than 100Å it is possible to obtain both ellipsometric angles, the phase difference (Δ) and amplitude attenuation (ψ), whereas for thinner films it is only possible to obtain Δ[84]. For monolayers on a liquid subphase it is impossible to obtain an unambiguous ellipsometric characterisation of the system. The reason for this is that one ellipsometric measurement parameter is affected by two independent film properties, the geometrical thickness, d, and the refractive index, n. The refractive index of Langmuir monolayers is anisotropic due to their high degree of molecular ordering[90]. The diameter of the ellipsometric light spot (~ 2 mm diameter) greatly exceeds the size of domains of uniform tilt or bond orientation (~20 μm)[91,92]. It is therefore often sufficient to interpret the ellipsometric measurements uniaxially with the optical axis normal to the surface[93].

Attempts have been made to resolve the ambiguity of the interpretation of ellipsometric data and to decrease the number of parameters requiring determination. The parameters consist of one measurable parameter, Δ, and two parameters which must be determined, i.e., n and d. Different wavelength ellipsometry experiments have been attempted to resolve ambiguities in the data[94,95]. It was found that a unique characterisation of thin films was only possible if both the substrate and surface film were highly dispersive. The use of multiple angle ellipsometry did not yield any additional information[96,97] but did have the advantage of optimising the fitting of the experimental data and for minimising errors. Paudler et al[98] showed how multiple angle ellipsometry could convey sets of experimental data amenable to computer analysis although no unique characterisation of ultrathin, uniaxial, nonabsorbing films was claimed.

The last twenty years have seen ellipsometry applied to air/liquid interfaces including systems such as synthetic polymers and biological materials[99,100] adsorbed from solution and long chain acid monolayers[101]. The difference in refractive index between the film

and subphase is much smaller than that for solid substrate systems making the technique more difficult.

A number of monolayers of spread homopolymers have been investigated using ellipsometry. Kawaguchi et al[88,89] have described ellipsometry measurements on spread monolayers of various polymers of expanded and condensed type. The expanded type included poly(ethylene oxide) and poly(vinyl acetate) while the condensed type was poly(methyl methacrylate). Sauer et al[102] studied the same homopolymers, having almost exact molecular weight characteristics, and reported comparable results for the changes in $\delta\Delta$ (the difference in Δ between pure water and a polymer covered water surface) with increasing surface concentration.

Mixed polymer films have also been investigated[103-107] using ellipsometry so that the compatibility of the mixed polymers may be determined. The compatability of two polymers in the two-dimensional state can be determined from the dependence of the mean areas at a constant surface pressure and/or that of the collapse surface pressures on the molar fraction of one component in the binary mixtures. A significant contribution to the investigation of the compatibility of polymer mixtures has been made by Gabrielli and co-workers[103-106] and they concluded that the compatibility of two polymers at the air/water interface depends strongly on their interfacial orientations. Kawaguchi et al[107] applied ellipsometry, in addition to surface pressure measurements, to binary mixtures of poly(ethylene oxide) (PEO) and poly(methyl methacrylate) (PMMA) spread at the air/water interface. The compatibility of the PEO and PMMA mixtures was examined using the molar composition dependence of both the mean surface areas at a constant surface pressure and collapse surface pressures. The values of $\delta\Delta$ and $\delta\psi$, the changes in Δ and ψ between the clean water surface and the film covered water surface were obtained as a function of the surface concentration of PMMA. It was found that Δ and

$\delta\Delta$ increased with increasing surface concentration and the values reached a plateau at a PMMA surface concentration of 1.7 mg/m^2 in the mixtures.

These homo and mixed polymer films showed the sensitivity and limitations of ellipsometry for the study of air/water interfacial systems. Kawaguchi[88] used the experimental sensitivity in the phase retardation to estimate values of d as a function of surface concentration and also calculated the refractive index of the film[89] thereby giving the adsorbed amount. An independent determination of d and n depends on the ellipsometry measurements being sensitive to both the measured parameters i.e., Δ and ψ. The problem encountered by Kawaguchi et al[88] was that the amplitude attenuation only exceeded experimental errors at high surface concentrations for two polymers studied. The other three polymers studied had zero amplitude attenuation values and the authors' claim of calculating both d and n uniquely was difficult to justify.

Kawaguchi et al[89] proposed the use of a Lorentz-Lorenz type relation for an estimation of n since the refractive indices of polymer, subphase and air were known. An estimate of the layer thickness, d was made by solving the Drude equation. Sauer et al[108] used this type of data analysis in a study of polystyrene-poly(ethylene oxide) diblock copolymer at the air/water interface. Two approaches to the data analysis were attempted, the Lorentz-Lorenz macroscopic approach of weighted averaging of n to obtain d, and various microscopic theories[109,110] predicting a linear dependence of the phase retardation on the fractional coverage of the surface. In the model used the contribution of the PEO segments was neglected and the surface was modelled as being partially covered with PS blobs, becoming squashed together with increasing surface concentration.

1.2.4 Surface Quasi-Elastic Light Scattering

The non-perturbative nature of light scattering allows the surface tension and viscosity to be accessible for simple liquids, and for monolayers on liquids. Parameters such as film elasticity and viscosity can also be measured since they affect the light spectrum.

An early review of surface quasi-elastic light scattering[111] acknowledged previous predictions[112] that in addition to bulk scattering from colloidal solutions, there is a degree of scattering from the surface. In the same paper[111] a theory was developed for the scattering of light from soap films for a light beam polarised normal to the plane of incidence. Limited experimental results were presented and were interpreted as the interfacial properties being dependent on a balance of electrostatic and Van der Waals stabilising forces in the films. It was not possible to progress the experiments further due to limitations in the optical technology available at that time.

Advances in laser optics[113] greatly improved the surface light scattering technique and the spectral modification of light scattered by a liquid surface was demonstrated. At about the same time experimental work led to resolution of the spectral data in both the frequency and time domains[114,115], and the existence of two different modes of capillary evolution, propagating and overdamped, were shown.

Hård et al[116] used a diffraction grating as a local oscillator to generate a heterodyne beat signal thereby enabling the simultaneous detection of scattered and reference intensities at the same wavenumber value. This was a major advance for the detection of the small frequency shifts caused by surface fluctuations. Earnshaw et al[117-118] applied the technique to time domain surface correlation methods and the experimental operation of the technique was improved by Hård and Neuman[119] who positioned the diffraction grating before the liquid surface thereby allowing focusing of the diffraction spots on the

surface. These ideas have since been used and have yielded excellent results[120], with important results reported by Earnshaw et al[121] for ultra fast data acquisition.

Surface Quasi-Elastic Light Scattering has been applied to a variety of interfacial systems. Examples of liquids studied include water[118,122,123], ethanol[122], glycerine[118] and mercury[124]. Studies of monolayers on liquid subphases include fatty acids[118,123,125-127], monoglycerides[120,128], and polymers[129-134].

The studies of polymeric monolayers have included poly(vinyl acetate)[129,131,133,134], poly(ethylene oxide)[131-133], and poly(methyl methacrylate)[133,138]. To some extent graft[135,136] and block copolymer[130,137] monolayers have been investigated using SQELS. Cao et al[135] studied graft copolymers composed of a poly(ethyl acrylate) (PEA) main chain and pendant polystyrene (PS) grafts. The PEA in the graft copolymers provided sufficient hydrophilicity to form stable monolayers. The results showed that at low surface concentration the surface pressure of the copolymers was influenced mainly by the PEA backbone. It was shown for higher surface concentrations that the surface pressure deviated from that of the PEA homopolymer and depended on the number of PS grafts, which was due to the overlap of the grafted PS chains. Preliminary studies of graft copolymers composed of a PMMA backbone and pendant PEO blocks have also been made[136]. Sauer et al[130] have investigated spread films of a PEO-PS diblock copolymer at both the air/water and heptane/water interfaces. The studies allowed the dynamic viscoelastic parameters, i.e. surface tension, dilational modulus, transverse viscosity, and dilational viscosity to be deduced. At the heptane/water interface the surface pressure and transverse viscosity were obtained. The transverse viscosity was found to be zero over the whole surface concentration range studied and possible chain conformations of the copolymer were speculated. In the context of the work presented in

this thesis SQELS measurements were made on the PMMA-b-PEO copolymers as a function of surface concentration and capillary wave frequency[137].

1.3 Neutron Reflectivity

Neutrons can be used to investigate the density profile of a layered material in a direction normal to the plane of the incident surface from the reflected intensity when the neutrons are incident at angles greater than the critical angle for total reflection. The reflected beam consists of specularly reflected neutrons and scattered neutrons from the interface and subphase respectively, the scattered neutrons contributing a flat background intensity to the total signal and subtraction of this from the reflected beam intensity gives the reflectivity. This reflectivity varies with the scattering vector Q depending on the scattering length density profile normal to the surface which in turn depends upon the atomic constitution of the material at the interface.

The processes which occur on reflection from a flat surface are:

a) specular reflection - angle of incidence equals angle of reflection

b) transmission into the bulk

c) scattering from the bulk - which occurs due to a number of scattering processes, i.e. incoherent scattering from protons, or coherent scattering from polymer structure in the substrate

d) non-specularly scattered radiation - which occurs due to a surface which is not perfectly smooth.

Due to the small angle of incidence used in the technique, the path length traversed by the beam transmitted through the interface is large and all the transmitted beam is scattered several times. This background scattering is a limiting factor on the resolution of the technique and is characteristic of neutron reflection.

At the boundary between two media the neutron refractive index may be defined by

$$n = k_1/k_0 \qquad (1.3.1)$$

$\mathbb{k}_1$ and $\mathbb{k}_0$ being the neutron wave vectors inside and outside the medium. For a uniform medium this refractive index may be expressed as

$$n = 1-(\lambda^2/2\pi)Nb + i\lambda N\sigma_a/4\pi \qquad (1.3.2)$$

where λ = neutron wavelength

N = atomic number density

b = atomic coherent scattering length

σ_a = adsorption cross-section

Since $N\sigma_a \approx 0$ then equation 1.3.2 may be simplified to

$$n = 1-(\lambda^2/2\pi)Nb \qquad (1.3.3)$$

The factor Nb is the scattering length density, ρ, of the medium and this terminology will be used from here on. The refractive index of any medium is usually less than unity, (1-n) being about 10^{-6} and this means that the total external reflection is observed at very low critical glancing angles.

1.3.1 Specular reflection

Using Snell's law, the critical glancing angle for total reflection, θ_c, is related to n by

$$\cos\theta_c = n \qquad (1.3.4)$$

i.e. $$\theta_c = \lambda(Nb/\pi)^{1/2} \qquad (1.3.5)$$

It is possible to calculate ρ for a molecular unit from the sum of its coherent scattering lengths of its constituent nuclei

$$\rho = \Sigma b_i d\, N_{av}/M_m \qquad (1.3.6)$$

where d is the density, N_{av} is Avogadro's number and M_m is the molecular weight of the species

Table 1.3.1 shows the coherent scattering lengths of some common nuclei. These values were used to calculate values of ρ for molecular species used in the neutron

Nuclei	Coherent Scattering Length, $b/10^{-4}$Å
^{1}H	-0.374
^{2}H	0.667
^{12}C	0.665
^{14}N	0.937
^{16}O	0.580

Table 1.3.1 Coherent Scattering Lengths of common nuclei

Molecular Unit	$\Sigma b_i / 10^{-4}$Å	$\rho / 10^{-6}$Å^{-2}
H_2O	-1.68	-0.56
D_2O	1.92	6.35
air	-	0
methyl methacrylate	1.49	0.90
methyl methacrylate - d_8	9.82	6.02
ethylene oxide	0.41	0.57
ethylene oxide - d_4	4.58	6.32

Table 1.3.2 Scattering Length Densities for relevant materials

reflectivity experiments discussed later which are tabulated in Table 1.3.2. The values for H_2O and D_2O have opposite sign, the negative value of H_2O being due to a change of phase on scattering. It is possible to obtain water with a scattering length density equal to zero by mixing specific quantities of H_2O and D_2O. This is known as null reflecting water (nrw) and since it is contrast matched to air then it is invisible to neutrons. Deuterated polymer spread on this subphase then appears to incident neutrons as a layer on an invisible subphase. The reflectivity produced is due only to the spread polymer after correct background subtraction and is a direct measure of the quantity of material at the surface. In contrast, the presence of hydrogenous polymer on D_2O subphase means that the reflectivity will be dominated by this subphase, but depressed from that of pure D_2O due to the hydrogenous material at the surface.

By spreading hydrogenous or deuterated polymers on nrw or D_2O then a number of contrast conditions may be obtained. The presence of a sufficient number of these contrast conditions allows calculation of both the layer thickness of each interfacial component and subsequently an indication of the spatial organisation of components at the surface.

1.3.2 The Optical Matrix Method

An exact expression for specular reflectivity from a smooth liquid surface may be described by the Fresnel reflectivity which is the square of the amplitude of the reflected beam

$$R_F = \left| \frac{Q - (Q^2 - Q_c^2)^{1/2}}{Q + (Q^2 - Q_c^2)^{1/2}} \right|^2 \qquad (1.3.7)$$

where Q is the scattering vector normal to the interface between the medium 1 and 2 (figure 1.3.1) and

$$Q_c = 4\pi^{1/2}(\rho_2 - \rho_1)^{1/2} \qquad (1.3.8)$$

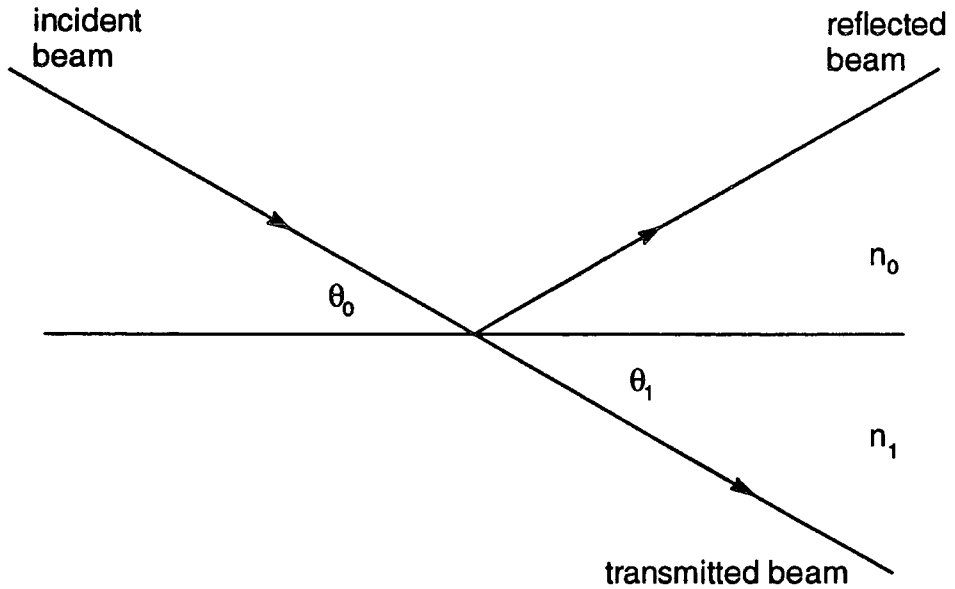

Figure 1.3.1 Reflection at a planar interface between two bulk media of refractive index n_0 and n_1

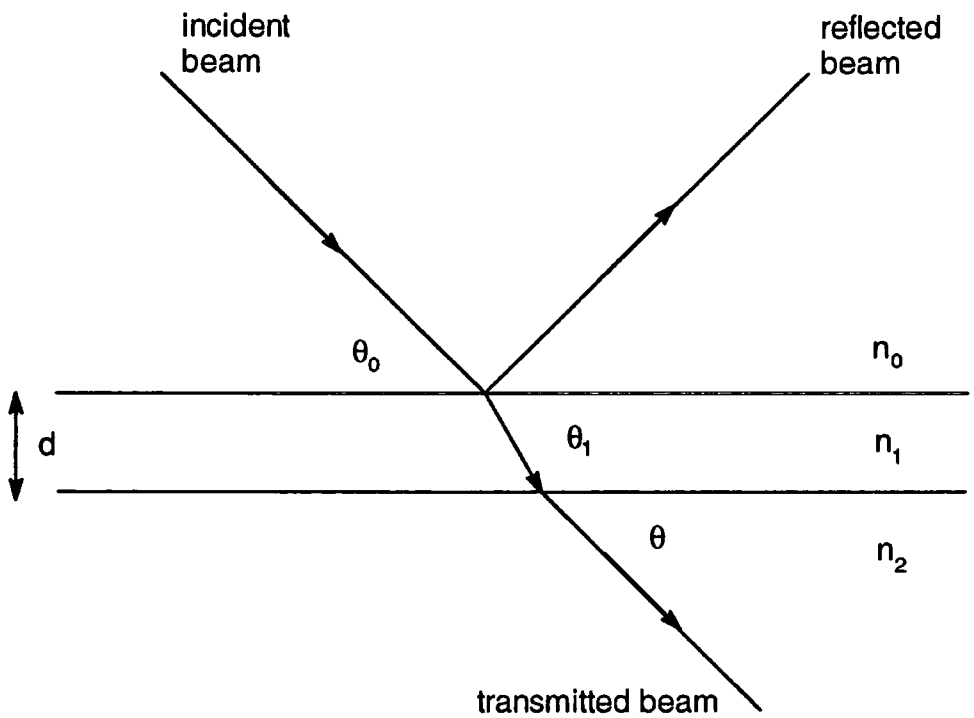

Figure 1.3.2 A thin film having thickness d and refractive index n_1 between two media of refractive index n_0 and n_2.

which is the critical value below which total reflection takes place. When $Q >> Q_c$ then from equations 1.3.7 and 1.3.8 the following expression is obtained

$$R_F = 16\pi^2(\rho_2-\rho_1)^2/Q^4 \qquad (1.3.9)$$

For the case where medium 2 has a layer of finite thickness on a thick substrate (figure 1.3.2) of scattering length density, ρ_3, then when $Q >> Q_c$

$$R_F = 16\pi^2[(\rho_2 - \rho_1)^2 + (\rho_2 - \rho_3)^2 + 2(\rho_1-\rho_2)(\rho_2-\rho_1)\cos Qd]/Q^4 \qquad (1.3.10)$$

which shows that the reflectivity at a large scattering vector is proportional to the sum of the squares of the differences between the jumps in the scattering length density of the polymer. For the case where the variation of the refractive index normal to the interface is continuous then the layer structure may be approximated by dividing it into a number of layers parallel to the surface having the same change in scattering length density from layer to layer and a possible change in layer thickness. The individual layers may be described by a characteristic optical matrix $[M_k]$ where

$$\left[M_k\right] = \begin{bmatrix} \cos\beta_k & -(1/k_k)\sin\beta_k \\ -ik\sin\beta_k & \cos\beta_k \end{bmatrix} \qquad (1.3.11)$$

where $k_k = (2\pi/\lambda)\sin\theta_k$

$\beta_k = (2\pi/\lambda)nkd_k\sin\theta_k$

and d_k is the thickness of the kth layer. The reflected amplitude is given by the product of the individual matrices for each layer at the interface. This amplitude is

$$A_R = \frac{(M_{11} + M_{12}k_k)k_1 - (M_{21} + M_{22})k_n}{(M_{11} + M_{12}k_n)k_1 + (M_{21} + M_{22})k_n} \qquad (1.3.12)$$

where the elements of the reflectivity amplitude matrix are denoted by M_{ij} and $R_F = |A_R|^2$. Obtaining the reflectivity as a product of matrices makes the data amenable to analysis by computer software.

For the case where an interface is not smooth, the surface roughness usually decreases the specular reflectivity and the description of reflection may be modified by application of a Debye-Waller factor to a Gaussian distribution of the interface[138]

$$I(\lambda) = I_0(\lambda)\exp(-Q^2\sigma^2) \qquad (1.3.13)$$

where σ is the root mean square roughness, which is the standard deviation of the interface relative to the average position of the interface assuming a Gaussian distribution about the average position. When incorporated into the matrix calculation the reflectivity is modified to

$$R = R_F \exp(-4k^2 \sin\theta_0 \sin\theta_1 \langle\sigma\rangle^2) \qquad (1.3.14)$$

where $\langle\sigma\rangle^2$ is the mean-square roughness.

1.3.3 Kinematic Approximation

While it is possible to analyse the reflectivity profiles by assuming a structural model for the interface and calculating the reflectivity exactly by applying the optical matrix method, this method can become complicated if the structure is complex. A number of approximate methods have been considered by Lekner[139] for the calculation of reflectivity. These methods have been used to describe the reflection of light, but so far have not been applied to neutron reflection and will not be discussed further. The most useful method is based on developments in approximate kinematic scattering theory by Crowley[140]. Application of the kinematic approximation to the analysis of the specular reflectivity is a simpler method of calculating reflectivity. The kinematic approximation for weak elastic scattering assuming a macroscopically smooth surface has a specular reflectivity expressed as

$$R(Q) = \frac{16\pi^2}{Q^2}|\rho(Q)|^2 \qquad (1.3.15)$$

where $\rho(Q)$ is the one dimensional Fourier transform of $\rho(z)$, the distribution in scattering length density normal to the interface

$$\rho(Q) = \int_{-\infty}^{\infty} \exp(iQz)\,\rho(z)dz \qquad (1.3.16)$$

where $\rho(z)$ is the mean scattering length density at level z in the interface. An equivalent expression to equation 1.3.15 describes R(Q) in terms of the Fourier transform of the derivative of the scattering length density profile, $\rho'(z) = d\rho/dz$ where

$$R(Q) = \frac{16\pi^2}{Q^4}\left|\rho'(Q)\right|^2 \qquad (1.3.17)$$

and

$$\rho'(Q) = \int_{-\infty}^{\infty} \exp(iQz)(d\rho / dz)dz \qquad (1.3.18)$$

When Q = 0 equation 1.3.18 reduces to

$$\rho'(0) = \Delta\rho \qquad (1.3.19)$$

where $\Delta\rho$ is the scattering length density between the two bulk media. The reflectivity can then be written as

$$R(Q) = R_s(Q)h'(Q) \qquad (1.3.20)$$

where

$$R_s(Q) = \Delta\rho^2(16\pi^2/Q^4) \qquad (1.3.21)$$

Equation 1.3.21 is the same as 1.3.9 and is the kinematic expression for the reflectivity of the sharp interface with a step in scattering length density $\Delta\rho$ and

$$h'(Q) = \left|\frac{\rho'(Q)}{\rho'(0)}\right| \qquad (1.3.22)$$

is a normalised form factor modulating $R_s(Q)$ in accordance with the shape of the width of the interfacial region. For the case where $Q\tau << 1$, where τ is the mean width of the interface, $h'(Q) \approx 1$ and the surface has a sharp appearance. Total reflection occurs when Q is about 10^{-2}Å^{-1} and therefore the reflectivities from sharp or gradual interfaces are indistinguishable in this region unless the variation of $\rho'(z)$ has a length scale greater than 10Å. At higher Q values h'(Q) rapidly decreases and R(Q) becomes depressed below the

sharp interface value, R(Q) being further depressed for broader interfacial profiles. It is possible to Fourier transform $|\rho(Q)|^2$ or $|\rho'(Q)|^2$ giving the Patterson function for the scattering length density correlation, P(z), or its derivative respectively. P(z) is the average of the product of the scattering length densities at two points separated by a distance u normal to the surface

$$P(z) = \int_{-\infty}^{\infty} \rho(z)\rho(z-u)du \qquad (1.3.23)$$

which is obtained by Fourier transforming $|\rho(Q)|^2$. It is possible that P(z) may allow an unambiguous determination of $\rho(z)$ under certain conditions. Obtaining h'(Q) by this Fourier transformation method usually gives limited information concerning the interface. This limitation is due to h'(Q) depending on the whole scattering length profile and it does not allow the different interfacial components to be distinguished. These problems can be overcome by obtaining and separating the individual number density profiles from each other.

1.3.3.1 Partial structure factors

For multicomponent systems, determining a unique profile for the scattering length density does not necessarily allow the distribution of each interfacial component at the interface to be identified. For an a-b diblock copolymer at the air/liquid interface there are three distributions requiring resolution. These three distributions are those pertaining to block a, block b and the subphase. By substituting equation 1.3.6 into 1.3.15 then

$$R(Q) = \frac{16\pi^2}{Q^2}\sum b_i b_j h_{ij}(Q) \qquad (1.3.24)$$

$$h_{ii}(Q) = |n_i(Q)|^2 \qquad (1.3.25)$$

$$h_{ij}(Q) = \mathrm{Re}\{n_i(Q)n_j(Q)\} \qquad (1.3.26)$$

where $n_i(Q)$ are the Fourier transforms of the distributions of number density of each interfacial component and $h_{ij}(Q)$ are the partial structure factors.

By isotopically labelling an interfacial component then $n_i(z)$ may be determined for it. In order to obtain the surface organisation for a diblock copolymer at the air/liquid interface then three pieces of information must be known:

(i) the extension of each block normal to the interface

(ii) the mean centre to centre separation of the distributions of the two blocks

(iii) the mean centre to centre separation between each block and the liquid subphase distribution

The scattering length density profile across the interface may be written in terms of the number densities of these three groups, combining equations 1.3.6 and 1.3.24 gives

$$\rho(z) = b_a n_a(z) + b_b n_b(z) + b_s n_s(z) \qquad (1.3.27)$$

where the subscripts a,b and s refer to the two blocks and liquid subphase respectively.

$$R(Q) = \frac{16\pi^2}{Q^2}\left[b_a^2 h_{aa}(Q) + b_b^2 h_{bb}(Q) + b_s^2 h_{ss}(Q) + 2b_a b_b h_{ab}(Q) + 2b_a b_s h_{as}(Q) + 2b_b b_s h_{bs}(Q)\right] \qquad (1.3.28)$$

By substituting the derivative of 1.3.27 into 1.3.17 then an equivalent expression is obtained in terms of $h_{ij}'(Q)$

$$R(Q) = \frac{16\pi^2}{Q^4}\left[b_a^2 h_{aa}'(Q) + b_b^2 h_{bb}'(Q) + b_s^2 h_{ss}'(Q) + 2b_a b_b h_{ab}'(Q) + 2b_a b_s h_{as}'(Q) + 2b_b b_s h_{bs}'(Q)\right] \qquad (1.3.29)$$

Isotopic substitution allows each of the six partial structure factors in equation (1.3.29) to be obtained by using reflectivity data from six different contrast conditions, i.e. different values of b_a, b_b and b_s. This is achieved by deuterium labelling of one or both blocks of a diblock copolymer and contrasting against suitably labelled subphases. Examples of such subphases are D_2O and that consisting of a mixture of H_2O and D_2O in such proportions that the total scattering length density is zero, which is commonly referred to as null reflecting water (nrw).

Self Partial Structure Factors

The partial structure factor analysis allows the individual components of the reflectivity to be identified. An example of the application of equation (1.3.29) is where a diblock copolymer having one block deuterated is spread on nrw. By approximating ρ_b to zero for the hydrogenous block then the only contribution to the reflectivity is from ρ_a of the deuterated block and all other terms disappear. By multiplying the reflectivity profile by $Q^4/16\pi^2 b_a^2$ then h_{aa}' is obtained. The simplest methods for the analysis of the polymer at the surface are to assume either uniform composition or Gaussian distribution profiles for the layer.

For a uniform layer

$$n_a(z) = n_{a1} \qquad -d/2 < z < d/2 \qquad (1.3.30)$$

where d is the layer thickness and n_{a1} its number density,

$n_a(Q)$ and $h_{aa}(Q)$ are given by

$$n_a(Q) = \frac{2n_{a1}}{Q}\sin(Qd/2) \qquad (1.3.31)$$

$$Q^2 h_{aa}(Q) = 4n_{a1}^2 \sin^2(Qd/2) \qquad (1.3.32)$$

from which the surface excess is

$$\Gamma_a = n_{a1}d \text{ / molecules Å}^{-2} \qquad (1.3.33)$$

For a half Gaussian distribution

$$n_a(z) = n_{a1}\exp(-4z^2/\sigma^2) \qquad z > 0 \qquad (1.3.34)$$

$n_a(Q)$ and $h_{aa}(Q)$ are given by

$$n_a(Q) = n_{a1}(\pi^{1/2}\sigma/2)\exp(-Q\sigma/16) \qquad (1.3.35)$$

$$h_{aa}(Q) = (n_{a1}^2)(\pi\sigma^2/4)\exp(-Q^2\sigma^2/8) \qquad (1.3.36)$$

where $\sigma/2$ is the full width of the half Gaussian when it has decayed to a value of n_{a1}/e. The surface excess is

$$\Gamma_a = \sigma n_{a1} \pi^{1/2}/2 \text{ / molecules Å}^{-2} \quad (1.3.37)$$

The liquid subphase forms a layer at the surface different from the bulk which may be described by either a uniform distribution or a hyperbolic tangent profile (tanh).

For a uniform distribution

$$h_{ss}(Q) = (1/Q^2)\left[n_{s0}^2 + 4n_{s1}(n_{s1} - n_{s0})\sin^2(Qd_s/2)\right] \quad (1.3.38)$$

for molecules in the uniform surface layer of thickness d_s, where n_{s0} is the bulk number density of the subphase and n_{s1} the number density of subphase.

For a tanh profile

$$n_s = n_{s0}\left(0.5 + 0.5\tanh\left(\frac{z}{\zeta}\right)\right) \quad (1.3.39)$$

where ζ is the width parameter of the profile

$$Q^2 h_{ss} = n_{s0}^2\left(\frac{\zeta\pi Q}{2}\right)^2 \operatorname{cosech}^2\left(\frac{\zeta\pi Q}{2}\right) \quad (1.3.40)$$

Cross partial structure factors

Although the self partial structure factors, h_{ii}, are informative about the distribution of each interfacial component at the interface, they give no information concerning the organisation of the components relative to each other. This spatial organisation is obtained from the cross partial structure factors, h_{ij}. For a distribution which is a distance δ from its origin then its Fourier transform becomes altered by a phase factor

where $n'(z) = n(z-\delta)$ (1.3.41)

and $n'(Q) = n(Q)\exp(iQ\delta)$ (1.3.42)

For two shifted distributions the cross term is

$$h_{ij}(Q) = \text{Re}\{n_i'(Q)n_j'(Q)\exp[iQ(\delta_1-\delta_2)]\} \quad (1.3.43)$$

or $$h_{ij} = \pm (h_{ii}h_{jj})^{1/2}\exp(iQ\delta) \quad (1.3.44)$$

where δ is the mean centre to centre separation of the two distributions. This equation shows that the distributions may be either odd or even about their centres and a degree of ambiguity becomes evident. The distributions of the blocks become zero when the values of z are either highly positive or negative and can be approximated as even functions. The liquid subphase term is regarded as being negative. For an a-b diblock copolymer, assuming that $n_s(z)$ is odd about its centre and that $n_a(z)$ and $n_b(z)$ are even, then from equation (1.3.44)

$$h_{as} = \pm (h_{aa}h_{ss})^{1/2}\sin Q\delta_{as} \qquad (1.3.45)$$

and

$$h_{ab} = \pm (h_{aa}h_{bb})^{1/2}\cos Q\delta_{ab} \qquad (1.3.46)$$

It is therefore possible to obtain the mean centre to centre separation, δ, of the distributions from experimental data.

1.4 Ellipsometry[141,142]

Ellipsometry is a non-perturbative method useful in the study of surfaces and thin films. The non-perturbative nature of the technique is due to the use of polarised visible light as the incident radiation. The ellipsometric technique works on the principle that when linearly or elliptically polarised light is reflected from a surface the components of its electric vector E undergo a phase change related to the refractive index and layer thickness. The reflected beam becomes polarised and can be used to determine the thickness and composition of the film.

The reflectivity of light for a one layer model is shown as a schematic in figure 1.4.1. The amplitude reflection coefficients (R_p and R_s) describe the polarisation characteristics of the incident and reflected beams and are related to the two ellipsometric angles, the phase difference (Δ), and the amplitude attenuation (ψ) between the orthogonal p and s waves. These ellipsometric angles Δ and ψ may be combined with the overall reflectivity coefficients of the surface by a basic equation of ellipsometry

$$\frac{R_p}{R_s} = \tan\psi \exp(i\Delta) \qquad (1.4.1)$$

where R_p and R_s are the complex reflection coefficients. R_p and R_s are functions of the complex refractive indices n_i of all the media, the layer thickness d_1, the wavelength λ and the angle of incidence ϕ as indicated in figure 1.4.1. By denoting air as layer 0, the film as layer 1, and the aqueous phase as layer 2 then

$$R = \left[r_{01} + r_{12}\exp(-i\beta)\right] / \left[1 + r_{01}r_{12}\exp(-i\beta)\right] \qquad (1.4.2)$$

where

$$\beta = 4\pi n_1 d_1 \cos\phi_1/\lambda_0 \qquad (1.4.3)$$

n_1 being the average refractive index of the film and ϕ_1 is the incident angle in the film, and λ_0 is the laser wavelength. The quantity β is the phase shift of the multiply reflected

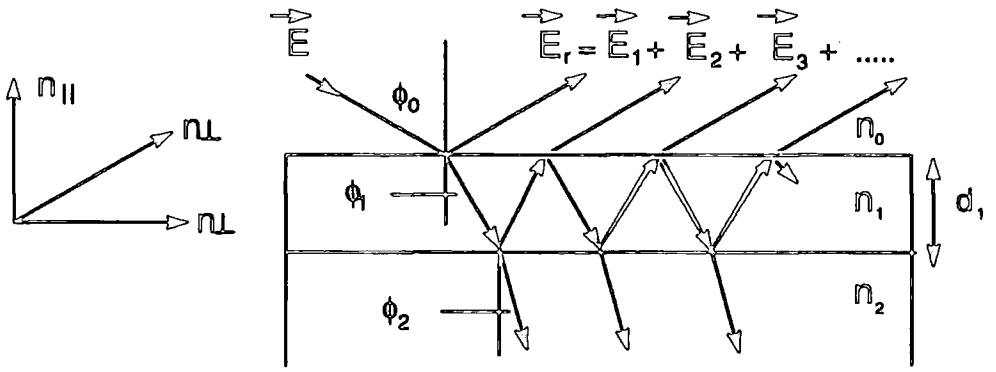

Figure 1.4.1 Reflection of light on a one layer model. The left hand side shows the co-ordinate system used for the description of uniaxial films

wave inside the film as it traverses from one interface to the other with respect to the directly reflected wave. Equation 1.4.2 is valid for either p or s polarisation where

$$r_{p01} = [n_1 \cos\phi_0 - n_0 \cos\phi_1] / [n_1 \cos\phi_0 + n_0 \cos\phi_1] \qquad (1.4.4)$$

$$r_{s01} = [n_0 \cos\phi_0 - n_1 \cos\phi_1] / [n_0 \cos\phi_0 + n_1 \cos\phi_1] \qquad (1.4.5)$$

where r_{p01} and r_{s01} are the Fresnel coefficients for reflection between layer 0 and layer 1. It is possible to obtain similar expressions of r_{p12} and r_{s12} for layers 1 and 2, thereby allowing the calculation of Δ by equation 1.4.1. The incident angles for layers 1 and 2 are calculated using Snell's law knowing the incident angle in air and the refractive indices n_0 = 1.002 for air and n_2 = 1.332 for water, and an estimated value of n_1 which is an average refractive index depending on the polymer.

Experimentally the values of Δ and ψ are determined for the clean water surface and then at various polymer surface concentrations, Δ' and ψ'. The change in phase angle $\delta\Delta$ between these two states is defined as

$$\delta\Delta = \Delta - \Delta' \qquad (1.4.6)$$

The values of $\delta\Delta$ are directly proportional to the film thickness d_1.

If the substrate is nonabsorbing then the amplitude attenuation difference

$$\delta\psi = \psi - \psi' \qquad (1.4.7)$$

is essentially zero according to both the approximate and full Drude equations. The result of this is that information concerning the interface may only be obtained from the value of $\delta\Delta$.

1.5 Surface Quasi-Elastic Light Scattering[128]

In a macroscopic sense, the surface of a liquid is flat. On a microscopic scale, the surface at an air-liquid interface is randomly roughened by molecular motion and thermal agitation. This roughening results in surface ripples consisting of capillary (transverse) and longitudinal (dilational) fluctuations in the monolayer (figure 1.5.1). Capillary waves have been studied extensively in past years[143-148] and the properties characterizing them (their wavelength and damping coefficient) are determined by stress conditions at the surface of the liquid. Coverage of this surface with a monolayer provides the surface with elastic properties and it will resist the periodic surface expansion and compression accompanying the wave motion. The result of this is a change in liquid flow below the surface which causes higher energy dissipation by viscous friction and a corresponding higher damping coefficient than that of a bare liquid surface.

Both types of waves may scatter light but the intensity scattered by longitudinal waves is much lower than that of transverse waves[128]. However, due to a degree of coupling between the transverse and longitudinal waves, the dilational parameters may be obtained under certain circumstanses. The theoretical background of SQELS is discussed here and the means by which several visco-elastic parameters may be extracted from the data are set out.

1.5.1 Capillary Waves

The random thermally induced roughening of a fluid surface causes a displacement (ξ) from its equilibrium plane. This surface can then be Fourier decomposed into a series of surface modes having a wavenumber q. The plane is defined as the x-y plane (Figure 1.5.2) and the amplitude from the equilibrium plane of a capillary wave propagating in the x direction is described by

$$\xi(x,t) = \xi_o \exp(i(qx + \omega t)) \qquad (1.5.1)$$

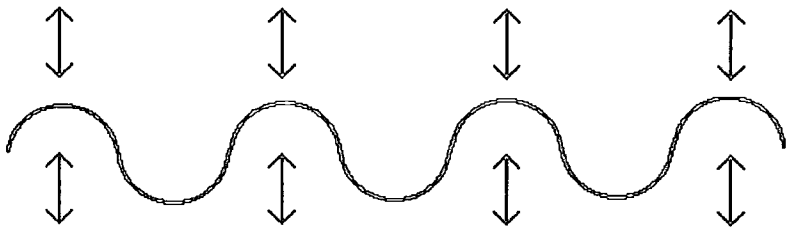

Figure 1.5.1a) Fluctuations of capillary waves at the surface of a liquid

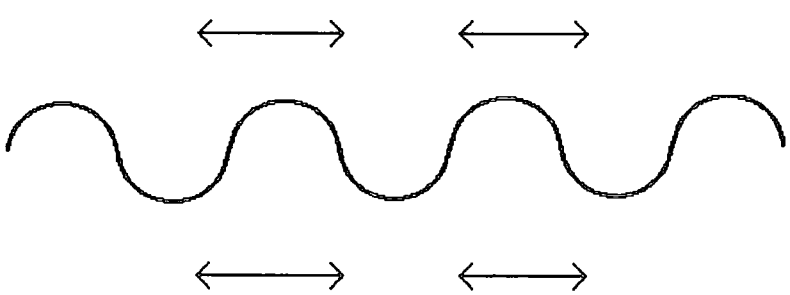

Figure 1.5.1b) Fluctuations of longitudinal waves at the surface of a liquid

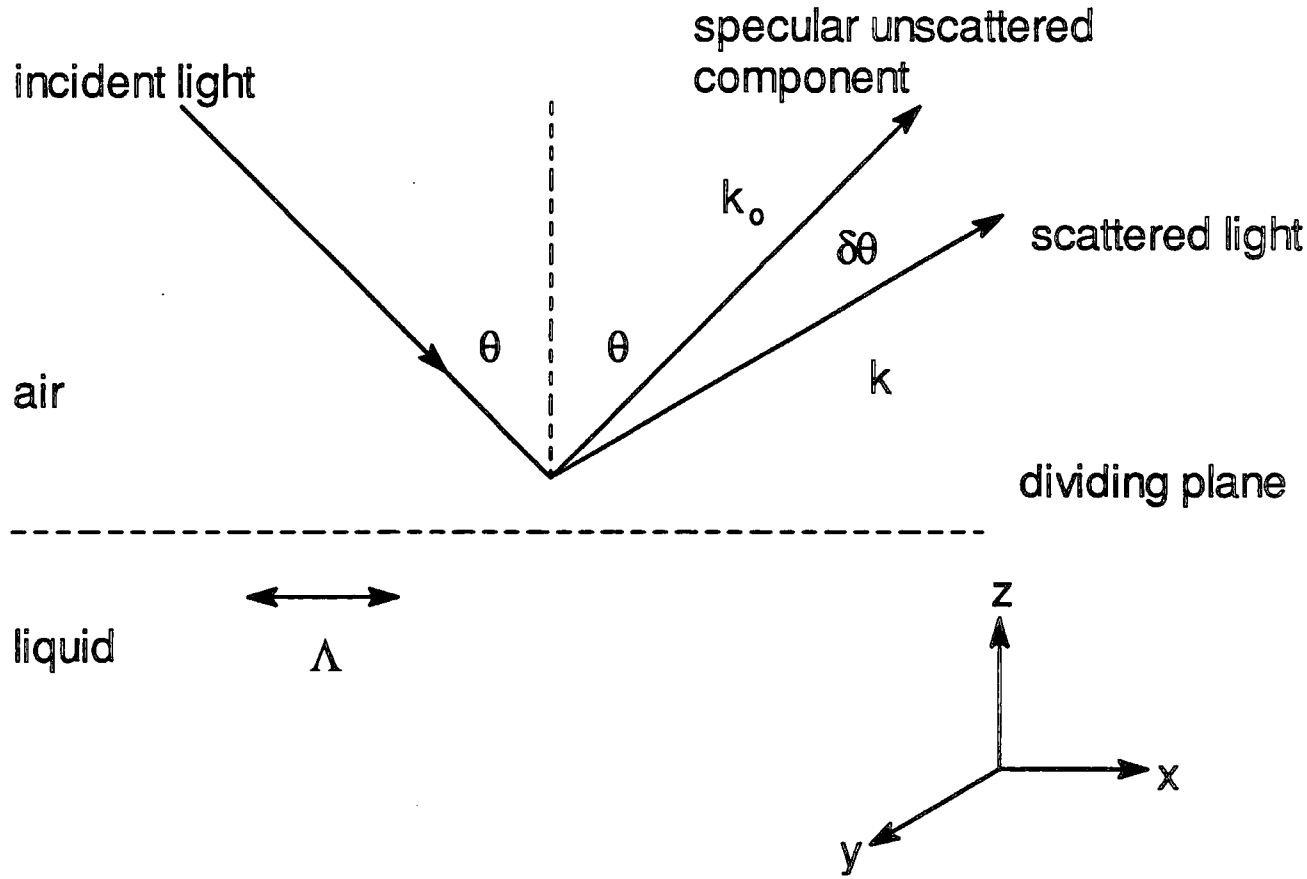

Figure 1.5.2 Light Scattered by Thermally Induced Surface Ripples

where $q = 2\pi/\Lambda$ = interfacial wavenumber

and Λ = wavelength of capillary wave

the wave frequency, ω, being a complex quantity describing the time evolution of the surface caused by fluctuations having frequency ω_0 (the capillary propagation frequency), Γ being the decay constant determining the damping of the waves, where

$$\omega = \omega_0 + i\Gamma \qquad (1.5.2)$$

The surface therefore acts as a weak phase grating which scatters incident light at an angle $\delta\theta$ from the specular reflection, θ, from the liquid surface. When considering small angles of scatter then

$$q = 2k_o \sin(\delta\theta/2).\cos\theta \qquad (1.5.3)$$

where $2k_o \sin(\delta\theta/2) = K$, the scattering vector.

Since the capillary waves have a spectrum of wavelengths and frequencies then the interfacial wavenumber, q, is used to probe capillary waves of wavelength λ ($q=2\pi/\lambda$). The complex frequency of the waves is related to q through a dispersion relationship which involves the viscoelastic properties of the surface. The Lamb-Levich equation[149,150] is the common form of the dispersion expression $D(\omega)$ for the free surface of a liquid

$$D(\omega) = (\omega + 2\nu q^2)^2 + gq + \gamma q^3/\rho - 4\nu^2 q^3(1 + \omega/\nu q^2)^{1/2} \qquad (1.5.4)$$

where γ is the surface tension, ν the kinematic viscosity, g the gravitational acceleration and ρ the density of the liquid. It is possible to ignore the gravitational term if the waves studied are of sufficiently short wavelength ($\lambda < 330\ \mu m$).

Equation (1.5.4) may be reduced to

$$D(S) = (S+1)^2 + Y - (2S + 1)^{1/2} = 0 \qquad (1.5.5)$$

where

$$S = \omega/(2\nu q)^2 \quad \text{and} \quad Y = \gamma/4\nu^2\rho q^2 = \gamma\rho/(4\eta^2 q). \qquad (1.5.6)$$

and η is the dynamic viscosity.

Reduced group variable Y represents a balance between driving forces and dissipative forces in wave propagation.

A numerical solution of reduced variable S when $Y > 0.145$, where the capillary waves are underdamped, shows that it has complex conjugate roots. A first order approximation to the solution of the dispersion equation (1.5.4) gives an expression for the wave frequency in the propagation mode,

$$\omega_0^2 = \gamma q^3/\rho \qquad (1.5.7)$$

and a proportional dependence of the wave damping to the liquid viscosity,

$$\Gamma = 2\nu q^2 \qquad (1.5.8)$$

i.e. $$\omega = \omega_0 + i\Gamma = (\gamma q^3/\rho)^{1/2} + i2\nu q^2 \qquad (1.5.9)$$

Viscoelastic properties at the surface due to the presence of a surface film affect capillary wave propagation[151,152]. As well as ω and q, the dispersion equation depends on density, viscosity, surface tension, γ, and the dilational modulus, ε, of the liquid surface. The dilational modulus occurs due to compression (longitudinal modes) of the surface film, which scatter light weakly. These longitudinal modes are coupled with transverse modes (capillary waves), the amplitude of which is governed mainly by γ. Because energy can be dissipated in the surface film as it relaxes to its equilibrium position after a pertubation, then γ and ε are viscoelastic quantities

$$\gamma = \gamma_o + i\omega_0\gamma' \qquad (1.5.10)$$

$$\varepsilon = \varepsilon_0 + i\omega_0\varepsilon' \qquad (1.5.11)$$

where γ_o and ε_o are the elastic moduli which describe the response of the system to transverse shear and dilation within the plane of the interface. The effect of the complex term in (1.5.10) is to increase the dissipative influence in the balance of propagation and damping. Substituting (1.5.10) into (1.5.9) gives

$$\omega = [(\gamma_o + i\omega_0\gamma')q^3/\rho]^{1/2} + 2i\nu q^2$$

$$\approx(\gamma_o q^3/\rho)^{1/2} + i[2\nu q^2 + \gamma' q^3/2\rho] \qquad (1.5.12)$$

It can be seen that the value of γ' will have a greater effect as q increases. This equation predicts that the transition from propagating to overdamped modes will occur at a slightly lower value of q from that predicted in the absence of surface specific viscoelastic effects.

The capillary waves are affected by the dilational modulus because longitudinal fluctuations in the film couple to them and recent work has given a deeper insight into the consequence of this. Resonance between the two surface modes is a well known effect[153] which occurs when the real frequencies of the two modes are the same. The frequencies coincide for $\varepsilon_0/\gamma_0 \approx 0.16$ over the q range studied. The overall damping, Γ, is due to contributions from the capillary wave damping, Γ_C, and dilational wave damping, Γ_D. At the resonance frequency, Γ_C increases to about twice the value for that of a clean surface, thereafter dropping off to a plateau. The surface viscosities also have an effect on the damping. The transverse shear viscosity, γ', has the effect of increasing Γ_C while the dilational surface viscosity, ε', has the effect of increasing Γ_D, causing Γ_C to fall which reduces the magnitude of the resonance.

1.5.2 The Power Spectrum

The light scattered by thermally excited capillary waves can be expressed by a power spectrum[154]

$$P(\omega) = K_B T/(\pi\omega).(\rho/4\eta^2 q^3)\mathrm{Im}\{1/D(S)\} \qquad (1.5.13)$$

The spectrum is approximately Lorentzian, having a peak frequency f_s and linewidth Δf_s which may be identified with ω_0 and Γ obtained from the dispersion equation. The surface properties present at the interface affect $P(\omega)$ in a number of ways. This fact allows a single experimental observation of the spectrum to be analysed in terms of the four properties which affect $P(\omega)$.

1.5.3 Monolayer spread surfaces - modification of the dispersion equation and power spectrum

A monolayer present at the suface of a liquid modifies the dispersion equation $D(\omega)$ due to introduction of explicit terms due to the properties of the monolayers. This form is[155,156]

$$D(\omega) = [\varepsilon q^2 + i\omega\eta(q + m)] \times [\gamma q^2 + i\omega\eta(q + m) - \omega^2\rho/q] - [i\omega\eta(q-m)]^2 = 0 \quad (1.5.14)$$

where $m = (q^2 + i\rho\omega/\eta)^{1/2}$ and $Re(m) > 0$.

where ε is the dilational modulus of the monolayer

$$\varepsilon = d\gamma / d \ln(A) \quad (1.5.15)$$

and A is the molecular area of the film.

The modified form of the power spectrum[155] is

$$P(\omega) = -k_B T/\pi\omega \, Im[i\omega\eta(q + m) + \varepsilon q^2) / D(\omega)] \quad (1.5.16)$$

This spectrum is again approximately Lorentzian in form, deviations from $P(\omega)$ being well known[157,158]. The surface properties mentioned all have an effect on $P(\omega)$ to some degree or fashion allowing a single experimental observation of the spectrum to be analysed in terms of these properties. For the following experiments it is the field autocorrelation function of scattered light $g(\tau)$ that is measured, i.e. the Fourier transform of $P(\omega)$, taking into account instrumental broadening by including it in the expression for $g(\tau)$.

1.5.4 Viscoelastic Relaxation

Although microscopic theories of rheological behaviour at an interface do not exist, it is possible to apply classical rheological theory [159] in a phenomenological way. An elastic deformation is a function of stress which is expressed in terms of strain[160] (i.e. relative displacement). This strain can be expressed in terms of a relative change in a measurement such as volume or length. Elastic bodies which act ideally have reversible

deformation to the original dimensions. Polymers in both their bulk and solution states have viscous and elastic properties which must be accounted for.

1.5.4.1 Mechanical Models

Simple rheological models are used as an aid to explain the complex rheology of viscoelastic materials[159,161]. It is assumed that the viscous response to an applied stress is due to a Newtonian fluid which is represented as a dashpot. This dashpot is simply a piston which operates in a cylinder containing a Newtonian fluid. The elastic response is assumed to be an ideal elastic solid which is represented by a spring. The dashpot is representative of a system which dissipates energy as heat, while the spring is a system which stores energy. Figure 1.5.3 shows stress-strain diagrams for the dashpot and spring systems. In the dashpot system stress is relieved due to viscous flow and is independent of strain, the resultant plot therefore having a constant value of stress. The spring system has a direct dependence of the stress on strain, the ratio of the two being the modulus E.

The simplest mechanical models[160] are shown in figure 1.5.4. In the Voigt-Kelvin model the spring and dashpot are in parallel. This model is characteristic of a solid material since the deformation produced by a force depends only on the spring. The Maxwell model is of a dashpot and spring in series. A material exhibiting this behaviour is liquidlike due to the application of stress yielding a permanent deformation. The Burgers model combines both these models in series, being a good model of a linear viscoelastic material.

1.5.4.2 Dynamic Behaviour

Using classical notation[160,161] then rheological behaviour can be analysed using complex variables representing stress and strain. The complex stress ($\tau^* = \tau_0 e^{i\omega t}$) and

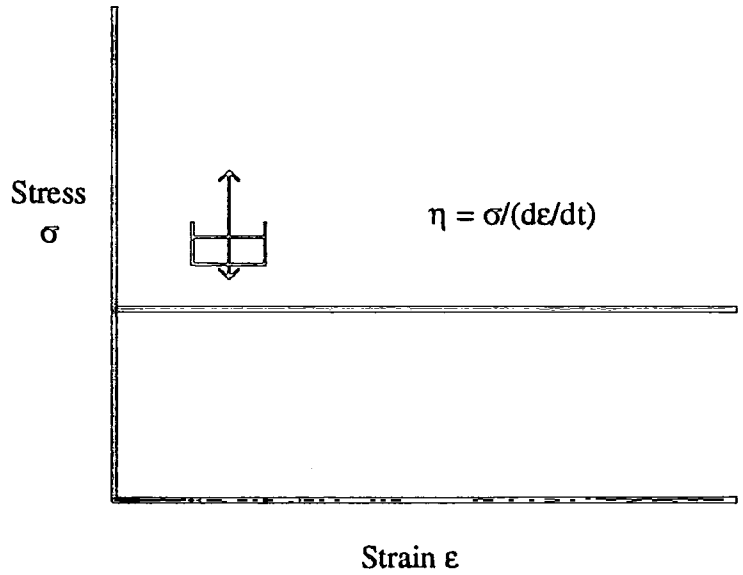

Figure 1.5.3a) Stress-strain diagram - For a dashpot of viscosity η the stress is independent of the strain

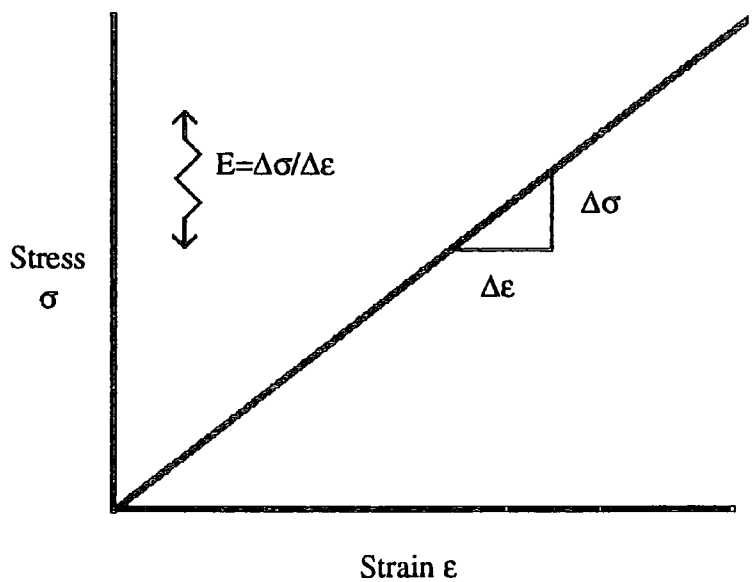

Figure 1.5.3b) Stress-strain diagram - For a spring of modulus E the slope is the modulus which is independent of the speed of testing

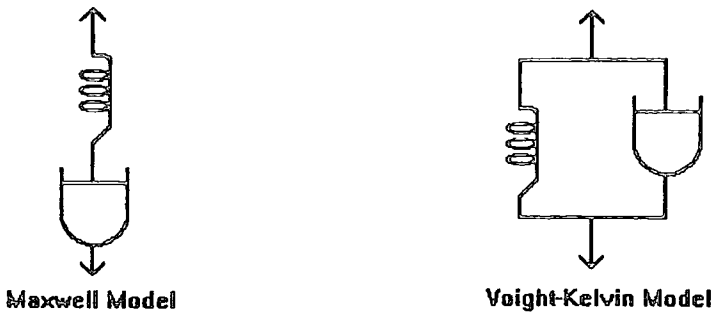

Figure 1.5.4a) Mechanical models for viscoelastic behaviour
Maxwell and Voight-Kelvin Models

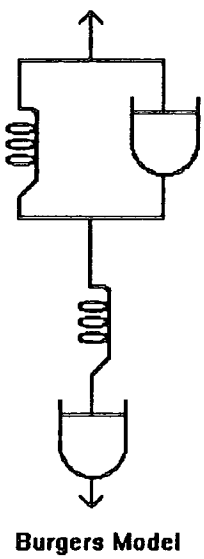

Figure 1.5.4b) Mechanical model for viscoelastic behaviour
Burgers Model

complex strain ($\gamma^* = \gamma_0 e^{i(\omega t-\delta)}$) are related by the complex dynamic modulus, $G^*(\omega)$, which is the ratio of the complex stress and strain

$$G^*(\omega) = \tau^*/\gamma^* \qquad (1.5.17)$$

this dynamic modulus can also be resolved into two components

$$G^*(\omega) = G'(\omega) + iG''(\omega) \qquad (1.5.18)$$

The storage modulus $G'(\omega)$ is a measure of elasticity and is in phase with the real components of γ^* and τ^*. The value of $G'(\omega)$ is a measure of the amount of energy stored during elastic deformation. The loss modulus $G''(\omega)$ occurs due to the out of phase components of γ^* and τ^* which are due to damping effects.

For an interfacial system then the storage modulus, $G'(\omega)$, corresponds to the surface tension, γ_0,(or dilational modulus, ε_0) while the loss modulus $G''(\omega)$ is analogous with $\omega\gamma'$ (or $\omega\varepsilon'$). Here only the two simplest models, the Voigt-Kelvin viscoelastic solid and the Maxwell fluid models are discussed. In the Voigt-Kelvin model both $G'(\omega)$ and $G''(\omega)/\omega$ are constant. For a Maxwell fluid model having a single relaxation process then

$$G'(\omega_0) = G_e + G\omega_0^2\,\tau^2/(1+\omega_0^2\tau^2) \qquad (1.5.19)$$

$$G''(\omega_0) = G\omega_0\tau/(1+\omega_0^2\tau^2) \qquad (1.5.20)$$

where G_e is the equilibrium elastic modulus at infinite relaxation time ($\omega\rightarrow 0$), which is analagous with the surface tension obtained from classical methods using surface force apparatus. G is simply the amplitude of the relaxation process. The Burgers model presents a more complex case and will not be referred to hereafter.

1.6 Micellization in Solution

Amphiphilic block copolymer solutions have been studied in past years due to their similarities with surfactant solutions. In certain solvents these block copolymers can self-assemble into micelles, capable of solubilizing hydrophobic particles. These properties find uses in industrial and biomedical situations such as drug delivery and separation processes. Micellization processes may be studied by using any physical property which depends on the particle size or on the number of particles. Examples of techniques used include static and dynamic light-scattering, membrane osmometry, UV spectroscopy, calorimetry and transmission electron microscopy, where the physical quantities are measured as a function of concentration.

1.6.1 Micellization Systems

1.6.1.1 Small Amphiphiles

Much work has been carried out on the determination of the critical micelle concentration (cmc) for a number of systems of low molecular mass surfactants. For systems consisting of nonionic and ionic surfactants in water then linear relationships have been reported between the logarithm of the measured cmc values and the number of C atoms in the hydrophobic tail of the surfactant[162]. It was noted that as the number of carbon atoms increased (up to ca. 16 C atoms) then the cmc decreased. Another observation was that ionic surfactants have higher cmc values than nonionic surfactants containing equivalent hydrophobic groups. When surfactants contain more than one hydrophilic group per molecule then they have higher cmc values than those with one hydrophilic group. In aqueous solutions the cmc values give an indication of the amount of binding of the counterion to the micelle, increases in binding of the counterion causing decreases in the cmc of the surfactant[163].

1.6.1.2 Nonionic Block Copolymers

Although there has been much work concerning the micellization of low molecular mass amphiphiles, less work has been carried out on block copolymers. When a block copolymer is dissolved in an organic solvent which is selectively poor for one of the blocks, the block copolymer may associate in solution to form micelles. These micelles consist of a swollen core of the least soluble blocks surrounded by a flexible fringe (corona) of the other blocks. Studies of block copolymer micelle systems are concerned with the nature of the core, the corona, and the solvent. Two kinds of systems may be envisaged for nonionic block copolymers. The first system is where a block copolymer is composed of two different hydrophobic segments and the second is where the block copolymer is amphiphilic.

The thermodynamics of micellization of polystyrene-block-poly(ethylene/propylene) copolymer (PS-b-PEP) in organic media has been studied in past years by Price[154], and more recently by Katime[165-168]. Price et al[164] have studied dispersions of the copolymer in decane, alkanes being selective solvents for the copolymer, i.e. good solvents for PEP but precipitants for PS. The dependence of the critical micelle temperature (cmt), on concentration was investigated using light scattering for three PS-b-PEP copolymers. For particles isolated from solution, electron microscopy showed the narrow size distribution of the micelles and the micellization could be treated as a closed association process. From the light scattering results ΔG°, ΔH° and ΔS° were calculated. Values of ΔH° were found to be large and negative and were very dependent on the molecular weight of the polystyrene block. Values of ΔG° on the other hand were found to be similar to each other. The standard entropy contributions were found to be unfavourable to micelle formation. Katime et al[165] studied (PS-b-PEP) block copolymer in a number of n-alkanes, n-hexane, n-heptane, n-octane, n-decane, and n-dodecane. From the results,

values of ΔH° were found to be large and negative, the magnitude of which depended on the carbon number for the lower n-alkane chain which was dependent on the temperature, with a maximum for n-octane at 85°C. For the copolymer in decane the values of ΔG°, ΔH°, and ΔS° were similar to those of Price et al[164]. The reason for the different behaviour of the n-alkanes studied was explained by taking into account differences in the polystyrene /n-alkane interactions. Further work by Katime et al[166] centred around the effect of molar mass and chemical composition of the PS-b-PEP copolymer, i.e. the same PS block length but differing PEP lengths. The solvents chosen for the study were n-octane and 5-methylhexan-2-one, two oppositely selective solvents for PEP and PS blocks. In this system, n-octane is a good solvent for the PEP block and a precipitant of the PS block, while 5-methylhexan-2-one is a good solvent for the PS block and a precipitant of the PS block. From the cmt and concentration data, the characteristics of the copolymer and block location in the micelle structure were found to influence the thermodynamics of the micellization process. The copolymers had negative standard Gibbs energies in both solvents, the copolymer with the larger PEP block having the more negative value. This difference in magnitude was greater in 5-methylhexan-2-one solutions because the micelle core was formed by the larger PEP blocks which favoured micellization. The greater negative values of ΔH° for 5-methylhexan-2-one solutions with respect to n-octane solutions was due to the differing block length that the copolymers showed. Further work[167] investigated micellization of PS-b-PEP block copolymer in several ketones (methyl ethyl ketone, methyl propyl ketone, diethyl ketone, methyl isobutyl ketone, dipropyl ketone, 5-methyl-2-hexanone and 5-methyl-3-heptanone). These liquids are good solvents for the PS block and poor solvents for the PEP block. Light scattering determined the dependence of temperature on the cmc for different ketones. This technique also yielded the weight average molar

mass, M_w, the second virial coefficient, A_2, and the apparent radius of gyration, $R_{g,app}$, of the micelles. Micelles were not formed in solutions of 5-methyl-3-heptanone. Values of ΔG°, ΔH°, and ΔS° were negative for all the ketones studies. ΔG° and ΔH° were found to depend on the polar nature of the ketone. Katime et al[168] studied micelle formation by PS-b-PEP in n-dodecane/1,4-dioxane mixtures. Here, n-dodecane was a good solvent for the PEP block and a poor solvent for the PS block, while 1,4-dioxan was a good solvent for the PS block and a poor solvent for the PEP block. Temperature dependence of the cmc was determined at differing copolymer concentrations using light scattering intensity measurements as a function of temperature. From the light scattering results ΔG°, ΔH°, and ΔS° were found to be negative and dependent on the composition of the solvent mixture. Standard entropies were unfavourable to micelle formation, and the standard enthalpies were solely responsible for micelle formation. Micelle structures were not detected in n-dodecane/1,4-dioxane mixtures with similar percentages of both solvents. Price et al[169] studied the dependence of the cmt on concentration for four polystyrene-block-polyisoprene copolymers PS-b-PI in n-hexadecane. The results were used to estimate ΔG°, ΔH°, and $-T\Delta S$. Values of ΔG° and ΔH° were found to be strongly dependent on the molecular weight of the polystyrene block, both becoming more negative with increasing molecular weight. Increasing the molecular weight of the polyisoprene block also made ΔH° more negative but had a negligible effect on ΔG°. The same copolymer when dispersed in N,N'-dimethylacetamide[170] was found to form wormlike micelles but these were thought to be metastable thermodynamically with respect to spherical micelles. Other workers have found that the copolymer structure, solvent, and temperature greatly influence the free chain-micelle equilibrium, micelle structure, and the unimer-micelle exchange[171-174].

Studies of nonionic diblock copolymers containing hydrophobic and hydrophilic blocks are of great importance. Micellization in these systems has been studied in both polar and nonpolar solvents. The properties of these systems such as the size of the aggregates, cmc values and structure of the micelles have been studied in relation to the molecular parameters of the copolymer and solvent[175-182]. Both static and dynamic light scattering studies of amphiphilic diblock and triblock copolymers having polystyrene cores suggested the existence of micelles in two narrowly distributed populations[183,184]. A study of PS-b-PEO micelles in water showed the existence of normal spherical core-shell micelles and loose micellar clusters composed of tens of micelles.

1.6.1.3 Ionic Block Copolymers

Block ionomers such as polystyrene/neutralised poly(methacrylic or polyacrylic acid) (PMAA or PAA) block copolymers may form micelles with an ionic core[185,186]. For block copolymers composed of short segments of poly(sodium methacrylate) attached to long PS chains then very stable reversed micelles were produced in organic solvents[186]. Work has been performed on systems where hydrophobic segments form the core and the ionic segments are in the corona[187-189]. Static and dynamic light scattering along with viscometry measurements have shown that block copolymers with ionic groups in the corona have much greater size even though they have very small aggregation numbers with respect to nonionic polymers. This greater size can be reasoned by taking into account repulsion effects of the ionic charges on the polymer in the corona.

Block polyelectrolyte systems containing micelles with a hydrophobic core and an ionic corona in aqueous solutions have been the attention of much study. A system consisting of PS-b-poly(4-vinylpyridinium) copolymers in water-methanol-LiBr mixtures has been studied[186]. Here, the micelles had a starlike structure and the micellization process was

strongly dependent on the solvent composition, temperature, salt concentration and insoluble polystyrene block length.

The behaviour of block polyelectrolyte systems is far more complicated than copolymer micelles containing non-ionic water-soluble blocks. The micelle behaviour is greatly influenced by the polyelectrolyte nature of the outer shell, which in itself may be affected by the presence of small ions. The formation and properties of PS-b-PMAA micelles therefore depended on pH and ionic strength[187-189].

1.6.1.4 Theory

It is possible to carry out a thermodynamic study of micelle formation from the temperature dependence of the critical micelle concentration (cmc). If it is assumed that micelle formation is a single stage equilibrium between unassociated copolymer molecules and micelles with an association number m

$$mA_1 \Leftrightarrow A_m \qquad (1.6.1)$$

It is assumed that m is independent of temperature and that the copolymer is ideally dilute apart from intramicelle interactions between the copolymer molecules. When micelles possess narrow size distribution, the standard Gibbs free energy of micellization per mole of copolymer chains is given by

$$\Delta G^o \approx RT\ln(cmc) - RTm^{-1}\ln([A_m]) \qquad (1.6.2)$$

When a copolymer system has a very high association number and low micelle concentration, the second term of equation 1.6.2 is very small, therefore

$$\Delta G^o \approx RT\ln(cmc) \qquad (1.6.3)$$

Assuming that the association number is independent of temperature it follows from equations 1.6.2 and 1.6.3 that

$$\Delta H^o \approx R\frac{d\ln(cmc)}{dT} \qquad (1.6.4)$$

From this equation an estimation of the contribution of the enthalpy term to the standard Gibbs energy of micellization may be gained. Using both of these values, the standard entropy of micellization, may be calculated

$$\Delta S^o = \frac{\Delta H^o - \Delta G^o}{T} \qquad (1.6.5)$$

Using calorimetric measurements to determine the standard enthalpy of micellization, ΔH^o, gives similar values as static light scattering. It is assumed from the results of the two methods that the block copolymers undergo closed association in dilute solutions to form micelles and that the association number is independent of the temperature. Block copolymer micelles have similar properties to surfactant micelles formed in aqueous solution. There are however very different thermodynamics responsible for the association in both cases. In the case of conventional surfactant molecules in aqueous solution, the main thermodynamic factor responsible for micelle formation is a positive standard entropy while the standard enthalpy of micellization, ΔH^o, can be positive or negative and is small. In contrast, block copolymers in organic solvents undergo micelle formation due only to ΔH^o. This value of ΔH^o is negative and due to the exothermic interchange energy accompanying the replacement of (polymer segment)-solvent interactions by (polymer segment)-(polymer segment) and solvent-solvent interactions on micelle formation. The block copolymer micelles are held together by net van der Waals interactions. The combined effect per copolymer chain is an attractive interaction similar in magnitude to that of a covalent chemical bond.

1.6.2 Experimental techniques for investigating the micellization of block copolymers in organic media

Osmometry may be used to determine the cmc of a block copolymer at different temperatures. Plots of π/cRT against c usually have a sigmoidal shaped curve which is

due to the effect of concentration on the micelle/unassociated-chain equilibrium. Due to the lack of definition of the transition of micelles to unassociated molecules, it is difficult to locate the cmc by this method. A better technique for obtaining thermodynamic functions is to determine the cmc at different concentrations. Since the intensity of scattered light is very dependent on the volume of the scatterer, then light scattering is an excellent technique for detecting the onset of micelle formation in micelle forming polymeric solutions. It is possible to initiate micelle formation by changing the temperature and obtaining the cmt. This can be studied experimentally by defining the cmt through the temperature dependence of either the integrated scattered light intensity or the hydrodynamic size of the particles, as long as the transition is reasonably sharp.

1.6.2.1 Outline of a light scattering experiment

Light is a type of electromagnetic radiation which propagates through a vacuum at a speed c_0 ($3x10^8 ms^{-1}$). and when it passes though a medium which is polarisable it is scattered. Light interacts with electrons bound in a material it is re-radiated as scattered light. When the light experiences no energy loss the scattering is termed 'elastic'. Light may interact with a system by changing the energy state of an electron being adsorbed rather than scattered. This adsorbed light may reappear as heat or light of a different wavelength. In order to measure scattered light then it needs to be separated from the incident source light. A laser is used to produce a well collimated intense monochromatic coherent light source. The laser beam has a Gaussian profile and the intensity decreases with the function $\exp(-x^2)$ where x is the distance from the centre.

1.6.3 Light Scattering

The excess scattered intensity versus temperature is usually measured for several different concentrations of copolymer solution at several scattering angles. Below a certain temperature value there is a large increase in the scattered intensity. The

transition occurs over a small temperature range and is characteristic of the specific solution concentration. This point is referred to as the critical micelle temperature (cmt) and is evident on all scattered intensity versus temperature curves. Above the cmt there is characteristically small but constant scattered intensities. It is possible by extrapolating the scattering data to infinite dilution to obtain the weight average molecular weight for single copolymer chains. Above the cmt, unassociated copolymer chains are present, while a decrease in temperature below the cmt causes micelle formation. This micelle formation causes the light scattering to increase substantially and a transition region is usually seen. By finding the intersection of the two straight line portions the cmt values may be estimated. By taking the concentration of each curve, this can be considered as the critical micelle concentration at the corresponding cmt. By noting the shift in cmt with increasing concentration, and the shift in cmc with decreasing temperature, conclusions about the micellization may be drawn.

1.6.3.1 Elastic light-scattering

For a micellar solution the Debye equation is applicable in the dilute solution regime

$$K(C\text{-}cmc)/R_{vv,\theta} = 1/M_w + 2A_2(C\text{-}cmc) \qquad (1.6.6)$$

where K ($= 4\pi^2 n_0^2 (dn/dC)^2 / N_A \lambda_0^4$) is an optical constant with N_A, n_0, and λ_0 being Avogadro's number, the refractive index of the solvent, and the wavelength of light in vacuo. $R_{vv,\theta}$ is the excess Rayleigh ratio at a scattering angle θ with vertically polarised incident and scattered beams, C is the total concentration (g/mL), and A_2 is the second virial coefficient. For solutions above the cmt, the forward and back scattering are the same, while below the cmt an angular dependence is usually observed. This latter case may be used to extrapolate R_{vv} values to zero scattering angle using equation 1.6.6. Additional information may also be obtained on the radius of gyration ($\langle R_g^2 \rangle_{z,app}$, apparent z-averaged squared radius of gyration for the block copolymer) from the

limiting slope of the $[K(C\text{-}cmc)/R_w]_{c=0}$ versus q^2 plot with q $(=4\pi/\lambda)\sin(\theta/2))$ being the scattering vector. The refractive index increment of the copolymer solution can be calculated using the relation

$$dn/dC = \omega_A(dn/dC)_A + \omega_B(dn/dC)_B \qquad (1.6.7)$$

where ω is the weight fraction and the subscripts A and B denote the component blocks. For block copolymers which are usually heterogeneous in chemical composition equation 1.6.6 yields an apparent molecular weight ($M_{w,app}$) rather than a true weight average molecular weight (M_w). A correction can be made by using the relation

$$M_{w,app}(dn/dC)^2 = M_w(dn/dC)_A(dn/dC)_B + [(dn/dC)_A^2 - (dn/dC)_A(dn/dC)_B]\omega_A M_w^A + [(dn/dC)^2_B - (dn/dC)_A(dn/dC)_B]\omega_B M_w^B \qquad (1.6.8)$$

where M_w^A and M_w^B are the weight average molecular weights of the components.

By looking at Debye plots over concentration ranges studied it is possible to prove that unimers and micelles exist at two extreme temperature regions. This is done by assuming that at high temperatures where only unimers exist then in equation 1.6.6 the total concentration may be used. At low temperatures the cmc term may be neglected due to its very small value. Much higher M_w and n_w values at higher temperatures than lower temperatures are proof of micelle formation.

1.6.3.2 Quasi-elastic light scattering

In the work discussed in Chapter 7 it was not possible to measure the refractive index increment of the copolymer solutions and therefore molecular weights could not be determined. However it is possible to use a method which would infer the dynamic properties of the copolymer solution.

Particles undergoing Brownian motion in solution produce spectral distributions in the scattered light. By measuring the line width of the scattered laser light using Photon correlation spectroscopy (PCS) then the translational diffusion coefficient may be

determined. PCS is simply a method of dynamic light scattering (DLS) using a correlator. The traditional method of investigating translational diffusion required a macroscopic concentration gradient, whereas PCS does not and the method is more amenable to investigations of association processes.

By assuming that the micelles are hydrodynamically equivalent spheres then in the Stokes-Einstein equation,

$$D_0 = kT/(6\pi\eta R_h) \qquad (1.6.9)$$

where D_0 is the diffusion coefficient at infinite dilution, R_h is the hydrodynamic radius and η the viscosity of the solvent. The reciprocal intercept of the plot is a measure of the particle size of interest, R_h. By plotting R_h (apparent) versus temperature then a curve may be obtained having three temperature regions being unimer, transition, and micelle regions, which appear in sequence with decreasing temperature. In the high temperature region above the cmt, relatively small, constant size and almost monodisperse particles are detected, which is expected assuming that only single copolymer chains are present above the cmt. The transition region below the cmt has two distinct features, an abrupt increase of the average particle size and a marked increase in the variance which both indicate that mixtures of unimer and micelle in equilibrium are present in this region. Further decrease in temperature leads to the micelle region where large particles with small variance are found.

1.7 Review of past work on the synthesis of amphiphilic block copolymers

In past years there have been four approaches to the preparation of amphiphilic block copolymers. These are coupling of individually synthesized blocks, living anionic or cationic polymerisations, macroradical initiations, and post polymerisation modification methods. The coupling technique has been used by Kennedy and Hongu[190,191] to synthesize polyisobutylene/PEO diblock and triblock copolymers. The same technique has been used by Galin and Mathis[192] in the preparation of poly(dimethylsiloxane)/PEO triblock copolymers. Anionic polymerisations have been used by Riess et al[193,194] and Khan et al[195] to synthesize polystyrene-b-PEO copolymers, and by Tomoi et al[196] to prepare poly(alkyl methacrylate)-b-PEO block copolymers. Macroradical initiation has been used by several workers for the preparation of polystyrene-b-PEO[197,198] and PMMA-b-PEO[191-201] block copolymers. An example of post-polymerisation modification is the preparation of amphiphilic poly(vinyl alcohol-acetate) which is obtained by partial alcoholysis of poly(vinyl acetate) with methanol.

Suzuki et al[202] synthesized block copolymers by the anionic polymerisation of MMA initiated with the sodium salt of PEO in the presence of a crown ether or a cryptate. However, a transesterification reaction occurred between PEO and the methoxy group in MMA during polymerisation which resulted in a PEO grafted block copolymer. This problem was overcome in later work[203] where the anionic polymerisation of MMA and tert-butyl methacrylate (BMA) was carried out using lithiated poly(ethylene glycol) diisobutyrate as initiator and THF as the solvent giving unimodal and relatively narrow molecular weight distributions.

Rathke et al[204,205] found that the α positions of acetic acid esters were easily, almost quantitatively lithiated by the use of lithium bis(tetramethylsilyl) amide or lithium dialkylamide. A further advance was reported by Lochmann et al[206] who initiated

polymerisation of MMA with the anion obtained by α-lithiation of methyl isobutyrate using lithium diisopropylamide. This initiation system polymerised MMA in high yield without side reactions.

Garg et al[207] synthesized di- and triblock copolymers of PEO with PMMA. The blockcopolymer PEO-b-PMMA was synthesized by polymerisation of MMA initiated with living PEO anions. The initiation of the MMA polymerisation occurred due to the enhancement in nucleophilicity of primary alkanoate anions of the metalated PEO chain. If the alkali metal salts initiate the polymerisation of MMA, then, there should not be any difference in the reactivity of these metalated chains of PEO and living chains of PEO. Transesterification was shown not to occur due to the absence of methanol by gas chromatographic analysis. The initiation of the polymerisation of MMA with living PEO anions resulted in a homogeneous ungrafted blockcopolymer. It was concluded that the PEO chains effectively capture the counterions to enhance the nucleophilicity of alkanoate anions of PEO which leads to the addition to the carbon-carbon bond in MMA.

The above work involving addition of MMA to living PEO is contrary to the scale of monomer reactivity proposed by Fetters[208]. In his work, Fetters divided up anionically polymerisable monomers into groups according to their reactivity. It was shown that PEO anions possess a lower reactivity with respect to MMA. The results of the above papers demonstrate that the polymerisation of MMA with living PEO anions as initiator do not fit in with the monomer reactivity proposed by Fetters.

Wang et al[209] compared both the sequential and reverse sequential addition of monomers for preparing copolymers anionically. The block copolymers prepared were well defined AB(BA) block copolymers of tert-butyl methacrylate (t-BMA) (A) and EO (B) by living anionic polymerisation of the two comonomers. Poly(t-BMA-b-EO) (AB)

was prepared by addition of the desired amount of initiator to THF, cooling to -78°C, and adding the required quantity of tBMA. The polymerisation lasted 2 hours after which an aliquot was withdrawn for analysis by GPC in order to obtain the molecular weight of the first block. Ethylene oxide was cooled down to -78°C and added. The temperature was slowly increased from -78°C to 35°C (ca. 0.5h). Copolymerisation was allowed to occur for 20 hours at that temperature. Poly(EO-b-tBMA) (BA) was prepared by the sequential addition of monomers. EO was added to the initiator solution in THF at -78°C. The temperature was raised to 35°C and EO polymerised for 24 hours. An aliquot was withdrawn from the reaction medium in order to determine the molecular weight of the PEO block. The reaction was cooled down to 20°C and the desired amount of tBMA added. Copolymerisation was continued for 5-15 minutes. On polymerisation of tBMA with a counterion (K) suitable for the EO polymerisation, it was of great importance to know if the anionic polymerisation of tBMA was living and if the related macroanion was stable enough to initiate quantitatively the EO polymerisation at a relatively high temperatue (ca. 0°C). Monofunctional polyanions of the tBMA type were used as macroinitiators for the EO polymerisation demonstrating an overall conversion being almost quantitative (95% as an average). Composition and molecular weight of the recovered block copolymers fitted very closely with the expected values. The molecular weight distribution was not much broader than the precursor. It was concluded that essentially pure diblock copolymers resulted from the anionic polymerisation of EO initiated with monofunctional polyanions of t-BMA in THF in the presence of a potassium counterion. The use of diphenyl methyl potassium as initiator had the advantage of producing narrow molecular weight distributions due to the experimental conditions (-78°C in THF) and the highly delocalized and sterically hindered state of the monofunctional diphenyl methyl potassium. This was in contrast to the results obtained

by Hardy Reuter et al[210] who reported tailing on the low molecular weight side when the t-BMA polymerisation was initiated with cumylpotassium in THF at 25°C, which was attributed to the occurrence of some side reactions under experimental conditions.

From the literature it would appear that there are optimum conditions which would give high conversion to products in the synthesis of MMA/EO diblock copolymers. Homogeneous initiation can be achieved by electron transfer in ether solvents such as THF using soluble electron transfer complexes formed by reaction of alkali metals with polycyclic aromatic compounds. An ideal initiator is diphenyl methyl potassium, formed by the addition of diphenylmethane to a THF solution of potassium naphthalide. The initiator is highly delocalized and sterically hindered and has the result of producing narrow molecular weight distributions compared to that of other initiators. These narrow molecular weight distributions are due to the elimination of transesterification reactions which had previously resulted in premature termination of propagating chains and formation of grafted copolymers.

References

1. Crisp, D.J., *J. Colloid Sci.*, 1946, 1, 49.

2. Crisp, D.J., *J. Colloid Sci.*, 1946, 1, 161.

3. Frisch, H.L., Simha, R., *J. Chem. Phys.*, 1957, 27, 702.

4. Singer, S.J., *J. Chem. Phys.*, 1948, 16, 872.

5. Huggins, M.L., *J. Phys. Chem.*, 1942, 46, 151.

6. Davies, J.T., *J. Colloid Sci., Suppl.*, 1954, No.1, 9.

7. Motomura, K., Matuura, R., *J. Colloid Sci.*, 1963, 18, 52.

8. de Gennes, P.G., *Scaling Concepts in Polymer Physics*, Cornell Univ. Press, Ithaca, New York, 1979.

9. Daoud, M, Jannink, G., *J. Phys. (Paris)*, 1976, 37, 973.

10. Le Guillou, J.C., Zinn-Justin, J., *Phys. Rev. Lett.*, 1980, 21, 3976.

11. Stephen, M.J., McCauley, J., *Phys. Lett. A*, 1973, 44, 89.

12. Stephen, M.J., *Phys. Lett. A*, 1975, 53, 363.

13. Grassberger, P.Z., *Phys. B: Condens. Matter*, 48, 255, 1982.

14. Derrida, B., *J. Phys. A: Math. Gen.*, 14, L-5, 1981.

15. Baumgartner, A., *J. Phys. (Les Ulis Fr.)*, 43, 1407, 1982.

16. Birshtein, T.M., Buldyrev, S.V., Elyashevitch, A.M., *Polymer*, 26, 1814, 1985.

17. Derrida, B., Saleur, H., *J. Phys. A: Math. Gen.*, 18, L-1075, 1985.

18. Marqusee, J.A., Deutch, J.M., *J. Chem. Phys.*, 75, 5179, 1981.

19. Llopis, J., Subirana, J.A., *J. Colloid Sci.*, 1961, 16, 618.

20. Jaffé, J., Berliner, C., Lambert, M., *J. Chem. Phys.*, 1967, 64, 499.

21. Kawaguchi, M., Yoshida, A., Takahashi, A., *Macromolecules*, 1983, 16, 956.

22. Langmuir, I., *J. Amer. Chem. Soc.*, 1917, 39, 1848.

23. Langmuir-Blodgett Films 3, Vols I and II, Mobius, D., Ed., Elsevier, New York.

24. Adam, N.K., *Trans. Faraday Soc.*, 1933, 29, 90.

25. Harkins, W.D., Carman, E.F., Ries, H.E. Jr., *J. Chem Phys*, 1935, 3, 692.

26. Shuler, R.L., Zisman, W.A., *J. Phys. Chem.*, 1970, 74, 1523.

27. Miller, I.R., *J. Colloid Sci., Suppl., No.1*, 1954, 9, 579.

28. Benson, G.C., McIntosh, R.L., *J. Colloid Sci.*, 1948, 3, 323.

29. Hotta, H., *J. Colloid Sci.*, 1954, 9, 504.

30. Llopis, J., Rebello, D.V., *J. Colloid Sci.*, 1956, 11, 543.

31. Schick, M.J., *J. Polymer Sci.*, 1957, 25, 465.

32. Ries, H.E., Jr., Ahlbeck, R.A., Gabor, J., *J. Colloid Sci.*, 1959, 14, 354.

33. Shuler, R.L., Zisman, W.A., *J. Phys. Chem.*, 1970, 74, 1523.

34. Cockbain, E.G., Day, K.J., McMullen, A.J., *Proc. Intern. Congr. Surface Activity,* 2nd, *London, 1957, 1, 56.*

35. Beredjick, N., Monomolecular Film Studies of Polymers, in Newer Methods of Polymer Synthesis and Characterisation, Ke, B., Ed., Interscience, New York, 1964.

36. Beredjick, N., Ries, H.E., Jr., *J. Polymer Sci.*, 1962, **62**, S64.

37. Beredjick, N., Ahlbeck, R.A., Kwei, T.K., Ries, H.E., Jr., *J. Polymer Sci.*, 1960, **46**, 268.

38. Ober, R., Vilanove, R., *Colloid & Polym. Sci.*, 1977, 255, 1067.

39. Vilanove, R., Rondelez, F., *Phys. Rev. Letts.*, 1980, **45**, 1502.

40. Takahashi, A., Yoshida, A., Kawaguchi, M., *Macromolecules*, 1982, 15, 1196.

41. Vilanove, R., Poupinet, D., Rondelez, F., *Macromolecules*, 1988, 21, 2880.

42. Poupinet, D., Vilanove, R., Rondelez, F., *Macromolecules*, 1989, 22, 2491.

43. Davies, J.T., *J. Colloid Sci.*, 1956, 11, 377.

44. Gaines, G.L., Insoluble Monolayers at Liquid-Gas Interfaces, Interscience, New York, 1966.

45. Mingins, J., Taylor, J.A., Owens, N.F., Brooks, J.H., *Adv. Chem. Ser.*, 1975, **144**, 28.

46. Davies, J.T., Llopis, J., *Proc. R. Soc. London Ser. A*, 1955, **227**, 537.

47. Allan, A.J.G., Alexander, A.E., *Trans. Faraday Soc.*, 1954, **50**, 863.

48. Bringuier, E., Vilanove, R., Gallot, Y., Selb, J., Rondelez, F., *J. Colloid Int. Sci.*, 1985, **104**, 95.

49. Fermi, E., Zinn, W., *Phys. Rev.*, 1946, **70**, 103.

50. Handel, P.H., *Z. Physik*, 1972, **252**, 7.

51. Hayter, J.P., Penfold, J., Williams, W.G., *Nature*, 1976, **262**, 569.

52. Buchaenko, M.R., Grundy, M.J., Richardson, R.M., Roser, S.J., *Thin Solid Films*, 1988, **159**, 253.

53. Felcher, G.P., Kampwirth, R.T., Gray, K.E., Felici, R., *Phys. Rev. Lett.*, 1984, **52**, 1537.

54. Felici, R., Penfold, J., Ward, R.C., Olsi, E., Matacotta, C., *Nature*, 1987, **329**, 523.

55. Stamm, M., Majkrzak, C.F., *Am. Chem. Soc. Polymer Prepr*, 1987.

56. Russell, T.P.,Karim, A., Mansour, A., Felcher, G.P., *Macromolecules*, 1988, **21**, 1890.

57. Fernandez, M.L., Higgins, J.S., Penfold, J., Ward, R.C., Shackleton, C., Walsh, D.J., *Polymer*, 1988, **29**, 1923.

58. Fernandez, M.L., Higgins, J.S., Penfold, J., Shackleton, C., Walsh, D.J., *Polymer*, 1990, **31**, 2146.

59. Fernandez, M.L., Higgins, J.S., 3rd Int. Conference on Diffusion of Polymers, York, UK, 13-15th Feb. 1991.

60. Composto, R.J., Stein, R.S., Kramer, E.J., Jones, R.A.L., Mansour, A., Karim, A., Felcher, G.P., *Physica B*, 1989, **156 & 157**, 434.

61. Jones, R.A.L., Norton, L.J., Kramer, E.J., Composto, R.J., Stein, R.S., Russell, T.P., Mansour, A., Karim, A., Felcher, G.P., Rafailovich, M.H., Sokolov, J., Zhao, X., Schwarz, S.A., *Europhys. Lett.*, 1990, 12, 41.

62. Lee, E.M., Thomas, R.K., Penfold, J., Ward, R.C., *J.Phys. Chem.*, 1989, 93, 381.

63. Penfold, J., Lee, E.M., Thomas, R.K., *Mol. Phys.*,1989, 68, 33.

64. Richardson, R.M., Roser, S.J., *Langmuir*, 1991, 7, 1458.

65. Grundy, M.J., Richardson, R.M., Roser, S.J., Penfold, J., Ward, R.C., *Thin Solid Films, 1988, 159, 43.*

66. Lu, J.R., Simister, E.A., Lee, E.M., Thomas, R.K., *Langmuir*, 1992, 8, 1837.

67. Simister, E.A., Lee, E.M., Thomas, R.K., Penfold., *Macromolecular Reports, A29(Suppl. 2), 1992, 155.*

68. Simister, E.A., Lee, E.M., Thomas, R.K., Penfold, J., *J. Phys. Chem.*, 1992, 96, 1373.

69. Lyttle, D.J., Lu, J.R., Su, T.J., Thomas, R.K., Penfold, J., *Langmuir*, 1995, 11, 1001.

70. Simister, E.A., Lee, E.M., Lu, J.R., Thomas, R.K., Ottewill, R.H., Rennie, A.R., *Penfold, J., J. Chem. Soc., Faraday Trans., 1992, 88 (20), 3033.*

71. Lee, A.M., Thomas, R.K., Rennie, A.R., *Europhys. Lett.*, 1990, 13, 135.

72. Rennie, A.R., Crawford, R.J., Lee, E.M., Thomas, R.K., Crowley, T.L., Roberts, S., Qureshi, M.S., Richards, R.W., *Macromolecules*, 1989, 22, 3466.

73. Guiselin, O., Lee, L.T., Farnoux, B., Lapp, A., *J. Chem. Phys.*, 1991, 95, 4632.

74. Lee, L.T., Guiselin, O., Farnoux, B., Lapp, A., *Macromolecules*, 1991, 24, 2518.

75. Cosgrove, T., Heath, T.G., Phipps, J.S., Richardson, R.M., *Macromolecules*, 1991, 24, 94.

76. Satija, S.K., Majkrzak, C.F., Russell, T.P., Sinha, S.K.,Sirota, E.B., Hughes, G.J., *Macromolecules, 1990, 23, 3860.*

77. Cosgrove, T., Phipps, J.S., Richardson, R.M., *Colloids and Surfaces*, 1992, 62, 199.

78. Henderson, J.A., Richards, R.W., Penfold, J., Shackleton, C., Thomas, R.K., *Polymer, 1991, 32, 3284.*

79. Lee, L.T., Mann, E.K., Langevin, D., Farnoux, B., *Langmuir*, 1991, 7, 3076.

80. Hodge, P., Towns, C.R., Thomas, R.K., Shackleton, C., *Langmuir*, 1992, 8, 585.

81. Kent, M.S., Lee, L.T., Farnoux, B., Rondelez, F., *Macromolecules*, 1992, 25, 6240.

82. Gissing, S.K., Richards, R.W., Rochford, B.R., *Colloids and Surfaces A: Physicochemical and Engineering Aspects, 1994, 86, 171.*

83. Richards, R.W., Rochford, B.R., Webster, J.R.P., *Faraday Discuss.*, 1994, **98**, 263.

84. Azzam, R.M., Bashara, N.M., *Ellipsometry and Polarised Light*, North Holland, New York, 1987.

85. Kim, M.W., Sauer, B.B., Yu, H., Yazdanian, M., Zografi, M., *Langmuir*, 6, **1990**, 236.

86. Englesen, D.D., Koning, B.D., *J. Chem. Soc., Faraday Trans. 1*, 1974, **70**, 1603.

87. Rasing, T., Hsiung, H., Shen, Y.R., Kim, M.W., *Phys. Rev. A: Gen. Phys.*, 1988, **37**(7), 2732.

88. Kawaguchi, M., Tohyama, M., Mutoh, Y., Takahashi, A., *Langmuir*, 1988, **4**, 407.

89. Kawaguchi, M., Tohyama, M., Mutoh, Y., Takahashi, A., *Langmuir*, 1988, **4**, 411.

90. Ducharme, D., Max, J., Salesse, C., Leblanc, R.M., *J. Phys. Chem.*, 1990, **94**, 1925.

91. Möhwald, H., *Thin Solid Films*, 1988, **159**, 1.

92. Garoff, S., *Thin Solid Films*, 1987, **152**, 49.

93. Englesen, D.D., *J. Opt. Soc. Am.*, 1971, **61**(11), 1460.

94. Ayoub, G.T., Bashara, N.M., *J. Opt. Soc. Am.*, 1978, 68(7), 978.

95. Antippa, A.F., Leblanc, R.M., Ducharme, D., *J. Opt. Soc. Am.*, 1986, 3(11), 1794.

96. Johnson, J.A., Bashara, N.M., *J. Opt. Soc. Am.*, 1971, 61(4), 457.

97. Ibrahim, M.M., Bashara, N.M., *J. Opt. Soc. Am.*, 1971, 61(12), 1622.

98. Paudler, M., Ruths, J., Riegler, H., *Langmuir*, 1992, 8, 184.

99. Benjamins, J., de Feitjer, J.A., Evans, M.T.A., Graham, D.E., Phillips, M.C., *Discuss. Farad. Soc.*, 1975, 59, 218.

100. de Feitjer, Benjamins, J., Veer, F.A., *Biopolymers*, 1978, 17, 1759.

101. Rasing, T., Hsiung, H., Shen, Y.R., Kim, M.W., *Phys. Rev. A*, 1988, 37, 2732.

102. Sauer, B.B., Yu, H., Yazdanian, M., Zografi, G., Kim, M.W., *Macromolecules*, 1989, 22, 2332.

103. Gabrielli, G., Puggelli, M., Faccioli, R., *J. Colloid Interface Sci.*, 1973, 44, 177.

104. Gabrielli, G., Puggelli, M., Ferroni, E., *J. Colloid Interface Sci.*, 1974, 47, 145.

105. Gabrielli, G., Baglioni, P., *J. Colloid Interface Sci.*, 1980, 73, 582.

106. Gabrielli, G., Puggelli, M., Baglioni, P., *J. Colloid Interface Sci.*, 1982, 86, 485.

107. Kawaguchi, M., Nagata, K., *Macromolecules*, 1990, 23, 3957.

108. Sauer, B.B., Yu, H., Kim, M.W., *Langmuir*, 1989, 5, 278.

109. Rasing, T., Hsiung, H., Shen, Y.R., Kim, M.W., *Phys. Rev. A*, 1988, 37, 2732.

110. Bootsma, G.A., Meyer, F., *Surf. Sci.*, 1969, 14, 52.

111. Vrij, A., *J. Colloid Sci.*, 1964, 19, 1.

112. Von Smoluchowski, M., *Ann. Physik.*, 1913, 41, 609.

113. Katyl, R.H., Ingard, U., *Phys. Rev. Lett.*, 1967, 19, 64.

114. Bouchiat, M.-A., Meunier, J., *C.R. Acad. Sci. Paris*, 1968, 266B, 301.

115. Katyl, R.H., Ingard, U., *Phys. Rev. Lett.*, 1968, 20, 248.

116. Hård, S., Hamnerius, Y., Nilsson, O., *J. Appl. Phys.*, 1976, 47, 3433.

117. Byrne, D., Earnshaw, J.C., *J. Phys. D: Appl. Phys.*, 1977, **10**, 207.

118. Byrne, D., Earnshaw, J.C., *J. Phys. D: Appl. Phys.*, 1979, **12**, 1133.

119. Hård, S., Neuman, R.D., *J. Colloid Int. Sci.*, 1987, **115**, 73.

120. Crilly, J.F., Earnshaw, J.C., *J. Physique*, 1987, **48**, 485.

121. Earnshaw, J.C., McGivern, R.C., *J. Colloid Int. Sci.*, 1989, **131**, 278.

122. Earnshaw, J.C., McGivern, R.C., *J. Phys. D: Appl. Phys.*, 1987, **20**, 82.

123. Earnshaw, J.C., McGivern, R.C., *J. Colloid Int. Sci.*, 1988, **123**, 36.

124. Bird, M., Hills, G., *Physicochemical Hydrodynamics* vol 2, ed. D.B. Spalding, London, pp 609-25.

125. Langevin, D., *J. Colloid Interface Sci.*, 1980, **80**, 413.

126. Winch, P.J., Earnshaw, J.C., *J. Phys: Condens. Matter.*, 1989, **1**, 7187.

127. Earnshaw, J.C., Winch, P.J., *J. Phys: Condens. Matter.*, 1990, **2**, 8499.

128. Earnshaw, J.C., McGivern, R.C., Winch, P.J., *J. Phys. Fr.*, 1988, **49**, 1271.

129. Kawaguchi, M., Sano, M., Chen, Y.-L., Zografi, G., Yu, H., *Macromolecules*, 1986, **19**, 2606.

130. Sauer, B.B., Yu, H., Tien, C.-F., Hager, D.F., *Macromolecules*, 1987, **20**, 393.

131. Sauer, B.B., Kawaguchi, M., Yu, H., *Macromolecules*, 1987, **20**, 2732.

132. Sauer, B.B., Yu, H., *Macromolecules*, 1989, **22**, 786.

133. Kawaguchi, M., Sauer, B.B., Yu, H., *Macromolecules*, 1989, **22**, 1735.

134. Yoo, K.-H., Yu, H., *Macromolecules*, 1989, **22**, 4019.

135. Cao, B.H., Kim, M.W., Peiffer, D.G., *Langmuir*, 1995, **11**, 1645.

136. Peace, S.K., private communication.

137. Richards, R.W., Rochford, B.R., Taylor, M.R., unpublished results.

138. Nevot, L., Croce, P., *Phys. Appl.*, 1980, **15**, 761.

139. Lekner, J., *Theory of Reflection*, Nijhoff, Dordrecht, 1987.

140. Crowley, T.L., Lee, E.M., Simister, E.A., Thomas, R.K., *Physica B*, 1991, 173, 143.

141. Zaininger, K.H., Revesv, A.G., *Ellipsometry - A valuable tool in surface research*, in RCA *Review*, Princetown, New Jersey, 1964.

142. Sauer, B.B., Yu, H., Yazdanian, M., Zografi, G., Kim, M.W., *Macromolecules*, 1989, 22, 2232.

143. Hansen, R.S., Mann, J.A., *J. Appl. Physics*, **1964**, 35, 152.

144. van den Tempel, M, van de Riet, R.P., *J. Chem. Physics*, **1965**, 42, 2769.

145. Lucassen, J., Hansen, R.S., *J. Colloid Interface Sci.*, **1966**, 22, 32.

146. Lucassen, J., Hansen, R.S., *J. Colloid Interface Sci.*, **1967**, 23, 319.

147. Lucassen, J., *Trans. Faraday Soc.*, **1968**, 64, 2221.

148. Lucassen, J., *Trans. Faraday Soc.*, **1968**, 64, 2230.

149. Lamb, H., *Hydrodynamics*, **1945**, Dover, New York.

150. Levich, V.G., Physicochemical Hydrodynamics, Prentice Hall, Englewood Cliffs, NJ, 1962.

151. Tejero, C.F., Rodriguez, M.J., Baus, M., *Phys. Lett.*, **1983**, 98A, 371.

152. Goodrich, F.C., *Proc. R. Soc.*, **1981**, 374, 341.

153. Earnshaw, J.C., McCoo, E., *Langmuir*, **1995**, 11, 1087.

154. Bouchiat, M.A., Meunier, J., *J. Physique*, **1971**, 32, 561.

155. Langevin, D., Meunier, J., Chatenay, D., Surfactants in Solution, Edited by L. Mittal and B. Lindman, Plenum, New York, 3, 1984, pp. 1991-2014.

156. Lucassen-Reynders, E.H., Lucassen, J., *Adv. Colloid Interface Sci.*, **1969**, 2, 347.

157. Bouchiat, M.A., Langevin, D., *C.R. Hebd. Sean. Acad. Sci. B*, **1971**, 272, 1357.

158. Wu, E.S., Webb, W.W., *Phys. Rev. A*, **1973**, 8, 2077.

159. Ferry, J.D., Viscoelastic Properties of Polymers, Wiley, New York, 1980.

160. Encylopedia of Polymer Science and Technology, Wiley, New York, **1988**, 14,472.

161. Introduction to Polymer Science, R.J. Young and P.A. Lovell, Chapman and Hall, London, **1991**, 322.

162. Otterwill, R.H., In *Surfactants*, Tadros, Th. F., Ed., Academic Press, London, 1984, pp 1-18.

163. Mukerjee, P., *Adv. Colloid Interface Sci.*, 1967, **1**, 241.

164. Price, C., Stubbersfield, R.B., El-Kafrawy, S., Kendall, K.D., *Br. Polymer J.*, 1989, **21**, 391.

165. Quintana, J.R., Villacampa, M., Munoz, M., Andrio, A., Katime, I.A., *Macromolecules*, 1992, **25**, 3125.

166. Quintana, J.R., Villacampa, M., Salazar, R., Katime, I.A., *J. Chem. Soc. Faraday Trans*, 1992, **88**, 2739.

167. Quintana, J.R., Villacampa, M., Salazar, R., Katime, I.A., *Polymer*, 1993, **34**, 2380.

168. Quintana, J.R., Villacampa, M., Salazar, R., Katime, I.A., *Macromolecules*, 1993, **26**, 601.

169. Price, C., Chan, E.K.M., Stubbersfield, R.B., *Eur. Polym. J.*, 1987, **8**, 649.

170. Price, C., Booth, C., Canham, P.A., Naylor, T., Stubbersfield, R.B., *Br. Polymer J.*, 1984, **16**, 311.

171. Tuzar, Z., Konak, C., Stepanek, P., Plestil, J., Kratochvil, P., Prochazka, K., *Polymer*, 1990, **31**, 2118.

172. Prochazka, K., Bednar, B., Svoboda, P., Trnena, J., Mukhtar, E., Almgren, M., *J. Phys. Chem.*, 1991, **85**, 4563.

173. Plestil, J., Hlavata, D., Hrouz, J., Tuzar, Z., *Polymer*, 1990, **31**, 2113.

174. Prochazka, K., Medhage, B., Mukhtar, E., Almgren, M., Svoboda, P., Trnena, J., Bednar, B., *Polymer*, 1993, 34, 103.

175. Munch, M.R., Gast, A.P., *Macromolecules*, 1990, 23, 745.

176. Nakamura, K., Endo, R., Takeda, M., *J. Polym. Sci., Polym. Phys. Ed.*, 1976, 14, 135 and 1287.

177. Linse, P., Malmsten, M., *Macromolecules*, 1992, 25, 5434.

178. Nicolas, C.V., Luo, Y.-Z., Deng, N.-J.,Attwood, D., Collett, J.H., Price, C., Booth, C., *Polymer*, 1993, 34, 138.

179. Zhou, Z., Chu, B., *Macromolecules*, 1988, 21, 2548.

180. Mortenson, K., Pedersen, J.S., *Macromolecules*, 1993, 26, 805.

181. Zulaut, M., Weckstrom, K., Hayter, J.B., Degiorgio, V., Corti, M., *J. Phys. Chem.*, 1985, 89, 3411.

182. Nagarajan, R., Barry, M., Ruckenstein, E., *Langmuir*, 1986, 2, 210.

183. Xu, R., Winnik, M.A., Hallett, F.R., Riess, G., Croucher, M.D., *Macromolecules*, 1991, 24, 87.

184. Khan, T.N., Mobbs, R.H., Price, C., Quintana, J.R., Stubbersfield, R.B., *Eur. Polym. J.*, 1987, 23 (3), 191.

185. Zhong, X.F., Varshney, S.K., Eisenberg, A., *Macromolecules*, 1992, 25, 7160.

186. Desjardins, A., Eisenberg, A., *Macromolecules*, 1991, 24, 5779.

187. Cao, T., Munk, P., Ramireddy, C., Tuzar, Z., Webber, S.E., *Macromolecules*, 1991, 24, 6300.

188. Prochazka, K.,Kiserov, D., Ramireddy, C., Tuzar, Z., Munk, P., Webber, S.E., *Macromolecules*, 1992, 25, 454.

189. Kiserov, D., Prochazka, K., Ramireddy, C., Tuzar, Z., Munk, P., Webber, S.E., *Macromolecules*, 1992, 25, 461.

190. Kennedy, J.P., Hongu, Y., *Polym. Bull.*, 1985, 13, 115.

191. Kennedy, J.P., Hongu, Y., *Polym. Bull.*, 1985, 13, 123.

192. Galin, M., Mathis, A., *Macromolecules*, 1981, 14, 677.

193. Marti, S., Nervo, J., Riess, G., *Progr. Coll. & Polym. Sci.*, 1975, 58, 114.

194. Riess, G., Nervo, J., Rogez, D., *Polym. Prepr.*, 1977, 18(1), 329.

195. Khan, T.N., Mobbs, R.H., Price, C., Quintana, J.R., *Eur. Polym. J.*, 1987, 23(3), 191.

196. Tomoi, M., Shibayama, Y., Kakiuchi, H., *Polym. J.*, 1976, 8(2), 190.

197. Niwa, M., Katsurada, N., Matsumoto, T., Okamoto, M., *J. Macromol. Sci. Chem.*, 1988, A25(4), 445.

198. Niwa, M., Higashi, N., *Macromolecules*, 1989, 22, 1002.

199. Minoura, Y., Kasuya, T., Kawamura, S., Nakano, A., *J. Polym. Sci.: Part A-1*, 1967, 5, 43.

200. Napper, D.H., *J. Colloid & Interface Sci.*, 1970, 32(1), 106.

201. Galin, J.C., Galin, M., Calme, P., *Makromol. Chem.*, 1970, 134, 273.

202. Suzuki, T., Murakami, Y., Takegami, Y., *Polymer Journal*, 1980, 12, 183.

203. Suzuki, T., Murakami, Y., Yamada, O., Takegami, Y., *J. Macromol. Sci.-Chem.*, 1982, A18(5), 817.

204. Rathke, M.W., *J. Am. Chem. Soc.*, 1970, 92, 3222.

205. Rathke, M.W., Lindert, A.J., *J. Am. Chem. Soc.*, 1971, 93, 2318.

206. Lochmann, L., Rodová, M., Trekoval, J., *J. Polym. Sci., Polym. Chem. Ed.*, 1974, 12, 2091.

207. Garg, , D., Höring, S., Ulbright, J., *Makromol. Chem., Rapid Commun.*, 1984, 5, 615.

208. Fetters, L.J., *J. Polym. Sci. C.*, 1969, 26,1.

209. Wang, J., Varshney, S.K., Jerome, R., Teyssie, P., *Journal of Polymer Science: Part A: Polymer Chemistry*, 1992, 30, 2251.

210. Reuter, H., Berlinova, I.V., Höring, S., Ulbright, J., *Eur. Polym. J.*, 1991, 27,

CHAPTER 2 - EXPERIMENTAL

2.1 Synthesis and Characterisation

A. Synthesis

2.1.1 Anionic High Vacuum Polymerisation

Diblock copolymers of methyl methacrylate/ethylene oxide were synthesised using high vacuum anionic polymerisation. In principle this allows a high degree of control over molecular weight and polydispersity. The use of fully deuterated monomers meant one or both blocks could be isotopically labelled. The high vacuum line (figure 2.1.1) consisted of a tubular glass master manifold having a total of three valved O ring/sleeve and/or ball/socket connection joints. All glassware, tap fittings, piston barrels etc. were supplied by Young's Scientific Glassware, Acton, England, and a standardised nominal glassware diameter of 10mm was used. Tap fittings were of the PTT type and vacuum seals were of OS Teflon type. High vacuum was obtained by a combination of an Edwards roughing rotary pump model E2195 with an Edwards backing diffusion pump model 63. The rotary pump reduced the pressure from atmospheric to about $8x10^{-5}$ atm and by backing down from this pressure with the diffusion pump a vacuum of around 10^{-13} to 10^{-14} atm was achieved. The pump apparatus was supplied by Edwards High Vacuum, Crawley, Sussex. A dry nitrogen line was used in conjunction with the vacuum line. Nitrogen purging of air or moisture sensitive materials was allowed while maintaining a high vacuum.

2.1.1.1 Preparation of reagents

Methyl methacrylate (Aldrich MS,590-9, 99%) as supplied contained 65ppm hydroquinone monomethyl ether which acted as a polymerisation inhibitor during storage. This was removed by cycles of washing with 10% sodium hydroxide solution and then water using liquid-liquid extraction. The monomer was then dried over calcium chloride followed by distillation under reduced pressure. Deuterated methyl methacrylate

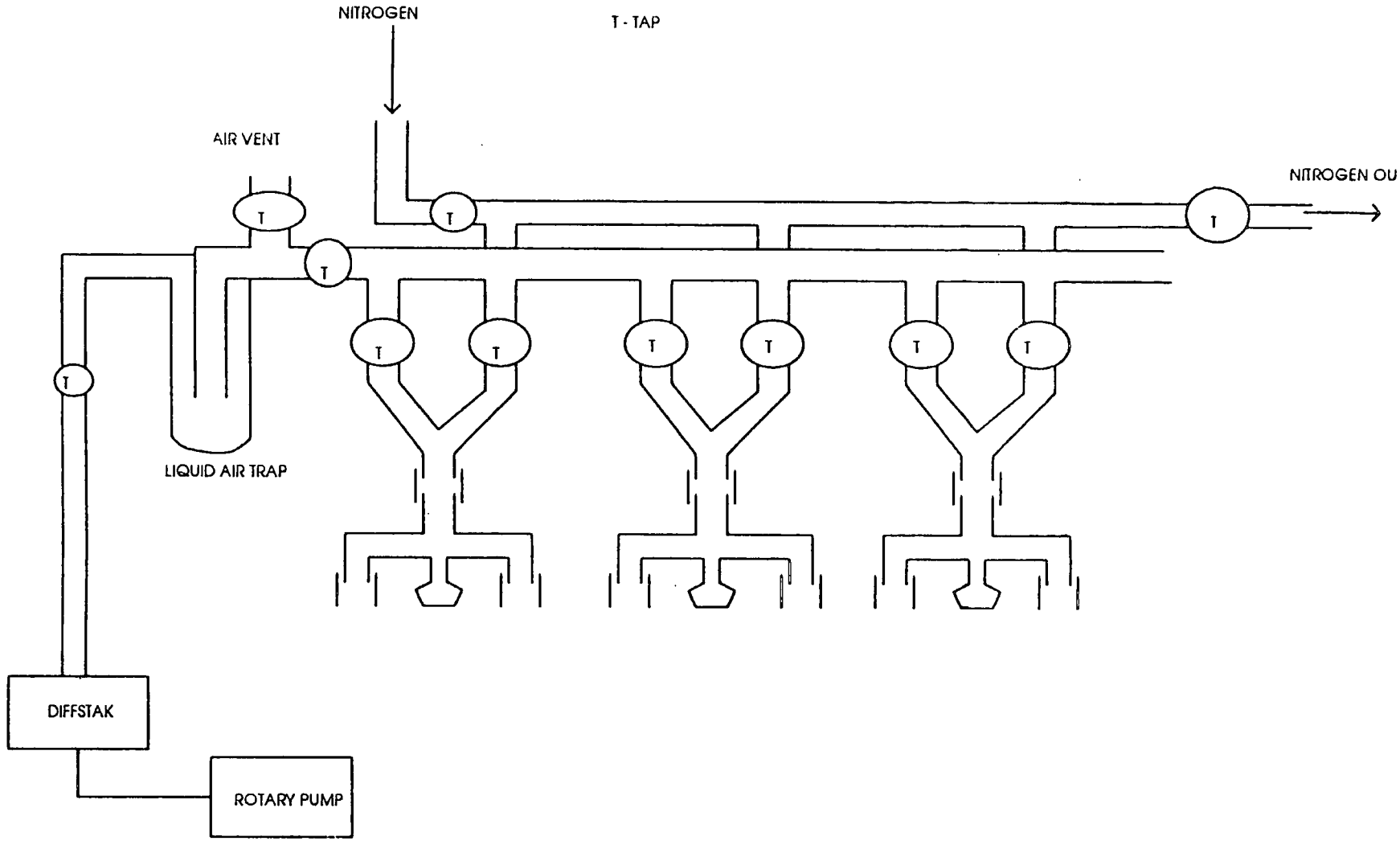

Figure 2.1.1 High Vacuum Anionic Polymerisation Line

(Cambridge Isotope Laboratories) was inhibited with 4-methoxyphenol which was removed using the above extraction procedure but using NaCl solution instead of water due to the higher density of the deuterated material. For both isotopic variations, storage was maintained under vacuum while standing over calcium hydride.

Ethylene oxide, a highly volatile and very poisonous gas at room temperature, as supplied (hydrogenous - Fluka Chemika, 99.8% pure; deuterated d8- C/D/N Isotopes), was transferred by molecular distillation (via acetone/dry ice cooled glassware) to a valved round bottom flask containing calcium hydride and stored under vacuum prior to use.

Tetrahydrofuran (BDH laboratory reagent stored over sodium wire) as supplied had already been highly purified. Sodium wire was added to a flask containing a volume of THF, to this was added a small amount of benzophenone. A deep blue/purple coloured solution resulted which was indicative of the complex formed. This complex prevented the formation of peroxide radicals in the uninhibited tetrahydrofuran and ensured that the THF was dry.

All reagents were stored on the vacuum line using glass joints sealed with Apiezon N type high vacuum grease. Before use all reagents were degassed by means of successive freeze-thaw cycles. Practically, this meant repeated cycles of freezing the liquid using liquid air, pumping down the frozen material, isolating the flask, thawing the reagent, and stirring (using a magnetic stirrer) for several hours. The purpose of stirring was to aid the release of dissolved gases from the liquid and ensure intimate mixing of the liquid and drying agent. The material was regarded as being fully degassed when no rapid rise in pressure occurred on opening the tap to the flask.

2.1.1.2 Preparation of glassware

The glassware was initially washed out with permanganic acid before use. Between syntheses the reaction flasks were washed repeatedly with acetone and methanol. Prior to distilling in reagents, reaction flasks were dried with heat gun to remove any water adsorbed on the glass surface. A living polystyryl-lithium solution, which consisted of a small amount of styrene monomer dissolved in benzene, initiated by injection of a few microlitres of 2.5M n-butyl lithium in hexane, was used to wash out the flasks.

2.1.1.3 Synthesis of initiator

The initiator used was diphenyl methyl potassium. This was prepared by adding potassium metal to dried distilled THF ($60cm^2$) in a $250cm^3$ flask, cooled to 273K in ice. Naphthalene (Aldrich 14,714-1, 99%) was added and the reaction carried out under a dry nitrogen atmosphere. A mole ratio of ca. 0.66:1 between naphthalene and potassium ensured complete consumption of the naphthalene. On mixing of the two reagents, a dark green colour appeared along with the evolution of heat. The mixture was left to stir overnight until total consumption of the potassium. An excess (ca. 10mL) of diphenyl methane (Aldrich, D20, 931-7, 99%) was injected quickly into the reaction flask and the contents stirred at room temperature for two days. The initiator was finally obtained as a dark red/purple solution and stored in a suba-sealed bottle under dry nitrogen.

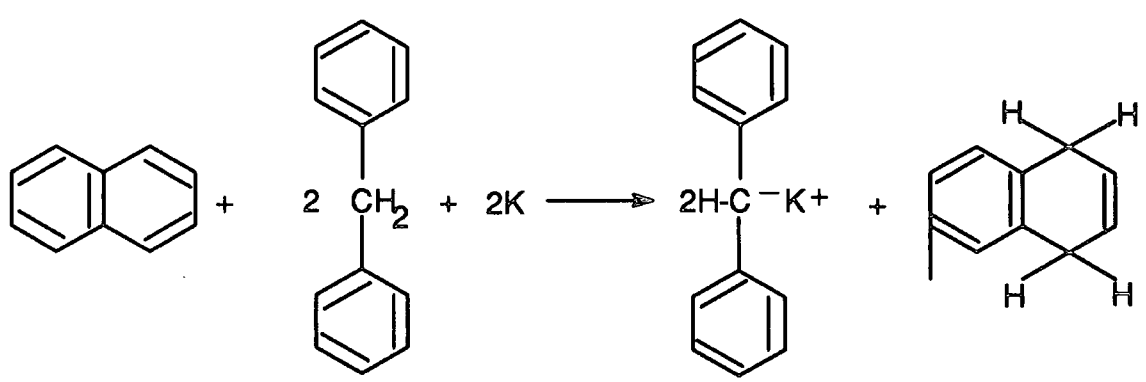

2.1.1.4 Estimation of initiator concentration

The concentration of the initiator was estimated by performing several polymerisations of methyl methacrylate with different amounts of initiator. Molecular weights determined from Gel Permeation Chromatography (GPC) allowed the concentration of the initiator to be calculated for a specific molecular weight.

2.1.1.5 Polymerisation

When required for further purification and/or polymerisation, the reagents were transferred by molecular distillation under high vacuum. The transfer procedure consisted of immersion of the receiver vessel in liquid air for both MMA and THF, while immersion in a dry/ice acetone bath was suitable for EO.

2.1.2 Poly(methyl methacrylate-ethylene oxide) diblock copolymers

2.1.2.1 PMMA block

THF (ca. 50mL) was distilled into a clean, dry reaction vessel (figure 2.1.2). Into this was distilled a known weight of MMA. By immersion in a dry ice /acetone bath the temperature of the reaction mixture was allowed to rise to about -78°C. The reaction was initiated by rapid injection of the required volume of diphenyl methyl potassium. Instantaneous polymerisation was accompanied by formation of a deep yellow colour in the solution, which turned colourless after a few seconds. A sidearm sample was taken after about 30 minutes and terminated by injection of 50μL degassed methanol.

2.1.2.2 PEO block

Ethylene oxide monomer was dried more thoroughly by exposure to sodium mirrors. In the case of the deuterated monomer this exposure also removed the polymerisation inhibitor. A small piece of sodium in a $100cm^3$ round bottom flask was heated under vacuum with a gas/oxygen flame until it boiled. On vaporisation a fresh metal coating

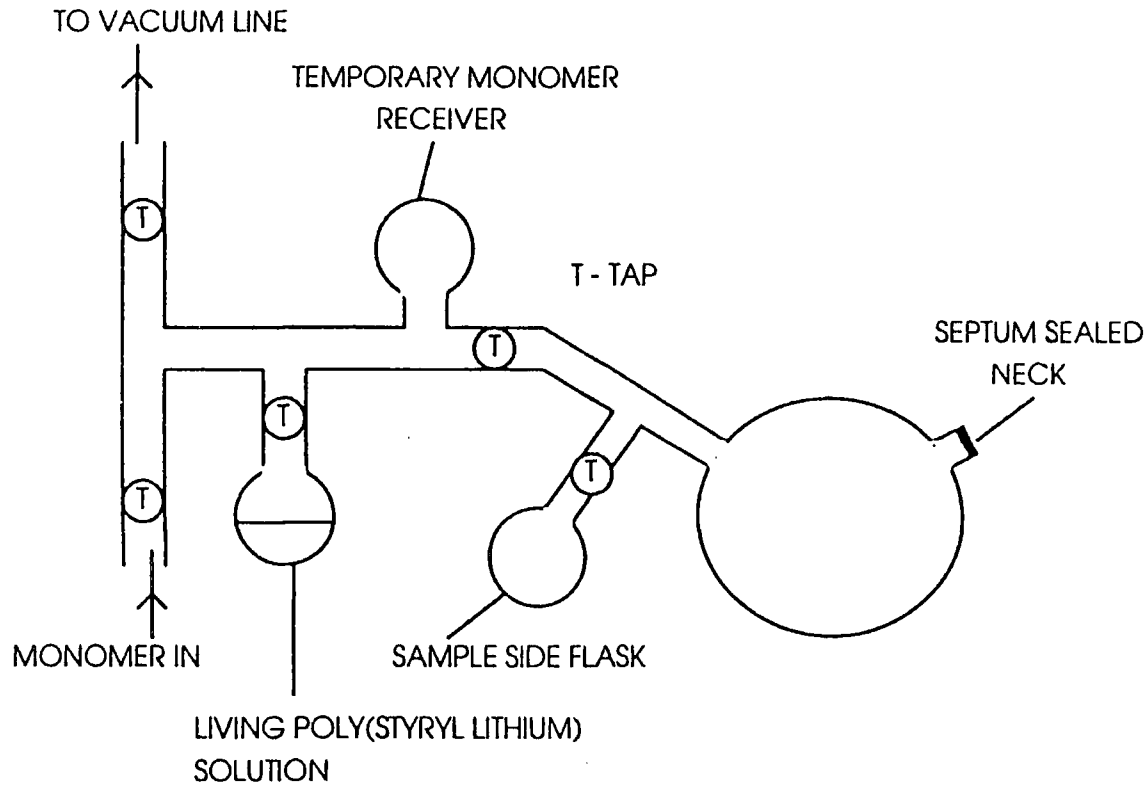

Figure 2.1.2 Anionic Polymerisation Reaction Vessel

condensed on the surface of the flask. The required amount of monomer was distilled into the flask and shaken gently to ensure good contact with the fresh metal. In order to prevent build up of vapour pressure and a subsequent explosion it was important to keep the temperature of the flask below 10^{0}C. The process was repeated until the mirror was not tarnished by exposure to the monomer. About five sodium mirrors were required.

The sodium dried monomer was distilled into a newly cleaned prepolymerisation flask (figure 2.1.3). The monomer was distilled directly to the septum fitted bulb where a few crystals of 9-Fluorenone (BDH laboratory reagent) had been previously placed. About 50μL of 2.5M n-butyl lithium was injected to give a bright yellow colour. The monomer was distilled into the receiver bulb leaving residual impurities. The highly purified monomer was distilled directly to the polymerisation reaction flask which was immersed in a dry ice /acetone bath. The polymerisation flask was allowed to rise to room temperature overnight, during which time a characteristic pale yellow colour developed in the solution. The flask was immersed in an oil bath for four days at 75°C. Termination of the polymerisation was effected by injection of 500μL degassed glacial acetic acid. The copolymer and sidearm homo-PMMA were precipitated into ten volumes of stirred n-hexane.

A number of copolymers were prepared with varying compositions, molecular weight and isotopic labelling.

B. Characterisation

2.1.3 Molecular Weight Determination

Molecular weights of the diblock copolymers and sidearm PMMA samples were determined by size exclusion chromatography using two PL gel 10μm mixed columns, a Waters differential refractometer as detector, chloroform as the carrier solvent and with

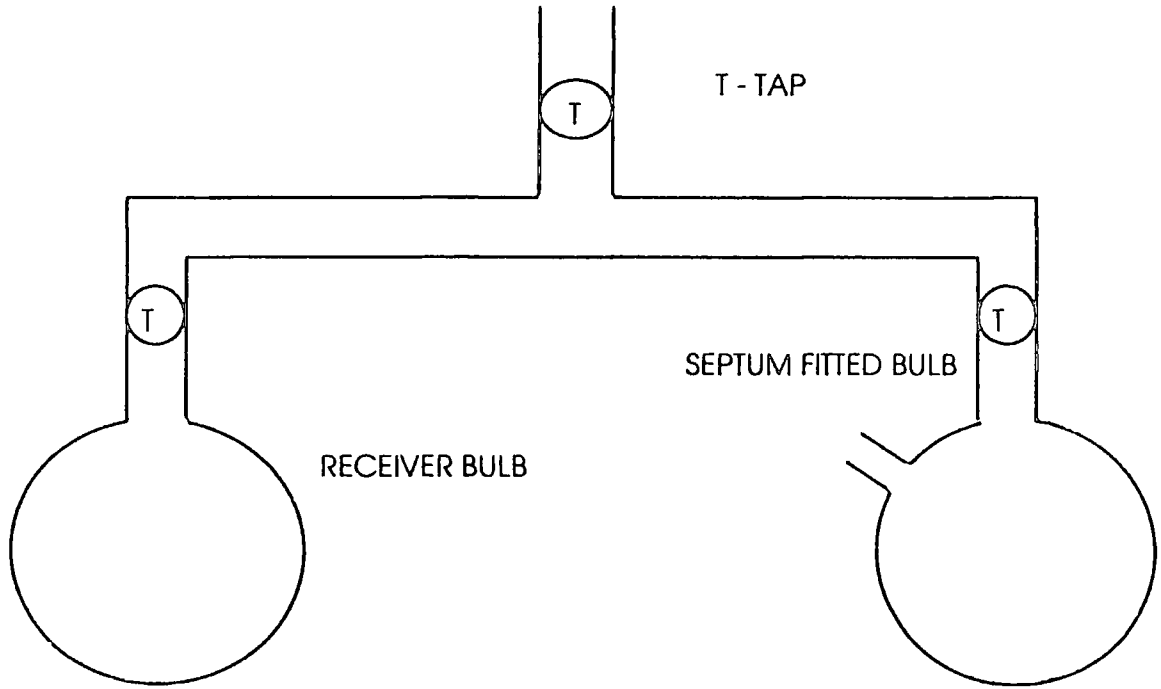

2.1.3 Pre-polymerisation Flask

respect to polystyrene standards. This method gave the number average and weight average molecular weights relative to the polystyrene standards (Table 2.1).

Figure 2.1.4 shows a GPC trace of a typical side-armed PMMA block and its PMMA-b-PEO block copolymer. It can be seen that a shift in polymer retention time occurs on addition of the PEO block indicating an increase in molecular weight. The fact that the block copolymer peak remains unimodal suggests that the polymerisation system is totally living i.e. there is no homo-PMMA remaining.

2.1.4 FTIR

FTIR spectra were recorded on a Perkin Elmer 1700 spectrometer.

A typical FTIR spectrum of a side-armed PMMA fraction is shown in Figure 2.1.5. This spectrum shows three aliphatic C-H stretching peaks at 3000, 2950, and 2850 cm^{-1} respectively. A single C=O carbonyl peak at 1730 cm^{-1} is due to the ester group in the methyl methacrylate units. The absence of aromatic C-H out-of-plane bending at 730 cm^{-1}, indicates the absence of aromatic (nonfunctional) prematurely terminated PMMA. Figure 2.1.6 shows the FTIR spectra of the corresponding PMMA-b-PEO copolymer (BR29) which shows strong C-H stretching at 2900 cm^{-1}, symmetric C-O-C stretching within the PEO block at 1100 cm^{-1} and a strong C=O carbonyl absorption at 1730 cm^{-1}.

2.1.5 NMR studies

The 400 MHz ^{1}H NMR spectra of these copolymers is only applicable to totally hydrogenous analogues since deuterium has very poor sensitivity to the technique with respect to hydrogen. A typical spectrum (figure 2.1.7) shows resonances of the methylene protons of PEO ($\delta = 3.64$) and of methoxy protons of PMMA ($\delta = 3.60$). The composition of the block copolymers with respect to PMMA and PEO was calculated from the ratio of integral intensities of these resonances (figure 2.1.8). Comparison of the

		PMMA block /10^3			PMMA-b-PEO /10^3			mol%	triad tacticity /%
sample code	isotopic structure	Mw	Mn	Mw/Mn	Mw	Mn	Mw/Mn	MMA:EO	I H S
BR10	HMHE	72.0	36.5	1.98					
BR11	HMHE	118.3	40.7	2.92	277.9	56.4	4.93		
BR13	HMHE	60.2	44.0	1.37	68.6	29.3	2.34		
BR14	HMHE				112.7	57.2	1.97	90:10	
BR15	HMHE	60.5	41.6	1.45	116.8	67.0	1.74	93:7	
BR16	HMHE	77.0	51.0.	1.51	225.5	98.3	2.29	90:10	
BR17	HMHE	46.3	26.0	1.78	57.0	21.5	2.66		
BR18	HMHE	61.4	44.2	1.39	40.4	20.9	1.93		
BR19	DMHE				76.0	55.4	1.37		
BR20	DMHE	38.0	28.1	1.35	62.8	43.5	1.44	50:50	7 55 39
BR21	HMHE	51.2	38.2	1.34	97.8	54.3	1.80	67:33	
BR22	HMHE	32.8	24.1	1.36	67.3	32.1	2.10	35:65	8 54 37
BR23	HMDE	34.1	28.7	1.19	46.3	34.0	1.36	95:5	
BR24	DMDE	21.5	18.7	1.15	25.0	19.9	1.26	95:5	
BR26	HMDE	24.3	21.1	1.15	32.7	24.6	1.33	78:22	9 53 38
BR27	DMDE	21.2	18.2	1.67	45.4	25.6	1.77	49:51	0 51 49
BR29	HMDE	20.7	15.1	1.37	45.5	19.3	2.34	30:70	0 35 65
BR30	HMDE	277.0	40.9	6.76	260.0	29.1	8.93		

Table 2.1 Molecular weights of diblock copolymers and tacticity of PMMA block

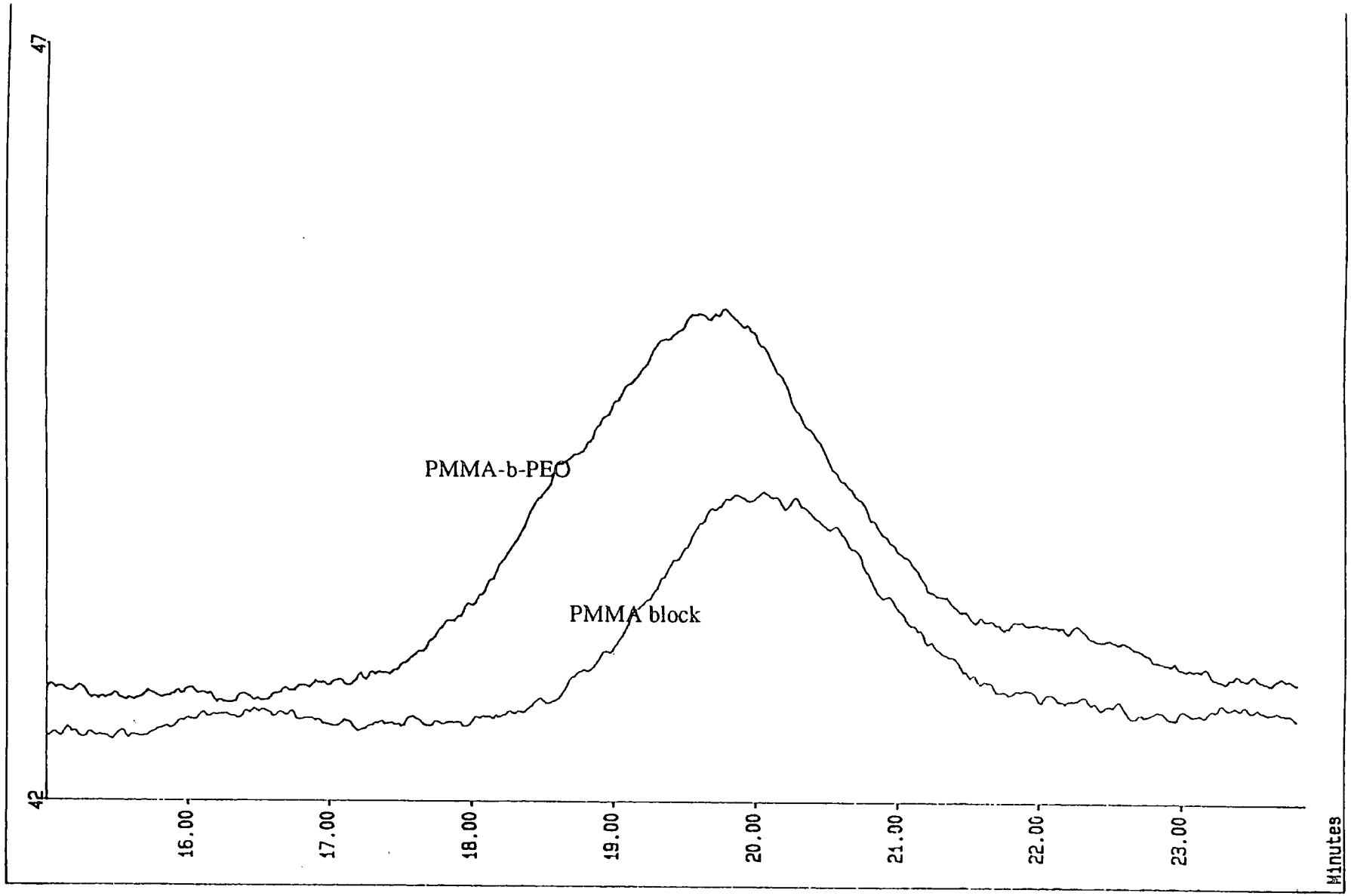

Figure 2.1.4 GPC trace of PMMA-b-PEO copolymer

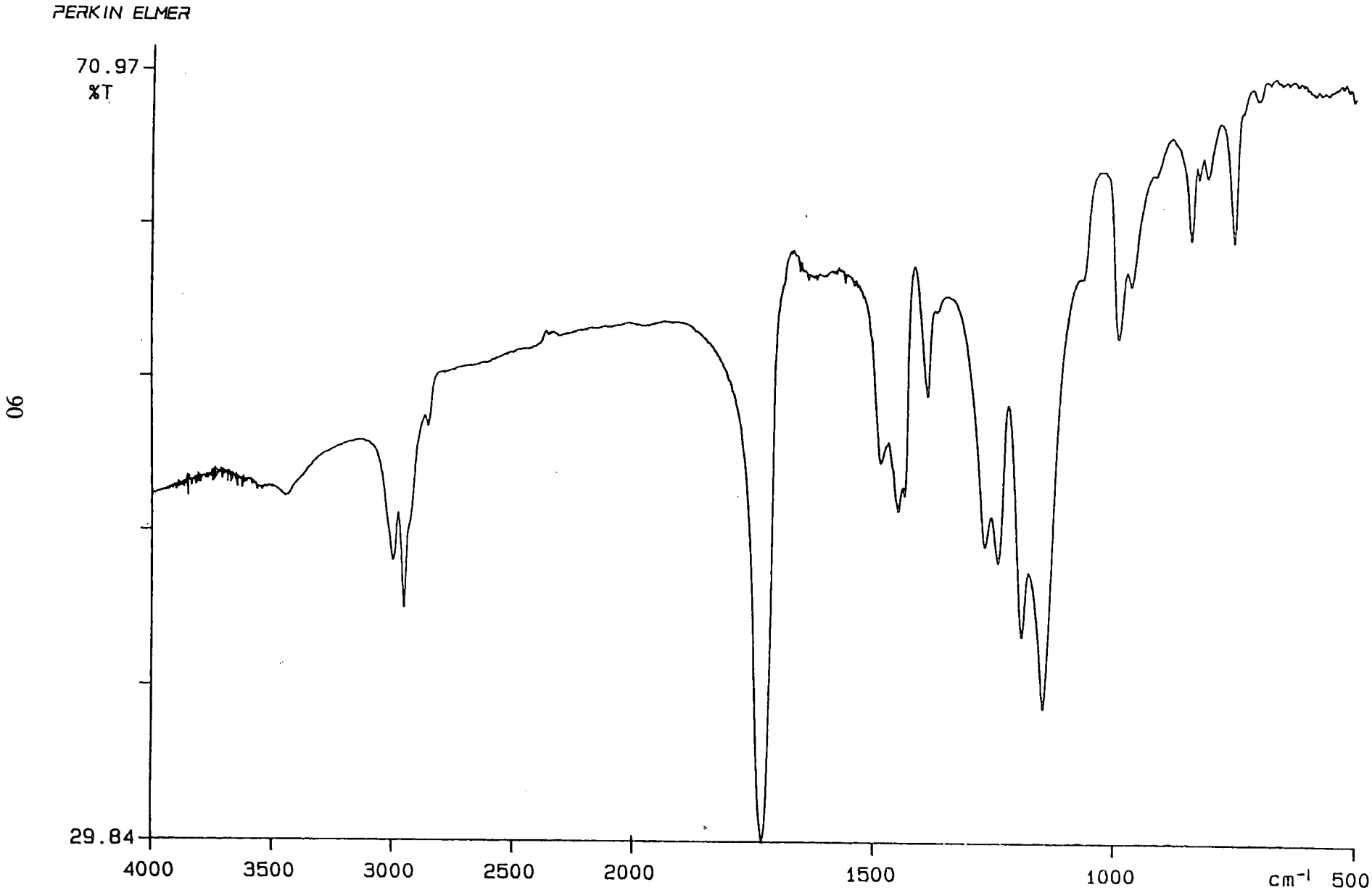

Figure 2.1.5 FTIR spectrum of side-armed PMMA fraction

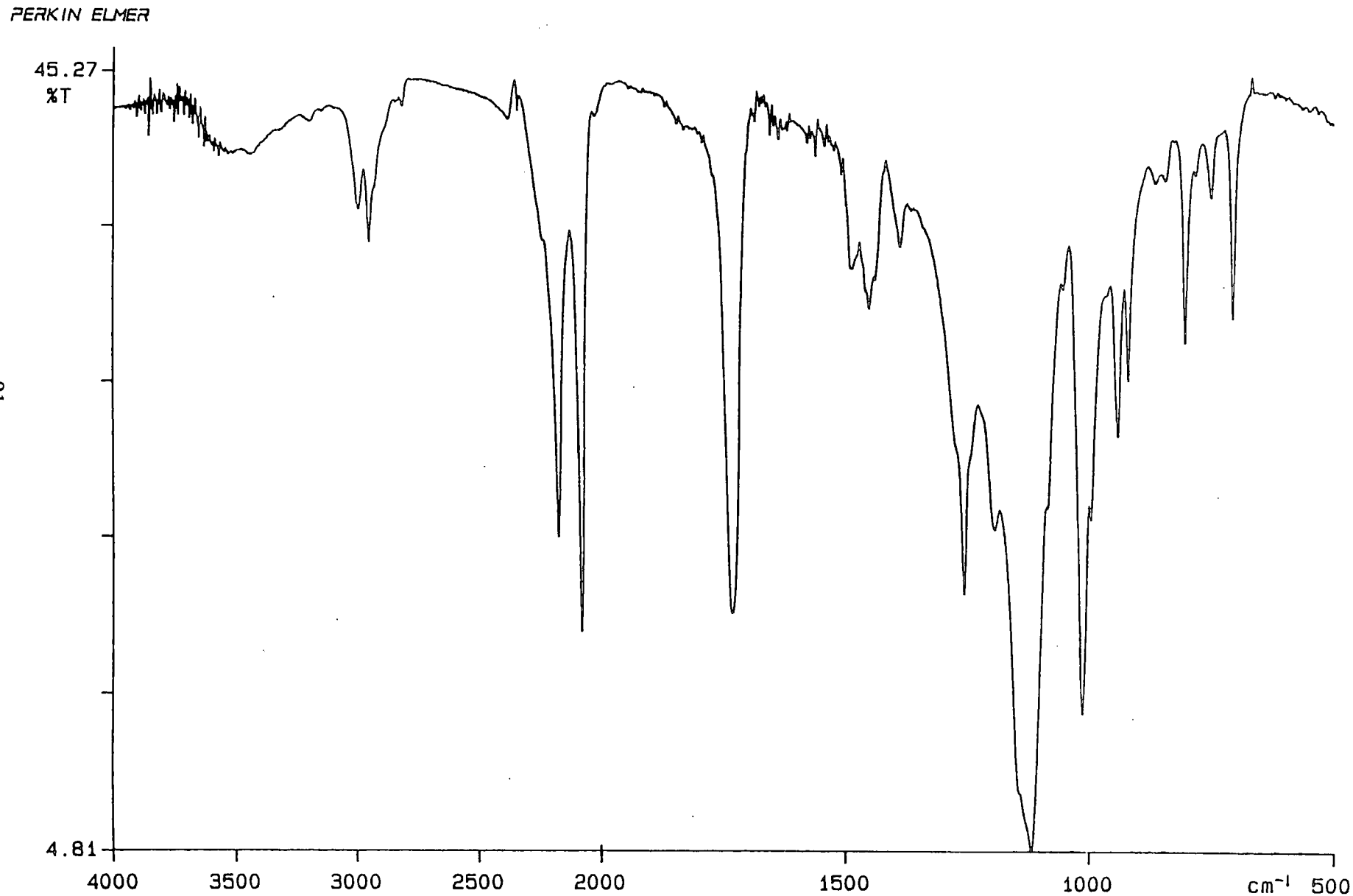

Figure 2.1.6 FTIR spectra of PMMA-b-PEO copolymer

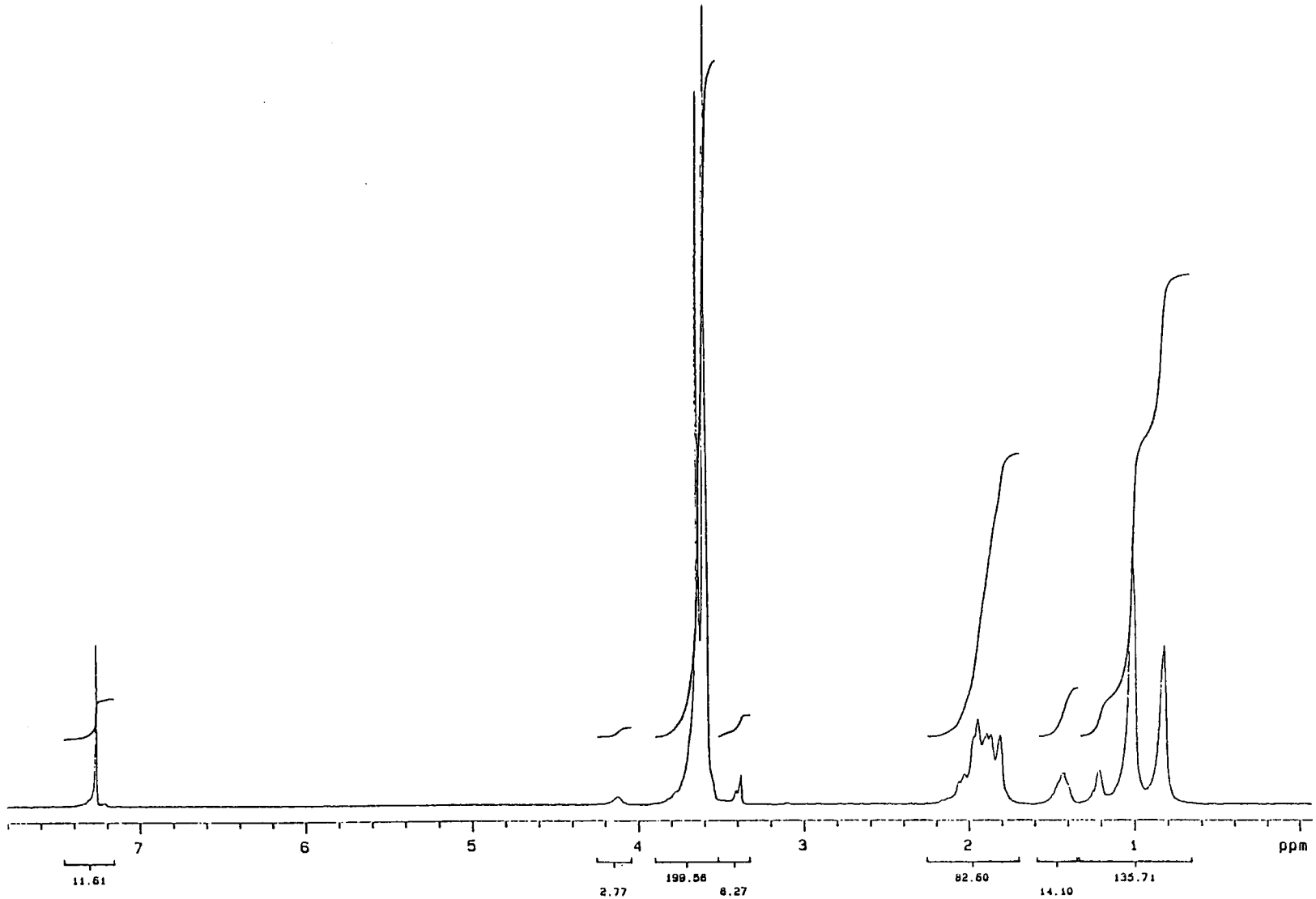

Figure 2.1.7 Typical ^{1}H NMR spectrum for PMMA-b-PEO copolymers

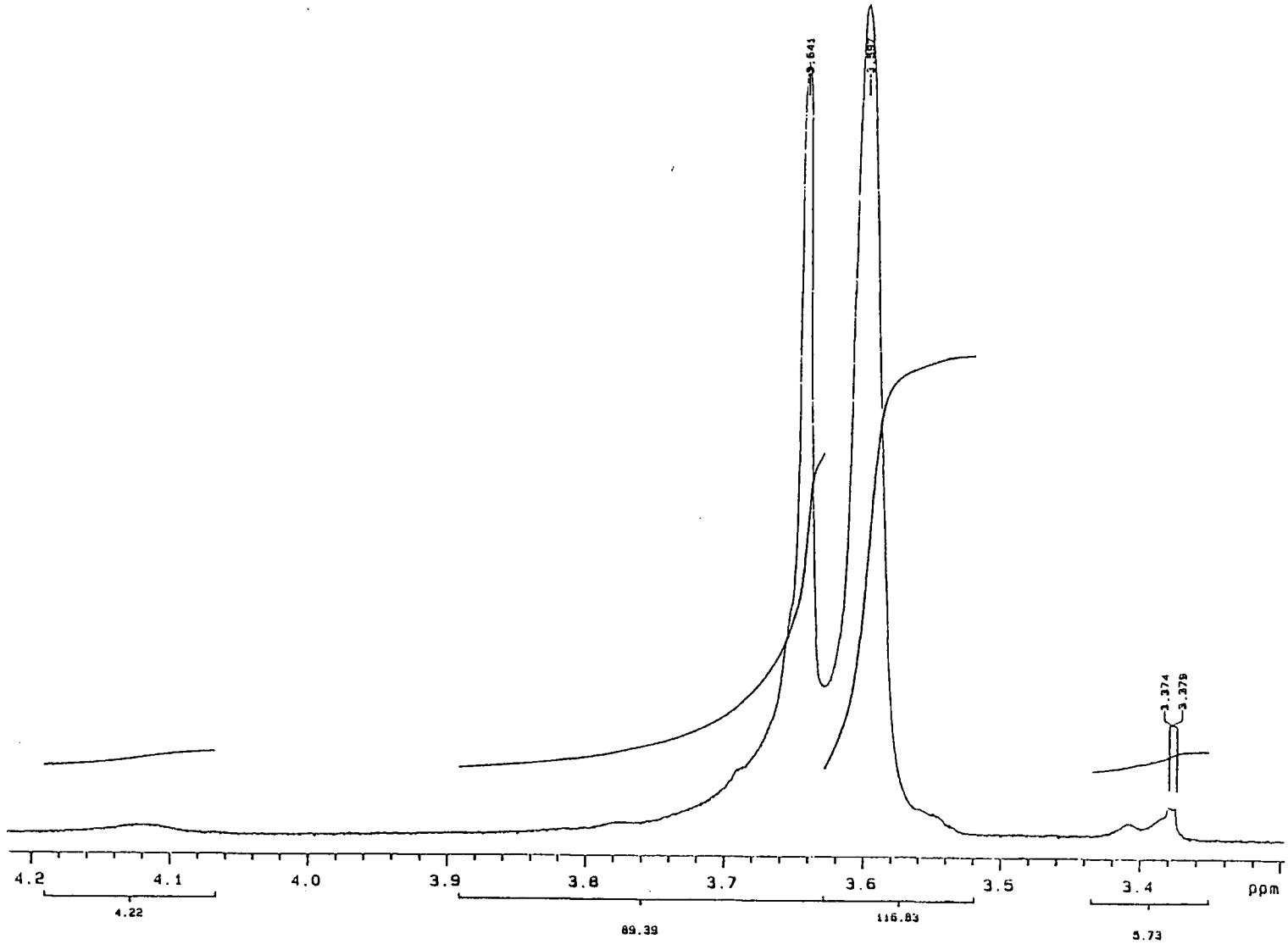

Figure 2.1.8 ^{1}H NMR spectrum showing integral intensities of methylene protons of EO (δ = 3.64) and methoxy protons of PMMA (δ = 3.60)

relative intensities of the absorptions of methoxy and α-methyl protons shows them to be about the same proving the absence of transesterification reactions.

The 400MHz ^{13}C NMR spectra were found to be best for determining the composition of the partly and fully deuterated copolymers. A typical spectra (figure 2.1.9) clearly shows the typical resonances of the methylene group of PEO at 70.6 ppm.

For further confirmation that transesterifications had not occurred, the relative intensity ratios of the signals of the carbonyl carbons at 175.7 - 178.5 ppm and methoxy carbons at 20ppm were measured. The signal intensity ratios were approximately unity. Since no transesterification was detected within experimental error then it was assumed that linear diblock copolymers were obtained. The tacticities of the copolymers were determined by observing the carbonyl signal at around 176-178ppm (figure 2.1.10) which is sensitive to slight change in shift according to the chain tactic sequences around it. Since the experimental resolution of NMR technology has increased, assignments up to and including heptads have been assigned.

All the NMR data are summarised in Table 2.1. The stereosequence distributions of the poly(methacrylate) part in the copolymer appeared rich in syndiotactic dyad due to using THF as a solvent. The low dyad tacticity is as expected for MMA monomer initiated in a polar solvent such as THF. The initiation of the polymerisation of MMA with diphenyl methyl potassium therefore results in wholly linear diblock copolymers, traces of homo-PMMA or homo-PEO being absent.

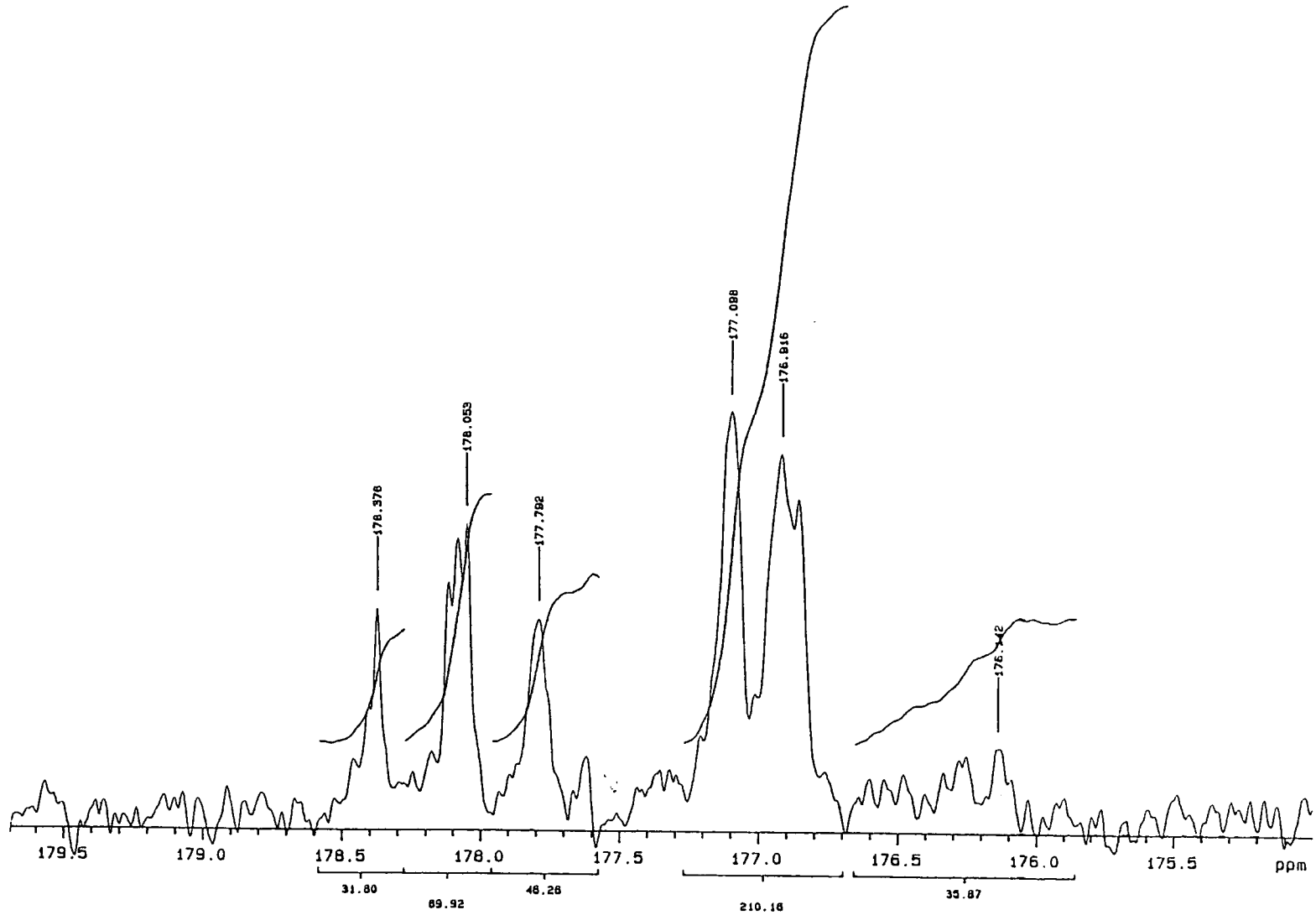

Figure 2.1.9 ^{13}C NMR spectrum showing resonance of PEO at 70.6 ppm

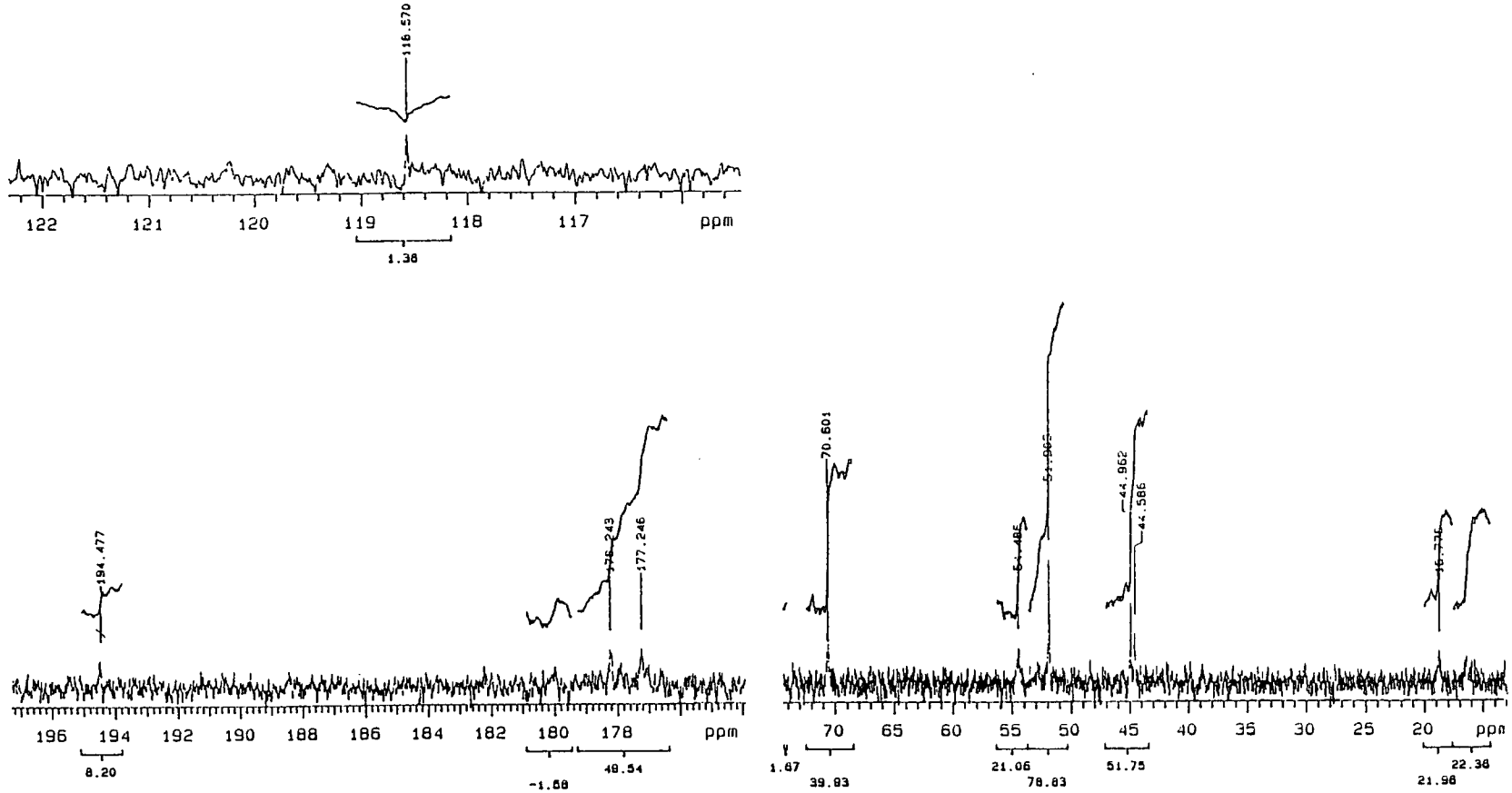

Figure 2.1.10 ^{13}C NMR spectrum showing intensity ratios of carbonyl carbons at 175.7 to 178.5 ppm

2.2 Surface Pressure Studies

The surface pressure isotherms were measured on a circular Teflon Langmuir trough (Nima Technology Ltd., Coventry, UK) having an area of 980cm^2. The trough rested on an optical vibration isolation table (75 cm by 40 cm). The temperature of the trough was controlled by means of circulating water through tubes in the base of the trough using a Neslab RTE-100 thermostat.

The surface pressure of the spread PMMA-b-PEO copolymers were measured by the Wilhelmy technique using a 10mm wide paper plate attached to a sensitive force balance which contained a displacement transducer. The force required to keep the paper plate in a stationary vertical position was converted into an electrical signal by the displacement transducer which was then converted to the corresponding surface pressure. The available surface area could be altered by either opening or compressing two Teflon barriers which were controlled by stepper motors. In this way the surface pressure could be measured in real time as a function of either area or surface concentration using the software provided by Nima and a 486 PC. The trough used is shown in figure 2.2.1.

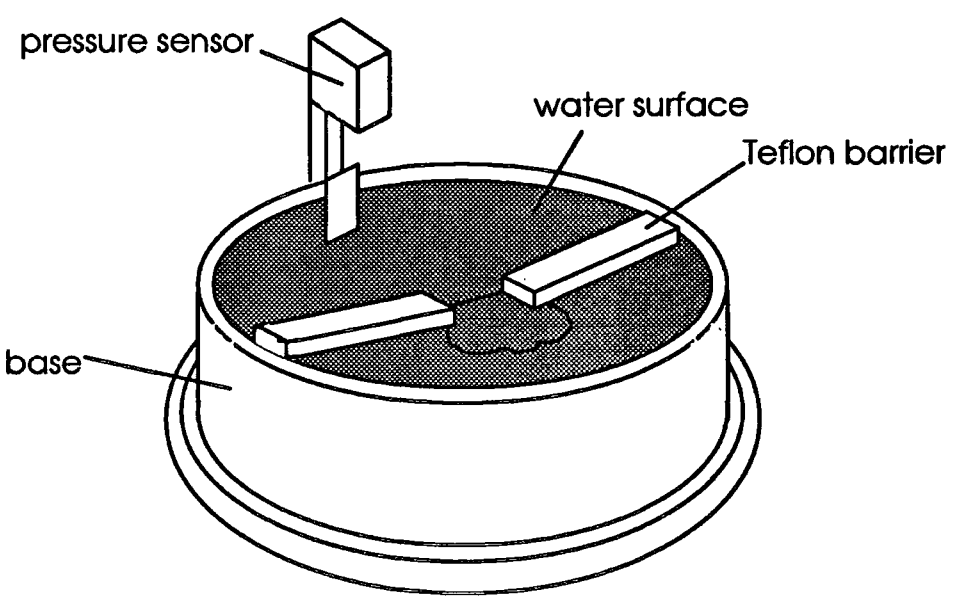

Figure 2.2.1 Nima Langmuir Trough

2.3 Neutron Reflectometry

The neutron reflection experiments were carried out on the CRISP instrument which operated from the pulsed spallation source, ISIS, at the Rutherford Appleton Laboratory, Oxfordshire. Figure 2.3.1 shows a schematic representation of the experimental setup. The Langmuir trough was constructed of Teflon with a maximum area of about 600cm^2 and the surface concentration was controlled by means of a stepper motor driven Teflon barrier. The trough was contained in a perspex box which had fused glass silica windows at either end which allowed the incident and reflected neutron beams to pass through. For each neutron reflection experiment a monolayer was deposited by spreading chloroform solutions of a copolymer. Increases in surface concentration were obtained by compressing the Teflon barrier until a specific surface area was obtained. In order to allow equilibration of the monolayer system, i.e. evaporation of solvent and the polymeric material to spread into the available are, about fifteen minutes were allowed. All experiments were conducted at ambient temperatures of about 298K.

2.3.1 The CRISP Reflectometer

The CRISP instrument (Critical Reflection Spectrometer) is a time of flight reflectometer for critical reflection studies on surfaces, figure 2.3.2 shows a diagram of the instrument. The incident neutron beam has a multi-wavelength, with wavelengths between 0.5 and 13 Å, and usually operates at a fixed incident angle of 1.5°. This incident angle gives a momentum transfer range Q of 0.05 to 0.65Å^{-1}. CRISP operates from the N4 beamline of the ISIS neutron source, the raw neutron beam being cooled by a 25K H_2 moderator. A horizontal slit geometry is used which gives beam dimensions typically 40 mm in width by 0.5 to 6 mm in height. The wavelength is filtered by means of a 50Hz wavelength limiting chopper at 6 m from the source, wavelengths below 0.5Å

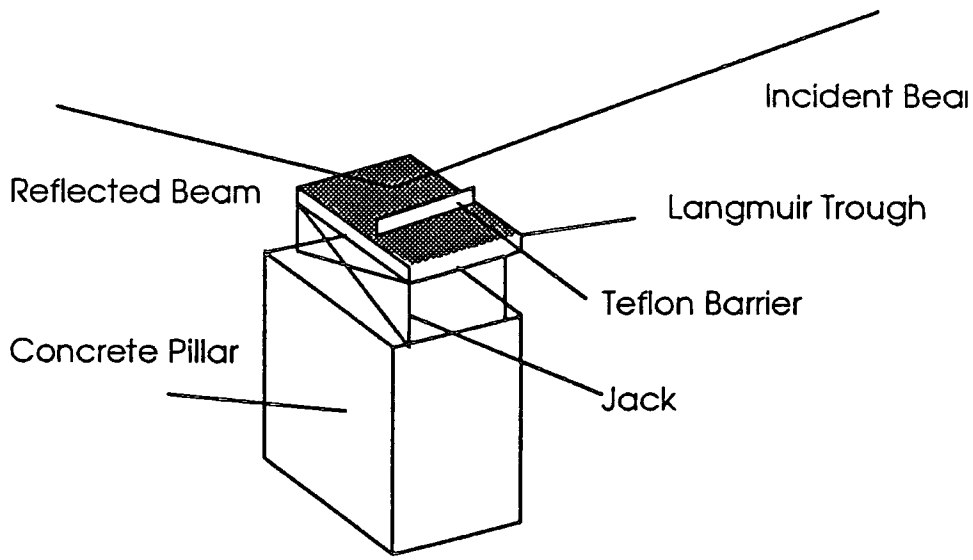

Figure 2.3.1 Schematic representation of the experimental setup

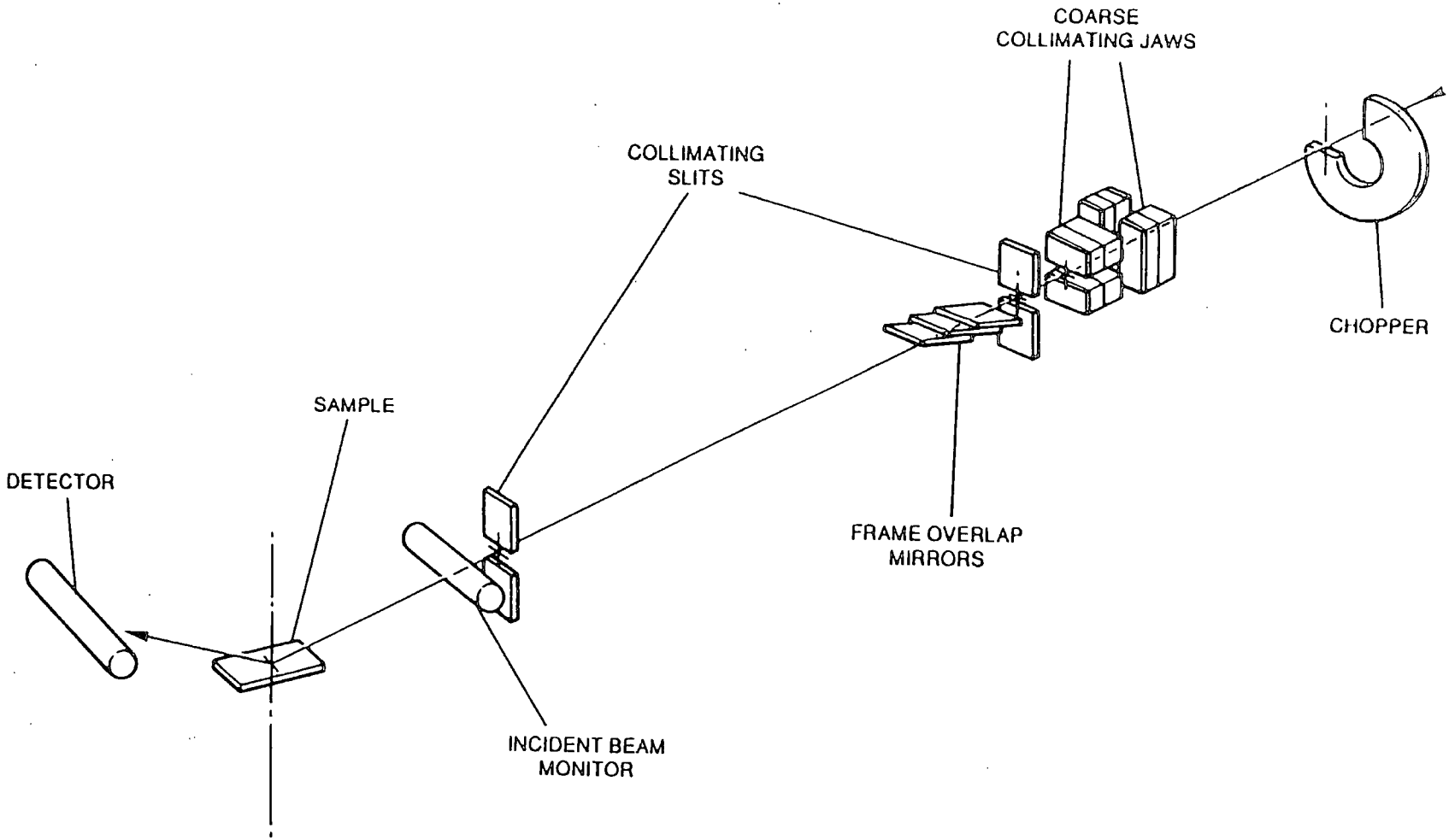

Figure 2.3.2 The CRISP Spectrometer

and above 13Å being rejected. Lower Q values can be measured by including a non-polarising supermirror in the beamline which deflects the neutron beam to shallower incident angles from 1.5°. The lowest value of Q accessible is 0.01$Å^{-1}$ which is achieved by an angle of 0.4°. The sample position is 10.25m distance from the moderator and is mounted on a large concrete anti-vibration pillar. An adjustable jack is used to alter the height of the sample position in relation to the incident beam. The reflected neutrons are detected by a one dimensional position sensitive detector which is 1.75 m distance from the sample. Alignment of the sample and detector were achieved by using a laser beam, manipulation of which was effected by mirrors colinear with the path of the neutron beam.

The intensity of the reflected beam pulse was analysed as a function of the slight differences in arrival time of the reflected neutrons of different wavelengths at the detector. These differences in arrival time are commonly referred to as 'time of flight'. The reflectivity is obtained from this raw data from the ratio of the reflected intensity to the intensity of the incident pulse measured by a scintillation monitor mounted in the incident neutron beamline. Momentum transfer was calculated by rebinning the time analysed data packages into wavelength sets which were then combined with the known incident angle. All data was acquired on a Vaxstation 3200 computer terminal. Data acquisition typically took 2-3 hours at 1.5°, whereas at an angle of 0.79° this acquisition took as little as 20 minutes.

2.4 Ellipsometry

The ellipsometry measurements were performed on a Jobin-Yvon Uvisel phase-modulated ellipsometer at the Cavendish Laboratory, Cambridge University, Cambridge. Figure 2.4.1 shows a schematic representation of the instrument used. In a scan the ellipsometric measurements give the phase difference (Δ) and the azimuth (ψ) of the amplitude ratio (between the p and s waves) for light polarised parallel and normal to the plane of incidence using a fixed wavelength of polarised light (λ = 413.3nm). In the experiments light was incident at two separate angles of 53.2° and 53.4° measured relative to the axis normal to the surface. The incident and detection arms of the ellipsometer were pivoted around a solid metal plate which was fixed perpendicular to the surface of the trough. The incident light was polarised perpendicular to the plane of incidence using a quartz wave plate retarder (QWP) and the incident angles chosen were close to the Brewster angle, where maximum sensitivity in the measured parameters occurs. The reflected signal was then minimised by the analyser (identical component to polariser). The combination of the polariser, analyser and QWP allowed the disinclination of the elliptically polarised incident field to be obtained giving the values of Δ and ψ from the following equations

$$\tan\Delta = \sin\beta \tan(\pi/2 - 2P_o) \qquad (2.4.1)$$

$$\cos 2L = -\cos\beta \cos 2P_o \qquad (2.4.2)$$

$$\tan\psi = \cot L \tan(-A_o) \qquad (2.4.3)$$

where β = retardation of QWP

P = polariser azimuth setting

A = analyser azimuth setting

L = thickness of QWP

and the subscript o represents the extinction setting.

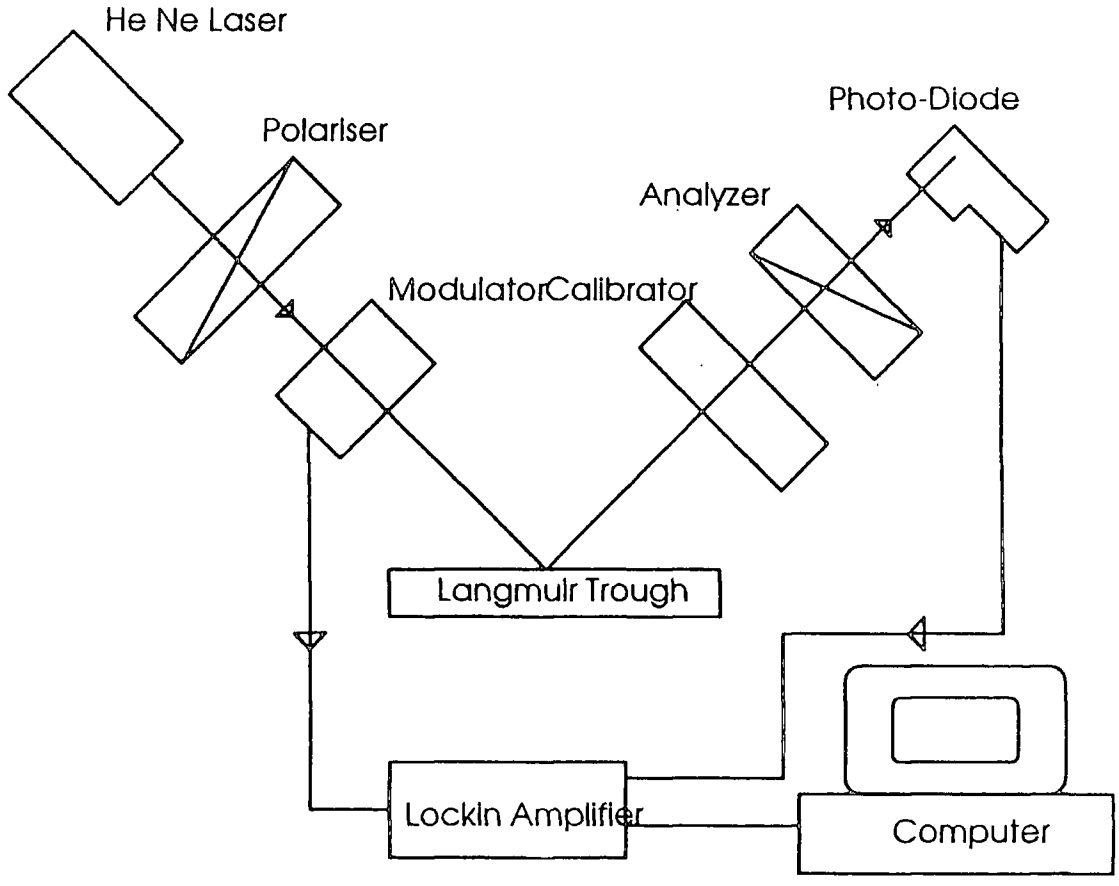

Figure 2.4.1 Schematic Representation of the Ellipsometry Experiment

The instrument was controlled and data recorded using Ellipsometric Software Version 3.0 on a 486 PC. The polariser and analyser were moved by means of stepper motors controlled by the computer. The experiments were performed on a Langmuir trough filled with water and surface pressure was measured using the Wilhelmy plate method. The Teflon coated trough had a maximum area of about 600cm^2 and was mounted on an optical anti-vibration table. Monolayers were formed by depositing chloroform solutions of the copolymer at the water surface. After equilibration of the monolayer system (ca. 15 mins.) the surface concentration was controlled by means of a sliding Teflon barrier. The water surface was cleaned by aspiration and checked before each run by compressing several times until a zero surface pressure was produced. Room temperature was maintained throughout the experiments. Surface pressure measurements and ellipsometric data were recorded simultaneously.

2.5 Surface Quasi-Elastic Light Scattering

Light scattered by capillary waves is detected using heterodyne methods. This allows the weak nature of the surface scattering effects to be utilised by measuring the small frequency shifts of the scattered light. This frequency shifted scattered light falling upon the photo multiplier detector (PMT) is mixed with a reference beam originating from the original laser beam, unshifted in frequency. The output of the detector is modulated by the beating of the scattered and reference beams with each other. The heterodyne intensity function is given by[1]

$$G(\tau) = (I_s + I_r)^2 + 2I_rI_sg^{(1)}(\tau) + I_s^2[g^{(2)}(\tau) - 1] \qquad (2.5.1)$$

where $g^{(1)}(\tau)$ is the field autocorrelation function of the scattered field, the Fourier transform of its power spectrum, while $g^{(2)}(\tau)$ is the intensity correlation function. The output of the detector is modulated by beats between the scattered and reference beams. It is important that the beat term dominates the time dependence of the correlation function, this is achieved when the reference beam intensity (I_r) is greatly in excess of the scattered light intensity (I_s). As long as I_s/I_r is smaller than about 10^{-3} then the last term of equation 2.5.1 becomes negligible and the first order term $2I_sI_rg^{(1)}(\tau)$ dominates the expression[2] for $G(\tau)$.

The determination of the q value is crucial for understanding the results of the scattering experiments. The value of q is the component of the scattering vector parallel to the liquid surface (figure 2.5.1) and is given to a good approximation by

$$q = 4\pi/\lambda.\sin(\delta\theta_n/2).\cos\theta \qquad (2.5.2)$$

where θ is the angle of incidence and $\delta\theta_n$ is the angular separation from the zero-order beam of the n^{th} diffracted beam. This value of q is used as a fixed value in the direct fitting method where $P(\omega)$ is calculated as a function of the surface properties.

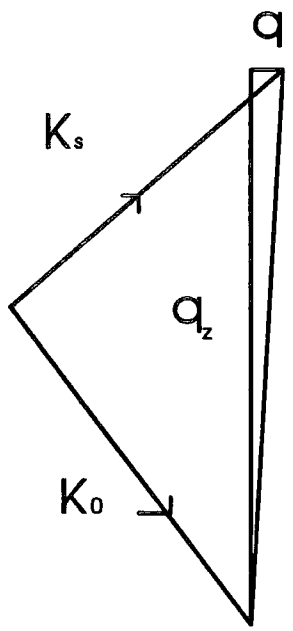

Figure 2.5.1 SQELS vector diagram

Light scattering measurements are greatly affected by instrumental effects arising from the finite extent of the laser beam on the surface. The observed spectrum is a convolution of $P(\omega)$ with an instrumental function. Providing the laser beam has a Gaussian profile the observed correlation functions may be written as[3]

$$G(\tau) = B + Af(\tau)\exp(-\beta^2\tau^2/4) \qquad (2.5.3)$$

where β is the standard deviation of the instrumental function in the frequency domain and $f(\tau)$ is the time dependence of the correlation function expected from waves of a selected q value.

Data analysis

Two different methods of data analysis may be applied to the correlation data. Both of these involve using non-linear least-squares fitting with appropriate mathematical forms. The wave frequency ω_b and damping Γ may be determined using equation (2.5.3) in conjunction with an exponentially damped cosine time dependence

$$f(\tau) = \cos(\omega_b|\tau| + \phi)\exp(-\Gamma\tau) \qquad (2.5.4)$$

where the phase term ϕ accounts for the deviations of $P(\omega)$ from the exact Lorentzian form. The full equation therefore becomes

$$G(\tau) = B + A\cos(\omega_0\tau + \phi)\exp(-\Gamma\tau).\exp(-\beta^2\tau^2/4) \qquad (2.5.5)$$

where A is an amplitude factor and B represents instrumental background mainly due to I_r. The Gaussian multiplicative term in β represents the instrumental line broadening. It was found by Earnshaw and McGivern that this factor had a significant effect on the shape of the function at q values above $700cm^{-1}$. Best fits of the experimental data using such a function (equation 2.5.5) give values of ω_0 and Γ which are related to the viscoelastic properties of the surface film via the dispersion equation.

The exact spectral form of equation 1.5.16 may also be used in the fitting of experimental data[4]. This method is a direct fitting method which calculates the power spectrum from estimates of the four surface properties (γ_o, γ', ε_o, and ε'). This calculated spectrum is fitted using equation (2.5.5) with a time dependence defined by the Fourier transform of $P(\omega)$ formulated as a function of these four properties. The viscosity and density of the subphase are assumed to have their accepted values.

Experimental Setup

The Surface Quasi-Elastic Light Scattering (SQELS) experiments were performed on a home built spectrometer using the same Langmuir trough as used for the static surface pressure isotherms. The experimental setup is shown in figure 2.5.2. The SQELS apparatus was constructed around the Langmuir balance using components purchased from Ealing Electro-optics, Watford, UK. The Langmuir trough was placed on an optical vibration isolation table (JRS, Affoltern, Switzerland), which was mounted on a large stationary steel table. The apparatus consisted of two parallel lengths of optical track which were fixed so as they were equivalent distances either side of the trough. The first track allowed manipulation of the incident beam on to the air-water interface while the

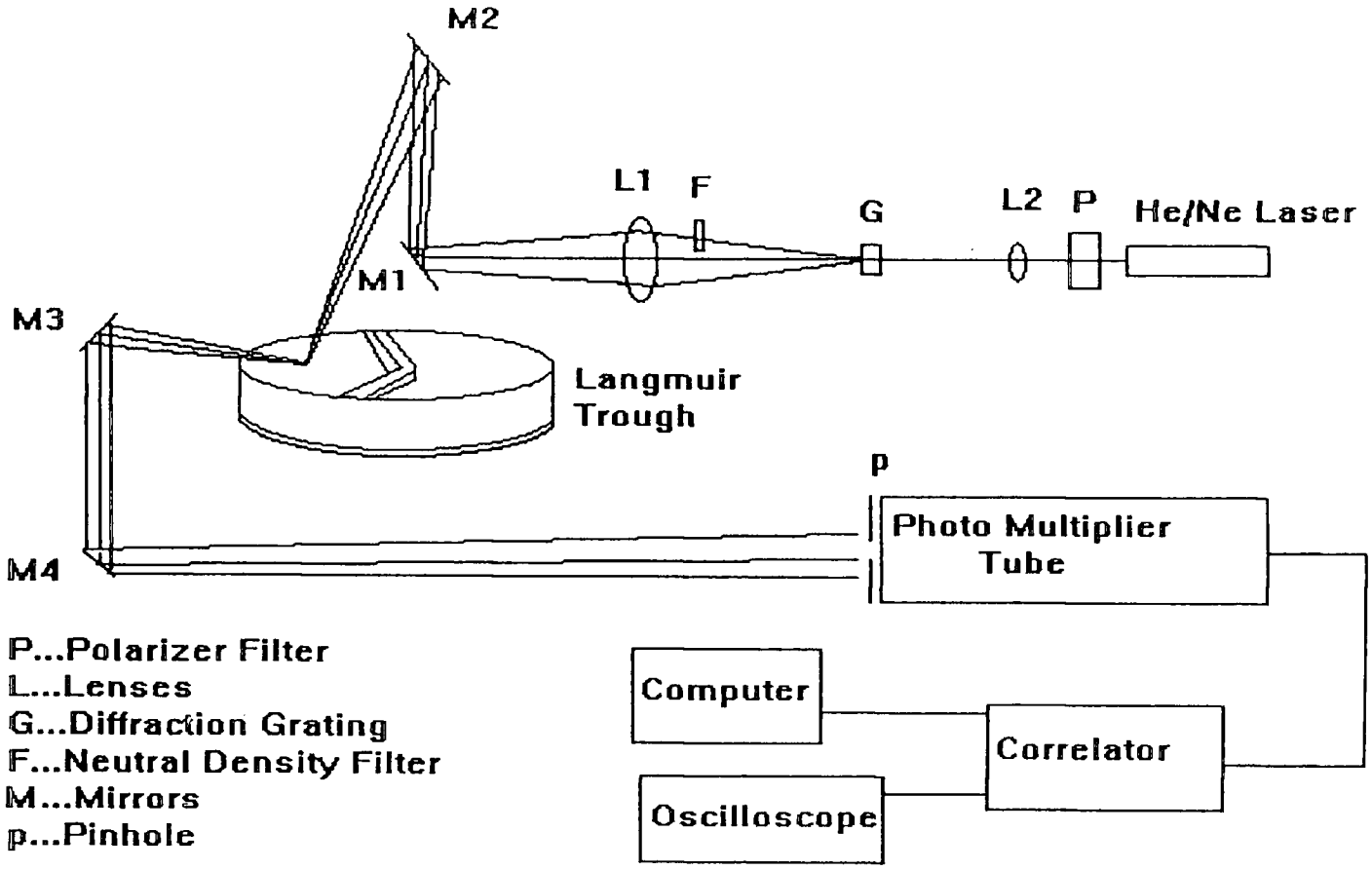

Figure 2.5.2 Surface Quasi-Elastic Light Scattering Experimental Setup

purpose of the second was to guide the reflected light so it could be collected at the PMT detector.

Light from a Siemens He/Ne laser (λ = 632.8nm), power rating 35mW, model No. LGK7626, had its radiation polarised normal to the plane of incidence. After passing through lens L_1 where the focused beam was split into a number of diffraction beams by a transmission diffraction grating (Datasights Ltd., Enfield, Middlesex, UK), G, which acted as a local oscillator. The first diffraction grating (used for surface concentration dependence at fixed q values) consisted of a number of 10μm CrO_2 parallel lines having a centre-centre separation of 100μm, while the second grating consisted of 10μm CrO_2 parallel lines having a centre-centre separation of 150μm. The transmission through this grating was about 90 per cent. Intensities from the second grating were therefore of a greater magnitude. The beam was aligned on the water surface by two research standard mirrors, the first diverting the beam from a horizontal to a vertical orientation, the second turning the beam 90° to the normal with respect to the optical track and downwards on to the liquid surface at about 55°. By optimising the distances between L_1, L_2, and G then the divergent diffraction beams reconverged as a single spot (about 5mm) on the water surface. The beam reflected from the surface was collected by two more research standard mirrors and guided back to a horizontal orientation. The beam consisted of a horizontal series of diffracted reference beams appearing as a series of spots. The central spot was the specular reflection from the main beam and was the brightest but this is not used in SQELS data collection, while the others were the specular reference spots from the diffracted beams (with scattered light mixed in). By adjusting M_4 it was possible to direct any reference beam into the pinhole of the photomultiplier. Several neutral density filters (Kodak Wratten gel filters) were used to attenuate these reference beams to a greatly reduced intensity giving an I_s/I_r ratio where

heterodyne beating was maximised. The output of the PMT was analysed using a 128 channel multi-bit photon correlator (Malvern K7025) with the signal being displayed live on an oscilloscope. The correlator was controlled by means of software on a 486 microcomputer which also stored the data in ASCII file format. Selection of different reference beams allowed values of the wave vectors, q, to be investigated over the range 301 to 900cm^{-1}.

The subphase was pure water (18MΩ resistivity) obtained from an Elgastat UHQ ultrafiltration unit. Before deposition of the monolayer the water surface was aspirated using a Pasteur pipette attached to a vacuum source to remove any surface contamination. The monolayers were spread dropwise as chloroform solutions from a micro syringe. After deposition of the monolayers, about 15 minutes were allowed for solvent evaporation and equilibration of the system. The film was compressed by moving two Teflon barriers at the interface. The surface temperature was maintained at 25°C ±0.1°C by circulating thermostated water through the base of the trough. Simultaneous use of the SQELS and static surface pressure measurements allowed surface pressure to be monitored allowing a direct comparison of results between the two techniques.

2.6 Light Scattering

2.6.1 Materials and sample preparation

Methanol dispersions of the PMMA-b-PEO copolymer were prepared. The methanol solvent (analytical grade) was further purified using a methanol still in order to remove trace amounts of water. The solvent was clarified by filtration at room temperature. A stock solution was prepared by dissolving the copolymer in pure solvent and copolymer solutions were then prepared from this stock solution. The solvent and solutions were filtered through solvent inert Millipore filters of pore size 200 nm. The solutions were held at 50°C overnight in order to allow the formation of unimers, then they were filtered. This process of heating and filtration was repeated several times, the copolymer solutions finally being filtered directly into Burchard light scattering cells which were then sealed.

2.6.2 Light Scattering Measurements

Measurements were made using a Malvern 4700 C system, having a K7032 CE 8-Multibit correlator. An Argon ion laser operating at 488 nm wavelength (Uniphase model No. 2213) was used as the light source. Figure 2.6.1 shows a schematic diagram of the Malvern 4700 Photon Spectrometer. The laser emits monochromatic light which is focused onto the sample cell which is held in a glass vat filled with xylene. The beam is narrowest at its 'waist of focus' which coincides with the axis of rotation of the spectrometer. The xylene in the vat has a similar refractive index as quartz in order to reduce flare occurring at the vat and sample cell interfaces. The xylene in the vat also served the purpose of coupling the sample thermally with the temperature sensor and temperature control element so that the vat contents were within 0.1°C of the required temperature. The optical system used to collect the scattered light is commonly referred to as 'Pusey optics' and the light is sensed by a highly sensitive photomultiplier (P.M.)

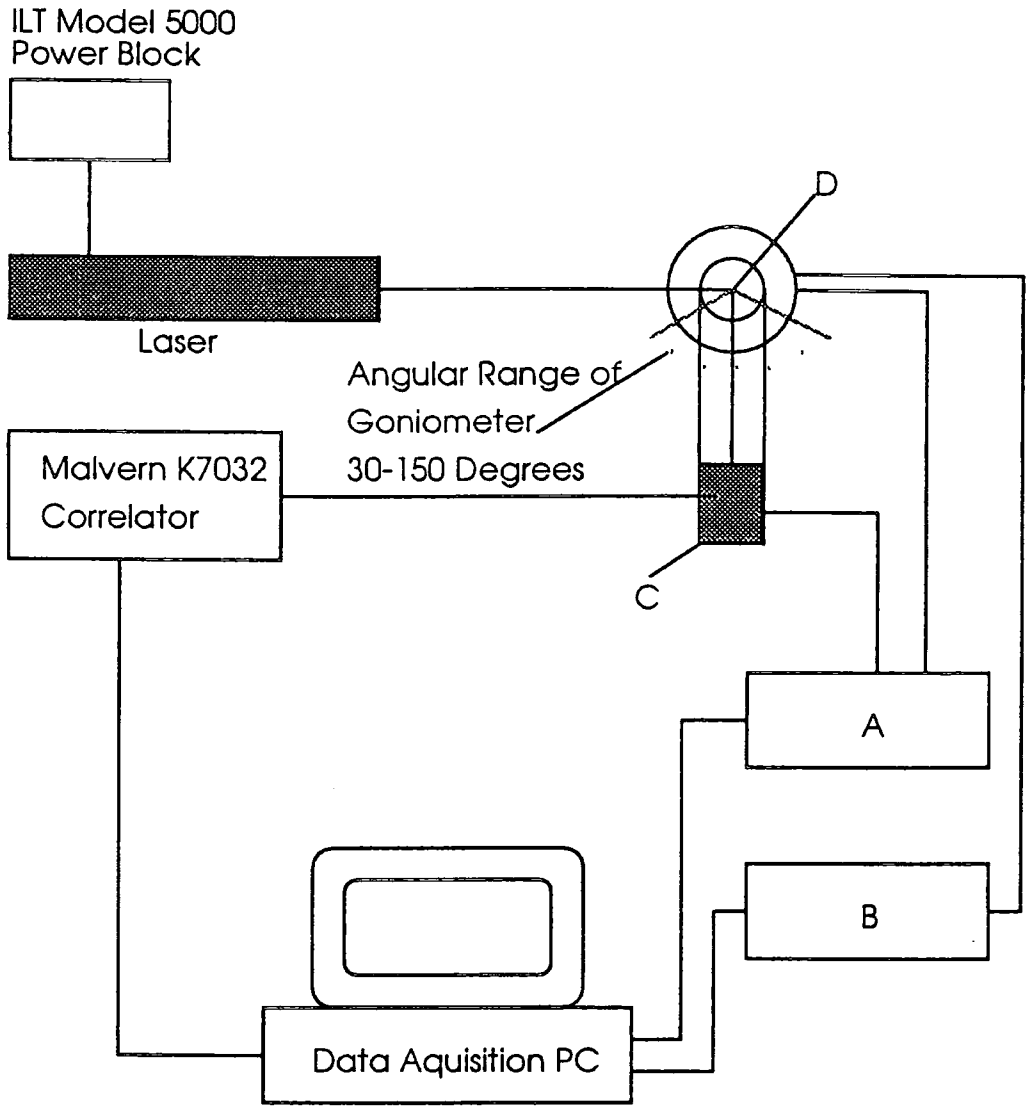

KEY

A. Temperature Controller and P.M. Power Supply

B. Goniometer Controller

C. 488nm Sensitive P.M. Tube Mounted on Goniometer Arm

D. Index Matching Cell

Figure 2.6.1 Malvern 4700 Photon Spectrometer

which can count individual photons. The amount of scattered light detected may be altered by means of an aperture selector located between the optics and the P.M.. Prior to reaching the photomultiplier, the light passes through a narrow band filter and only light with the wavelength of the laser is detected. The P.M. is mounted on an arm which is controlled by a stepper motor controller connected to the computer. Scattering angles between 10° and 150° were possible but here an angle of 90° was used throughout which enabled accurate ratioing of the incident and scattered intensities. These scattering angles are defined as the angle between the detected light and the beam after passing through the sample cell.

The 4700 C system may be used for two types of experiment which both involve variation of both the solution concentration and temperature. The first of these is intensity measurements where the measured quantity is the flux of light reaching the detector from the sample. The second type of experiments analyse fluctuations in the intensity with time scales from a few nanoseconds to seconds. These fluctuations in intensity are due to molecules diffusing under Brownian motion. In this type of experiment the scattered light must be measured from a small volume of sample over a narrow angle. These scattering processes are termed 'coherent' since the phase as well as the amplitude of the scattered radiation determines the instantaneous intensity.

2.6.2.1 Static Light Scattering

Previous work on the thermodynamics of micellization of block copolymers in organic solvents have shown that it is best to have an experimental protocol where the scattered light intensity is measured as a function of temperature at several solution concentrations. The critical micelle temperature (cmt) at these concentrations is taken as the temperature at which micelle formation can just be detected.

2.6.3 Quasi-elastic light scattering

In solution a polymer molecule scatters light due to its refractive index being different from that of the solvent. By allowing laser light to pass through a solution then each polymer molecule acts as a radiating dipole and the total amplitude of the scattered light is the sum of the amplitudes due to single molecules. The incident laser light is vertically polarised and the scattered light is collected in the horizontal plane at an angle θ to the incident radiation. Figure 2.6.2 shows the scattering geometry based upon the von Laue approach to scattering theory. Here, the phase difference between an imaginary particle at the origin and light scattered by the *i*th point particle is

$$\varphi_i = \mathbb{k}.r_i - \mathbb{k}_s - r_i \qquad (2.6.1)$$

where $\mathbb{k}$ is the wave vector of the incident light and has a value of $2\pi n/\lambda_0$ where λ_0 is the wavelength of the incident radiation and n the refractive index of the solution. The shift in wavelength on scattering is negligible and the magnitudes of the scattered wave vector $\mathbb{k}_s$ and $\mathbb{k}$ are equal. The phase difference may be expressed as

$$\varphi_i = (\mathbb{k} - \mathbb{k}_s).r_i = \mathbb{K}.r_i \qquad (2.6.2)$$

where $$|Q| = (4\pi/\lambda_0)\sin(\theta/2) \qquad (2.6.3)$$

In PCS measurements Q is an important parameter which allows the phase difference ϕ_{ij} between two point scatterers i and j, a distance r_{ij} apart, to be determined

$$\phi_{ij} = Q.r_{ij} \qquad (2.6.4)$$

The total amplitude E of scattered light may be obtained from the summation of scattering from individual scatterers

$$E = \Sigma a_i \exp(iQ.r_i) = a\Sigma\exp(iQ.r_i) \qquad (2.6.5)$$

for N identical particles with amplitude factor *a*. The average value of the intensity (I) will remain constant but the instantaneous value of I(t)(= E(t)E*(t)) fluctuates about the

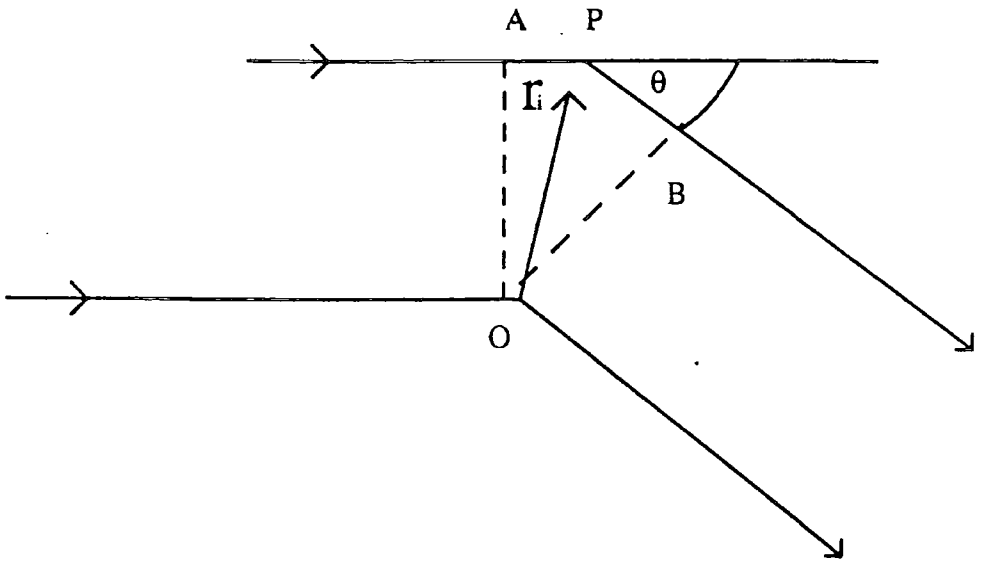

Figure 2.6.2a) Path difference (between source and detector) for light scattered through an angle θ by particles at O and P is APB

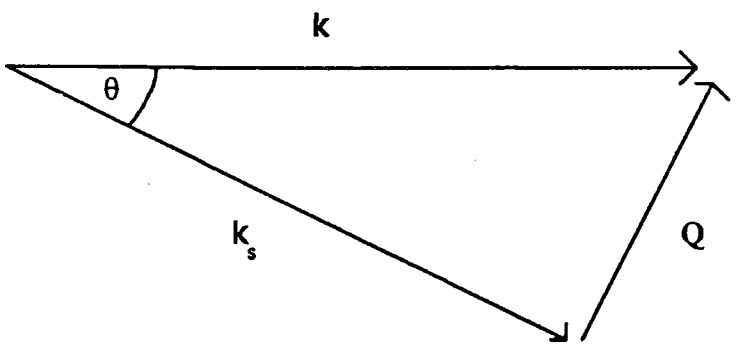

2.6.2b) The scattering vector $\mathbf{Q} = \mathbf{k} - \mathbf{k}_s$

mean value due to particle movement. By considering diffusion processes then the mean square displacement of a particle in a time τ is

$$\overline{\Delta r^2} = 6D\tau \qquad (2.6.6)$$

where D is the diffusion coefficient.

Information concerning the dynamics of the motion of molecules may be extracted from the correlation function $C(\tau)$ of the scattered light using a digital correlator

$$C(\tau) = \frac{\langle I(t)I(t+\tau)\rangle}{\langle I^2(t)\rangle} = \frac{\lim_{T\to\infty}\frac{1}{T}\int_0^T I(t)I(t+\tau)dt}{\lim_{T\to\infty}\frac{1}{T}\int_0^T I^2(t)dt} \qquad (2.6.7)$$

where the term on the denominator normalises the function. $C(\tau)$ is the time-averaged value of the product of the instantaneous intensities at two discrete times which are separated by an interval τ.

Since the system is a stationary process where the average values of quantities such as intensity do not change over the experimental duration then $C(\tau)$ is an average over the behaviour of all the particles. It is possible to express $C(\tau)$ in terms of the amplitude of the optical field $E(\tau)$ when it is a second order correlation function of E. The symbol $G^{(2)}(\tau)$ is used to represent the unnormalised form

$$G^{(2)}(\tau) = \langle I(t)I(t+\tau)\rangle = \langle E(t)E^*(t)E(t+\tau)E^*(t+\tau)\rangle \qquad (2.6.8)$$

while the normalised form is given the symbol $g^{(2)}(\tau)$. For light with Gaussian statistics, the Siegert relation relates $g^{(2)}(\tau)$ to the first-order correlation function $g^{(1)}(\tau)$

$$g^{(2)}(\tau) = 1 + |g^{(1)}(\tau)|^2 \qquad (2.6.9)$$

where $$g^{(1)}(\tau) = \langle E(t)E^*(t+\tau)\rangle / \langle E(t)E^*(t)\rangle \qquad (2.6.10)$$

For a system consisting of scattering from N particles, $g^{(1)}(\tau)$ can be written in unnormalised form as $S(Q,\tau)$ which is called the dynamic structure factor

$$S(Q,\tau) = S(Q,0)\exp(-DK^2\tau) = S(Q,0)\exp(-\Gamma\tau) \qquad (2.6.11)$$

where D is the diffusion coefficient and $\Gamma = DK^2$.

References

1. Jakeman, E., Photon Correlation and Light Beating Spectroscopy, Edited by H.Z. Cummins and E.R. Pike, Plenum, New York, 1974, pp. 75-149.
2. Oliver, C.J., Photon Correlation and Light Beating Spectroscopy, Edited by H.Z. Cummins and E.R. Pike, Plenum, New York, 1974, pp. 151-223.
3. Earnshaw, J.C., McGivern, R.C., Winch, P.J., *J. Phys. (Paris)*, **1988**, 49, 1271.
4. Earnshaw, J.C., McGivern, R.C., McLaughlin, A.C., Winch, P.J., *Langmuir*, **1990**, 6, 649.

CHAPTER 3 - SURFACE PRESSURE STUDIES

3.1 Copolymers spread on water subphase

Surface pressure isotherms were measured for each block copolymer used in the neutron reflectivity experiments to be discussed later in Chapter 4. It was important that the isotherms of the selectively deuterated and hydrogenous block copolymers had similar behaviour since the neutron reflectivity data from each was analysed together to characterise the interface. All measurements were repeated several times under identical conditions to reduce uncertainty in the results.

Figure 3.1 shows an example of a surface pressure isotherm obtained at a barrier compression rate of 30cm^2/min and superimposed are the isotherms of the corresponding PMMA and PEO homopolymers. The 'lift off' in surface pressure is observed at 0.6mg/m^2, the characteristic 'knee' in the isotherm being attributed to the poly(ethylene oxide) block of the copolymer. In this region the surface pressure rises steeply from zero to a flatter region between 6 and 8mN/m. This behaviour is similar to that of PEO homopolymer where the isotherm reaches a plateau at 10mN/m, regarded as its collapse surface pressure. At about 1.6mg/m^2 there is a transition point where the surface pressure increases steeply and this is attributed to the presence of the PMMA block. The monolayer collapses at about 3.00mg/m^2 and the surface pressure at this point is slightly less than that for PMMA homopolymer.

Figures 3.2 and 3.3 show repeated measurements of the same surface pressure isotherm in order to assess the reproducibility of the data. Surface pressure measurements at low surface concentrations were very reproducible, but at higher surface concentrations there were deviations in the data. These deviations were due mainly to minute differences in the amount of copolymer at the surface caused by minute differences in the spread volume. These differences become more apparent at high surface concentration due to the high compression of the film. Another factor responsible for the lack of

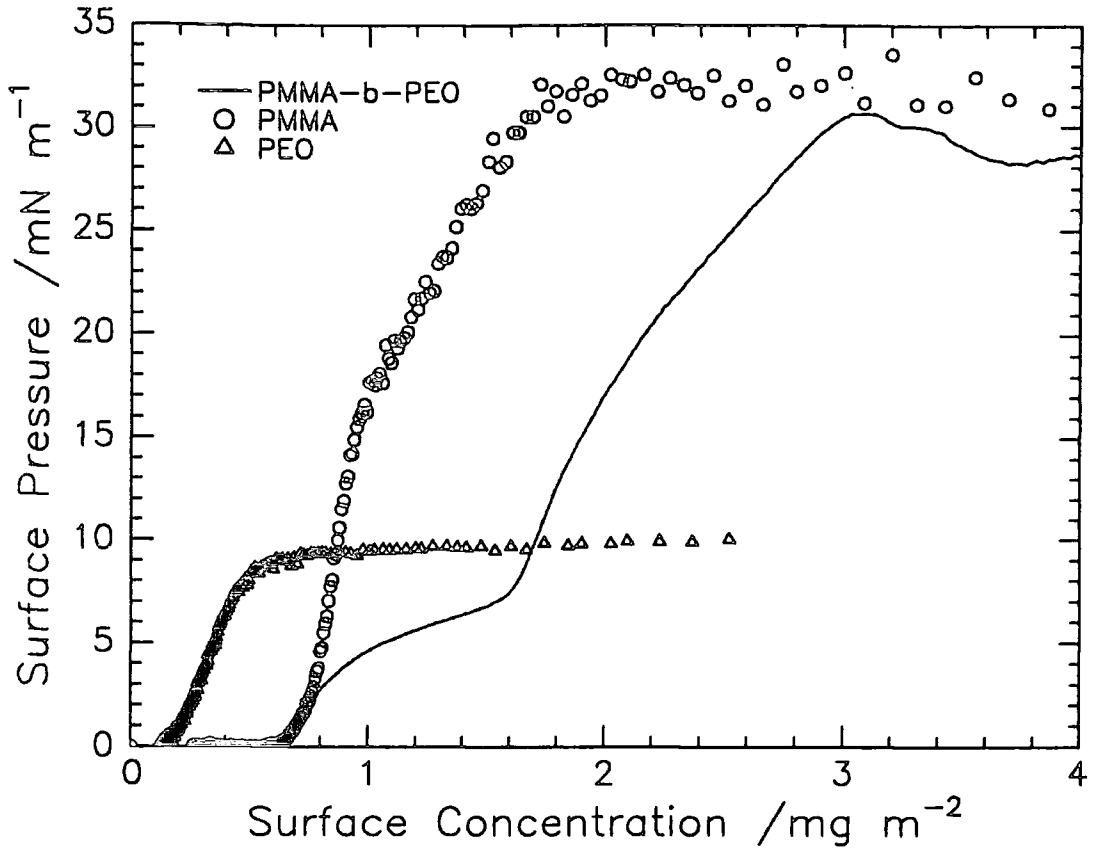

Figure 3.1 Surface Pressure Isotherms PMMA and PEO homopolymers superimposed on DMHE isotherm at 25°C

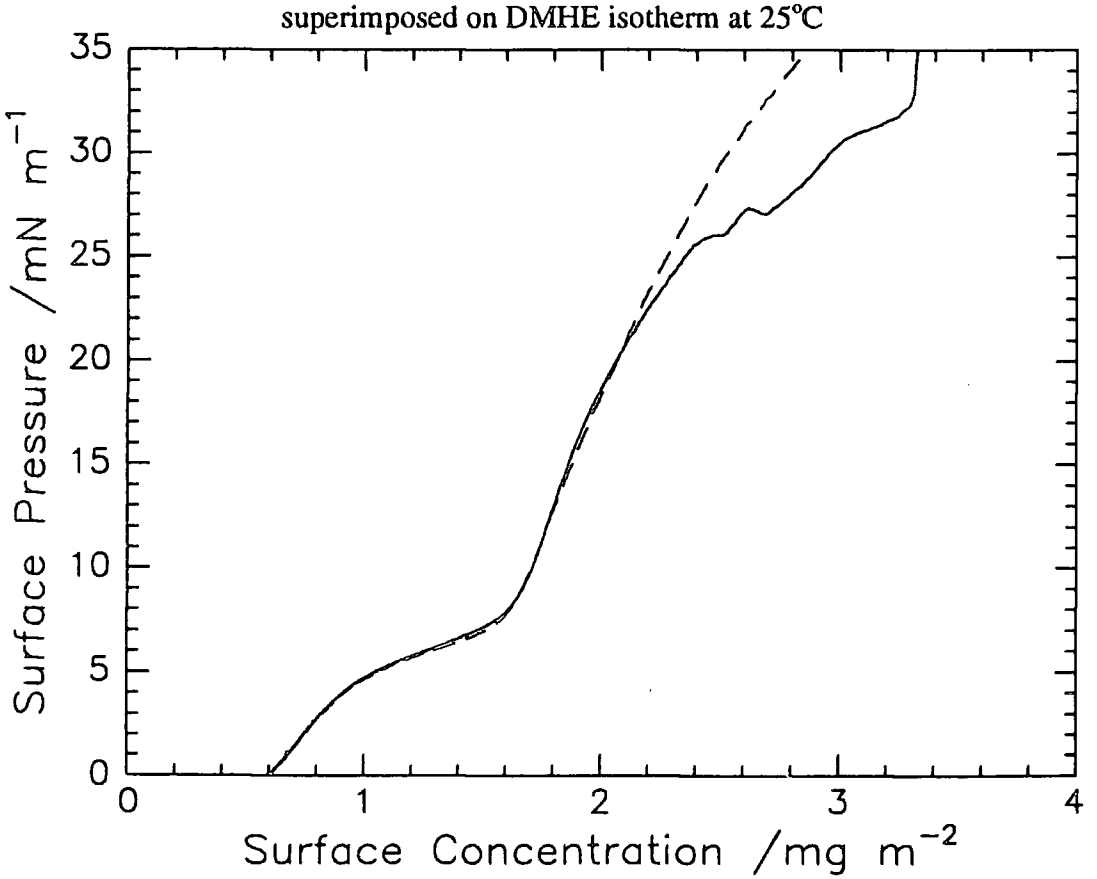

Figure 3.2 Repeated Surface Pressure Isotherms for DMHE at 20°C

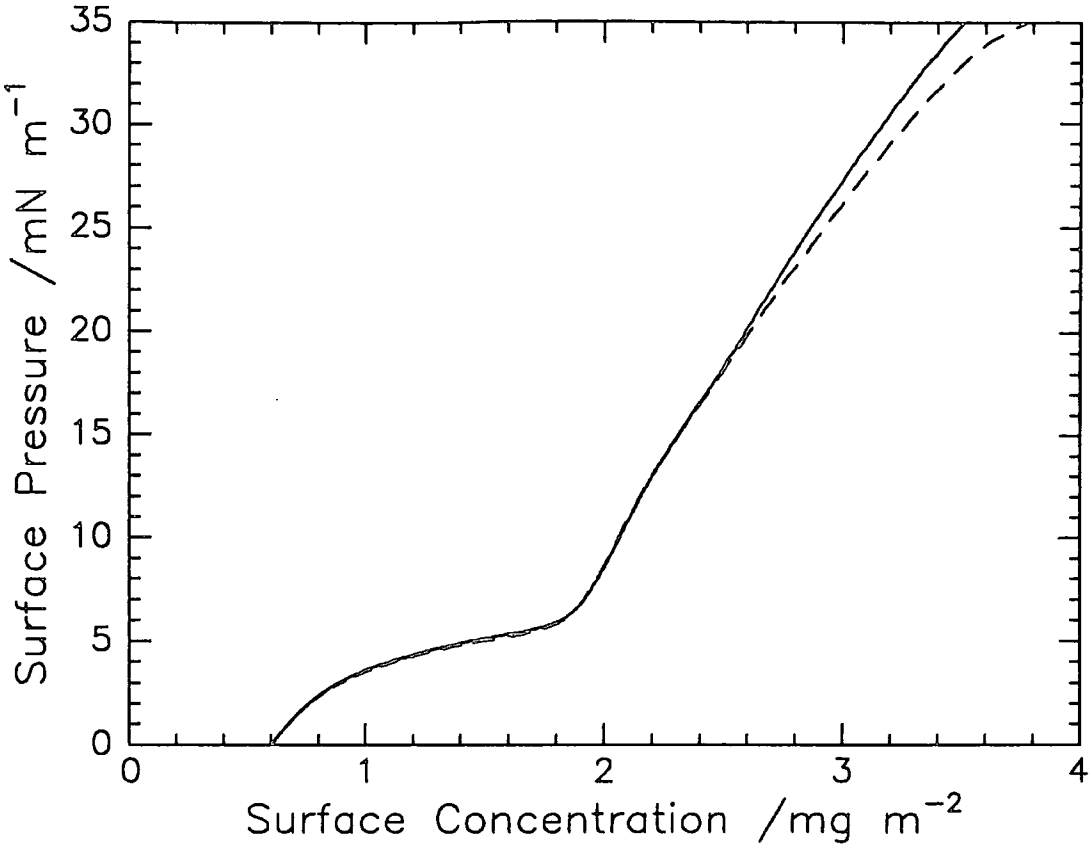

Figure 3.3 Repeated Surface Pressure Isotherms for DMDE at 25°C

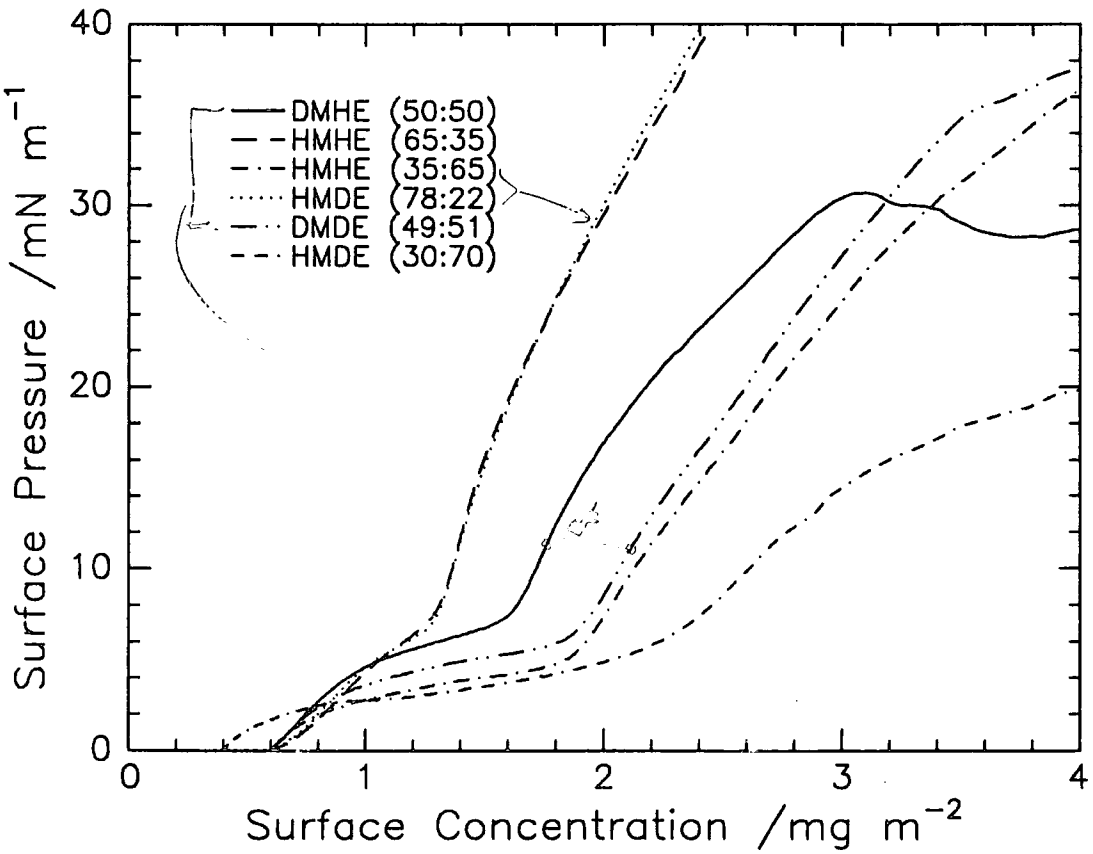

Figure 3.4 Effect of Composition on Surface Pressure Isotherms.
Inset shows mole ratios MMA:EO

reproducibility at high surface concentration is surface contamination. This contamination is difficult to eradicate completely even by cleaning the surface by several repeated cycles of sweeping the surface with the barriers then aspirating until no rise in surface pressure is noticed on compression of the barriers. Theories used in the analysis of surface pressure data are relevant in the semi-dilute region so deviations at high surface concentration lose their significance.

Figure 3.4 compares the effect of copolymer composition on the surface pressure isotherms. It can be seen that the width of the 'knee' regions increases with the molar fraction of PEO in the copolymer. The limiting area per molecule is classically used to describe surface pressure isotherms and is obtained by extrapolating the initial steep rise in surface pressure to zero concentration. For macromolecular films the limiting area per monomer (apm) is used which is obtained using the limiting surface concentration and the monomer molecular weight. The limiting surface concentrations and corresponding limiting areas per monomer unit of surface pressure onset for the PMMA block are shown in Table 3.1. The apm values, calculated by taking an average value of the monomer molecular weight, were slightly less than that for PMMA homopolymer but significantly smaller than that of PEO homopolymer.

Further information can be extracted from the surface pressure isotherms by re-plotting the data as double logarithmic plots, allowing values of the critical scaling exponent ν (the exponent in two-dimensional scaling laws) to be determined for each copolymer block as described in Chapter 1. For copolymers the value of ν depends on both intramolecular and intermolecular interactions with the subphase and is not as physically realistic as that obtained for homopolymers. Figure 3.5 shows an example of a double logarithmic plot fitted using linear least squares analysis and the magnitude of the slope y was used to calculate ν from the relationship $y = 2\nu/(2\nu-1)$. Figures 3.6 to 3.10 show the

Polymer	Γ_{lim}/mg m^{-2}	apm$_{lim}$/Å
homo PMMA	1.10	15
homo-PEO	0.17	43
DMHE (BR20)	1.32	10
HMHE (BR21)	1.14	12
HMHE (BR22)	1.59	7
HMDE (BR26)	1.23	12
DMDE (BR27)	1.55	8
HMDE (BR29)	1.84	6

Table 3.1 Limiting Surface Concentrations and area per monomer for PMMA block

Polymer	T/K	slope	ν
DMHE (BR20)	288	5.07	0.62
	293	4.61	0.64
	298	4.86	0.63
	303	4.36	0.65
	308	3.73	0.68
HMHE (BR21)	288	6.28	0.59
	293	6.77	0.59
	298	5.77	0.60
	303	5.42	0.61
	308	4.46	0.64
HMHE (BR22)	288	6.44	0.59
	293	6.07	0.60
	298	5.04	0.62
	303	4.84	0.63
	308	4.42	0.65
HMDE (BR26)	288	6.76	0.59
	293	7.05	0.58
	298	5.90	0.60
	303	5.55	0.61
	308	4.85	0.63
DMDE (BR27)	288	6.40	0.59
	293	5.02	0.62
	298	4.84	0.63
	303	4.15	0.66
	308	3.91	0.67

Table 3.2 Critical Scaling Exponents for PMMA block

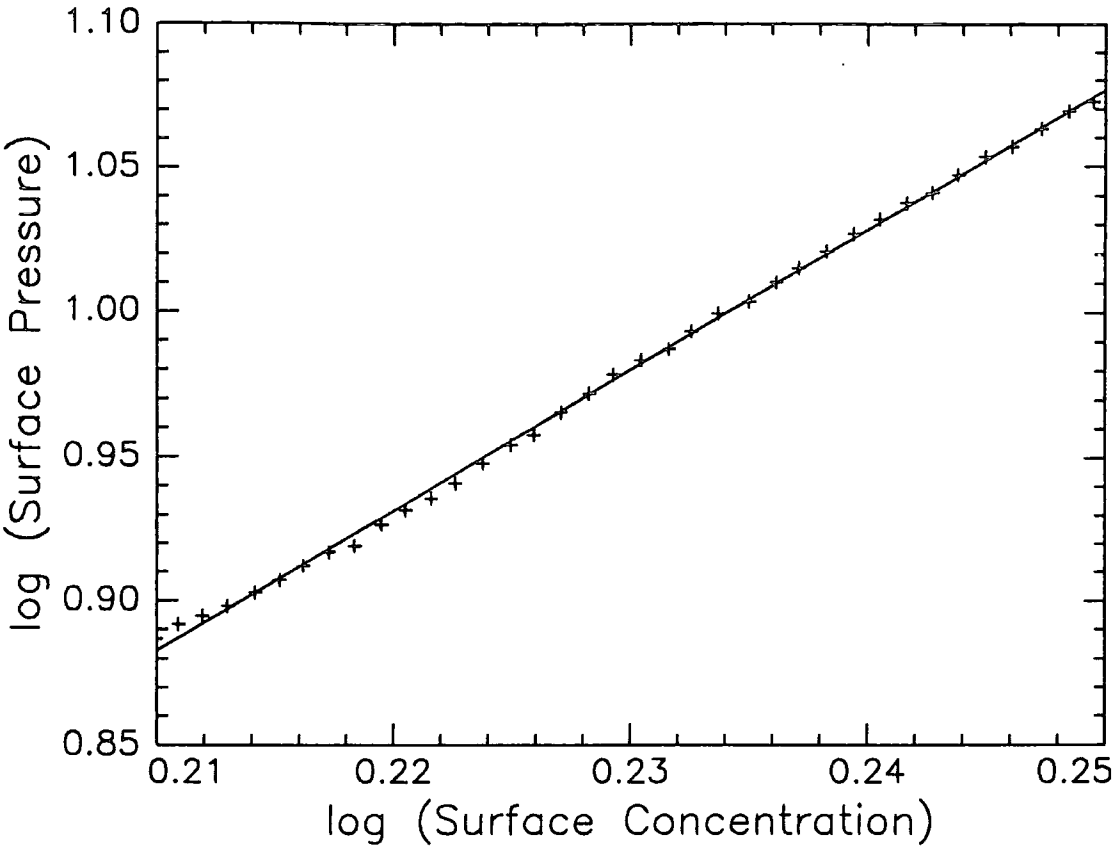

Figure 3.5 Double Logarithmic Plot of Surface Pressure Isotherm of DMHE at 25°C

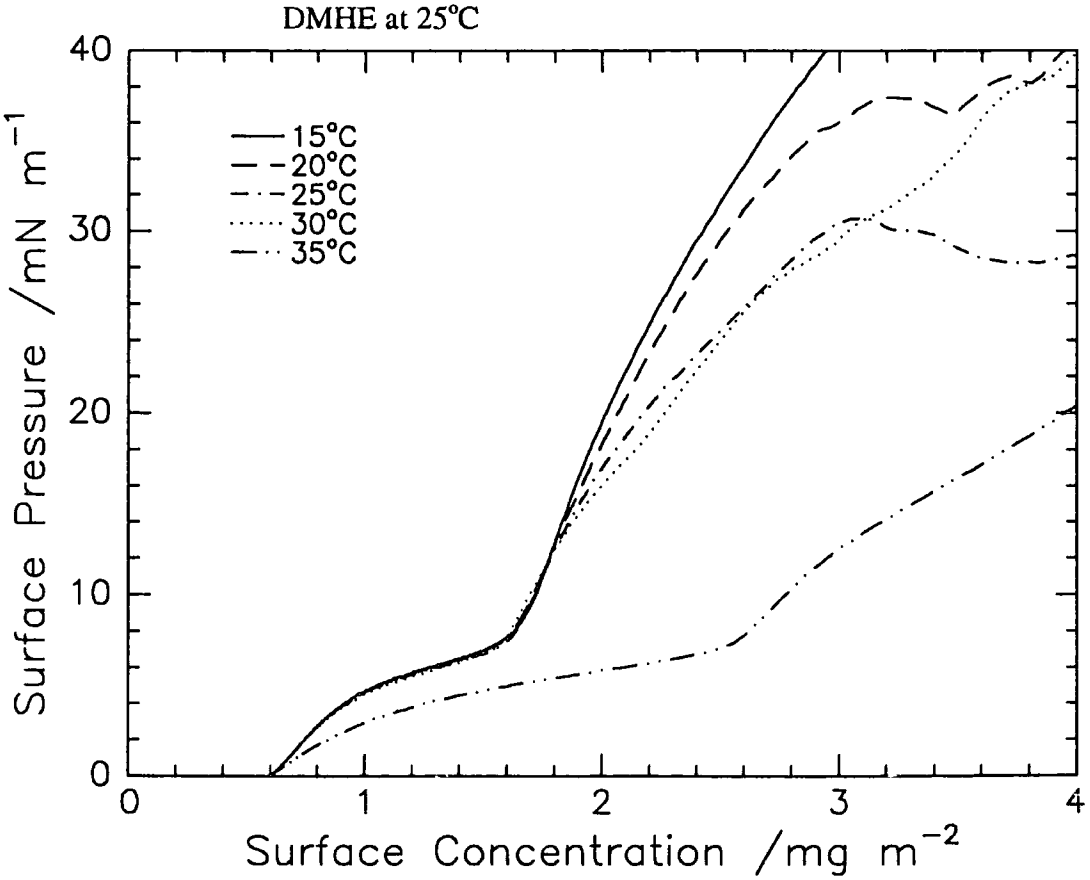

Figure 3.6 Temperature Dependence of DMHE (BR20) Surface Pressure Isotherms

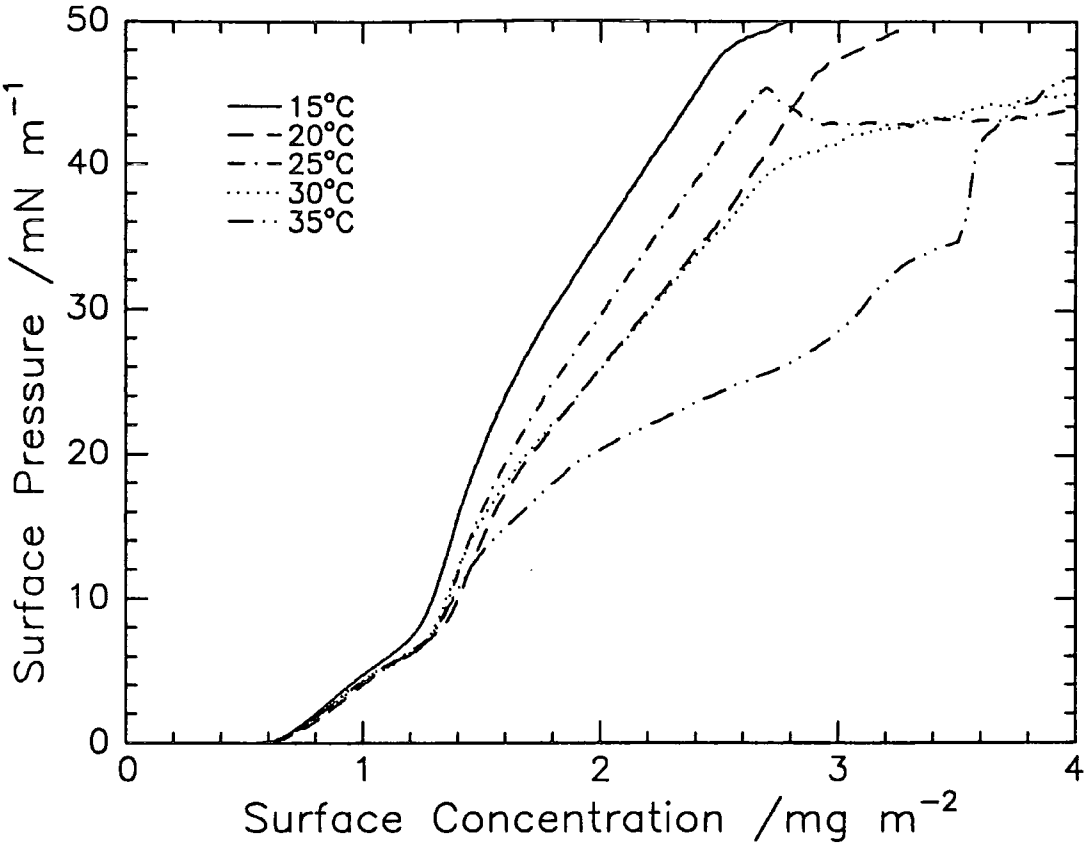

Figure 3.7 Temperature Dependence of HMHE (BR21) Surface Pressure Isotherms

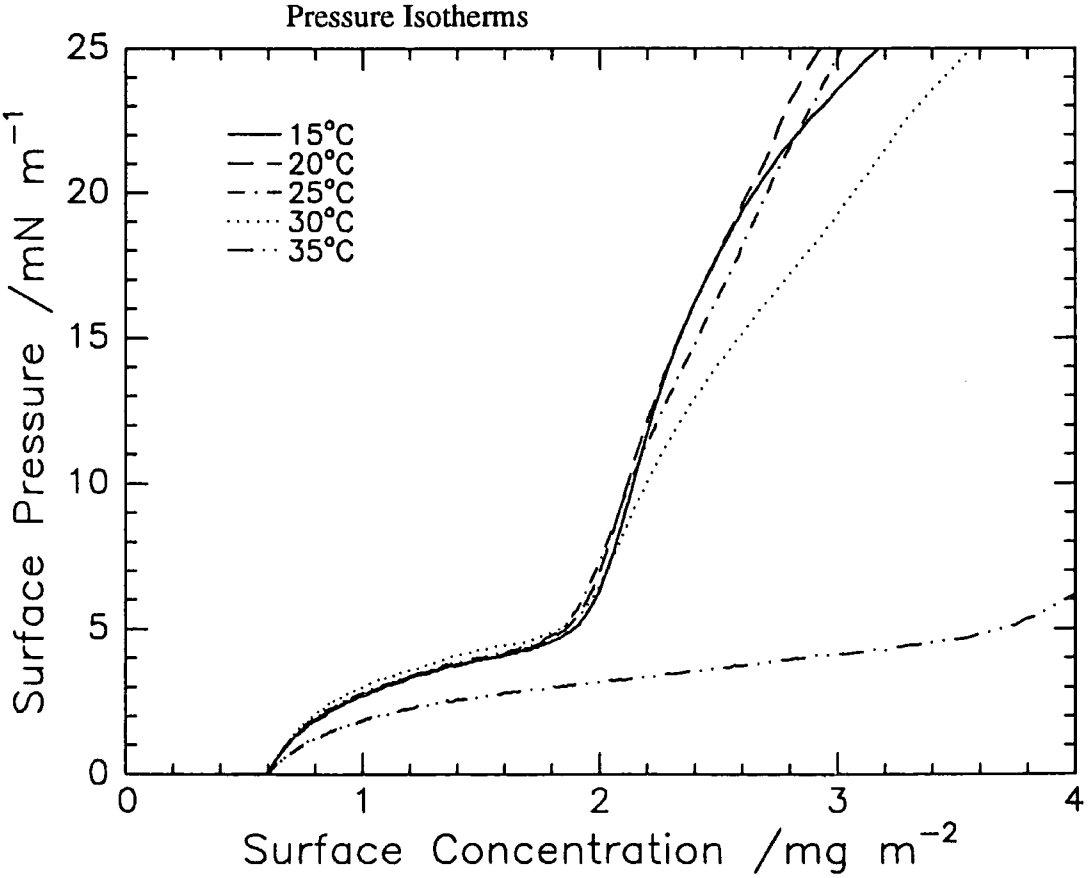

Figure 3.8 Temperature Dependence of HMHE (BR22) Surface Pressure Isotherms

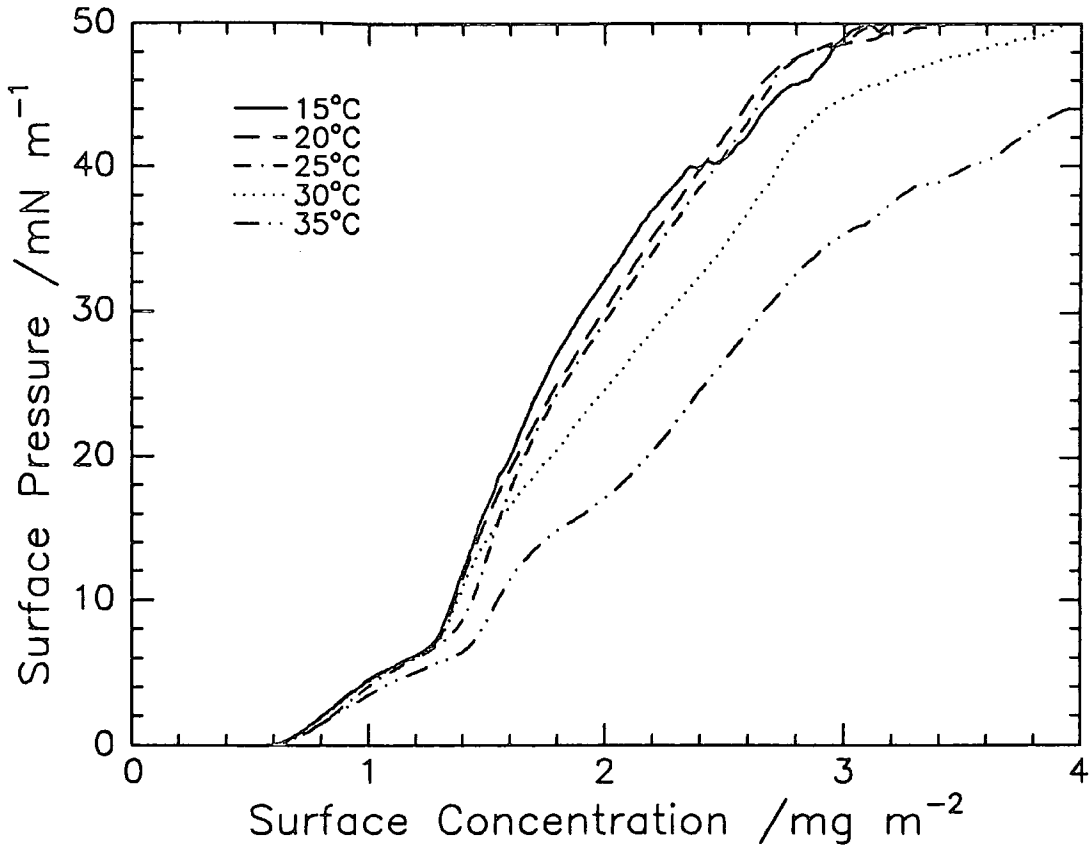

Figure 3.9 Temperature Dependence of HMDE (BR26) Surface Pressure Isotherms

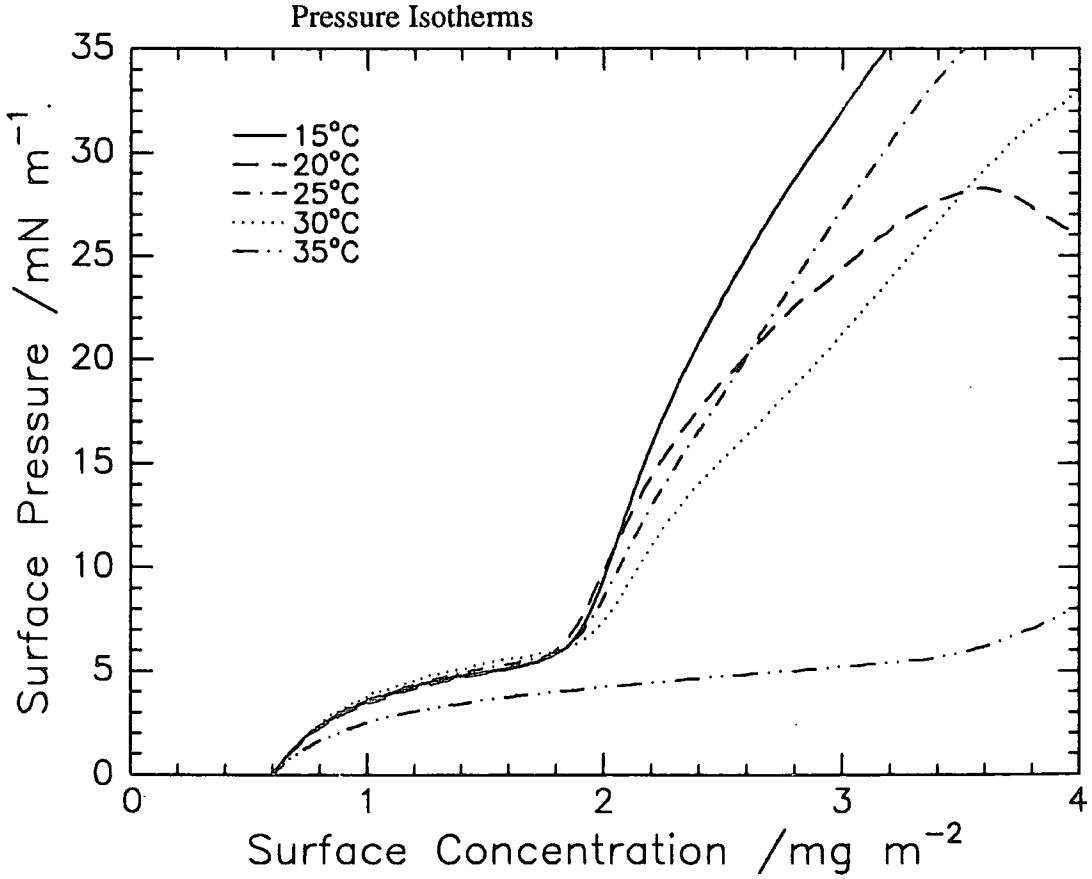

Figure 3.10 Temperature Dependence of DMDE (BR27) Surface Pressure Isotherms

temperature dependence of the surface pressure isotherms for each copolymer and the values are summarised in Table 3.2. The values of ν for the copolymer differ from those of PMMA and PEO homopolymer. Rondelez et al[1] obtained $\nu = 0.53$ for several narrow fractions of syndiotactic PMMA with a range of molecular weights from 3,300 to 1,600,000, this value was also temperature independent. Rondelez also obtained $\nu = 0.77$ for isotactic PMMA. The PMMA block of the copolymers in this work were predominantly atactic and contained about 2-4% isotacticity. The value of ν was obviously due to the combined effect of the PMMA and PEO blocks, the isotactic content of the PMMA having a negligible effect.. These values are intermediate between monolayers in the theta condition ($\nu = 0.56$) and those in good 2-D solvent conditions ($\nu = 0.77$). Higher values of ν are indicative of the film being in good solvent conditions, i.e. favourable segment-solvent conditions. PEO homopolymer has a value of $\nu = 0.77$ and this could explain the intermediate value. Table 3.2 shows that the value of ν approaches good solvent conditions as the temperature increases. Since the solubility of PEO in water decreases with increasing temperature then the PEO block would be expected to be more intermixed with the PMMA block giving rise to a liquid expanded behaviour.

3.2 K_2SO_4 subphases

Surface pressure isotherms were obtained using various aqueous K_2SO_4 subphases of 0.20M, 0.40M, 0.60M and 0.70M solution concentration (figure 3.11). These measurements were taken at a temperature of 298K and an additional measurement made at 307K with a 0.45M K_2SO_4 subphase. This additional measurement was at bulk theta conditions for PEO homopolymer. The surface pressure was lower for copolymer spread on 0.7M K_2SO_4 subphase, indicative of more polymer being in the immediate surface layer. Table 3.3 summarises the apm values and a slight increase can be seen with

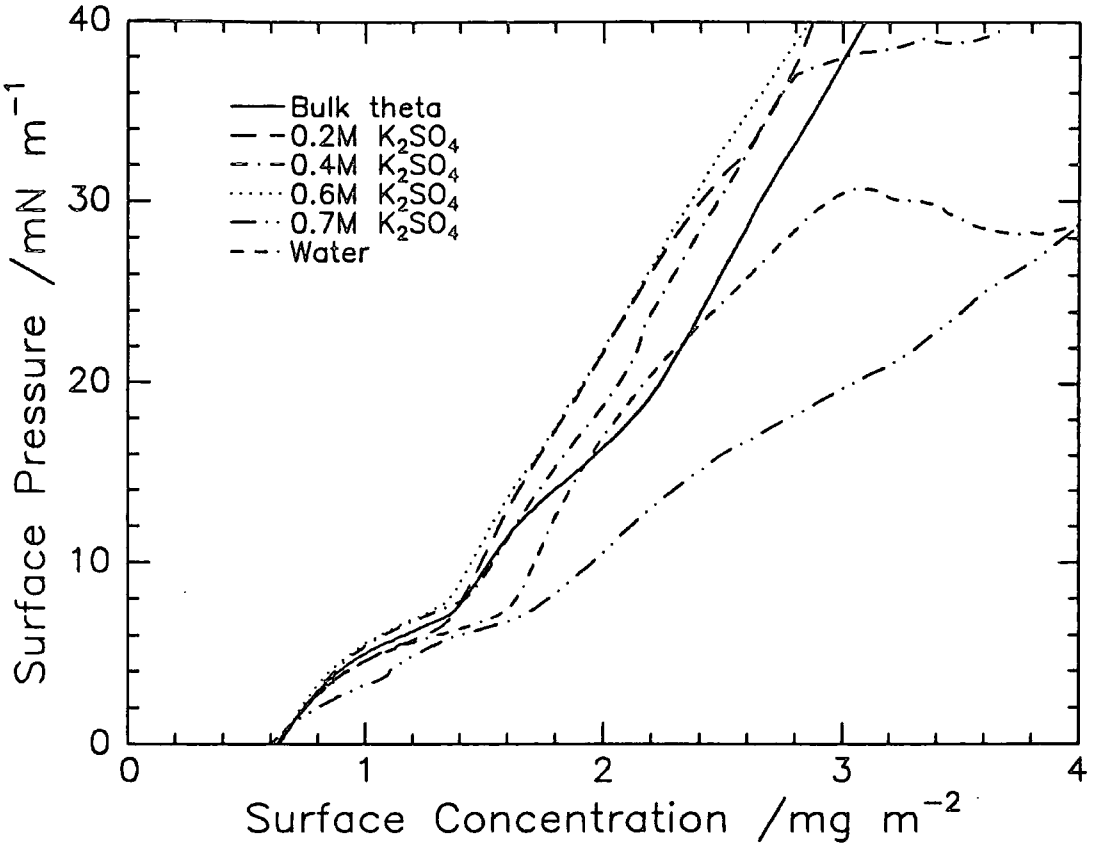

Figure 3.11 Surface Pressure Isotherms for DMHE (BR20) spread on an aqueous subphase with K_2SO_4 molarities indicated. Bulk theta indicates a subphase of 0.45M K_2SO_4 at a temperature of 307K.

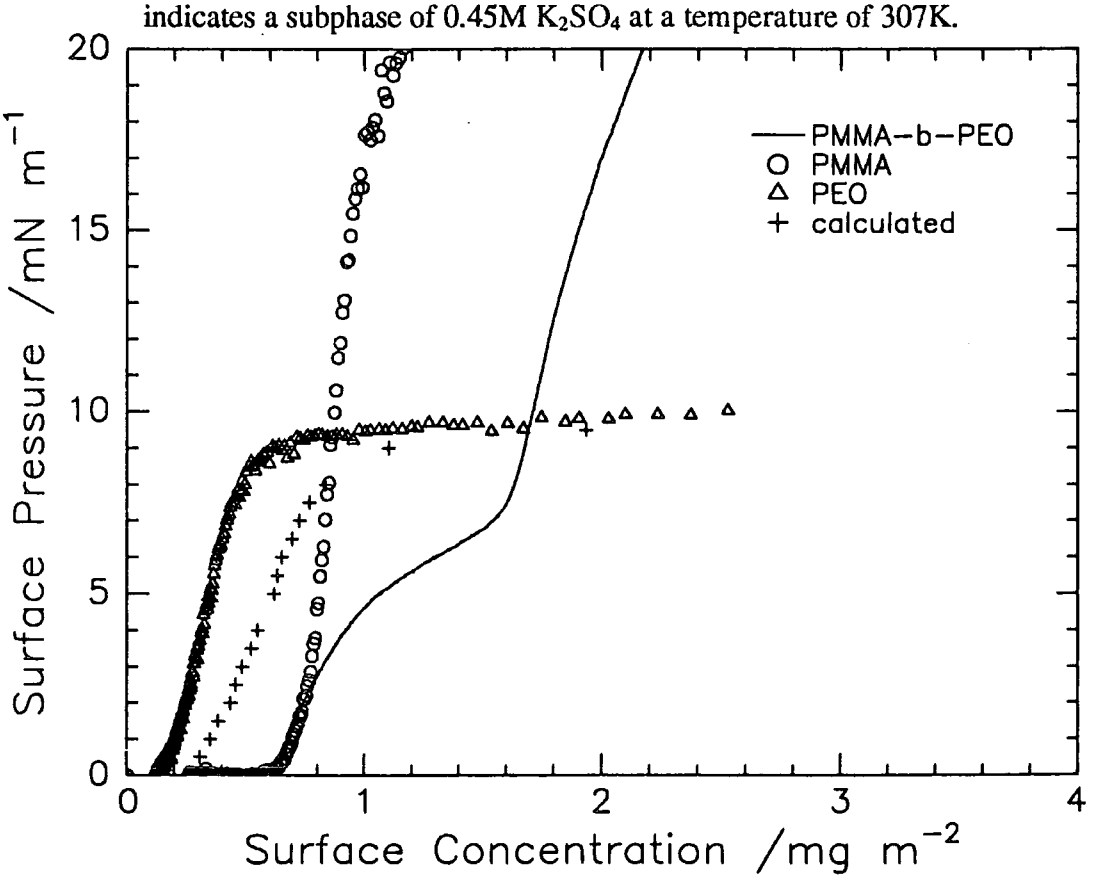

Figure 3.12 Goodrich-Gaines area additivity at given π values (calculated from isotherms of PMMA/PEO homopolymers) compared with actual surface pressure isotherm of DMHE (BR20) at 25°C

Subphase	T/K	Γ_{lim}/mg m^{-2}	apm$_{lim}$/Å
H_2O	298	1.32	10
0.20M K_2SO_4	298	1.08	12
0.40M K_2SO_4	298	1.05	12
0.60M K_2SO_4	298	0.98	13
0.70M K_2SO_4	298	1.08	12
0.45M K_2SO_4	307	0.97	13

Table 3.3 Limiting Surface Concentrations and area per monomer for PMMA block of copolymer on K_2SO_4 subphase

Subphase	T/K	slope	ν
H_2O	298	5.07	0.62
0.20M K_2SO_4	298	3.74	0.68
0.40M K_2SO_4	298	3.27	0.72
0.60M K_2SO_4	298	3.15	0.73
0.70M K_2SO_4	298	2.28	0.89
0.45M K_2SO_4	307	3.06	0.74

Table 3.4 Critical Scaling Exponents for PMMA block of copolymer on K_2SO_4 subphase

Copolymer	Mole ratio MMA:EO	ΔG^E J/mole monomer
BR29	30:70	-741
BR22	35:65	-687
BR27	49:51	-482
BR20	50:50	-409
BR21	65:35	-391
BR26	78:22	-301

Table 3.5 Excess Gibbs free energy of mixing, ΔG^E for the block copolymers at 25°C

increasing K_2SO_4 concentration. Table 3.4 summarises the ν values for the PMMA block and they increase slightly with increasing concentration of K_2SO_4 in the subphase. This trend is indicative of a change in the thermodynamics of the interaction between the copolymer and the subphase. The PEO-water interaction decreases with increasing temperature and the PMMA-PEO interaction increases thereby raising ν. The results suggest that the average segment adopts a more extended conformation at 0.45M and 0.60M K_2SO_4 subphase

3.3 Effect of rate of compression of barriers

The rate of compression of the barriers had little effect on the surface pressure isotherms. At higher surface concentrations overcompression led to overshoot of the surface pressure or premature collapse of the film. The effect of overcompression was largely due to the mobility of the chains in the film and the time taken for them to respond to the compression. At low surface concentrations the chains in the monolayer are less constrained and have a very small relaxation time compared with the barrier speed. At high surface concentrations the chains were much closer to each other and their mobility was decreased, therefore their relaxation times increased.

3.4 Thermodynamics of the monolayers

Diblock copolymers are analagous to a binary polymer system consisting of two homopolymers when spread at the air/water interface. In the following, two approaches have been attempted for the investigation of the thermodynamic nature of the monolayers.

3.4.1 Method 1

The miscibility of binary systems at the air/water interface can investigated by applying the ideas of Goodrich and Gaines (an area additivity rule) to the surface pressure isotherms[2]. Systems studied fall into three categories (i) immiscibility, (ii) ideal

miscibility, (iii) nonideal miscibility. The Goodrich-Gaines thermodynamic model may be applied to ideal miscible and immiscible monolayers. For polymeric systems the usual convention is to use area per monomer unit rather than area per molecule. For a two component polymer system the average area per monomer unit, $\langle A \rangle$, is

$$\langle A(\Pi) \rangle^{ideal} = \langle A(\Pi) \rangle^{immiscible} = X_1 A_1^{\circ}(\Pi) + X_2 A_2^{\circ}(\Pi) \qquad (3.1)$$

where X_1 and X_2 are the mole fractions of homopolymers 1 and 2, and A_1° and A_2° are the areas per monomer unit of the component homopolymers at the same surface pressure. The superscripted dots refer to quantities of the pure component films. Here surface concentration Γ is used as the abscissa and is the sum of the component partial surface concentrations at each surface pressure. Equation 3.1 then becomes

$$\langle \Gamma(\Pi) \rangle^{ideal} = \langle \Gamma(\Pi) \rangle^{immiscible} = X_{mma} \Gamma_{mma}^{\circ}(\Pi) + X_{eo} \Gamma_{eo}^{\circ}(\Pi) \qquad (3.2)$$

where X_{mma} and X_{eo} are the mole fractions of the MMA and EO blocks respectively in the copolymer, and Γ_{mma}° and Γ_{eo}° are surface concentrations of the constituent homopolymers. The surface concentration was therefore calculated for each surface pressure (upto the collapse surface pressure of PEO at 10mN/m) from the corresponding surface concentration. Figures 3.12 to 3.17 compare the surface pressure isotherms for the homopolymers, the Goodrich-Gaines additivity and the actual surface pressure isotherm of each diblock copolymer.

The surface pressures of the co-added partial surface concentrations in figures 3.12 to 3.17 are below the PEO collapse pressure and are confined mainly between the isotherms of the homopolymers. The experimental surface pressure isotherms exhibit large negative deviations from the calculated isotherms. Similar negative excess areas were reported for binary mixtures of poly(vinyl acetate)/polydimethylsiloxane (PVA/PDMS)[3] and PDMS with PMMA and cellulose acetate[4]. These systems were interpreted in terms of the interactions occurring between the polymers assuming a miscible monolayer structure.

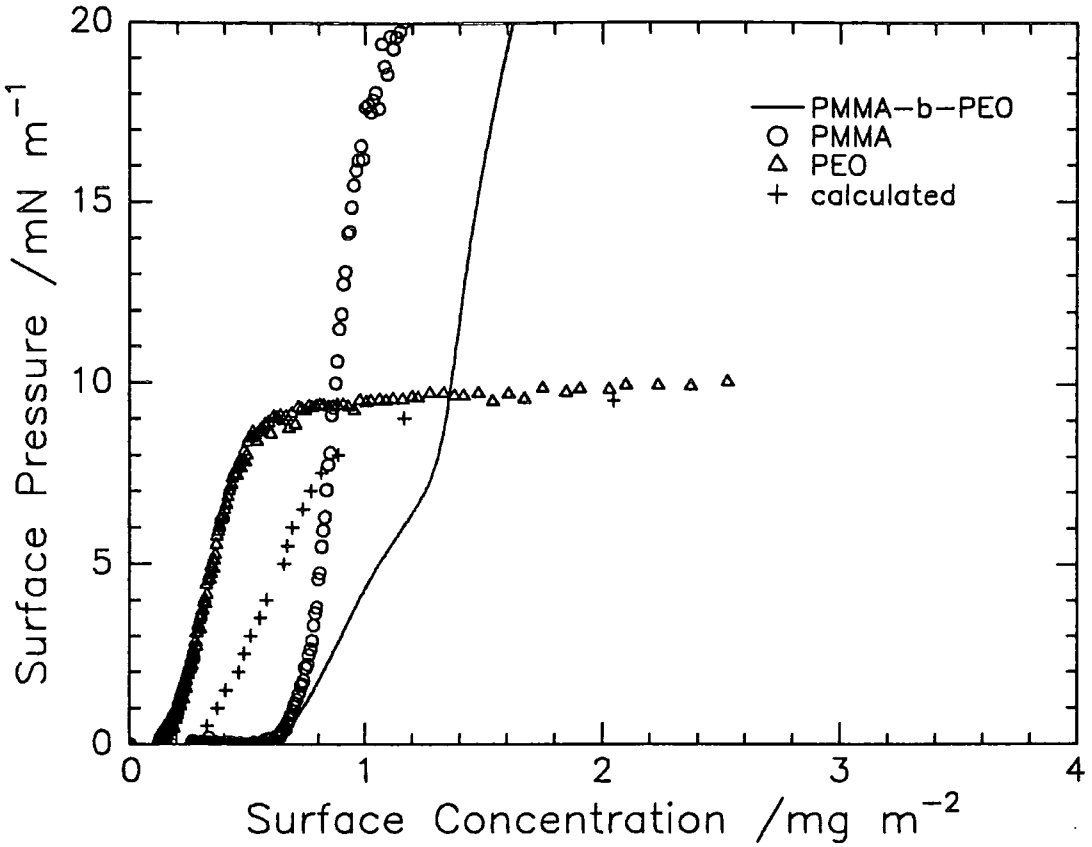

Figure 3.13 Goodrich-Gaines area additivity at given π values (calculated from isotherms of PMMA/PEO homopolymers) compared with actual surface pressure isotherm of HMHE (BR21) at 25°C

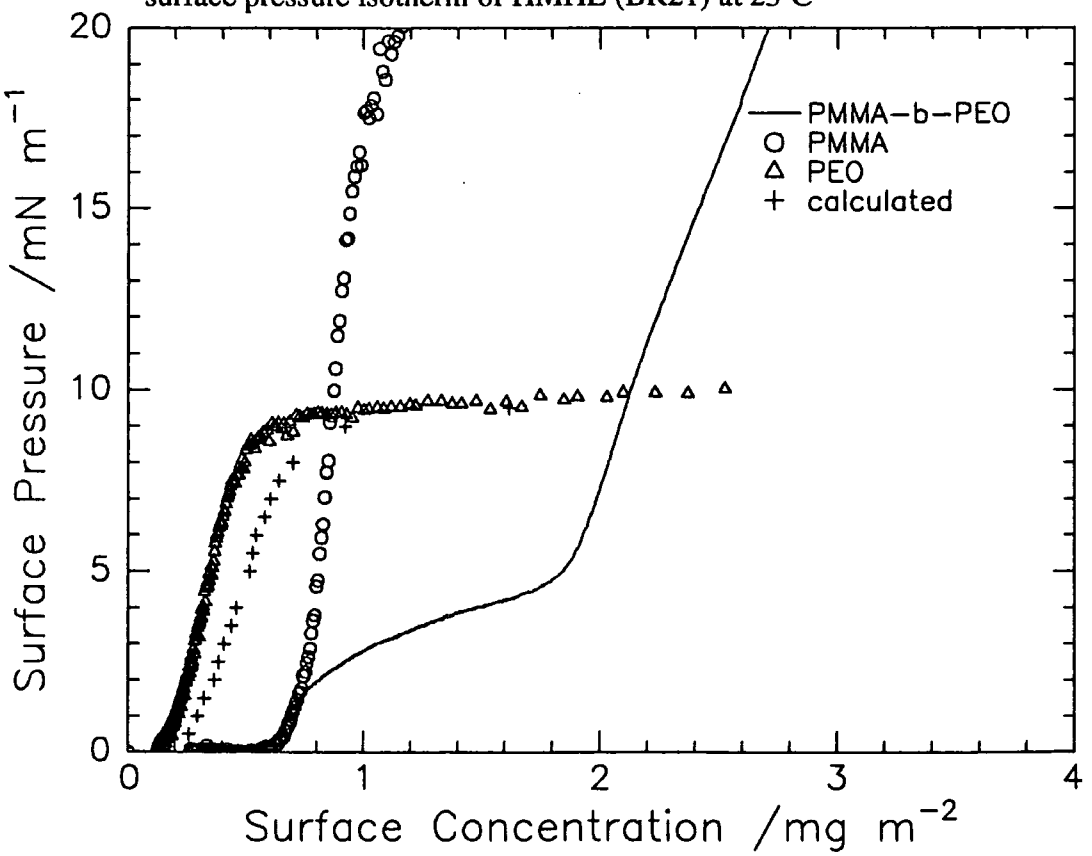

Figure 3.14 Goodrich-Gaines area additivity at given π values (calculated from isotherms of PMMA/PEO homopolymers) compared with actual surface pressure isotherm of HMHE (BR22) at 25°C

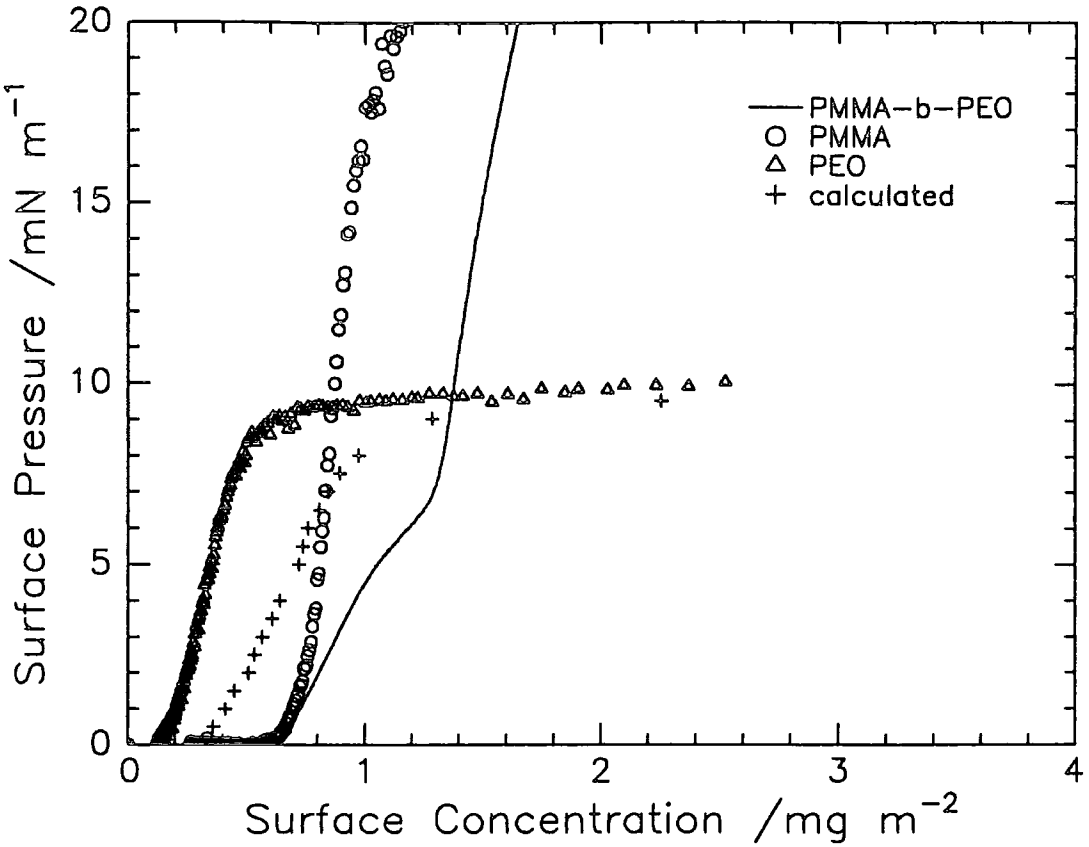

Figure 3.15 Goodrich-Gaines area additivity at given π values (calculated from isotherms of PMMA/PEO homopolymers) compared with actual surface pressure isotherm of HMDE (BR26) at 25°C

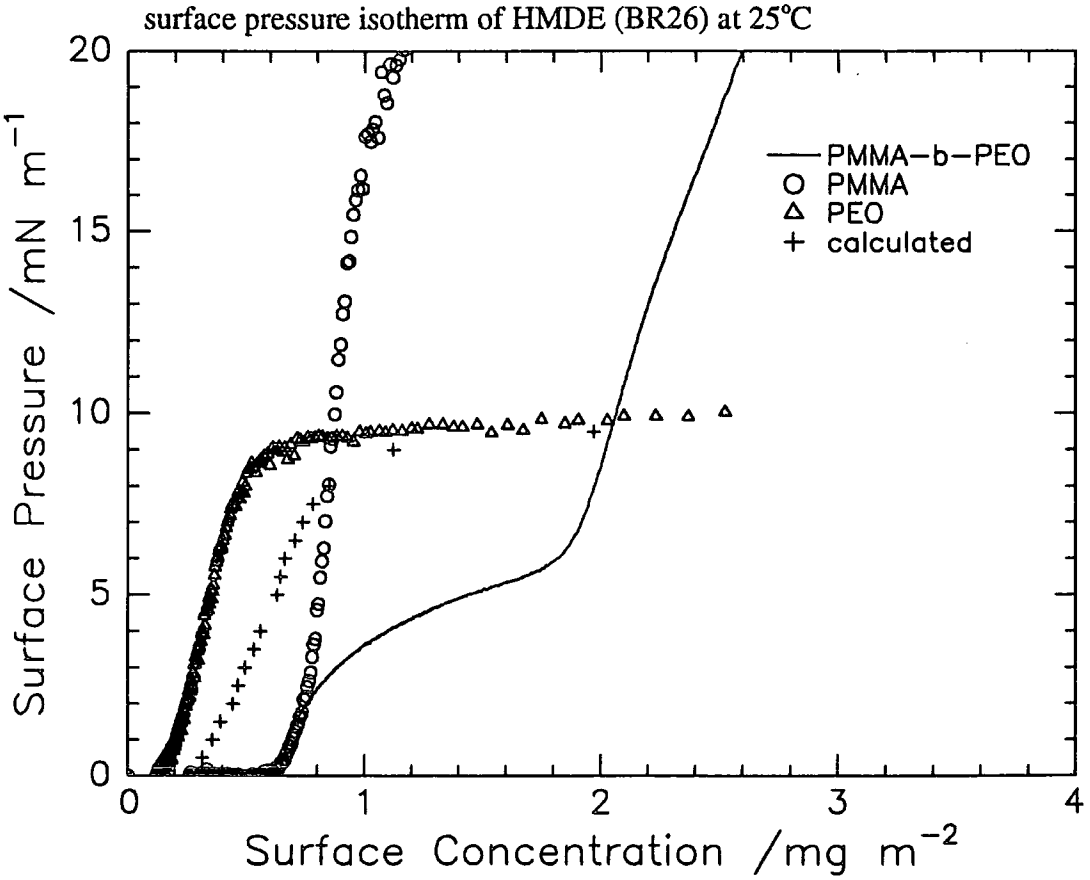

Figure 3.16 Goodrich-Gaines area additivity at given π values (calculated from isotherms of PMMA/PEO homopolymers) compared with actual surface pressure isotherm of DMDE (BR27) at 25°C

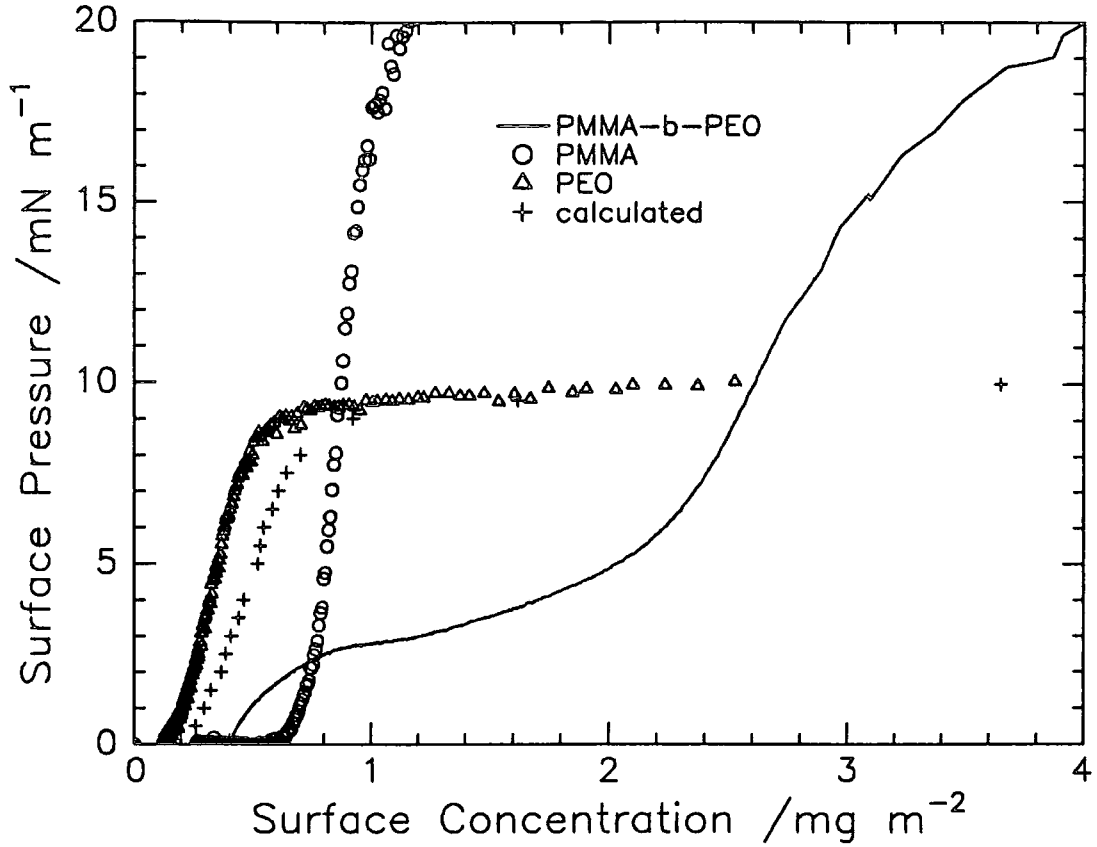

Figure 3.17 Goodrich-Gaines area additivity at given π values (calculated from isotherms of PMMA/PEO homopolymers) compared with actual surface pressure isotherm of DMDE (BR27) at 25°C

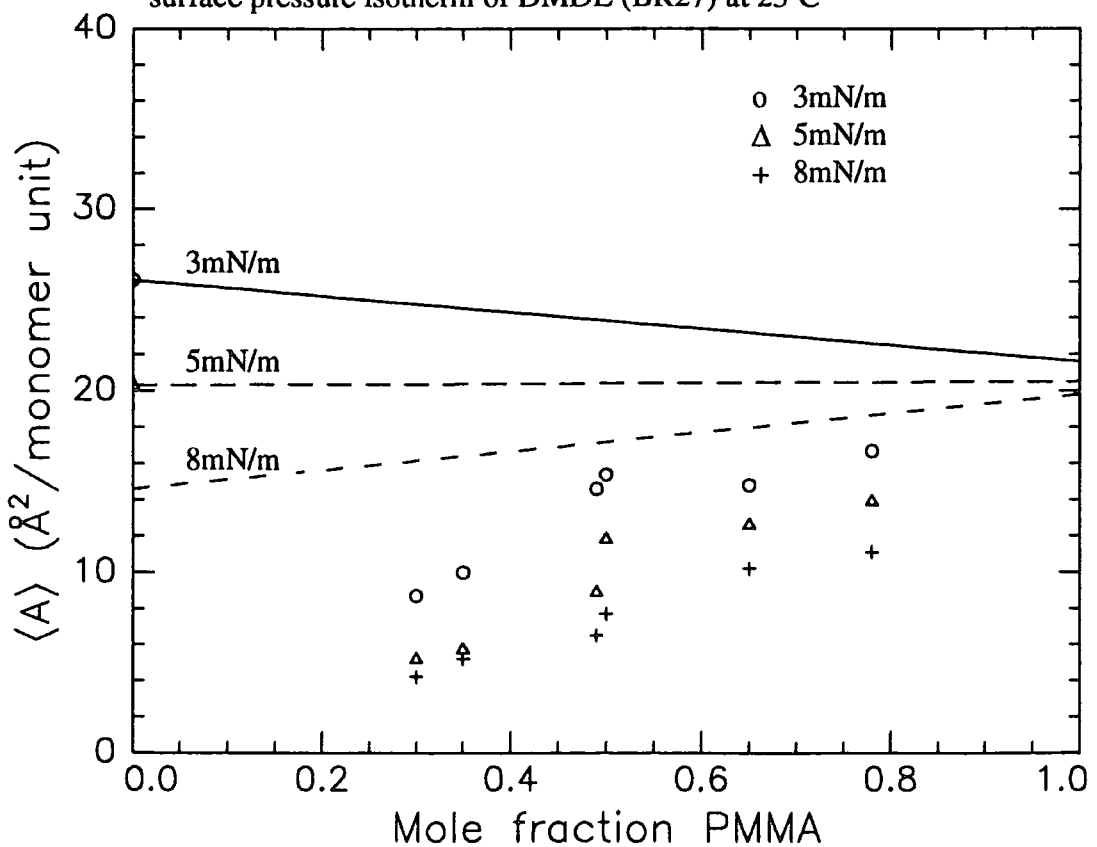

Figure 3.18 Average areas per monomer in PMMA-b-PEO as a function PMMA mole fraction. The lines represent ideal films.

It is possible to obtain an excess area, ΔA^E, which is the difference between the actual and ideal area

$$\Delta A^E(\Pi) \equiv \langle A(\Pi)\rangle - \langle A(\Pi)\rangle^{ideal} \tag{3.3}$$

Values of ΔA^E at the air/water interface have previously been reported as mainly zero or negative[5,6]. It is possible to obtain the excess Gibbs free energy of mixing, $\Delta G^E(\Pi)$ (assuming ideal miscibility for $\Pi \rightarrow 0$) from

$$\Delta G^E(\Pi) = \int_0^{\pi} \Delta A^E d\Pi \tag{3.4}$$

Figure 3.18 shows a plot of the average area of the films at 3, 5, and 8mN/m surface pressure. The lines represent the averaged areas of the PMMA and PEO homopolymers in ideal or immiscible films. The greatest deviation between the experimental and linear combination data is at 0.30 and 0.35 PMMA mole fraction. The limiting surface area for PMMA homopolymer[7] is about 18Å and the experimental data extrapolate to approximately this value. Similar negative excess areas have been reported for binary mixtures of PDMS with PMMA[6] and cellulose acetate[4] as second components, and were regarded as being due to energetic interactions between the polymers assuming a miscible monolayer structure. The excess Gibbs free energy of mixing for each copolymer was obtained by numerical integration of ΔA^E-Π plots in terms of equation 3.4, the results are shown in Table 3.5. The values were about 10 times higher than those relating to PMMA/PnBMA. The PMMA and PEO blocks would be expected to have only dipole-dipole interactions and a low ΔG^E compared to the situation where ion-dipole interactions occur corresponding to large ΔG^E. Deviations of ΔG^E from zero indicate the extent to which the mixtures are non-ideal. It would appear that the copolymers with the lower PEO mole fractions are therefore more mixed but increases in the PEO mole fraction lead to non-miscible behaviour. Apart from this latter deduction

this method does not allow the monolayer behaviour to be understood on a molecular basis.

3.4.2 Method 2

Another method for the analysis of the surface pressure isotherm data was suggested by Runge and Yu[8] where a binary PVAc/PDMS system at the air/water interface was described using a two-dimensional analogue of Dalton's law of partial pressures for an ideal gas mixture. In this method the surface pressures of the homopolymers are added together for the corresponding partial areas

$$\Pi(\langle A \rangle) = \Pi_1^{\circ}(A_1) + \Pi_2^{\circ}(A_2) \qquad (3.5)$$

where Π_1 and Π_2 are the surface pressures at the corresponding partial areas A_1 and A_2. Figures 3.19 to 3.24 show the surface pressure isotherms calculated by co-adding the surface pressures of each homopolymer at the corresponding partial surface concentration. Equation 3.5 assumes that no interaction occurs between the two copolymer blocks. In an actual monolayer, polymer-polymer interactions are negligible in the dilute regime where the films behave as an ideal gas. At higher surface concentrations these interactions have a greater effect. The surface pressure isotherms calculated using this method have similar lift off points in surface pressure and follow the surface pressure isotherms more closely. The experimental surface pressure becomes depressed from the calculated values with increasing PEO content indicating less polymeric material at the surface. This observation could be explained by a reduction in MMA-EO interactions for copolymers with higher PEO mole fractions.

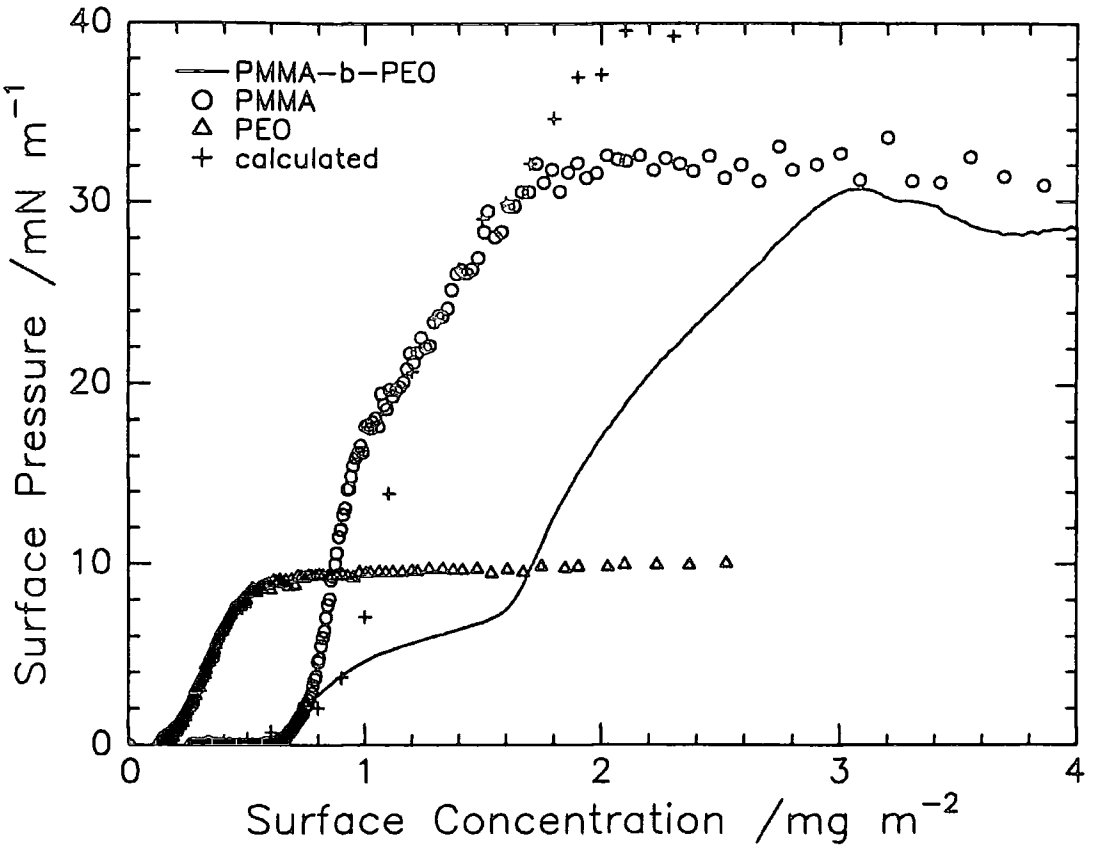

Figure 3.19 Surface Pressure Isotherms for DMHE (BR20), homo PMMA and homo PEO films at 25°C compared with that calculated from one component films

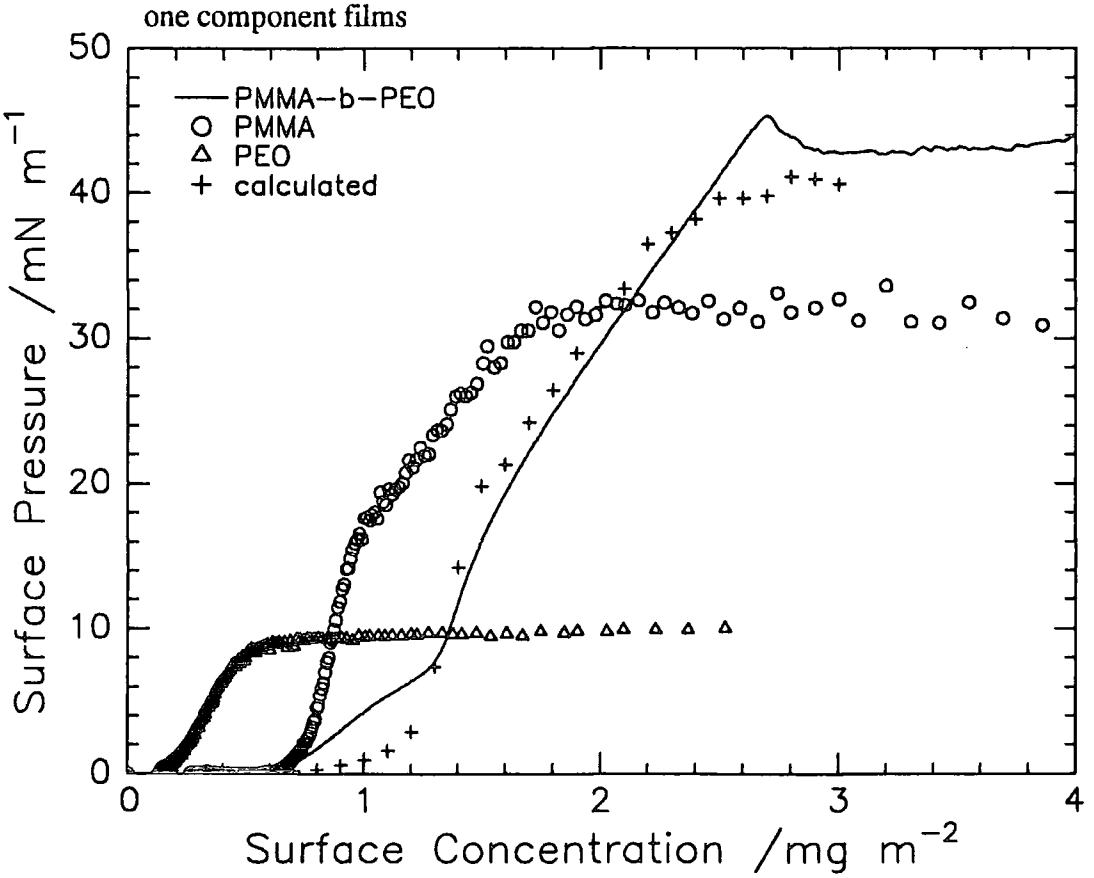

Figure 3.20 Surface Pressure Isotherms for HMHE (BR21), homo PMMA and homo PEO films at 25°C compared with that calculated from one component films

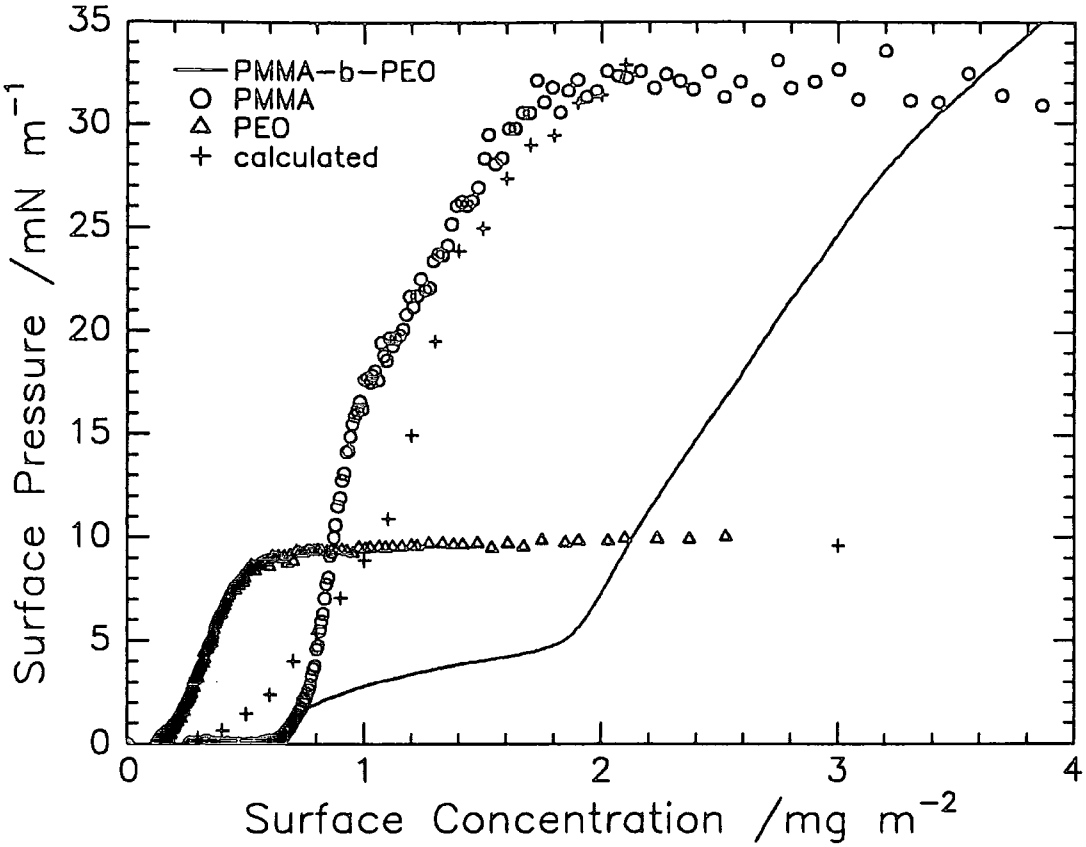

Figure 3.21 Surface Pressure Isotherms for HMHE (BR22), homo PMMA and homo PEO films at 25°C compared with that calculated from one component films

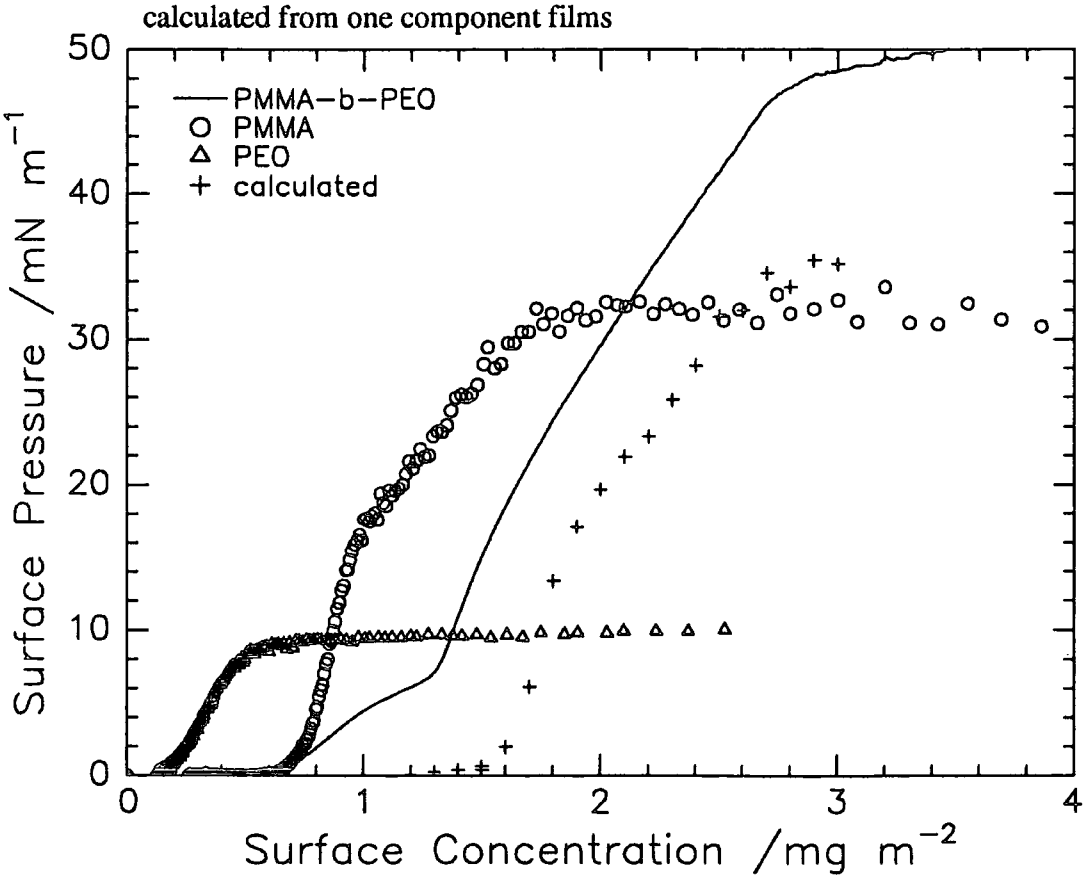

Figure 3.22 Surface Pressure Isotherms for HMDE (BR26), homo PMMA and homo PEO films at 25°C compared with that calculated from one component films

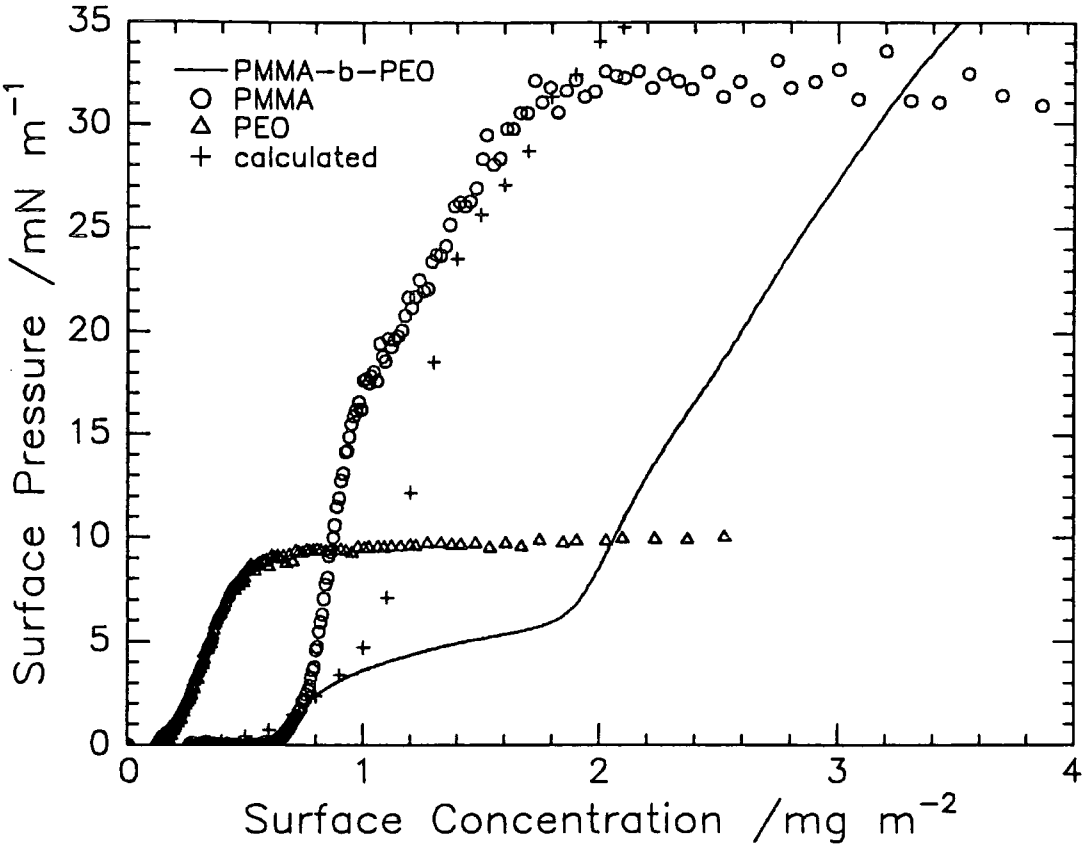

Figure 3.23 Surface Pressure Isotherms for DMDE (BR27), homo PMMA and homo PEO films at 25°C compared with that calculated from one component films

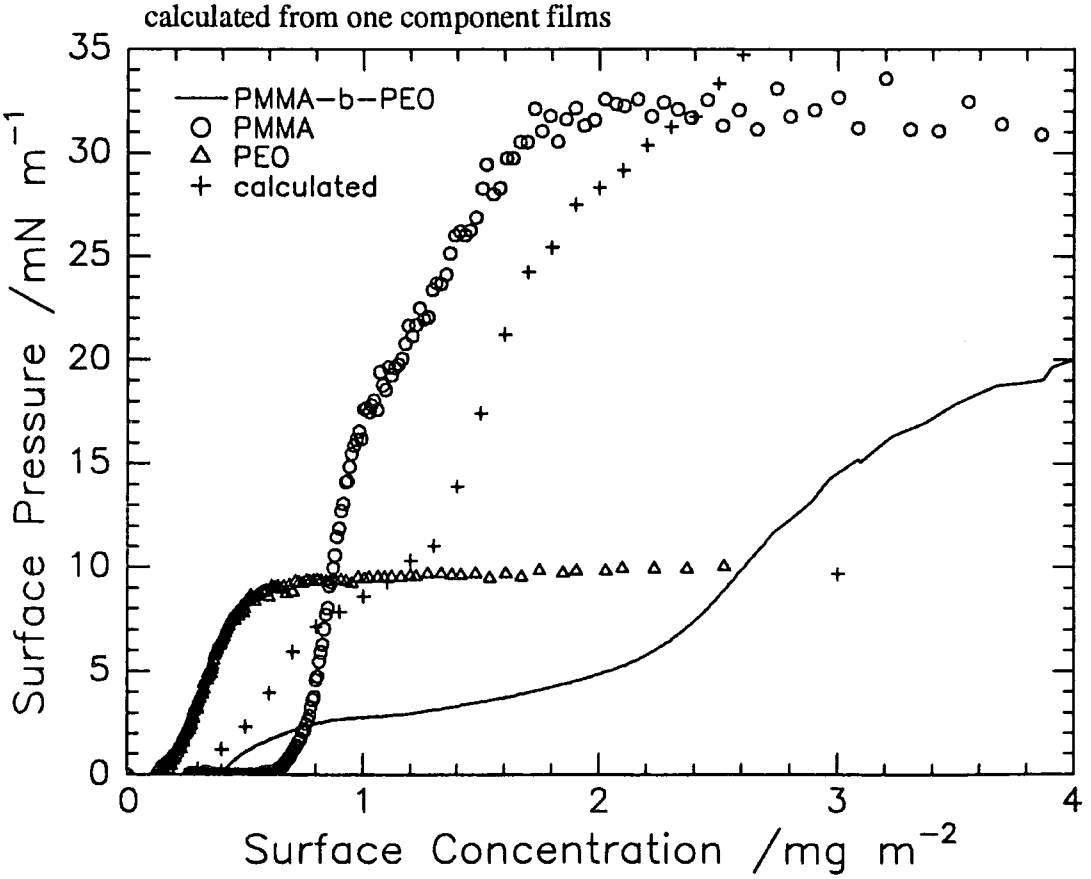

Figure 3.24 Surface Pressure Isotherms for HMDE (BR29), homo PMMA and homo PEO films at 25°C compared with that calculated from one component films

References

1. Vilanove, R., Poupinet, D., Rondelez, F., *Macromolecules*, 1988, **21**, 2880.

2. Gaines, G.L., Jr. *Insoluble Monolayers at Liquid-Gas Interfaces*, Wiley Interscience, New York, 1966.

3. Ries, H.E., Walker, D.C., *J. Colloid Sci.*, 1961, **16**, 361.

4. Gabrielli, G., Baglioni, P., *J. Colloid Interface Sci.*, 1980, **73**, 582.

5. Wu, S., Huntsberger, J.R., *J. Colloid Interface Sci.*, 1969, **29**, 138.

6. Gaines, G.L., Jr., *Adv. Chem. Ser.*, 1975, **144**, 338.

7. Henderson, J.A., Ph.D. thesis, University of Durham, 1992.

8. Runge, F.E., Yu, H., *Langmuir*, 1993, **9**, 3191.

CHAPTER 4 - NEUTRON REFLECTOMETRY

Summary

Neutron reflectometry has been used to study several isotopic analogues of PMMA-b-PEO spread as monolayers at the air-water interface. The target composition of the copolymers was 50:50 MMA:EO mole composition. However, this was difficult to achieve although high vacuum anionic polymerisation allowed a degree of control over the PMMA block length.

The measurements were taken using two sets of contrast conditions. By spreading partially or fully deuterated polymer on null reflecting water (nrw) it is possible to obtain a direct measure of the deuterated material at the surface. Totally hydrogenous polymer spread on D_2O subphase is very sensitive to the amount of water present in the layer.

Initially, the measurements were made using a neutron beam with a fixed incident angle of 1.5° to the surface giving an accessible neutron beam scattering vector range of $0.052 \leq Q/Å^{-1} \leq 0.65$. Four constant surface pressures, corresponding to different surface concentrations, were studied. Distributions of the MMA and EO blocks across the interface could not be distinguished effectively because of the limited Q range studied and furthermore the upper Q range is limited by the water substrate background causing a low signal to noise ratio. These results however indicated that there was separation between the MMA and EO blocks, which increased at higher surface concentrations. Another problem was that the HMDE/nrw contrast had a very low reflectivity due to the low DEO content of the copolymer. This contrast was replaced in the solution of the kinematic approximation by a DMDE/D_2O contrast which meant that four D_2O contrasts and only two nrw contrasts were used. The necessity to do this was thought to be responsible for the large overestimation of the number densities of the EO block and the smaller overestimation for that of the MMA block.

The measurements were repeated at two constant surface concentrations, the area of the trough remaining constant. The Q range was extended to a lower limit of Q but ensuring the critical edge was not approached. This extended Q range was $0.027 \leq Q/Å^{-1} \leq 0.65$. A new HMDE copolymer having a larger DEO content was synthesised, giving the HMDE/nrw contrast a higher reflectivity and allowing its use in the solution of the kinematic approximation.

This chapter is therefore divided into two parts. Part A describes the initial work carried out at constant surface pressure, while Part B describes the work at constant surface concentration involving the extended Q range and uses an improved HMDE/nrw contrast.

PART A: REFLECTOMETRY DATA AT $0.052 \leq Q/Å^{-1} \leq 0.65$

Neutron reflectometry was used to study BR20, 22, 26 and 27 copolymers at the air-water interface. These polymers were used to obtain the following contrast conditions: DMHE/nrw, DMDE/nrw, HMDE/nrw, DMHE/D_2O, DMDE/D_2O, HMDE/D_2O, HMHE/D_2O. The reflectivity profiles for each contrast condition were measured at constant surface pressures of 1, 2, 5 and 10mN/m.

The measurements were made at a fixed incident angle of 1.5° and the reflectivity placed on an absolute scale using clean D_2O as a calibrant. Neutron reflection theory predicts that for a clean surface reflectivity has an inverse dependence on Q, i.e. it decreases with Q^4. This is seen in the following experimental data in which the reflectivity is plotted in logarithmic form as a function of Q. The reflectivity profiles decrease in this way until the instrumental background is reached. These instrumental backgrounds were determined for each profile from the low scattering level at high Q and were subtracted from the reflected beam intensity. The background is mainly due to isotropic incoherent scattering and depends on the contrast conditions used. Since ^1H nuclei have a higher incoherent scattering cross section than ^2H nuclei, a higher background is obtained for highly protonated systems. The expected background for nrw systems is about $1x10^{-5}Å^{-2}$ which is higher than for D_2O systems having backgrounds of about $3x10^{-6}Å^{-2}$. These background levels are usually reached at Q values of about 0.30-0.35$Å^{-1}$. The error bars, which were very small except near the high Q background, are omitted for clarity but examples of single reflectivity profiles are shown.

4.1 Results

Figures 4.1 to 4.4 show reflectivity profiles obtained on CRISP for the copolymers spread on D_2O at 1, 2, 5 and 10mN/m, while figure 4.5 shows a typical background subtracted reflectivity profile with typical error bars included. The background

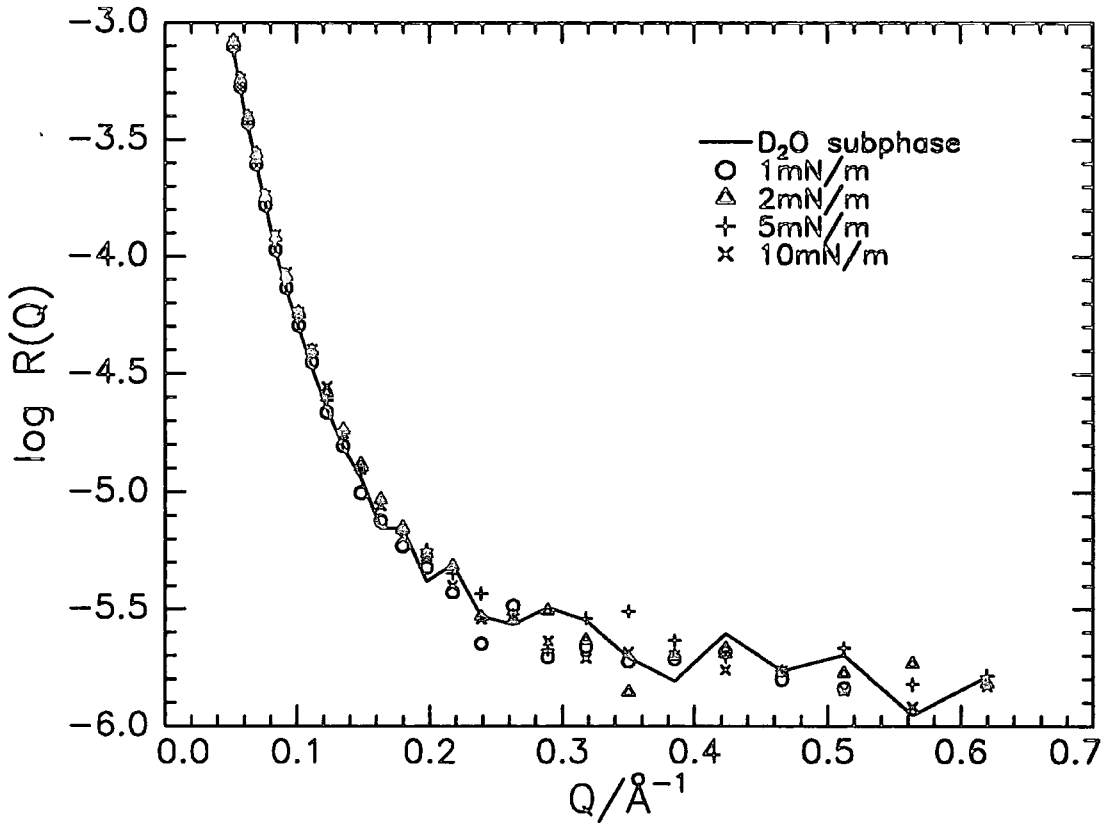

Figure 4.1 Neutron Reflectivity Profiles for DMDE on D_2O

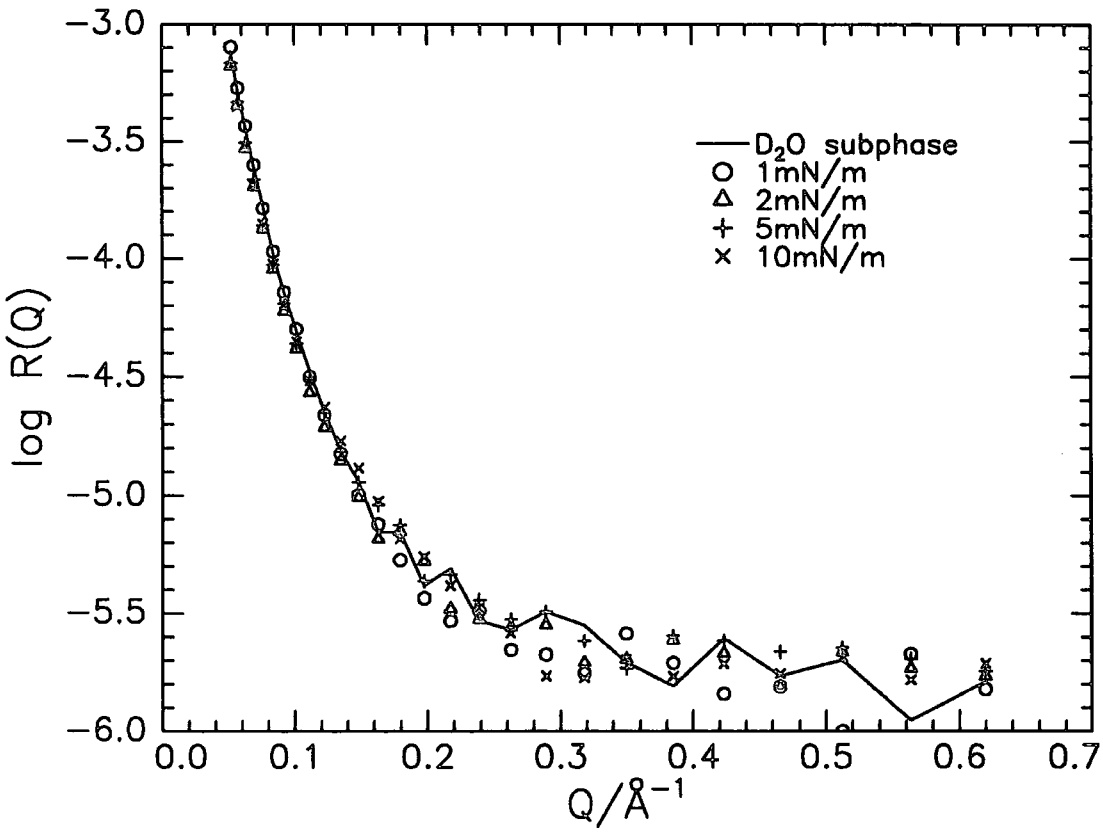

Figure 4.2 Neutron Reflectivity Profiles for DMHE on D_2O

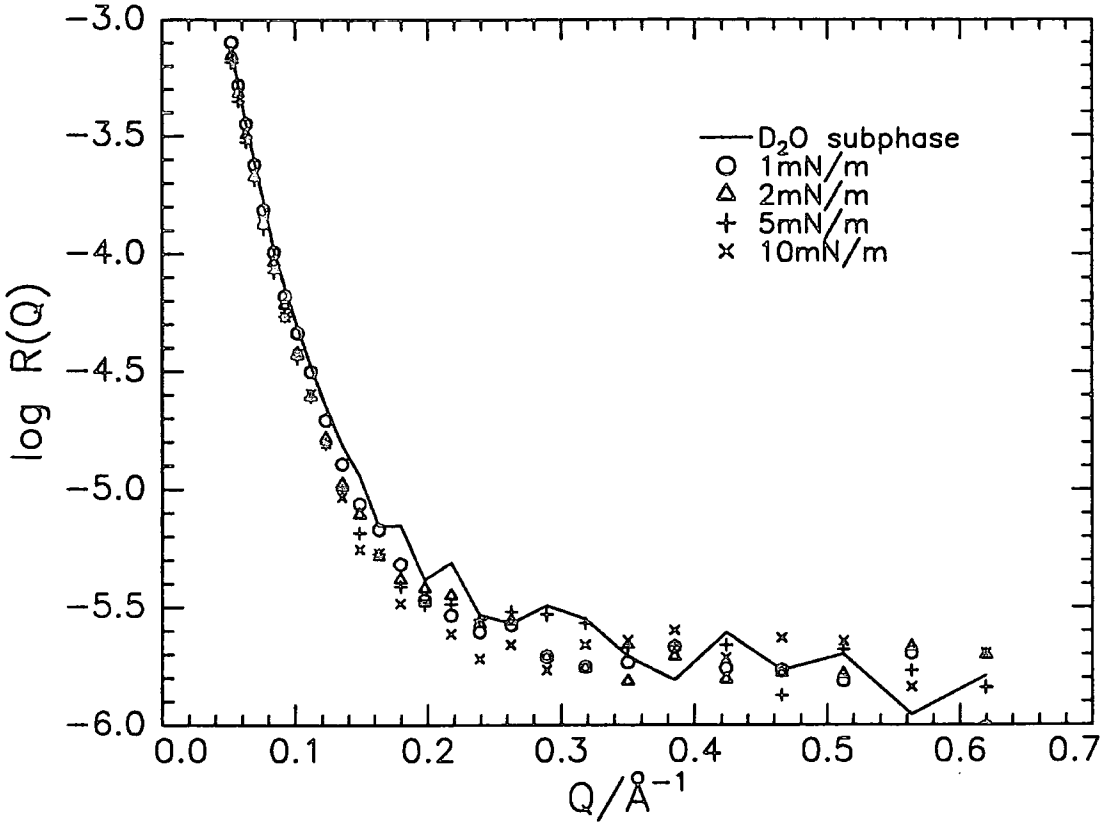

Figure 4.3 Neutron Reflectivity Profiles for HMDE on D_2O

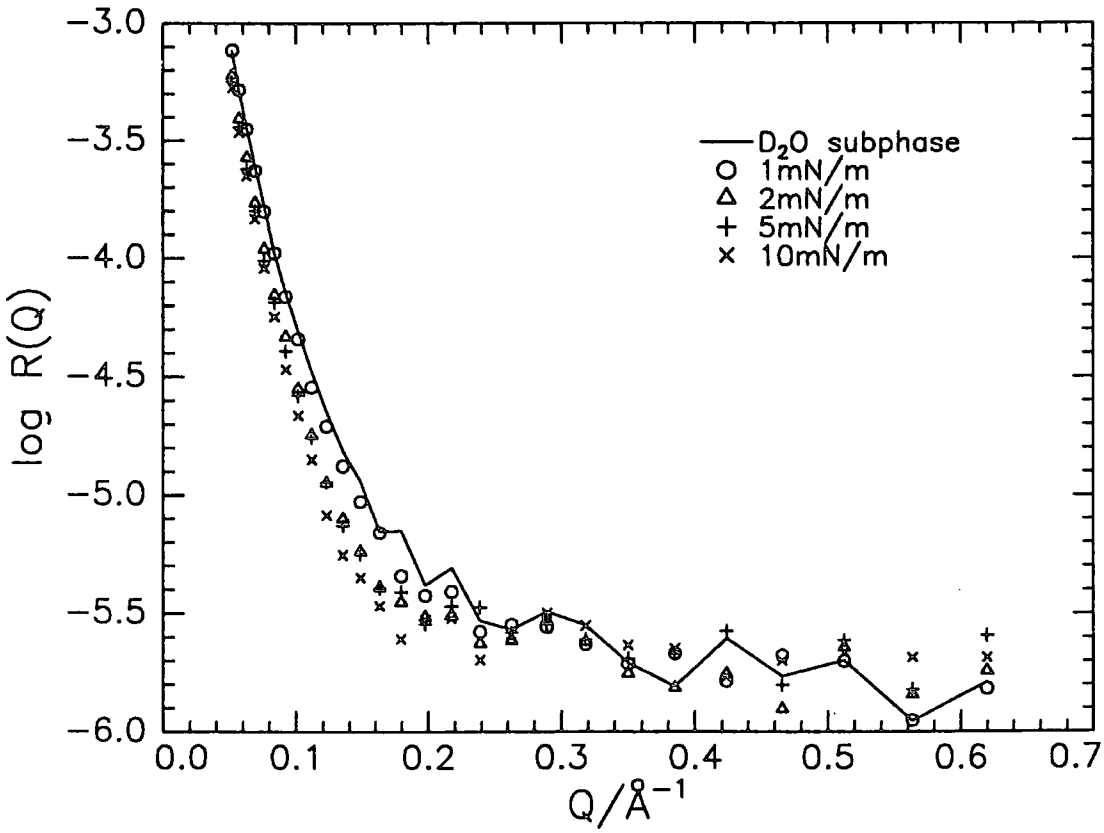

Figure 4.4 Neutron Reflectivity Profiles for HMHE on D_2O

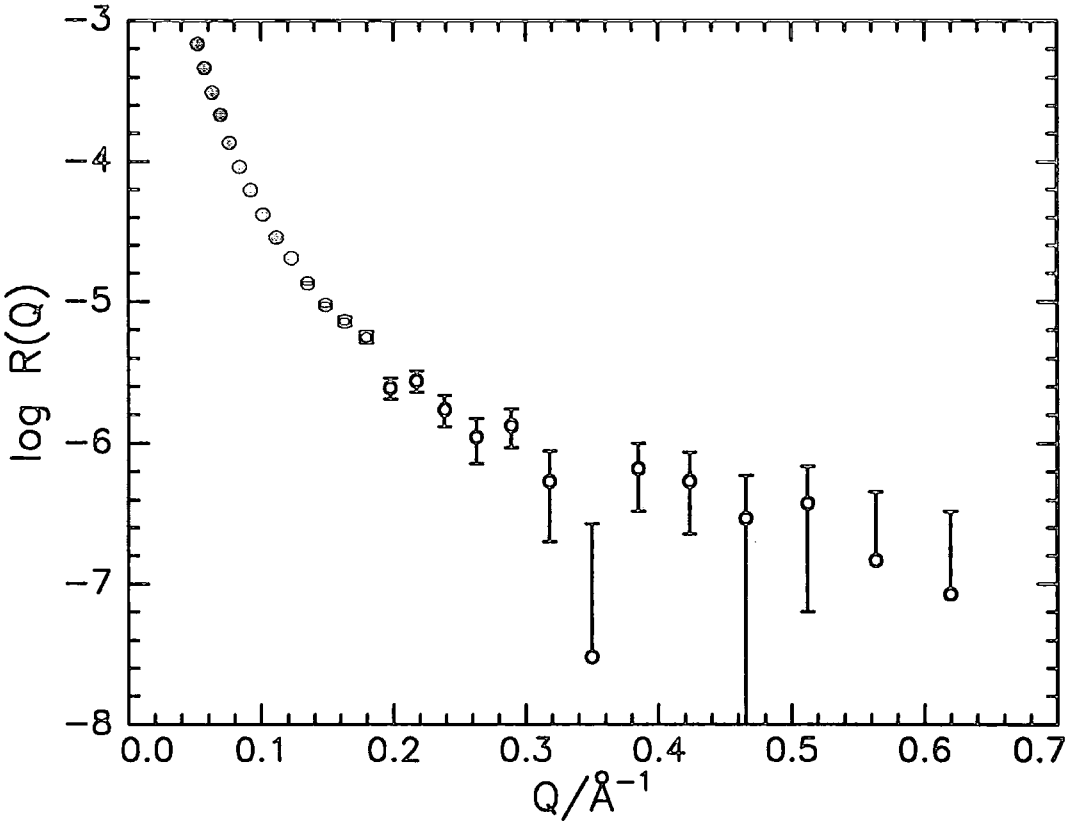

Figure 4.5 Background subtracted Neutron Reflectivity profile for DMHE/D_2O at 5mN/m

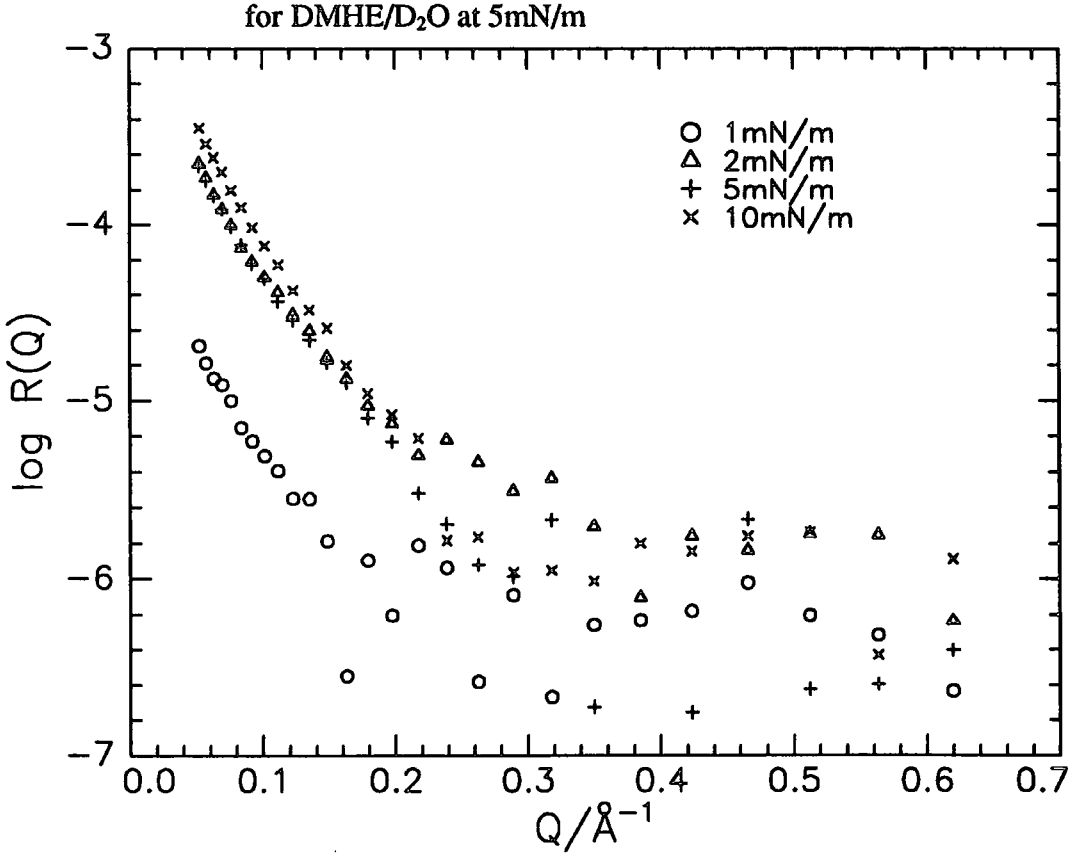

Figure 4.6 Background subtracted Neutron Reflectivity Profiles for DMHE on nrw

subtracted reflectivity profiles for the copolymers on nrw are shown for the same surface pressures in figures 4.6 to 4.8, figure 4.9 showing a typical background subtracted reflectivity profile with typical error bars included. At large surface pressures, representing higher surface concentrations, there is an increase in the nuclear density at the interface. For the DPMMA-DPEO copolymer spread on D_2O the effect of increasing the surface concentration of polymer was to increase the amount of deuterated material at the interface. The reflectivity profile therefore increased slightly from that obtained for pure D_2O. The layer scattering length density in this case was contributed to by the polymer and subphase material. In the case of DPMMA-HPEO, HPMMA-DPEO and HPMMA-HPEO copolymers the reflectivity was depressed with increasing surface concentration. This effect was greatest for the HMHE copolymer and was indicative of an increase in hydrogenous material at the interface. When the DPMMA-DPEO and DPMMA-HPEO copolymers were spread on nrw the experimental reflectivity rose with increasing surface concentration indicating a rise in deuterated material at the interface. Spread layers of HPMMA-DPEO on nrw did not show an appreciable reflectivity. Spread layers of HPMMA-HPEO on nrw would have been almost invisible to neutron reflection and time constraints forced these measurements to be omitted.

4.1.1 Uniform layer models

The data were initially fitted using the simplest of models, a uniform layer structure having one or two layers was assumed, the thickness (d) and scattering length density (ρ) of each layer (either single or two layer model) being varied to optimise the fits. The software package used was DRYDOC by A.R.Rennie which used non-linear least squares fitting of the reflectivity data from initial estimates of the parameters involved. The parameters of the fits were obtained by fixing a constant layer thickness and using the scattering length density as a fitting variable for each layer and subsequently

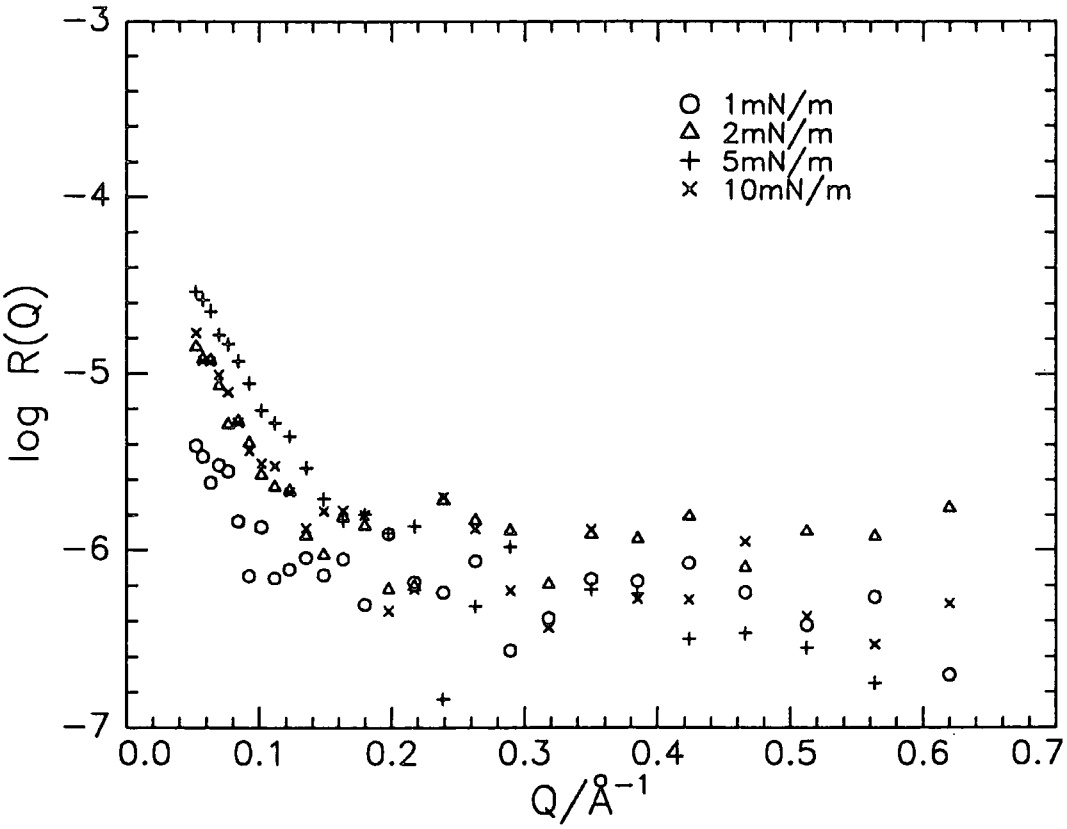

Figure 4.7 Background subtracted Neutron Reflectivity Profiles for HMDE on nrw

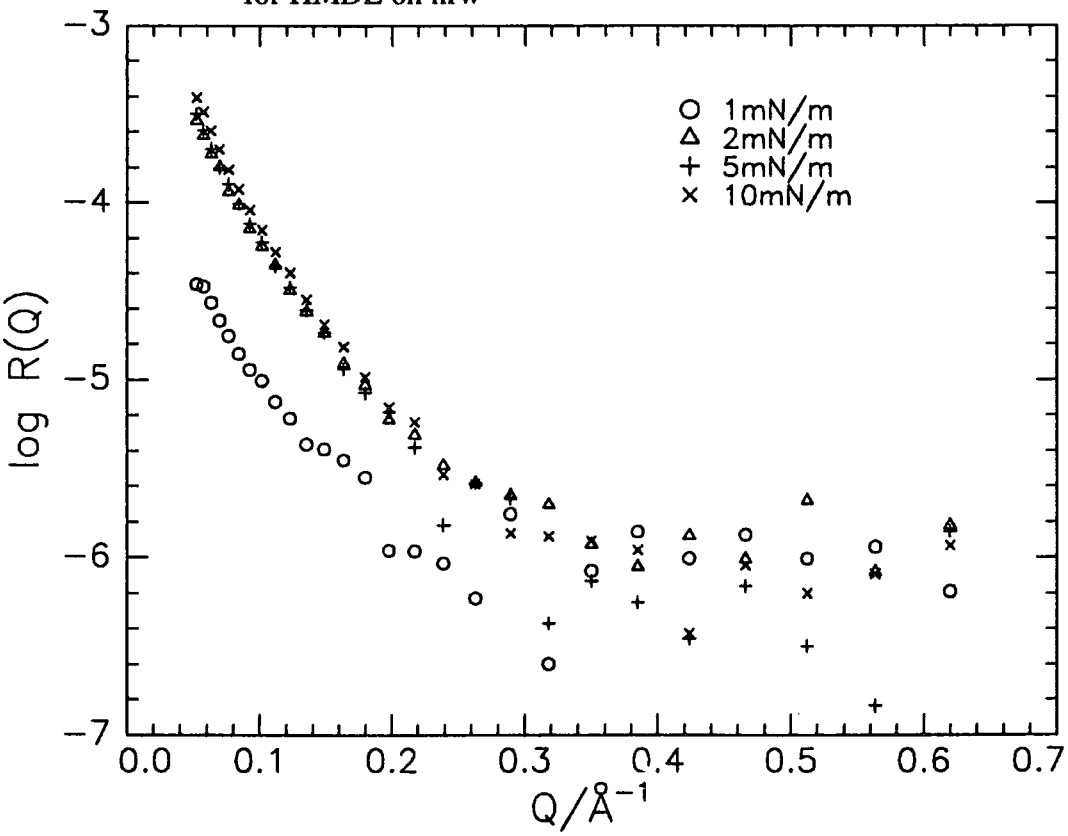

Figure 4.8 Background subtracted Neutron Reflectivity Profiles for DMDE on nrw

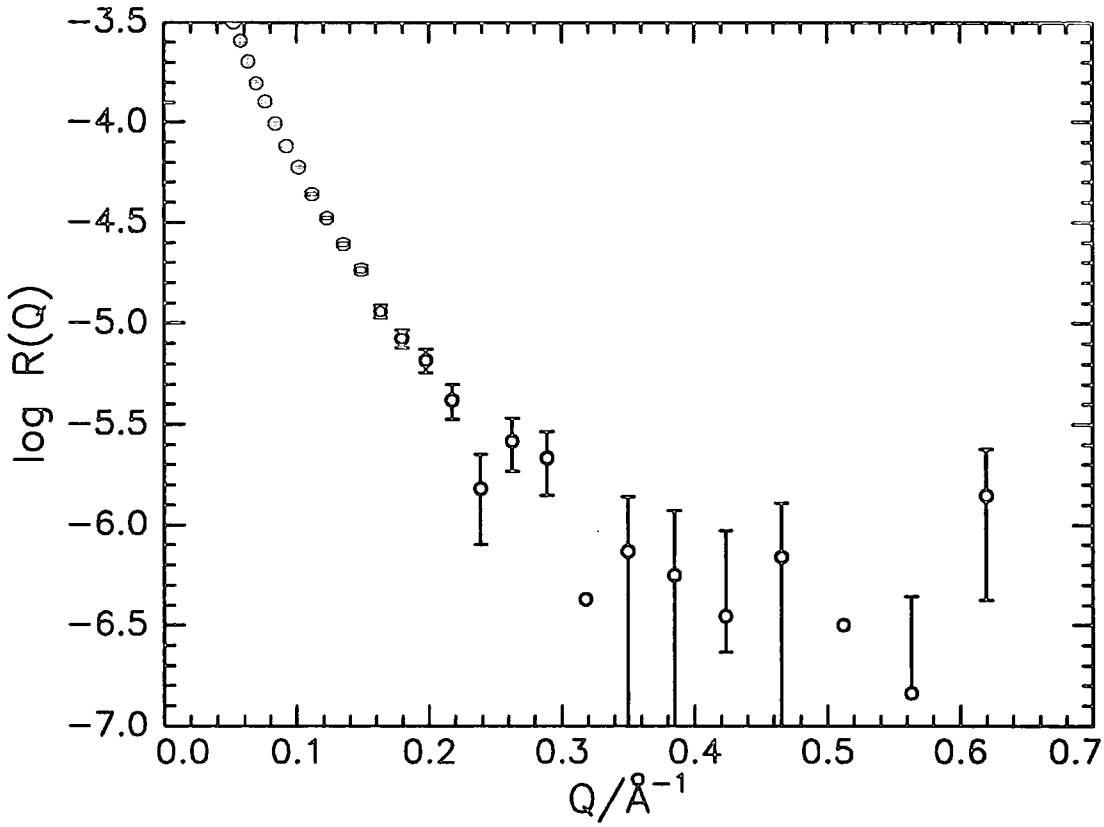

Figure 4.9 Background subtracted Neutron Reflectivity Profile for DMDE/nrw at 5mN/m

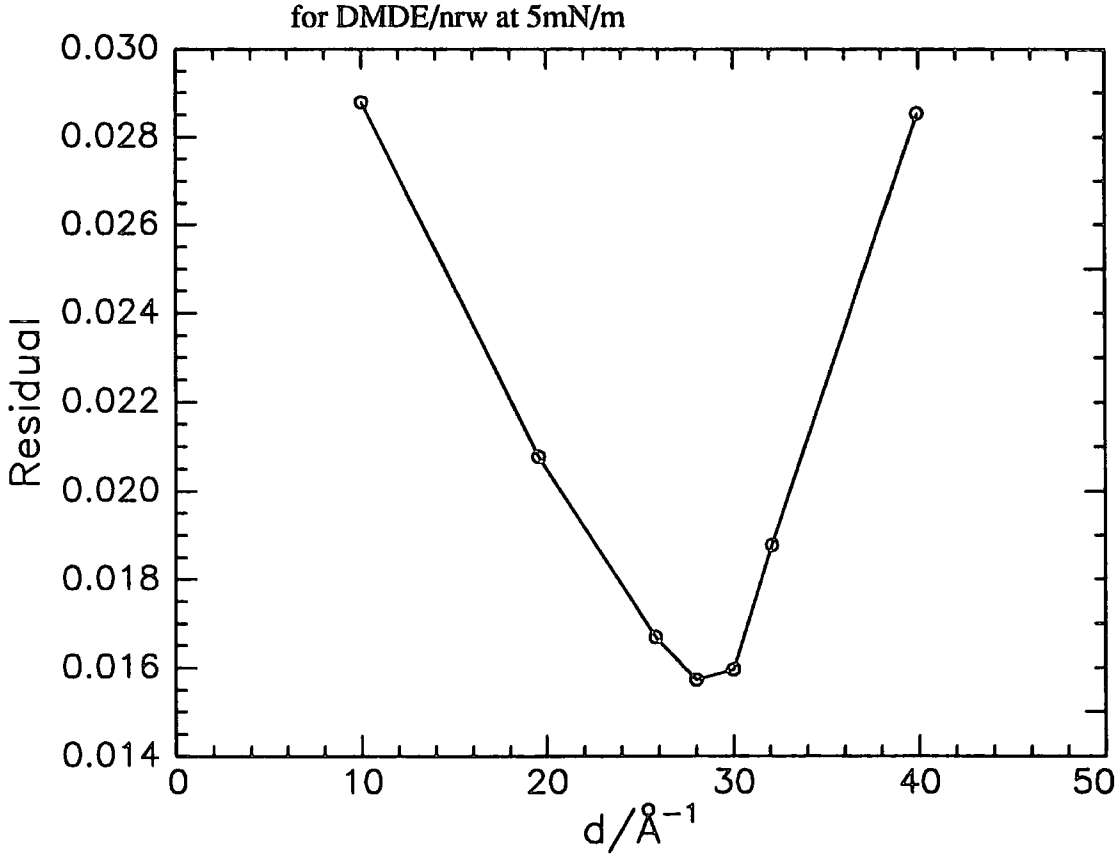

Figure 4.10 Plot of residual error as a function of layer thickness for DMHE/D_2O at 5mN/m

identifying the minimum in the residual error of the fits. Figure 4.10 shows such a plot of residual error as a function of layer thickness for DMHE/D_2O at 5mN/m surface pressure. In the same way ρ was fixed and the thickness varied to find a minimum for the copolymer at the same surface pressure.

4.1.1.1 Single uniform layer model

A typical fit obtained for the single uniform layer model is shown in figure 4.11 while Table 4.1 shows the layer thickness and scattering length densities obtained. Due to the high scattering length density of D_2O the overall reflectivity was much higher for copolymers spread on this subphase than those spread on nrw. The model fitted data for the copolymers spread on nrw subphase well, with the exception of HMDE spread on nrw which had a very low reflectivity. From the product of the fitted thickness, d, and the scattering length density, ρ, for deuterated material on nrw subphase, where the deuterated material is the only material contributing to the signal, it is possible to calculate area per monomer (apm) values at a given surface concentration. Apparent surface concentration values, Γ_a, may be determined for the deuterated portion of the copolymer by the following formulae

$$\text{Area per monomer} = \Sigma b_i/\rho.d \qquad (4.1)$$

and $$\Gamma_a = M_m/N_{av}.apm \qquad (4.2)$$

where Σb_i = sum of the coherent scattering lengths of the constituent nuclei in the unit

M_m = molecular weight of deuterated monomer unit

N_{av} = Avogadro's constant.

For the DMDE copolymer the apparent surface concentration of the whole deuterated copolymer is calculated, while for DMHE and HMDE the apparent concentration of the deuterated blocks are calculated. Table 4.2 summarises the parameters used in the

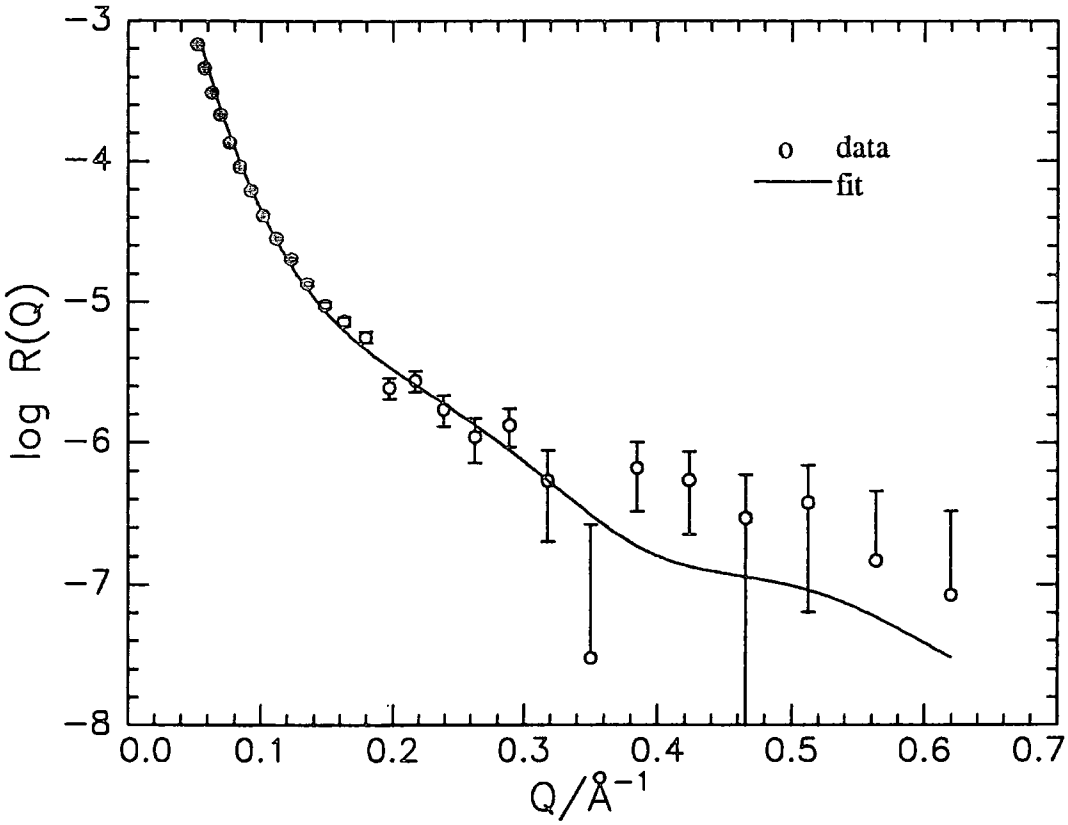

Figure 4.11 Fit to DMHE/D_2O reflectivity data at 5mN/m

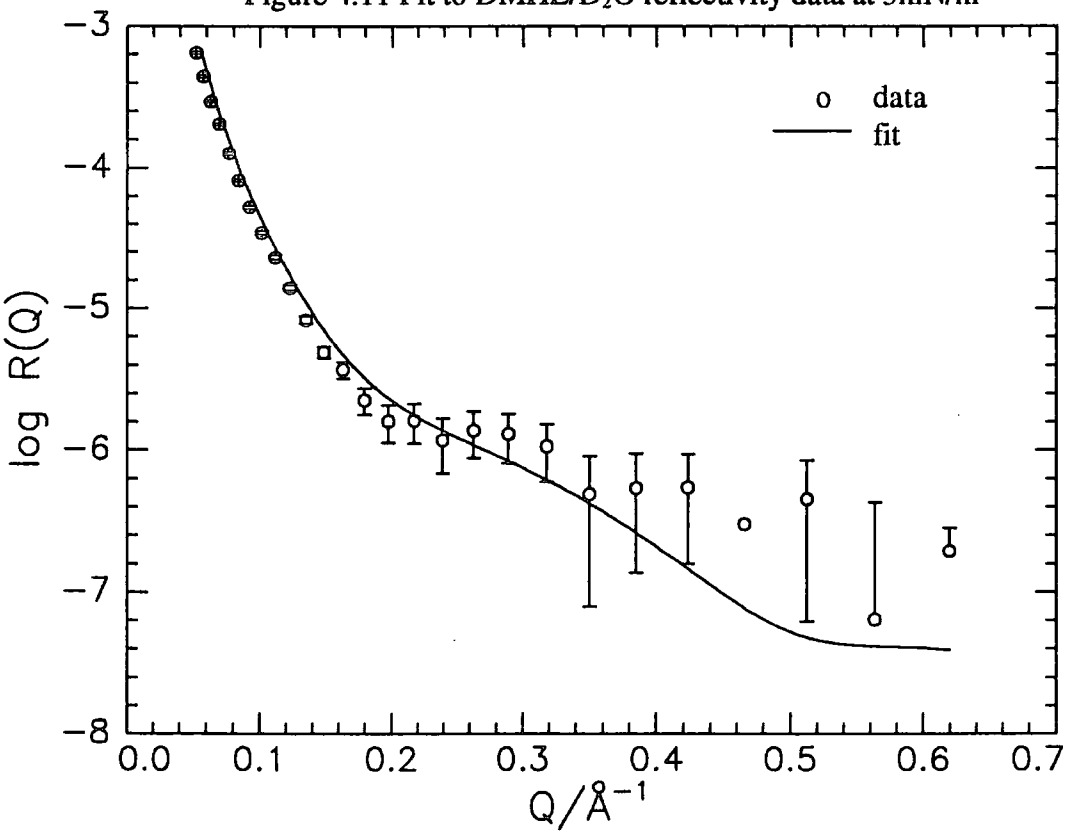

Figure 4.12 Fit to HMDE/D_2O reflectivity data at 5mN/m

Copolymer	π/mN m^{-1}	Subphase	d/Å	$\rho/10^{-6}$Å^{-2}	Residual
DMDE	1	D_2O	20	5.77	0.224e-1
	2		23	6.35	0.247e-1
	5		25	6.00	0.689e-2
	10		22	6.11	0.932e-2
	1	nrw	8	2.99	0.334e-1
	2		12	5.11	0.265e-1
	5		17	4.08	0.255e-1
	10		16	4.65	0.259e-1
DMHE	1	D_2O	20	5.74	0.275e-1
	2		24	5.60	0.212e-1
	5		28	5.69	0.157e-1
	10		32	5.75	0.912e-2
	1	nrw	17	4.56	0.214e-2
	2		9	6.44	0.205e-2
	5		17	3.68	0.600e-2
	10		17	4.56	0.214e-1
HMDE	1	D_2O	18	5.49	0.115e-1
	2		22	5.31	0.123e-1
	5		20	5.07	0.134e-1
	10		17	4.96	0.205e-1
	5	nrw	12	1.87	0.366e-1
HMHE	1	D_2O	21	5.57	0.165e-1
	2		21	4.87	0.267e-1
	5		20	4.61	0.304e-1
	10		21	4.46	0.432e-1

Table 4.1 Fitted parameters to single uniform layer model

Copolymer	Deuterated Species	π/mN m^{-1}	Γ_s/mg m^{-2}	$\rho_d.d/10^{-6}$Å^{-1}	apm/Å^2	Γ_s/mg m^{-2}
DMDE	DMDE	1	0.30	24.8	29	0.45
		2	0.60	49.0	15	0.89
		5	1.00	78.6	9	1.42
		10	2.40	81.8	9	1.48
DMHE	DMMA	1	0.36	26.2	38	0.48
		2	0.65	40.9	24	0.75
		5	1.00	63.3	16	1.16
		10	1.41	78.0	13	1.42
HMDE	DEO	5	0.16	22.3	21	0.39

Table 4.2 Surface Concentration calculated from fitted parameters

Contrast	Model	Layer thickness d/Å	Scattering length density $\rho/10^{-6}$Å^{-2}
HMDE/D_2O	Uniform	20	2.05
	Two layer		
	HMMA upper	18	0.90
	DEO lower	18	6.32
	DEO upper	18	6.32
	HMMA lower	18	0.90
DMHE/D_2O	Uniform	20	3.30
	Two layer		
	DMMA upper	18	6.02
	HEO lower	18	0.57
	HEO upper	18	0.57
	DMMA lower	18	6.02

Table 4.3 Parameters used in neutron reflectivity simulations

calculation of Γ_a. Apart from the DMDE/nrw contrast at 10mN/m, the values of Γ_a appear to be larger than Γ_s, the spread amount of deuterated material. The reason for this was an underestimation of Γ_s due to compression of the monolayer. This compression was due to the trough computer software compensating for unreal surface pressure readings caused by perturbation of the Wilhelmy plate. These unreal readings were caused by mechanical vibration and thermal agitation. For DMDE/nrw at 10mN/m the Γ_a value is less than Γ_s which indicates some 'lost' polymer which may be attributed to PEO segments stretching into the subphase and becoming highly diluted.

4.1.1.2 Two layer model

The background subtracted reflectivity profile of HMDE on D_2O at 5mN/m (figure 4.3) is slightly reduced from that of clean D_2O. If the copolymer film was a uniform mixture of both blocks then it would have a scattering length density of about 2×10^{-6}Å^{-2} which is a value is between that of air and D_2O. If the monolayer had this scattering length density then there would have been a more profound effect on the reflectivity due to deuterated material at the surface increasing the reflectivity. Since the scattering length densities of DEO and D_2O are about the same then a mixture of DEO and D_2O would give a reflectivity approximately that of D_2O. A proton rich upper layer of HMMA will almost be contrast matched to air and have a negligible effect on the reflectivity. The HMMA must constitute the upper layer at the air/water interface because an upper layer of DEO with a lower layer of HMMA would have a great effect on the reflectivity profile. Figure 4.13 shows reflectivity profiles for HMDE spread on D_2O at 5mN/m^{-1}. This data is compared with calculations for a uniformly mixed layer and two separate layers with the HMMA layer as the upper or lower layer. Layer thickness and scattering length densities used were those typical of the individual homopolymers, Table 4.3 summarises the parameters used in these simulations.

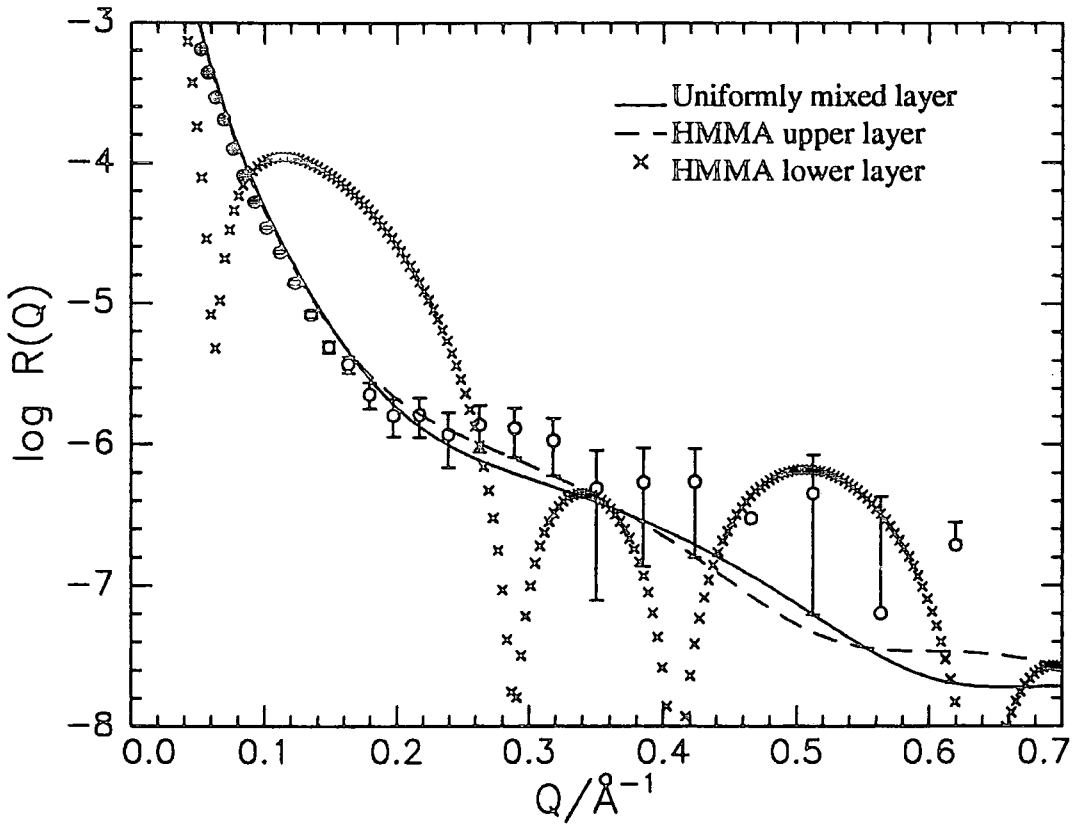

Figure 4.13 Simulated fits to neutron reflectivity data of HMDE on D_2O at 5mN/m

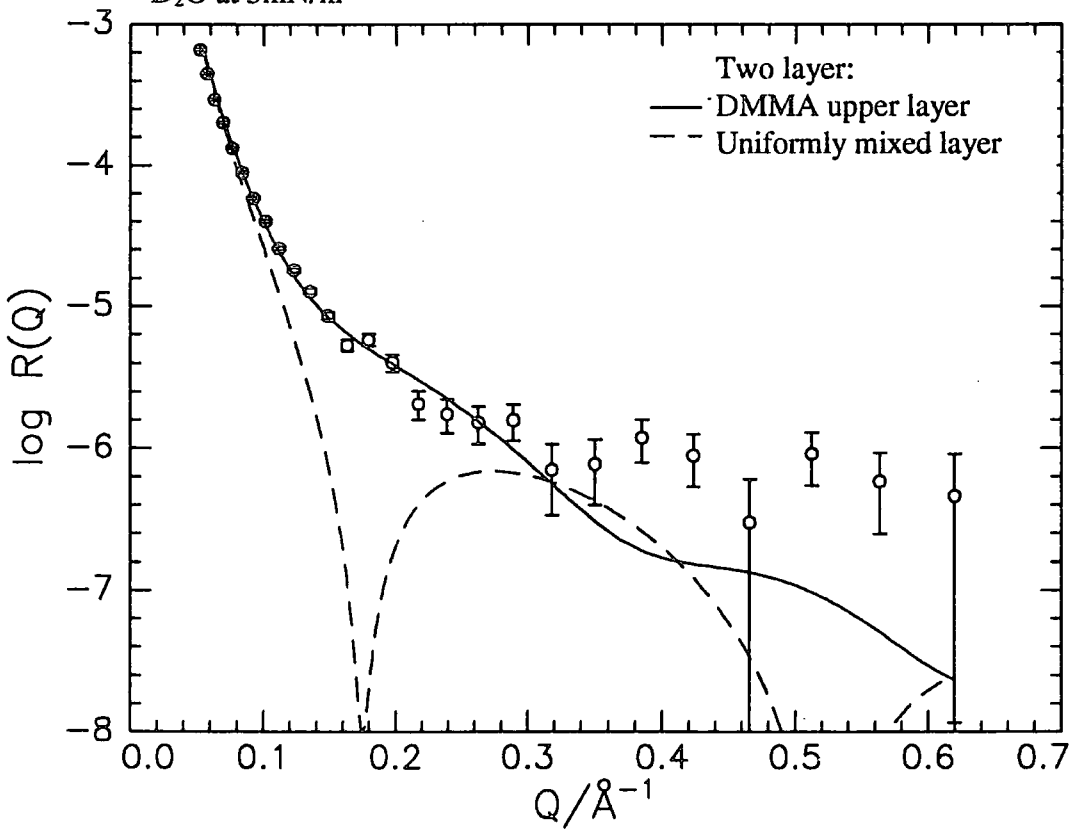

Figure 4.14 Neutron Reflectivity Profile for DMHE on D_2O at 2mN/m

The surface was divided into two uniform layers, each containing mainly PMMA or PEO. The reflectivity of the fully protonated copolymer spread on D_2O subphase (figure 4.4) is decreased from that of pure D_2O. This decrease is greatest at the highest surface coverage. Since the polymeric material has about the same scattering length as air, its contribution to the reflectivity is negligible. The scattering length density profile is therefore determined by the amount of D_2O incorporated in the layer. The observed decrease in reflectivity with increased surface coverage means that D_2O must be squeezed out of the layer. Figure 4.14 compares the experimental data obtained for DMHE on D_2O at 2mN/m with the calculated reflectivities for both a single uniform layer and a two layer model having the DMMA as the upper layer, the parameters used in the simulations are summarised in Table 4.3. It is evident that a two layer model is qualitatively better than a single layer model. Table 4.4 summarises the layer thickness and scattering length densities obtained for the two layer fits while figures 4.15 and 4.16 show examples of these fits. The results show that for DMHE on D_2O that the PMMA (layer 1) reflectivity is slightly decreased from that of clean D_2O and DMMA indicating some penetration of the DMMA by HEO. The greatest penetration of the DMMA by HEO is at 2mN/m, while the least penetration is at 10mN/m. For DMDE on nrw the reflectivity is decreased from that of DMMA, occurring to a lesser extent at 10mN/m indicating least penetration by water. These observations suggest that the PMMA and PEO blocks are intermixed at low surface coverage but separate at higher surface coverages.

This two layer model allows an initial estimate of the composition of the interfacial region. Assuming an upper layer of MMA then the composition may be obtained from the thickness of the PMMA and PEO layers, d_m and d_e, the fractions of these species in the upper block, f_m and f_e, and the volume fraction of water in each layer, ϕ^w_m and ϕ^w_e. By

Polymer	Subphase	π/mN m^{-1}	Layer 1		Layer 2	
			d/Å	$\rho/10^{-6}$Å^{-1}	d/Å	$\rho/10^{-6}$Å^{-1}
DMDE	nrw	2	10	5.90	15	1.19
HMHE	D_2O	2	10	1.01	15	1.63
DMDE	nrw	5	12	5.10	14	1.20
HMHE	D_2O	5	10	0.96	15	1.94
DMDE	nrw	10	10	6.17	15	1.55
HMHE	D_2O	10	8	1.46	15	1.93
DMHE	nrw	2	10	5.56	15	0.65
DMHE	D_2O	2	10	5.77	15	5.50
DMHE	nrw	5	12	4.48	15	0.98
DMHE	D_2O	5	12	5.74	15	5.75
DMHE	nrw	10	10	5.94	13	2.04
DMHE	D_2O	10	10	6.00	13	5.69

Table 4.4 Layer thicknesses and scattering length densities obtained from two-layer model

π/mN m^{-1}	f_m	f_e	A/Å^2	ϕ_m	ϕ_e
2	0.95	0.16	16	0.03	0.81
5	0.54	0.14	10	0.18	0.37
10	0.38	0.06	7	0.02	~1

Table 4.5 Values of f_m, f_e, A, ϕ_m and ϕ_e obtained from two-layer fits

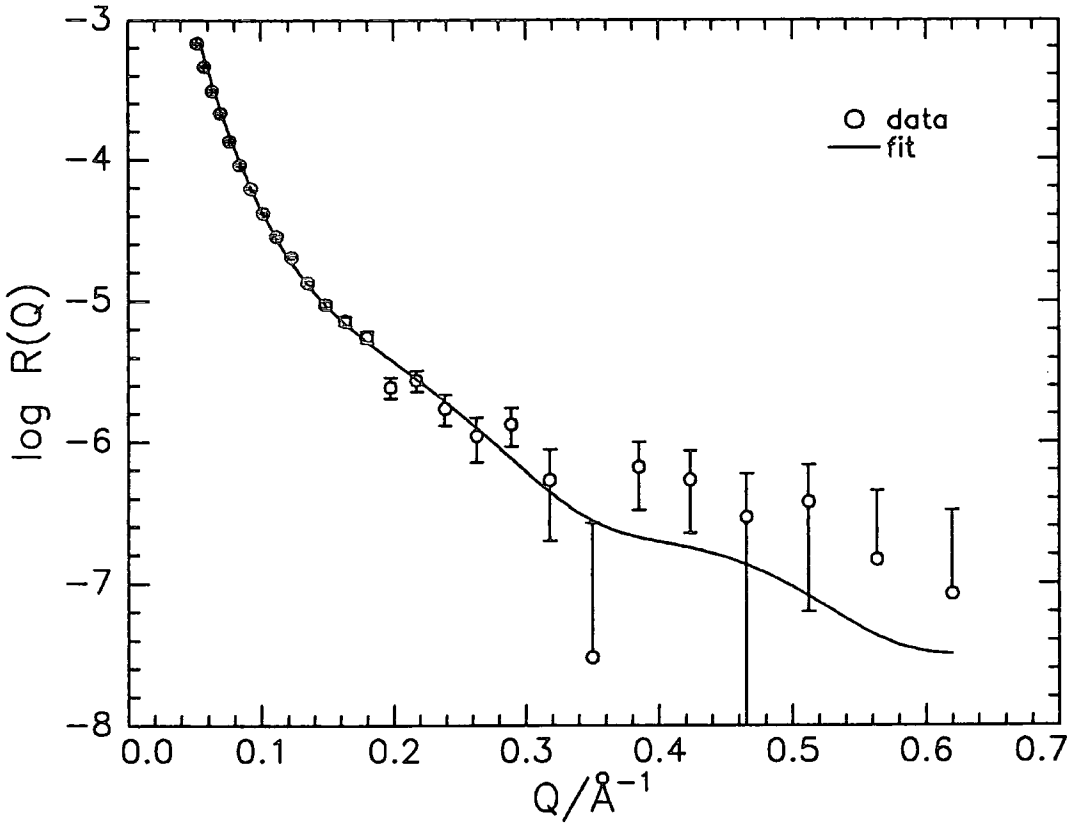

Figure 4.15 Two layer fit for DMHE/D_2O at 5mN/m

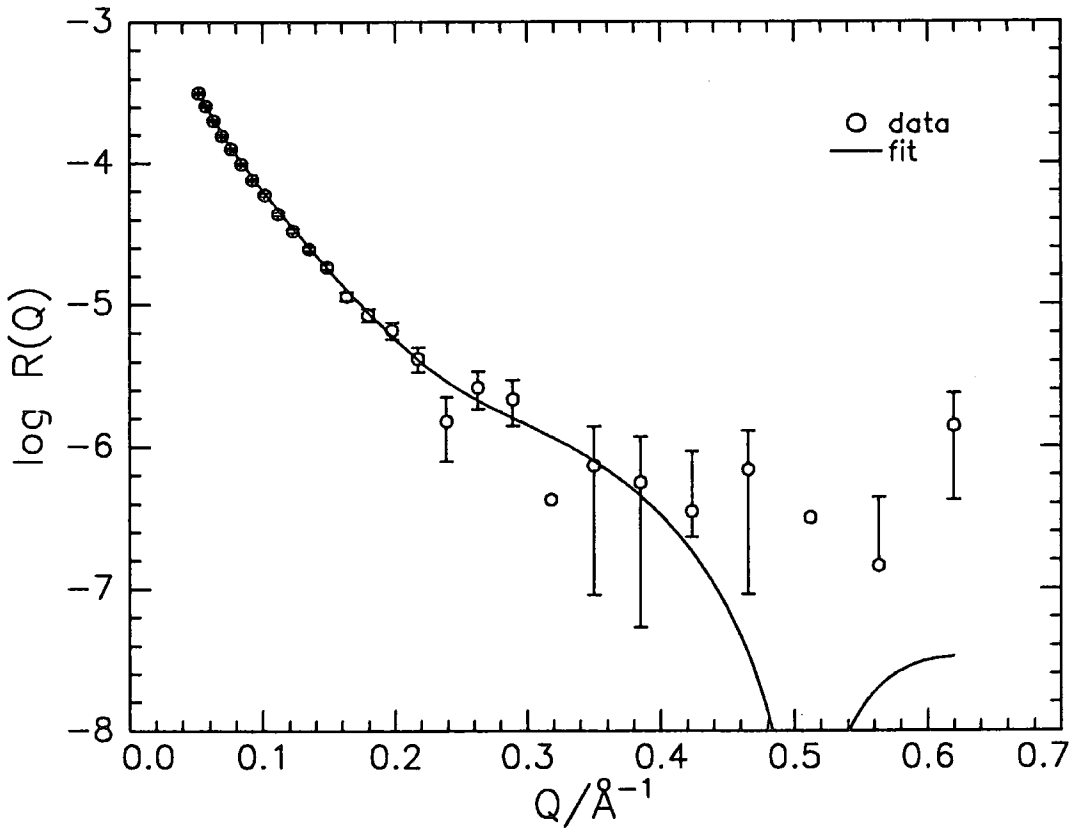

Figure 4.16 Two layer fit for DMDE/nrw at 5mN/m

allowing the average area occupied per segment to be A, then it is possible to write a number of equations relating the scattering length density for each layer to its components. The six equations are;

DMHE / D_2O

upper layer

$$\rho_m = [9.82 \times 10^{-4} f_m + 0.41 \times 10^{-4} f_c] / Ad_m + 6.35 \times 10^{-6} \phi^w_m$$

lower layer

$$\rho_c = [9.82 \times 10^{-4}(1-f_m) + 0.41 \times 10^{-4}(1-f_c)] / Ad_c + 6.35 \times 10^{-6} \varphi^w_c$$

DMHE / nrw

upper layer

$$\rho_m = [9.82 \times 10^{-4} f_m + 0.41 \times 10^{-4} f_c] / Ad_m$$

lower layer

$$\rho_c = [9.82 \times 10^{-4}(1-f_m) + 0.41 \times 10^{-4}(1-f_c)] / Ad_c$$

DMDE / nrw

upper layer

$$\rho_m = [9.82 \times 10^{-4} f_m + 4.58 \times 10^{-4} f_c] Ad_m$$

lower layer

$$\rho_c = [9.82 \times 10^{-4}(1-f_m) + 4.58 \times 10^{-4} f_c] / Ad_c$$

The values in Table 4.4 were used to solve the above equations giving f_m, f_c, A, ϕ^w_m and ϕ^w_c, the average values obtained are given in Table 4.5. This model, although giving values reasonable in appearance, has a number of weaknesses. Firstly, an equal area per segment for PEO and PMMA cannot be correct, secondly, during the fitting of the reflectivity profiles it is the product of the layer thickness and scattering length density which is used in the optical matrix method. Decreasing one of these parameters while increasing the other would give the same product and the uniqueness of this method becomes questionable. From this simplified model the following points can be deduced:

1. The top layer is PMMA having a small amount of PEO and water present

2. PEO is mainly in the lower layer and is highly diluted by the water subphase

3. The PMMA block penetrates the PEO/water layer, especially with increasing surface coverage.

4.1.2 Kinematic Approximation

As mentioned in Chapter 1, isotopically labelling a diblock copolymer allows six partial structure factors to be obtained under suitable contrast conditions. Application of equation (1.3.29) to the MMA/EO diblock copolymer allows these self and cross terms to be determined. Restating this equation explicitly in terms of the species of interest then

$$R(Q)=\frac{16\pi^2}{Q^4}\left[b_m^2 h_{mm}(Q)+b_e^2 h_{ee}(Q)+b_w^2 h_{ww}(Q)+2b_m b_e(Q)+2b_m b_w(Q)+2b_e b_w(Q)\right] \qquad (4.3)$$

where the subscripts m, e and w represent methyl methacrylate, ethylene oxide and water respectively.

4.1.2.1 Self Partial Structure Factors

The simplest models which may be used for the analysis of the self partial structure factors are the uniform layer and Gaussian distribution models. It was impossible to distinguish between these two models because of the resolution of the experiment due to the Q range used, the requirement allowing uniform and Gaussian distributions to be distinguished[1] is that $Q_{max}.d > 2\pi$.

A uniform layer model is described by

$$Q^2 h_{pp}(Q) = (4n_{pl}^2)\sin^2(Qd/2) \qquad (4.4)$$

where n_{pl} is the number density of polymer segments and d is the thickness of the uniform layer. A Gaussian distribution of the number density normal to the surface is usually assumed since this model is considered to be physically more realistic as Gaussian profiles normally describe polymer probability statistics. Gaussian distributions are given by

$$Q^2 h_{pp}(Q) = (n_{pl}^2)(\pi\sigma^2/4)\exp(-Q^2\sigma^2/8) \qquad (4.5)$$

where n_{pl} is the number density of polymer segments and σ is the relaxation distance of the half Gaussian distribution. The apparent surface concentration may therefore be given by

$$\Gamma_a = \sigma n_{lp}\pi^{1/2} / 2 \text{ molecules Å}^{-2} \quad (4.6)$$

Equations 4.5 and 4.6 then give

$$\ln(h_{pp}(Q) = 2\ln\Gamma_a - Q^2\sigma^2 / 8 \quad (4.7)$$

For the DMHE/nrw contrast, then in the kinematic approximation (eqn 4.3) if the scattering length of HEO is taken to be approximately zero then all except the first term disappear and

$$h_{mm}(Q) = (Q^2 16\pi^2/b_m^2)R(Q) \quad (4.8)$$

where b_m is the scattering length of the whole DM block. A similar equation may be written for DMDE for the whole copolymer. By using equation 4.7 then since DMHE and DMDE have almost exact molar composition then their data may be compared. Figure 4.17 shows plots similar to Guinier plots of small angle scattering, DMDE and DMHE data sets being plotted as h_{mm} v Q^2. These plots have a similar intercept indicating the absence of isotope effects at the air/water interface. Table 4.6 shows the parameters for these plots as well as those for HMDE. It can be seen that the HMDE intercepts differ from those of DMDE and DMHE which must be an effect of the rather short DEO chain. The DMHE/nrw and HMDE/nrw contrast data were used to calculate the MMA and EO self terms at 2,5 and 10mN/m, a typical fit is shown in figure 4.18 and the parameters obtained are shown in Table 4.7 assuming uniform and Gaussian distributions. It can be seen that there is good agreement between σ determined from both the Guinier and Gaussian methods. The apparent surface concentration Γ_a values are higher than the spread amount which is due to the problem encountered earlier for the uniform layer model, i.e. film collapse due to perturbation of the Wilhelmy plate. The

Polymer	π/mN m^{-1}	Γ_s/mg m^{-2}	slope	intercept	σ/Å
DMDE	2	0.60	-30.42	-16.27	16
	5	1.00	-33.83	-16.20	17
	10	2.40	-33.80	-16.00	16
DMHE	2	0.65	-21.52	-16.59	13
	5	1.00	-29.47	-16.55	15
	10	1.41	-30.20	-16.09	16
HMDE	2	0.13	-35.22	-14.87	17
	5	0.16	-33.55	-14.10	16
	10	0.23	-33.55	-14.77	16

Table 4.6 Parameters from self terms obtained using Guinier method

Model	Term	Subphase	π /mN m^{-1}	n_{il}/Å^{-3}	d/Å	σ/Å	Γ_s /mg m^{-2}	Γ_{app} /mg m^{-2}
uniform	DMHE	nrw	2	1.20e-5	15		0.65	1.14
	HMDE	nrw	2	1.07e-5	20		0.13	0.29
	HMHE	D_2O	2	7.94e-3	21			
	DMHE	nrw	5	1.06e-5	18		1.00	1.17
	HMDE	nrw	5	1.59e-5	20		0.16	0.44
	HMHE	D_2O	5	9.64e-3	21			
	DMHE	nrw	10	1.32e-5	17		1.41	1.42
	HMDE	nrw	10	1.11e-5	20		0.23	0.31
	HMHE	D_2O	10	1.11e-2	20			
Gaussian	DMHE	nrw	2	1.59e-5		13	0.65	1.16
	HMDE	nrw	2	1.42e-5		17	0.13	0.29
	DMHE	nrw	5	1.38e-5		16	1.00	1.21
	HMDE	nrw	5	2.10e-5		17	0.16	0.44
	DMHE	nrw	10	1.72e-5		15	1.41	1.46
	HMDE	nrw	10	1.49e-5		17	0.23	0.31

Table 4.7 Structural Parameters from the Partial Form Factors

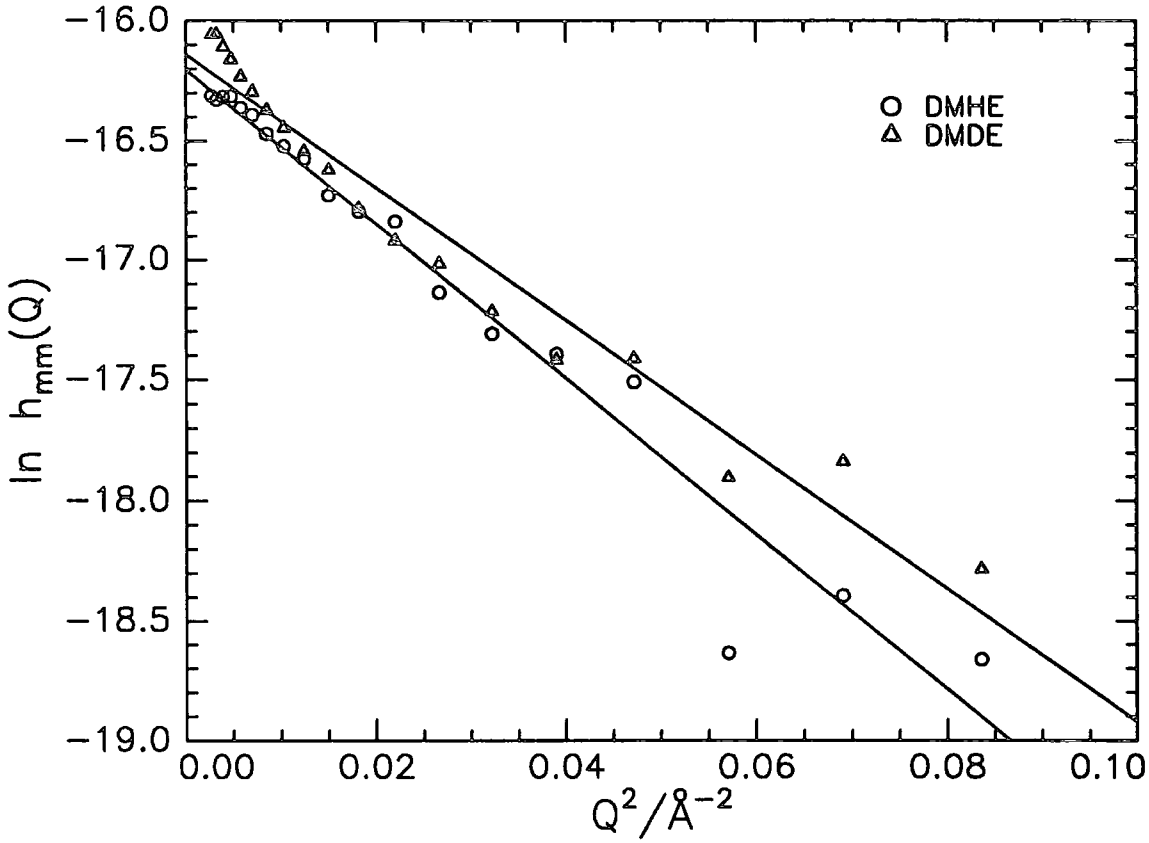

Figure 4.17 DMHE (O) and DMDE (Δ) spread on nrw at 10mN/m presented as Guinier plots

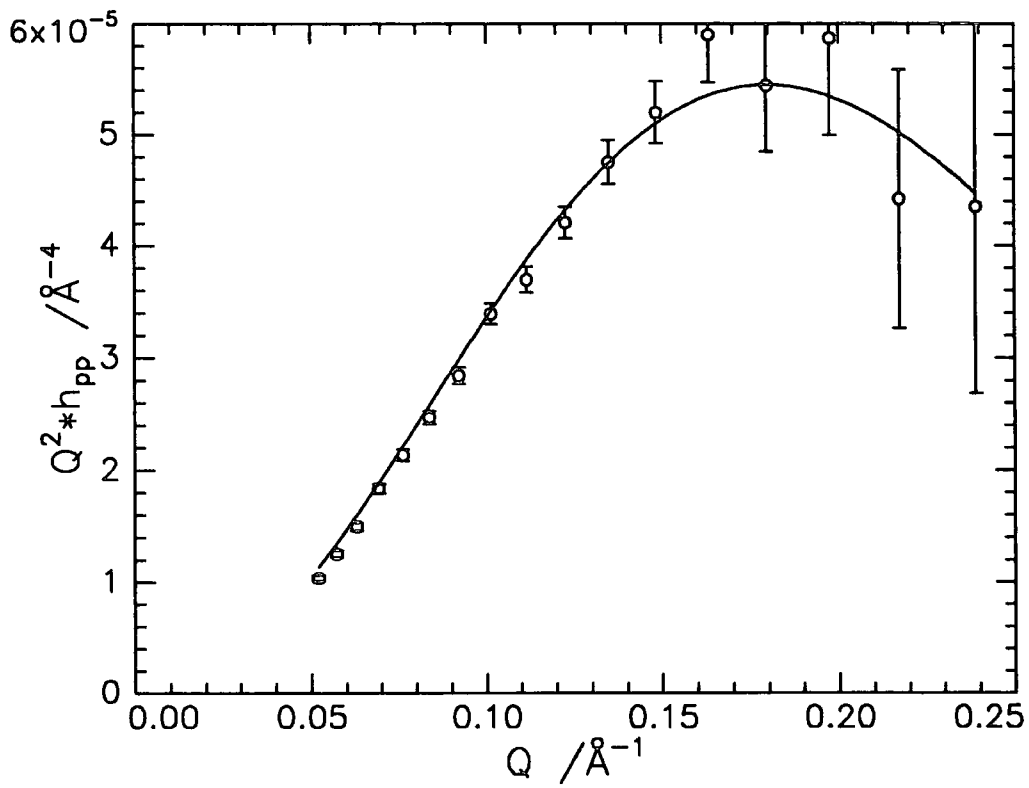

Figure 4.18 Fit to DMHE/nrw data at 5mN/m assuming a gaussian distribution of segments

HMHE/D_2O contrast data give an indication of the distribution of the water at the air/water interface. The partial structure factor describing this uniform model is

$$Q^2h_{ww}(Q) = [n_{w0}^2 + 4n_{w1}(n_{w1}-n_{w0})\sin^2(Qd_w/2)] \qquad (4.9)$$

where n_{w0} is the bulk number density of water subphase and n_{w1} is the number density of water at the interface having a thickness of d_w. A fit to a typical water self term is shown in figure 4.19 and the parameters are summarised in Table 4.7.

In order obtain the maximum information from the kinematic approximation and therefore the spatial organisation of the interfacial components, then several different contrast conditions must be used. Ideally, these contrast conditions should maximise the variation in coherent scattering length, b_i, of each interfacial component. This is achieved by spreading isotopically labelled copolymers on both D_2O and null reflecting water (nrw). These copolymers should have exact composition and molecular weight but this is difficult to achieve experimentally. Table 2.1 shows that the copolymers DMHE, DMDE and HMHE are similar enough in composition for their reflectivity data to be used. Seven contrast conditions were available in total which included DMDE/nrw, DMHE/nrw, DMHE/D_2O, HMDE/D_2O, HMHE/D_2O, HMDE/nrw and DMDE/D_2O although only six were required to solve the kinematic approximation. The six contrast conditions used represented a series of simultaneous equations for the three interfacial components. A least squares solution of these equations using the PARTIAL3 computer program developed by J. Penfold gave the six partial structure factors. This program required the six background subtracted reflectivity profiles and an input file. This file contained the coherent scattering lengths of the MMA and EO components weighted by factors equal to their degrees of polymerisation (Appendix A). It was not possible to obtain self and cross terms involving ethylene oxide when the HMDE/nrw contrast was used in conjunction with the first five of the above contrasts. The reason for this was thought to

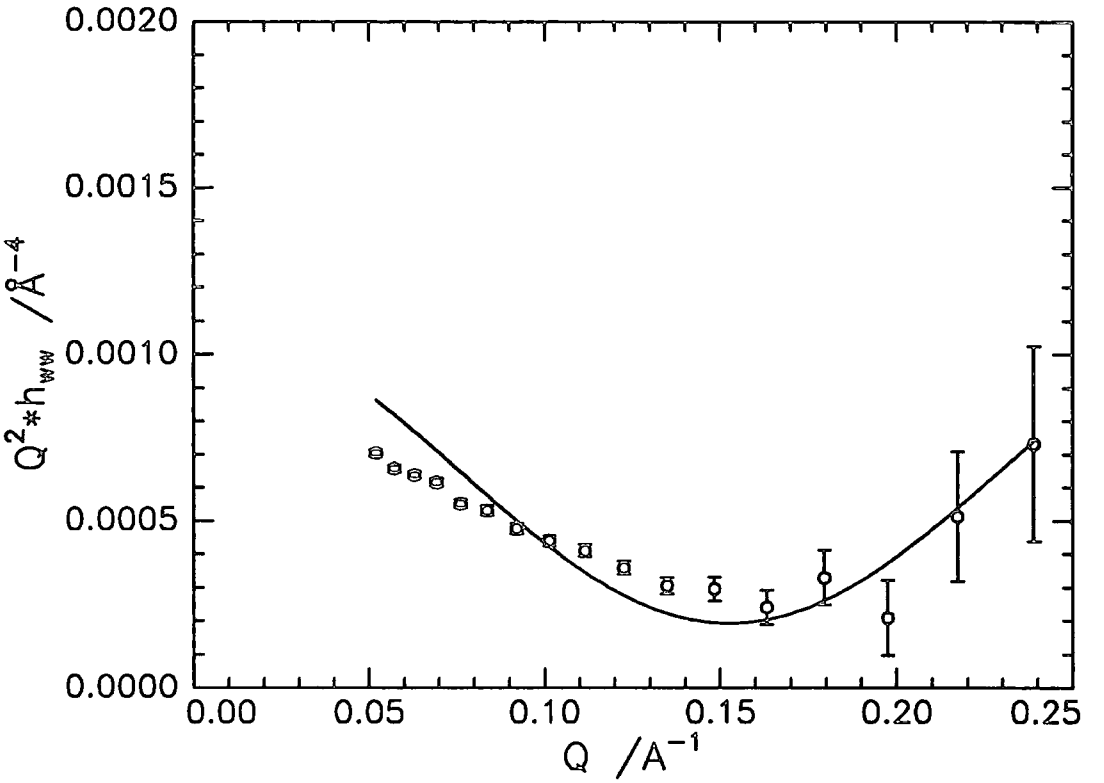

Figure 4.19 Fit to HMHE/D_2O data at 5mN/m assuming uniform layer of water

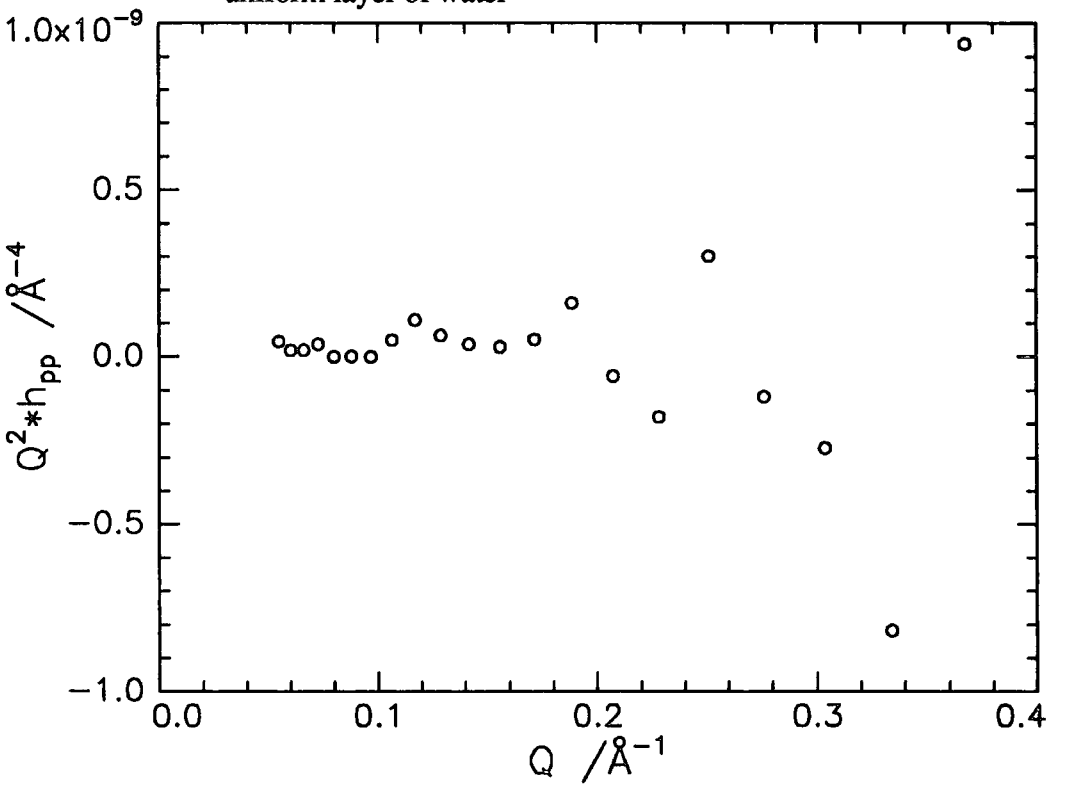

Figure 4.20 MMA self term at 1mN/m

be due to the very low reflectivity of the contrast. Better data were obtained by using the DMDE/D_2O contrast instead. Solving the kinematic approximation in this way with the computer software available produced data files without an error column, therefore error bars are missing from these plots.

The self term data were fitted assuming both uniform and Gaussian distributions of segments. Figures 4.20 to 4.27 show the data for the MMA and EO self terms fitted assuming a Gaussian distribution of segments. It was not possible to fit a model to the scattered data points of the partial structure factors at 1mN/m surface pressure (figures 4.20 to 4.21) or the EO self term at 10mN/m. Table 4.8 summarises the parameters from the fits of uniform and gaussian distributions. Figures 4.28 to 4.33 are typical Guinier plots for the self terms which show how appropriate the fits to the Gaussian distributions are. The parameters obtained from these straight line plots are summarised in Table 4.9, the values of σ and Γ agreeing well with those of the Gaussian distributions. Figures 4.34 to 4.37 show uniform layer fits to the water self terms and the parameters are summarised in Table 4.8.

The form factors h_{ii} give the profile of component i across the interface, but they contain no information about its structural correlation with component j. A knowledge of h_{ii} alone does not allow the spatial arrangement of the copolymer blocks in the layer to be deduced. This information is contained in the cross partial structure factors, h_{ij}. These may be calculated by restating equation (1.3.46) in terms of the species of interest

$$h_{me}(Q) = \pm(h_{mm}h_{ee})^{1/2}\cos(Q\delta) \qquad (4.10)$$

where δ is the mean centre to centre separation of the two distributions. The left hand side of equation 4.10 is the cross term produced by solving the kinematic approximation, while the right hand side was calculated using the parameters obtained from the self

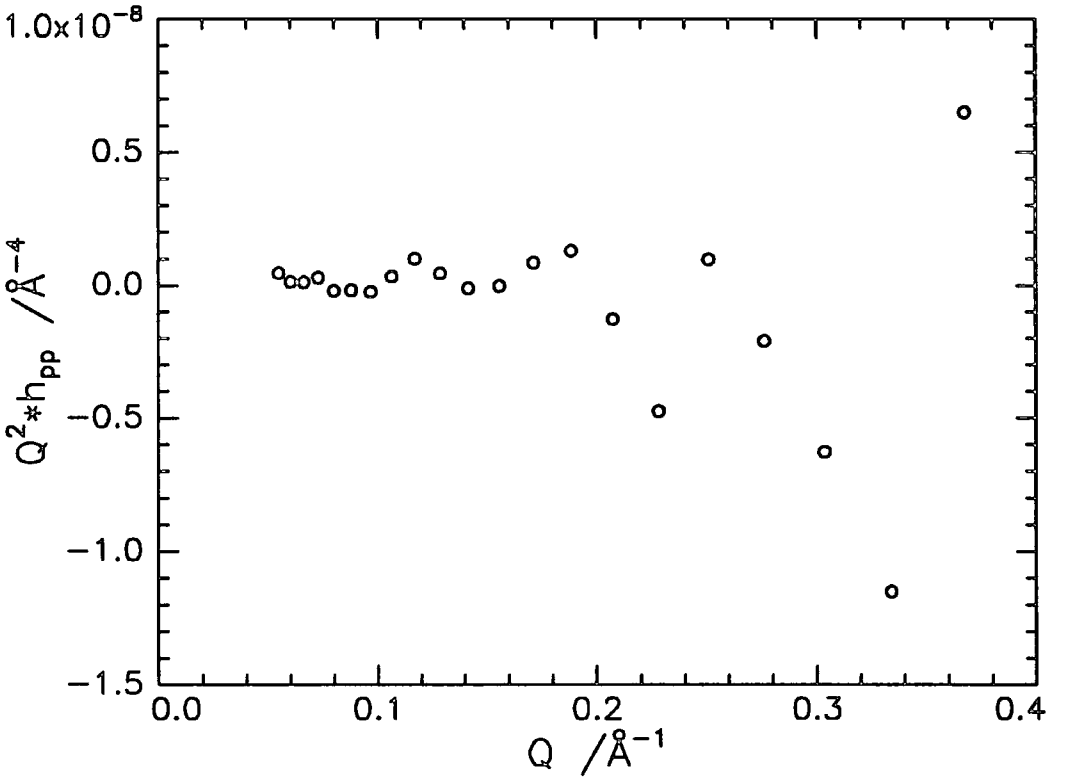

Figure 4.21 EO self term at 1mN/m

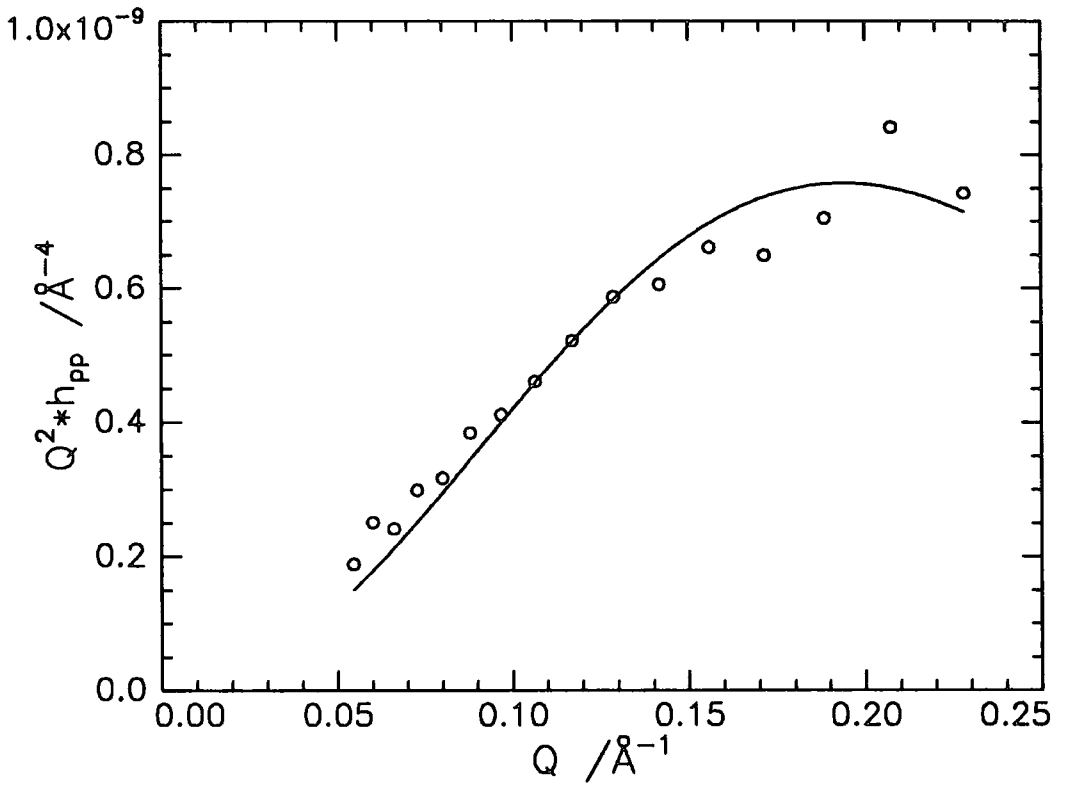

Figure 4.22 MMA self term at 2mN/m

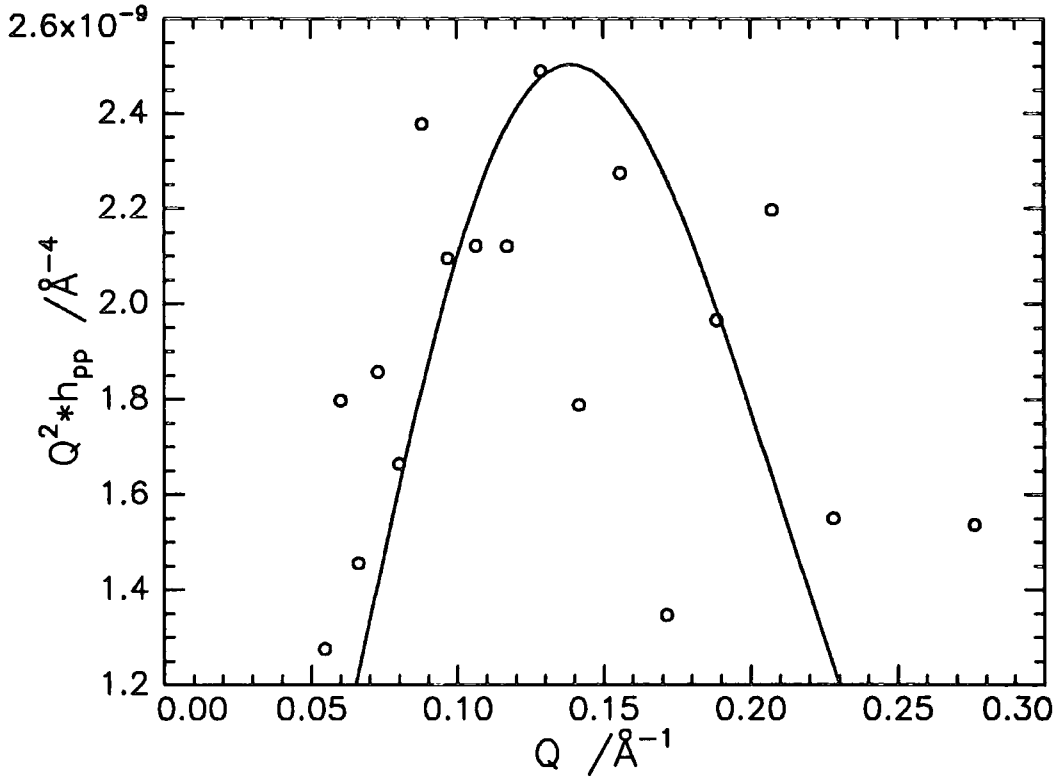

Figure 4.23 EO self term at 2mN/m

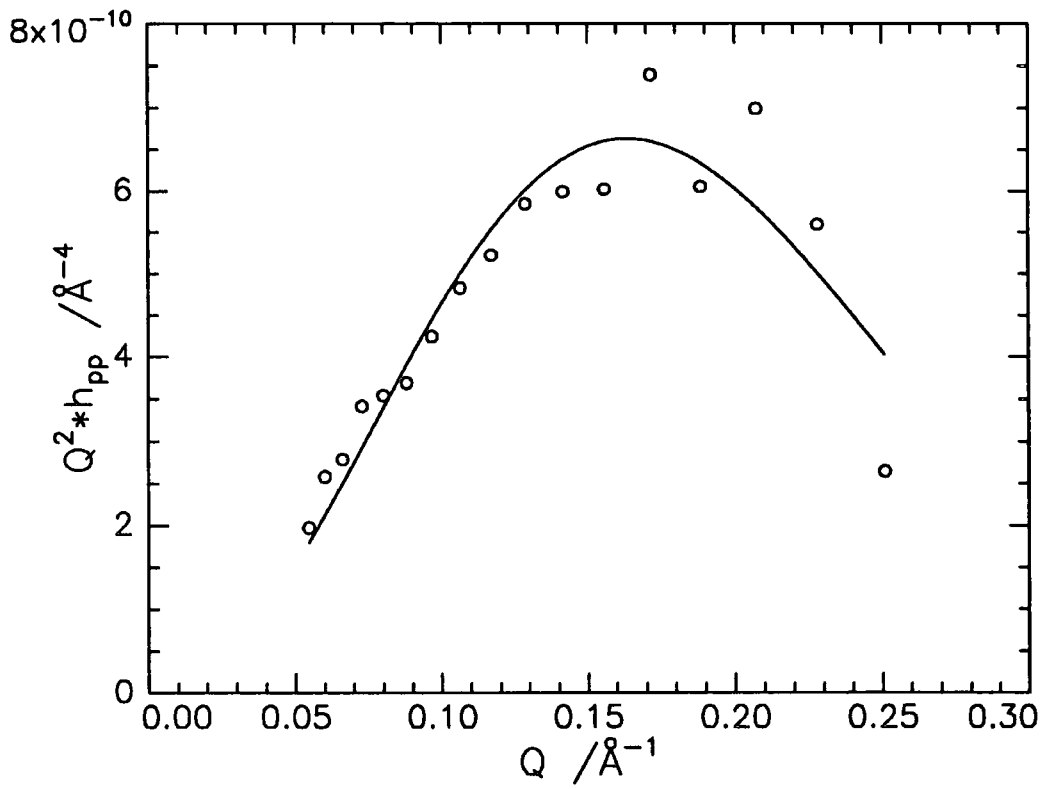

Figure 4.24 MMA self term at 5mN/m

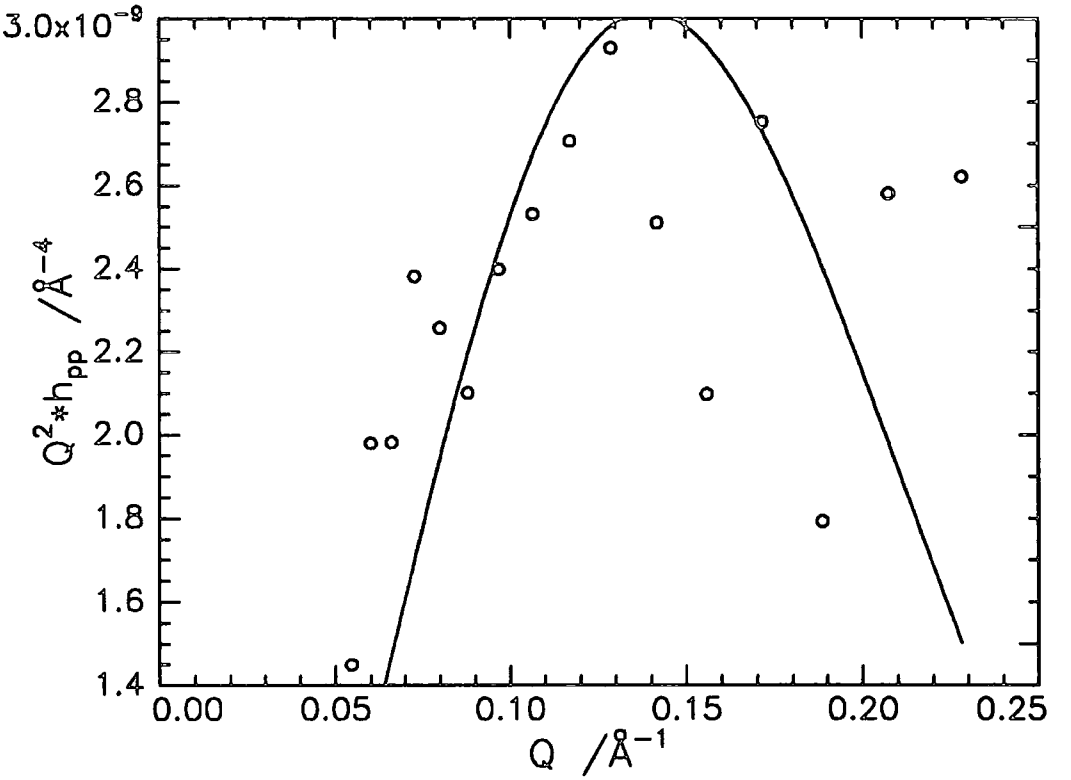

Figure 4.25 EO self term at 5mN/m

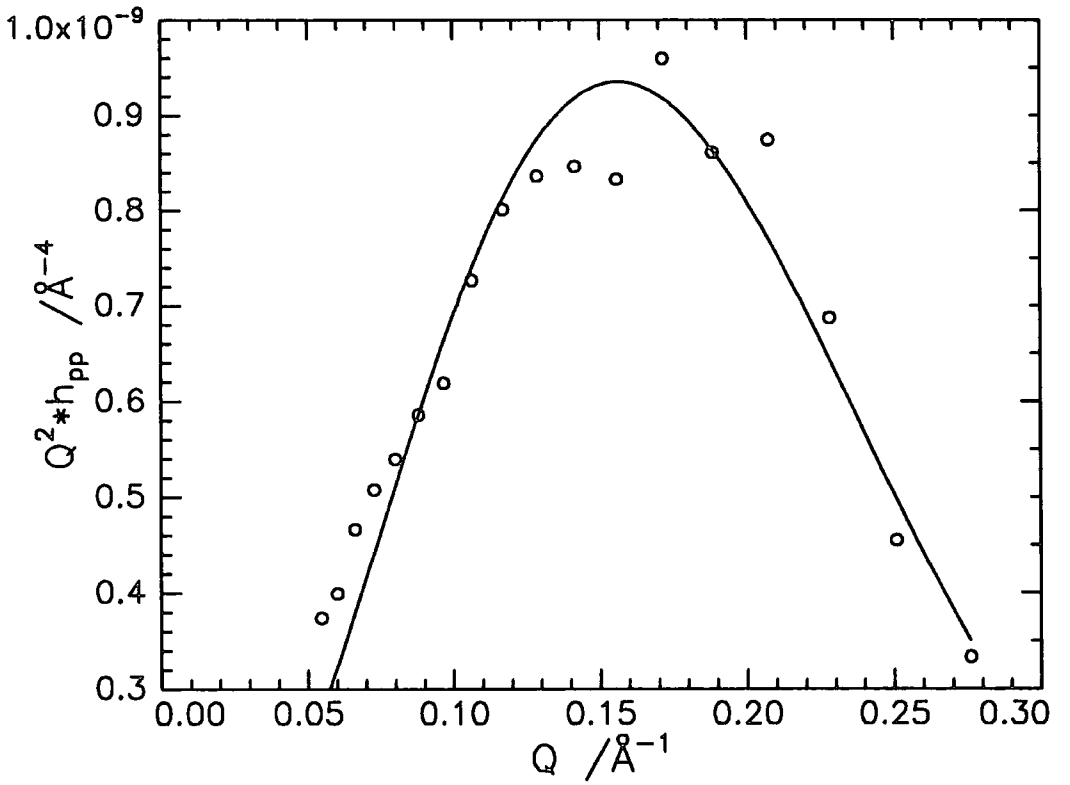

Figure 4.26 MMA self term at 10mN/m

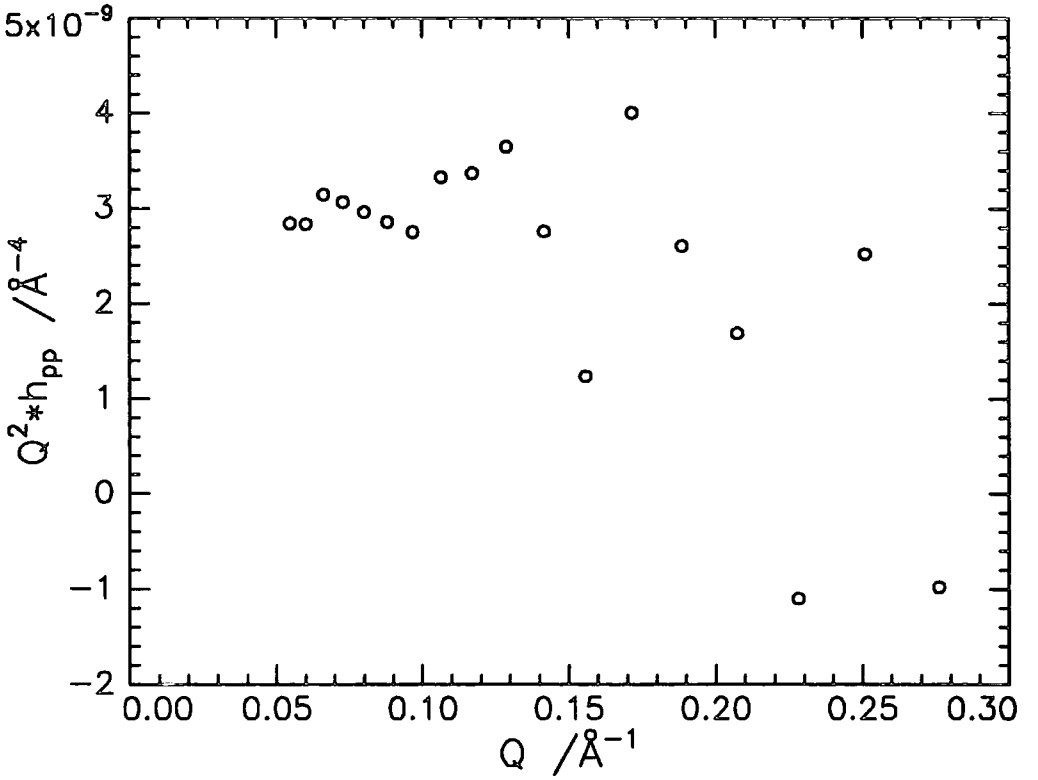

Figure 4.27 EO self term at 10mN/m

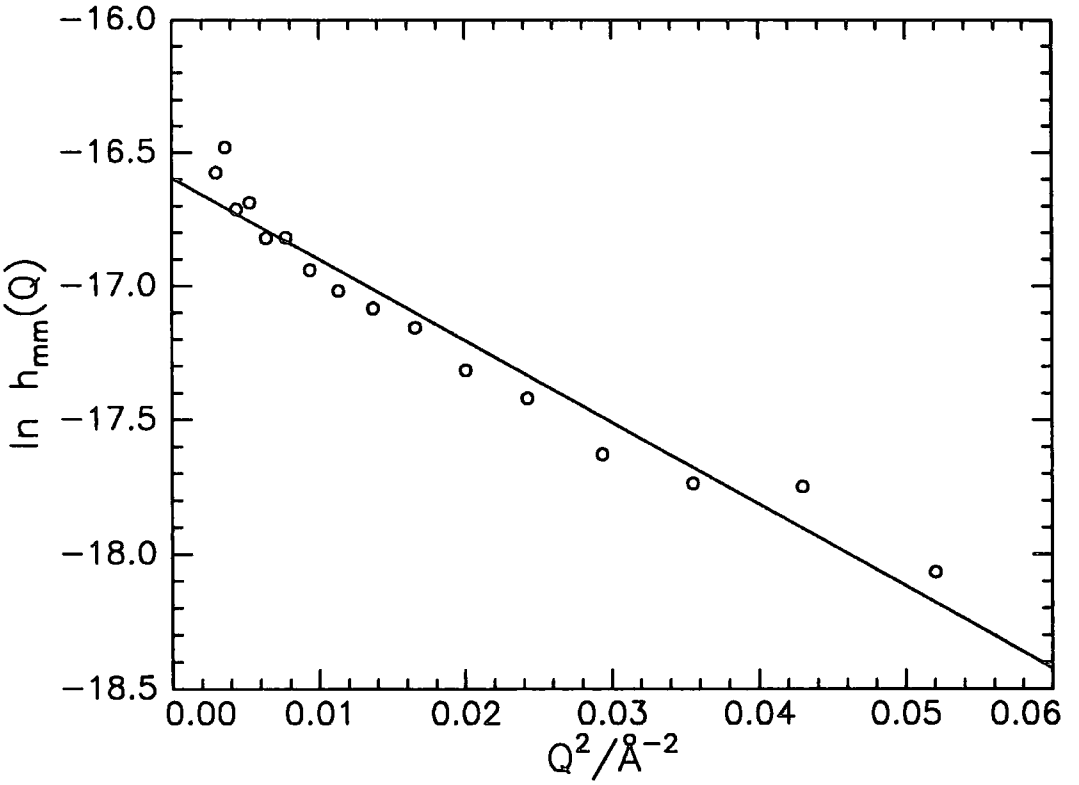

Figure 4.28 Guinier plot for MMA self term at 2mN/m

Model	Term	π /mg m^{-1}	n_{il}/Å^{-3}	d/Å	σ/Å	Γ_s /mg m^{-2}	Γ_{app} /mg m^{-2}	δ_{mc}/Å	δ_{mw}/Å	δ_{cw}/Å
none		2						4	5	0.8
		5						4	3.5	1.0
		10						5	5	0.5
uniform	h_{mm}	2	1.39e-5	16		0.70	1.08			
		5	1.32e-5	19		0.98	1.18			
		10	1.56e-5	19		1.48	1.41			
	h_{cc}	2	2.49e-5	25		0.30	1.97			
		5	2.72e-5	25		0.42	2.13			
		10	3.05e-5	25		0.65	2.38			
	h_{ww}	2	3.85e-3	21						
		5	5.35e-3	20						
		10	5.25e-3	22						
Gaussian	h_{mm}	2	1.81e-5		15	0.70	1.11			
		5	1.69e-5		17	0.98	1.23			
		10	2.01e-5		18	1.48	1.53			
	h_{cc}	2	3.29e-5		21	0.30	1.88			
		5	3.61e-5		20	0.42	2.04			
		10	4.10e-5		24	0.65	2.74			

Table 4.8 Structural Parameters from the Partial Form Factors using the Kinematic Approximation

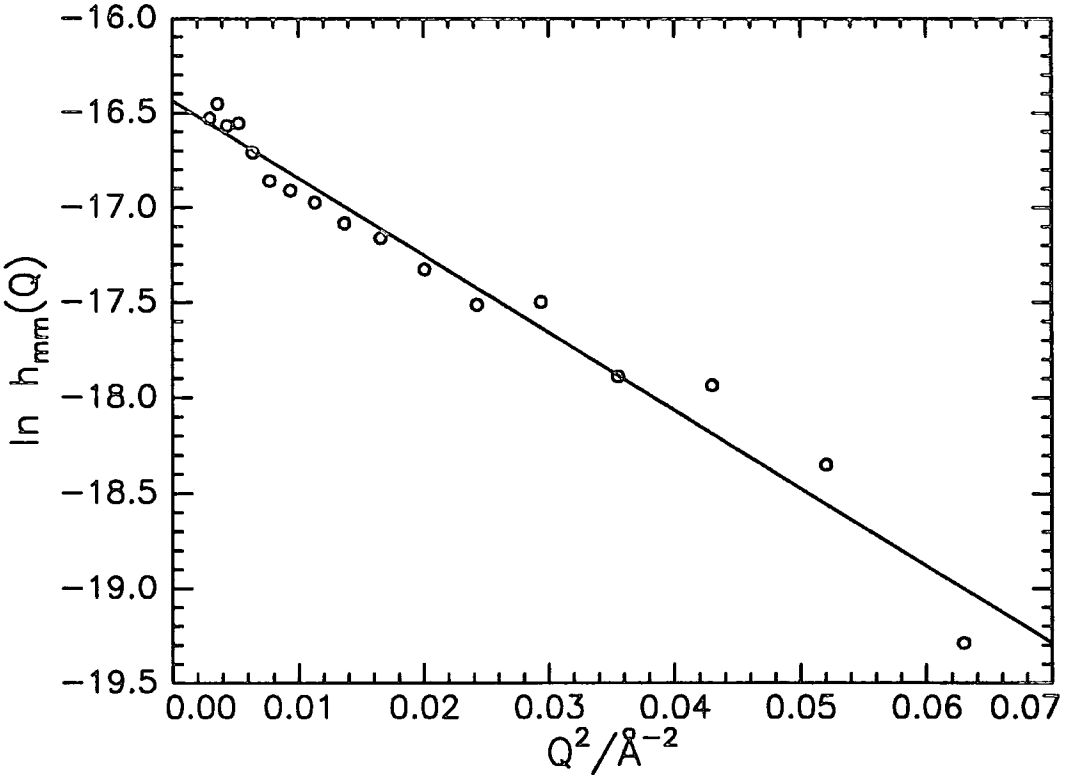

Figure 4.29 Guinier plot for MMA self term at 5mN/m

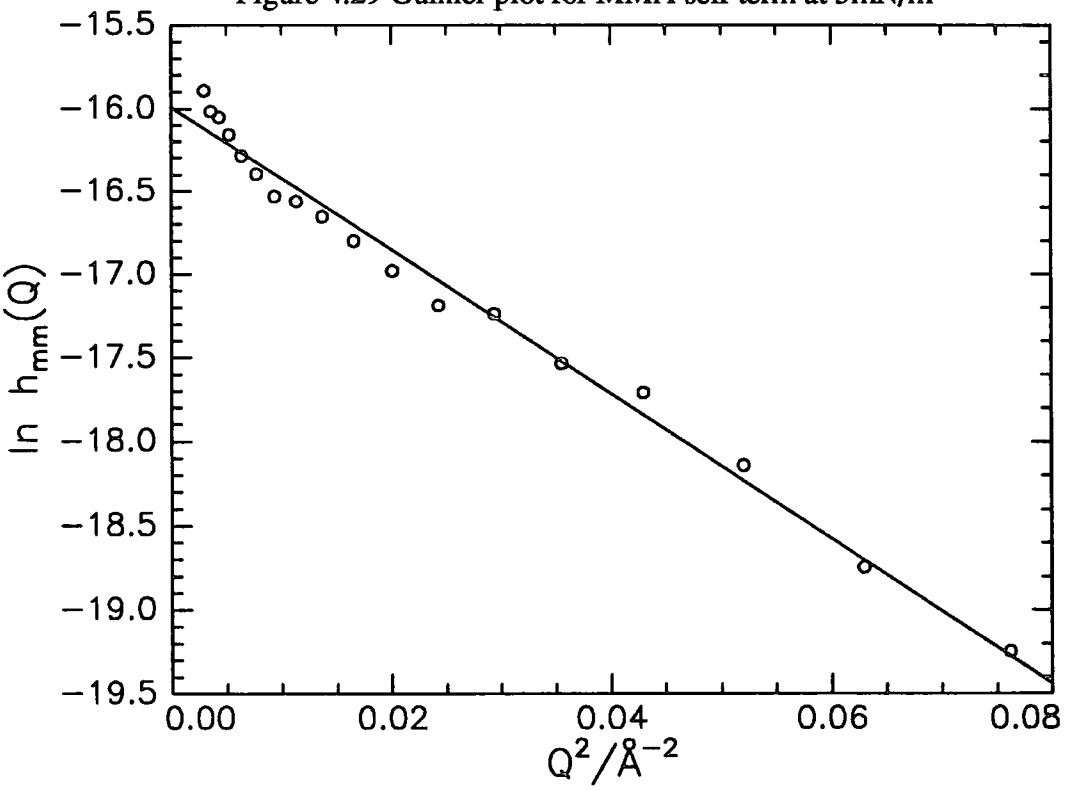

Figure 4.30 Guinier plot for MMA self term at 10mN/m

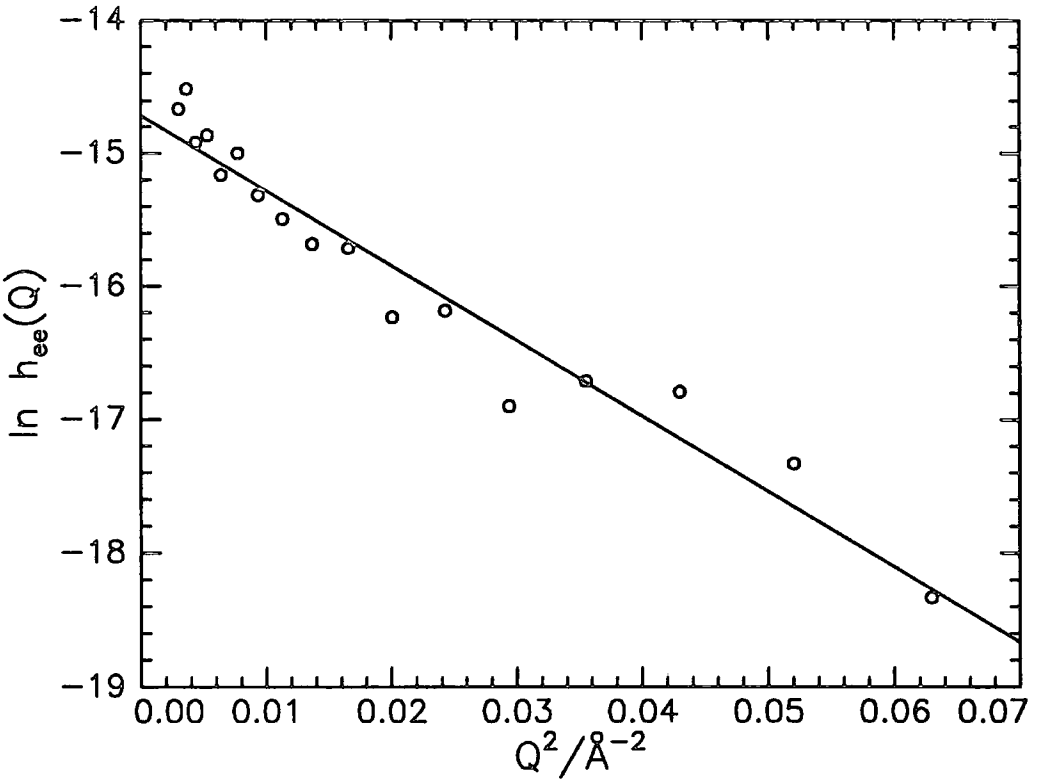

Figure 4.31 Guinier plot for EO self term at 2mN/m

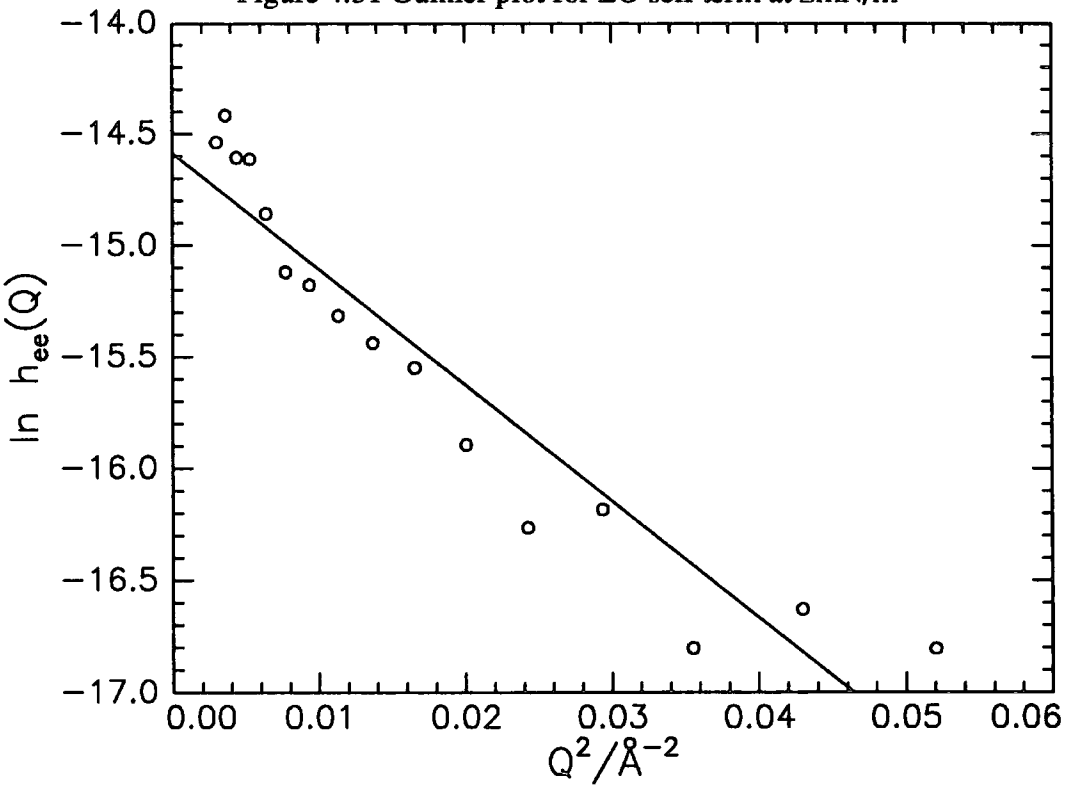

Figure 4.32 Guinier plot for EO self term at 5mN/m

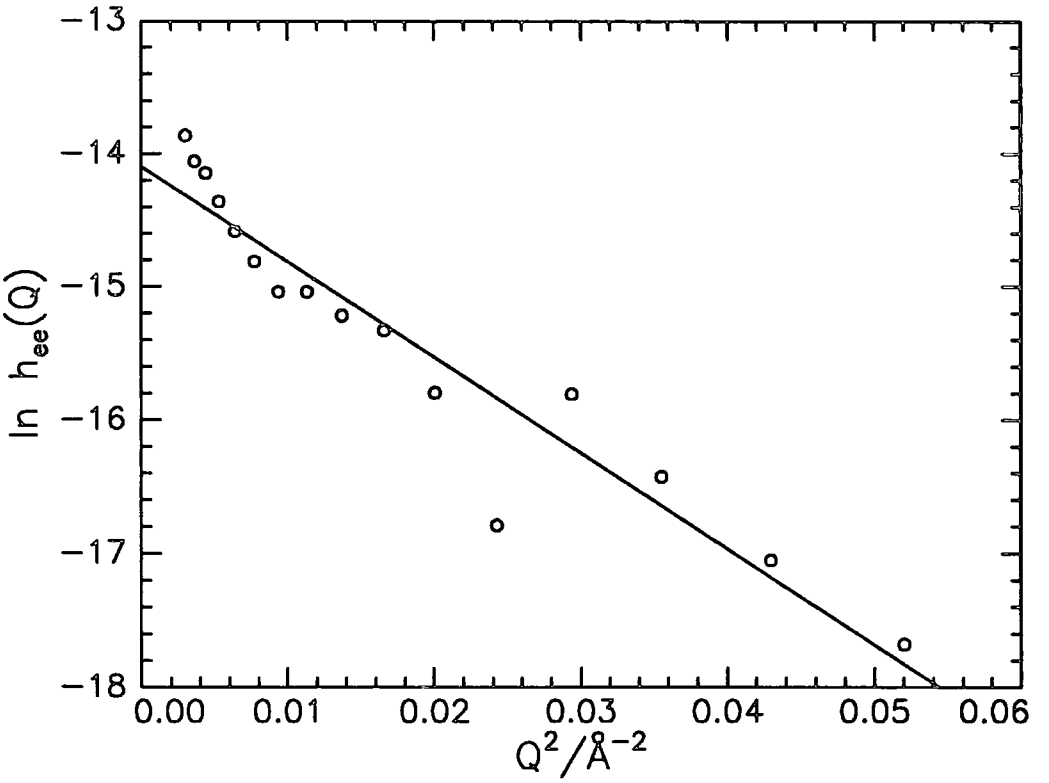

Figure 4.33 Guinier plot for EO self term at 10mN/m

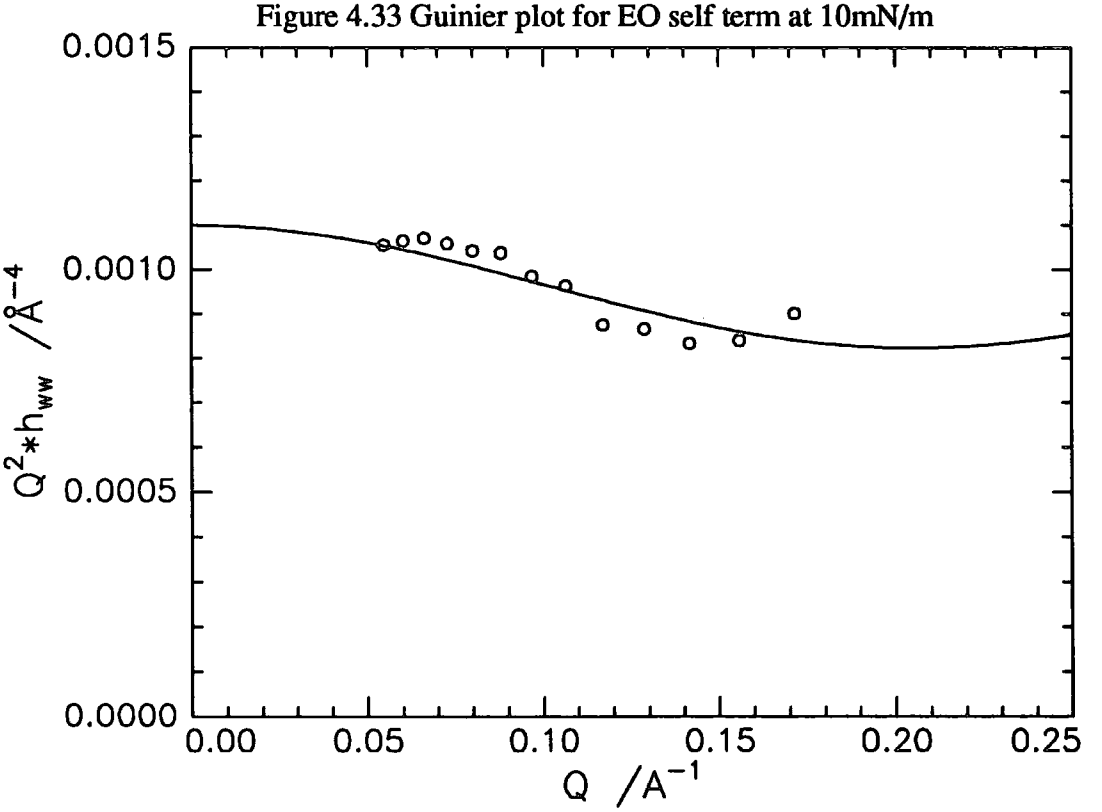

Figure 4.34 Uniform layer fit to water self term at 1mN/m

Term	π/mN m^{-1}	Γ_s/mg m^{-2}	slope	intercept	σ/Å
h_{mm}	2	0.70	-30.46	-16.59	16
	5	0.98	-40.74	-16.43	18
	10	1.48	-43.07	-15.99	19
h_{ee}	2	0.30	-55.67	-14.72	21
	5	0.42	-52.01	-14.58	20
	10	0.65	-71.77	-14.09	24

Table 4.9 Parameters from self terms obtained using Guinier method

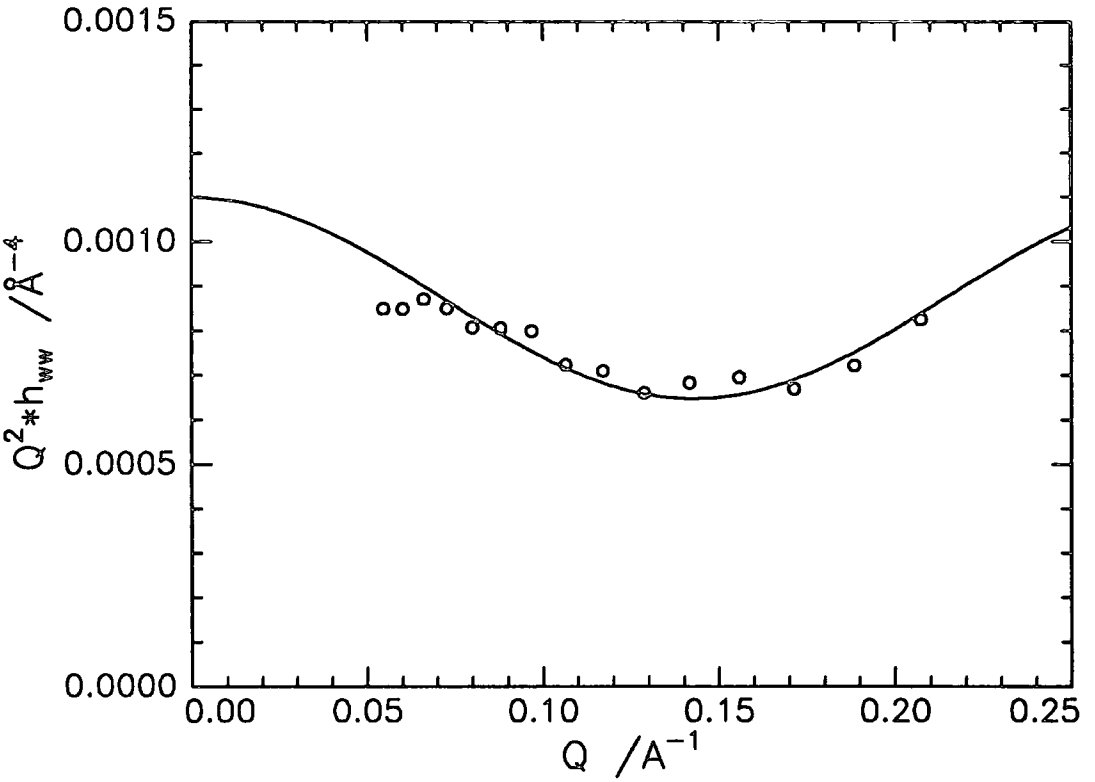

Figure 4.35 Uniform layer fit to water self term at 2mN/m

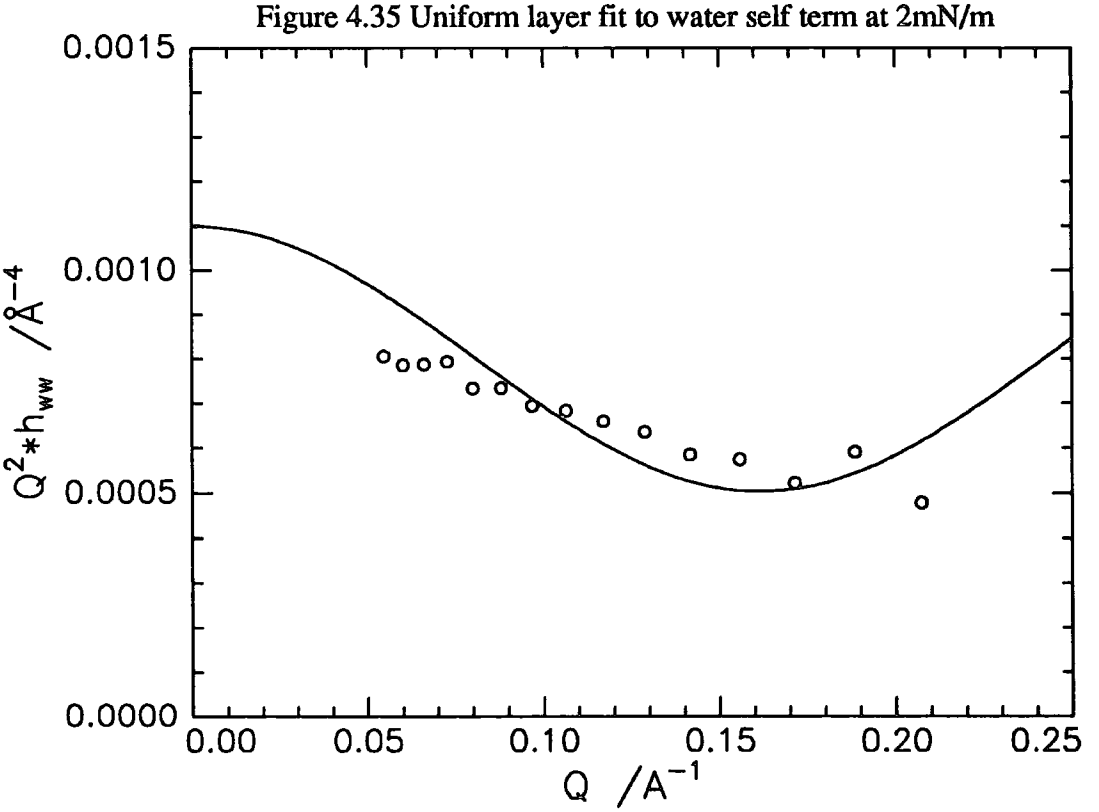

Figure 4.36 Uniform layer fit to water self term at 5mN/m

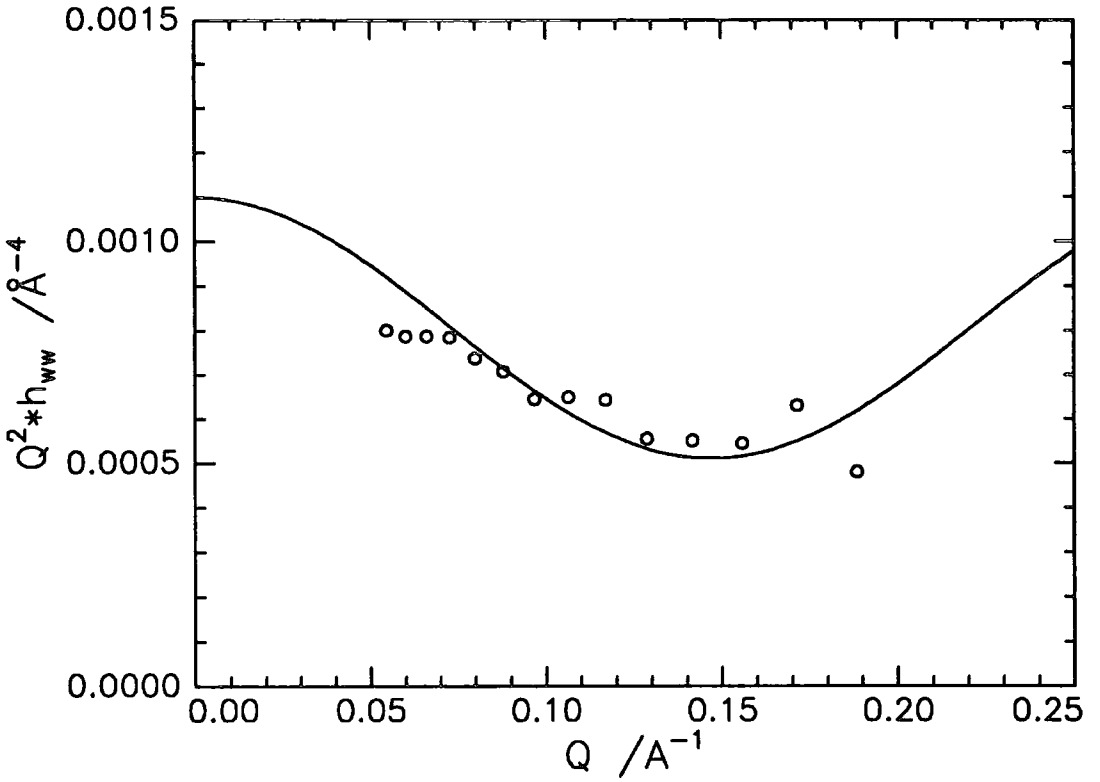

Figure 4.37 Uniform layer fit to water self term at 10mN/m

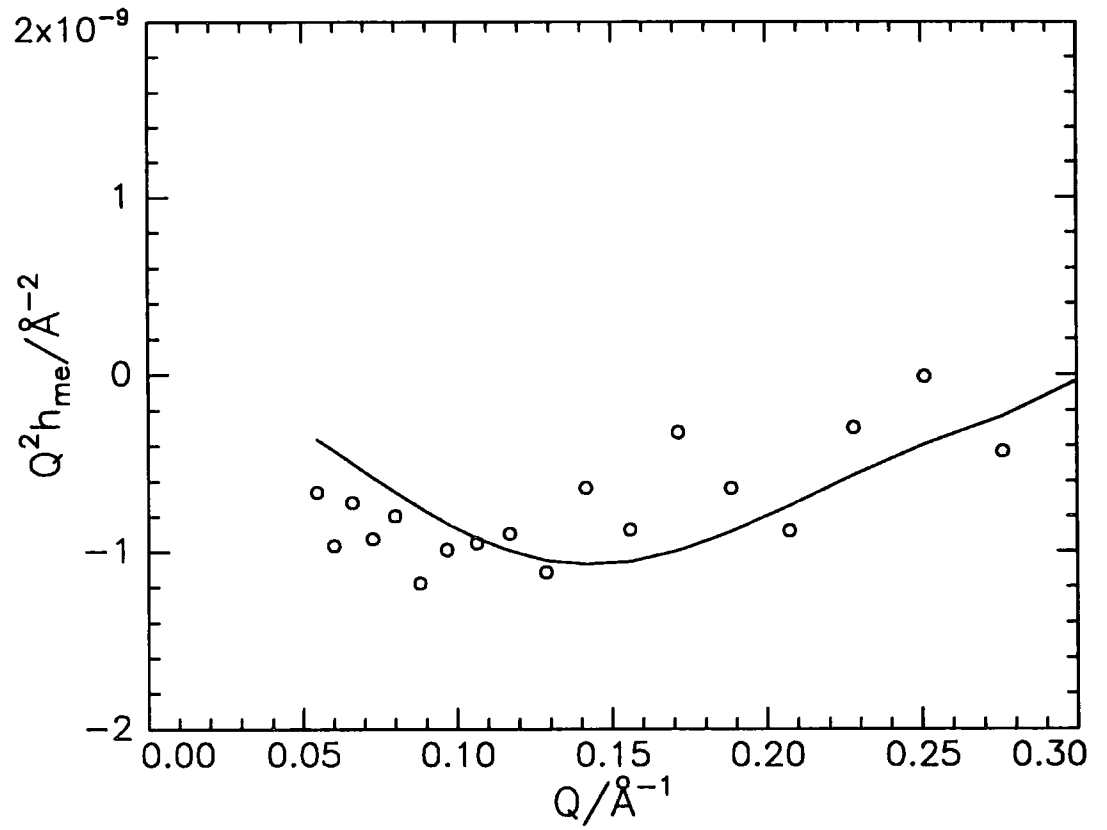

Figure 4.38 Fit to MMA/EO cross term at 2mN/m

terms (equation 4.5). By generating plots of $(h_{mm}h_{mm})^{1/2}\cos(Q\delta)$ having varying values of δ then the 'best fit' to the $h_{ij}(Q)$ data was obtained.

In the case of cross terms involving a solvent then equation (1.3.45) may be used

$$h_{iw}(Q) = \pm (h_{ii}h_{ww})^{1/2} \sin(Q\delta) \qquad (4.11)$$

where the subscript w denotes the water subphase and i = MMA or EO. Values of δ were obtained using the same method as for equation 4.10 and are shown in Table 4.7. Figures 4.38 to 4.46 show data and fits for the three cross terms. The structural parameters obtained for the Gaussian distribution are presented in figures 4.47 to 4.49 as distributions of the number density of each interfacial component at 2, 5 and 10mN/m. The results show that there is separation between the centres of the PMMA and PEO distributions. The mean separation is about 4Å at 2 and 5mN/m increasing to 5Å at 10mN/m. The widths of the two distributions indicate a large fraction of PEO segments in the PMMA layer. The mean centre to centre PMMA/water distribution is 5Å at 2 and 10mN/m, being 3.5Å at 5mN/m. The values of the PEO/water separations are about 1Å which shows that the water distribution is almost coincident with that of the PEO. At higher surface concentrations both the PMMA and PEO distributions become broader. Considering the 50:50 ratio of MMA:EO then the number densities of these distributions should be equal. By dividing the integrated number density by the corresponding layer thickness then the amount of PEO is overestimated by a factor of 2. In Table 4.7 the number densities of DMHE and HMDE on nrw are similar so the observed overestimation must due to inclusion of four D_2O contrasts and only 2 nrw contrasts in the matrix used to solve the kinematic approximation.

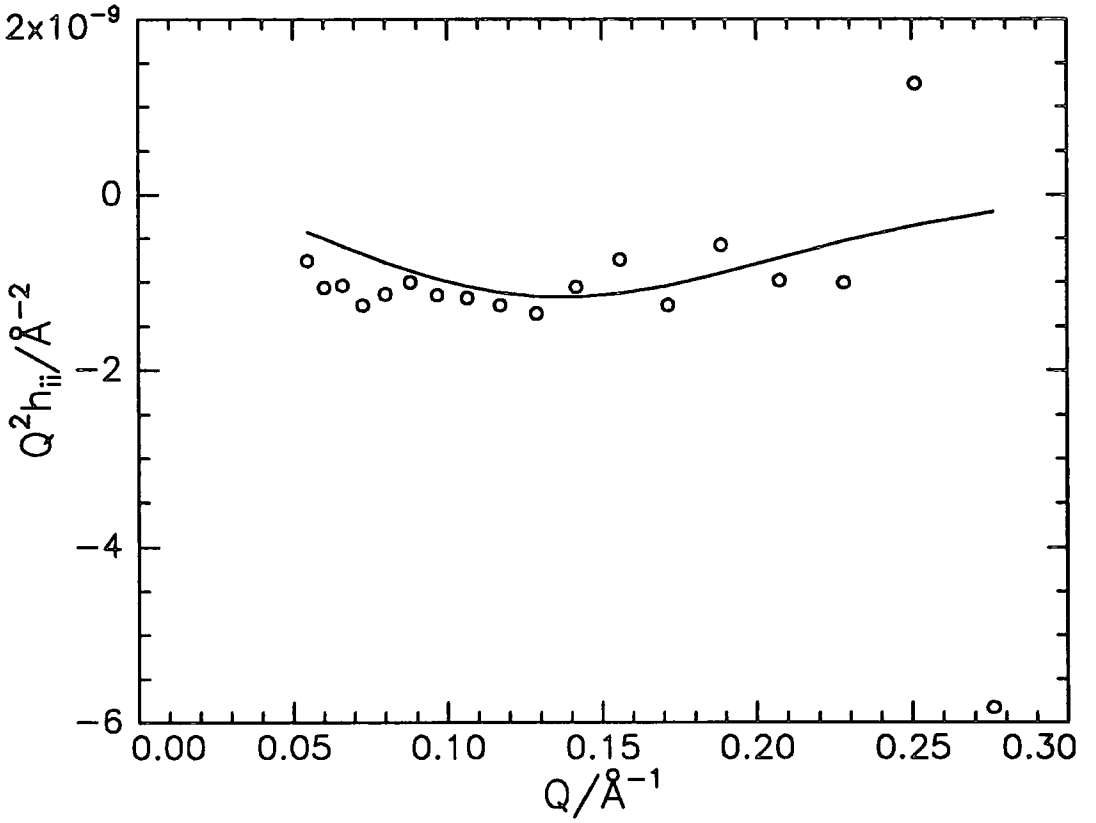

Figure 4.39 Fit to MMA/EO cross term at 5mN/m

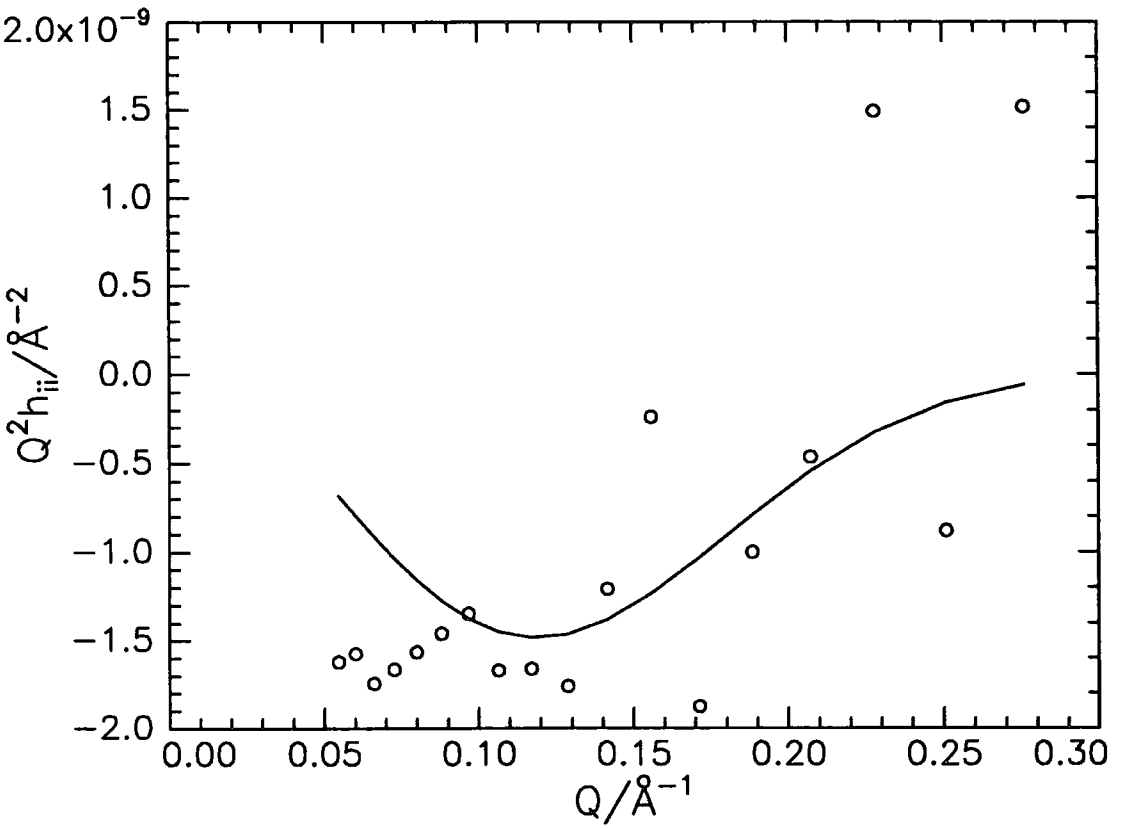

Figure 4.40 Fit to MMA/EO cross term at 10mN/m

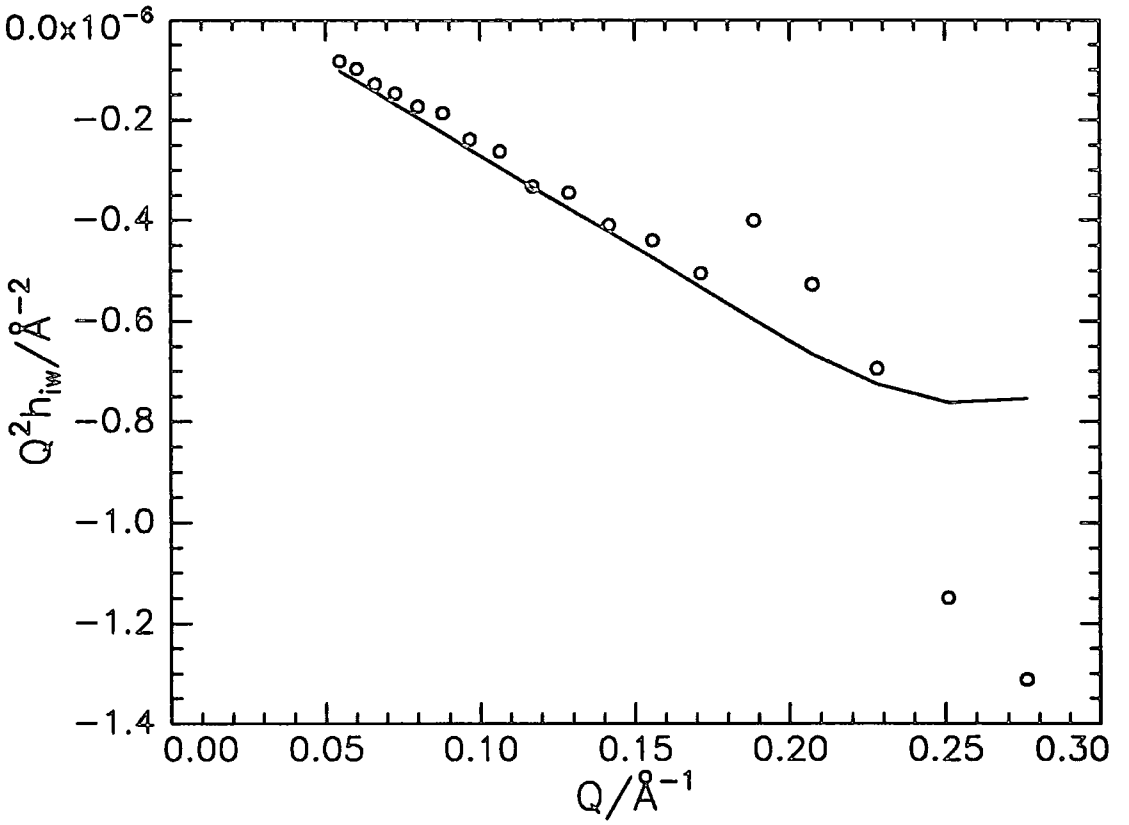

Figure 4.41 Fit to MMA/water cross term at 2mN/m

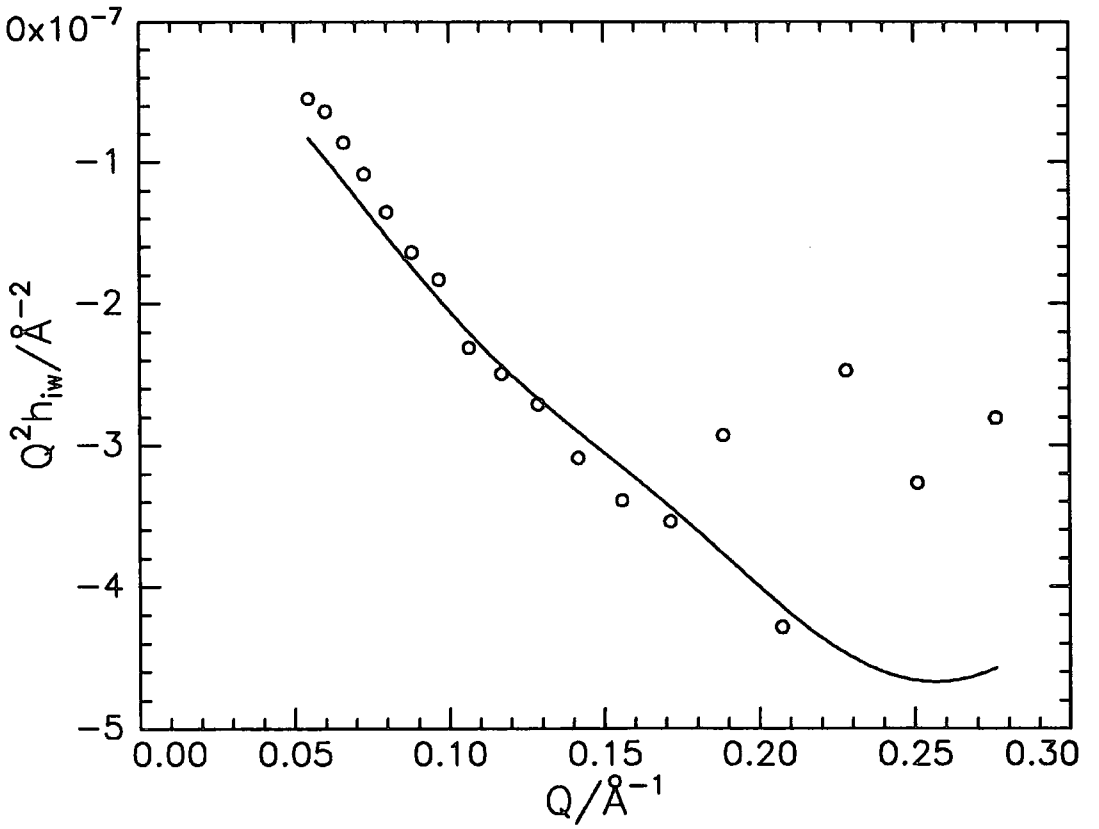

Figure 4.42 Fit to MMA/water cross term at 5mN/m

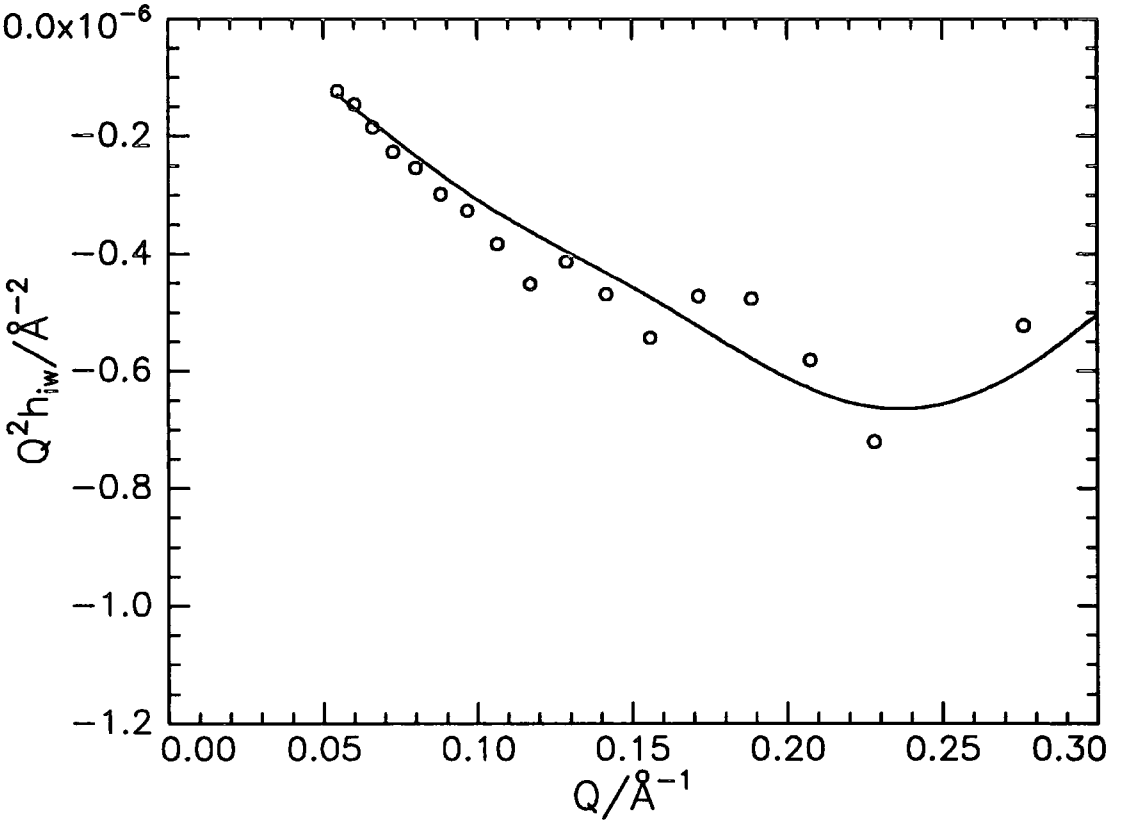

Figure 4.43 Fit to MMA/water cross term at 10mN/m

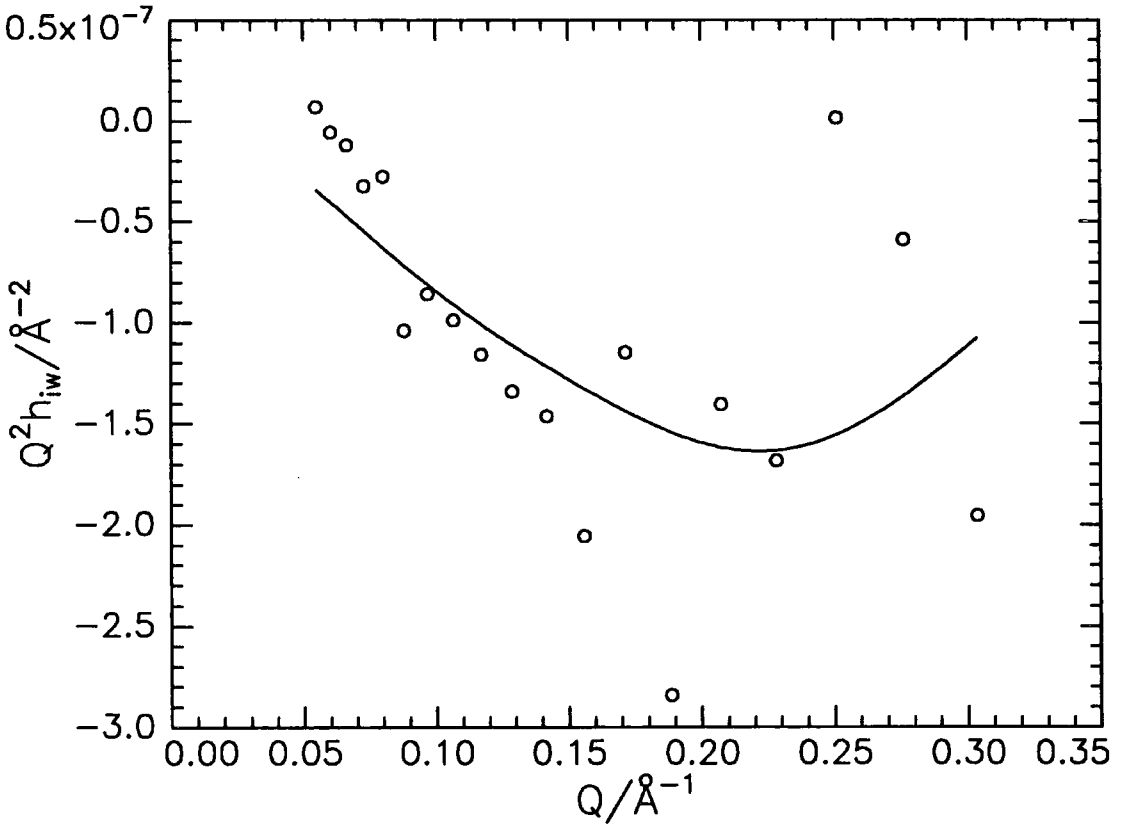

Figure 4.44 Fit to EO/water cross term at 2mN/m

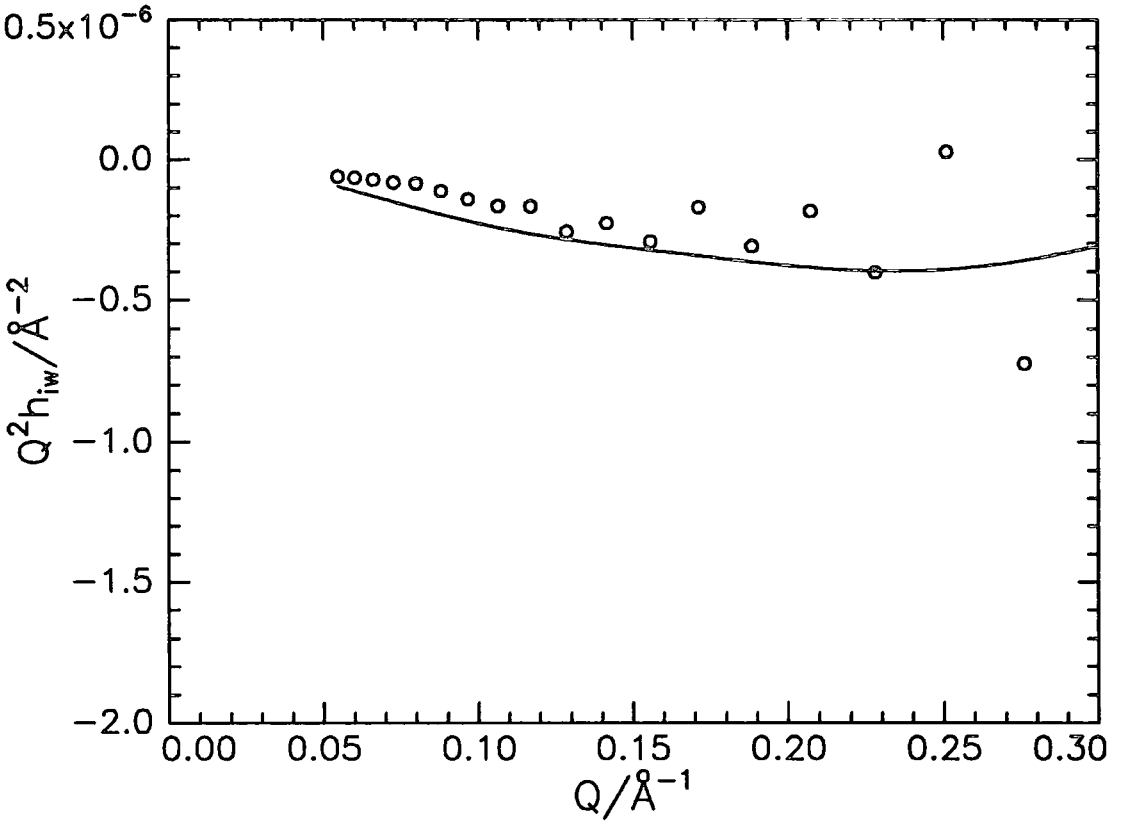

Figure 4.45 Fit to EO/water cross term at 5mN/m

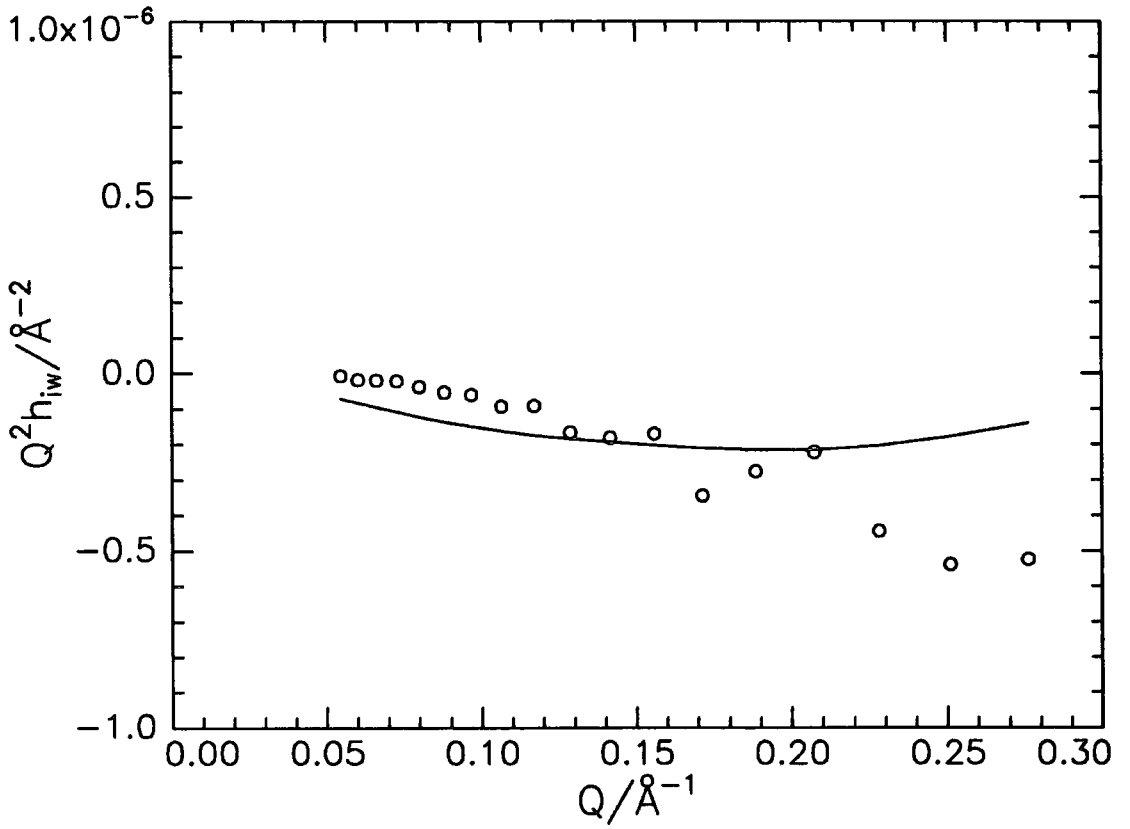

Figure 4.46 Fit to EO/water cross term at 10mN/m

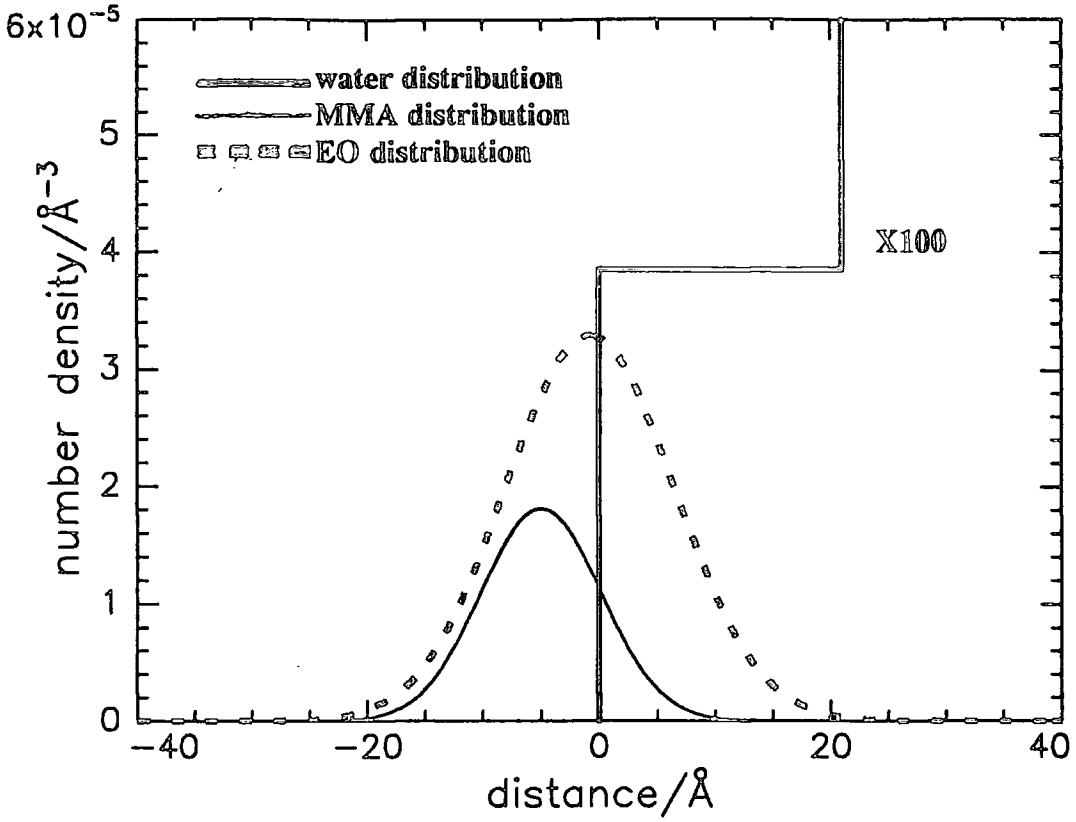

Figure 4.47 Distribution of interfacial components at 2mN/m

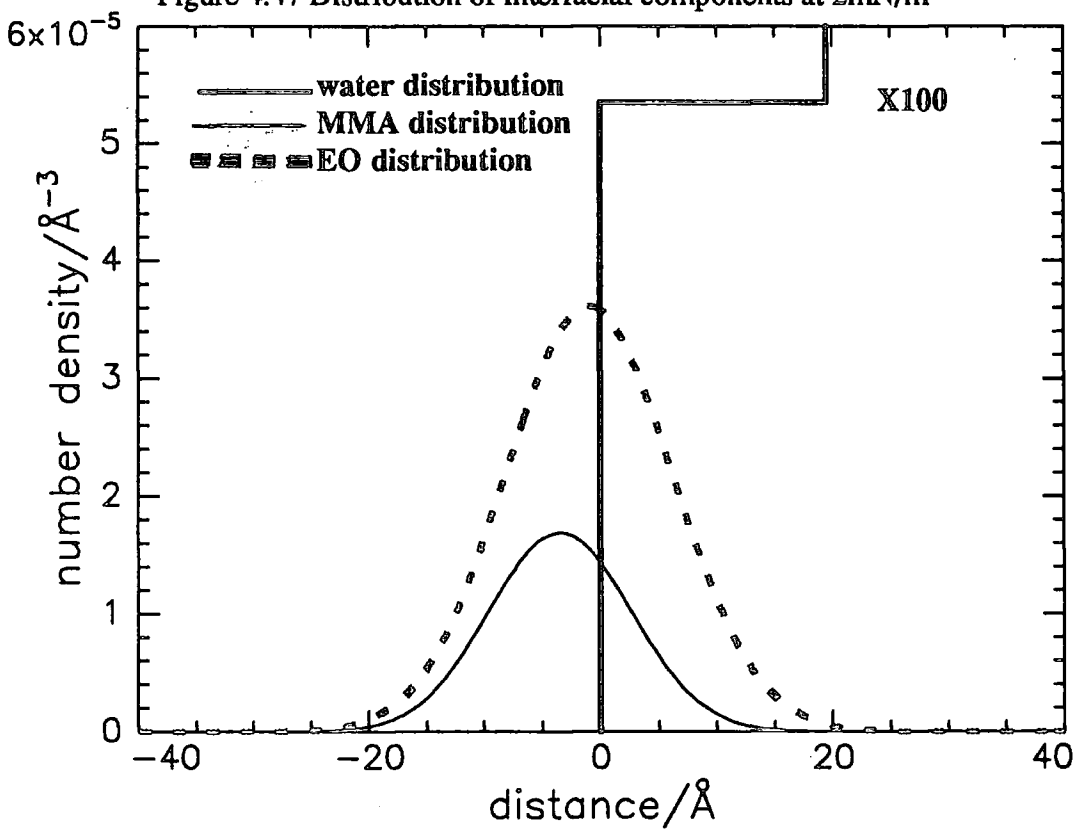

Figure 4.48 Distribution of interfacial components at 5mN/m

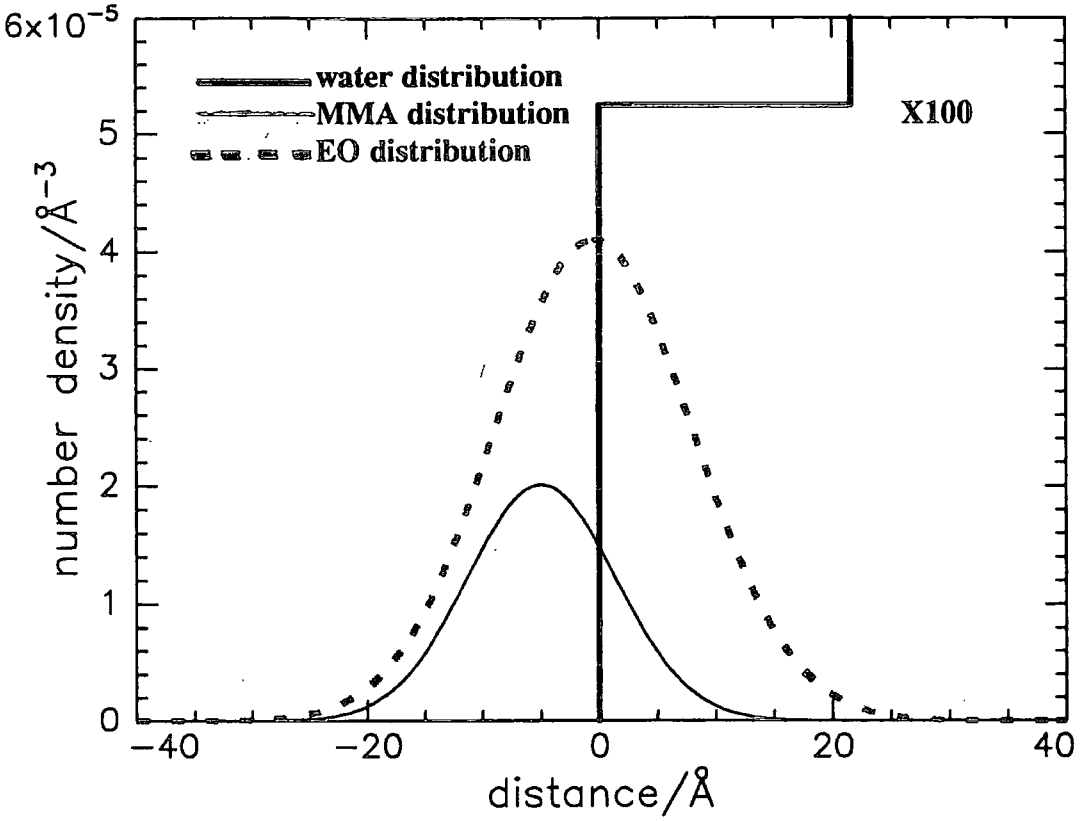

Figure 4.49 Distribution of interfacial components at 10mN/m

PART B: REFLECTOMETRY DATA AT $0.0267 \leq Q/Å^{-1} \leq 0.65$

The second part of the neutron reflectometry work involved using an HMDE copolymer having a much larger DEO content (BR29). The HMDE/nrw contrast therefore gave a higher reflectivity allowing it to be used to solve the kinematic approximation. In addition to using this copolymer, a larger Q range was studied. This time the reflectivity profiles for each contrast condition were measured at constant surface area. The reasons for this have been set out earlier, i.e. the constant surface pressure method had problems associated with perturbation of the Wilhelmy plate causing fluctuations in the barrier position and collapse of the film.

The measurements were made consecutively at two fixed angles of incidence of 0.79° and 1.5° and the reflectivity placed on an absolute scale using D_2O as a calibrant. The data sets produced at each angle were combined to give one data set representative of the whole Q range. The background was then subtracted as in Part A.

4.2 Results

Figures 4.50 to 4.53 show the reflectivity profiles for the copolymers spread on D_2O at 0.6 and 1.2mg/m^2, while figure 4.54 shows a typical background subtracted reflectivity profile with errors for the copolymers. Figures 4.55 to 4.57 show the reflectivity profiles for the copolymers spread on nrw and figure 4.58 shows a typical background subtracted reflectivity profile with errors for this subphase. For HMDE spread on D_2O (figure 4.50) an increase in surface concentration caused a higher reflectivity which contradicted the result from Part A where an increase in surface coverage caused a lower reflectivity. The reason for this is that the reflectivity of the HMDE in Part A was dominated by the HMMA block due to the small size of the DEO block. By using the new HMDE copolymer, then the enlarged DEO content would therefore be expected to dominate the reflectivity. The reflectivity of DMHE spread on D_2O did not change appreciably on

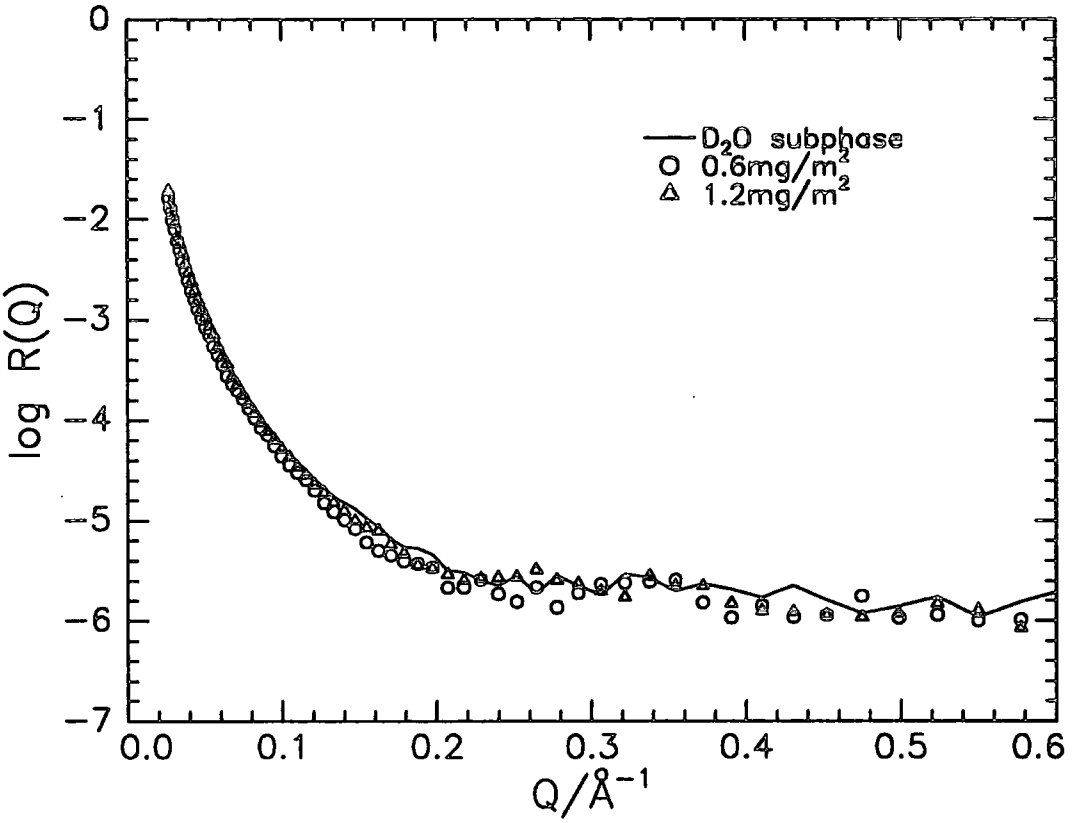

Figure 4.50 Neutron Reflectivity Profile for HMDE on D_2O

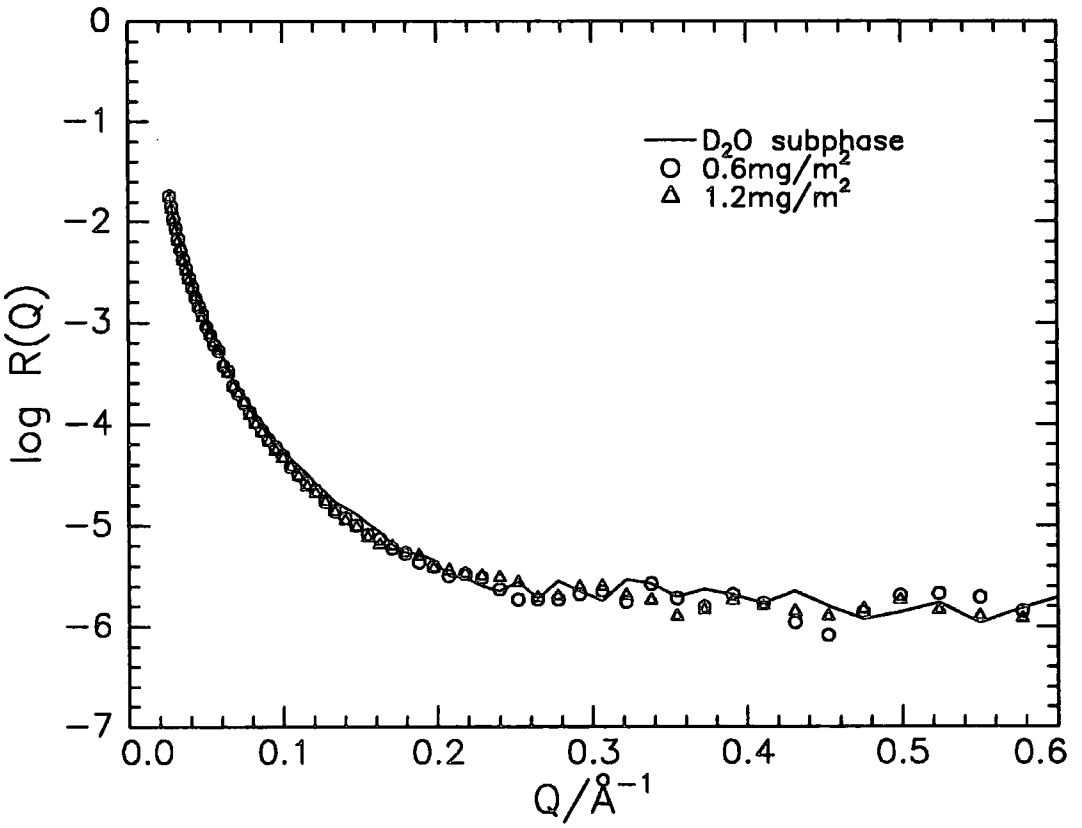

Figure 4.51 Neutron Reflectivity Profile for DMHE on D_2O

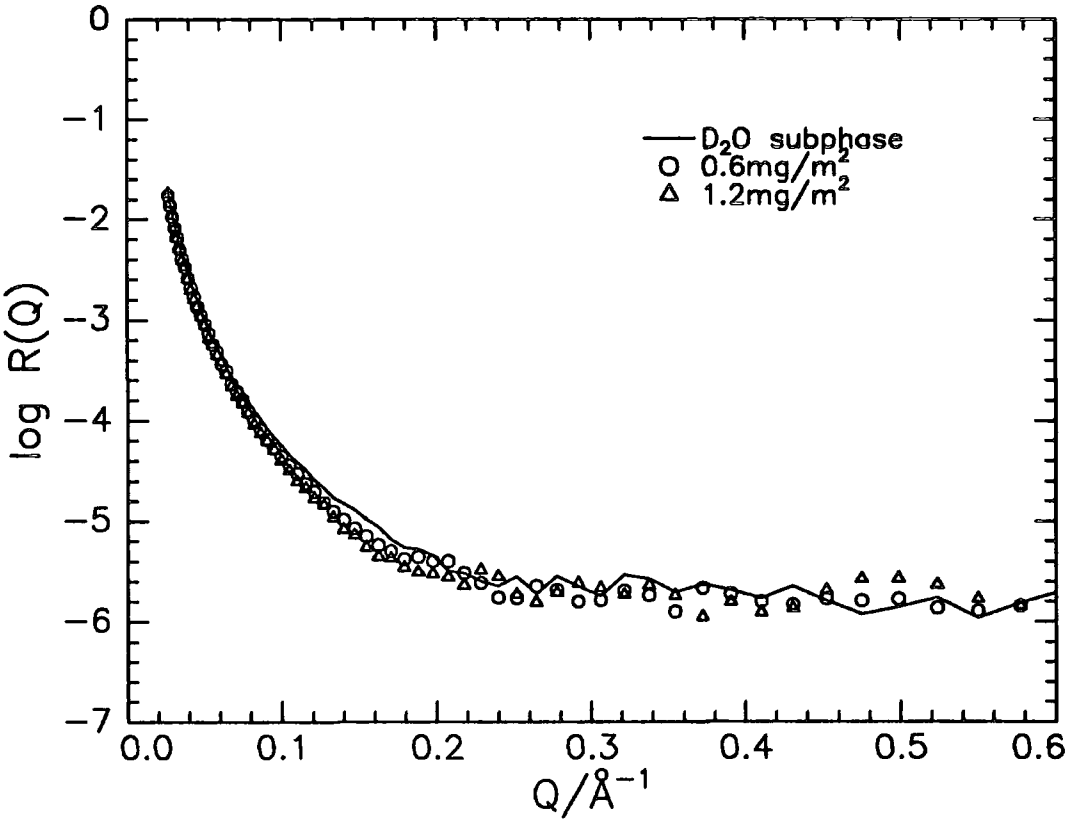

Figure 4.52 Neutron Reflectivity Profile for HMHE on D_2O

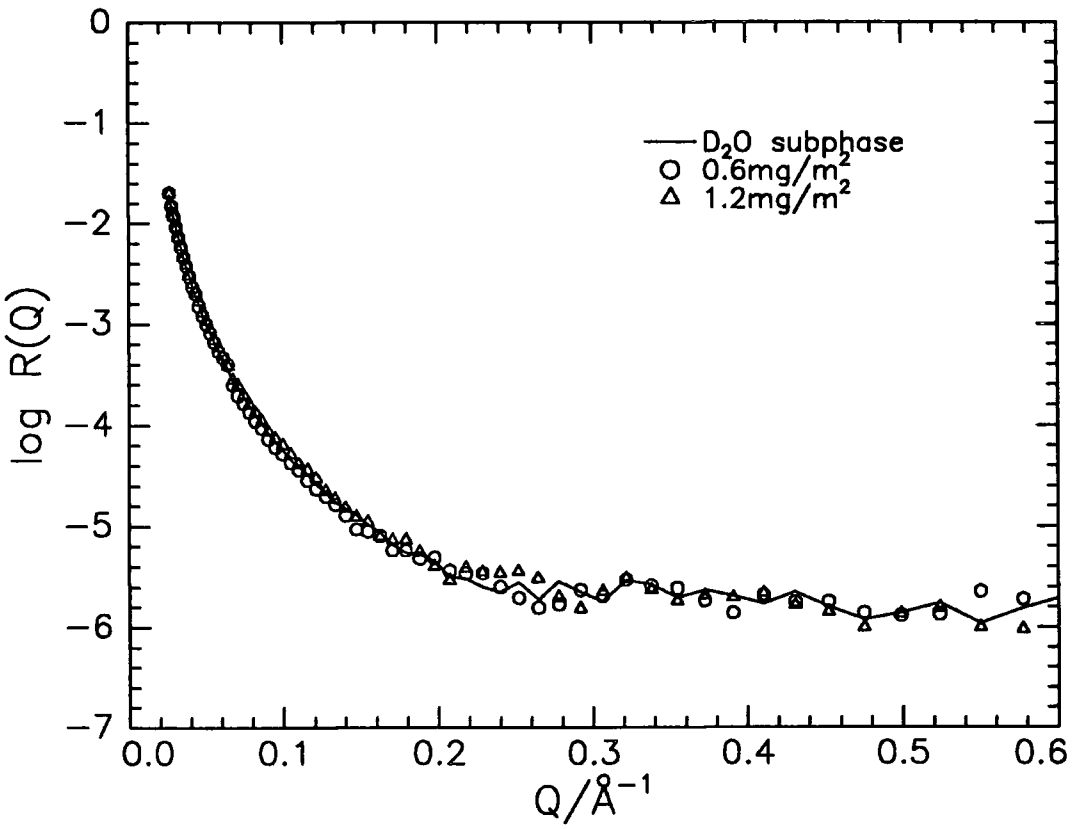

Figure 4.53 Neutron Reflectivity Profile for DMDE on D_2O

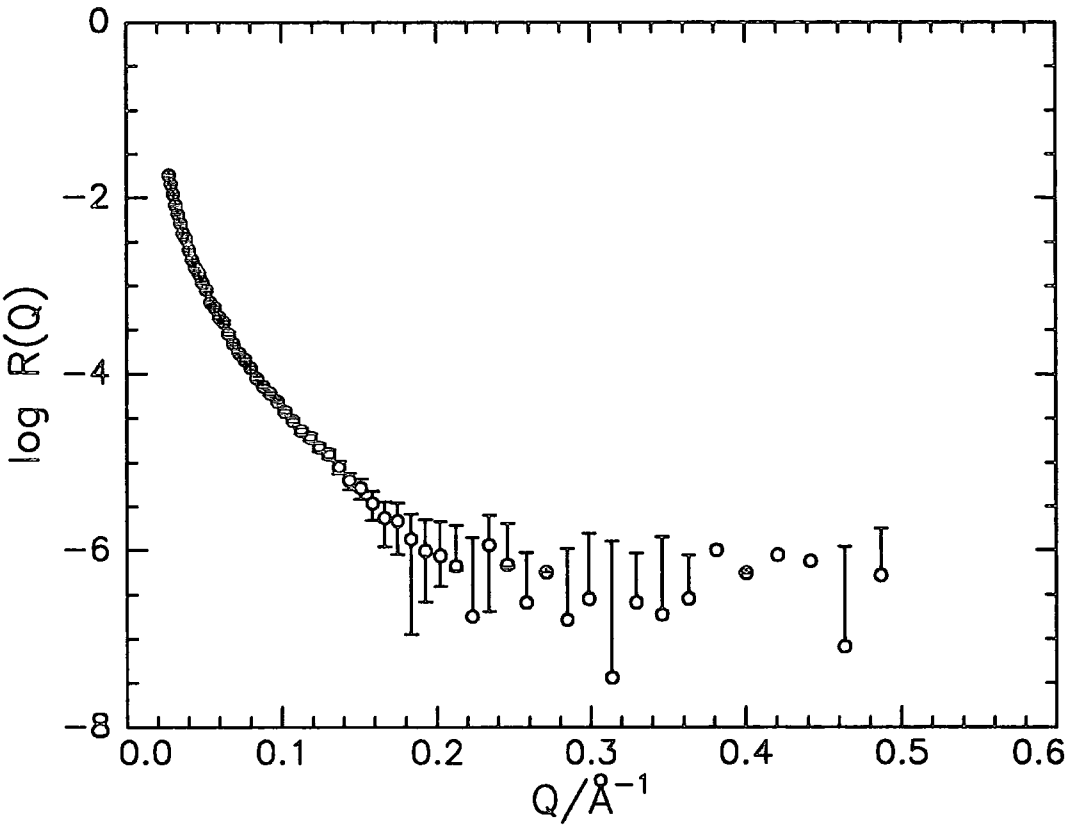

Figure 4.54 Background subtracted Neutron Reflectivity Profile for HMHE/D_2O at 1.2mg/m^2

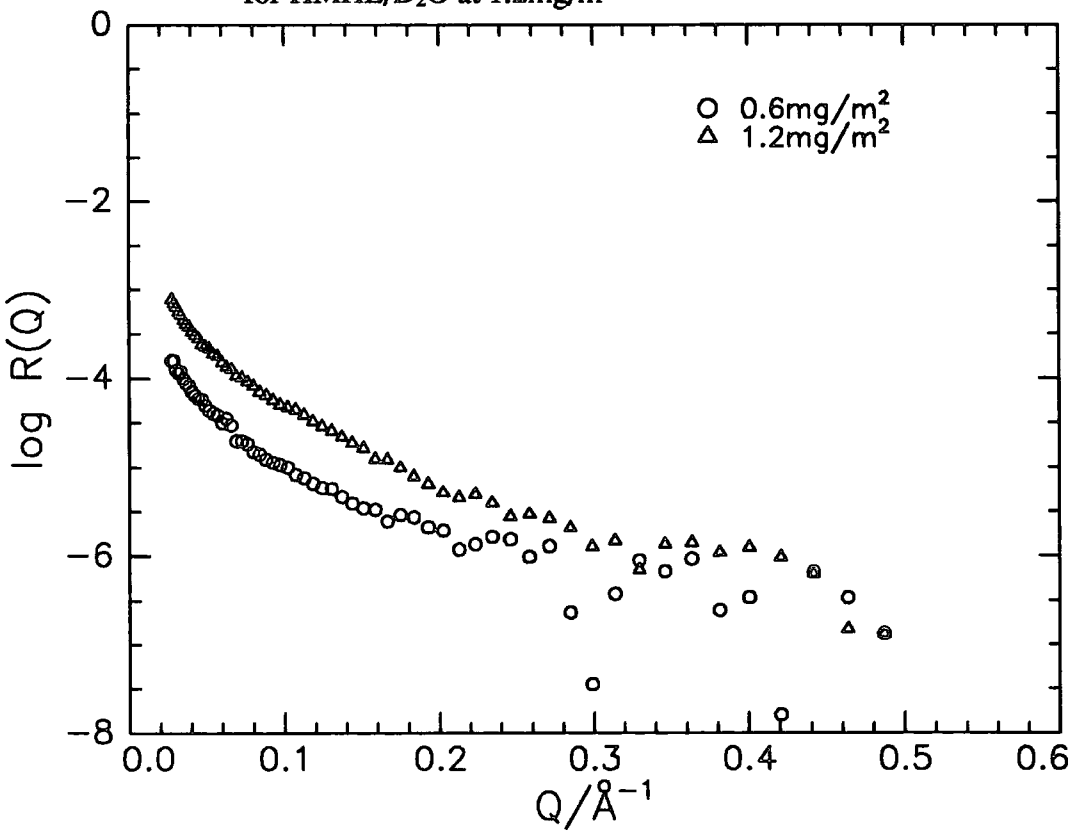

Figure 4.55 Background subtracted Neutron Reflectivity Profile for DMHE on nrw

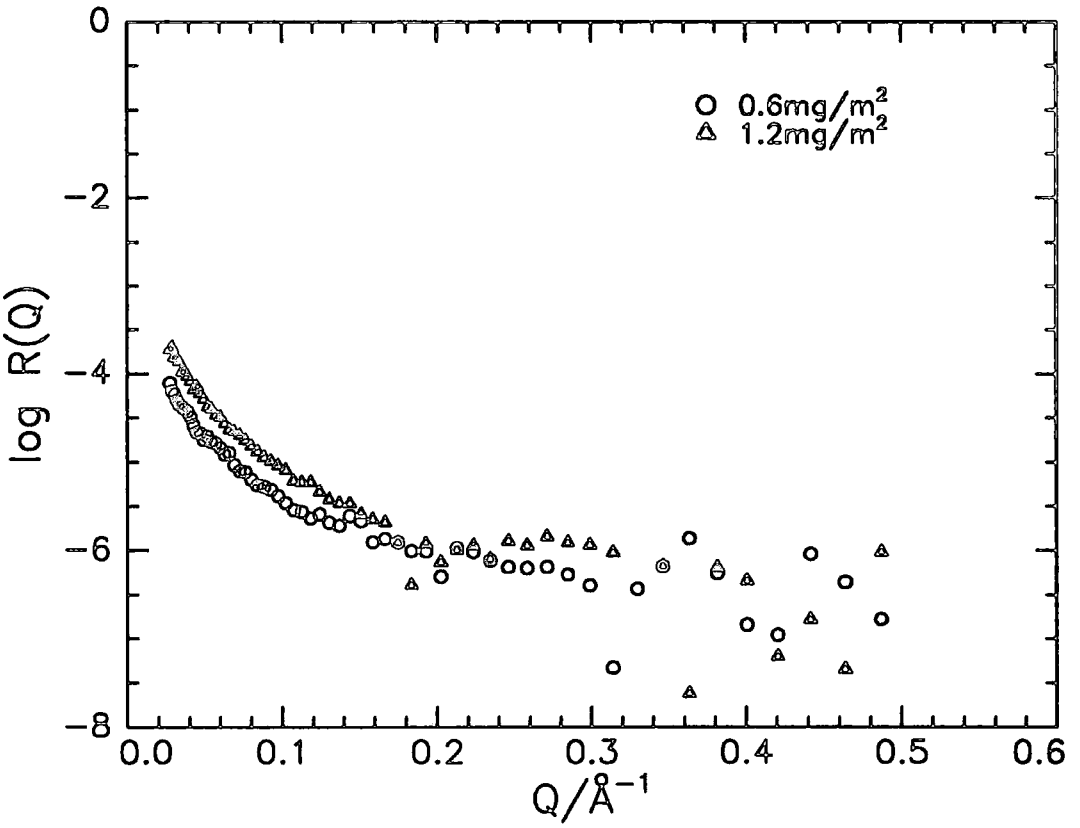

Figure 4.56 Background subtracted Neutron Reflectivity Profile for HMDE on nrw

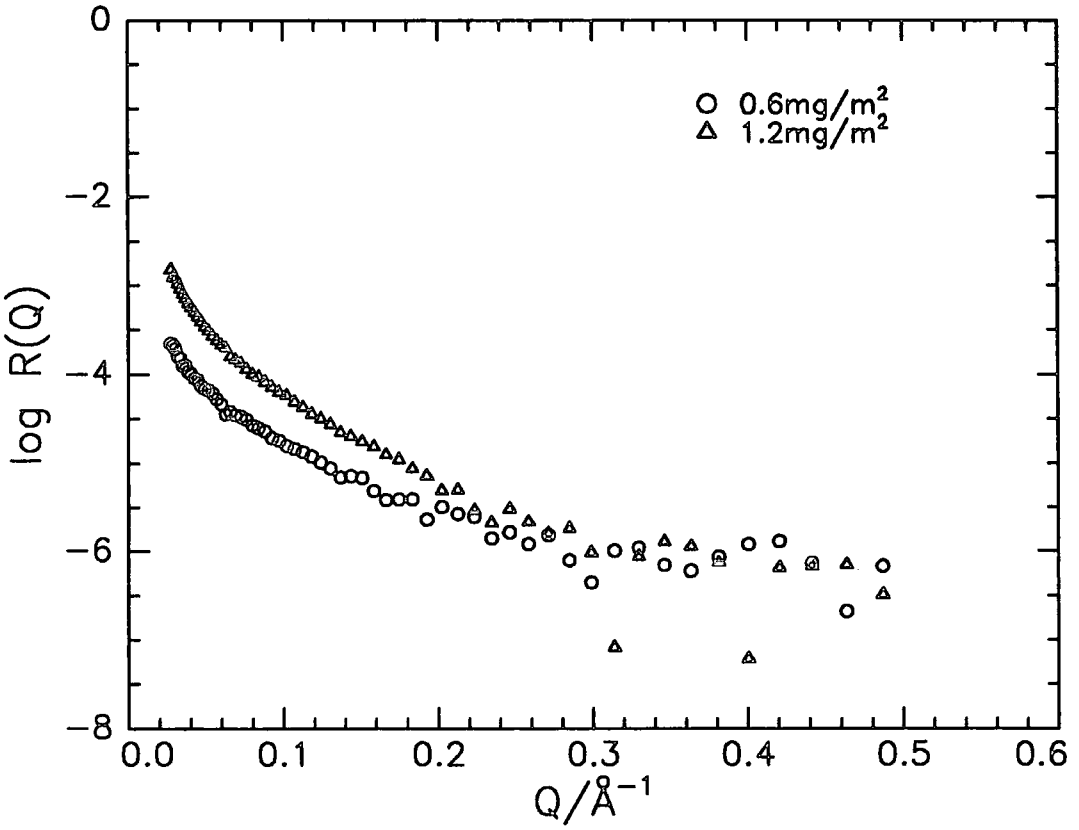

Figure 4.57 Background subtracted Neutron Reflectivity Profile for DMDE on nrw

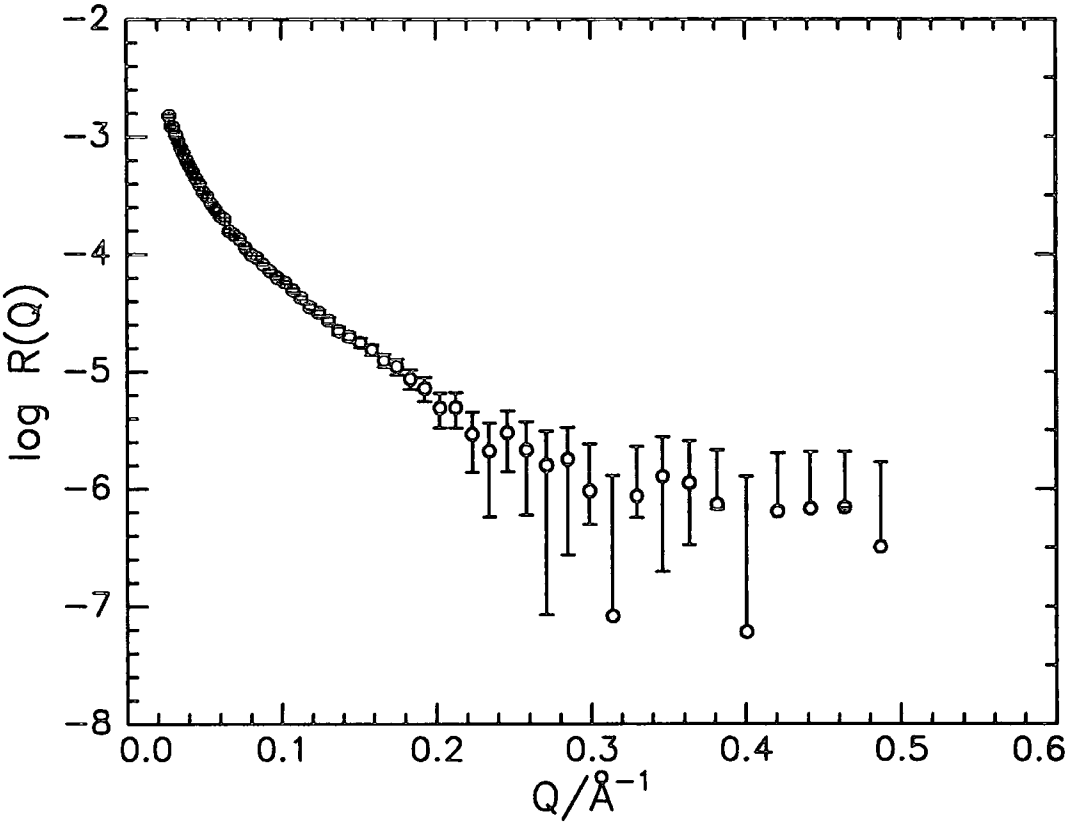

Figure 4.58 Background subtracted Neutron Reflectivity Profile for DMDE/nrw at 1.2mg/m^2

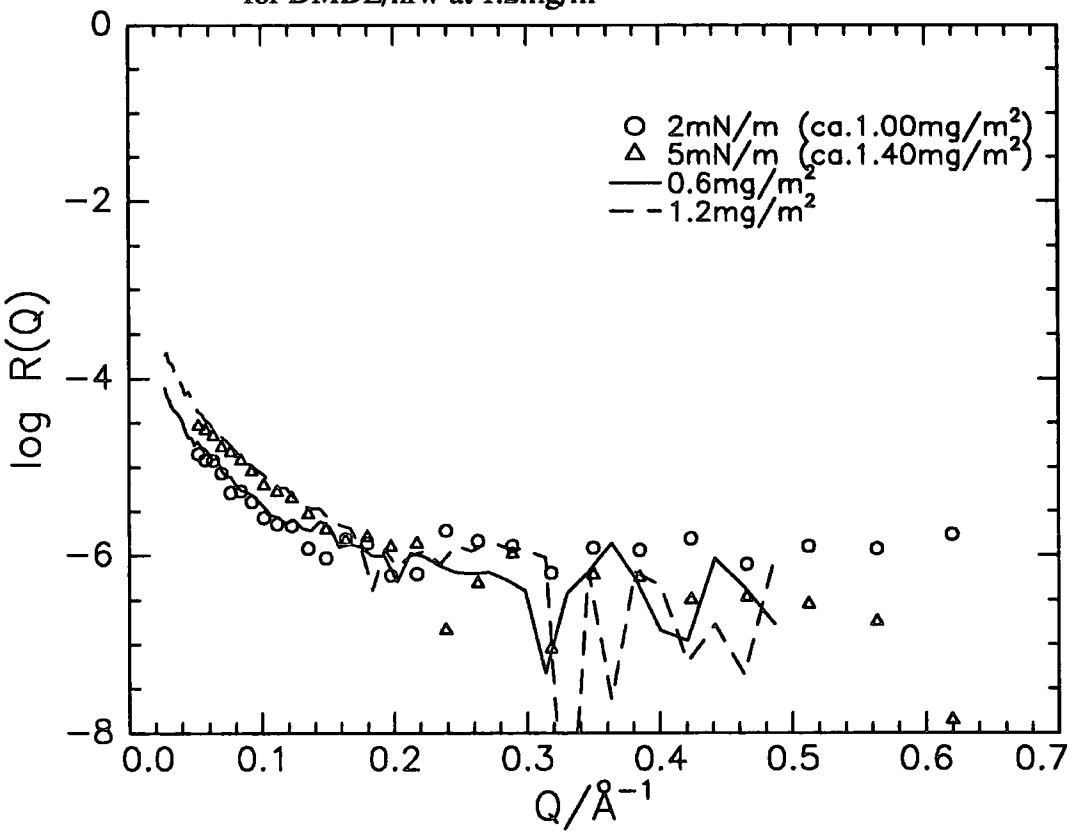

Figure 4.59 Comparison of reflectivities of the new and old HMDE/nrw contrasts

increasing the surface coverage, a slightly higher reflectivity being noted for $Q > 0.16Å^{-1}$. The decrease in reflectivity noted for the HMHE/D_2O contrast (figure 4.54) follows the expected trend as in Part A. It can be seen that the reflectivity of the DMDE/D_2O contrast (figure 4.53) is below that of the D_2O profile at 0.6mg/m^2, while at 1.2mg/m^2 it is above this reflectivity which agrees with the result of Part A. The DMHE, HMDE and DMDE copolymers spread on nrw displayed higher reflectivities with increasing surface coverage. Figure 4.59 compares the data at 0.6 and 1.2mg/m^2 for the new HMDE/nrw contrast with those of the 2 and 5mN/m data (ca. 1.00 and 1.40mg/m^2). The reflectivity of the new HMDE (BR29) copolymer is slightly higher than the old HMDE (BR26) copolymer and more importantly a greater curvature is observed in the reflectivity due to the lower Q range studied.

4.2.1 Uniform layer models

These models were used as a preliminary inspection of the reflectivity data. The thickness (d) and scattering length density (ρ) were obtained using the DRYDOC software package as in Part A.

4.2.1.1 Single uniform layer model

Typical fits to the single uniform layer model are shown in figure 4.60. Table 4.10 summarises the parameters obtained. The HMHE/D_2O contrast gives an indication of the amount of water in the layer. The reduction in the thickness with increasing surface coverage is due to water being squeezed out of the layer. For the copolymers spread on nrw it can be seen that there are large increases in the thickness of the deuterated material with increasing surface concentration. Table 4.11 shows apm and apparent surface concentration values, Γ_a, calculated as in Part A from the product of the fitted thickness, d, and the scattering length density, ρ, using equation 4.2. The data have good agreement between the Γ_s and Γ_a values for the deuterated material at 0.6mg/m^2, but at

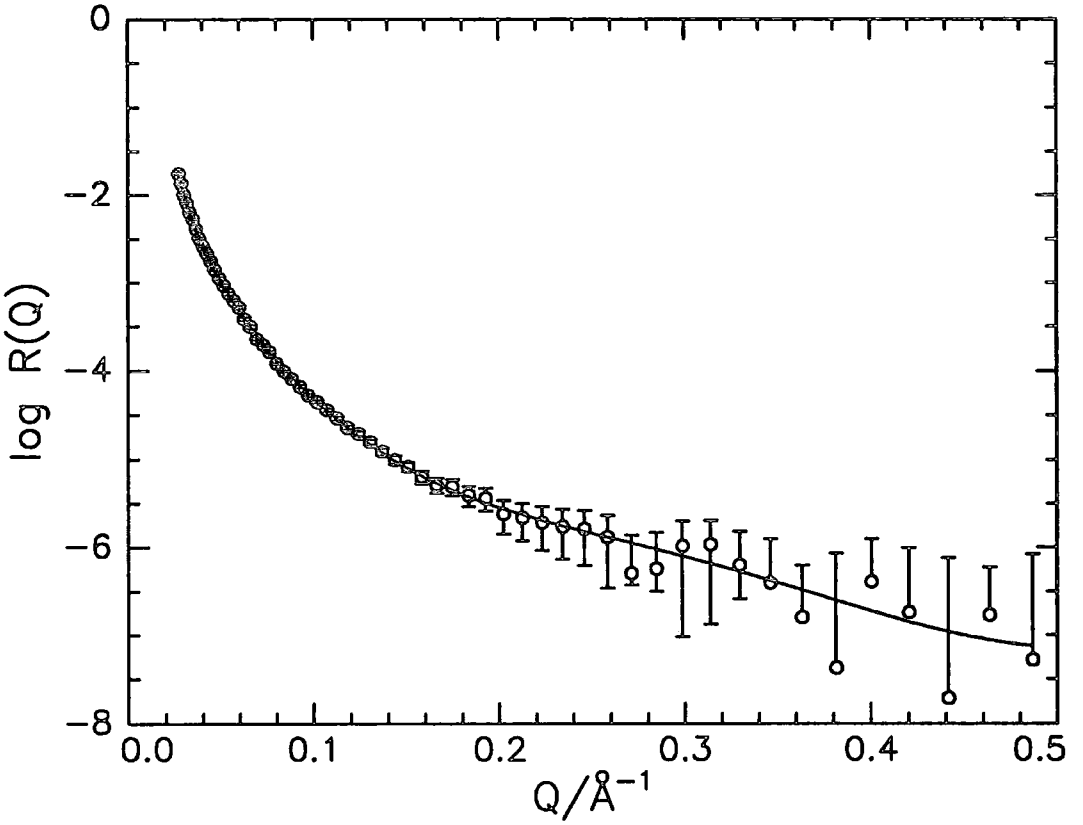

Figure 4.60a) Single uniform layer fit to DMHE/D_2O data at 1.2mg/m^2

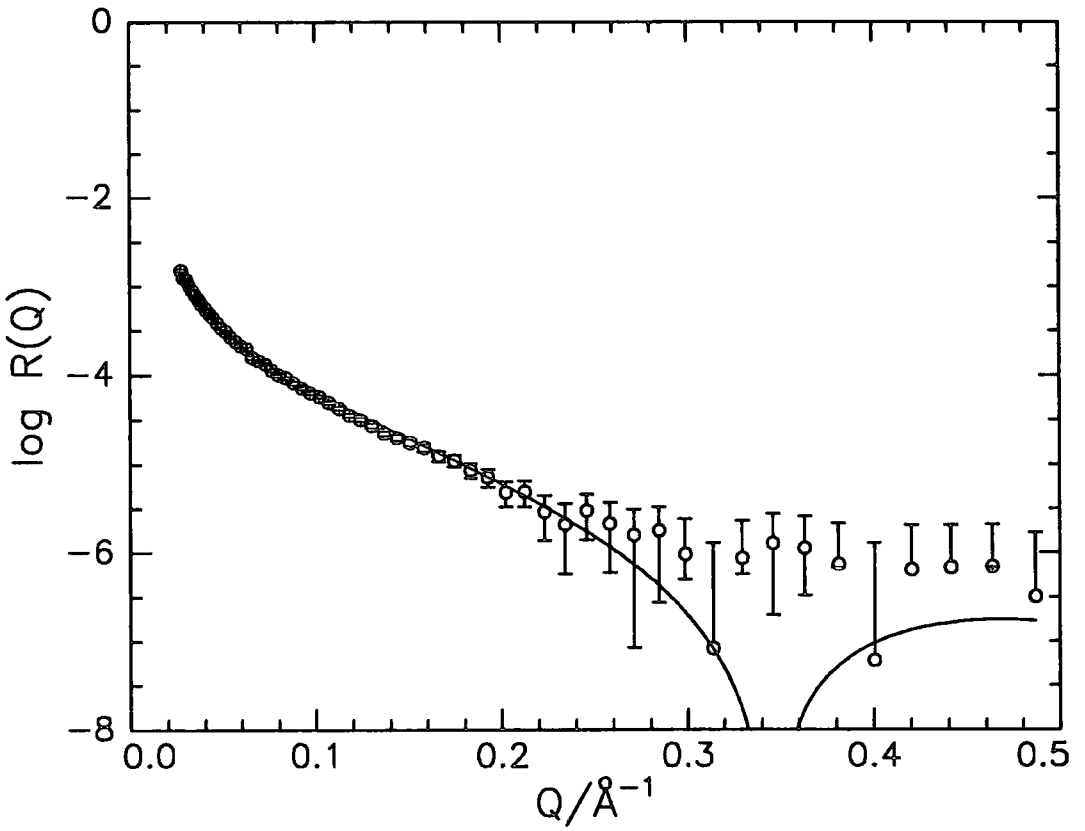

Figure 4.60b) Single uniform layer fit to DMDE/nrw data at 1.2mg/m^2

Copolymer	Γ /mg m^{-2}	Subphase	d/Å	ρ /10^{-6}Å^{-2}
DMDE	0.6	D_2O	17	5.82
	1.2		17	6.27
	0.6	nrw	11	3.02
	1.2		18	4.05
DMHE	0.6	D_2O	17	5.82
	1.2		21	5.71
	0.6	nrw	10	2.62
	1.2		14	4.37
HMDE	0.6	D_2O	10	5.81
	1.2		14	5.70
	0.6	nrw	10	1.79
	1.2		20	1.47
HMHE	0.6	D_2O	19	5.54
	1.2		15	4.68

Table 4.10 Fitted parameters to single uniform layer model

Copolymer	Γ /mg m^{-2}	Γ_s /mg m^{-2}	ρ_d.d /10^{-6}Å^{-1}	apm /Å^2	Γ_a /mg m^{-2}
DMDE	0.60	0.60	33.28	21	0.60
	1.70	1.70	73.91	10	1.34
DMHE	0.60	0.43	27.04	36	0.49
	1.20	0.85	59.52	17	1.09
HMDE	0.60	0.32	17.51	26	0.30
	1.20	0.63	28.72	16	0.50

Table 4.11 Surface Concentration calculated from fitted parameters

1.2mg/m^2 there is some overestimation for DMHE. For DMDE and HMDE at this surface concentration, Γ_a is less than Γ_s which indicates 'lost' polymer as in Part A.

4.2.1.2 Two layer model

The HMDE/D_2O contrast (figure 4.50) shows the slight decrease below the reflectivity of D_2O noticed in Part A. There is an important difference in that figure 4.3 suggests a decrease in reflectivity with increasing surface concentration, whereas figure 4.50 suggests the reverse. The reason for this must be the large HMMA content of the HMDE copolymer used in Part A. The reflectivity profile of figure 4.50 suggests that at 1.2mg/m^2 the HMMA forms the upper layer while the DEO forms the lower layer. The fact that at 0.6mg/m^2 the reflectivity is lower than that at 1.2mg/m^2 may suggest intrusion of D_2O or DEO into the HMMA layer. Figure 4.61 shows the reflectivity profiles for HMDE spread on D_2O at 0.6 and 1.2mg/m^2 and compares them with calculated data using the optical matrix method for a uniformly mixed layer and two separate uniform layers with the HMMA layer as the upper or lower layer. At 0.6mg/m^2 the interfacial components are more uniformly mixed, while at 1.2mg/m^2 a two layer model is more appropriate. Figure 4.62 shows typical fits to the two layer model, while Table 4.12 summarises the parameters obtained. Overall, layer thickness is slightly higher when a copolymer is contrasted against D_2O rather than nrw due to the extra contribution of the deuterated subphase to the reflectivity. For the DMHE/D_2O contrast the combination of the long DMMA chain and D_2O subphase gave an overestimated MMA layer thickness of 13Å. The thickness of the PEO layer is underestimated for those contrasts involving HEO due to the low contribution of this isotopic species to the reflectivity. The thickness of the DEO block in the HMDE/D_2O contrast is slightly higher due to its longer length. Ignoring this overestimation then the thickness of the MMA and EO layers are about 10Å and 15Å respectively at 1.2mg/m^2.

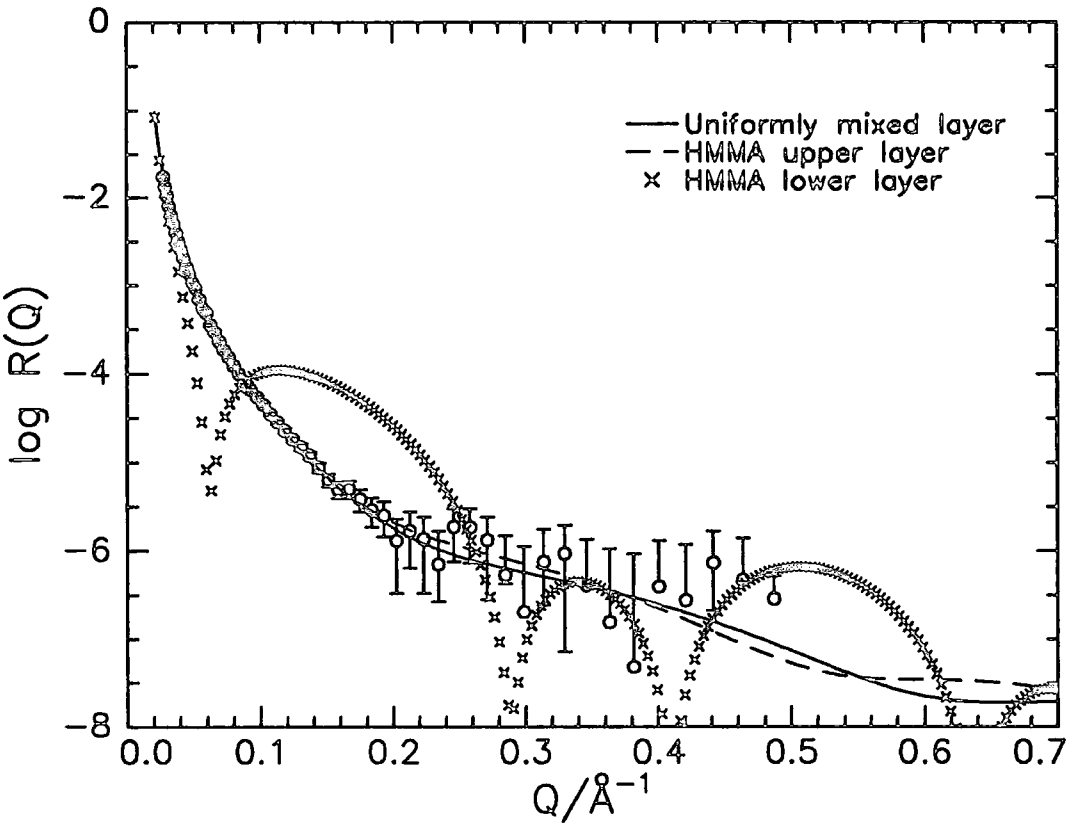

Figure 4.61a) Neutron Reflectivity Profile for HMDE_n/D_2O at 0.6mg/m^2 compared with uniform and two layer models

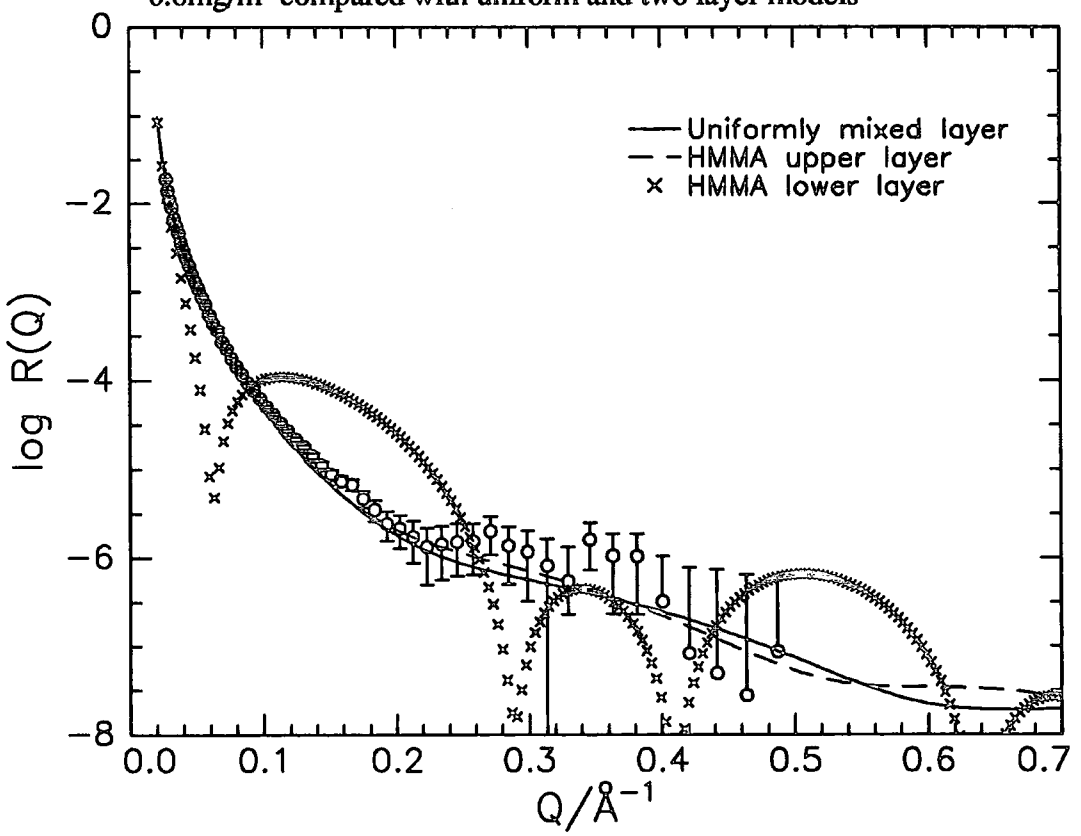

Figure 4.61b) Neutron Reflectivity Profile for HMDE_n/D_2O at 1.2mg/m^2 compared with uniform and two layer models

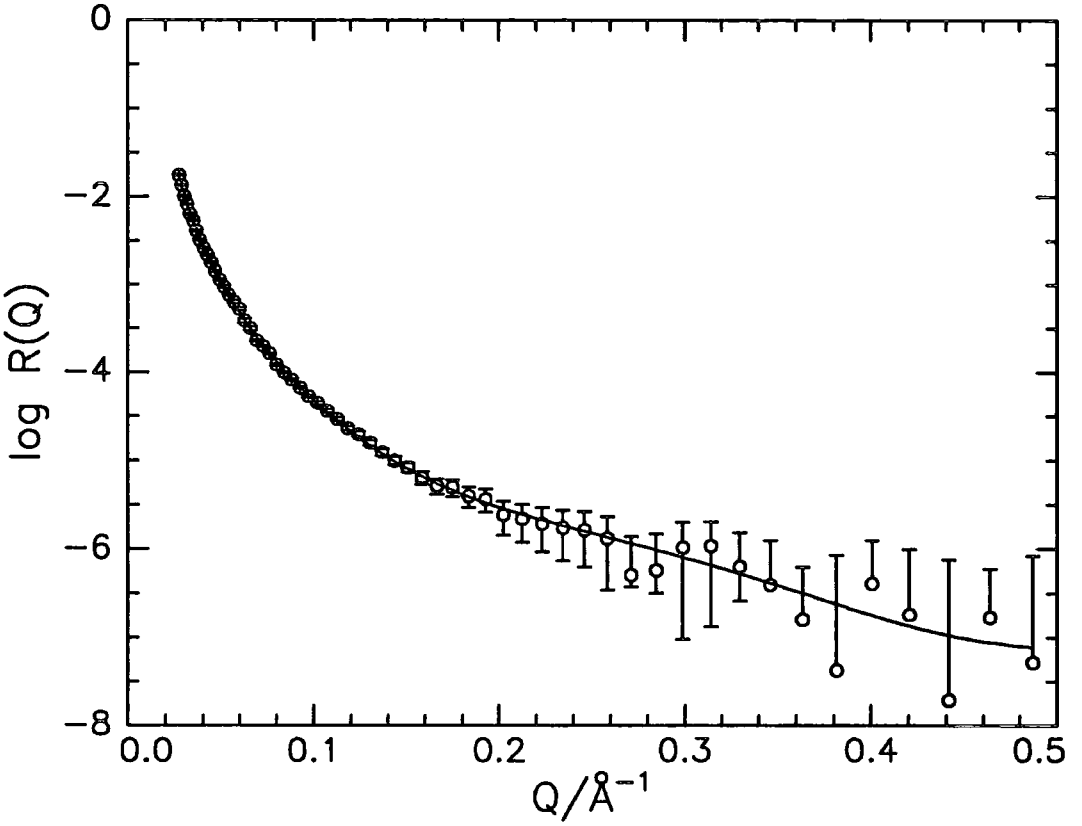

Figure 4.62a) Fit to DMHE/D_2O data at 1.2mg/m^2 using two layer model

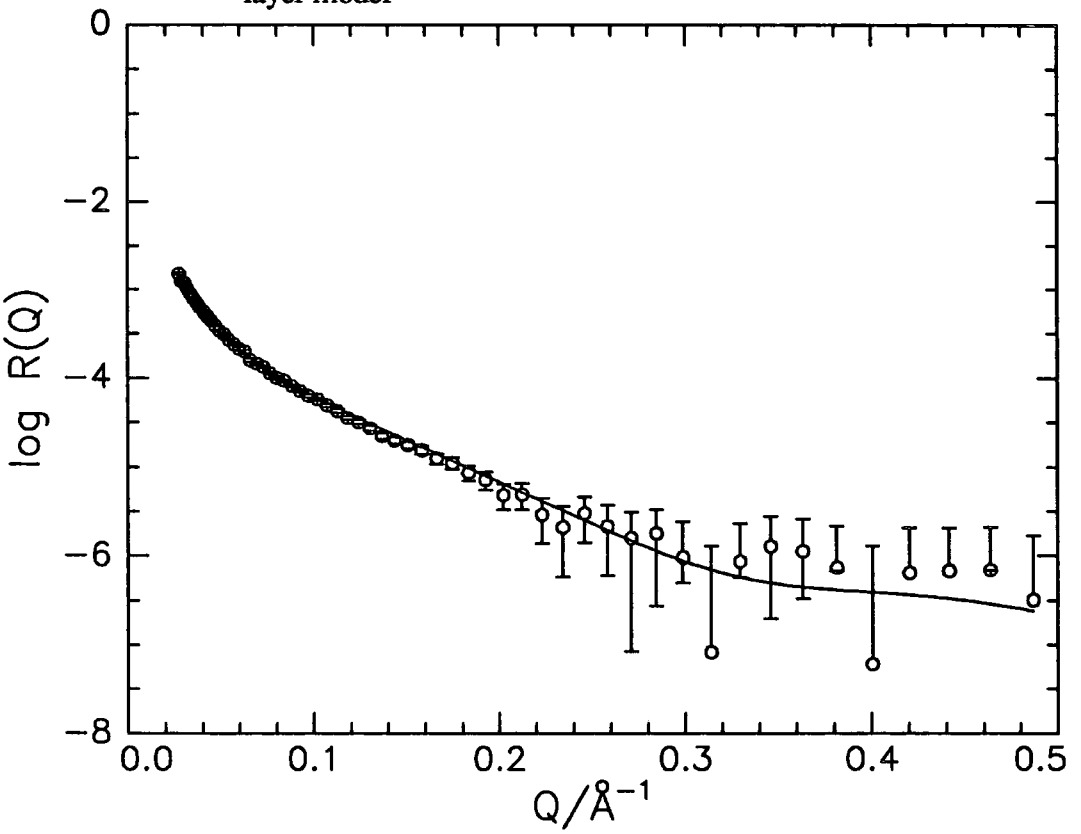

Figure 4.62b) Fit to DMDE/nrw data at 1.2mg/m^2 using two layer model

Polymer	Subphase	Γ /mg m^{-2}	Layer 1		Layer 2	
			d/Å	ρ /10^{-6}Å^{-1}	d/Å	ρ /10^{-6}Å^{-1}
DMDE	nrw	1.2	9	5.56	12	2.26
DMHE	nrw	1.2	10	5.23	8	1.82
DMDE	D_2O	1.2	10	6.42	14	6.19
DMHE	D_2O	1.2	13	5.72	8	5.7
HMHE	D_2O	1.2	10	1.00	8	2.68
HMDE	D_2O	1.2	10	0.57	16	6.40

Table 4.12 Layer thicknesses and scattering length densities obtained from two layer model

4.2.2 Kinematic Approximation

Uniform and Gaussian distribution models were again used in the analysis of the partial structure factors. For the DMHE and HMDE copolymers spread on nrw, the data were used to calculate the MMA and EO self terms at 0.6 and 1.2mg/m^2, figure 4.63 shows a typical fit assuming a Gaussian distribution. The HMHE/D_2O contrast data was best fitted assuming a tanh distribution of water at the surface rather than a uniform distribution. Tanh profiles have been used in the past to describe the diffuse liquid/vapour interface and its form is suitable to describe a gradual change of scattering density at an interface. The partial structure factor describing the tanh model is

$$Q^2h_{ss} = n_{s0}^2(\zeta\pi Q/2)^2\text{cosech}^2(\zeta\pi Q/2) \qquad (4.12)$$

where ζ is the width parameter, a typical fit is shown in figure 4.64. All the structural parameters for these form factors are summarised in Table 4.13. The new HMDE copolymer (HMDE_n), having a greater DEO content, allowed the kinematic approximation to be solved with more varied contrast conditions (Appendix A). The contrast conditions had a balance of nrw and D_2O contrasts thereby maximising the variation in coherent scattering length, b_i, of each interfacial component. Figures 4.65 to 4.68 show data for the self terms fitted assuming a Gaussian distribution of segments, while figures 4.69 and 4.70 shows the fits to the water self terms assuming a tanh profile. These structural parameters obtained from the form factors of the kinematic approximation are summarised in Table 4.14. It can be seen that the Gaussian distribution gives Γ_a values nearer the spread amount Γ_s. The spatial arrangement of the interfacial components was obtained by solving the cross partial structure factors. Figures 4.71 to 4.76 show fits to these cross terms. The values of δ, the mean centre to centre separation of the components, are also summarised in Table 4.14.

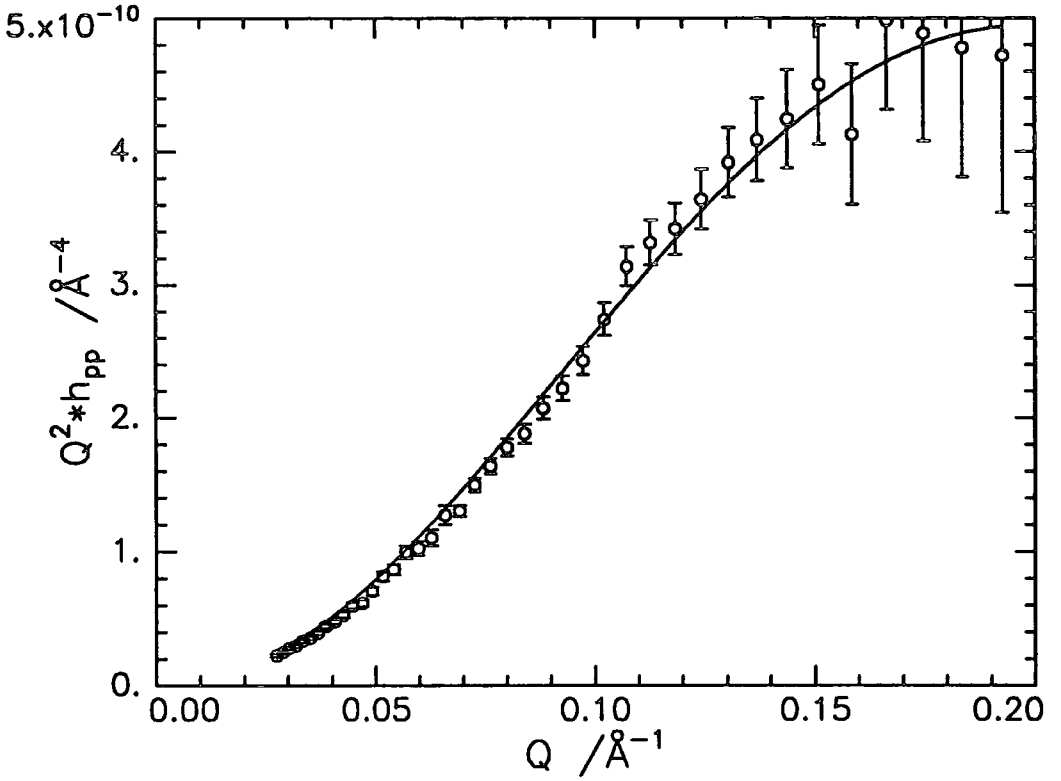

Figure 4.63 DMHE/nrw data at 1.2mg/m^2 used to calculate MMA self term assuming Gaussian distribution of segments

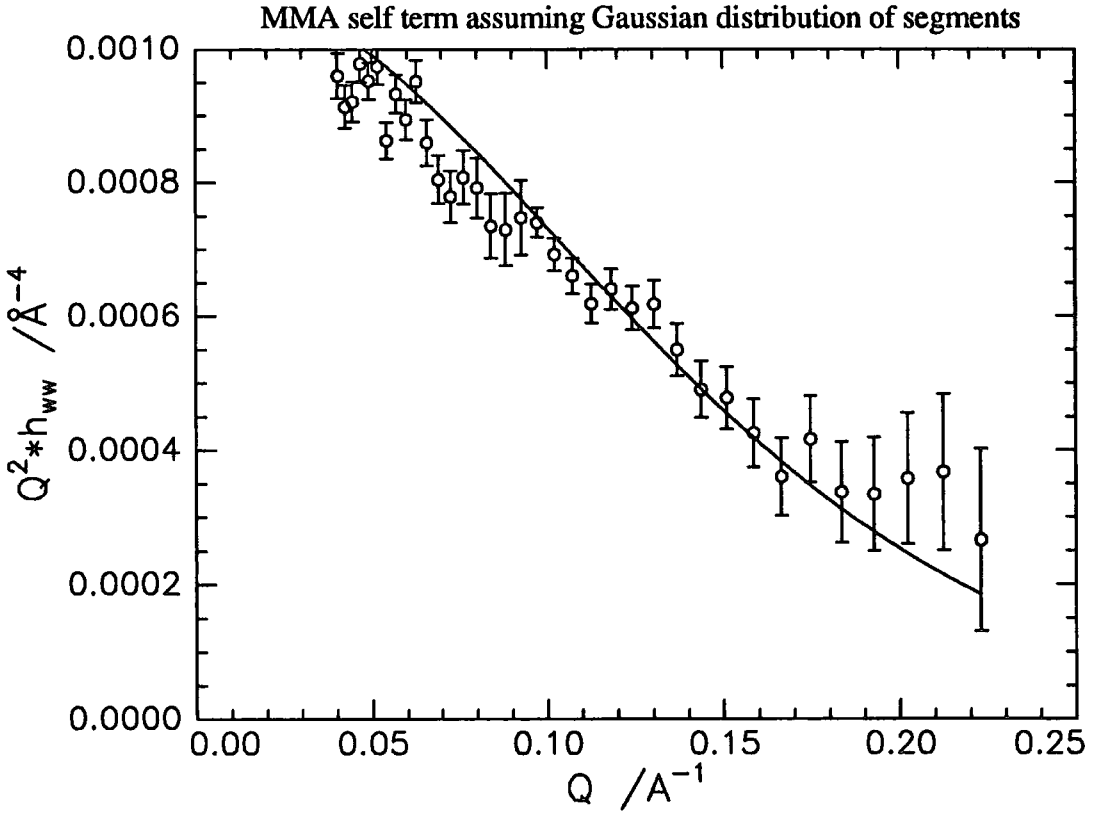

Figure 4.64 HMHE/D_2O data at 1.2mg/m^2 used to calculate water self term assuming tanh profile

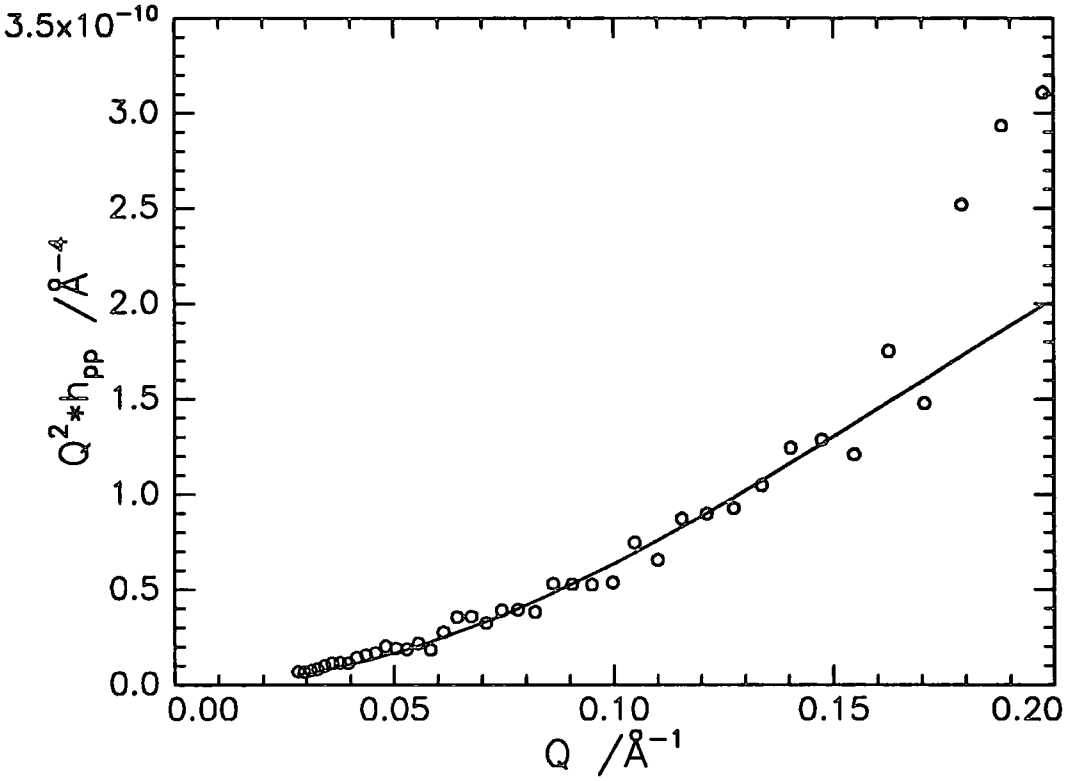

Figure 4.65 Fit to MMA self term at 0.6mg/m^2

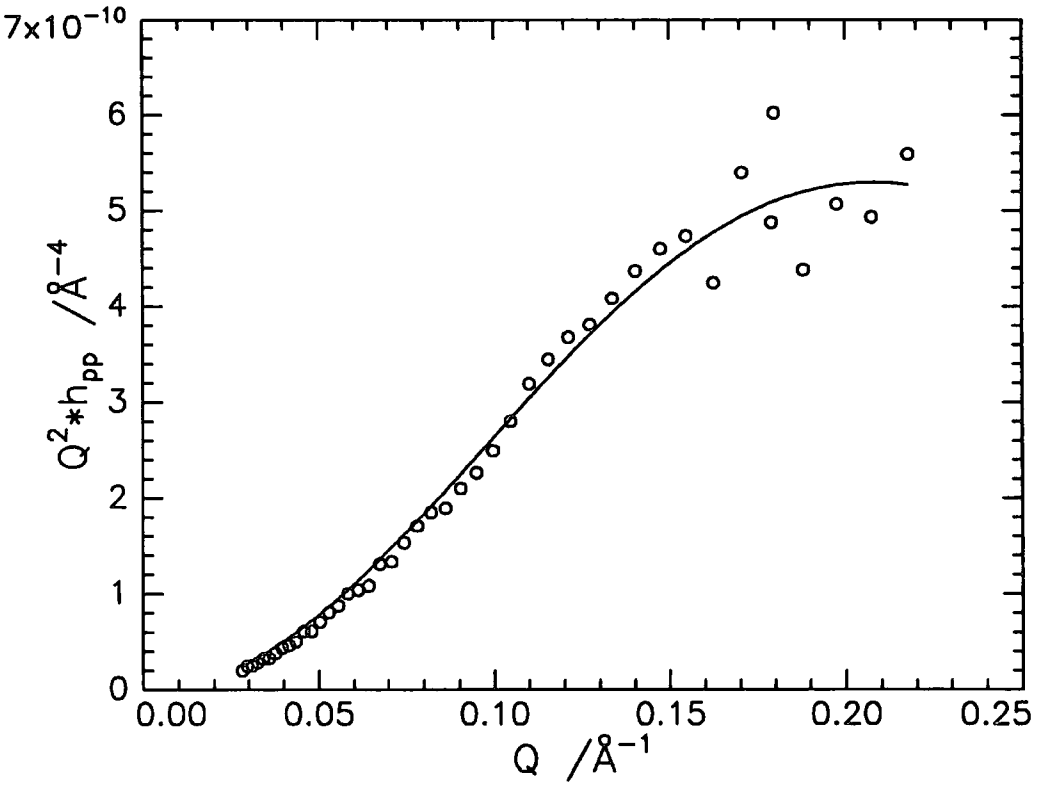

Figure 4.66 Fit to MMA self term data at 1.2mg/m^2

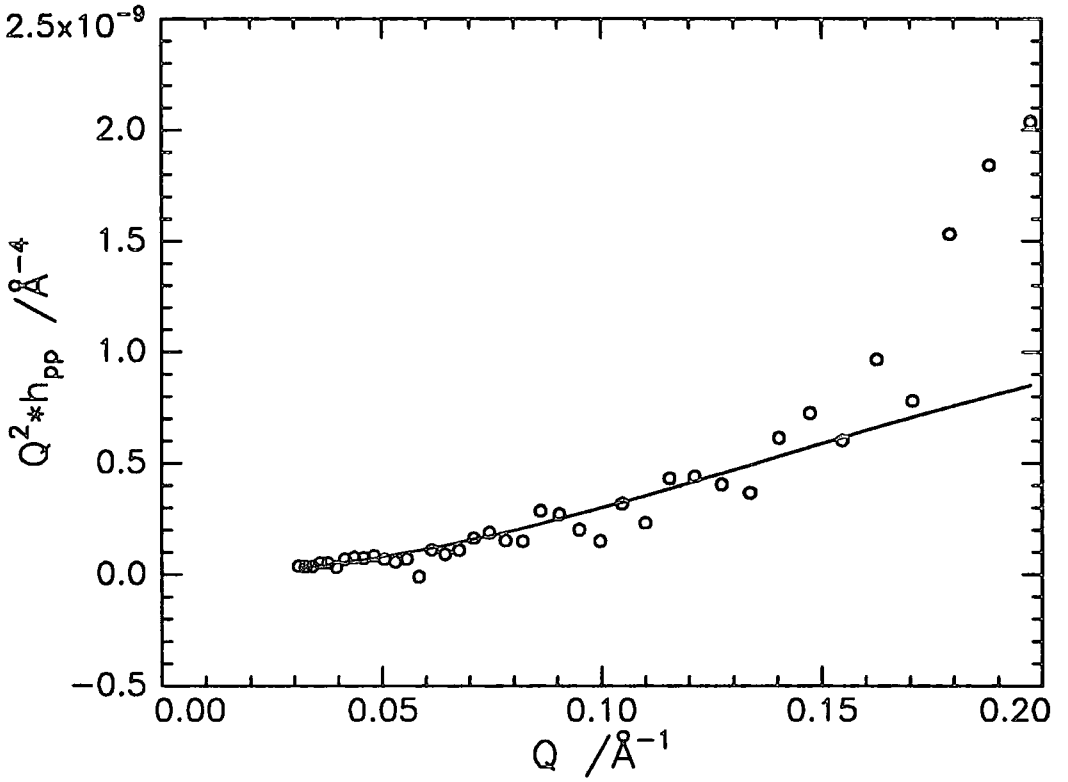

Figure 4.67 Fit to EO self term at 0.6mg/m^2

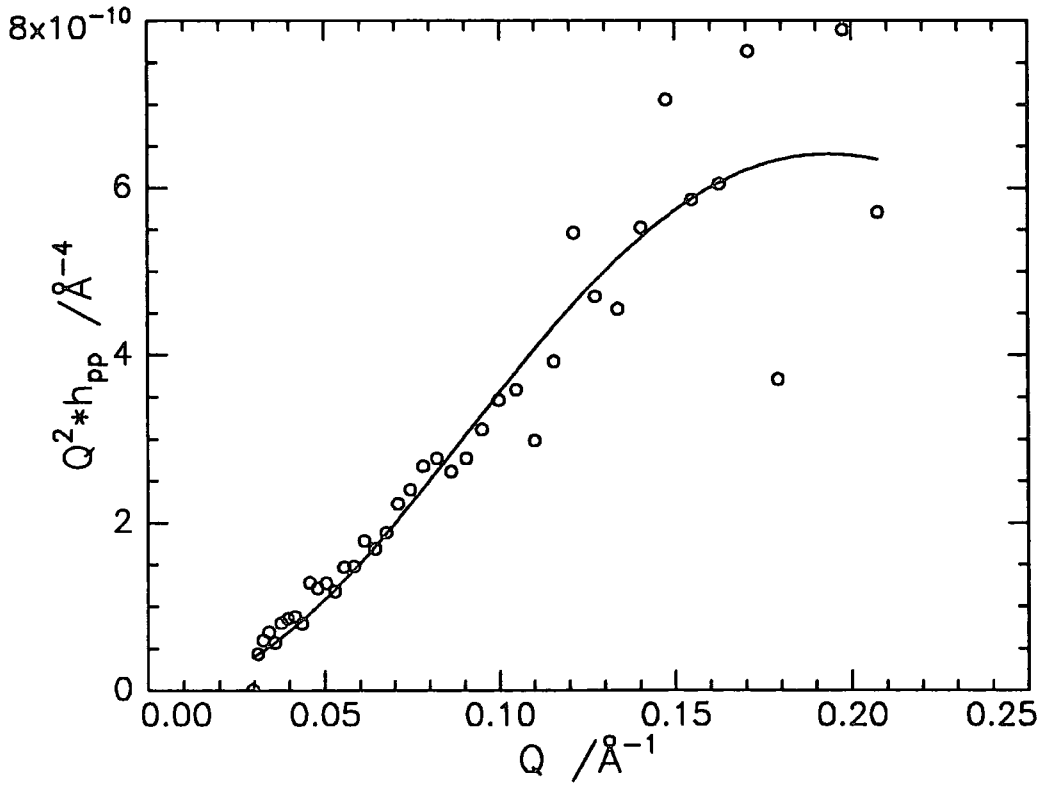

Figure 4.68 Fit to EO self term data at 1.2mg/m^2

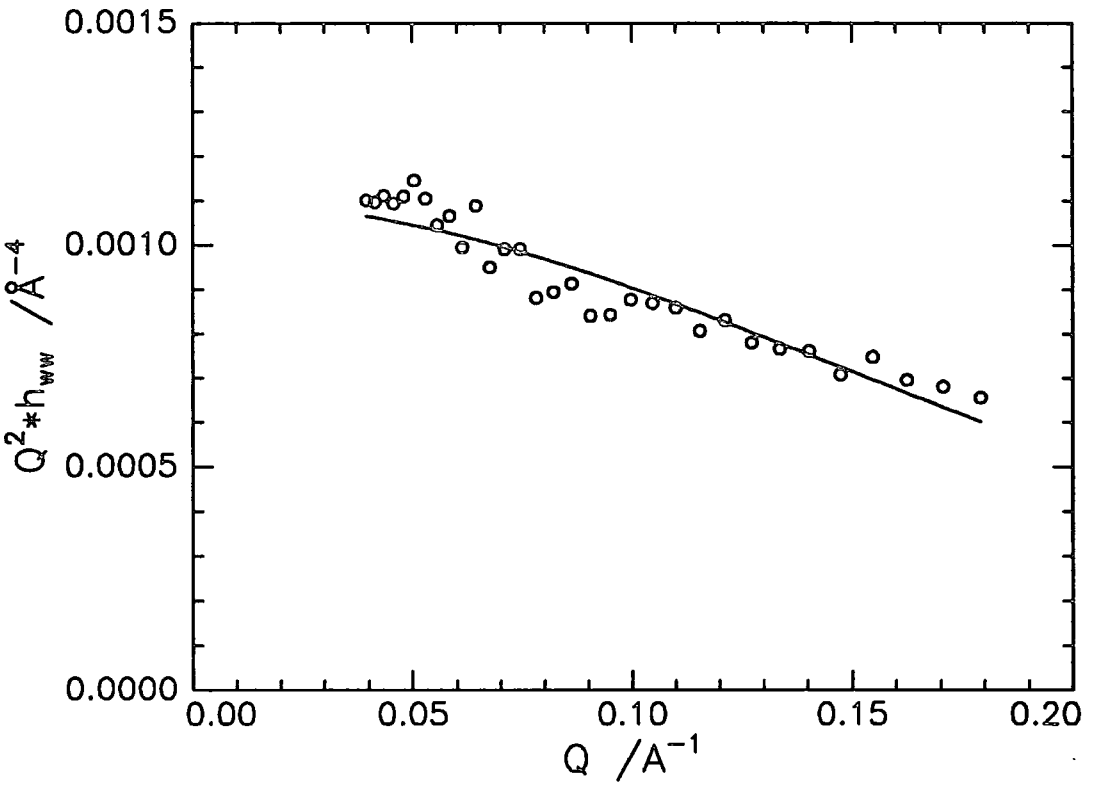

Figure 4.69 Tanh fit to water self term at 0.6mg/m^2

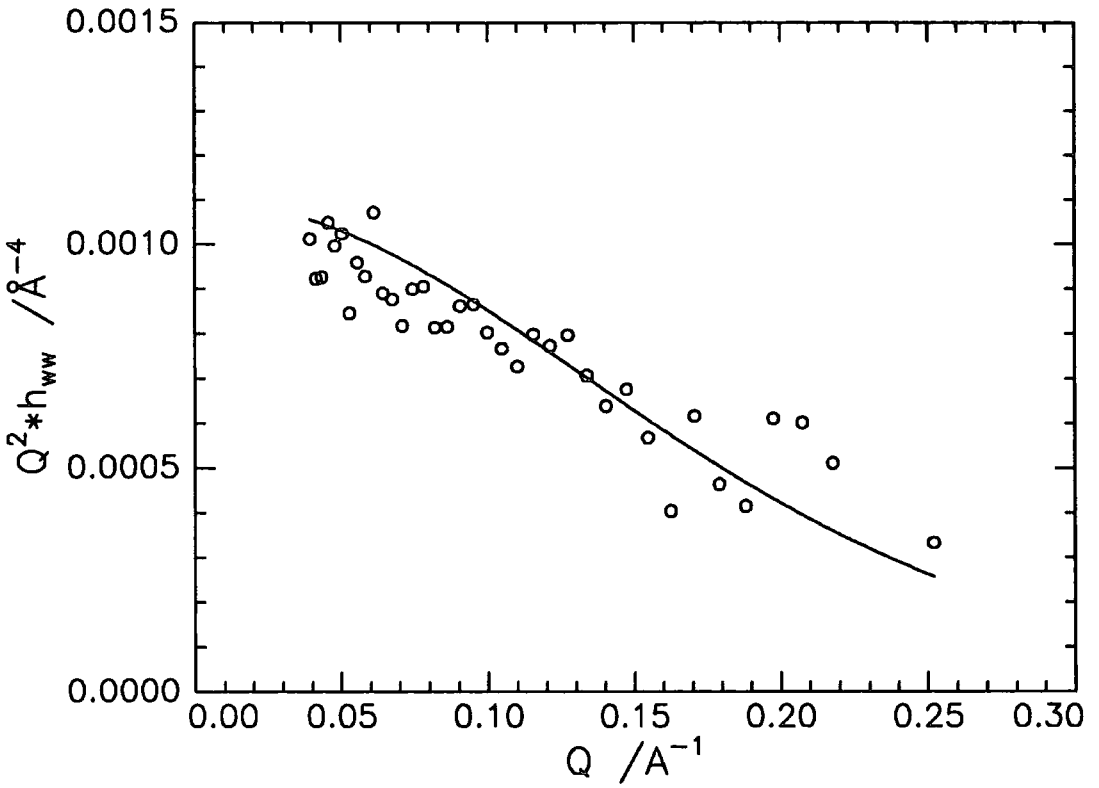

Figure 4.70 Tanh fit to water self term at 1.2mg/m^2

Model	Term	Γ /mg m^{-2}	n_{il}/Å^{-3}	d/Å	σ/Å	ζ/Å	Γ_s /mg m^{-2}	Γ_{app} /mg m^{-2}	δ_{mc}/Å	δ_{mw}/Å	δ_{cw}/Å
none		0.6							2	1	1
		1.2							10	6	1
uniform	h_{mm}	0.6	7.39e-6	12			0.35	0.40			
		1.2	1.14e-5	16			0.78	0.86			
	h_{cc}	0.6	1.41e-5	11			0.21	0.47			
		1.2	1.26e-5	17			0.51	0.66			
	h_{ww}	0.6	2.92e-2	15							
		1.2	5.20e-3	16							
Gaussian	h_{mm}	0.6	1.20e-5		8		0.35	0.35			
		1.2	1.51e-5		14		0.78	0.86			
	h_{cc}	0.6	2.20e-5		9		0.21	0.58			
		1.2	1.87e-5		12		0.51	0.65			
tanh	h_{ww}	0.6				4.9					
		1.2				5.7					

Table 4.14 Structural Parameters from the Partial Form Factors using the Kinematic Approximation

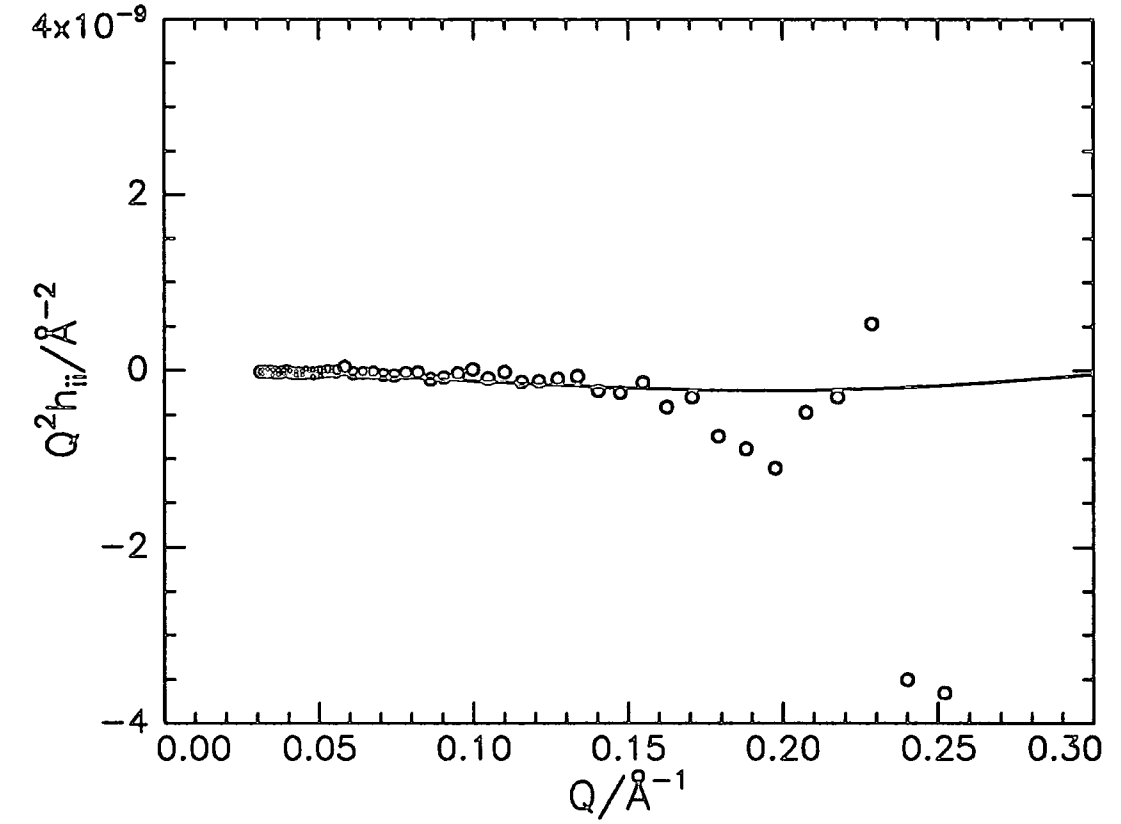

Figure 4.71 MMA/EO cross term data at 0.6mg/m^2

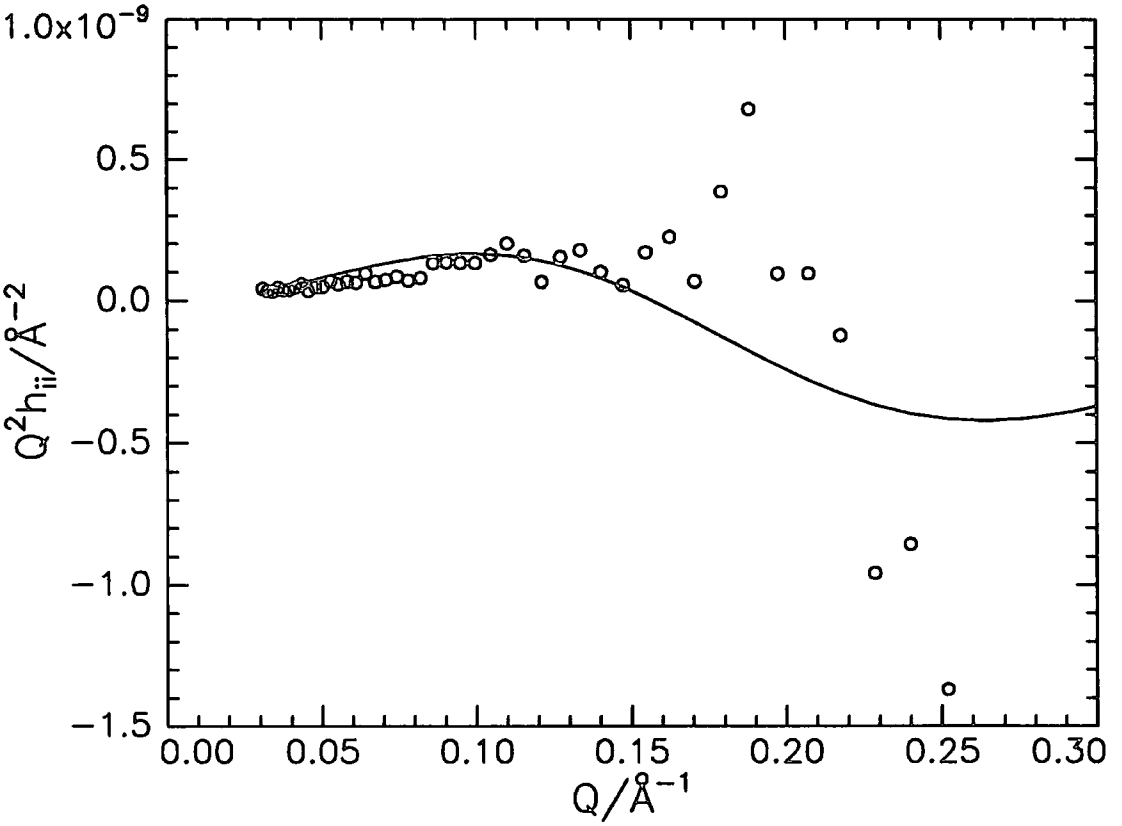

Figure 4.72 MMA/EO cross term data at 1.2mg/m^2

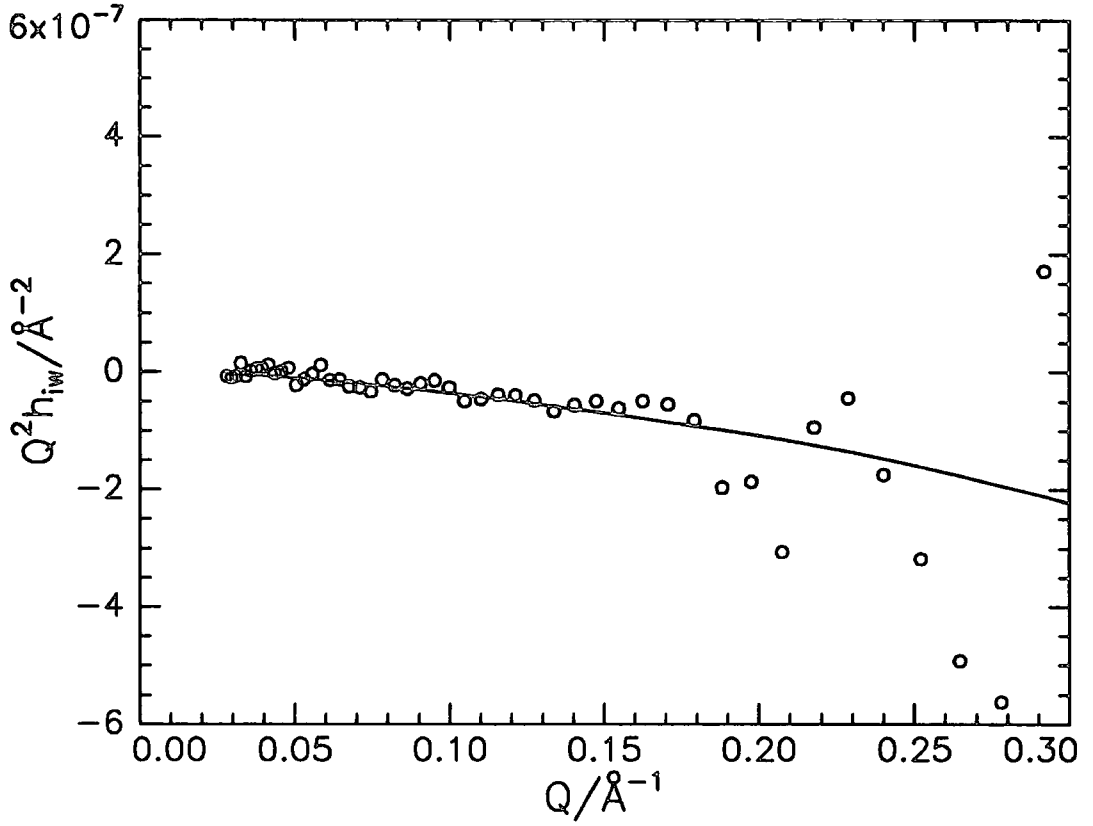

Figure 4.73 MMA/water cross term data at 0.6mg/m^2

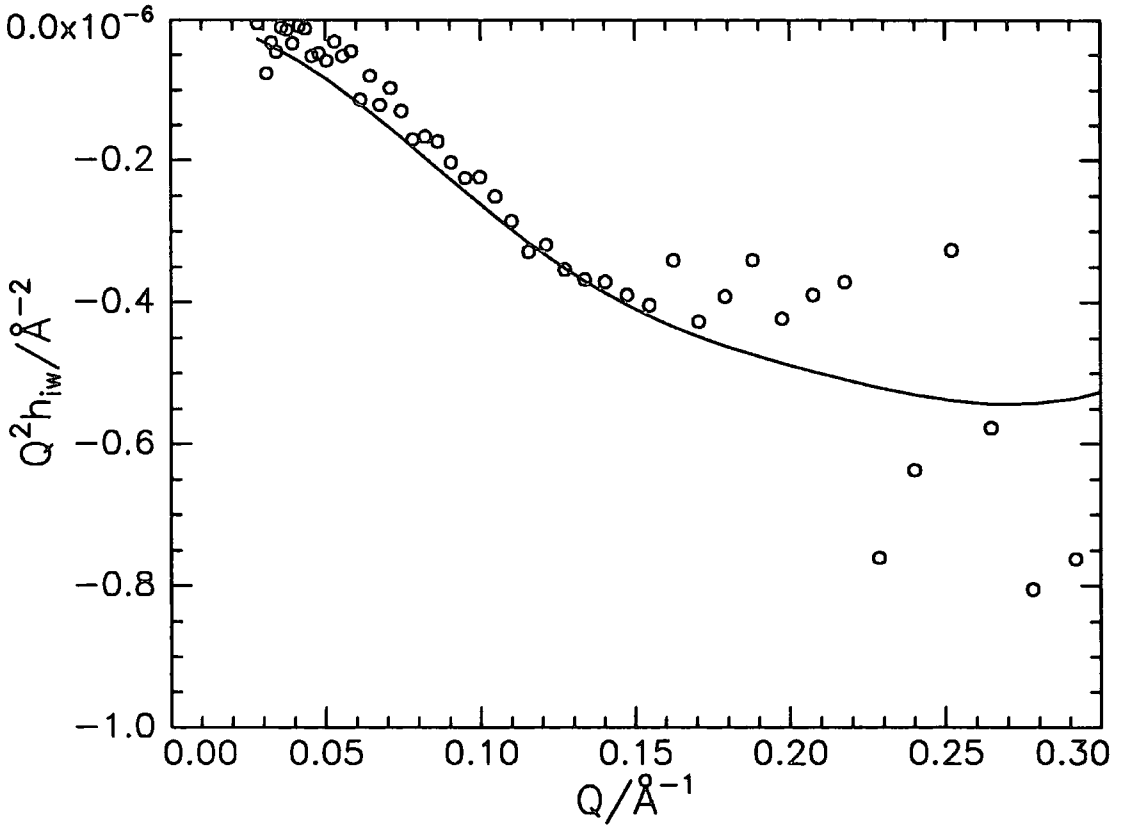

Figure 4.74 MMA/water cross term data at 1.2mg/m^2

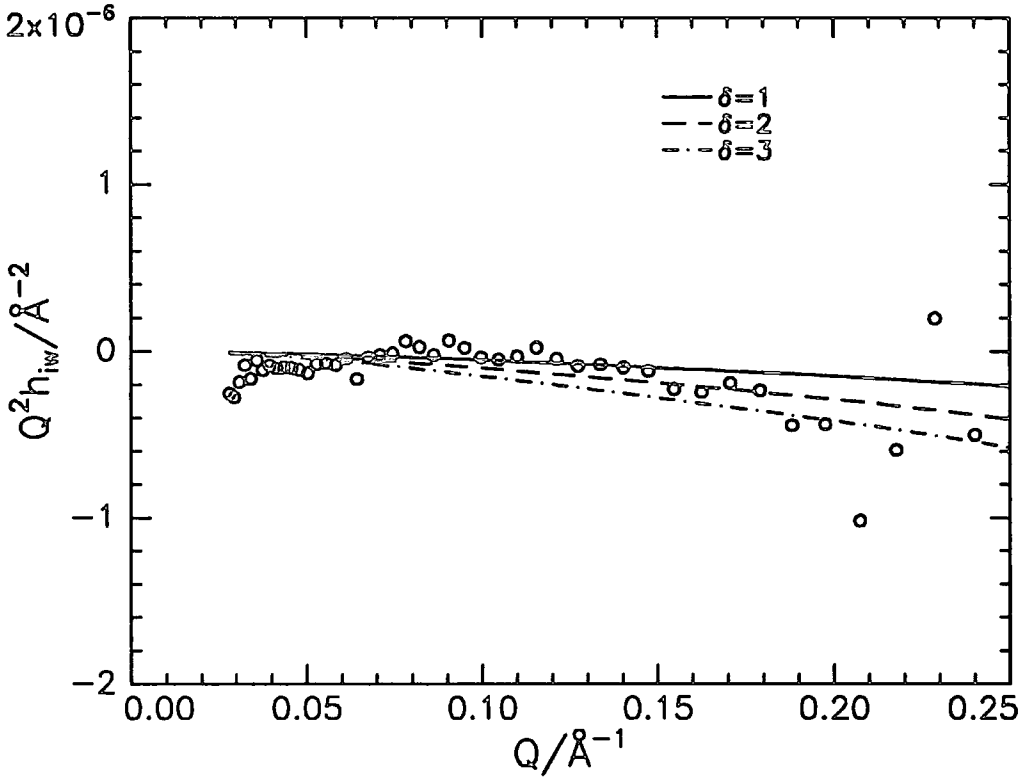

Figure 4.75 EO/water cross term data at 0.6mg/m^2

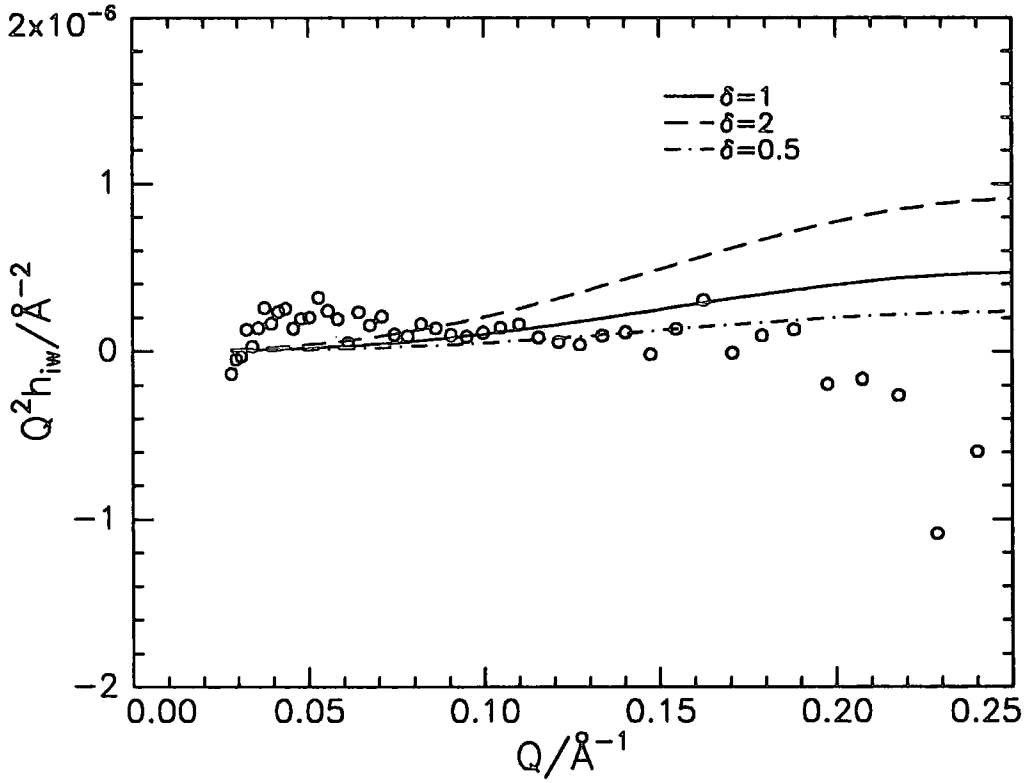

Figure 4.76 EO/water cross term data at 1.2mg/m^2

PART C: DISCUSSION

Application of the uniform layer model to the measured reflectivity profiles has allowed important inferences to be drawn from the results of the optical matrix method. The data for the copolymers spread on nrw show clear increases in layer thickness of the blocks with increasing surface coverage. For this constant area data these increases are sharper than those in Part A and include data for the improved HMDE/nrw contrast. At 0.6mg/m^2 there is good agreement between Γ_s and Γ_a. At the higher surface concentrations the DMDE and HMDE copolymers have lower Γ_a values than Γ_s, since this does not occur for the DMHE copolymer then it can be assumed that it is DEO segments which are effectively 'lost' to the neutron reflectivity technique. Figures 4.77 and 4.78 show the distribution of the interfacial components at 0.6 and 1.2mg/m^2. The amount of polymer at the surface is obtained by dividing the integrated number density by the layer thickness. At 0.6mg/m^2 the amount of EO is overestimated by a factor of two with respect to MMA, while at 1.2mg/m^2 the amounts of MMA and EO are about the same. This overestimation of the amount of EO was encountered in Part A and since here it only occurred at 0.6mg/m^2 it must be due to the presence of D_2O in the surface layer. The overestimation did not occur at 1.2mg/m^2 due to the D_2O being squeezed out of the layer. The MMA and EO components are presented as Gaussian distributions while the water is presented as a tanh profile. At 0.6mg/m^2 the full width, σ, of the MMA and EO distributions are about 8 and 9Å respectively. This surface concentration has significant interpenetration between the MMA and EO distributions, both blocks appearing to be uniformly mixed at the surface with a mean centre to centre separation of 2Å. Increasing the surface concentration from 0.6 to 1.2mg/m^2 had a dramatic effect on the organisation of the interfacial components. The widths of the MMA and EO distributions increased significantly to about 14 and 12Å respectively. The separation of the two distributions increased to 10Å and was accompanied by an MMA/water

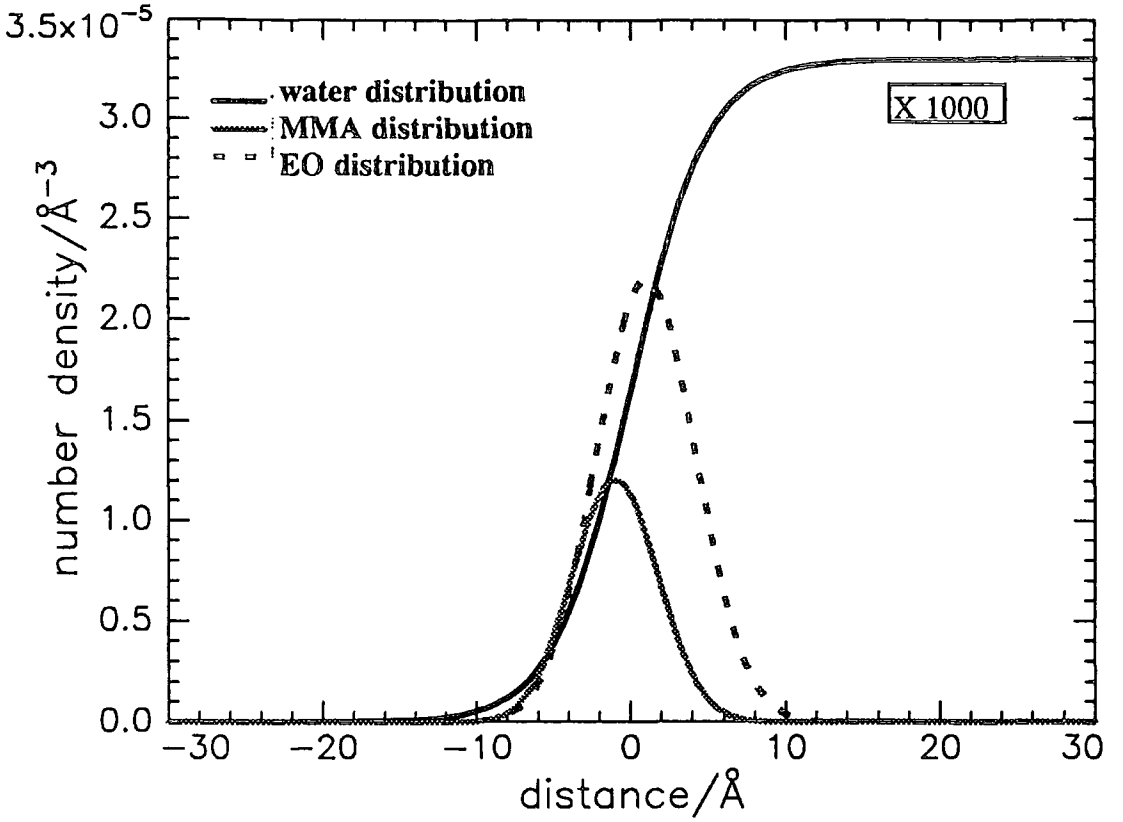

Figure 4.77 Distribution of interfacial components at 0.6mg/m^2

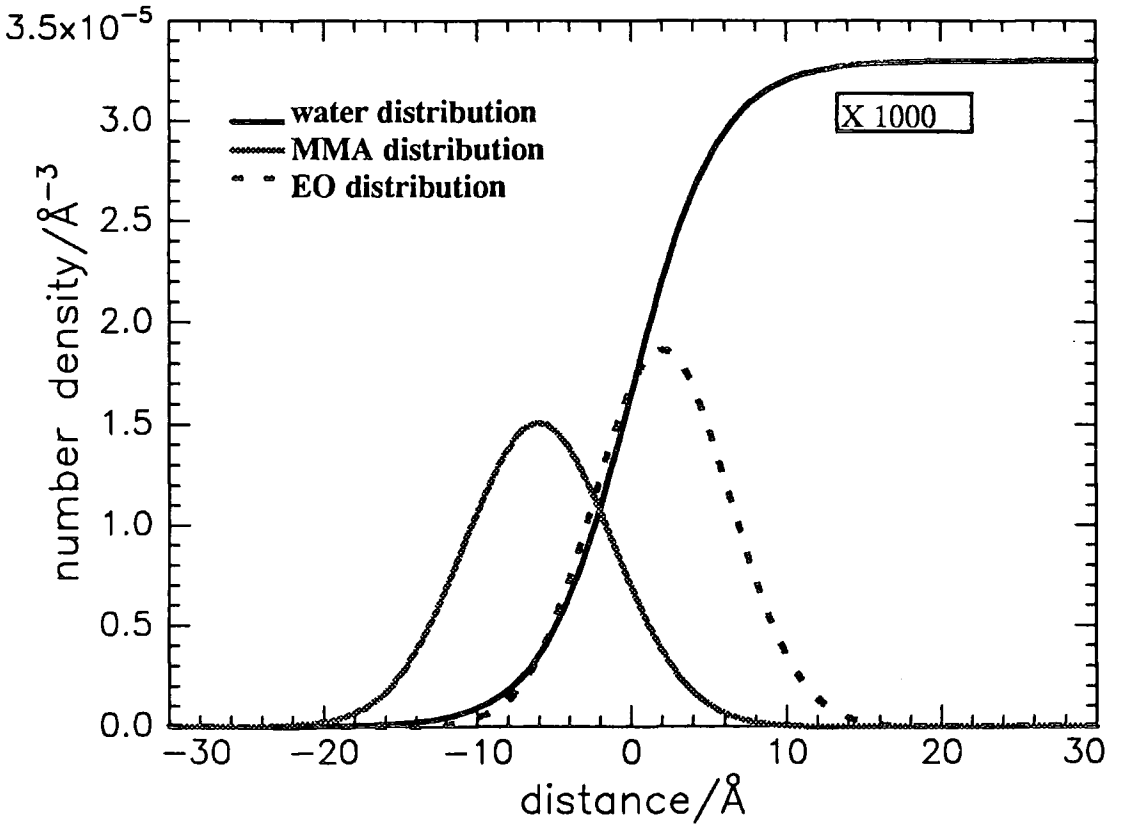

Figure 4.78 Distribution of interfacial components at 1.2mg/m^2

separation of 6Å. At 0.6mg/m^2 the MMA distribution is mainly on the air side of the interface with about 36% of it penetrating the water distribution, while at 1.2mg/m^2 about 9% of the distribution penetrates the subphase. A fraction of the PEO remains intermixed with the PMMA while the remainder is solubilized in the water subphase. The uniformity of the PMMA and PEO distributions disappears on increasing the surface concentration. At 1.2mg/m^2 there is obviously phase separation with the PMMA being confined mainly in the vicinity of the air-water interface while the PEO is highly solvated in the water subphase.

The system so far described is analogous with that of a 'tethered chain' system. An example of this type of system is an A-B diblock copolymer adsorbed from dilute solution onto a solid surface that attracts the A block and repels the B block in a nonselective solvent. For any terminally attached chain at a surface there exists a number of possible structures[2]. Figure 4.79 shows the theoretical structure for isolated chains, where the distance between the grafting points, D, is larger than the radius of gyration. The *mushroom* structure is extended normal to the surface with a dimension of about $2R_g$. For the *pancake* model the chain visits the surface a number of times and has a thickness similar to the segment size. When the surface density increases, the value of D being less than the radius of gyration, strong overlap occurs between the tethered chains and a significant change in structure occurs. It was predicted that the chains become stretched into a *brush* configuration allowing extra segments to be accommodated (figure 4.80). For the MMA/EO diblock copolymer at the air/water interface the PMMA is regarded as the anchor block at the surface while the PEO is termed the buoy block. For systems containing these chains a major component which must be considered is the degree of crowding. This crowding is commonly expressed as

$$\sigma^* = \sigma/\sigma_{01} \qquad (4.13)$$

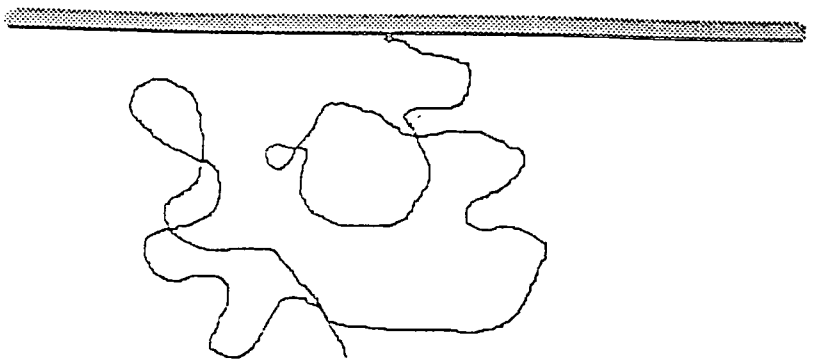

Figure 4.79a) Mushroom Configuration

Figure 4.79b) Pancake Configuration

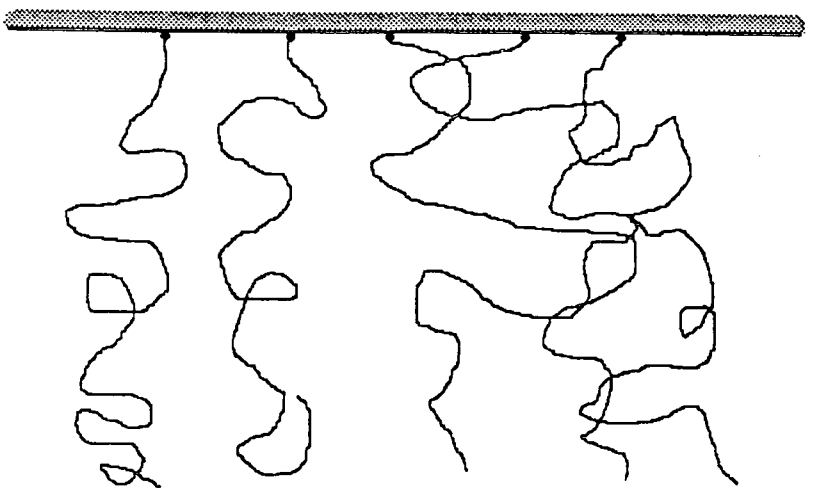

Figure 4.80 Brush Configuration

where σ^* is the reduced surface density

σ is the surface density (number of chains per unit area)

and $\sigma_{01} = 1/\pi R_g^2$ (4.14)

which is an estimate of surface density where the tethered chains just begin to overlap, R_g being the root mean square (rms) radius of gyration of a free coil in solution. At a solid/liquid interface the system consists of a soluble copolymer adsorbed from solution whereas in this work the system consists of a copolymer spread on water. Studies employing these ideas have been carried out on systems such as solid/liquid interfaces[3,4,5] and the ideas are applicable to air/liquid interfaces[6,7]. For an MMA/EO diblock copolymer spread on water then the surface tension (γ) of water is very much higher than PEO which means that the PEO will tend to be adsorbed at the air/water interface. Neutron reflectivity provides a number of advantages for this system over adsorbed systems at the solid/liquid interface. Firstly, the low surface roughness (~3Å) allows a higher range of momentum transfer (Q) to be measured than for solid/liquid interfaces. Secondly, σ^* can be varied by changing the surface concentration of the spread polymer. At the solid/liquid interface σ^* is fixed and variation is only possible by altering the chemical composition of the copolymer.

The adsorbed layer may be described by an asymmetry factor β_n, which for a diblock copolymer may be given by

$$\beta_N = (N_B/N_A)^{6/5} \quad (4.15)$$

where N_A and N_B are the degrees of polymerisation for each block. For a layer thickness L, then two regimes may be considered

Buoy regime; $\beta_n > N_A$

$$L \propto N_A^{2/5} N_B^{3/5} \quad (4.16)$$

Anchor regime; $1 < \beta_n < N_A$

$$L \propto N_B N_A^{-1/3} \quad (4.17)$$

Alexander[8] predicted that $L \propto N\sigma^{1/3}$, where N is the number of monomers per chain. Due to the difference in N for the copolymers used in the kinematic approximation then $L \propto \sigma^{*1/3}$ only. The parameters from the fits to the EO self term data were used to calculate values of σ^* (Table 4.15). Vennemann et al[9] have measured the radius of gyration of a monodisperse sample of PEO in water and their value was 73Å at 298K. Their PEO sample had a molecular weight of 19000g/mol, comparable to an average value of 18800 g mol^{-1} for the PEO blocks of the copolymers used in this work.

It is possible to make a qualitative comparison of self-consistent field theories to number density profiles obtained from the self partial structure factors. It can be seen for the constant π data that as σ^* increases from 10.0 to 14.6 there is an increase in the width of the Gaussian PEO distribution, σ_e. If the layer thickness L is taken to be approximately equal to σ_e then these increases in σ_e show an apparent $\sigma^{*1/3}$ dependence on L. The same dependence is evident for the constant area data, the lower values of $\sigma^{*1/3}$ being due to smaller number densities, n_{1e}, determined for the PEO blocks. For the constant surface pressure data it can be argued that these larger number densities are due to higher surface concentrations being used (and may be higher still due to barrier movement). Remembering that for the constant surface pressure data, the mole composition of PEO in each copolymer was 50% or less, then the number densities should be approximately equal to those of MMA. The values of n_{1e} are overestimated by about a factor of 2 *at all surface pressures*. This overestimation was thought to be due to using four D_2O contrasts and only two nrw contrasts, the extra D_2O contrast used being DMDE/D_2O. The constant area data show that at 0.6mg/m^2 the amount of EO is still overestimated but may be attributed to D_2O in the surface layer since at 1.2mg/m^2 the overestimation disappears as D_2O is squeezed out of the layer. At 1.2mg/m^2 the value

Surface Coverage	$n_{1c}/Å^{-3}$	$\sigma_o/Å$	Surface [a] density $\sigma/Å^2$	Reduced surface density σ^*	$\sigma^{*1/3}$	D/Å
2mN/m	3.42e-5	21	5.98e-4	10.0	2.16	41
5mN/m	3.81e-5	20	6.49e-4	10.9	2.22	40
10mN/m	4.38e-5	24	8.72e-4	14.6	2.44	34
$0.6mg/m^2$	1.00e-5	10	8.86e-5	1.5	1.14	74
$1.2mg/m^2$	1.87e-5	12	2.06e-4	3.5	1.51	68

Table 4.15 σ^* and $\sigma^{*1/3}$ calculated from parameters of EO self term fits

[a] The surface density above which PEO buoys will overlap
$= 1/(\pi Rg^2) = 5.97e\text{-}5Å^2$

[b] $D = (\sigma)^{-1/2}$ where D is the average distance between adsorbed chains

of the PEO number density decreases to a value comparable to that of the PMMA number density.

The literature shows that the range of surface densities possible varies significantly between experimental techniques[10-13]. Auroy et al[10-11] have reported values of σ^* greater than 70 for terminally grafted systems, while work on block copolymer adsorption at the solid/liquid interface[13] has yielded maximum values ranging from 4 to 7. Parsonage et al[4] have shown that the maximum σ^* values for adsorbed block copolymer systems are obtained using highly asymmetric copolymers. The maximum values of σ^* obtained in this work were 3.5 for the constant area data and 14.6 for the constant π data. Although the constant π values of σ^* may be overestimated the same trend as the constant area data is observed, where increasing values of σ^* are attributed to extension of the PEO segments into the water surface. Equation 4.14 gives a value 5.97e-5Å^2 for the surface density, σ_{01}, above which the PEO buoys overlap and form a semidilute solution in the adsorbed layer. Table 4.15 shows that for all surface coverages the surface density, σ, is much larger than σ_{01} meaning that there is strong overlap between the PEO blocks. The values of the surface density, σ, may be used to calculate a value D which is the mean distance between PMMA-PEO junction points from

$$\sigma = (1/D)^2 \qquad (4.18)$$

the values of which are included in Table 4.15 and are seen to decrease with increasing surface coverage. Assuming that the PEO blocks are tethered to the air/water interface then assumptions can be made about their configuration. The thickness of the PEO layer is much less than that characteristic of a *mushroom* structure which requires that the layer thickness be about $2R_g$ (ca. 146Å). The PEO layer is much thicker than that required for a *pancake* configuration which is of the order of segment size. A *brush* configuration is possible since the PEO blocks overlap strongly at the interface,

especially with increasing surface coverage, and it would be expected that the chains become stretched in order to accommodate extra PEO segments. At 0.6mg/m^2 there is a high degree of mixing between the two blocks at the interface and the PEO blocks do not extend far into the subphase, the PEO density distribution resembling a 'squashed mushroom'. The PEO distribution at 1.2mg/m^2 has more 'brushlike' characteristics than at 0.6mg/m^2, with loops of the PEO chains extending into the subphase, perhaps accounting for the segments 'lost' to the technique. The expected distributions of the interfacial components are shown as schematics in figures 4.81 and 4.82

It must be noted that the self partial structure terms for the PMMA and PEO blocks may be fitted well using either uniform layer models or Gaussian distributions. The fact that Q does not extend to a sufficiently high value where $Q_{max}.d > 2\pi$ means that it is impossible to distinguish between these two models. An upper Q value of about 0.45Å would therefore be needed to resolve the ambiguity. The constant area reflectivity data extend to the lowest Q value where the signal to noise ratio is lower and a better description of the distributions is therefore obtained.

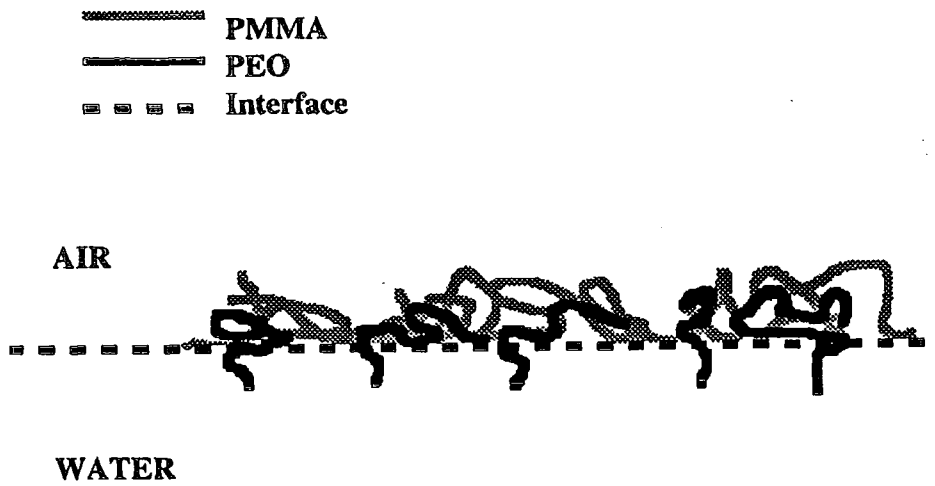

Figure 4.81 Schematic of distribution of components at 0.6mg/m^2

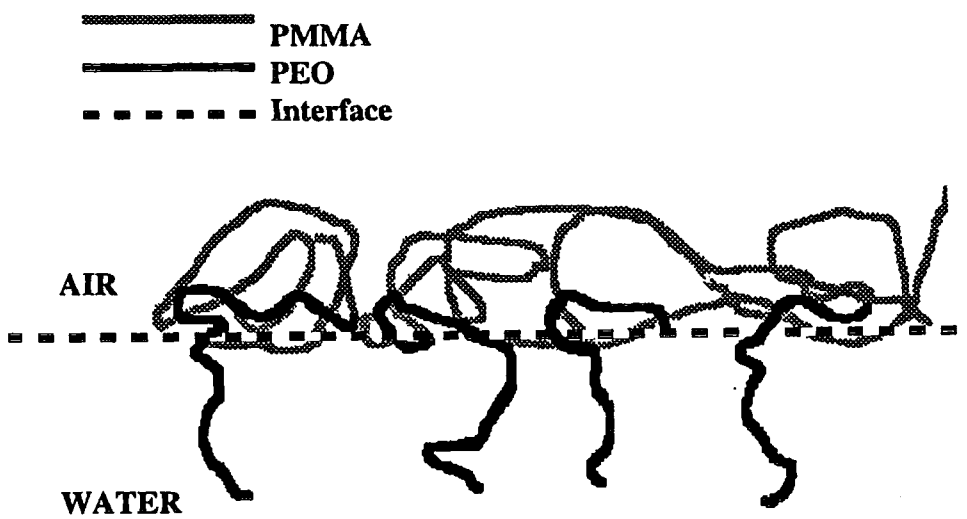

Figure 4.82 Schematic of distribution of components at 1.2mg/m^2

References

1. Lu, J.R., Hromadova, M., Thomas, R.K.,Penfold, J., *Langmuir*, 1993, 9, 2417.

2. Fleer, G.J., Cohen-Stuart, M.A., Scheutjens, J.M.H.M., Cosgrove, T., Vincent, B., *Polymers at Interfaces*, Chapman and Hall, London, 1993.

3. Marques, C.M., Joanny, J.F., *Macromolecules*, 1989, 22, 1454.

4. Parsonage, E., Tirrel, M., Watanabe, H., Nuzzo, R.G., *Macromolecules*, 1991, 24, 1987.

5. Mansfield, T.L., Iyengar, D.R., Beaucage, G., McCarthy, T.J., Stein, R.S., *Macromolecules*, 1995, 28, 492.

6. Rennie, A.R., Crawford, R.J., Lee, E.M., Thomas, R.K., Crowley, T.L., Roberts, S., Qureshi, M.S., Richards, R.W., *Macromolecules*, 1989, 22, 3466.

7. Kent, M.S., Lee, L.T., Farnoux, B., Rondelez, F., *Macromolecules*, 1992, 25, 6240.

8. Alexander, S., *J. Phys (Paris)*, 1977, 38, 977.

9. Vennemann, N., Lechner, M.D., Oberthür, R.C., *Polymer*, 1987, 28, 1738.

10. Auroy, P., Auvray, L., Léger, L., *Phys. Rev. Lett.*, 1991, 66, 719.

11. Auroy, P., Auvray, L., Léger, L., *Macromolecules*, 1991, 24, 2523.

12. Auroy, P., Auvray, L., Léger, L., *Macromolecules*, 1991, 24, 5158.

13. Cosgrove, T., *J. Chem. Soc., Faraday Trans.*, 1990, 86, 1323.

CHAPTER 5 - SURFACE QUASI - ELASTIC LIGHT SCATTERING

Summary

In the folowing chapter two types of data are presented, the first type being measured at a fixed wavenumber (q), comparing the difference between using constant surface pressure and constant area to obtain the surface concentration dependence of the viscoelastic parameters. The second type of data was measured at one surface concentration in the fully compressed state and investigated the variation of the viscoelastic parameters with q. Viscoelastic models are applied to the data with the purpose of obtaining relaxation times for the polymeric monolayers. The results are discussed and compared with those of other workers and with respect to results obtained from neutron reflectometry.

5.1 SQELS from Water

SQELS was used on the bare water surface to estimate the surface wavenumber (q) for each diffraction spot falling on the pinhole of the photomultiplier tube. These estimates were made by obtaining the frequency and damping constants of the thermally excited capillary waves on the water surface. Due to flare originating from the edge of the neutral density filter the lowest angle diffraction spot was disregarded. Non-linear least squares fitting of a doubly exponentially damped cosine function (eqn 1.6.4) to the experimental data gave values for the wave damping and propagation frequency of each run. Typical fitted data and their respective residuals are shown in figure 5.1. The scattered intensity (I_s), relative intensity of the scattered light I_s to the reference beam I_r (I_s/I_r), propagation frequency (ω_0) and damping constant (Γ) variation with q are shown in figures 5.2 and 5.3. The values of I_s and I_s/I_r are tabulated in tables 5.1a) and b), the difference in intensities between the two data sets being due to two diffraction gratings being used. Although the absolute values of the relative intensities of the scattered light

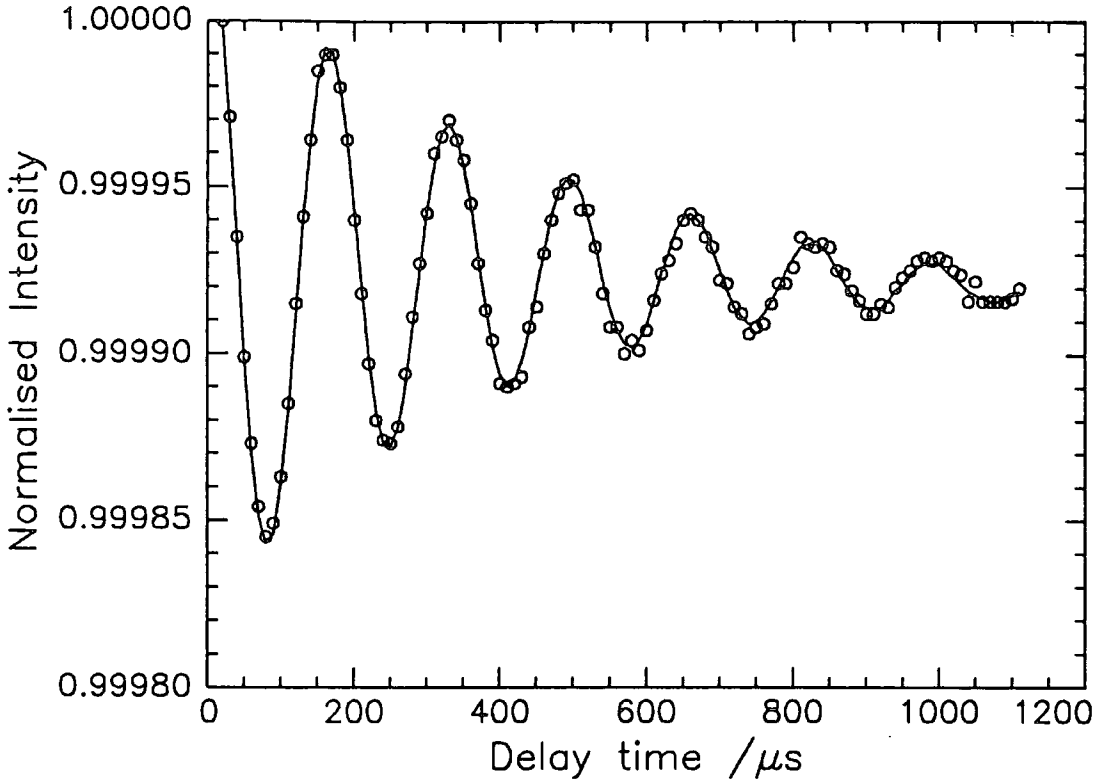

Figure 5.1a) Typical fit (-) to a correlation function obtained by SQELS

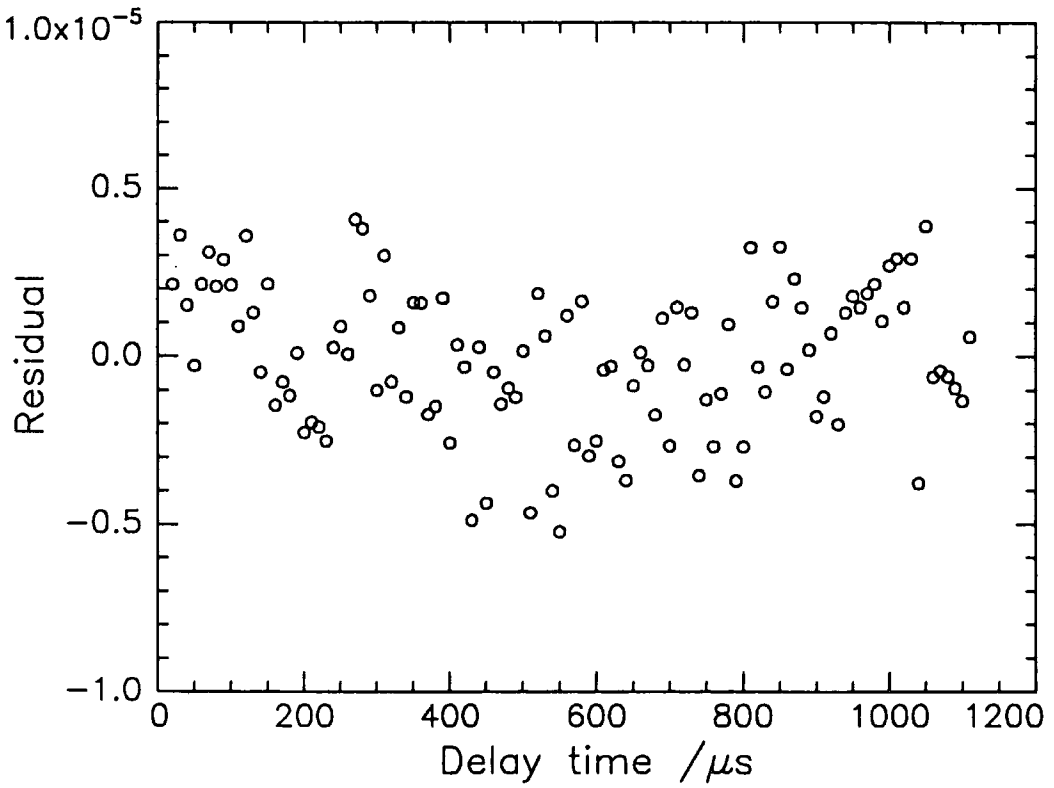

Figure 5.1b) Residuals of the above fit

q/cm^{-1} (from ω_0)	Is	Is/Ir	Damping Constant /s^{-1}	Frequency /s^{-1}
295	5.61e-5	9.67e-6	1808	42929
301	8.64e-5	1.50e-5	1818	44148
351	5.23e-5	1.01e-5	1419	44671
393	2.99e-5	9.73e-6	2669	66208
473	1.16e-4	5.63e-6	4086	87165
566		4.29e-5	5541	114159

Table 5.1a Fitted parameters from SQELS on the bare water surface using diffraction grating 1

q/cm^{-1} (from ω_0)	Is	Is/Ir	Damping Constant /s^{-1}	Frequency /s^{-1}
220	5.20e-4	9.38e-5	750	27547
332	1.77e-4	3.19e-5	1749	51217
438	1.84e-4	3.87e-5	3310	77765
552	8.27e-5	1.80e-5	4930	110208
667	1.88e-4	5.71e-5	7787	146408
786	1.91e-4	3.99e-5	10619	187340
909	6.74e-5	1.61e-5	15061	232972

Table 5.1b Fitted parameters for SQELS on the bare water surface using diffraction grating 2

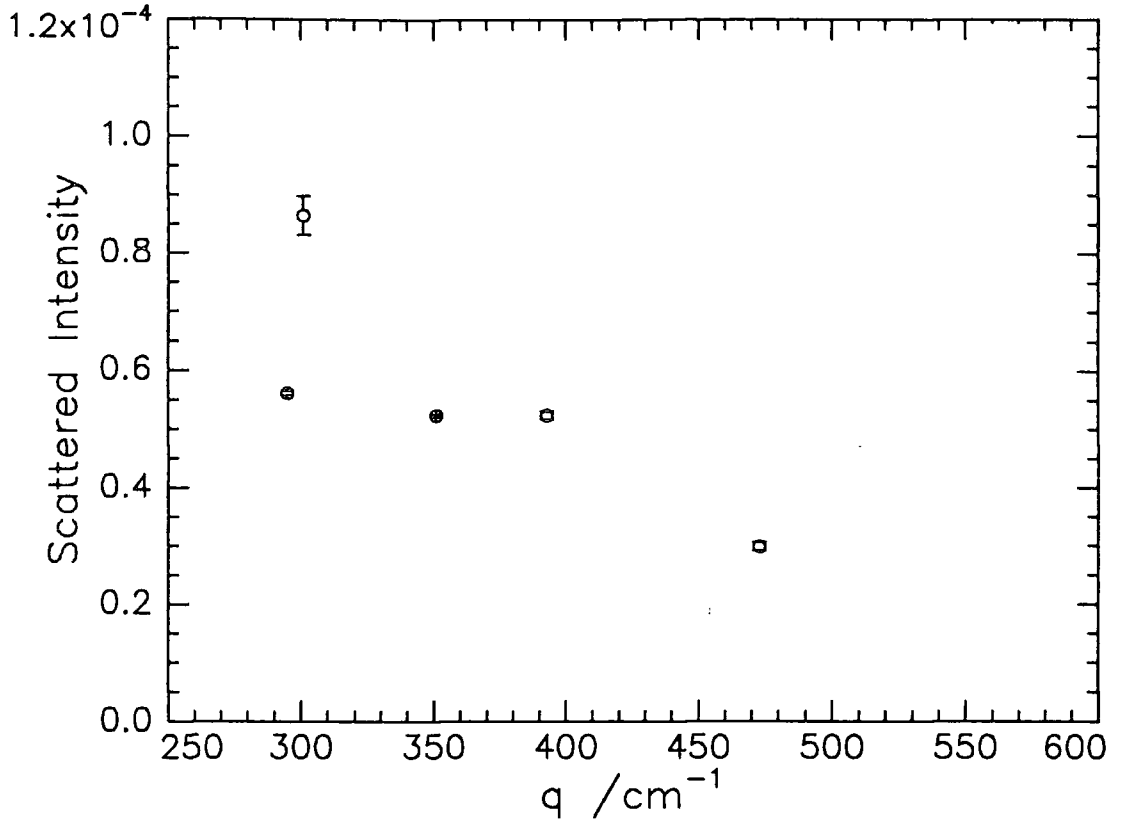

Figure 5.2a) Variation of Scattered Intensity as a function of q using diffraction grating 1

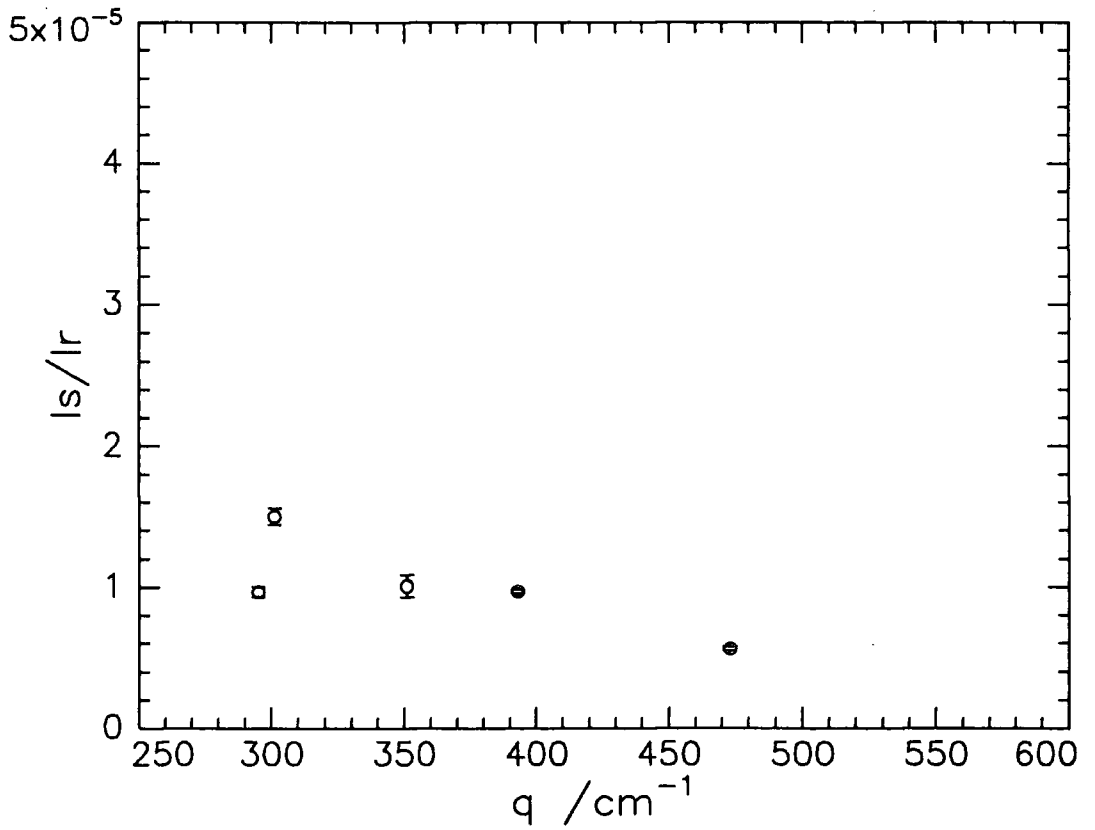

Figure 5.2b) The ratio of Scattered to Reference Intensities as a function of q using diffraction grating 1

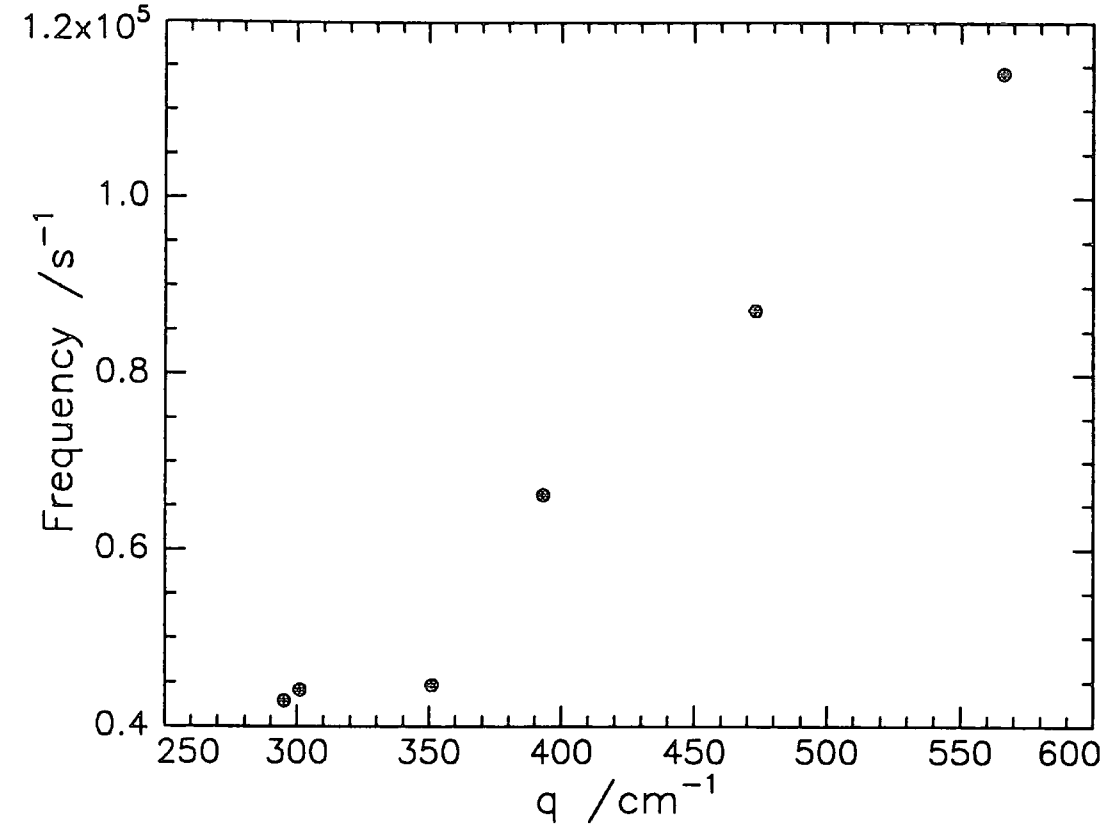

Figure 5.2c) Variation of capillary wave frequency as a function of q for diffraction grating 1

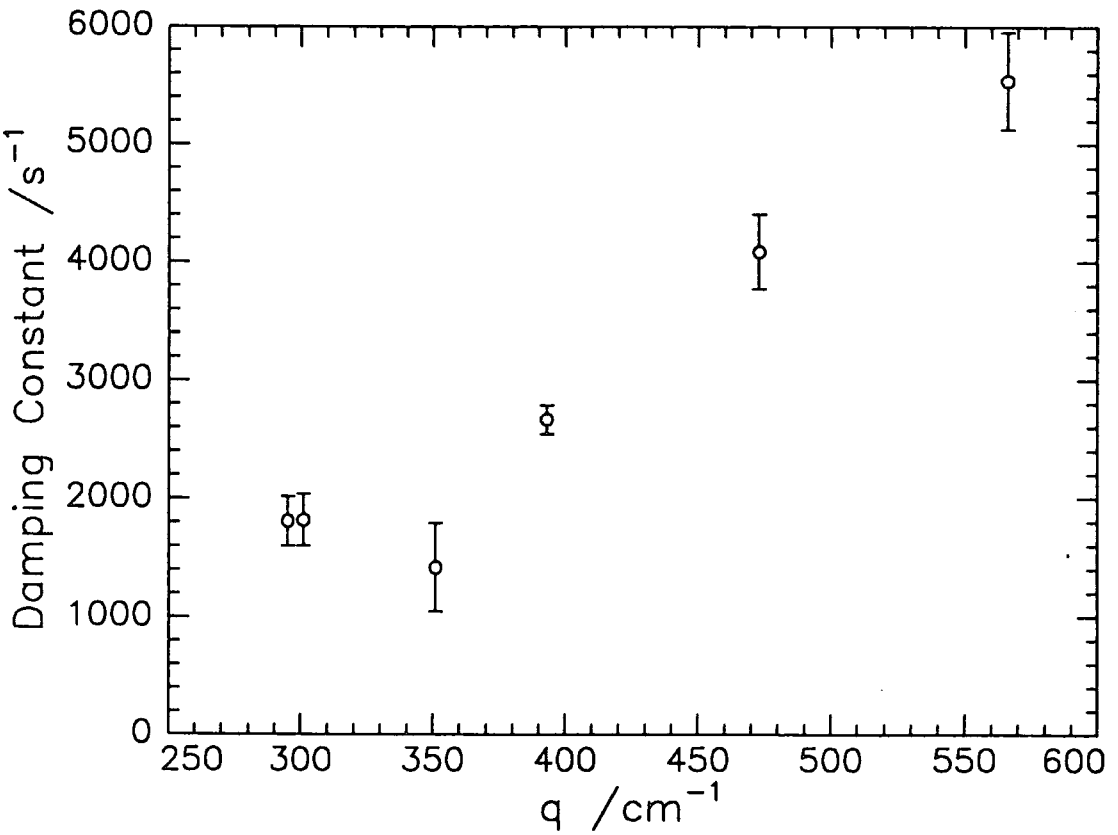

Figure 5.2d) Variation of Damping Constant as a function of q for diffraction grating 1

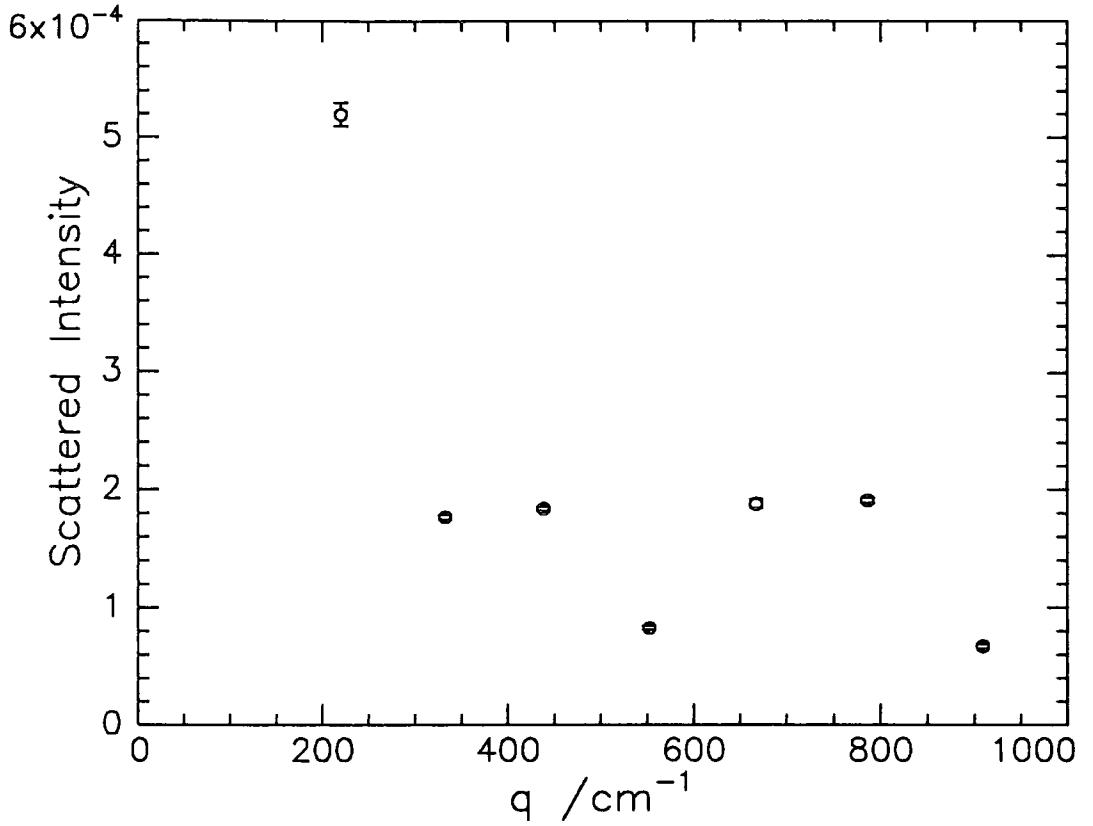

Figure 5.3a) Variation in Scattered Intensity as a function of q for diffraction grating 2

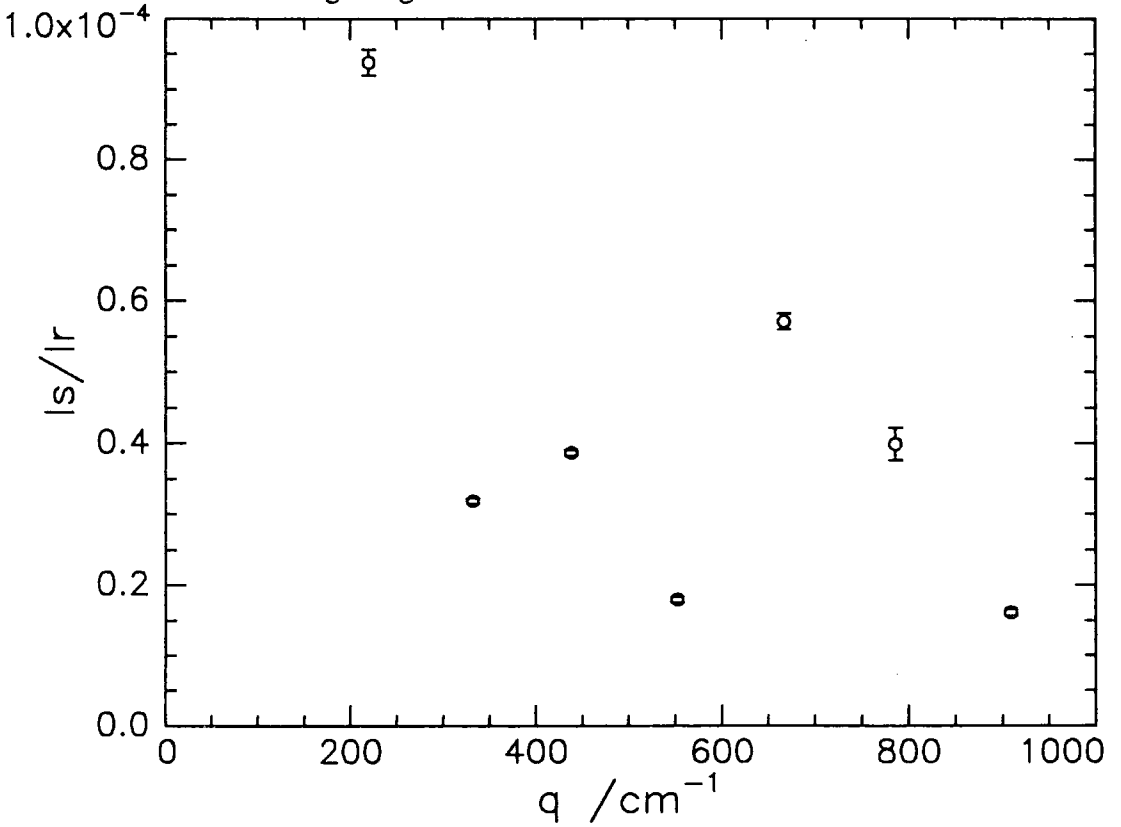

Figure 5.3b) The ratio of Scattered to Reference Intensities as a function of q using diffraction grating 2

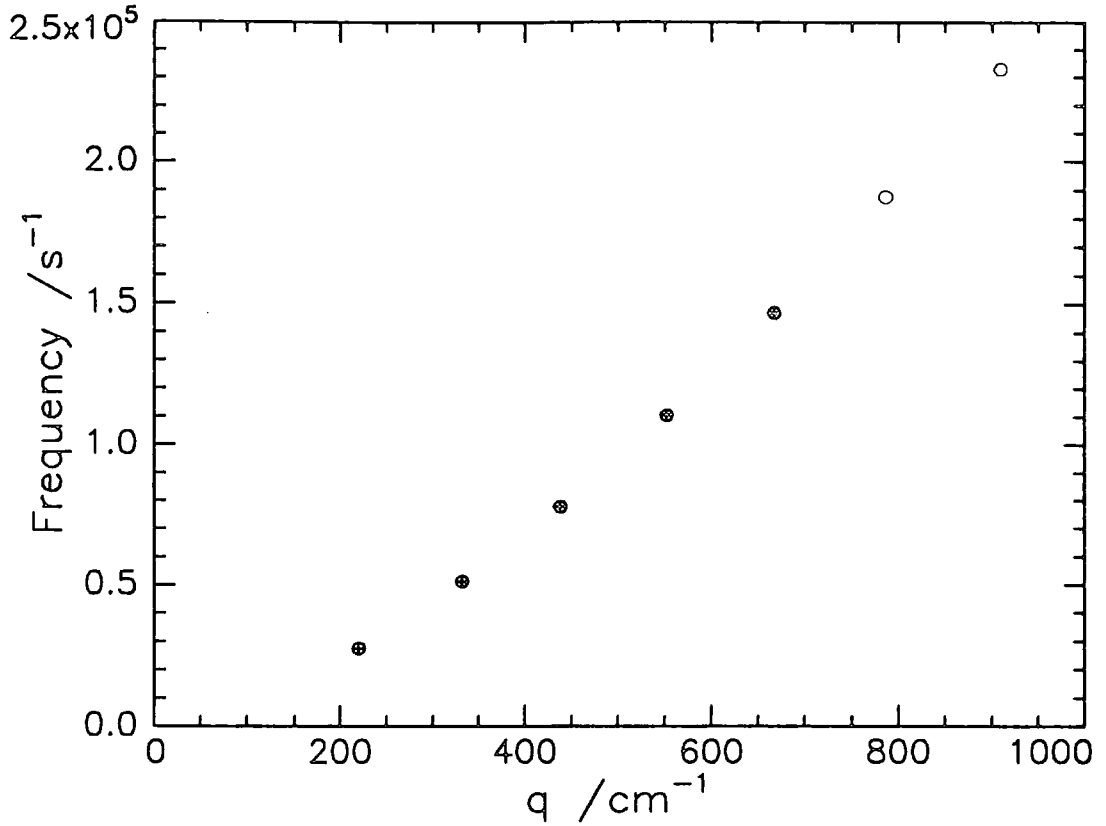

Figure 5.3c) Variation of capillary wave frequency as a function of q for diffraction grating 2

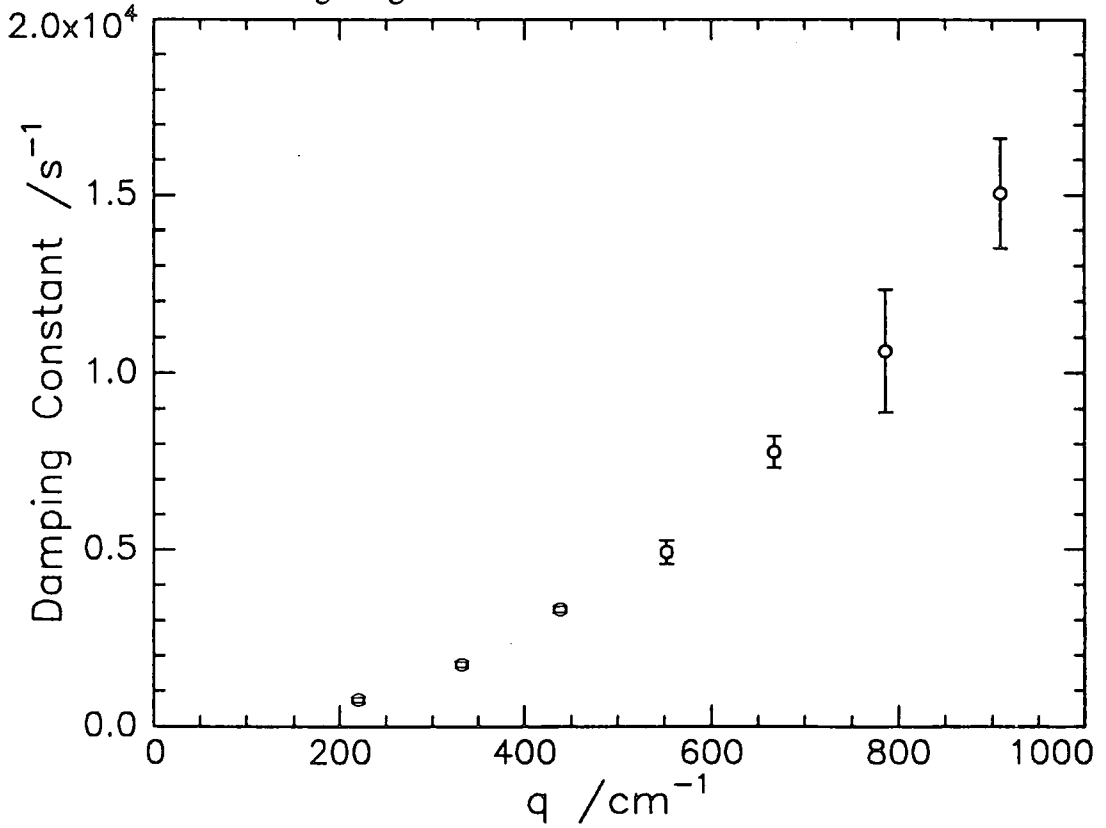

Figure 5.3d) Variation of Damping Constant as a function of q for diffraction grating 2

(I_s) and of the reference beam (I_r) cannot be obtained, it is possible to follow variations in their magnitude. The intensity data decrease in magnitude with increasing q in accordance with the relation

$$I_s \propto RkT/\gamma_0 q^2 \qquad (5.1)$$

where R is the interfacial reflectivity. Therefore I_s carries no structural information and is due only to the capillary waves. This decrease is followed approximately in figures 5.2-3a) and b), remembering that intensities of the scattered beam also depend on experimental variations such as the neutral density filter used and the position of the waveguide. It can be seen that both the propagation frequency and damping constant increase linearly with q as expected. Use of the approximation formulae (eqns 1.6.7 and 1.6.8) meant that ω_0 and Γ could be used to estimate the surface wavenumber q for each of the diffraction spots. The parameters obtained are shown in table 5.1 over a range of q values. It can be seen that the value of q depends on the magnitude of the propagation frequency and wave damping.

5.2 SQELS from PMMA-b-PEO copolymers

5.2.1 Measurements at a fixed wavenumber (q)

Spread monolayers of a PMMA-b-PEO block copolymer (BR20) at the air-water interface were investigated using SQELS. The classical surface pressure isotherm is shown in figure 5.4. The light scattering observations were initially carried out at constant surface pressure and subsequently at constant surface area. The advantage of having a constant surface area was that stationary barriers reduced perturbation of the monolayer and a surface concentration range upto 3.00mg/m^2 could be investigated.

A known volume of block copolymer solution was deposited on the water surface and sufficient time allowed for evaporation of the chloroform solvent. For the monolayer held at a specific surface pressure using a classical force balance and controlling the

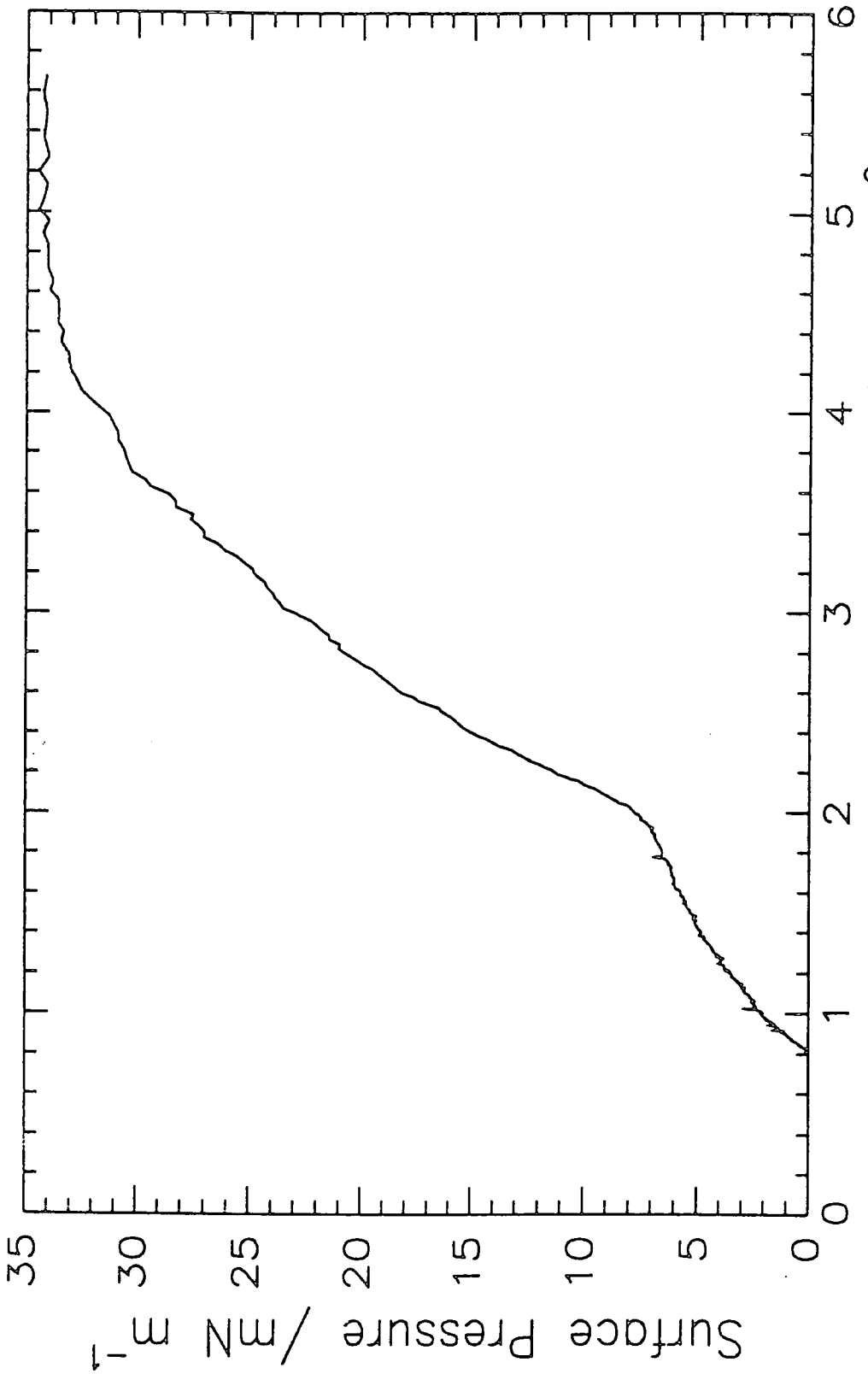

Figure 5.4 Surface pressure isothem for the copolymer studied

barrier positions automatically then a constant surface concentration was always maintained. The monolayers held at constant area were initially compressed to give the required surface concentration. All measurements were made at a constant temperature of 298K. A total of ten consecutive correlation functions were recorded for each surface concentration.

5.2.1.1 Measurements at constant surface pressure (π)

For the constant surface pressure measurements, I_s, I_s/I_r, ω_0 and Γ values are shown in figures 5.6-5.9 as a function of surface concentration at a q value of 295cm^{-1}. These fitted parameters are statistical averages of ten correlation functions. It can be seen that the I_s/I_r ratios are all below ca.10^{-3}, the value recommended by Earnshaw et al[4]. In equation 2.5.1 for the measured correlation function $G(\tau)$ the field autocorrelation function therefore predominates due to I_r being sufficiently larger than I_s. This means that the self beat term was much smaller than the random noise on the observed correlation functions. The scattered intensity was sufficiently high so that data acquisition was completed in times as small as forty seconds. The propagation frequency is seen to decrease with increasing surface concentration, except at very low concentrations where there is a slight increase in the values compared to that of the free water surface. The wave damping reaches a sharp maximum at 0.6mg/m^2 before decreasing to a plateau value with increasing surface concentration. These results are also presented as a function of constant surface pressure in figures 5.10-5.11.

The surface viscoelastic properties surface tension (γ_o), transverse shear viscosity (γ'), dilational elastic modulus (ε_o) and dilational viscosity (ε') were derived using the direct fitting method (Eq.1.6.16). A Fourier transformation routine was used to calculate a correlation function from the power spectrum generated by a given set of film viscoelastic parameters in the dispersion equation. Least squares minimisation of the

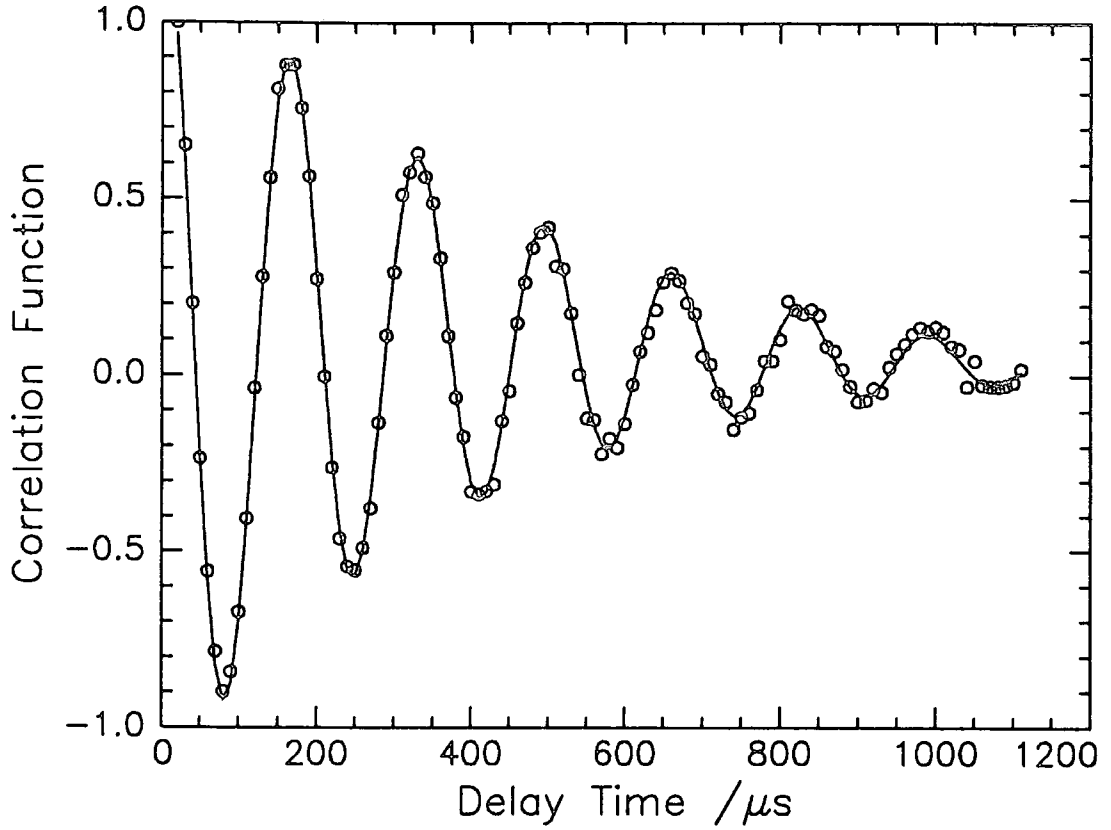

Figure 5.5a) Typical fit (-) to using full spectral fitting to correlation function data

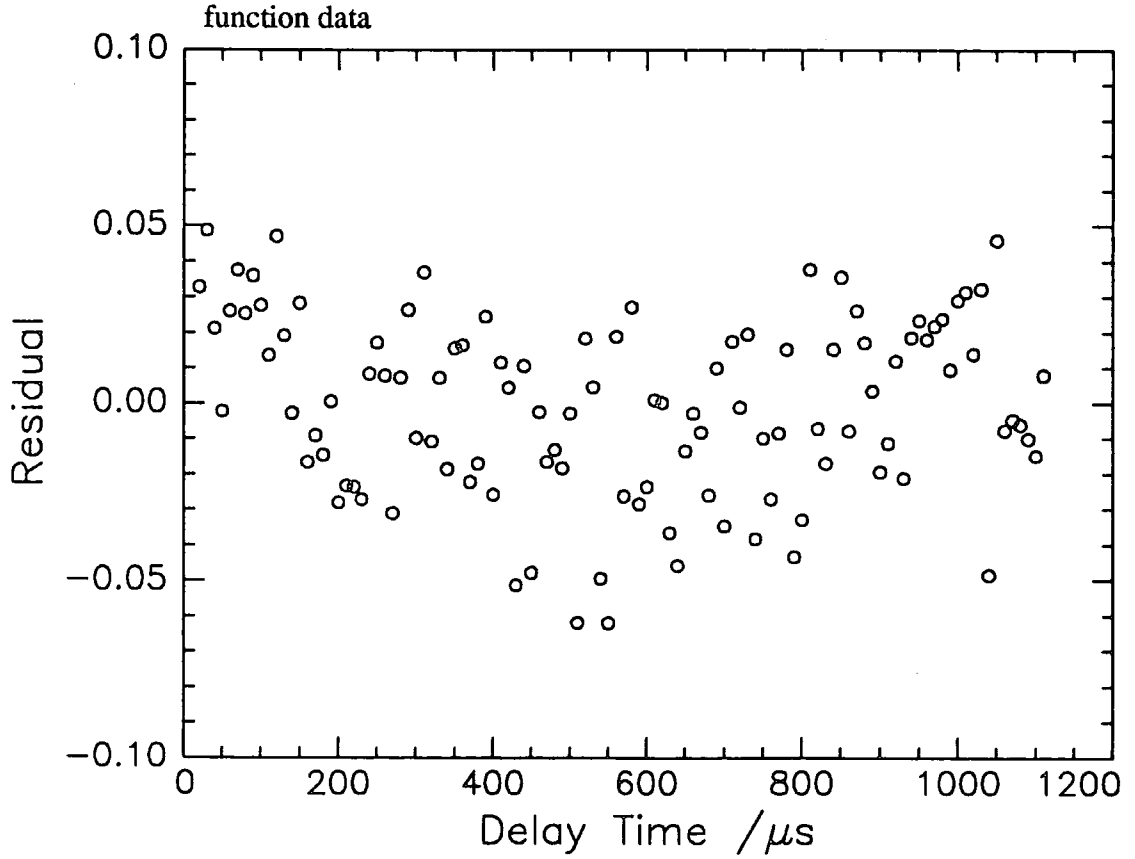

Figure 5.5b) Residuals to the above fit

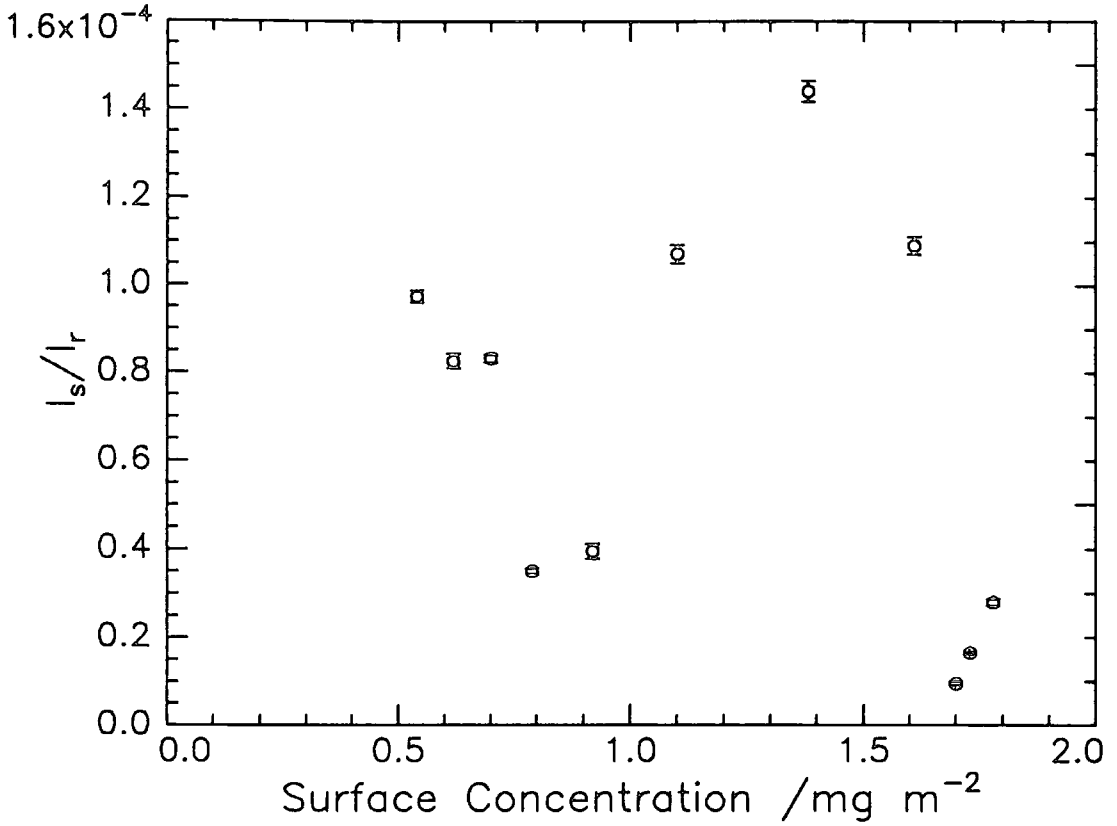

Figure 5.6 Variation the ratio I_s/I_r with surface concentration at constant pressure

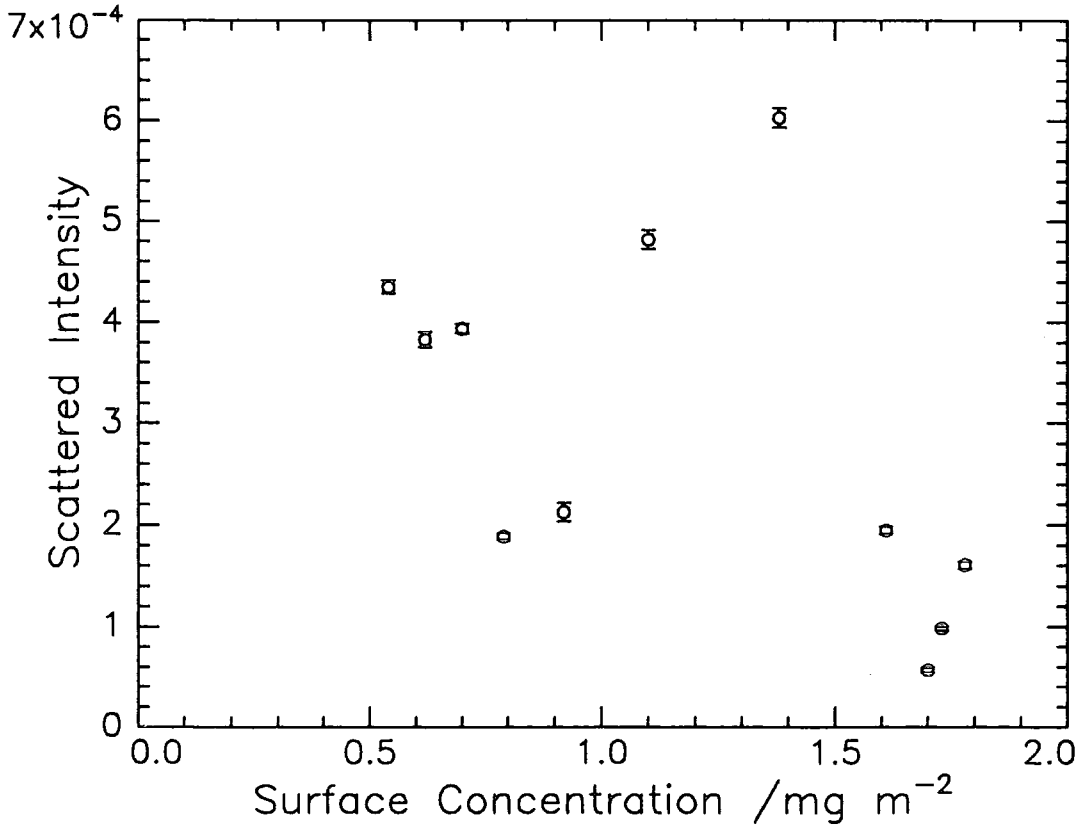

Figure 5.7 Variation of scattered intensity with surface concentration at constant pressure

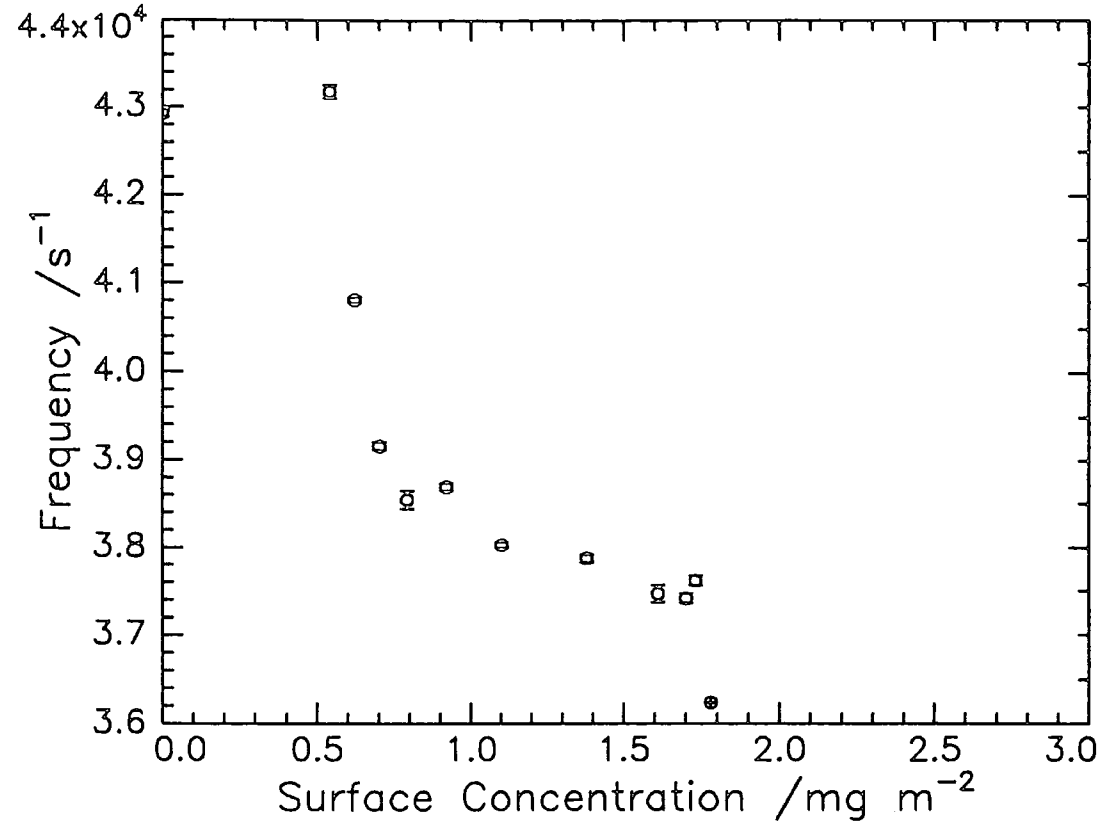

Figure 5.8 Variation of frequency with surface concentration at constant pressure

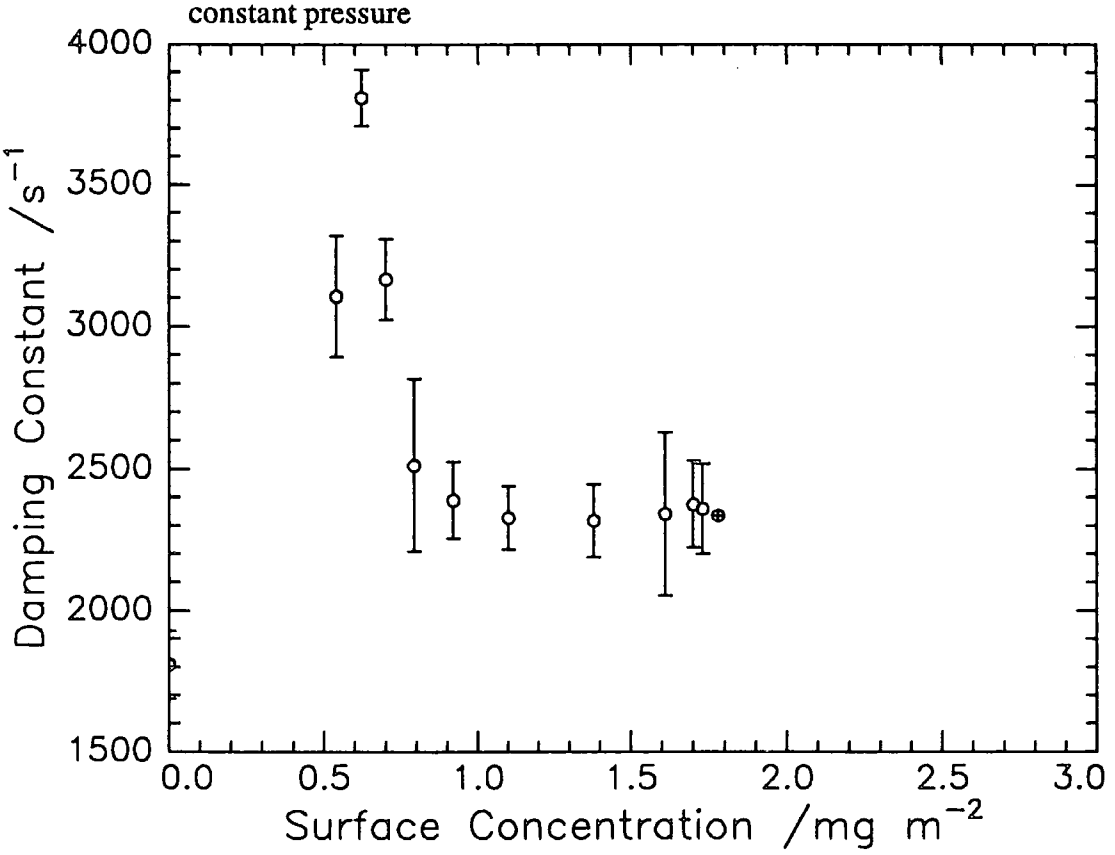

Figure 5.9 Variation of damping constant with surface concentration at constant pressure

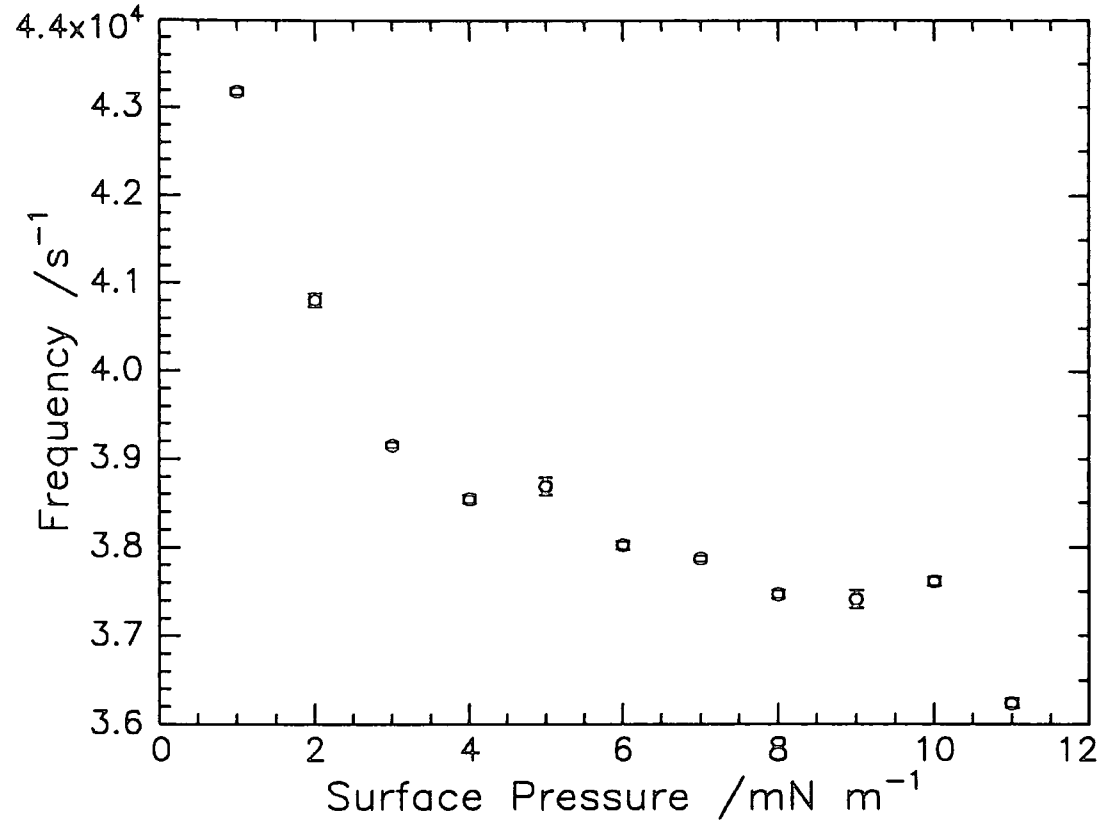

Figure 5.10 Variation of frequency with surface pressure at constant pressure

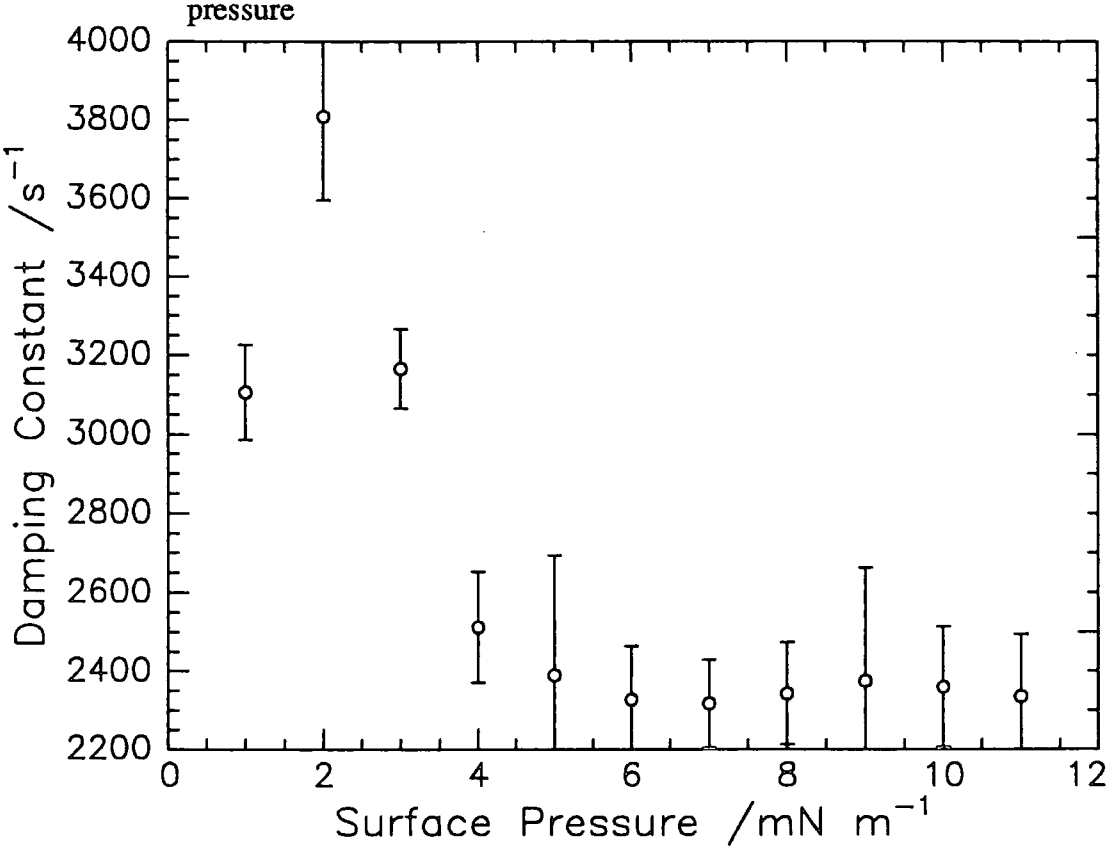

Figure 5.11 Variation of damping with surface pressure at constant pressure

viscoelastic parameters was used to fit the calculated correlation function directly to the experimental data. Figure 5.5 shows a typical fit with the residuals obtained. Analysis by averaging the correlation functions prior to fitting led to very poor fits. All data were analysed as separate correlation functions and statistical averages for each individual parameter were calculated. Initially, the parameters to the fits were unconstrained in the fitting program, thereafter constraints were added to the fitting ranges for each parameter to optimise the fitting conditions. The fits gave consistent values of surface properties for each of the ten consecutive correlation functions measured. Figures 5.12-5.15 summarise the film parameters obtained as a function of surface concentration for q=295 cm^{-1}. The very small errors in the data of figure 5.12 points to a strong dependence of the signal on surface tension. Figure 5.13 shows a sharp initial increase in transverse shear viscosity followed by a decrease. Figure 5.14 shows that the light scattering dilational elastic modulus (ε_0) values at low surface coverage greatly exceed those of the classical values. Values of the dilational viscosity (ε') appear to increase rapidly, then decrease sharply at 1.70mg m^{-2}.

It was not possible to sustain a monolayer long enough above 11mN m^{-1} (about 2 mg/m^2) constant surface pressure to obtain SQELS data. This was due to rapid barrier movement causing a large pertubation of the surface. SQELS taken during daytime (figure 5.16a) were avoided where possible. It can be seen from this variation of surface pressure and area with time that the surface pressure plot is rapidly changing around its set value and the surface area is also constantly changing to compensate this. This was due to air turbulence originating from ventilation systems causing perturbation of the Wilhelmy paper plate. From this movement of the paper plate the force balance registers an unreal change in surface pressure causing movement of the barriers. As a result it was difficult for the computer software to fit any of the data obtained during the daytime.

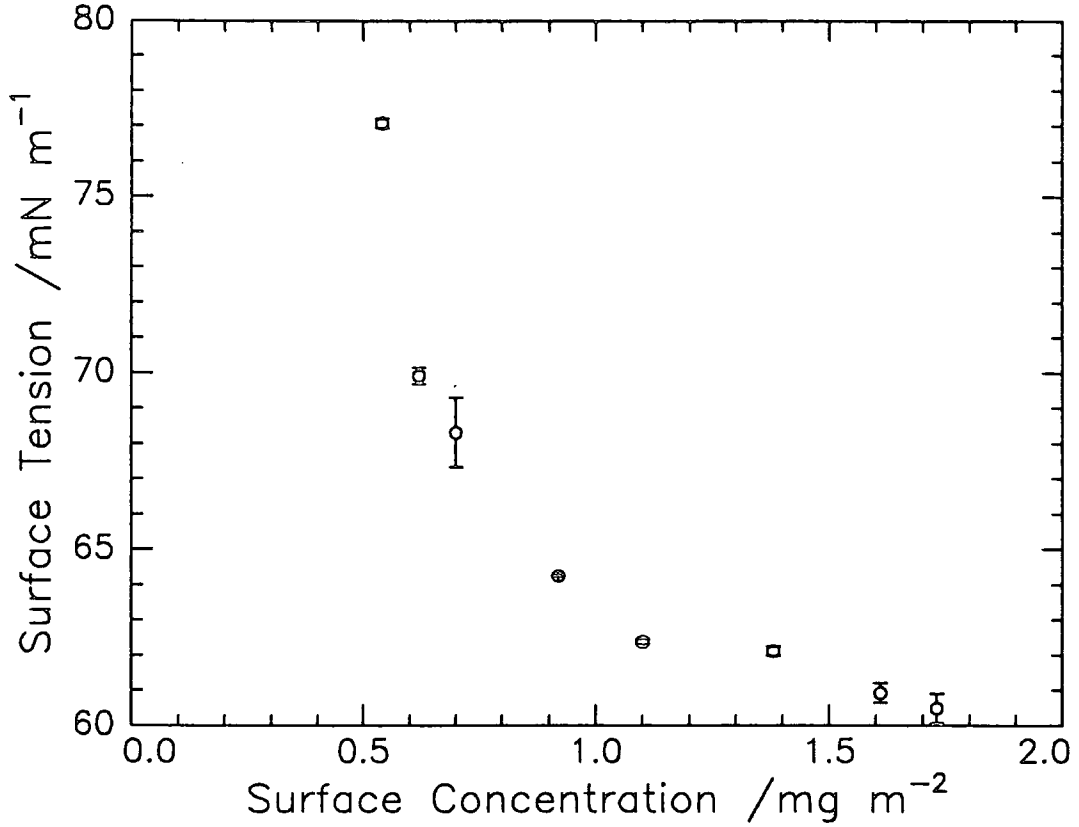

Figure 5.12 Variation of surface tension with surface concentration at constant pressure

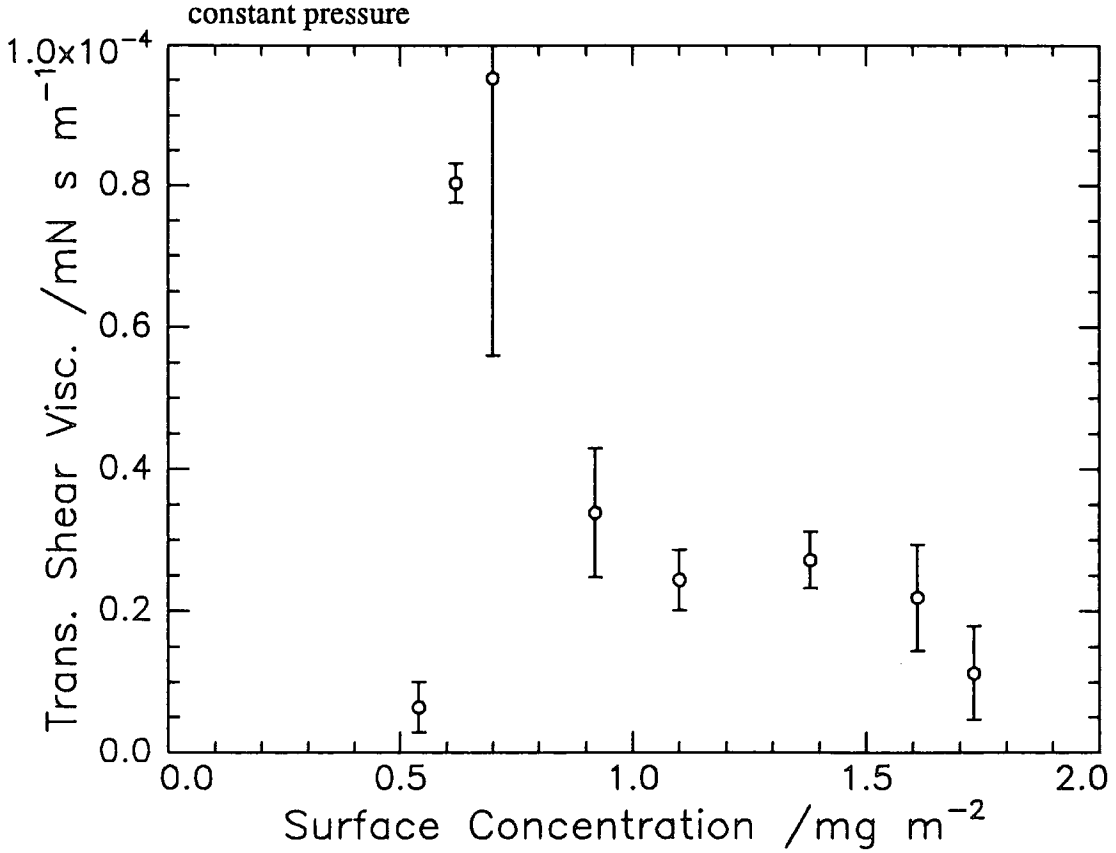

Figure 5.13 Variation of transverse shear viscosity with surface concentration at constant surface pressure

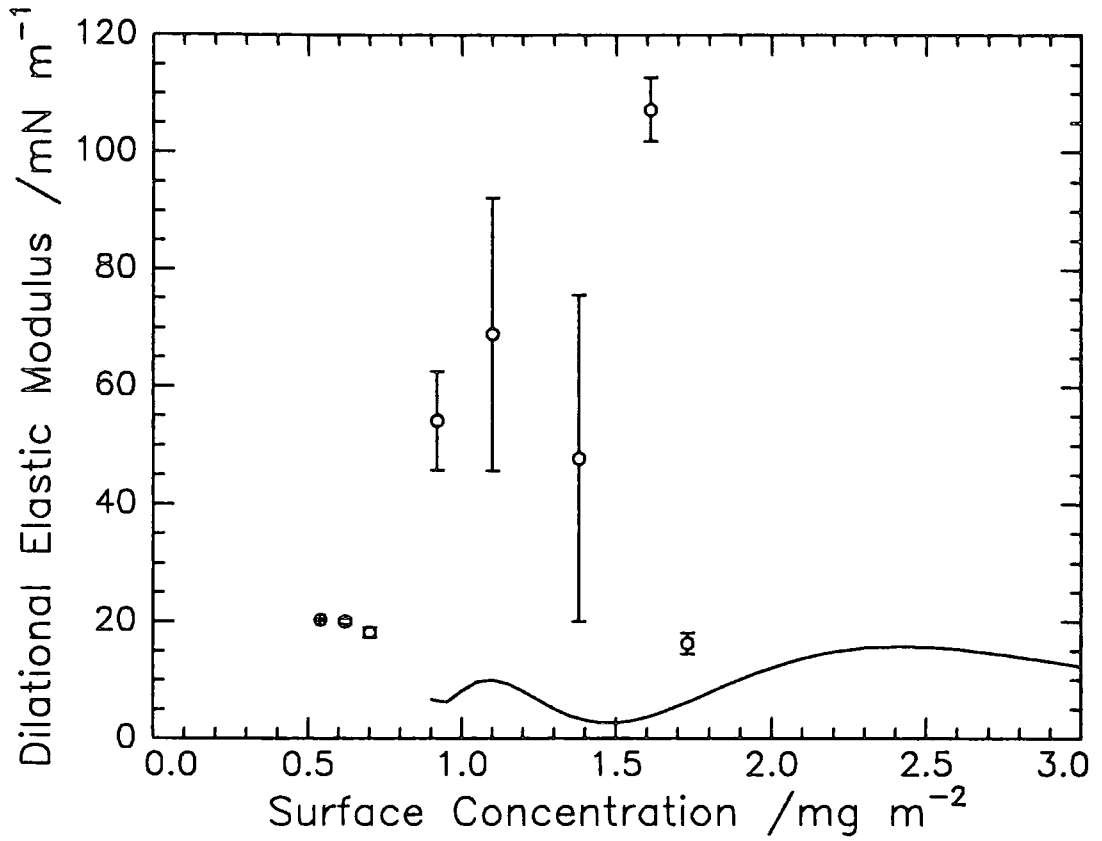

Figure 5.14 Comparision of classical (-) and SQELS (o) dilational elasticmodulus variation with surface concentration at constant pressure

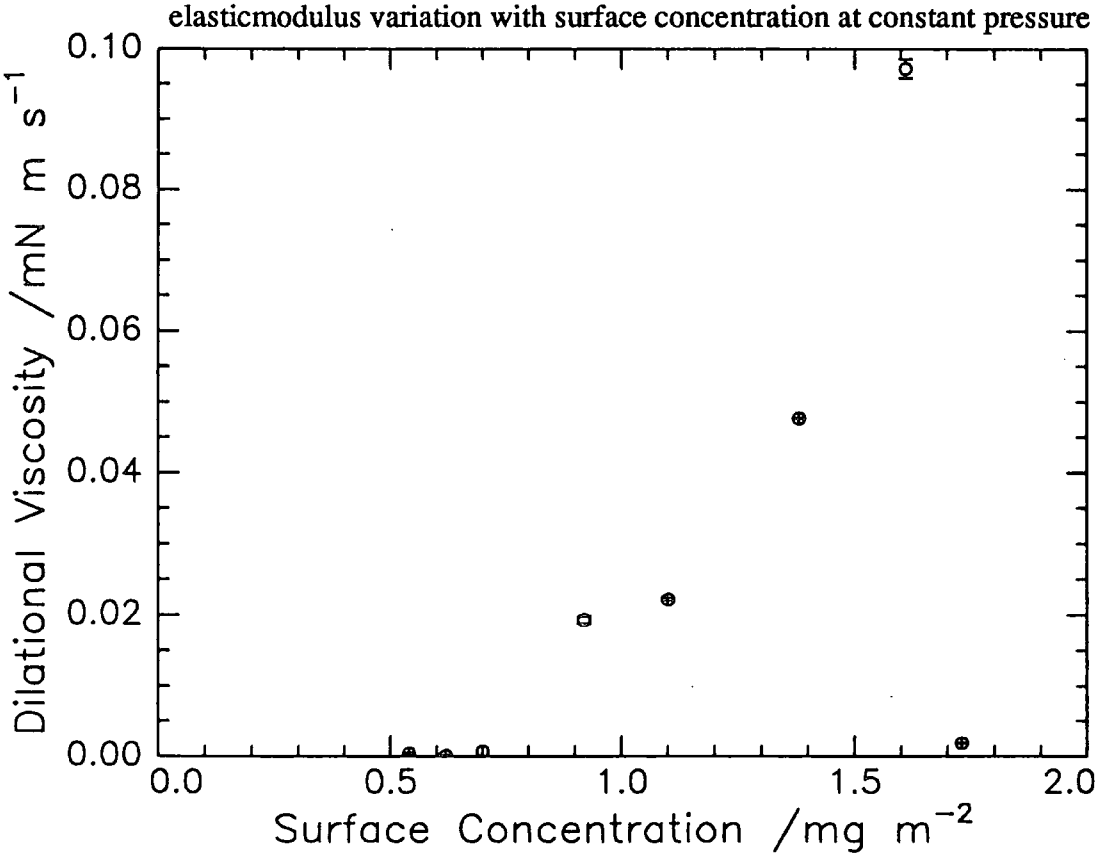

Figure 5.15 Variation of dilational viscosity with surface concentration at constant pressure

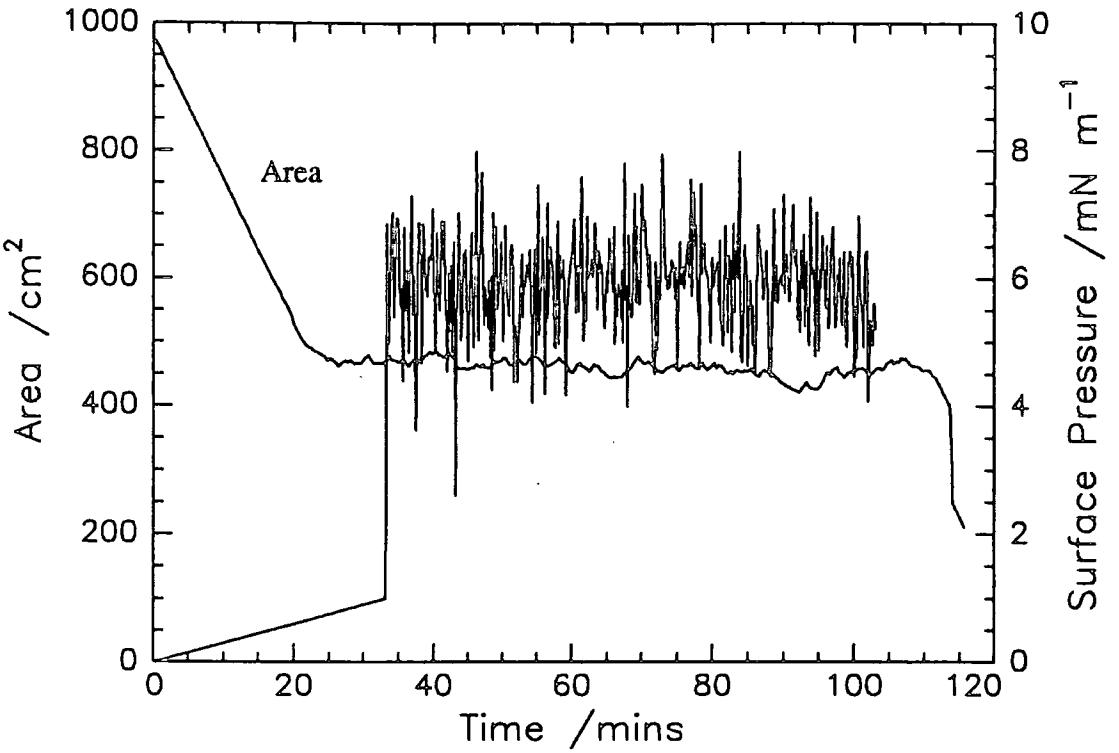

Figure 5.16a Variation of surface pressure and area with time
Data taken at day time during maximum air disturbance

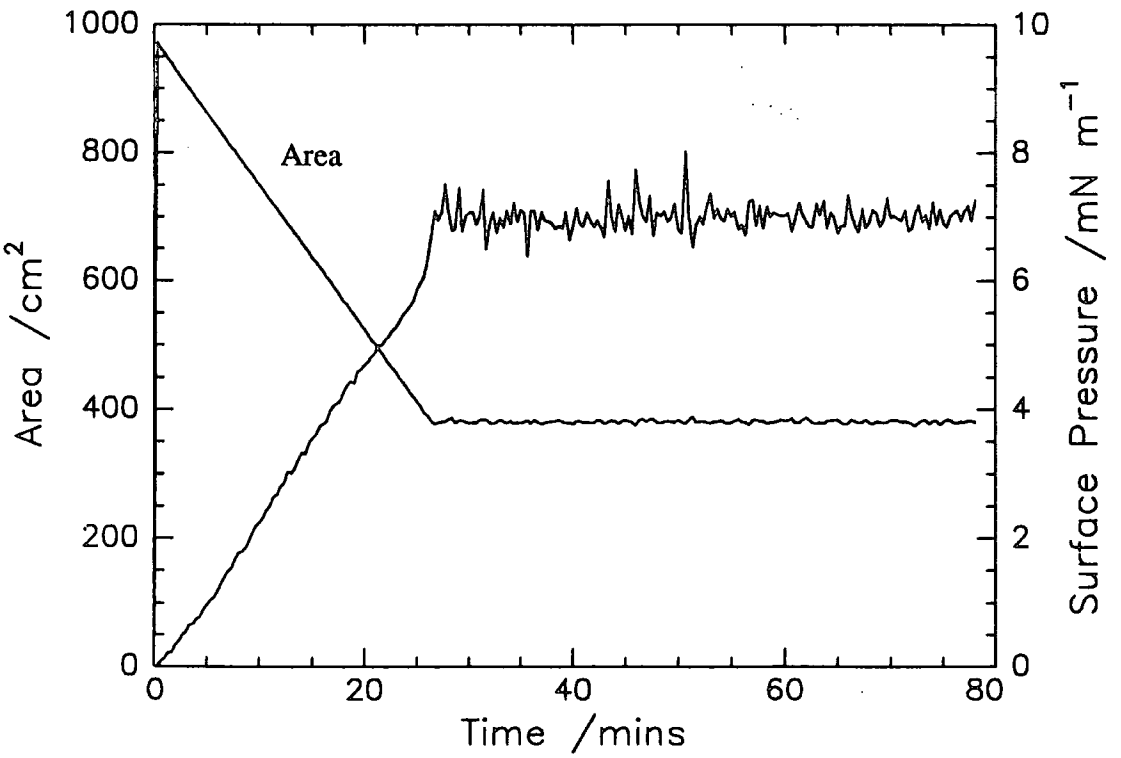

Figure 5.16b Variation of surface pressure and area with time
Data taken at night time during minimum air disturbance

Figure 5.16b shows that surface pressure and area variation during late evening are considerably smaller, although there is still some perturbation of the Wilhelmy plate due to thermal vibrations. Another problem associated with constant surface pressure measurements is the limited range of surface coverage which may be investigated due to the nature of the isotherm.

5.2.1.2 Measurements at constant surface concentration

It was found that better data could be obtained if the measurements were taken at constant surface area by spreading sufficient volume of polymer solution to give a specific surface concentration thereby avoiding movement of the barriers.

The values of the scattered intensity (I_s), the ratio of the reference to scattered intensity (I_s/I_r), the propagation frequency (ω_0) and the wave damping (Γ) are shown in figures 5.17-5.20 as a function of the enlarged surface concentration range. The I_s/I_r ratio (figure 5.18) is once again below ca.10^{-3}, while the variations in magnitude of both I_s and I_s/I_r (figure 5.17) are seen to increase then decrease with increasing surface concentration. The propagation frequency (figure 5.19) is seen to decrease with increasing surface concentration coinciding with transitions in the static surface pressure isotherm. Wave damping (figure 5.20) is seen to rise initially with increasing surface concentration before decreasing to a plateau of values.

The surface tension data (figure 5.21) show more features than those obtained by the constant surface pressure method. There appear to be transition points at about 0.6 and 1.8 mg/m^2 which match those of the classical surface pressure isotherm. Subtraction of these surface tension values from that of pure water gives surface pressure values which when overlaid on the classical isotherm (fig. 5.22) have similar features. The transverse shear viscosity (fig. 5.23) when plotted as a function of surface concentration has a peak at about 1.6 mg/m^2, which is about the value observed for the transition in the classical

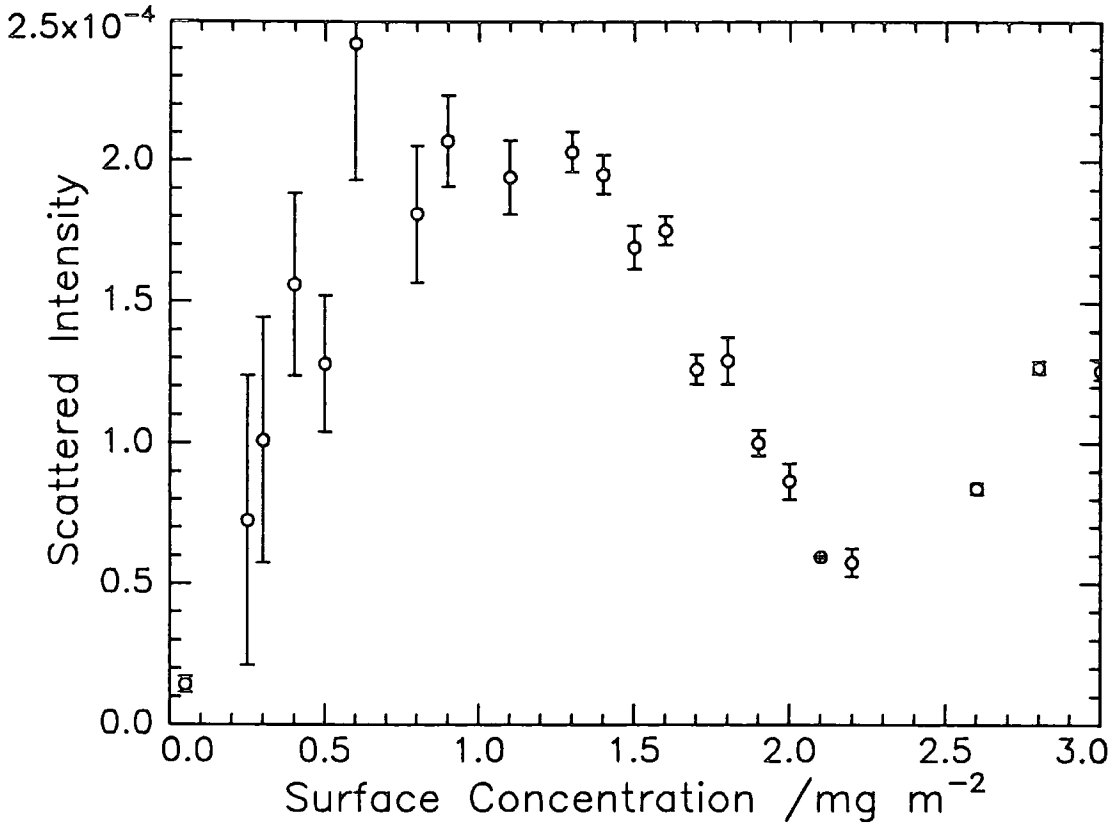

Figure 5.17 Variation of the scattered intensity with surface concentration at constant area q=351cm^{-1}

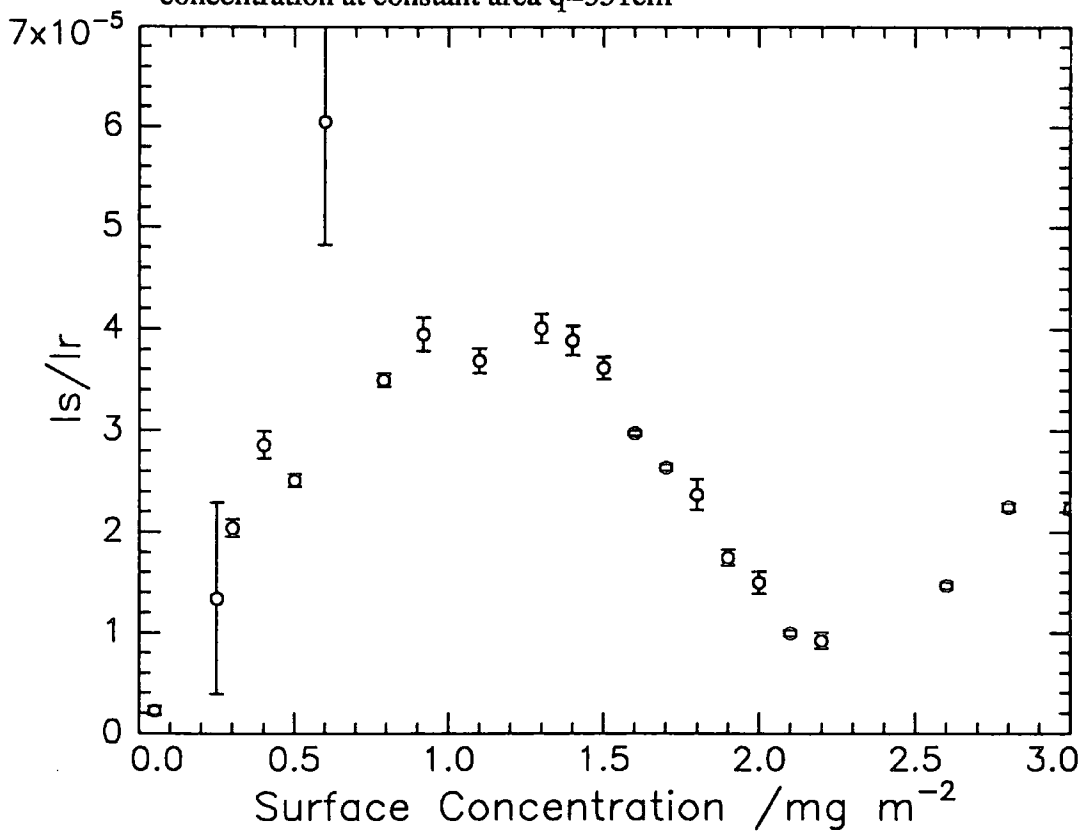

Figure 5.18 Variation of the ratio of scattered to reference intensities with surface concentration at constant area q=351cm^{-1}

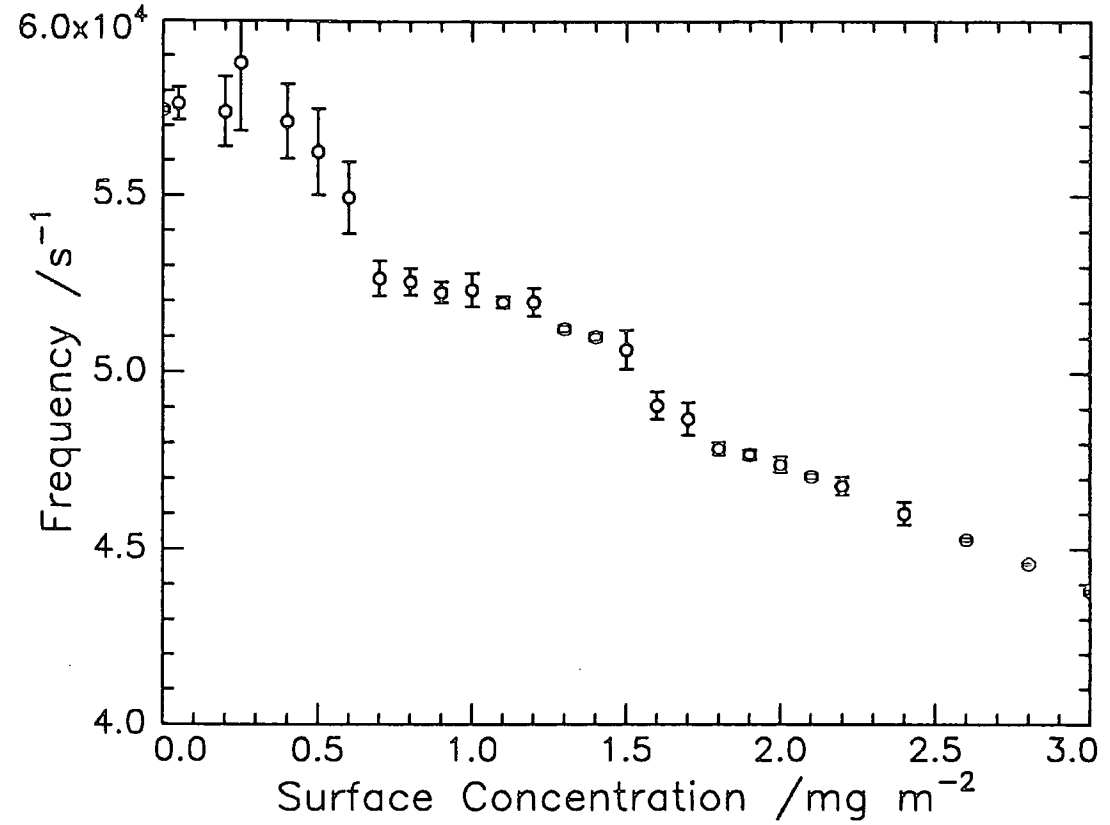

Figure 5.19 Variation of frequency with surface concentration at constant area q=351cm^{-1}

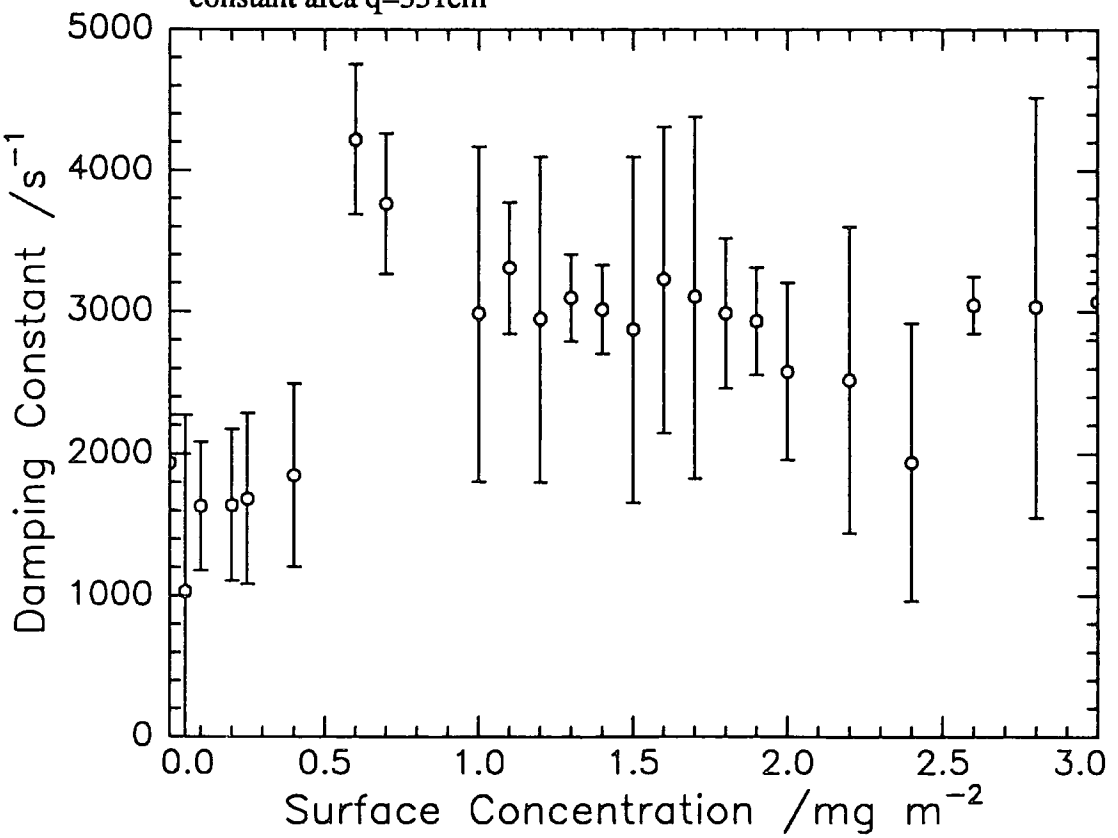

Figure 5.20 Variation of damping constant with surface concentration at constant area q=351cm^{-1}

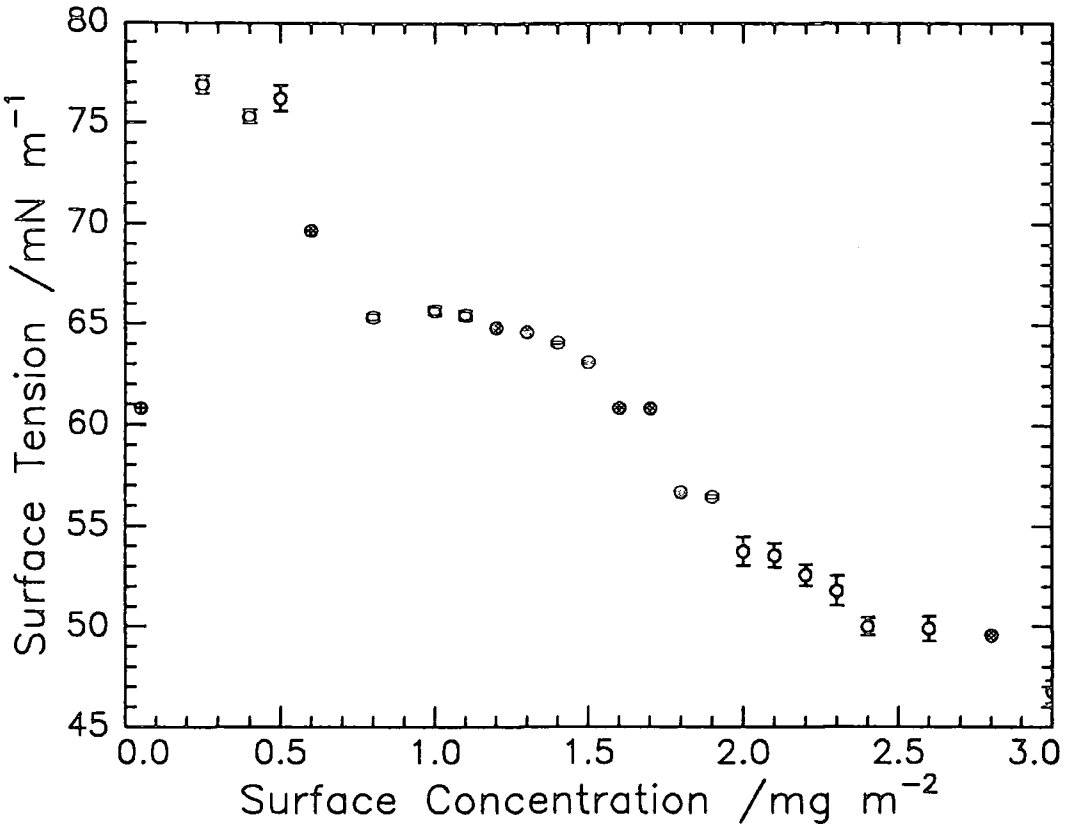

Figure 5.21 Variation of surface tension with surface concentration at constant area q=351cm^{-1}

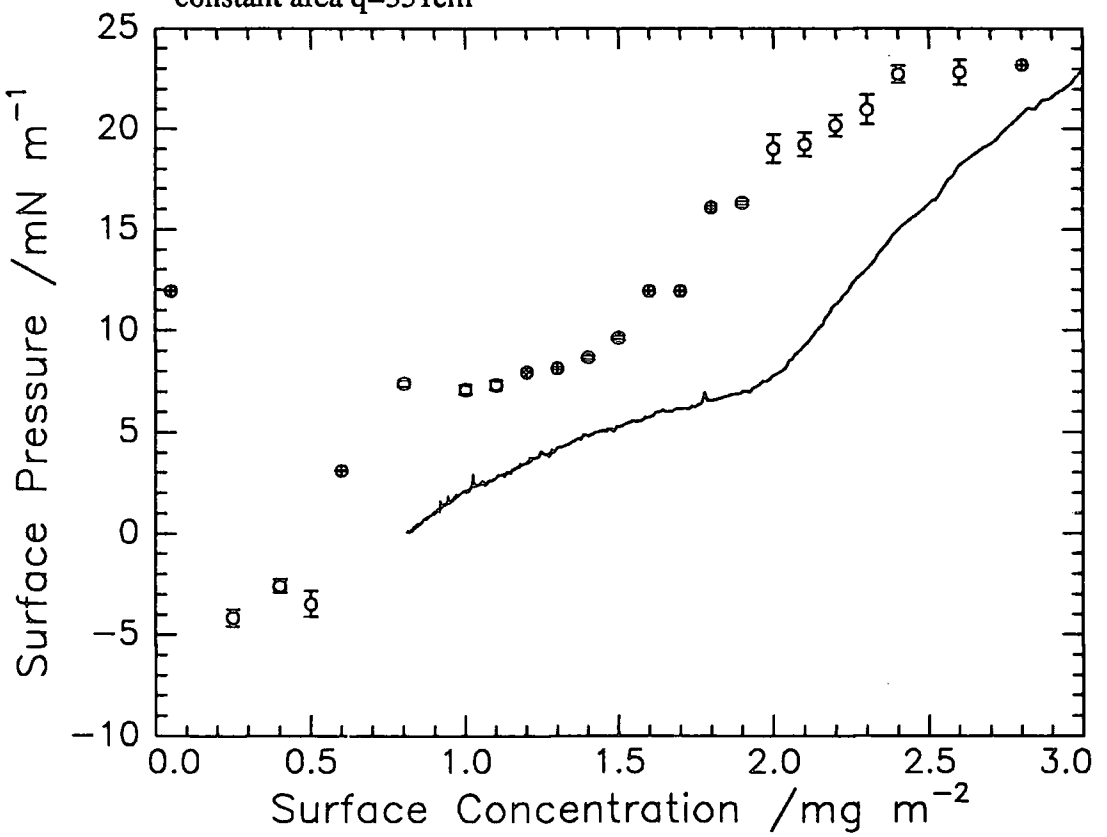

Figure 5.22 Surface pressure from SQELS (o) compared with classical Wilhelmy plate method (-) q=351cm^{-1}

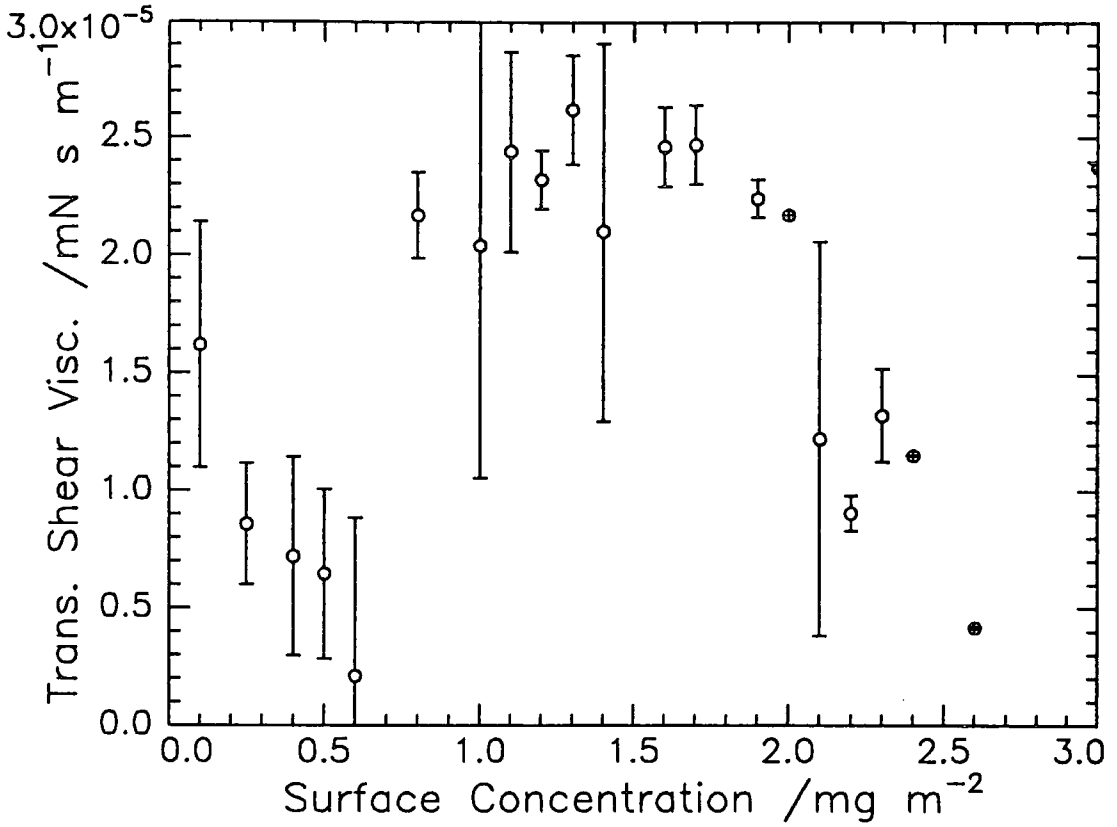

Figure 5.23 Variation of transverse shear viscosity with surface concentration at constant area q=351cm^{-1}

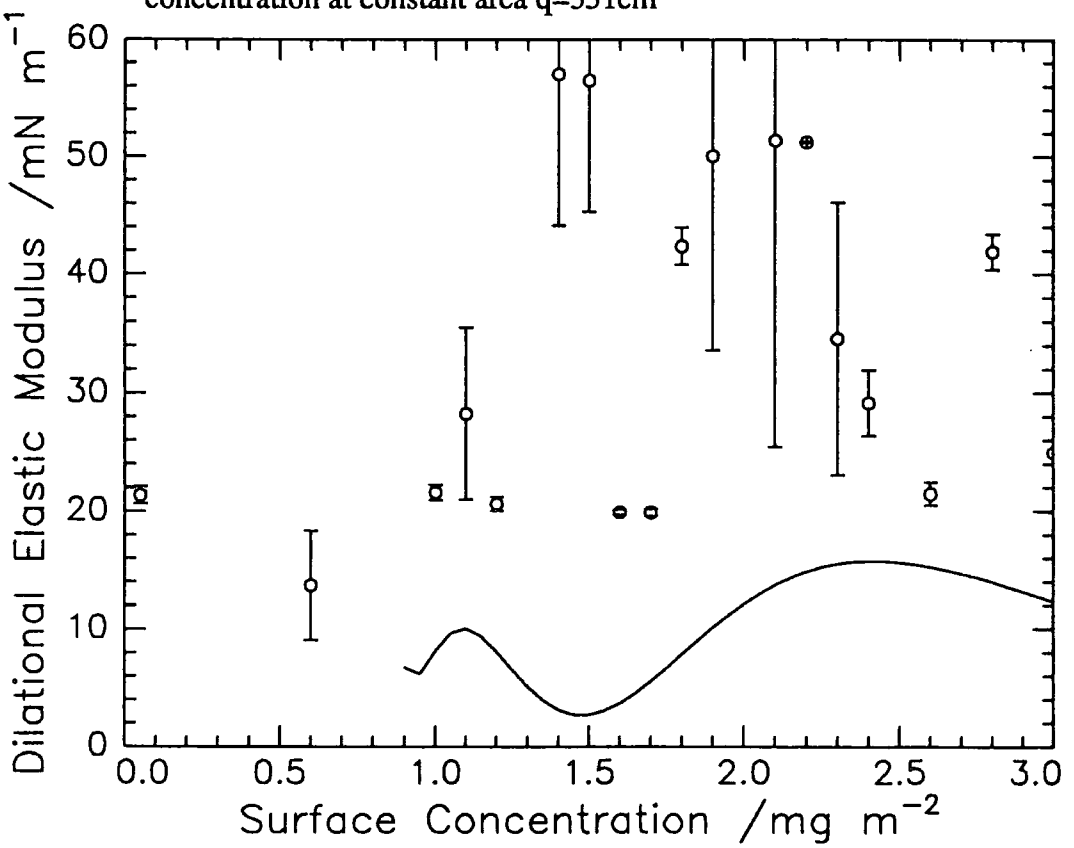

Figure 5.24 Comparision of classical (-) and SQELS (o) dilational elastic modulus variation with surface concentration at q=351cm^{-1}

isotherm. Data for the dilational modulus (figure 5.24) are those obtained from the direct fitting method and not from the light scattering π-Γ isotherm. The dilational viscosity (figure 5.25), although poorly defined, can be seen to have approximately similar behaviour as the transverse shear viscosity, which may indicate similarities in the underlying molecular mechanisms.

Due to the range of surface concentration available for SQELS measurements using the constant area method, the surface concentration dependence at higher q values was investigated. Figures 5.26 to 5.29 show the variation of the fitted values of the correlation function with surface concentration at q values of 301, 393, 473 and 566 cm^{-1} respectively. For the measurements taken at q=393, 473 and 566 cm^{-1} only several surface concentrations, reflecting the trends in the data, were investigated. It can be seen that the intensity data measured above q=351cm^{-1} does not follow the exact trends as the data measured for q=301 and 351cm^{-1}. This is due to difficulties associated with measuring correlation functions at high q values. Variation of the neutral density filters and waveguide to optimise experimental conditions allow these observed trends to be followed only approximately. For the γ_0 data obtained from these different q values the same variations, such as values above that of pure water at low surface concentrations were evident. In all cases, the transverse shear viscosity rose rapidly from circa 0.5mg/m^2 to a maximum at circa 1.6mg/m^2 then falling off towards a collapse value at about 2.6mg/m^2. The trends observed are similar to those for low molecular weight spread films, i.e. an increase in γ' with surface concentration followed by a decrease. The γ' values at q=301 and 351cm^{-1} show that at low surface concentrations there appears to be an initial decrease in γ' from 1.6×10^{-5} mN s/m to a minimum of about 2.0×10^{-6} mN s/m.

The precision of the determination of the dilational modulus decreased rapidly when q was larger than 351cm^{-1}. At low surface coverage the ε_0 values greatly exceeded those of

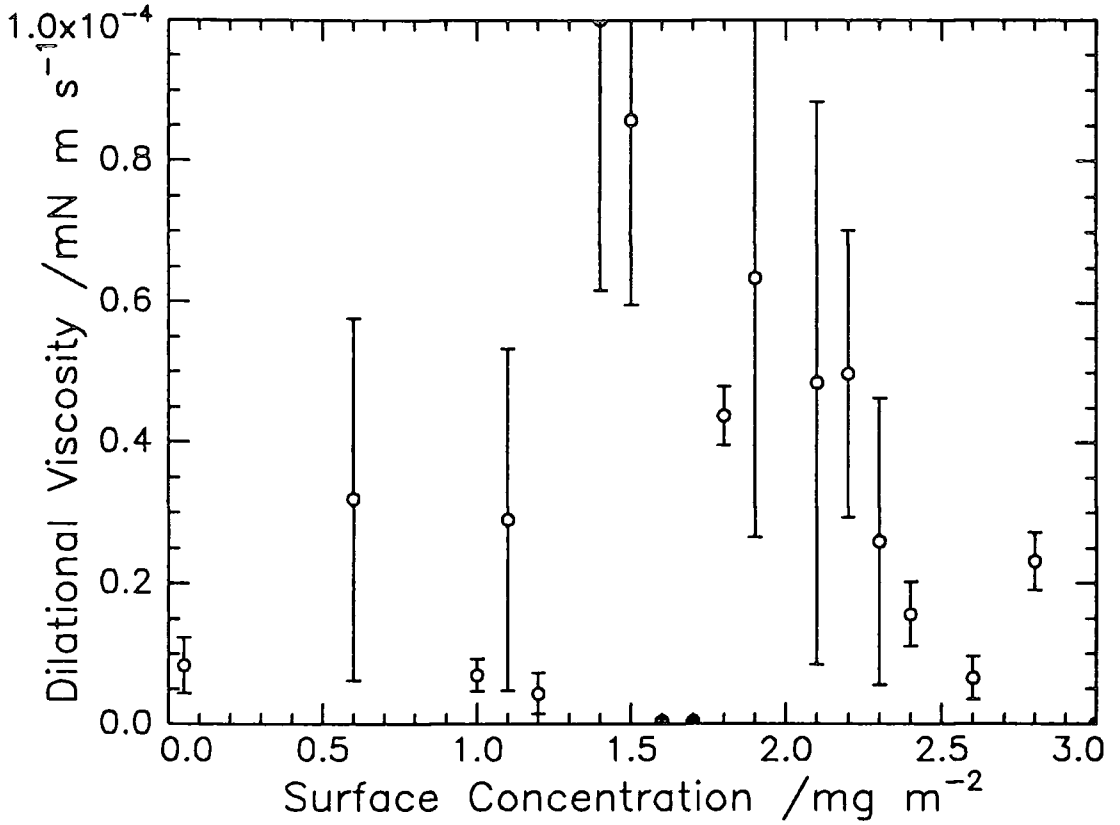

Figure 5.25 Variation of dilational viscosity with surface concentration at constant area q=351cm^{-1}

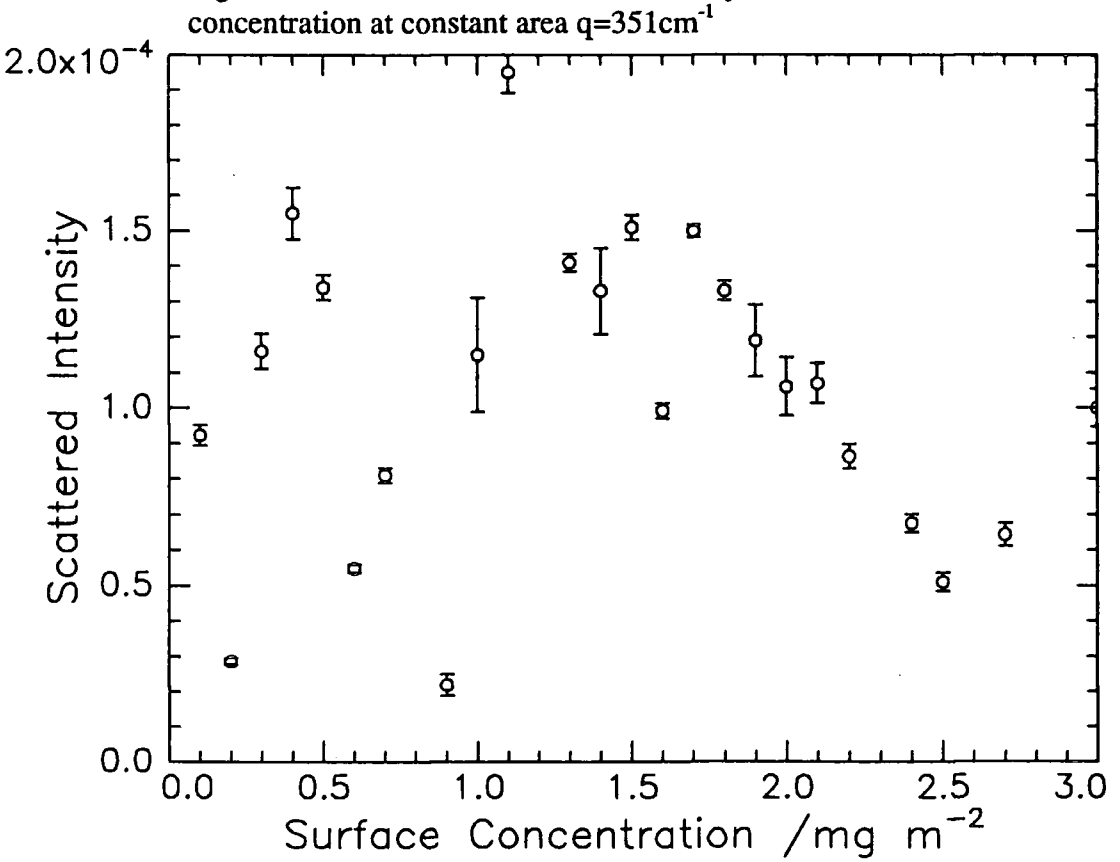

Figure 5.26a Variation of the scattered intensity with surface concentration at q=301cm^{-1}

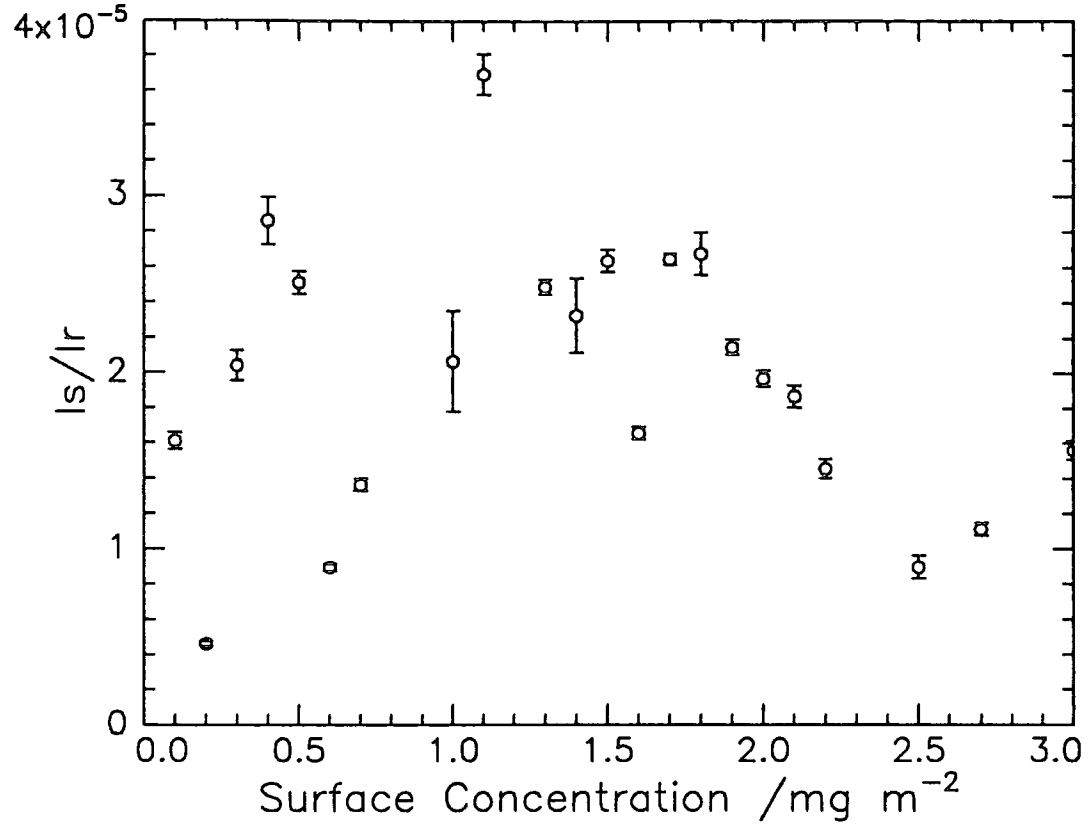

Figure 5.26b Variation of I_s/I_r with surface concentration at q=301 cm^{-1}

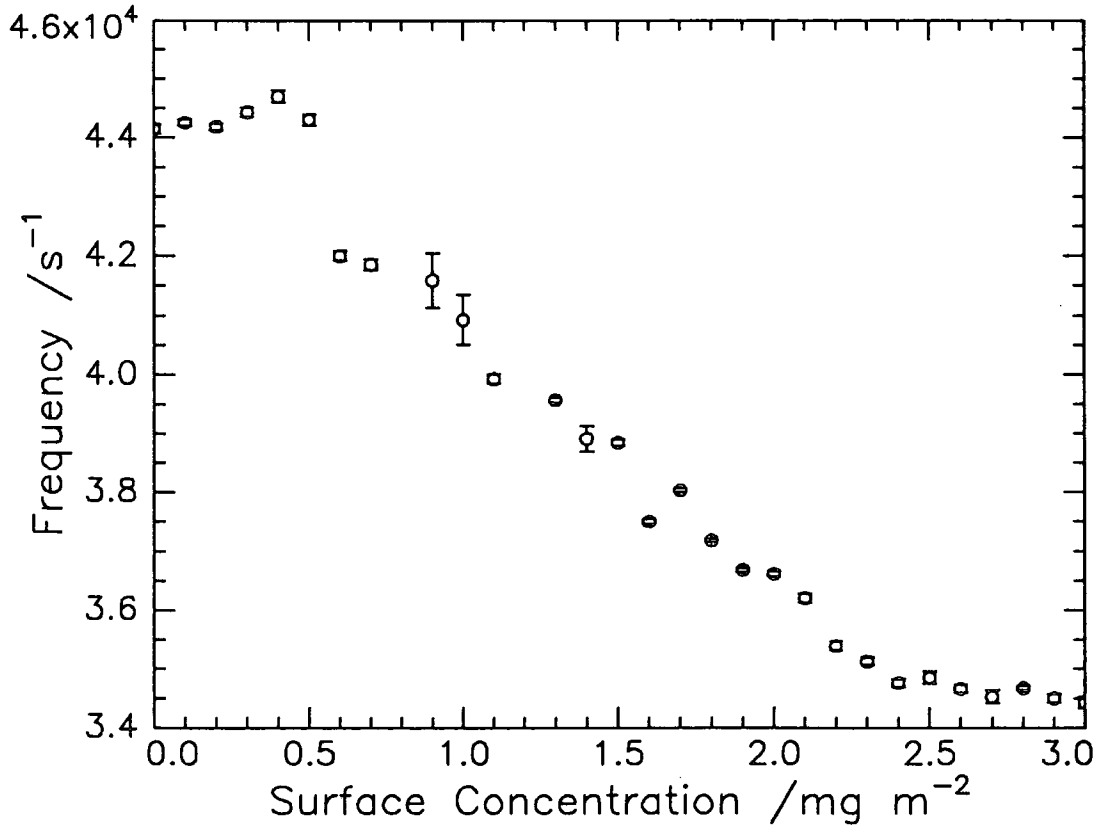

Figure 5.26c Variation of frequency with surface concentration at q=301 cm^{-1}

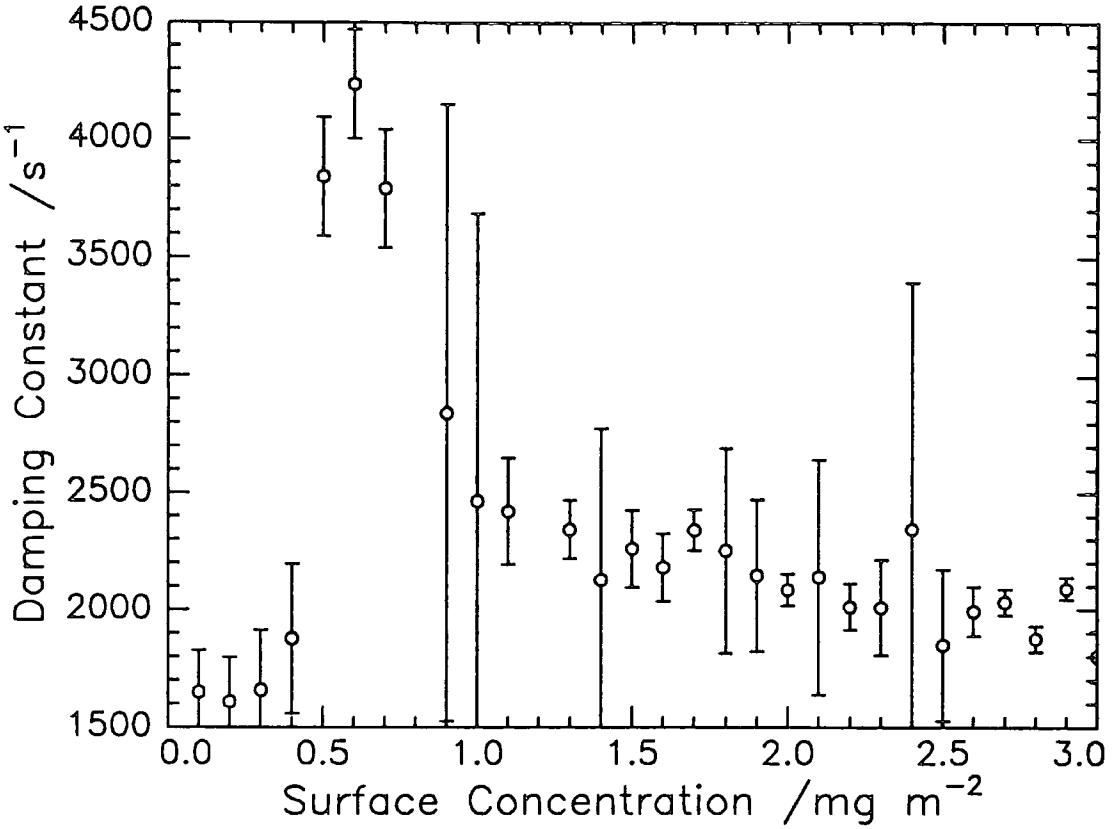

Figure 5.26d Variation of damping constant with surface concentration at q=301cm^{-1}

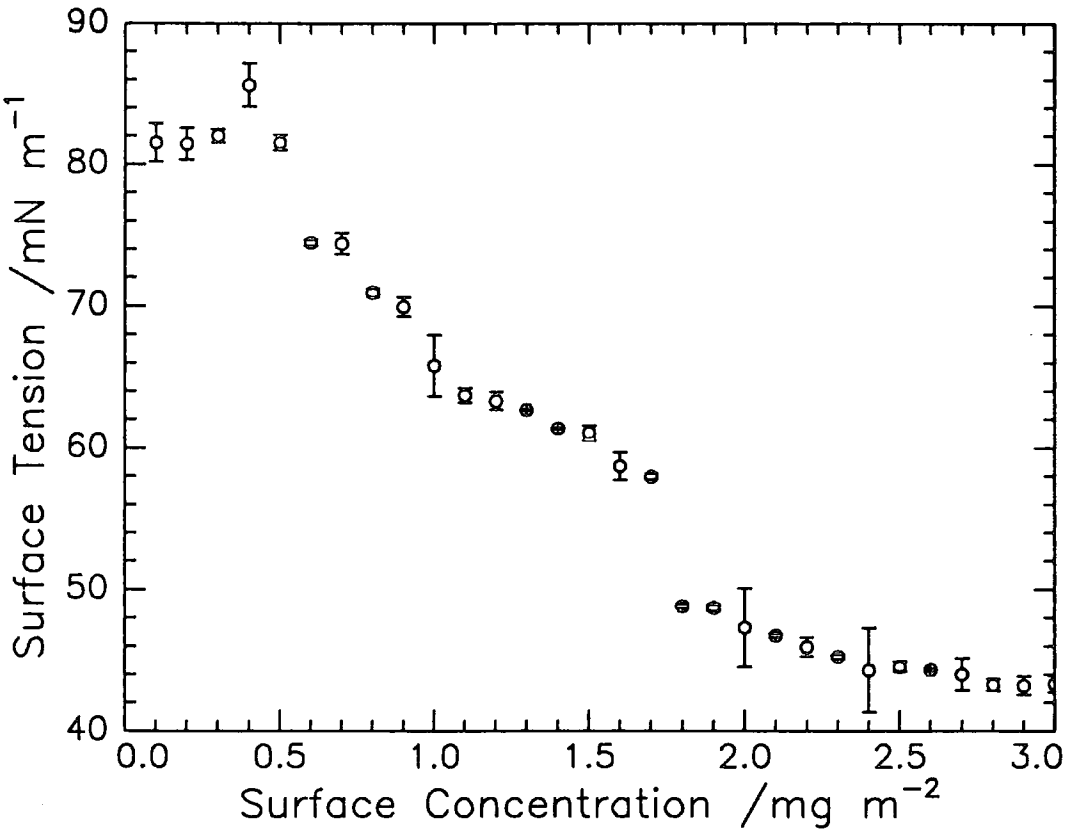

Figure 5.26e Variation of surface tension with surface concentration at q=301cm^{-1}

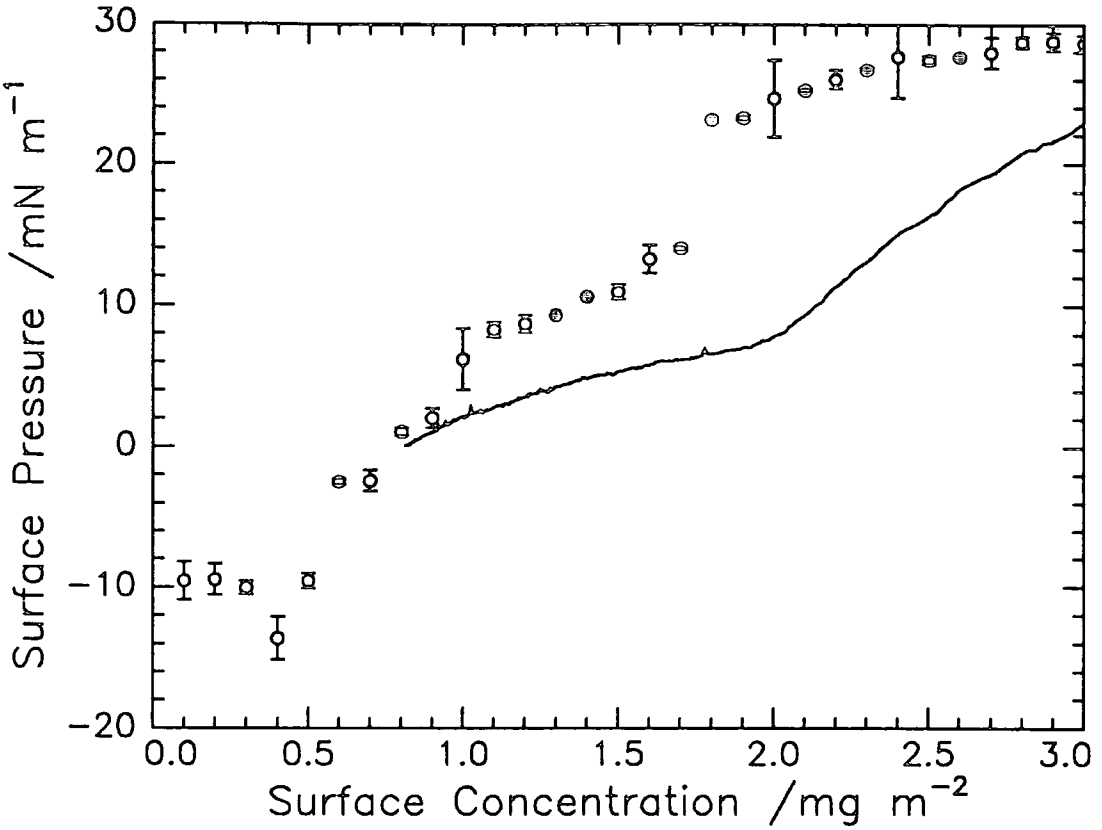

Figure 5.26f Surface pressure from SQELS (o) compared with classical Wilhelmy plate method (-) q=301cm^{-1}

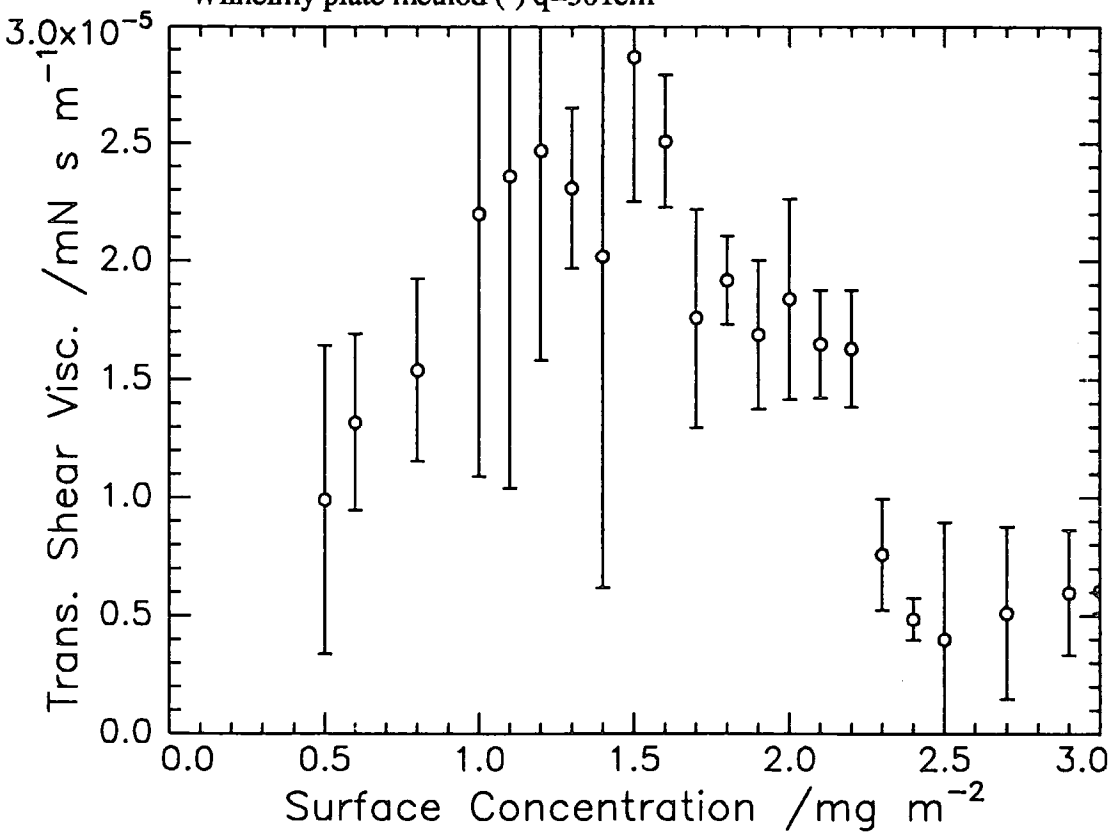

Figure 5.26g Variation in transverse shear viscosity with surface concentration at q=301 cm^{-1}

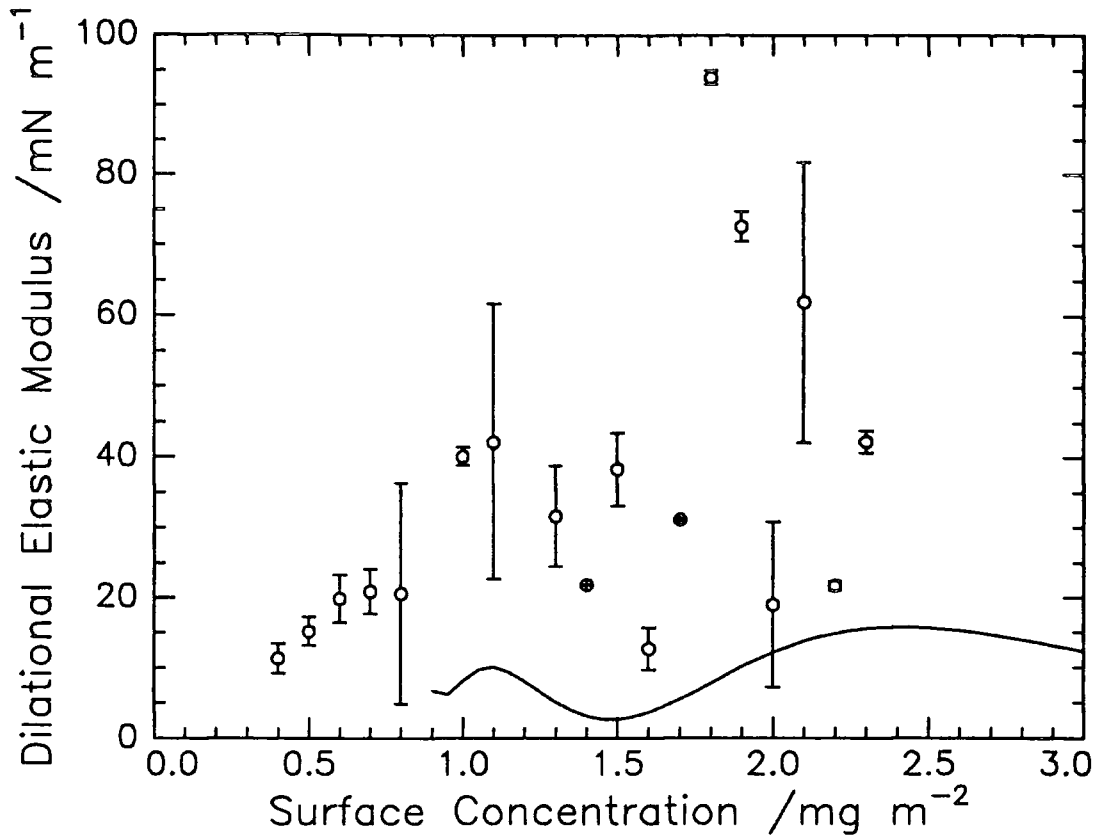

Figure 5.26h Comparision of classical (-) and SQELS (o) dilational elastic modulus variation with surface concentration at q=301cm^{-1}

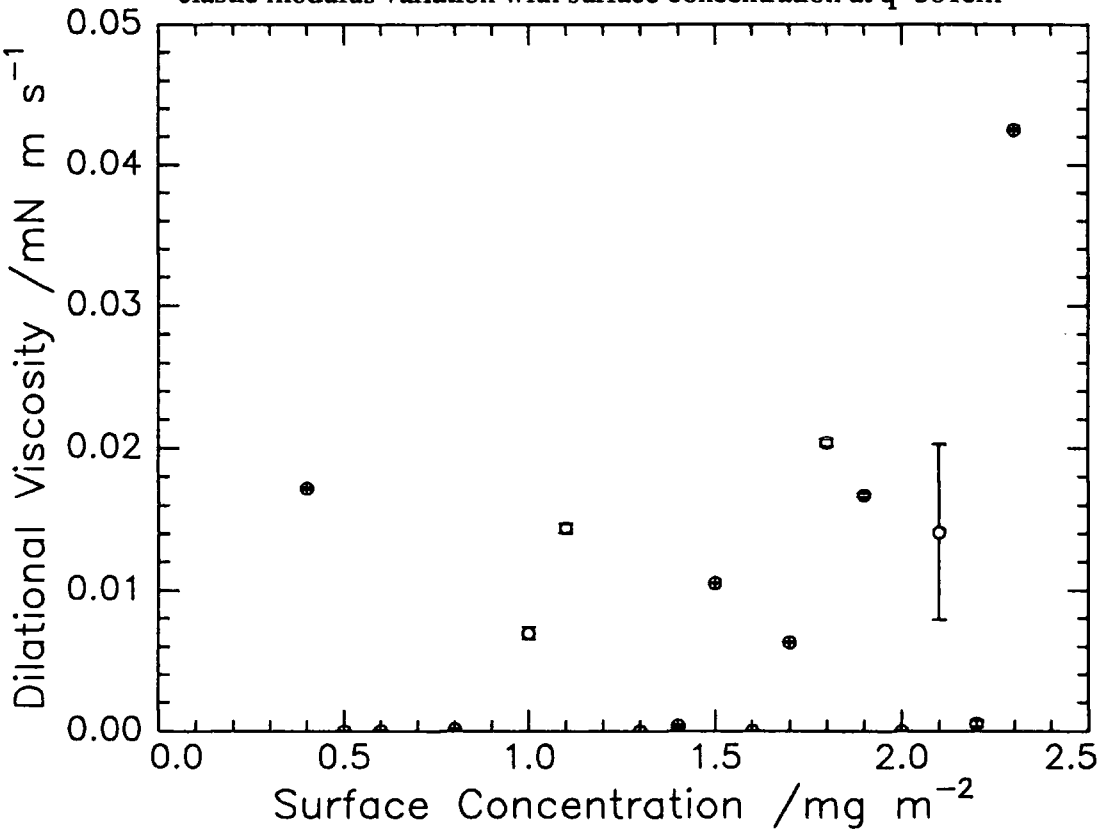

Figure 5.26i Variation of dilational viscosity with surface concentration at q=301cm^{-1}

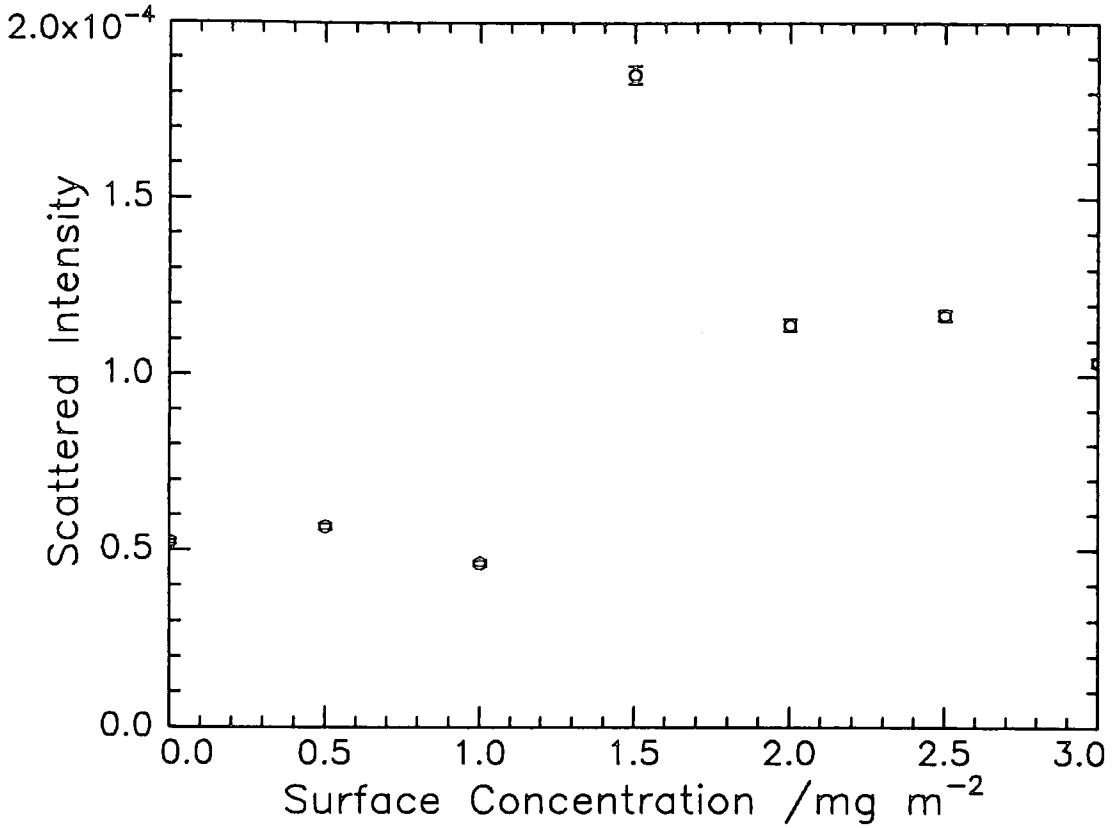

Figure 5.27a Variation of the scattered intensity with surface concentration at q=393cm^{-1}

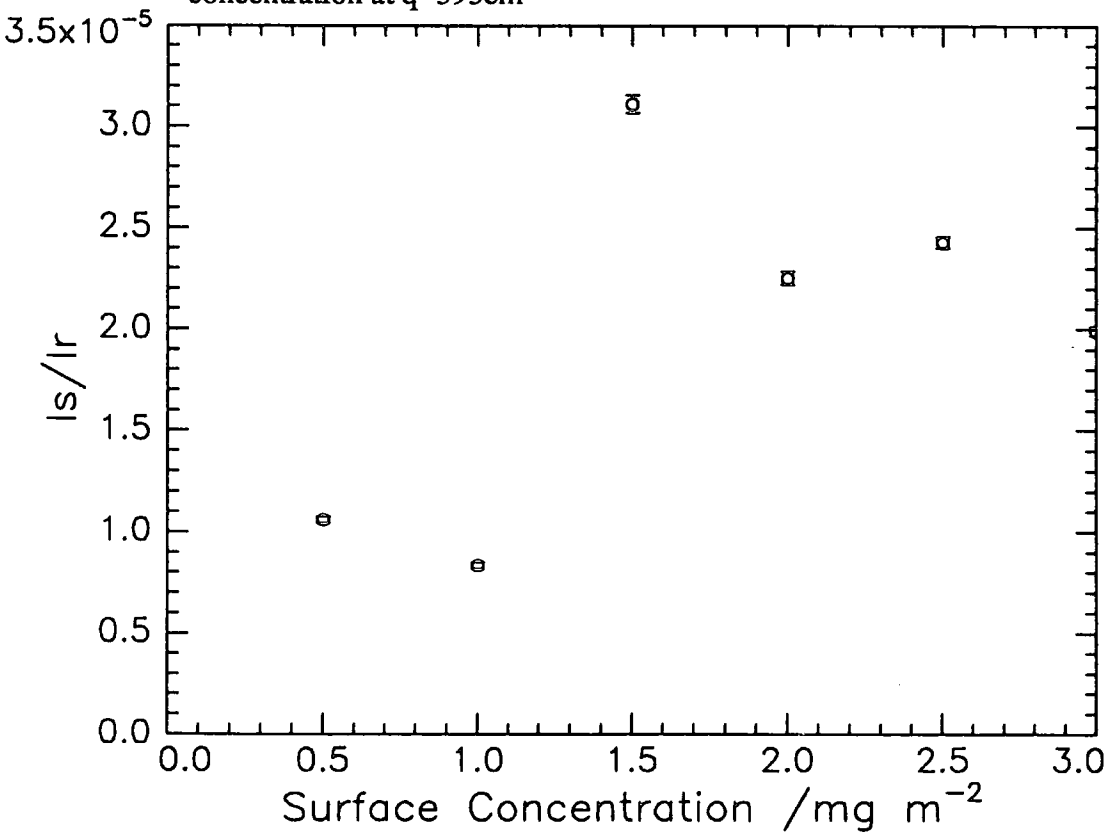

Figure 5.27b Variation of the ratio I_s/I_r with surface concentration at q=393 cm^{-1}

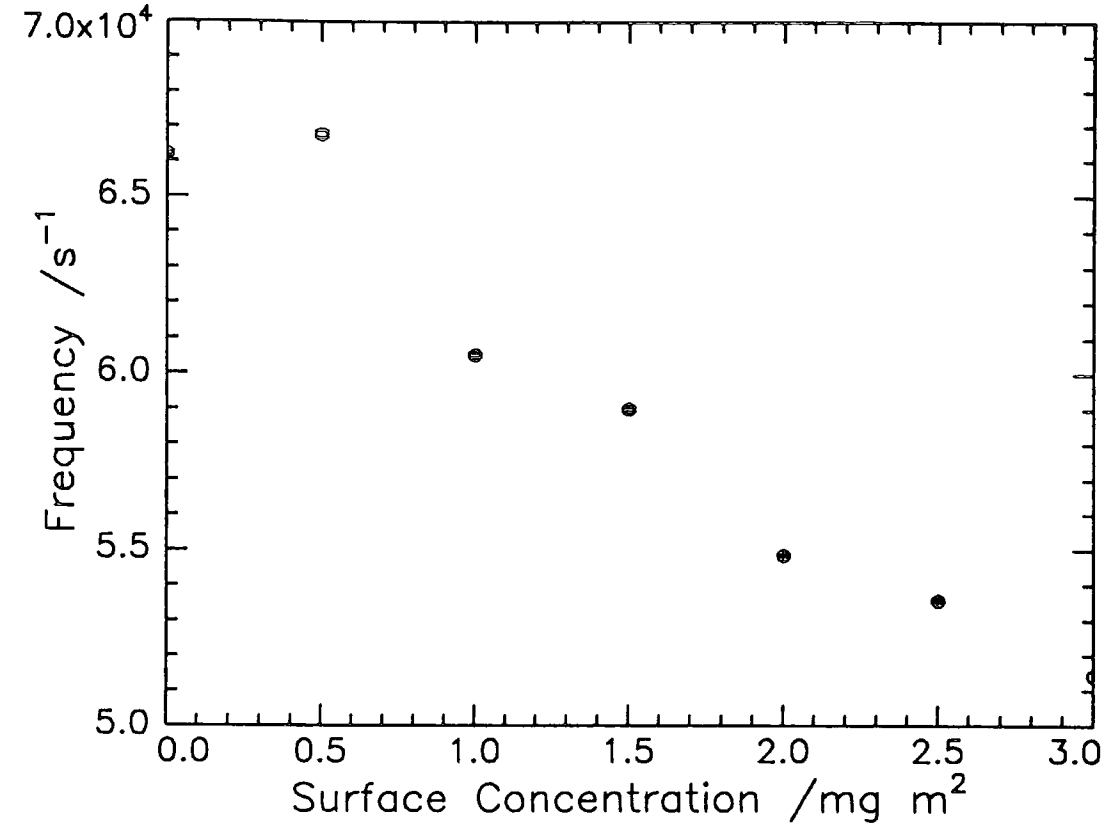

Figure 5.27c Variation of frequency with surface concentration at q=393 cm^{-1}

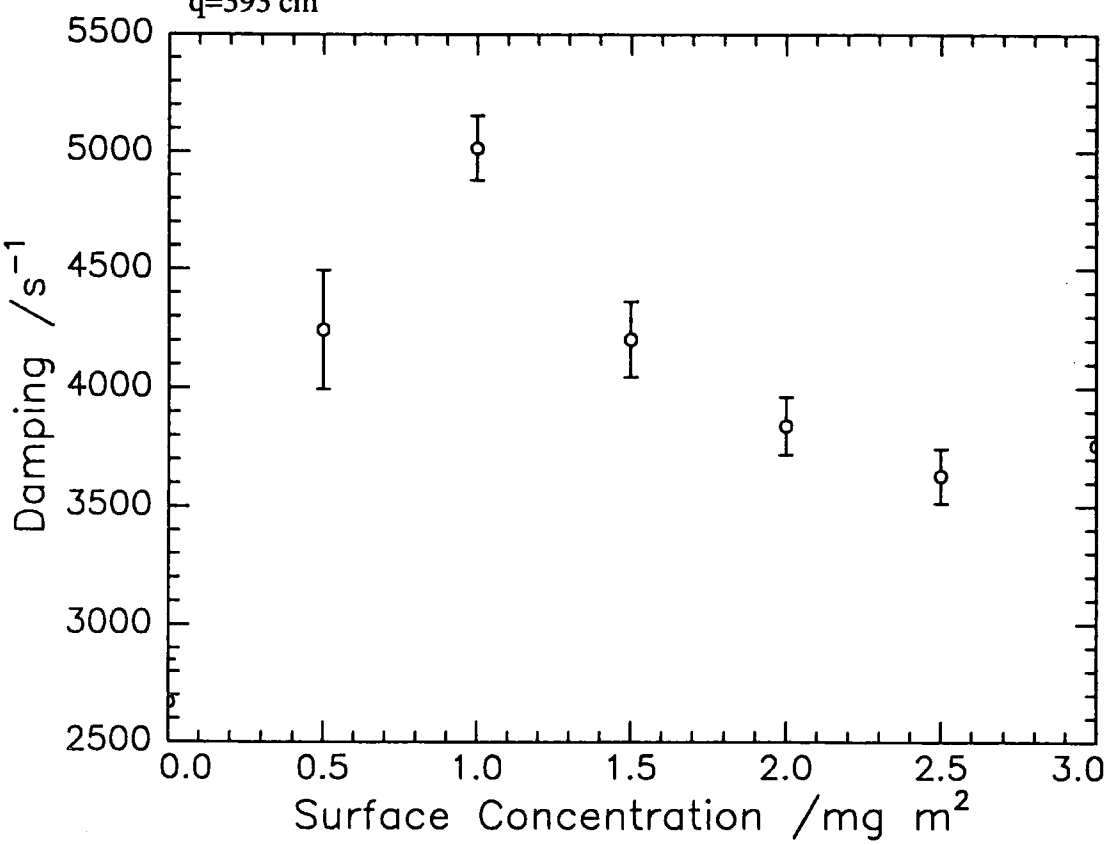

Figure 5.27d Variation of damping with surface concentration at q=393cm^{-1}

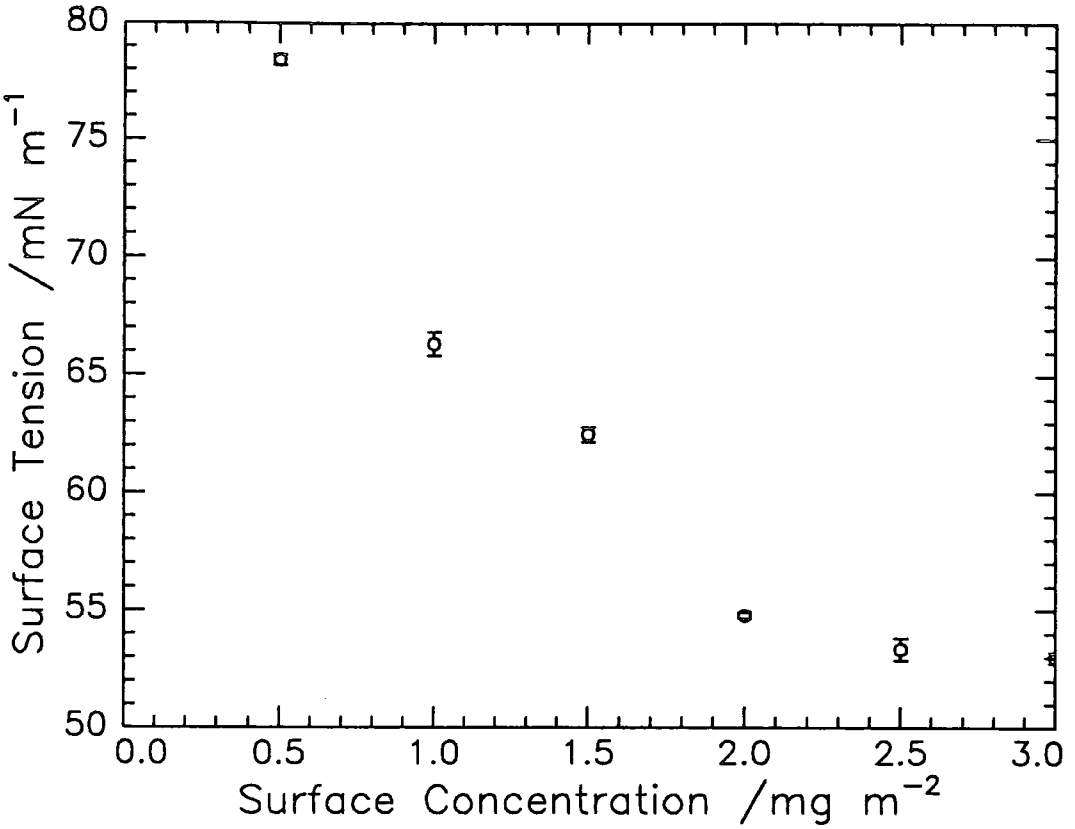

Figure 5.27e Variation of surface tension with surface concentration at q=393cm^{-1}

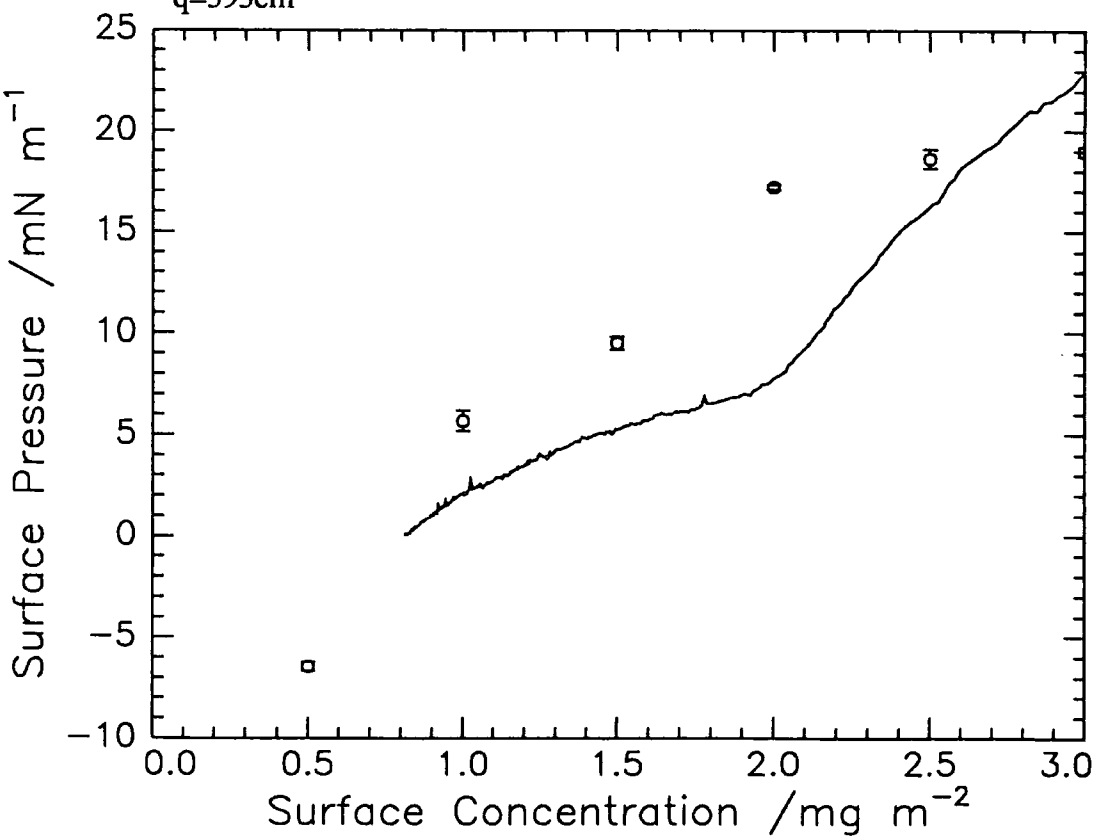

Figure 5.27f Surface pressure from SQELS (o) compared with classical Wilhelmy plate method (-) q=393cm^{-1}

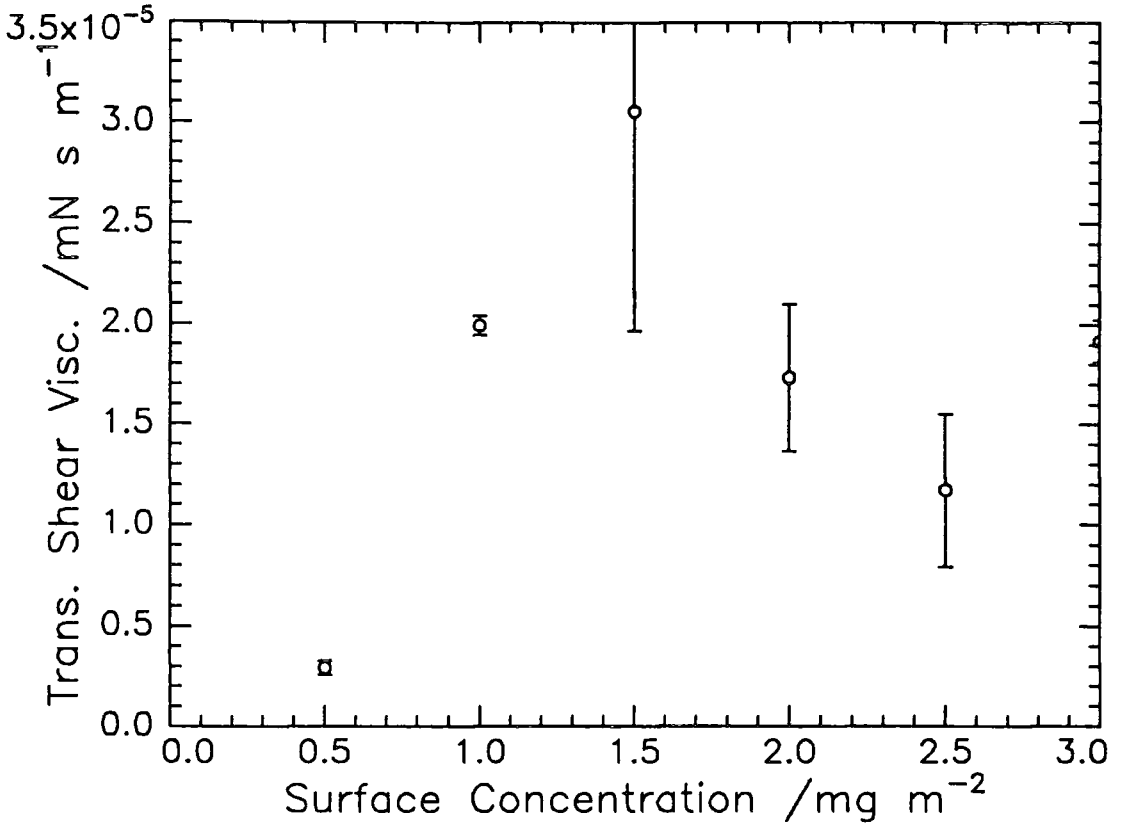

Figure 5.27g Variation of transverse shear viscosity with surface concentration at q=393cm^{-1}

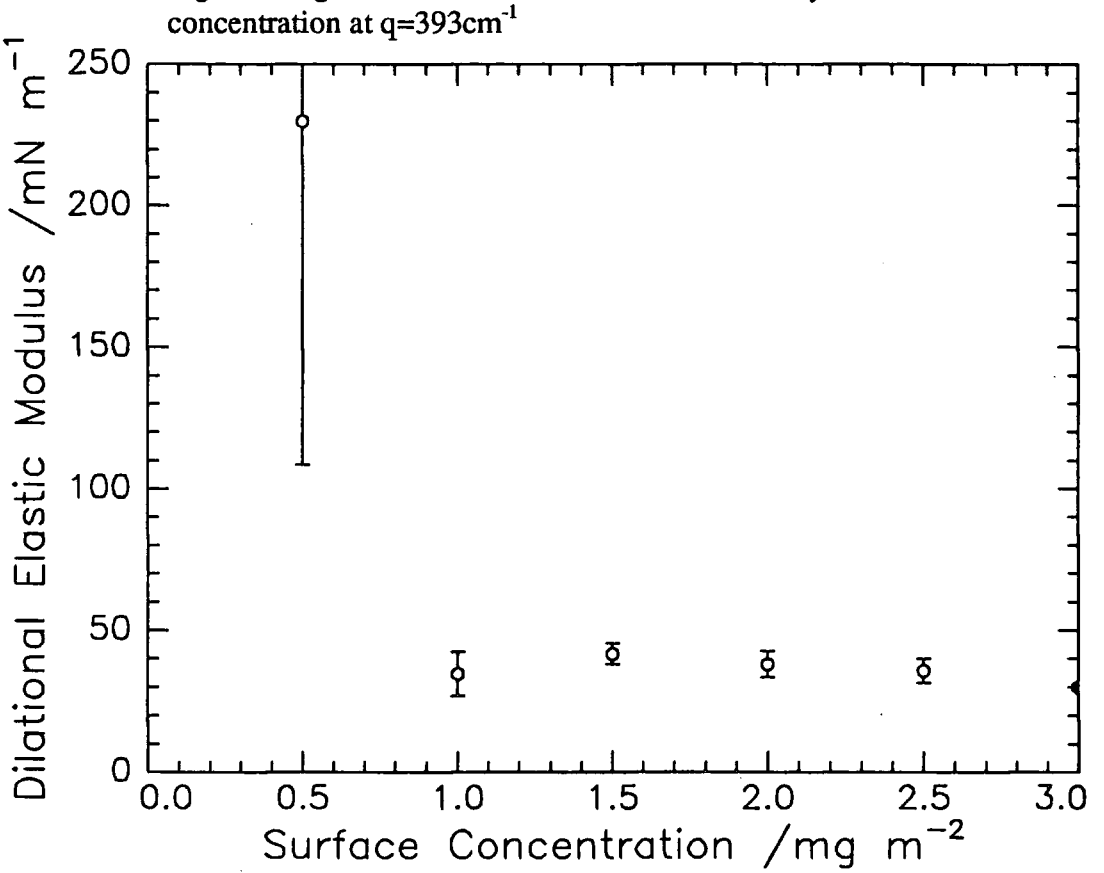

Figure 5.27h Comparision of classical (-) and SQELS (o) dilational elastic modulus variation with surface concentration at q=393cm^{-1}

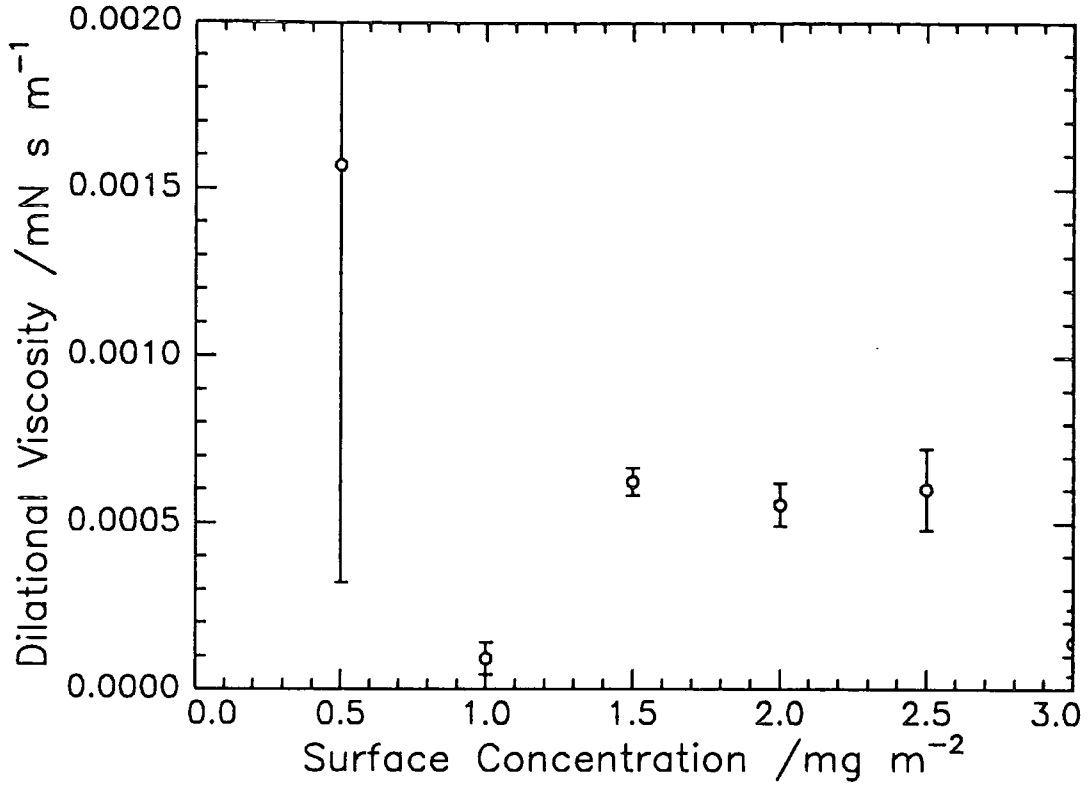

Figure 5.27i Variation of dilational viscosity with surface concentration at q=393cm^{-1}

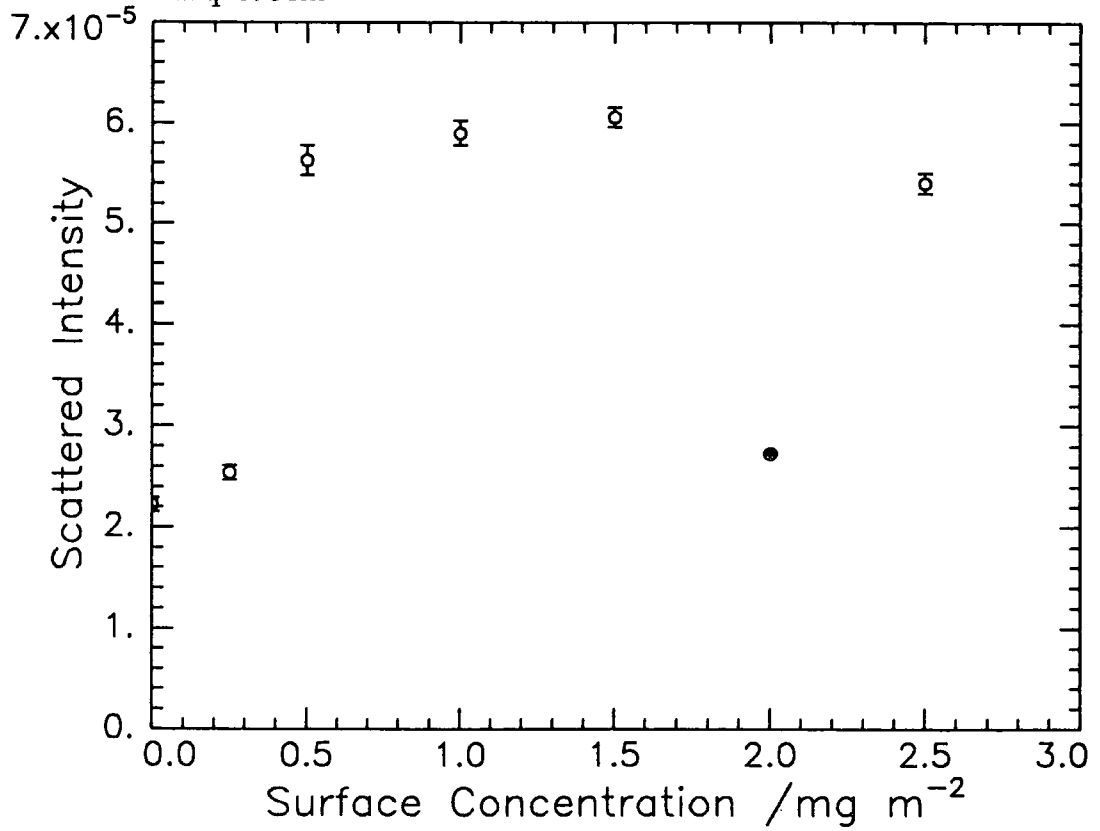

Figure 5.28a Variation of scattered intensity with surface concentration at q=473cm^{-1}

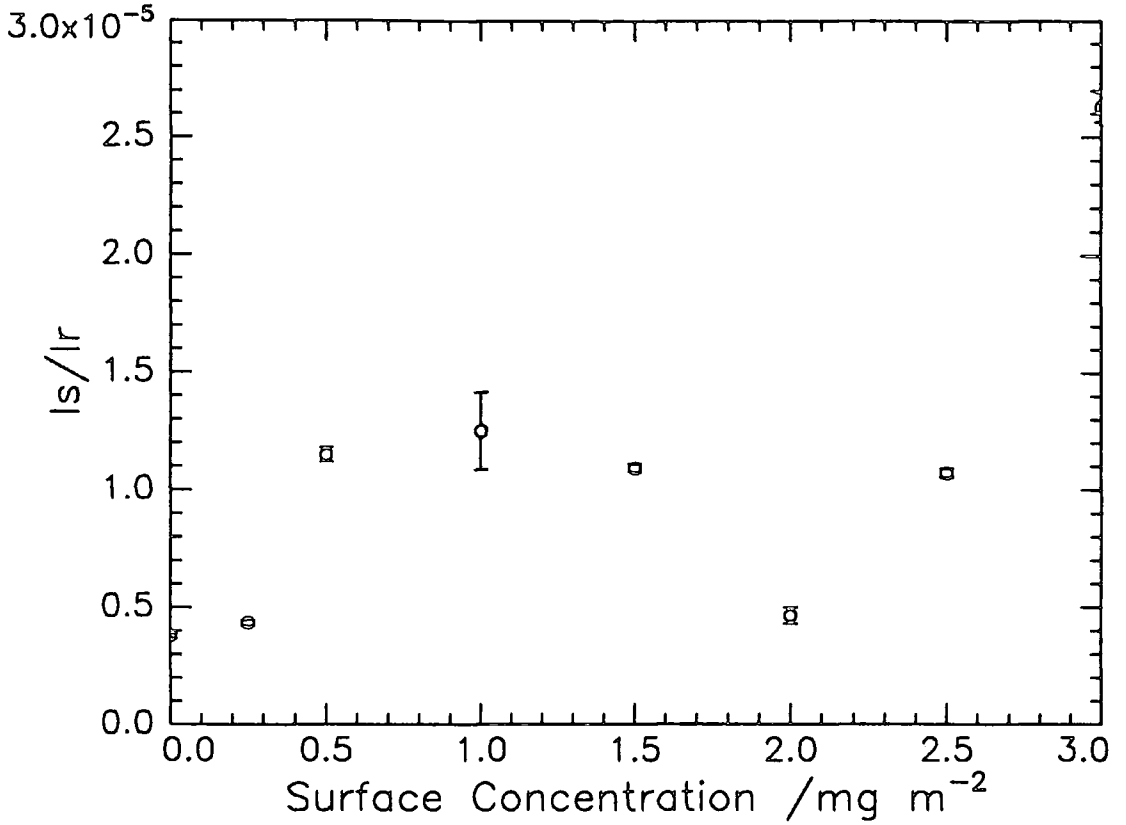

Figure 5.28b Variation of the ratio I_s/I_r with surface concentration at q=473cm^{-1}

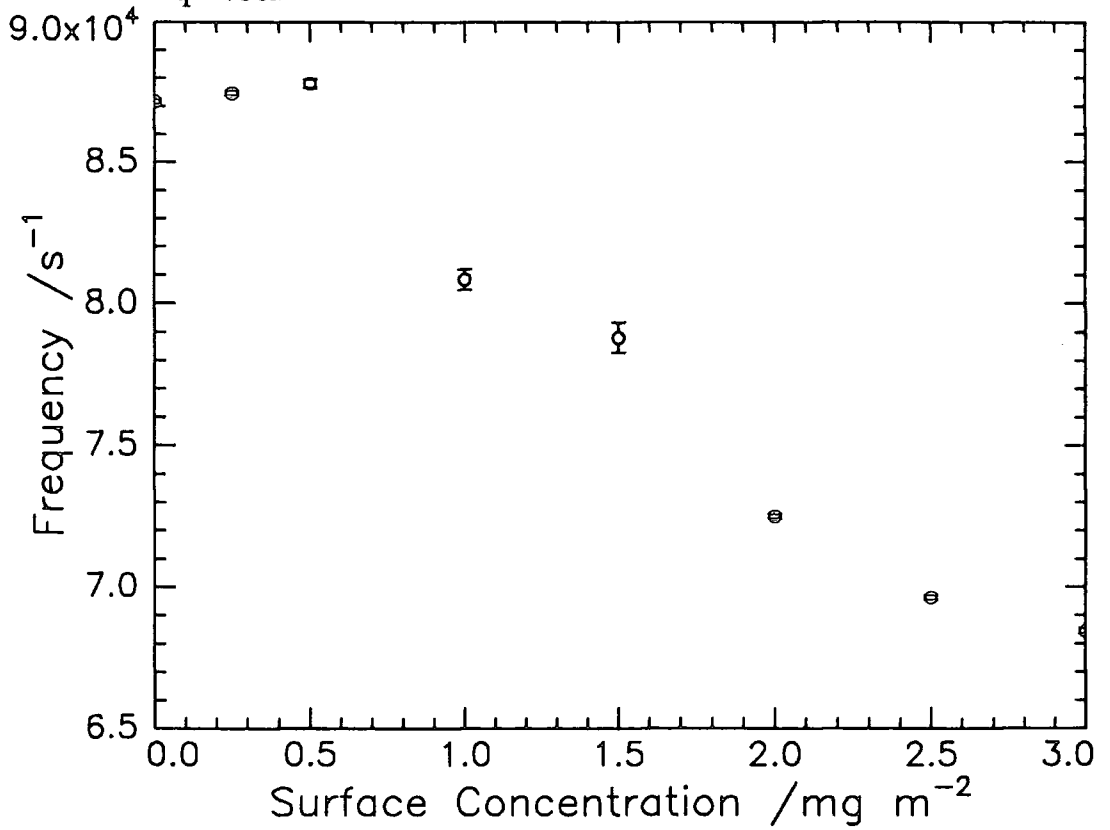

Figure 5.28c Variation of frequency with surface concentration at q=473cm^{-1}

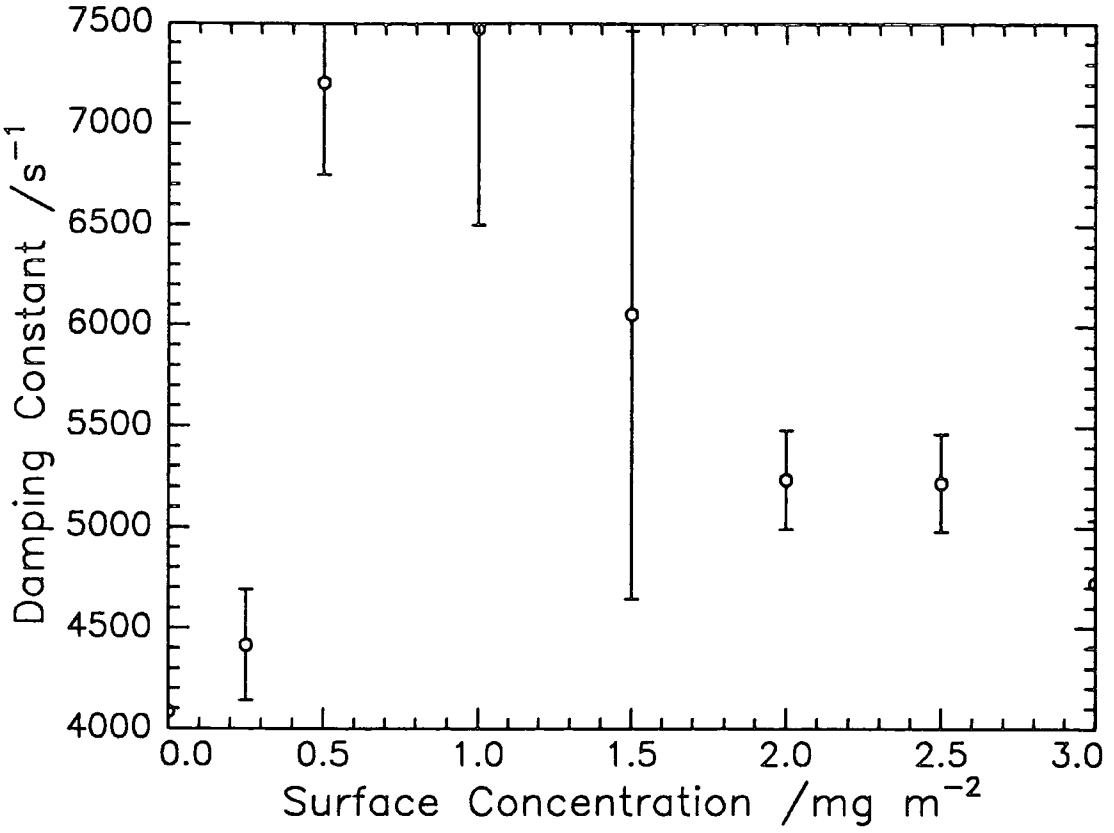

Figure 5.28d Variation of damping constant with surface concentration at q=473cm^{-1}

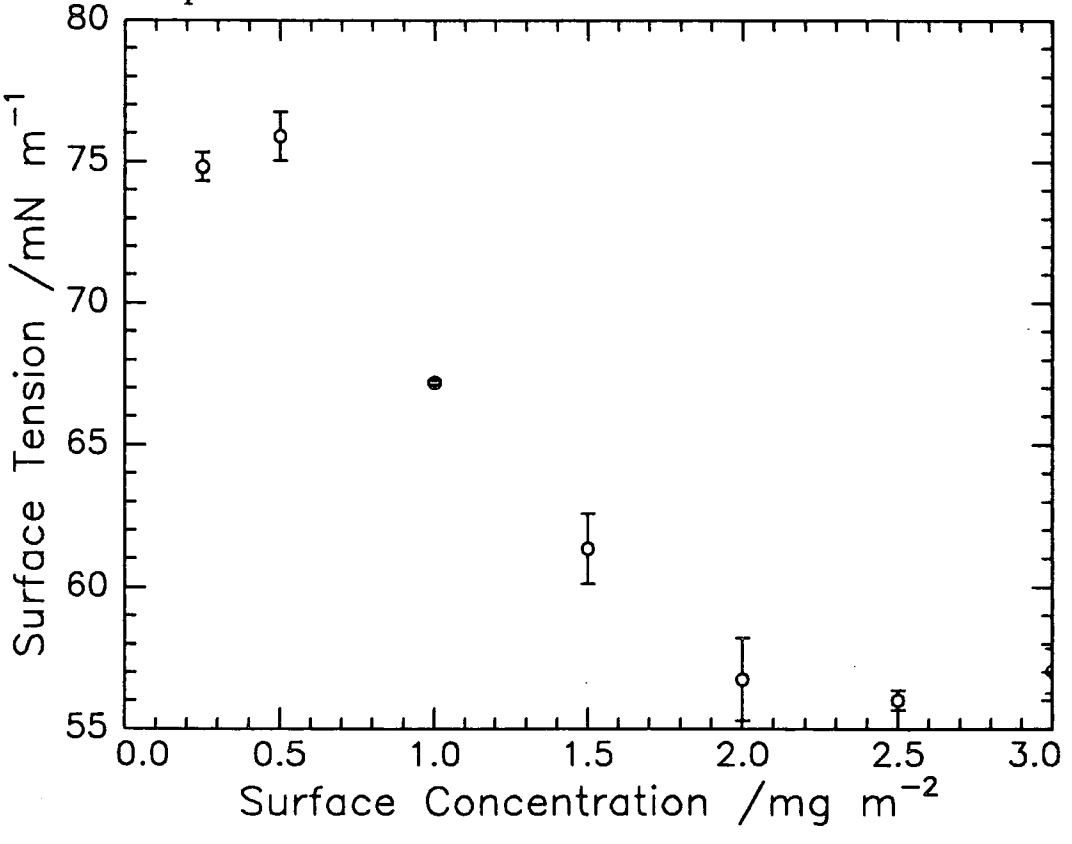

Figure 5.28e Variation of surface tension with surface concentration at q=473cm^{-1}

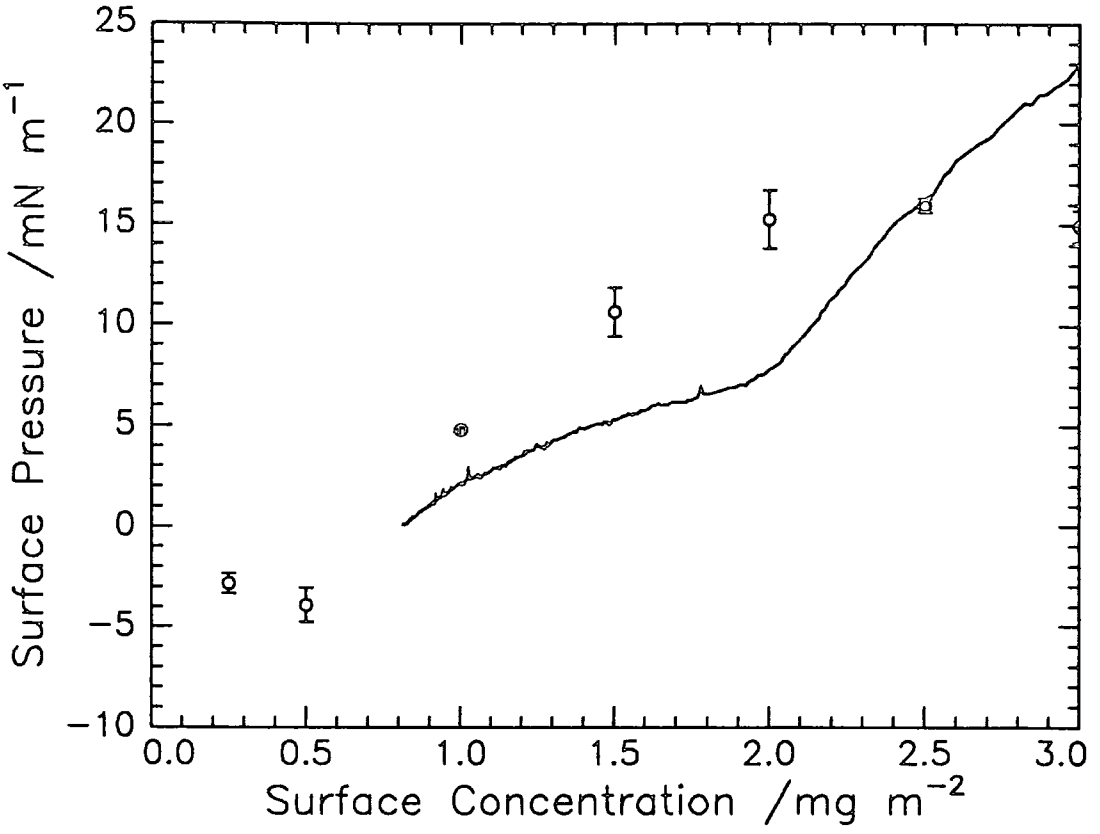

Figure 5.28f Surface pressure from SQELS (o) compared with classical Wilhelmy plate method (-) q=473cm^{-1}

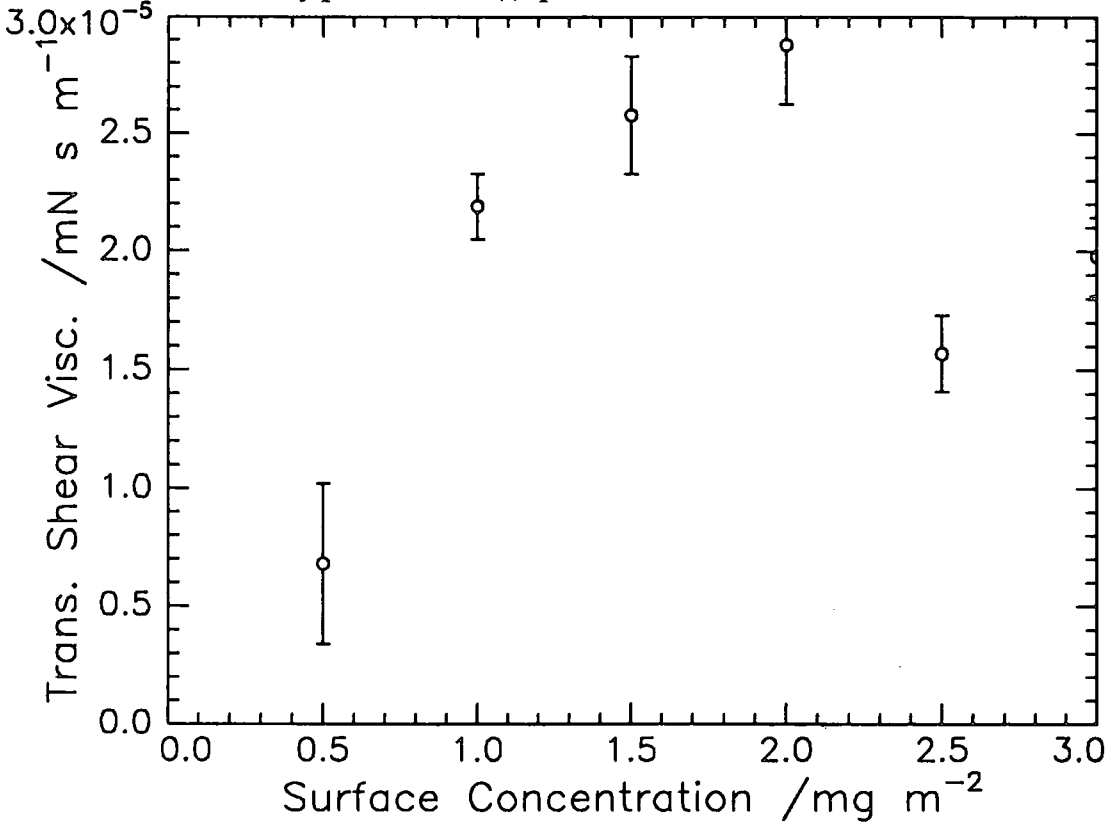

Figure 5.28g Variation of transverse shear viscosity with surface concentration at q=473cm^{-1}

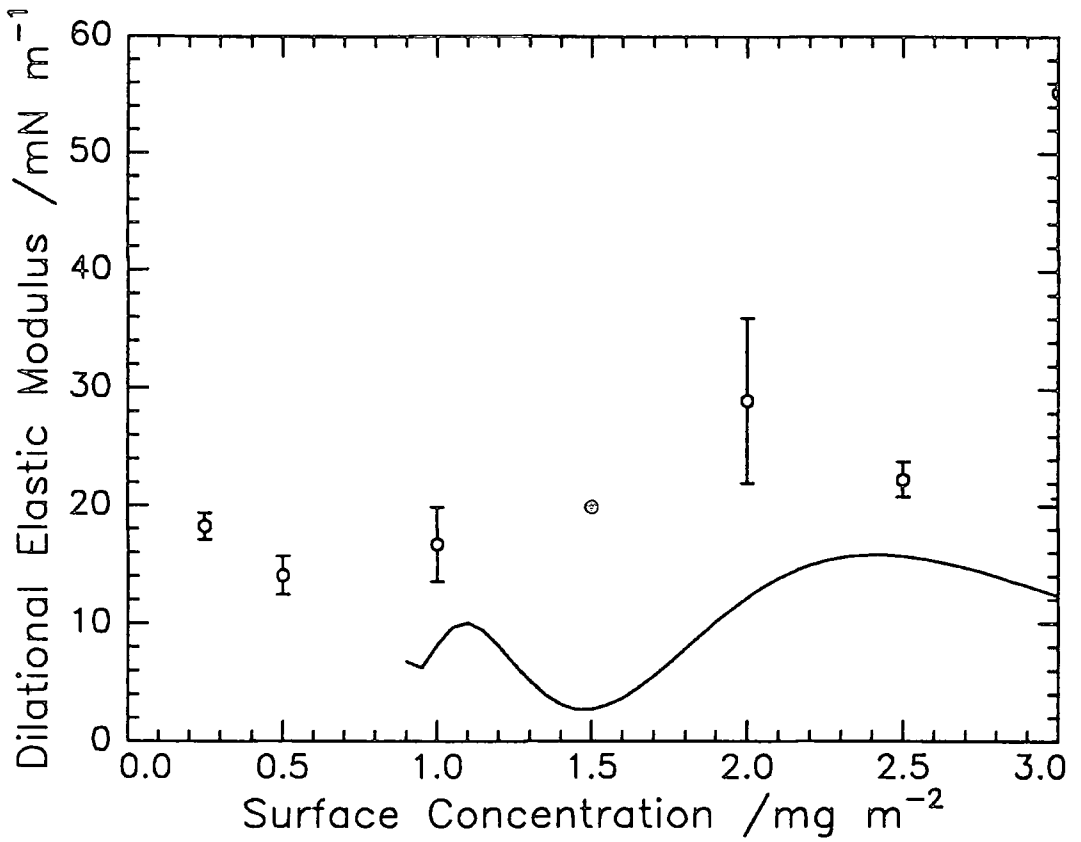

Figure 5.28h Comparision of classical (-) and SQELS (o) dilational elastic modulus variation with surface concentration at q=473cm^{-1}

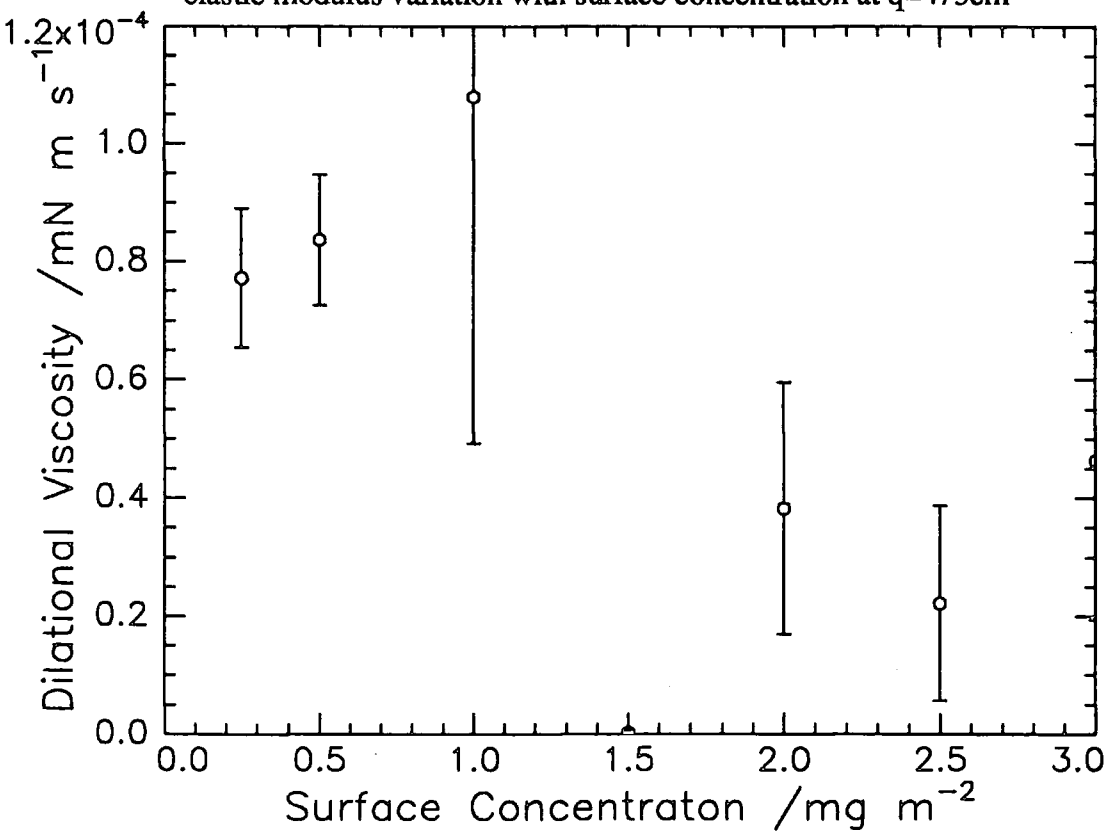

Figure 5.28i Variation in dilational viscosity with surface concentration at q=473cm^{-1}

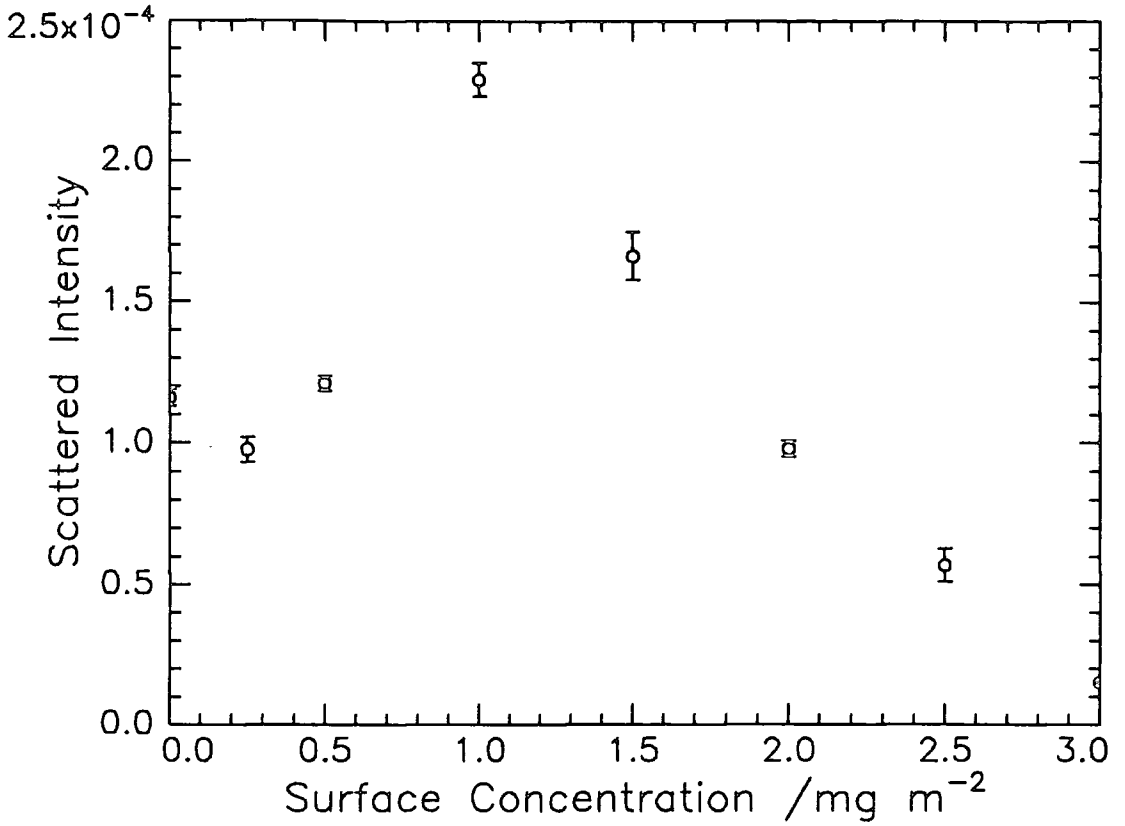

Figure 5.29a Variation of scattered intensity with surface concentration at q=566cm^{-1}

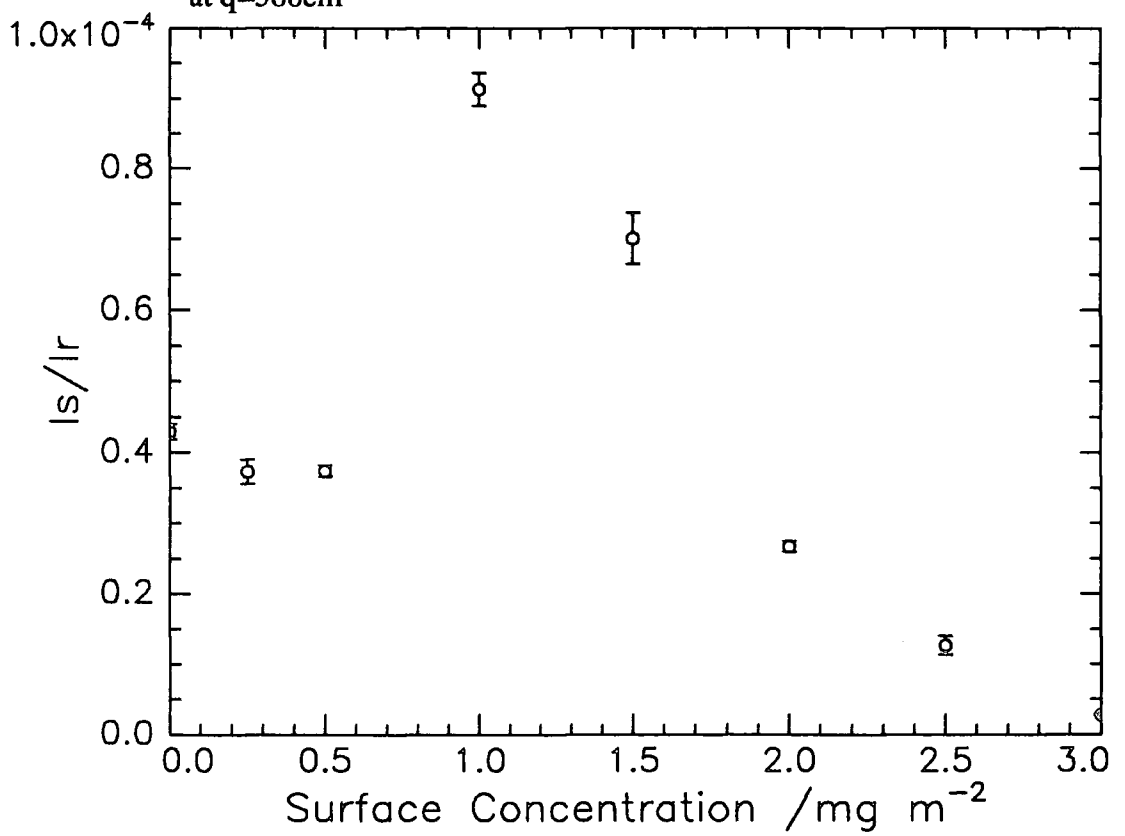

Figure 5.29b Variation of the ratio I_s/I_r with surface concentration at q=566cm^{-1}

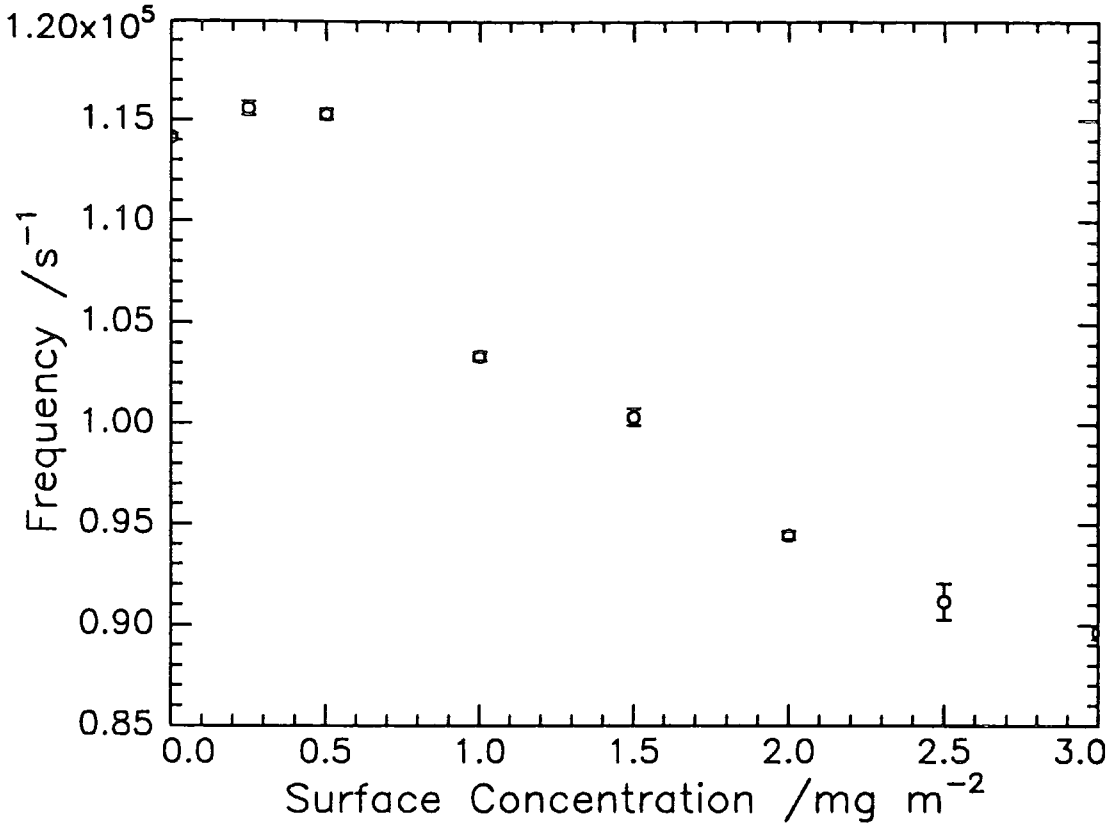

Figure 5.29c Variation of frequency with surface concentration at q=566cm^{-1}

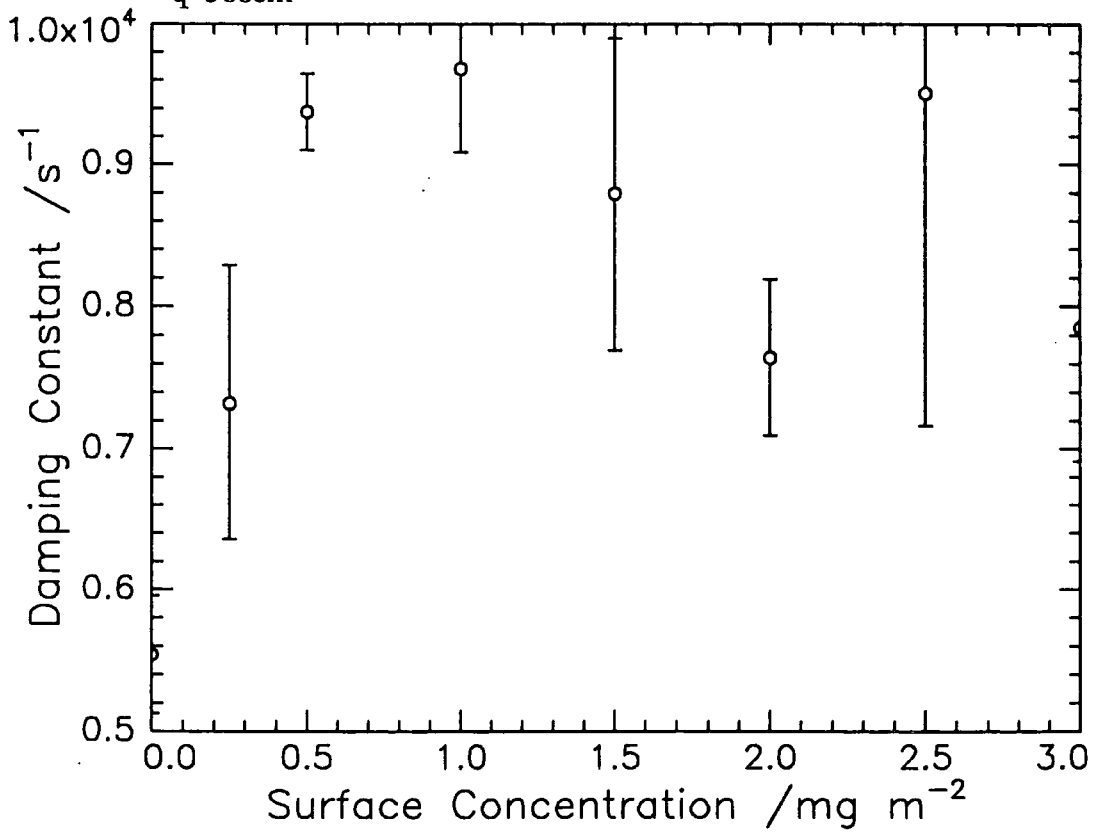

Figure 5.29d Variation of damping with surface concentration at q=566cm^{-1}

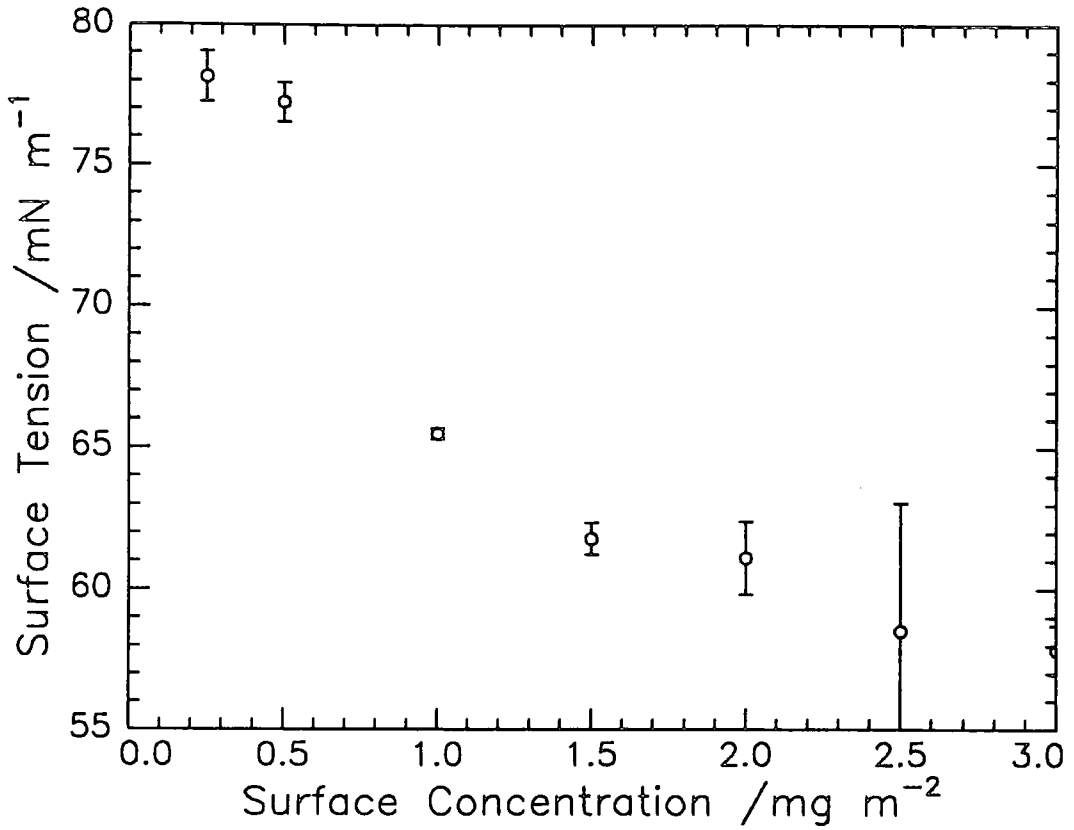

Figure 5.29e Variation of surface tension with surface concentration at 566cm^{-1}

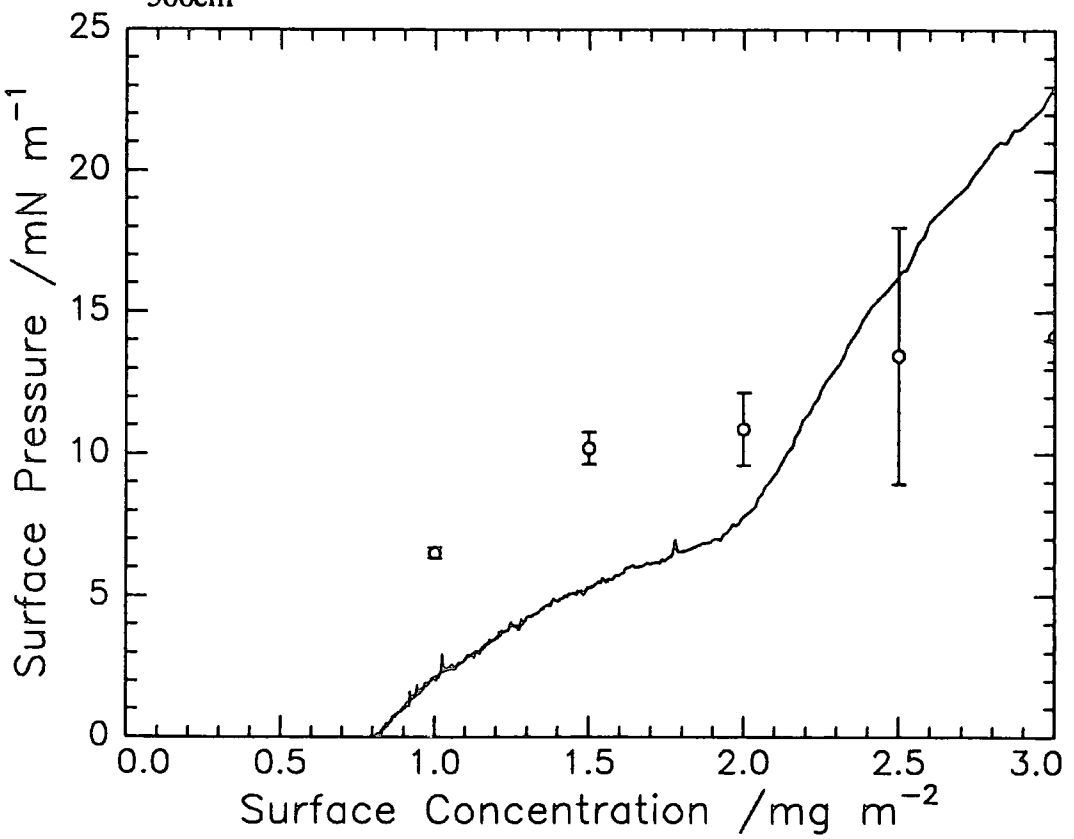

Figure 5.29f Surface pressure from SQELS (o) compared with classical Wilhelmy plate method (-) q=566cm^{-1}

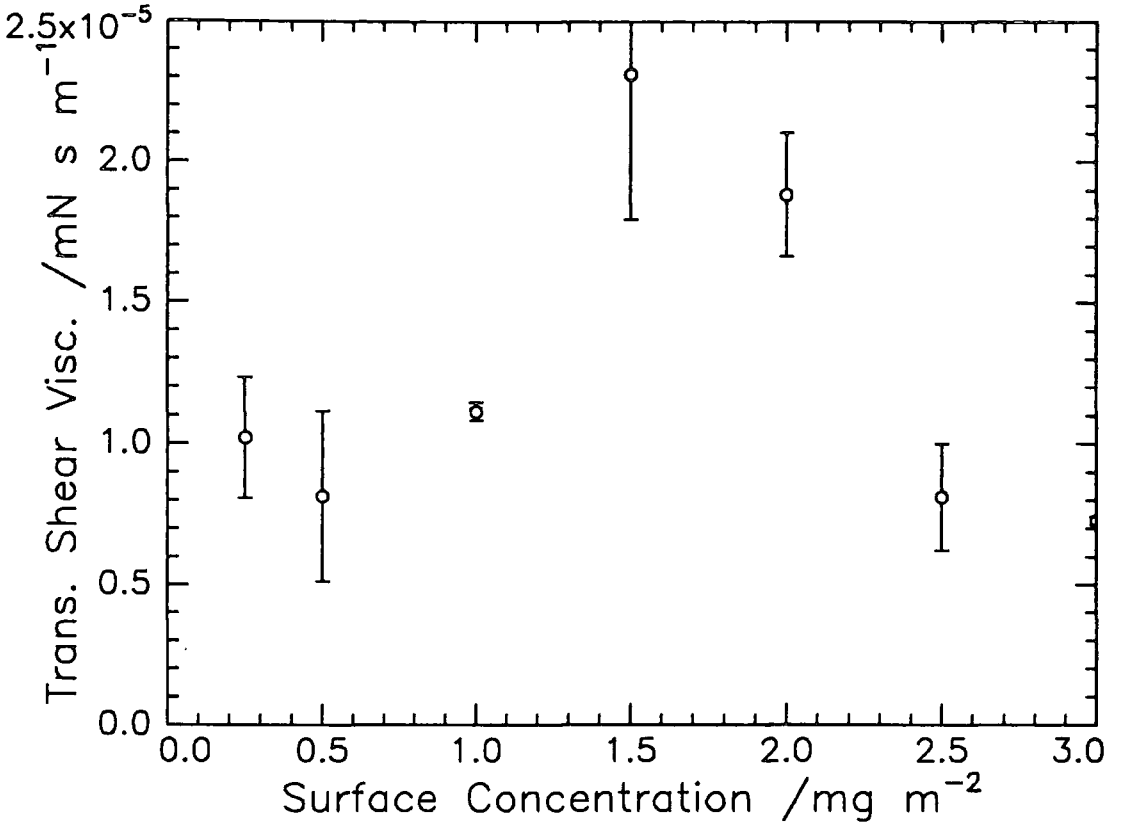

Figure 5.29g Variation in transverse shear viscosity with surface at q=566cm^{-1}

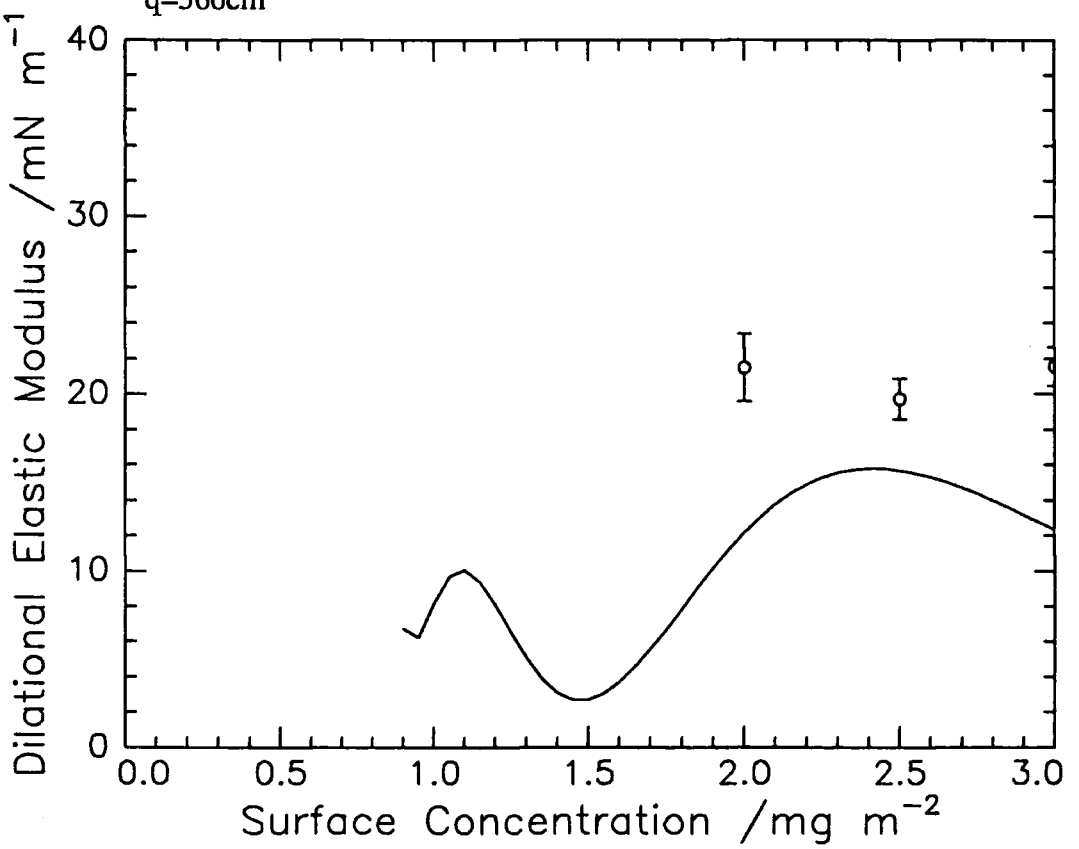

Figure 5.29h Comparision of classical (-) and SQELS (o) dilational elastic modulus variation with surface concentration at q=566cm^{-1}

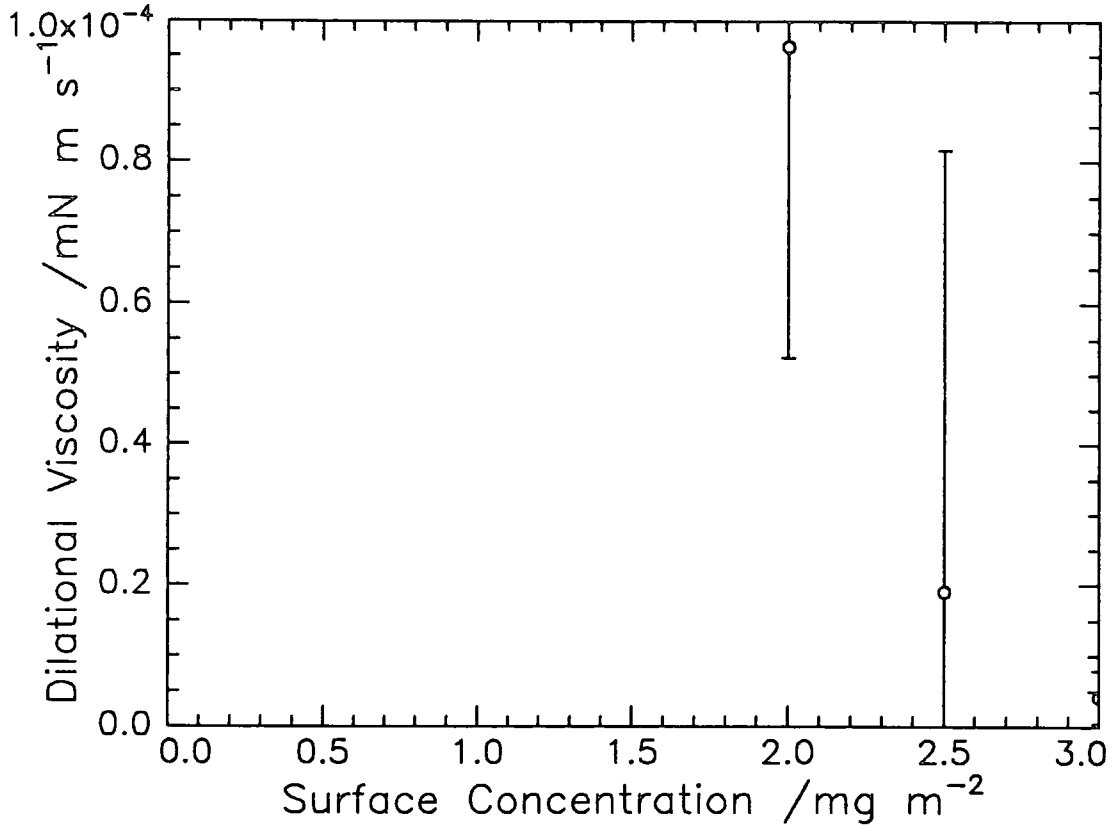

Figure 5.29i Variation in dilational viscosity with surface concentration at q=566cm^{-1}

the classical values, above 1.00mg/m^2 these values were approximately double those of the classical values. The ε' values were poorly determined over the q range studied.

5.2.2 Fully compressed state

The frequency dependence of the viscoelastic properties was studied in the fully compressed state which was taken to be 3.00mg/m^2. The measurements were taken at constant area over eight different q values ranging from q=220 to 909 cm^{-1}. Figure 5.30 shows the q dependence of ω_0 and Γ which increase in a similar linear fashion as those values determined for the bare water surface (figures 5.2 and 5.3). The γ_0 values (figure 5.31a) increased to a plateau value at higher frequency values the overall increase being about 8mN/m over the q range studied. The observed γ' (figure 5.31b) values decreased by about 60% over the frequency range studied. Figure 5.32 shows that the values of both ε_0 and ε' decrease with frequency, the magnitude of ε' falling off at a greater rate to almost zero values.

5.3 Discussion

5.3.1 Classical isotherm

It has been argued[1] that a plot of surface pressure as a function of surface concentration, rather than surface area, allows subtle effects due to phase changes in the monolayer to be evident. The surface pressure isotherm in figure 5.4 has features common to its constituent homopolymers. The shape of the low concentration range (0 to 2.00mg/m^2) is similar to that of PEO homopolymer, although the surface pressure values fall short of the plateau observed at 10mN/m. Above the transition point at about 2mg/m^2 the surface is no longer dominated by the PEO and the isotherm increases to a plateau at 35mN/m characteristic of syndiotactic PMMA.

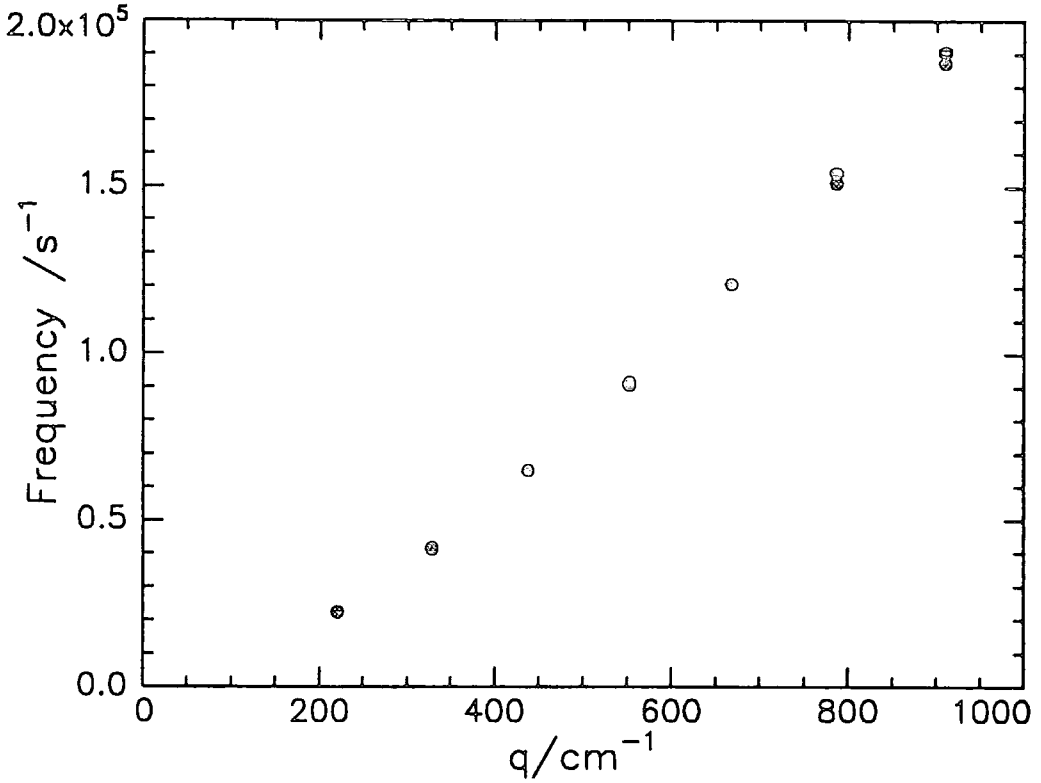

Figure 5.30a) Variation of frequency with q at 3.00mg/m^2

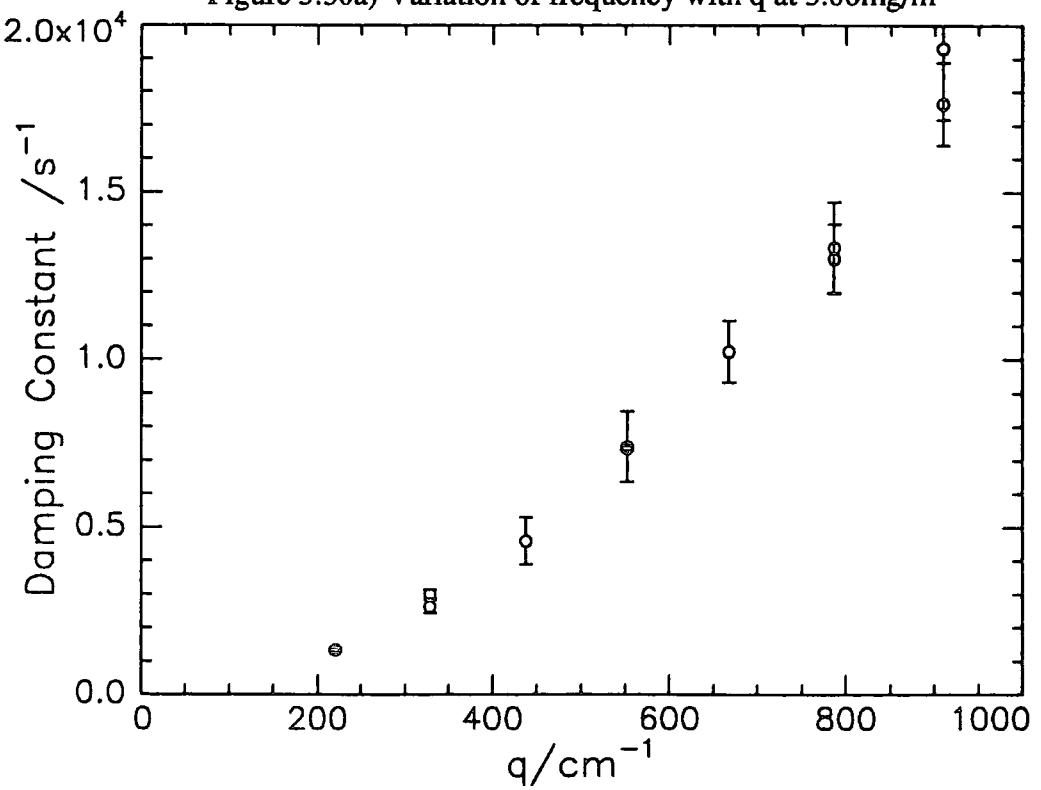

Figure 5.30b) Variation of damping constant with q at 3.00mg/m^2

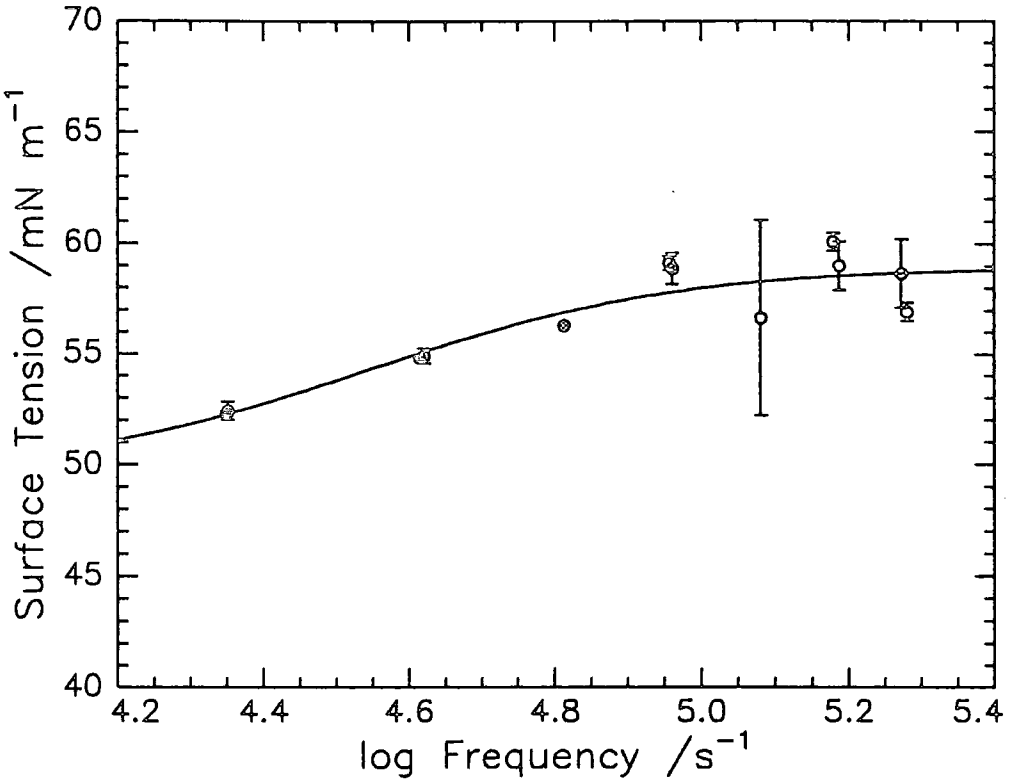

Figure 5.31a) Variation of surface tension with propagation frequency

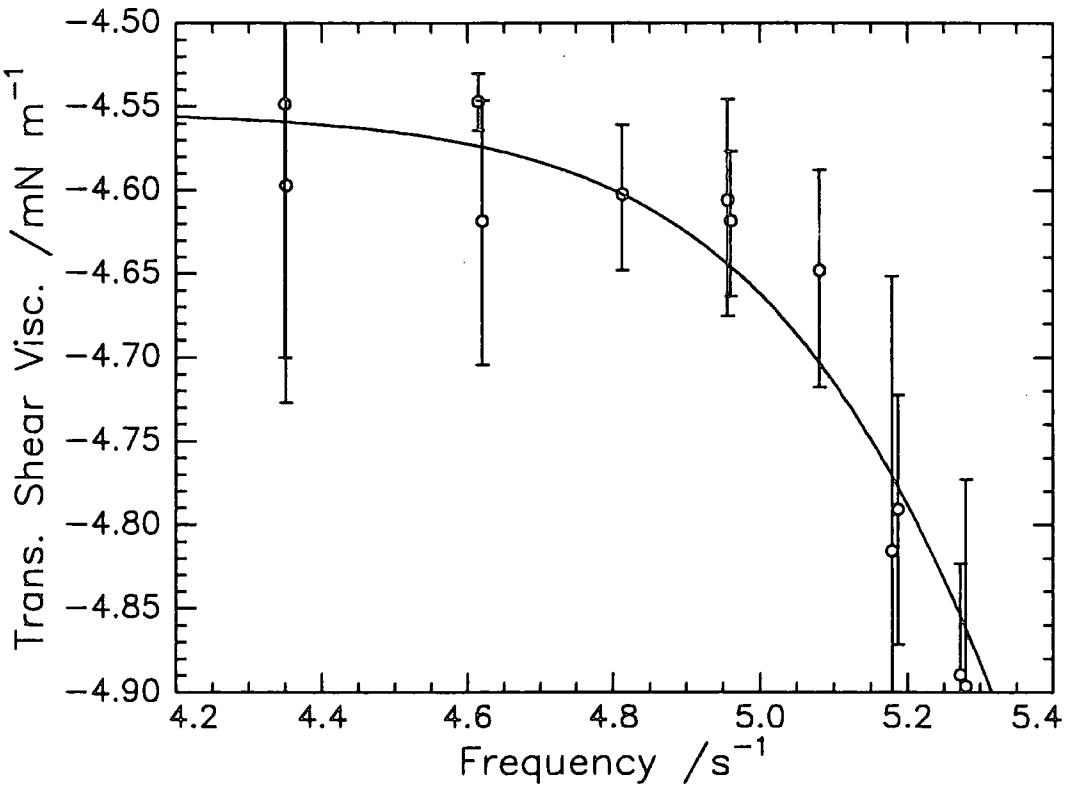

Figure 5.31b) Variation of transverse shear viscosity with frequency

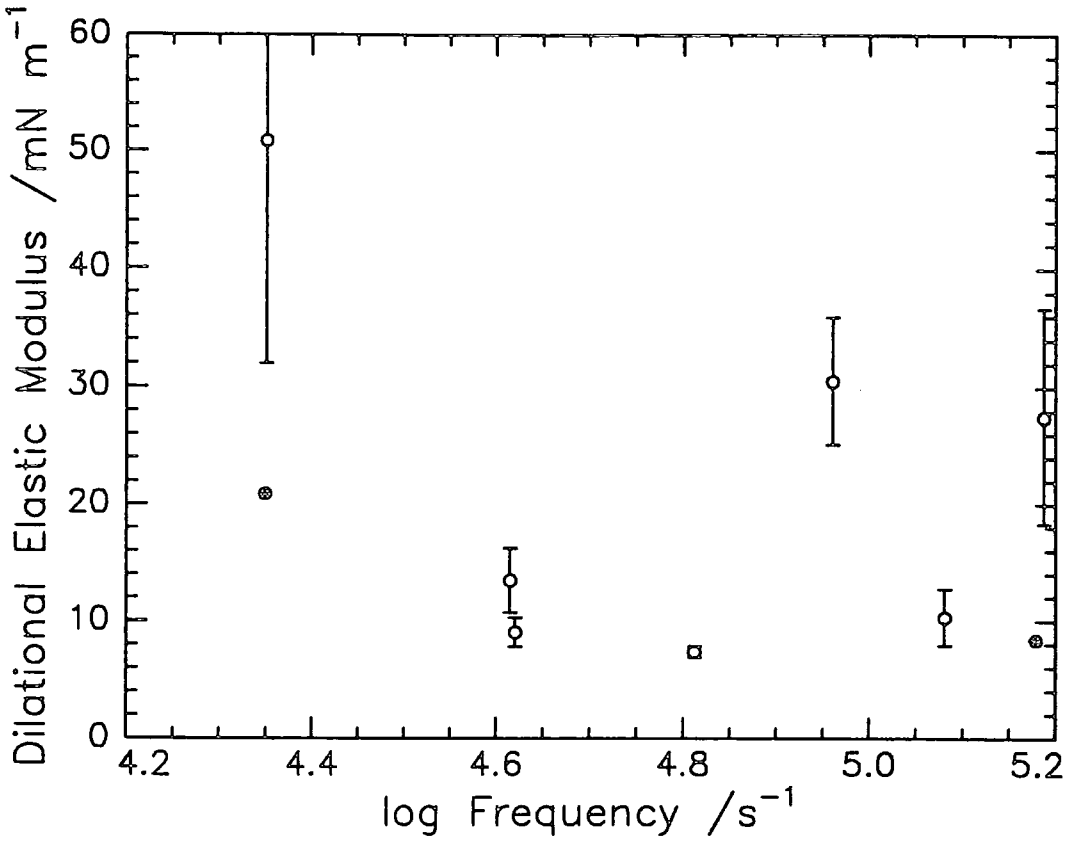

Figure 5.32a) Variation of dilational modulus with frequency

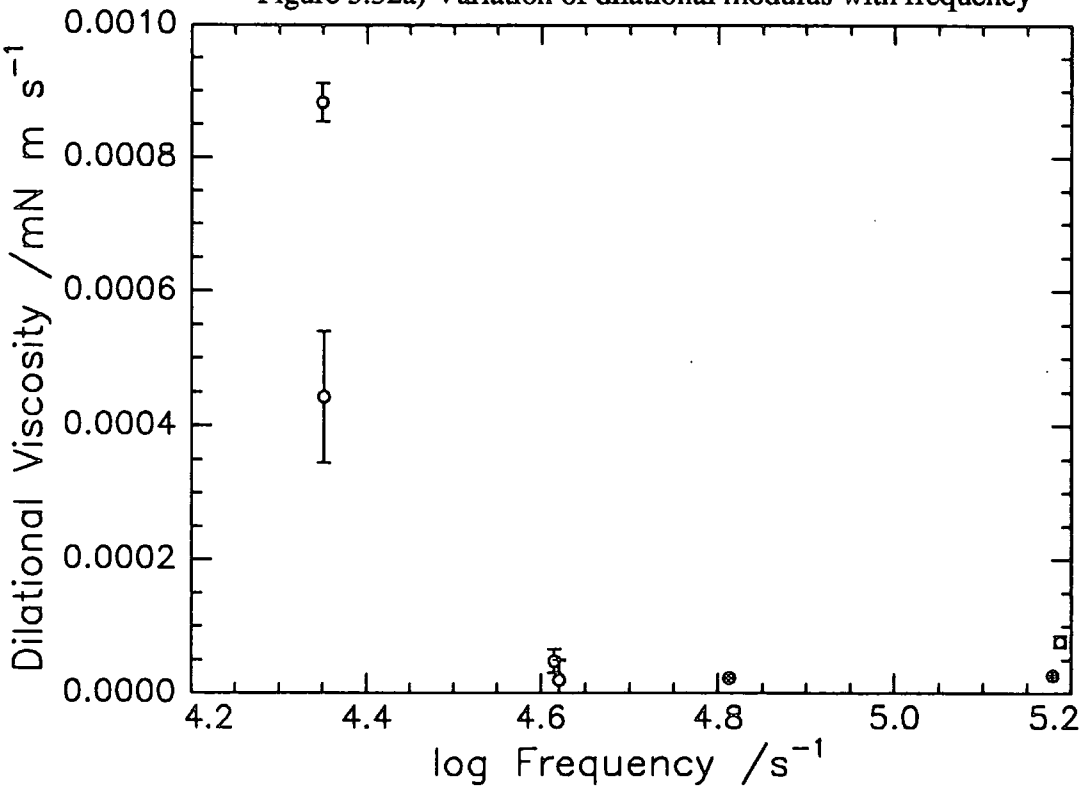

Figure 5.32b) Variation of dilational viscosity with frequency

5.3.2 Transverse shear modulus - γ

This section discusses two approaches to the analysis of the SQELS data. Firstly, data for q=301 and 351cm^{-1} are discussed in detail and compared with the classical static values. Secondly, the variaton of γ_0 and γ' with frequency and their relation to a viscoelastic model is also discussed.

5.3.2.1 Classical and light scattering surface tensions - γ_0.

Figures 5.22 and 5.26f (q=351 and 301cm^{-1} respectively) show that the light scattering surface pressures and those from the static Wilhelmy plate method have similar shapes but a number of anomalies are present. The fact that below 0.6mg/m^2 the light scattering surface tensions are higher than those for pure water suggests either incorrectly aligned apparatus, producing a false q value, or that the fitting procedure was inaccurate. These arguments can be discounted since the analysis of pure water gave surface tension values which agreed with the accepted value. The surface pressure isotherms calculated from the SQELS γ_0 data therefore had negative values in this low surface concentration region. Studies on syndiotactic PMMA homopolymer spread at the air-water interface[2] have shown negative surface pressure values using both the Wilhelmy plate and SQELS methods which was not observed for isotactic PMMA homopolymer[2] or PEO homopolymer[3]. The reason for this observation was thought to be due to the stereochemical nature of the polymer which has stronger intermolecular cohesive forces with itself than the water subphase. This also appeared to increase the cohesion of water and thus the surface tension. This behaviour therefore appears to be evident in the block copolymer since the PMMA portion has a degree of syndiotacticity.

The effect of the γ_0 on P(ω) is that it can be determined precisely, independent of the other surface viscoelastic parameters. The value of ω_0 is primarily dependent on γ_0, other viscoelastic properties having a very small effect. To a first order approximation then

$$\omega_0 \cong \sqrt{(\gamma_0 q^3 / \rho)} \qquad (5.2)$$

which is used to obtain apparent surface tension values. However, this approximation for ω_0 is affected by ε_0 especially when $\varepsilon_0/\gamma_0 > 0.13$.

5.3.2.2 Transverse shear viscosity - γ'

The transverse shear viscosity (γ') has the main effect on capillary waves of increasing their damping. To a first order approximation this increase in damping is

$$\Delta\Gamma = \gamma' q^3/(2\rho) \qquad (5.3)$$

which shows that light scattering becomes more sensitive to γ' with increasing values of q. The experimental γ' values determined for q=301 and 351cm^{-1} were therefore not as precise as those determined for higher q values, although the ease of data aquisition allowed a more detailed investigation of the surface concentration dependence.

The variations in γ' are consistent with the non-zero values of γ' observed in previous studies[4]. The non-zero nature of the surface viscosity has been suggested in the past to be due to inadequate correction for instrumental line broadening. This critisism can be countered by analysing the light scattering data for the clean, bare surface of water. Direct fitting of this data gives parameters in agreement with the known parameters of water, i.e. γ_0 = classical value, $\varepsilon_0 = \gamma' = \varepsilon' = 0$.

The surface viscosity was slightly less than that observed for PEO homopolymer for which $\gamma' \sim 3 \times 10^{-5}$ mN s/m. Since the copolymer was most viscous around 1.5mg/m^2 this could indicate increased chain-chain interactions of the PMMA segment as the PEO segments are forced into the water phase. At low surface coverage the PEO block dominates the interface, while at higher coverage the PMMA block plays a greater role. This corresponded to the rapid rise of γ'. The decrease in γ' could be attributable to further displacement of PEO segments from the interface and indicative of the phase separation of the blocks discussed in Chapter 4.

5.3.2.3 Viscoelastic Relaxation (γ)

Fully compressed state

A viscoelastic Voigt-Kelvin solid model cannot be applied to the data because this requires that both γ_0 and γ' be constant with increasing frequency. However, due to the observed variation of γ_0 and γ' with frequency, it is possible to apply a Maxwell fluid model (eqns 1.5.19 and 1.5.20) and figure 5.31 shows the fitted data assuming this model. The parameters of the least squares fit are shown in table 5.2 for the γ_0 and γ' variation with frequency.

Variation	τ/s	G/mN m^{-1}	Ge/mN m^{-1}
$\gamma_0(\omega_0)$	2.88e-5	9.5	49.5
$\gamma'(\omega_0)$	5.35e-6	5.2	-

Table 5.2 Fitted parameters of the least squares fit to the Maxwell fluid relations

It can be seen that there are differences in the values of G, the amplitude of the relaxation process and τ, the relaxation time. The constant G_e in equation 1.5.19 is present to allow for a discrete contribution to the relaxation spectrum when $\tau = \infty$. The value of G_e (49.49mN/m), the equilibrium elastic modulus ($\omega_0 \rightarrow 0$) is almost exactly the same as the surface tension (48.95mN/m) value calculated from the static surface pressure isotherm. In conventional rheological notation G is a nonnegative function of τ that fully characterises the relaxation of a material only when G_e is also given. The values of G and τ derived from equation 1.5.20 using γ' do not characterise the relaxation fully. Evidence that the combination of parameters G_e, G, and τ from equation 1.5.19 is more valid is supported by the fact that calculation of τ and G for each q value separately show that these parameters are dependent on the value of the wavenumber q. For the

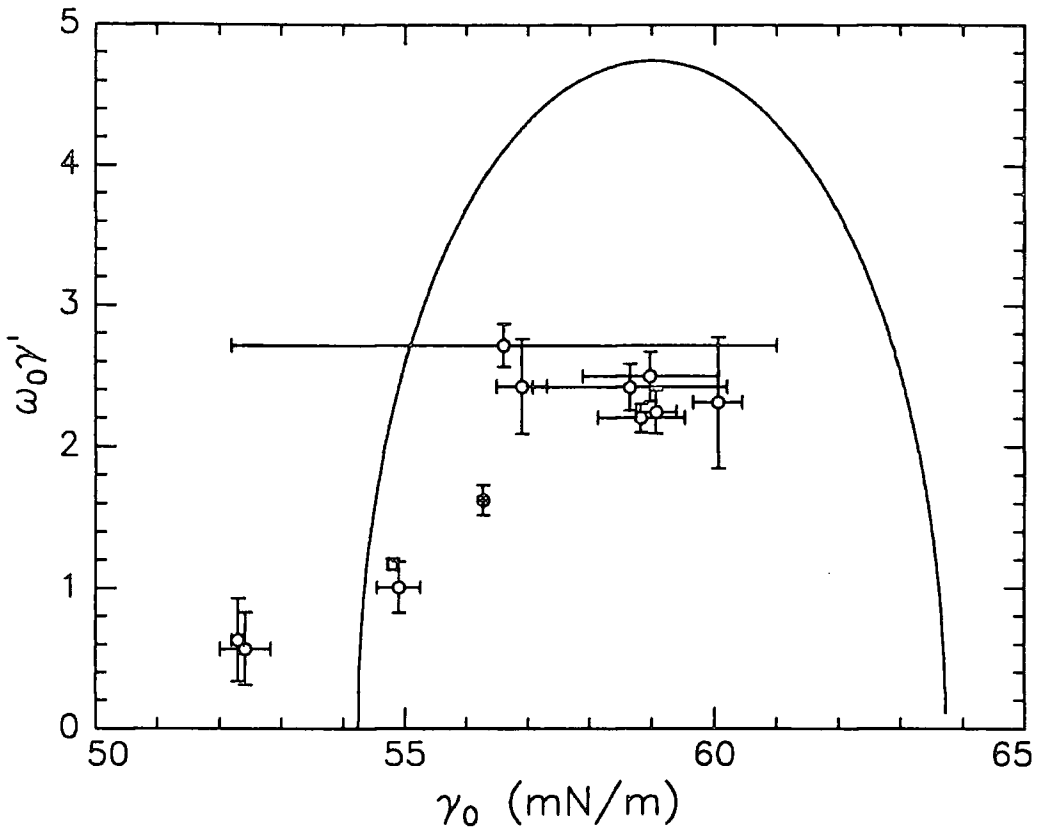

Figure 5.33 Cole-Cole plot of loss modulus (G") versus γ_0 for the data of figure 5.31

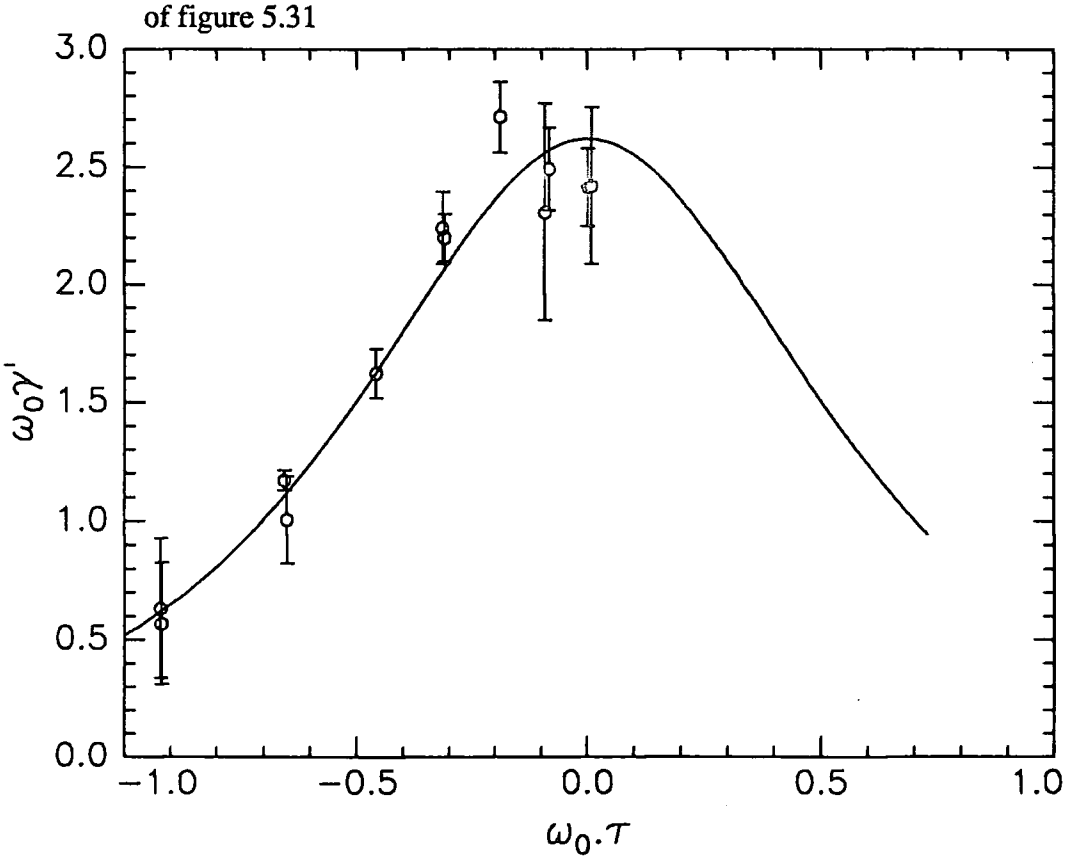

Figure 5.34 Dependence of G" on frequency. The line is the variation expected for the Maxwell fluid model.

range of q studied these calculated parameters are all within the range obtained from equation 1.5.19. This variation in the relaxation times suggests that a single relaxation process may not be present. These variations may be investigated further by plotting the loss modulus ($\omega_0\gamma'$) against the surface tension (storage modulus) which is known as a Cole-Cole plot. The modulus $G^*(\omega_0)$ should describe a semi-circle in the complex plane (eqns 1.5.19 and 1.5.20), centred upon the real axis. Figure 5.33 shows this Cole-Cole plot and the theoretical semi-circle trajectory calculated using the parameters obtained from equation 1.5.19. If a single exponential relaxation process is present then this semi-circle trajectory should be compatible with the data. The frequency range over which the measurements were taken obviously does not extend to a high enough value to match the surface tensions of the theoretical curve. The data seem to be broader than those predicted for the semi-circle and have smaller magnitudes than these theoretical values. This broadening is similar to that discussed by Davidson and Cole[5], where high frequency broadening was observed in the dielectric relaxation of glycerine and thought to be due to a distribution of relaxation times. The limited frequency range over which the measurements were taken meant that high frequency γ_0 and γ' values were not obtainable. These values would have shown the maximum value of the loss modulus in the Cole-Cole plot and provided an insight into the distribution of relaxation times in the high frequency range.

By looking at the dependence of the loss modulus ($\omega_0\gamma'$) on frequency (plotted as $\omega_0.\tau$) any departure from ideal single exponential behaviour will become evident (figure 5.34). Using the data from table 5.2 for the loss modulus, the experimental data in this case agrees with the variation expected for a Maxwell model. According to figure 5.34 the γ' data for $\omega_0\tau < 0$ show that slower processes do not contribute significantly to the relaxation. Since the data only extend to $\omega_0\tau \sim 0$, then much faster relaxation processes

may not be excluded. It would be possible to detect these faster relaxation processes if the ω_0 range could be extended.

It would therefore be reasonable to assume that at low frequencies a single relaxation process is present whereas at high frequencies the broadening of the Cole-Cole plot suggests that more than one relaxation process is present.

Variations with surface coverage

By using values of $\Delta\pi$ and γ' measured for q values of 301 and 351cm^{-1} over the surface concentration ranges studied it is possible to obtain G and τ. By rearranging equations 1.6.19 and 1.6.20 then

$$\tau = (G'(\omega_0)-G_e)/\omega_0.G''(\omega) \qquad (5.4)$$

$$= -\Delta\pi/\omega_0^2\gamma' \qquad (5.5)$$

By substituting τ back into equations 1.6.19 or 1.6.20 then G may be evaluated. The values of τ and G were plotted in semi-log form against both Γ and π (figures 5.35 and 5.36). The relaxation time (τ) data increased by approximately one and a half orders of magnitude for the q=301cm^{-1} data while for q=351cm^{-1} τ increased by about one order of magnitude over the surface concentration range studied. The range of relaxation times for q =301cm^{-1} are between 50μs and 2500μs, while those for q=351cm^{-1} are between 50μs and 560μs over the surface concentration range studied. The relaxation time is seen to decrease initially for q=351cm^{-1} but essentially increases over the surface coverage ranges studied. Using the values of the relaxation time then values of G can be calculated by rearranging equation 1.6.19 and calculating the loss modulus using values of γ'. Figures 5.37 and 5.38 show values of G as a function of surface coverage for the two q values. For q=301cm^{-1} the values of G are all in the range 2 to 20mN/m, while for q=351cm^{-1} the values are in the range 4 to 13mN/m. At both q values studied G has approximatly similar behavior. The minimum at 1.5mg/m^2 (5mN/m) and the maximum at

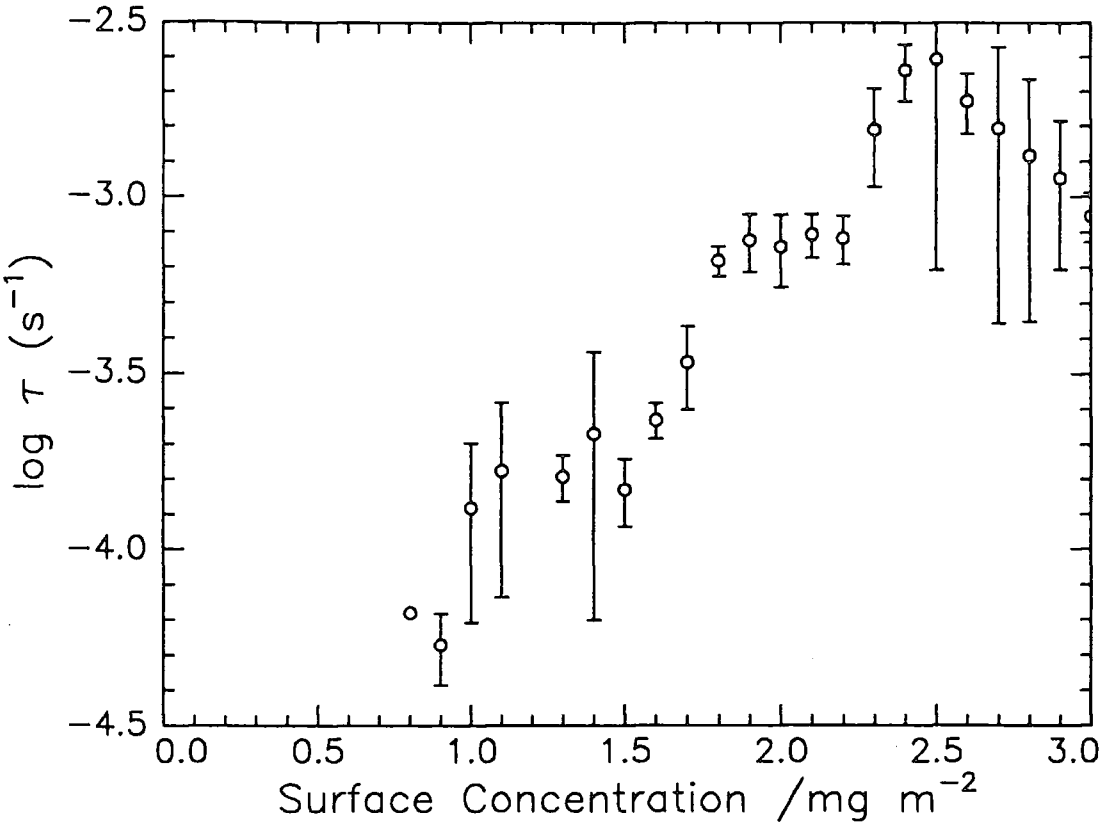

Figure 5.35a) Semi-log plot of τ versus surface concentration for q=301cm^{-1}

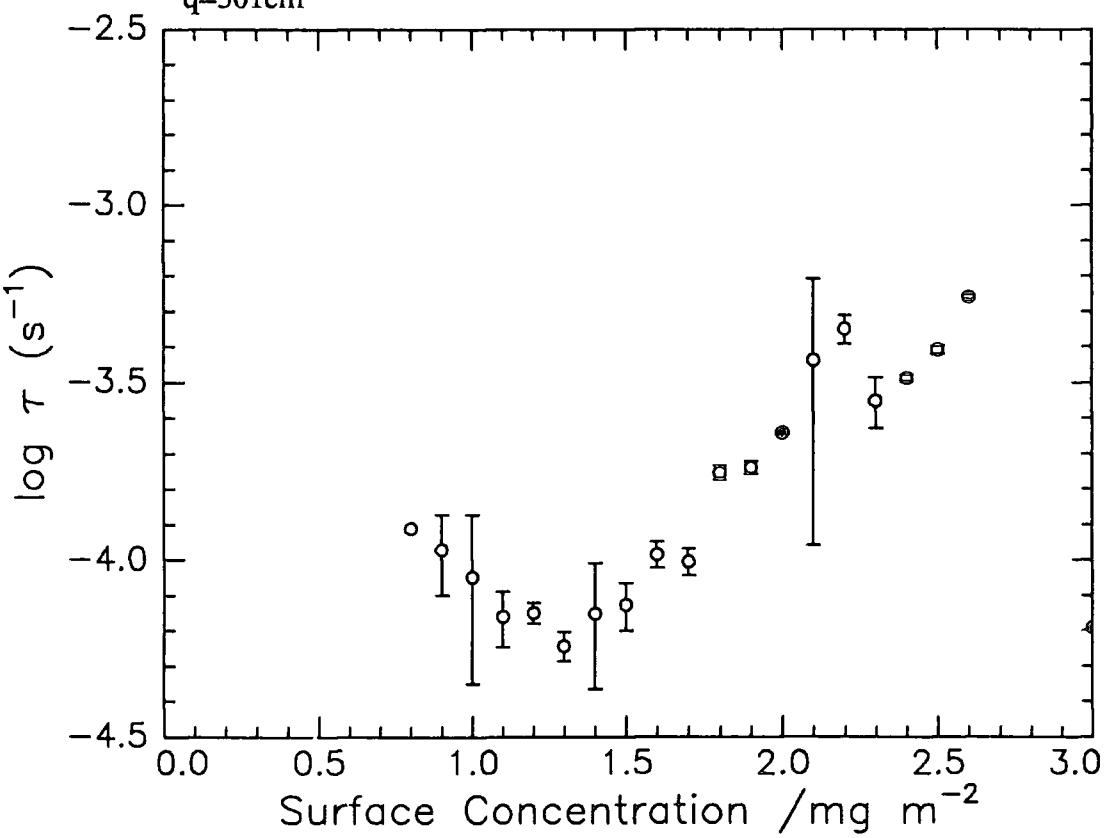

Figure 5.35b) Semi-log plot of τ versus surface concentration for q=351cm^{-1}

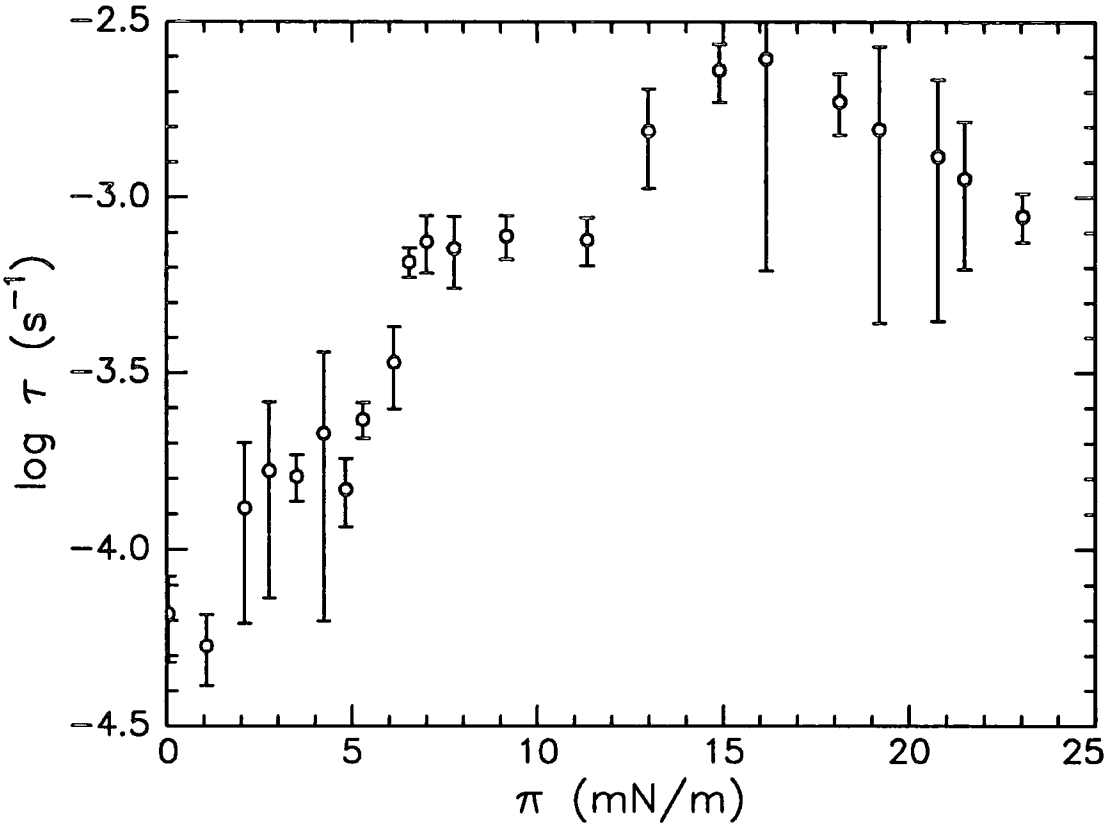

Figure 5.36a) Semi-log plot of τ versus surface pressure for q=301cm^{-1}

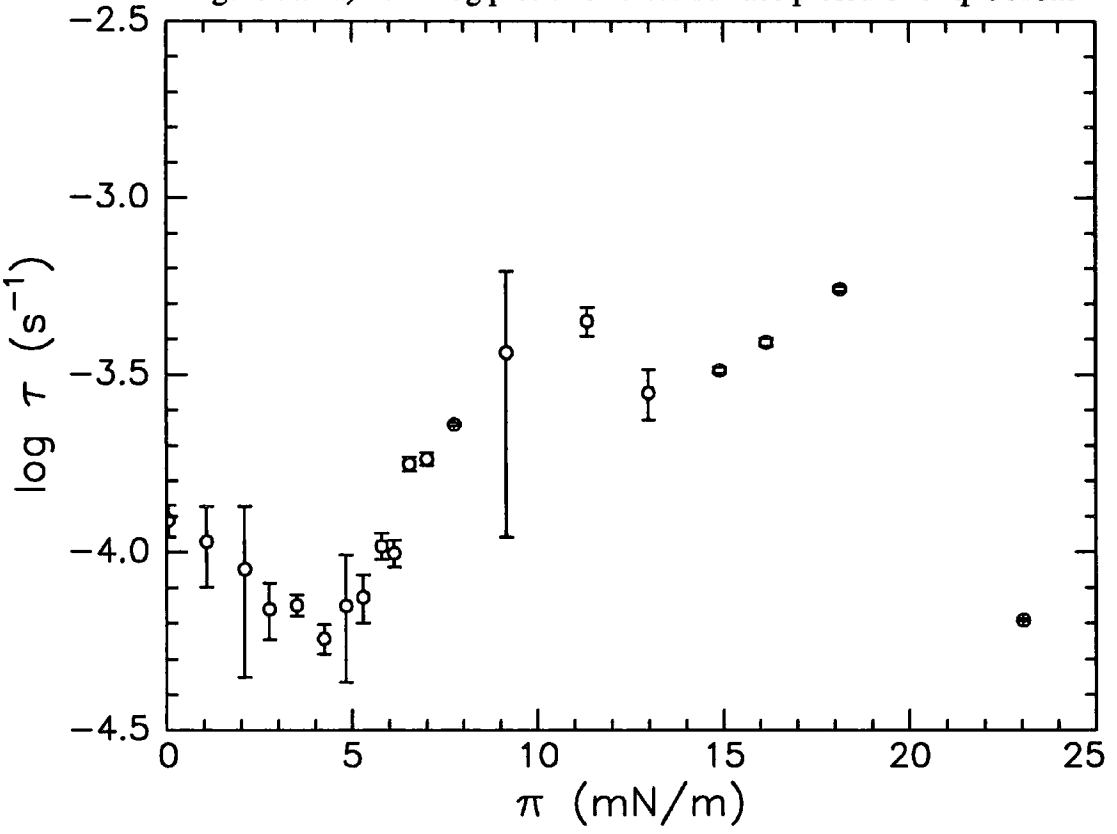

Figure 5.36b) Semi-log plot of τ versus surface pressure for q=351cm^{-1}

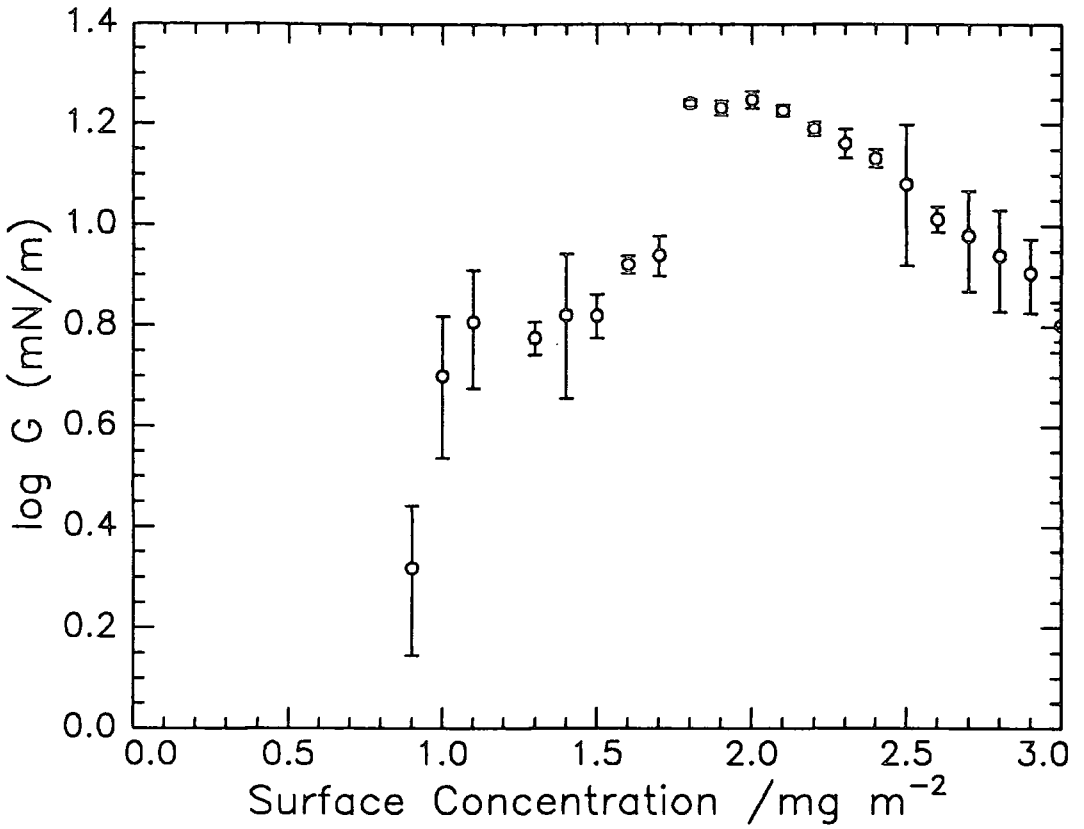

Figure 5.37a) Semi-log plot of G versus surface concentration for q=301cm^{-1}

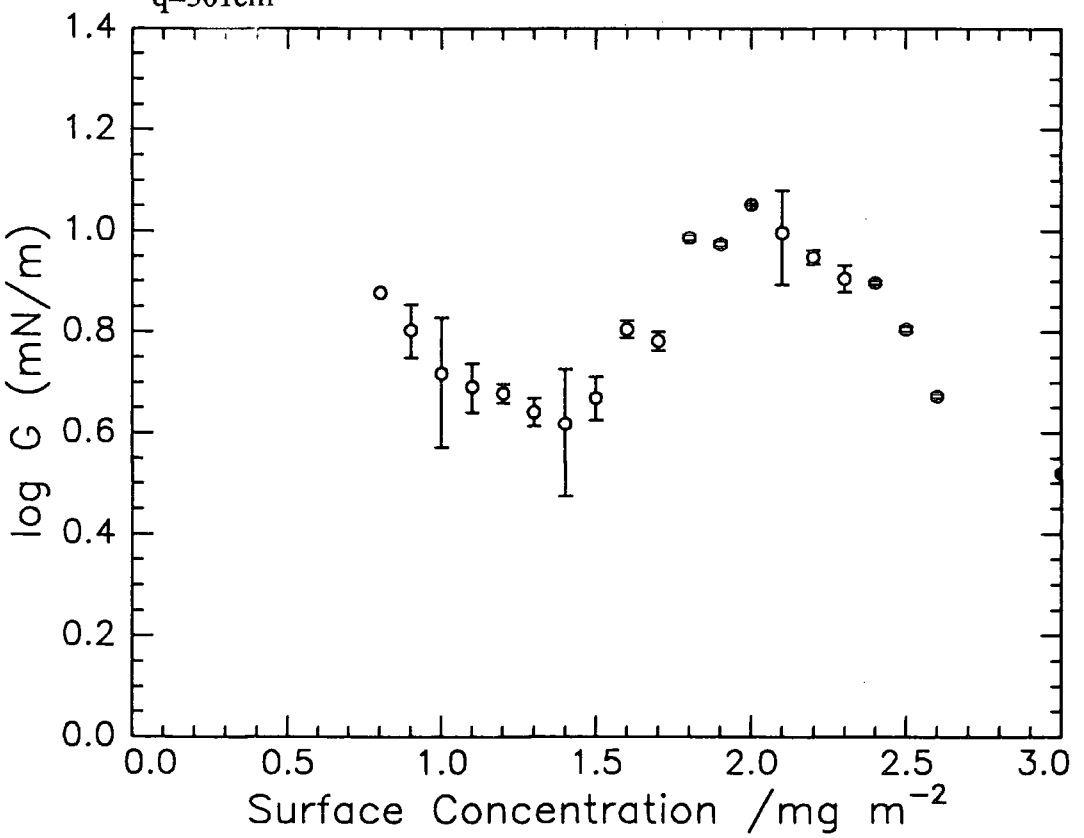

Figure 5.37b) Semi-log plot of G versus surface concentration for q=351cm^{-1}

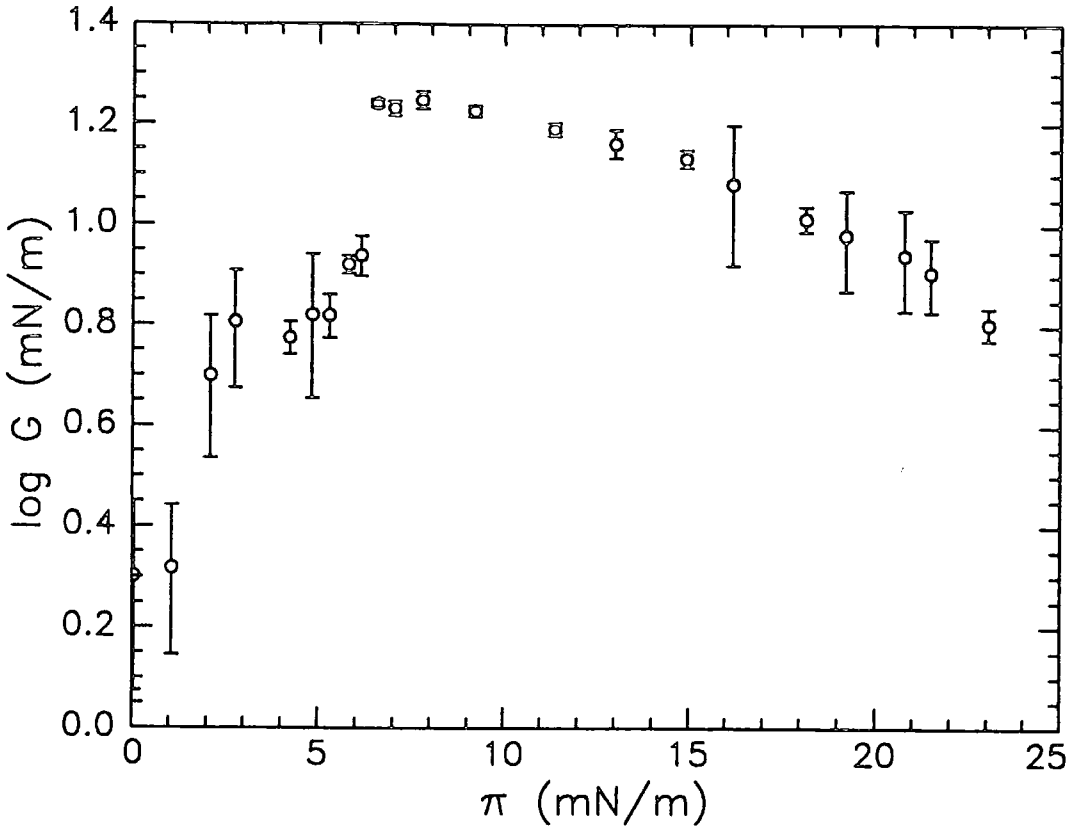

Figure 5.38a) Semi-log plot of G versus surface pressure at q=301cm^{-1}

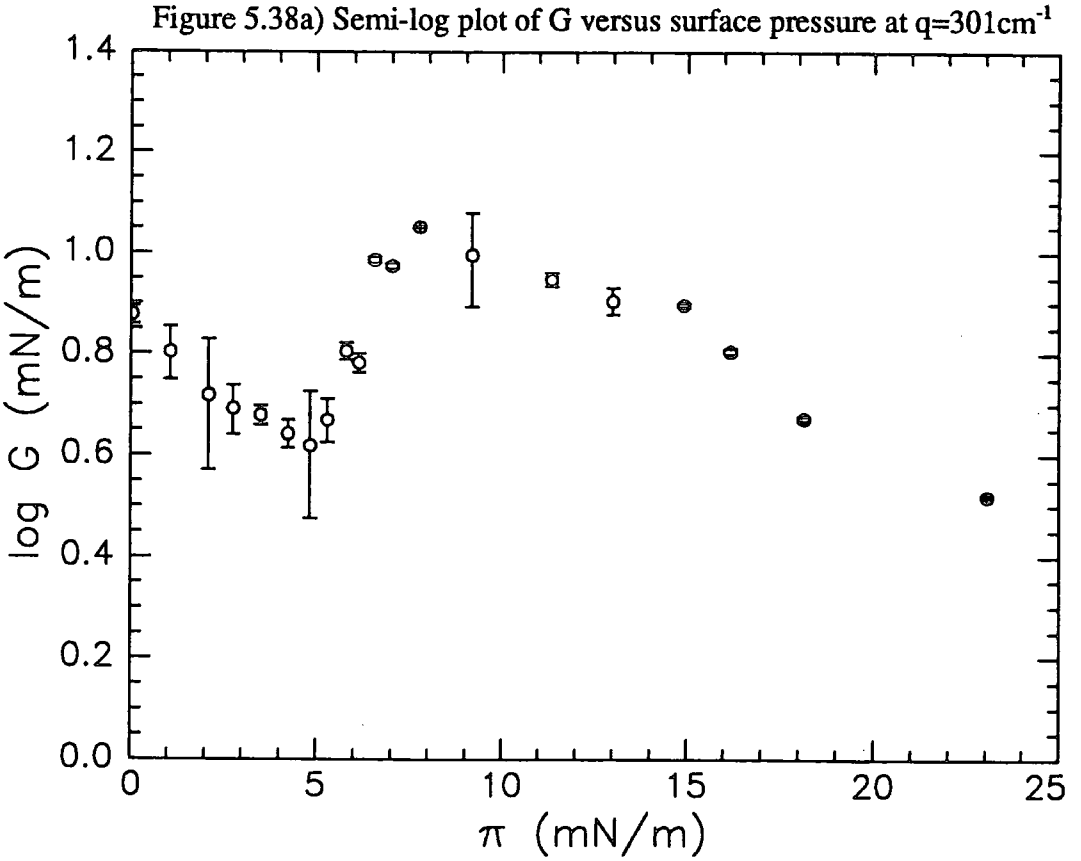

Figure 5.38b) Semi-log plot of G versus surface pressure for q=351cm^{-1}

2.0mg/m^2 (7mN/m) correspond to the transition point in the surface pressure isotherm. These trends in the data could suggest two underlying molecular mechanisms, one due to the PEO segments, the other due to the PMMA segments.

5.3.3 Dilational modulus - ε

The dilational modulus has an indirect influence on the capillary waves due to its effect on the longitudinal waves at the surface. The precision of the measurement of both ε_0 and ε' decreases at higher frequencies due to increased sensitivity in the SQELS technique. The dilational modulus is very susceptible to noise on the experimental correlation functions which increases at higher frequencies.

5.3.3.1 Dilational elastic modulus - ε_0

Values of ε_0 did not show any trends in surface concentration with respect to each q value above 351 cm^{-1}. It can also be seen from figure 5.32a) that no q dependency can be associated with the values of ε_0 at 3.00mg/m^2. For this reason only the variation of ε_0 with surface concentration at q=301 and 351 cm^{-1} is discussed.

Figures 5.24 and 5.26h (q=351 and 301 cm^{-1}) show the dicrepancies between the classical (Γ_s dπ/Γ_s) and light scattering dilational modulus. The values of the classical dilational modulus were calculated by fitting a polynomial to the surface pressure isotherm. Over the surface concentration values obtainable ε_0 greatly exceeds the classical values. The maximum and minimum values of the classical dilational modulus are not seen in the SQELS determined ε_0 values due to the size of the error bars and lower resolution of the data points.

5.3.3.2 Dilational viscosity - ε'

Figure 5.32b) shows that above q=351cm^{-1} (Γ=3.00mg/m^2) the values of ε' over the q range studied are essentially zero. For q=351cm^{-1} the values of ε' follow the trend of the values of γ' but have a greater magnitude. The ε' values obtained for q=301cm^{-1} appear

to be scattered although the intermediate surface concentrations appear to have similar values as the q=351cm^{-1} data.

5.3.3.3 Viscoelastic Relaxation (ε)

Variations with surface coverage

Since the values of ε_0 and ε' did not show any appreciable q dependency then only variations in the surface coverage were used to investigate the viscoelastic properties. Modification of equations 5.1 and 5.2 by replacing γ_0 and γ' by ε_0 and ε' allowed a dilational relaxation time, τ_ε (figures 5.39 and 5.40), and dilational amplitude of relaxation, G_ε (figures 5.41 and 5.42), to be calculated as a function of surface coverage. There was no apparent concentration dependence of the relaxation times. Apart from three points in the range 1.6-1.8mg/m^2 for the data at q=351cm^{-1} the values of τ_ε are in the range 200 to 3000μs with an average value of about 1300μs for q=301cm^{-1} and 440μs for q=351cm^{-1}. These ranges are approximately in agreement with values calculated from the transverse shear modulus data. The values of G_ε have much larger amplitudes than those calculated for the transverse shear modulus data and very approximately follow the same trends, especially for q=351cm^{-1}. Figure 5.39 shows much slower relaxation times at about 1.5mg/m^2 which is different from observed for the γ data where much faster relaxation times are observed.

5.3.4 Molecular mechanisms

No theoretical viscoelastic relaxation mechanisms have yet been developed for surface films, the viscoelastic models already discussed permit some speculation on the molecular mechanisms present. If the neutron reflectometry results are considered then the combination of both the surface organisation and SQELS viscoelastic parameters allow some cumulative discussion. In Chapter 4 the kinematic approximation was applied to the neutron reflectometry data due to the presence of a full set of contrast conditions

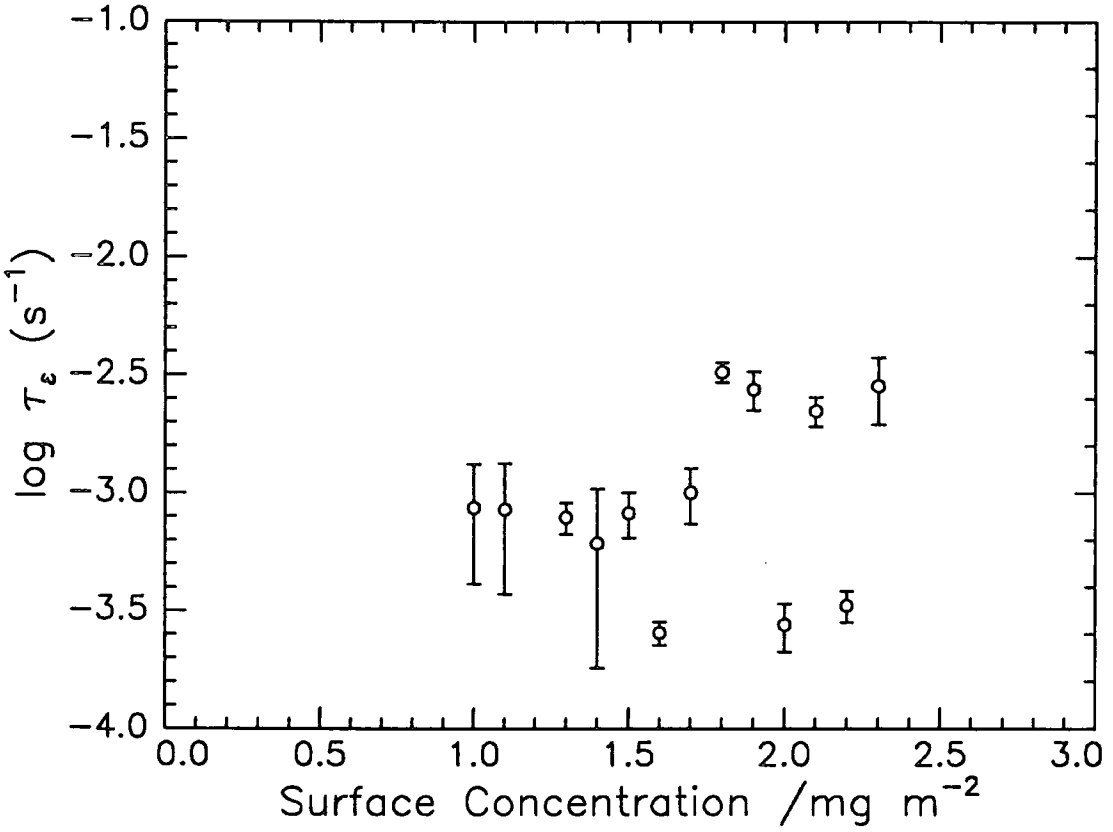

Figure 5.39a) Semi-log plot of τ_ε versus surface concentration for q=301cm^{-1}

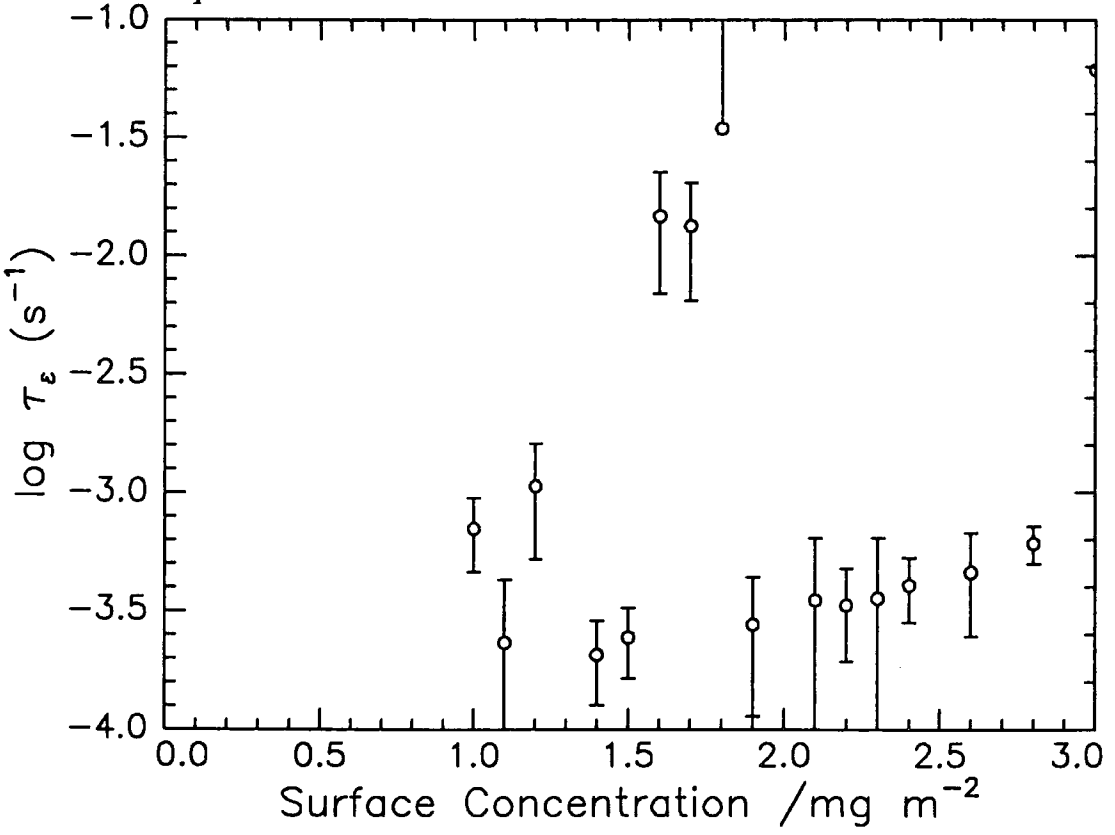

Figure 5.39b) Semi-log plot of τ_ε versus surface concentration for q=351cm^{-1}

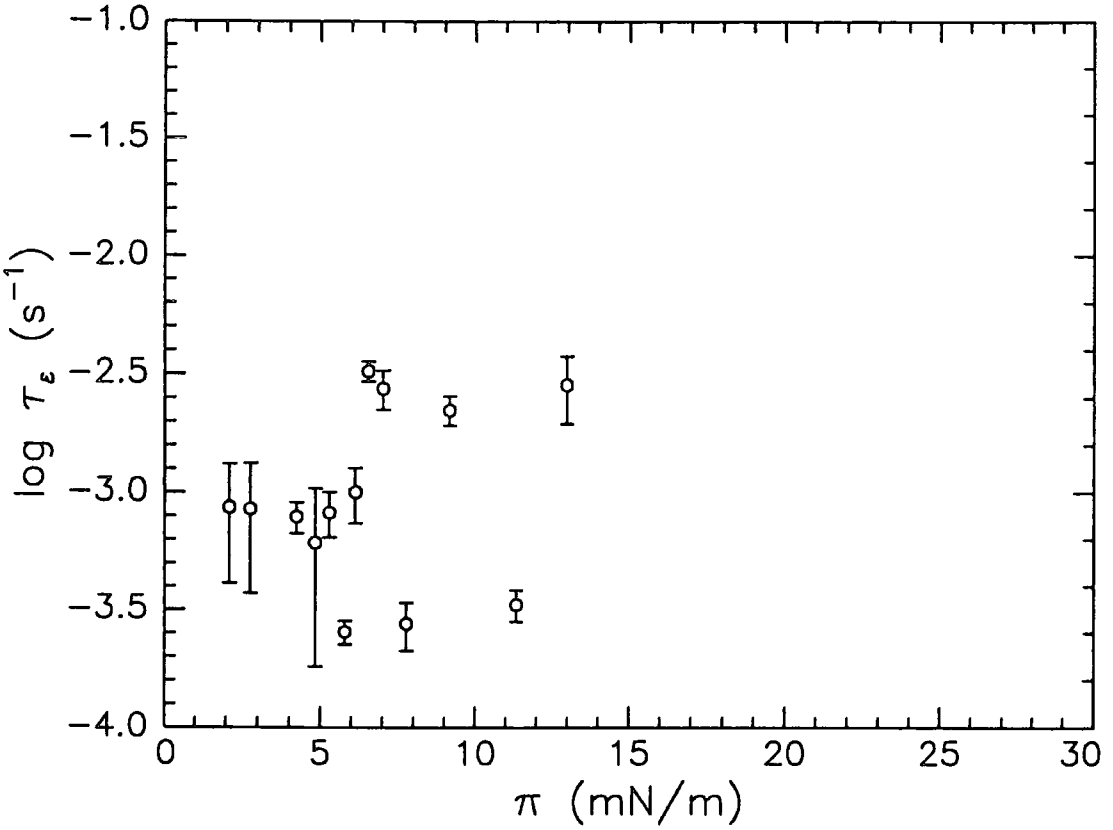

Figure 5.40a) Semi-log plot of τ_ε versus surface pressure forq=301cm^{-1}

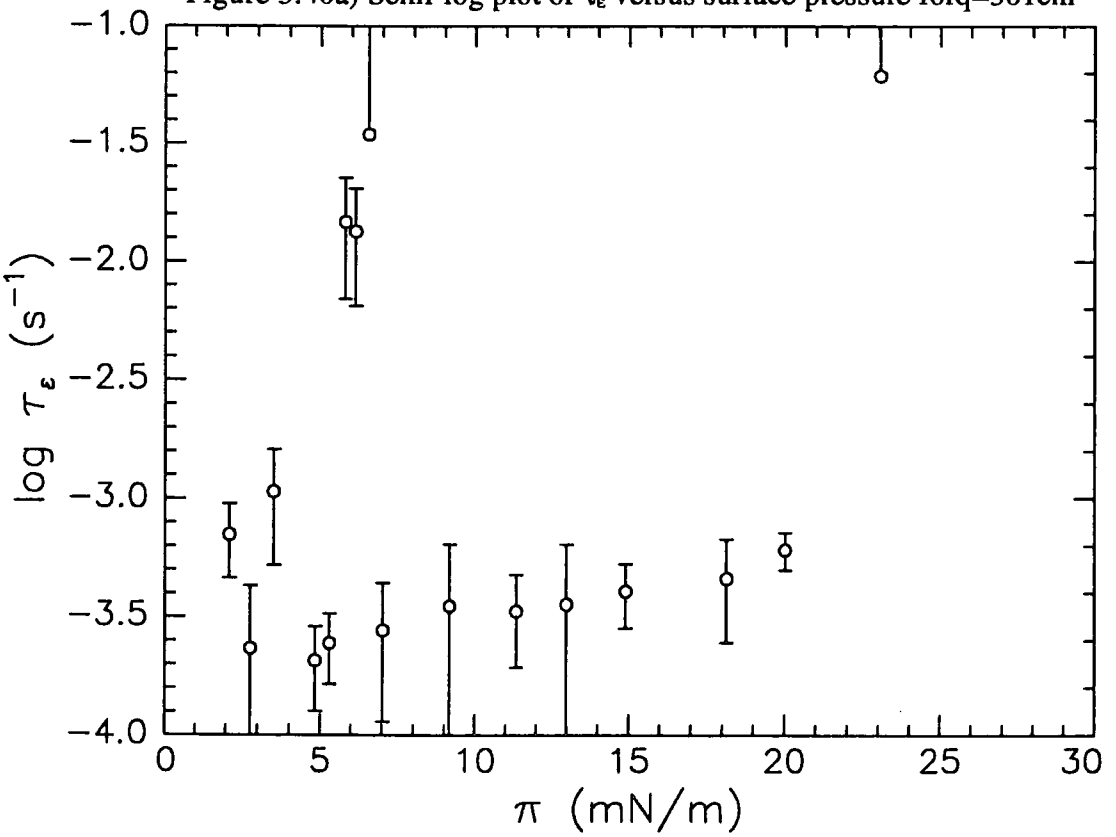

Figure 5.40b) Semi-log plot of τ_ε versus surface pressure for q=351cm^{-1}

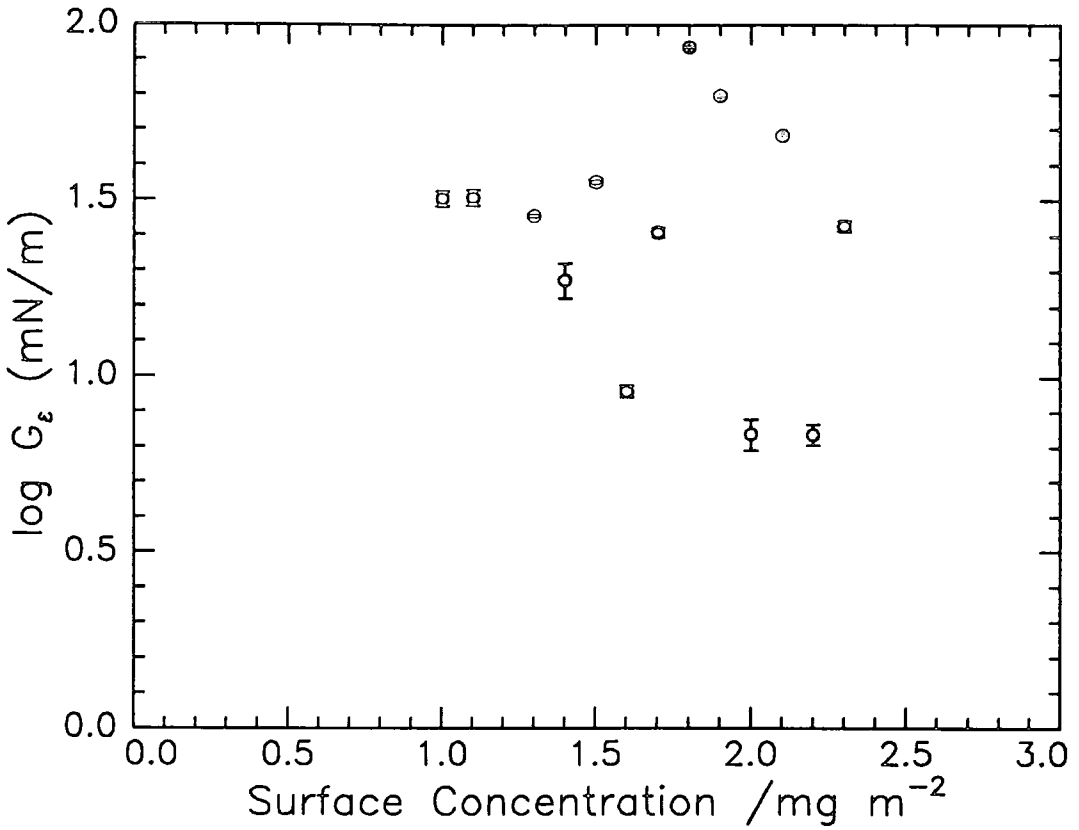

Figure 5.41a) Semi-log plot of G_ε versus surface concentration for q=301cm^{-1}

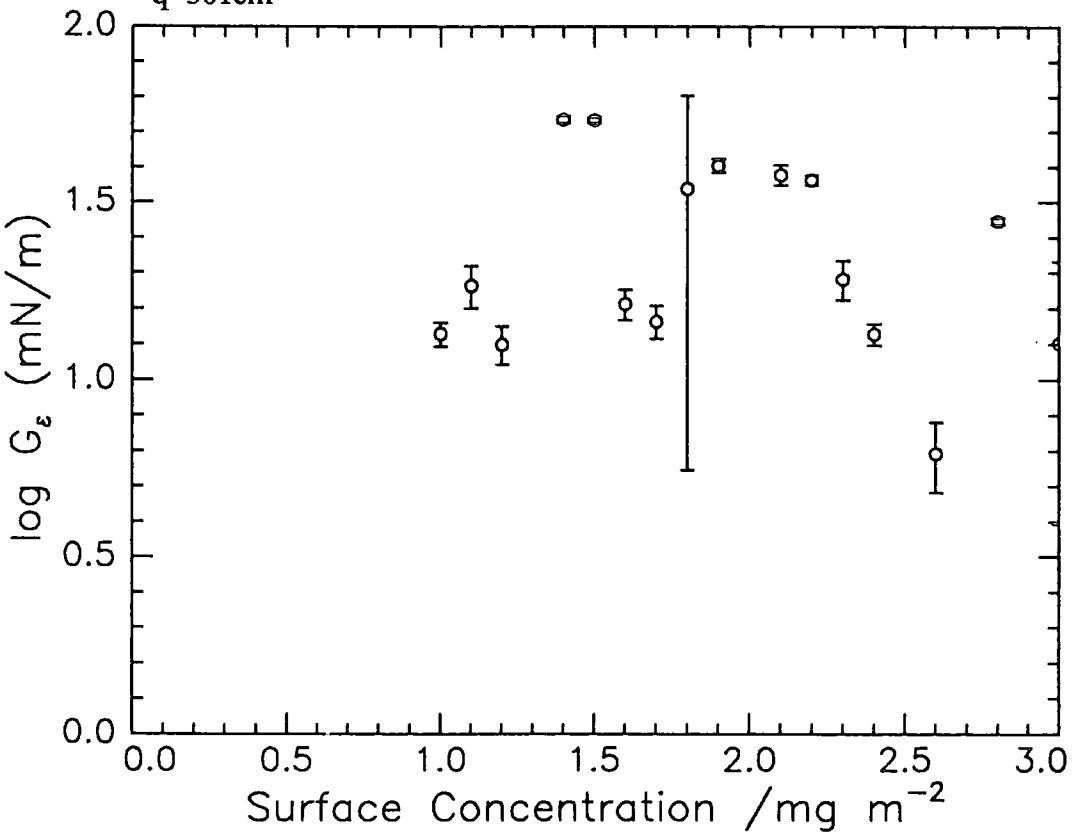

Figure 5.41b) Semi-log plot of G_ε versus surface concentration for q=351cm^{-1}

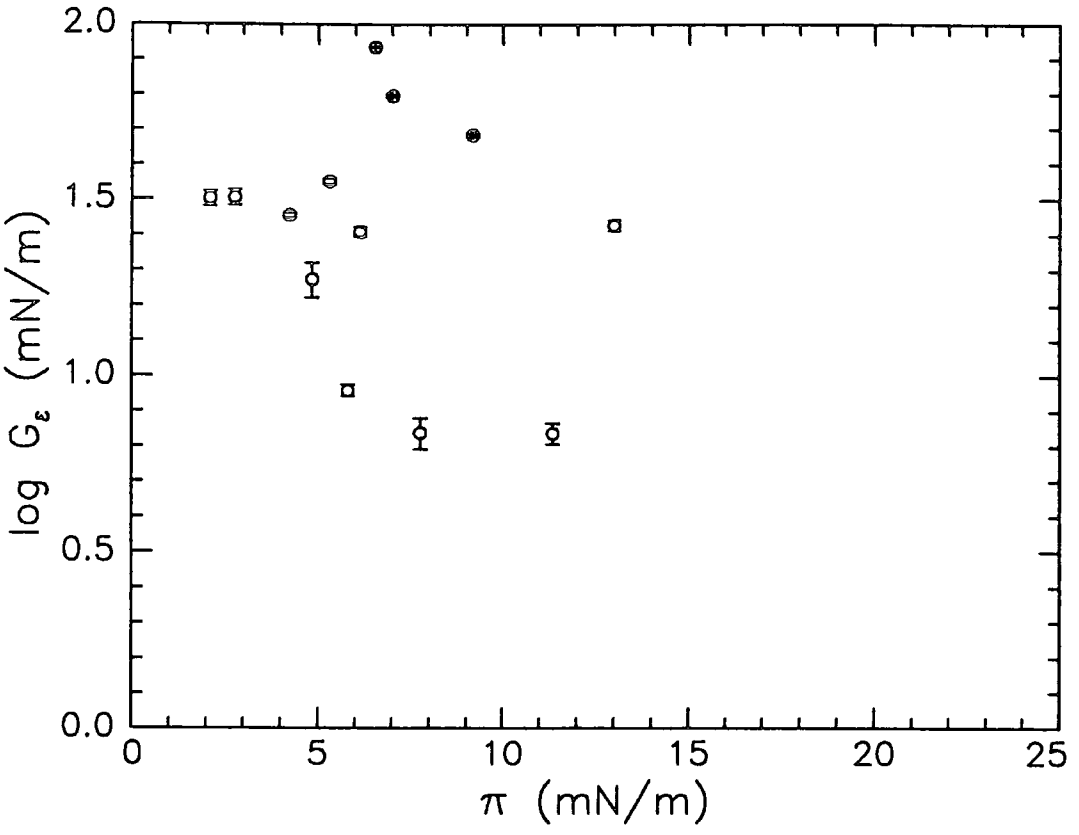

Figure 5.42a) Semi-log plot of G_ε versus surface pressure for q=301cm^{-1}

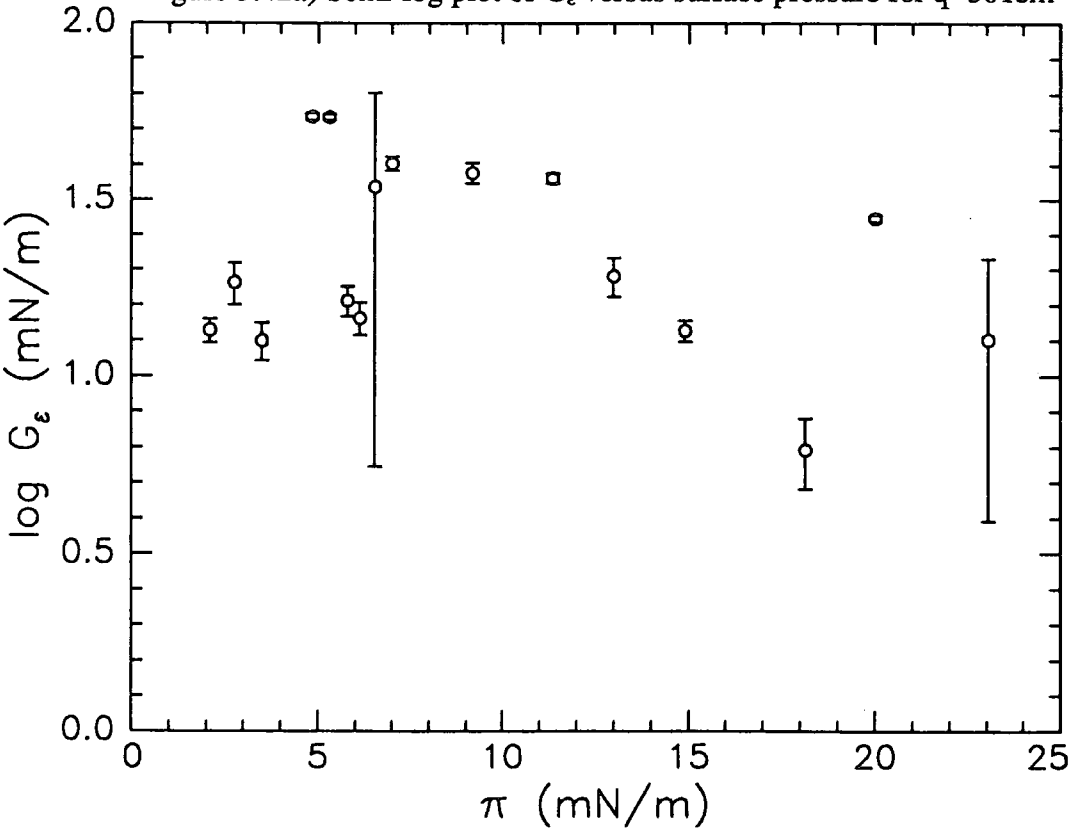

Figure 5.42b) Semi-log plot of G_ε versus surface pressure for q=351cm^{-1}

obtained by selective deuteration. These results were obtained at three specific surface concentrations and it was possible to show that phase separation of the blocks occurred on increasing the surface concentration. At a surface coverage of 0.6mg/m^2 both the PMMA and PEO blocks were uniformly mixed together at the surface. At a surface concentration of 1.2mg/m^2 and beyond phase separation occurred with the PMMA block being confined essentially in the vicinity of the air-water interface and the PEO block dangling in solution. The variation of the relative intensities of the scattered light (I_s) and of the reference beam (I_r) do not have absolute values but variations in their magnitude are informative (equation 5.1). I_s is proportional to the reflectivity R which depends upon the square of the layer thickness d^2. Figures 5.17 and 5.26a) show that the scattered intensities reach a maximum at about 1.5mg/m^2 then decrease which is the opposite of that expected when more material is present at the surface. The value of I_s is seen to decrease over the range of surface concentration noted for the transition in the surface pressure isotherm before increasing again at 2.5mg/m^2. This could be explained by taking into account that after phase separation occurs between the blocks then further compression causes the PEO segments to become more extended into the subphase. The PEO segments are no longer in the immediate surface layer and are diluted by the water subphase thereby decreasing their contribution to the scattered light.

Studies of PMMA homopolymer using SQELS have shown that γ_0 and γ' do not exhibit a frequency dependence, i.e. it behaves as a Voigt-Kelvin solid[3]. For the block copolymer studied here then only the PEO block contributes to the frequency dependent parameters. This could account for the much faster relaxation times in figure 5.35b) at about 1.3mg/m^2. The observed faster relaxation times in the lower concentration range could be accounted for by an increase in the EO-water interaction, allowing the EO blocks to become more mobile. At about 1.2mg/m^2 the phase separated PEO blocks are

mainly in the water subphase and further increases in surface concentration cause greater crowding of these blocks. The consequence of this increased crowding is greater extension of the PEO into the subphase and more 'brushlike' characteristics thereby decreasing the mobility of the chains and resulting in slower relaxation times.

Anomalous static and SQELS surface tension values were noted in the 0 to 0.6mg/m^2 range. These surface tension values are higher than those of pure water and are usually attributed to a desorption mechanism from the monolayer surface[2]. Other results from the SQELS data suggest that this mechanism cannot be true. The damping constants in the low concentration range are always less than the value for pure water, a fact also observed for spread monolayers of syndiotactic PMMA homopolymer[2]. Neither isotactic polymethyl methacrylate or polyethylene oxide homopolymer exhibit these surface phenomena. The overall damping, Γ, is due to contributions from the capillary wave damping, Γ_c, and dilational wave damping, Γ_D. Resonance between these two surface modes occurs when $\varepsilon_0/\gamma_0 \approx 0.16$ and Γ is at a maximum. At q = 301cm^{-1} the the overall damping was over two times that of a clean water surface. At higher q values corresponding to higher frequencies this ratio decreased. Decreases in Γ_c occur due to increases in Γ_D which are influenced by ε'. Therefore more than one high frequency relaxation process must be present. Two relaxation processes involving each of the transverse and dilational relaxation times are possible if they involve departure of the PEO from a 2-D system by chain looping and relaxation, penetrating to different depths into the water subphase. Neutron reflectivity suggest that on increasing the surface concentration to higher values causes water to be squeezed out of the layer and the ethylene oxide segment-water interaction increases until the blocks separate, the polyethylene oxide block becoming immersed mostly in the water subphase and the polymethyl methacrylate block confined at the vicinity of the air-water interface. The fact

that the γ' values decrease in figure 5.23 over the range 0 to 0.8mg/m^2 may be indicative of the film containing increasing amounts of water, i.e increased EO-water interactions. At higher surface concentrations (i.e. $\Gamma > 0.8$mg/m^2) the copolymer molecules interact to a greater extent thereby increasing the transverse shear viscosity. The similarity in the magnitude of the transverse and dilational relaxation times back up the possibility of these interactions.

The diblock copolymer exhibited combinations of features of its constituent components which can be compared with the work of Yu et al[6] for PEO and PMMA homopolymers. PEO homopolymer had a characteristic sharp damping peak at about 0.3mg/m^2 while the PMMA homopolymer damping reached its maximum at about 0.5mg/m^2 thereafter plateauing out. For the PEO homopolymer the dilational elastic modulus (ε_0) and dilational viscosity (ε') reached their maximum values at 0.4 and 0.5mg/m^2. PMMA homopolymer formed a highly viscoelastic monolayer having large ε_0 values which were approximately 70mN/m in magnitude and much larger than those reported for PEO. The PMMA/PEO diblock copolymer therefore follows the same trends as the PEO homopolymer, the ε_0 and ε' values both passing through peak values. Although the ε_0 maximum is at about 1.5mg/m^2, its magnitude is less than that of PMMA but much greater than that of PEO. Yu et al[6] found that the SQELS data for PMMA had magnitudes of ε_0 which greatly exceeded those derived from the classical surface pressure isotherm, while the data for the PEO had excellent agreement. The fact that the SQELS ε_0 data has a similar variation as PEO and magnitudes greater than the classical data does not mean that the viscoelasticity is necessarily a combination of that from the two homopolymers but is more likely to be a cumulative effect resulting from the organisation of the copolymer at the surface.

References

1. MacDonald, R.C., Simon, S.A., *Proc. Nat. Acad. Sci. USA*, 1987, **84**, 4089.

2. Henderson, J.A., Richards, R.W., Penfold, J., Thomas, R.K., *Macromolecules*, 1993, **26**, 65

3. Taylor, M.R., unpublished results

4. Earnshaw, J.C., McGivern, R.C., Winch, P.J., *J. Phys. France*, 1988, **49**, 1271.

5. Davidson, D.W., Cole, R.H., *J. Chem. Phys.*, 1950, **18**, 1417.

6. Kawaguchi, M., Sauer, B.B., Yu, H., *Macromolecules*, 1989, **22**, 1735.

CHAPTER 6 - ANCILLARY TECHNIQUES

This chapter describes other techniques relevant to the work of the previous chapters but which did not warrant a chapter of their own. Ellipsometric measurements provided additional information to the neutron reflectometry results of Chapter 4 about the layer thickness of the spread monolayers. Light scattering studies of methanol solutions of the copolymers allowed an investigation of the thermodynamics of micellization and of the corresponding association mechanism present.

6.1 ELLIPSOMETRY

6.1.1 Results

Ellipsometry was performed on a 50:50 molar MMA/EO diblock copolymer spread at the air/water interface using the ellipsometer described in Chapter 2. The ellipsometric measurements allowed the angles Δ and ψ to be obtained as a function of energy (eV) for different surface concentrations (figures 6.1 and 6.2). By selecting one energy value above the Brewster angle, identified by the minimum in ψ, then the statistical average values of Δ and ψ were calculated over 100 measurements. The values of Δ and ψ on a clean water surface were also measured at the same energy and the differences between a monolayer covered and clean water surface, $\delta\Delta$ and $\delta\psi$, were then obtained. The results are therefore presented in terms of the change in ellipsometric phase angle, $\delta\Delta$, change in amplitude attenuation, $\Delta\psi$, and surface pressure, Π, as a function of surface concentration, Γ. Figures 6.3 and 6.4 show the variation of $\delta\Delta$ at 2.9eV (λ = 4279Å) and 3.8eV (λ = 3265Å) respectively, the different energies due to measurements taken at two different incident angles of 53.20° and 53.40°. Figure 6.3 shows that $\delta\Delta$ rises monotonically as the surface pressure increases and the rate of increase drops off sharply at about 0.8mg/m^2 and the values seem to approach a plateau of about 120°, while figure 6.4 shows that the values of $\delta\Delta$ reach a plateau at about 1.50mg/m^2 of 80°. These

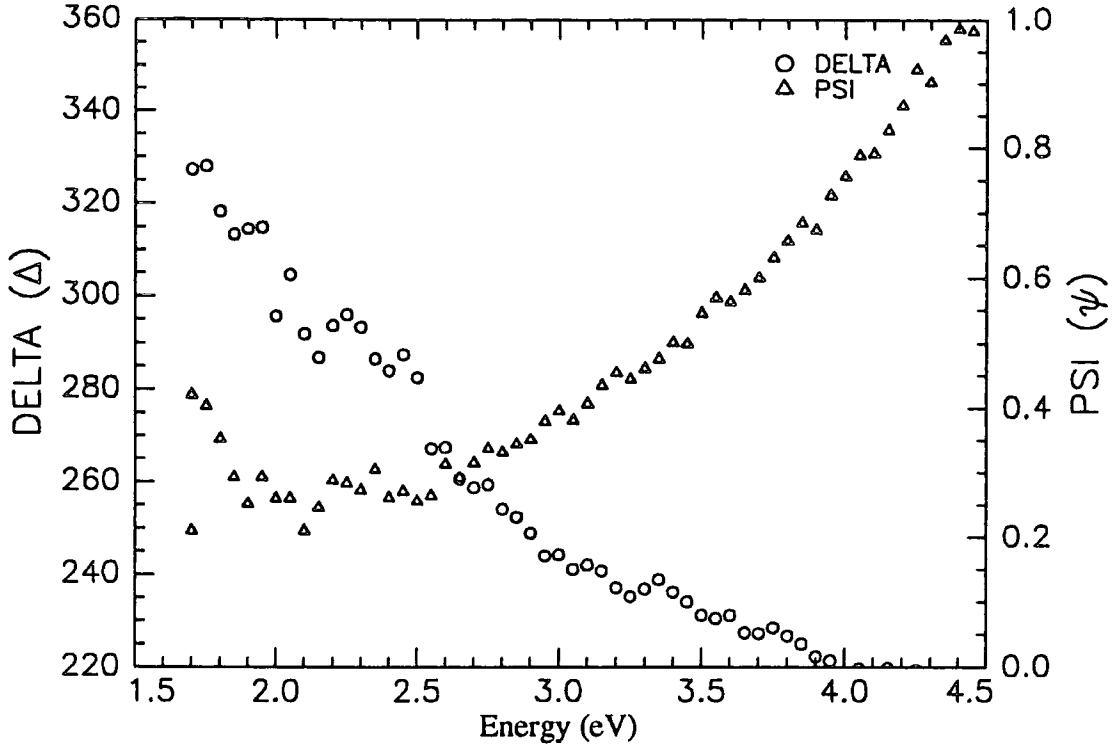

Figure 6.1 Ellipsometric angles Δ and ψ as a function of energy (eV) taken at 2.00mg/m^2 surface concentration and incident angle of 53.20°. Statistical averages over 100 measurements taken at 2.9eV.

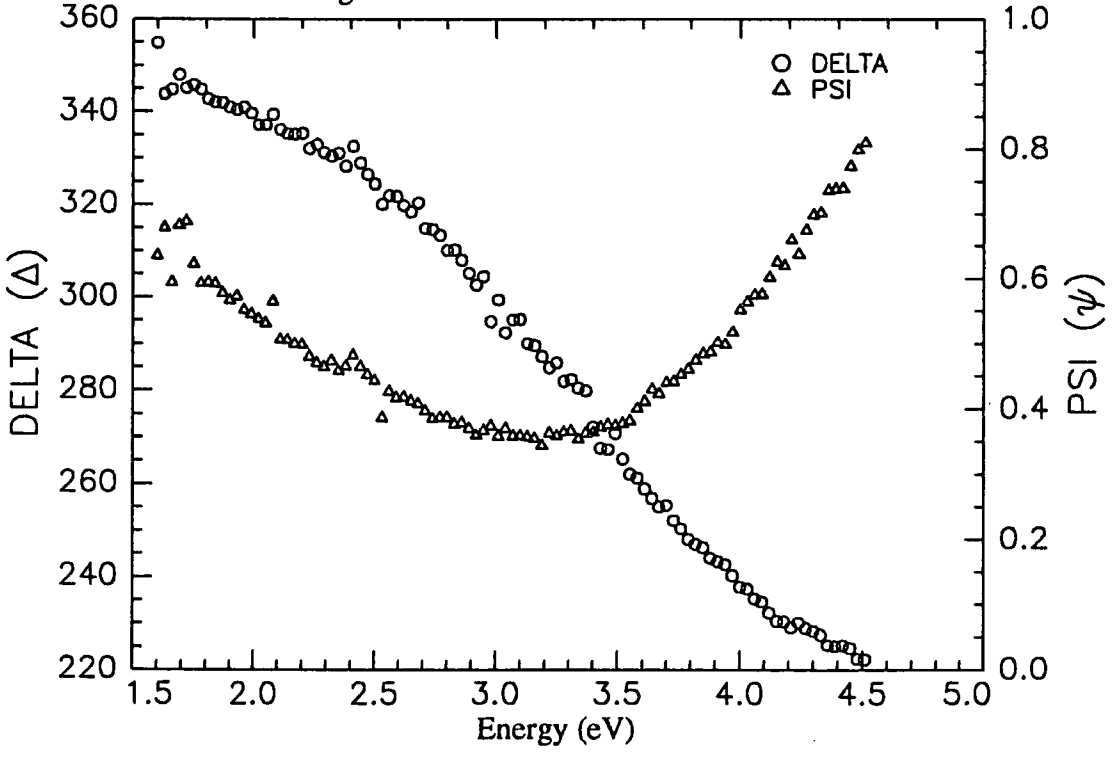

Figure 6.2 Ellipsometric angles Δ and ψ as a function of energy (eV) taken at 2.00mg/m^2 surface concentration and incident angle of 53.40° Statistical averages over 100 measurements taken at 3.8eV.

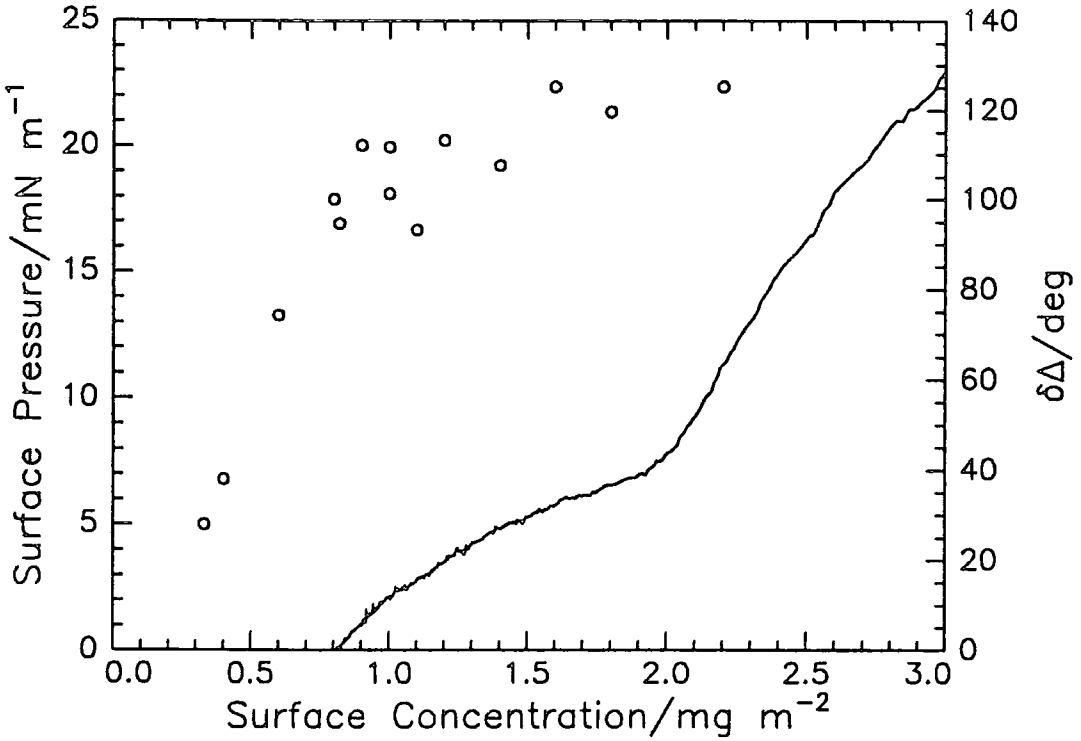

Figure 6.3 Surface pressure (-) and the change in ellipsometric phase angle δΔ (o) versus surface concentration at 2.9eV (λ = 4279Å)

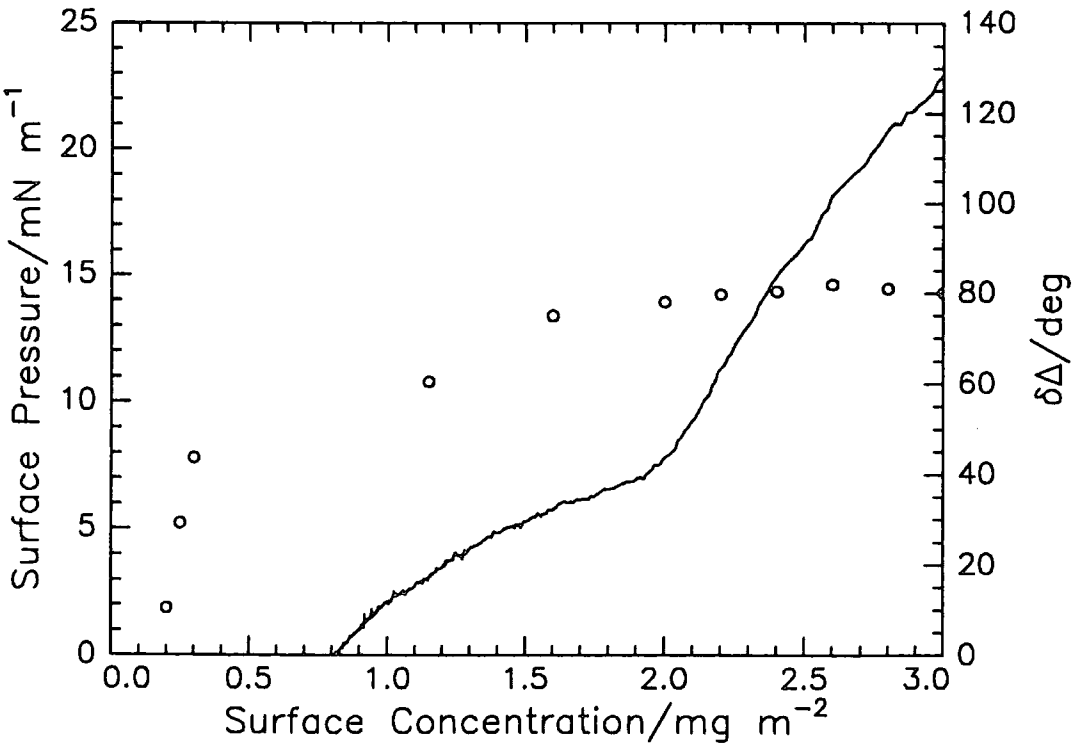

Figure 6.4 Surface pressure (-) and the change in ellipsometric phase angle δΔ (o) versus surface concentration at 3.8eV (λ = 3265Å)

increases in $\delta\Delta$ reflect changes in the monolayer since the value of $\delta\Delta$ is directly proportional to the layer thickness. Figures 6.5 and 6.6 show the variation of $\delta\psi$ corresponding to the same ellipsometric measurements of figures 6.3 and 6.4. It can be seen that $\delta\psi$ increases monotonically with surface concentration but the ranges over which this increase occurs are small being 0° to 0.30° and -0.3° to 0.2° for measurements at 2.9eV and 3.8eV respectively. An iteration method involving the Drude equation (equation 1.4.1) was used in an attempt to obtain the thickness and refractive index, which should have reproduced the measured ellipsometric angles of Δ and ψ. The values of $\delta\psi$ were significantly smaller than $\delta\Delta$ and it was not possible to obtain solutions for the Δ and ψ data.

An alternative method of data analysis was undertaken using computer software supplied with the Jobin-Yvon Uvisel ellipsometer. This software allowed calculation of the spectroscopic dependence of the ellipsometric angles Δ, ψ and the pseudo-dielectric function $\langle\varepsilon\rangle$ of a reflecting multilayer system. The program assumed that the substrate and each of the layers consisted of three material components. The effective dielectric function (EDF) of the substrate and the layers were then calculated using a Maxwell-Garnett (MG) model. This model describes a material consisting of inclusions which are completely surrounded by the material. In this model the volume fractions of f_1 and f_2 of inclusions 1 and 2 had to satisfy the conditions that $f_1 \ll 1$ and $f_2 \ll 1$. The dielectric functions (DF) were then approximated using the classical dispersion model

$$\varepsilon = \varepsilon_\infty + \frac{(\varepsilon_s - \varepsilon_\infty)}{\omega_t^2 - \omega^2 + i\Gamma_0\omega} \qquad (6.1)$$

where ω = energy in eV, ε_∞ and ε_s are high frequency and static dielectric constants respectively, Γ_0 is a damping factor, and ω_t is the transverse energy expressed in eV. A layer consisting of a PMMA volume fraction of 0.95 was assumed for all surface

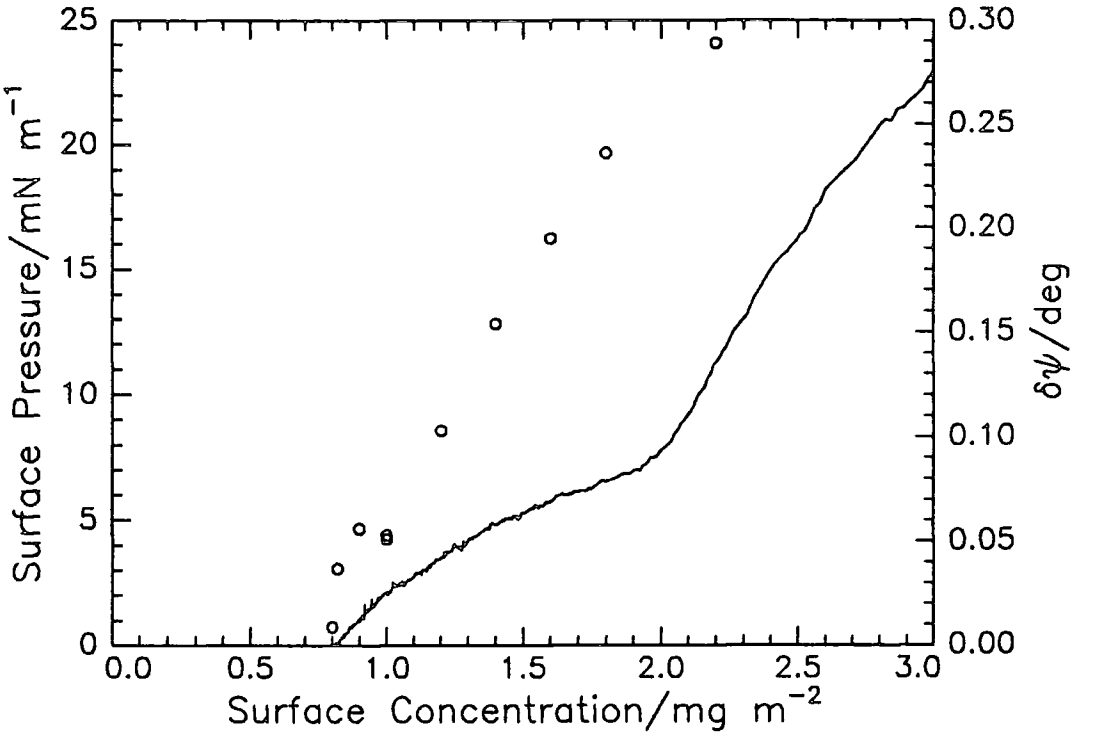

Figure 6.5 Surface pressure (-) and the change in amplitude attenuation $\delta\psi$ (o) versus surface concentration at 2.9eV (λ = 4279Å)

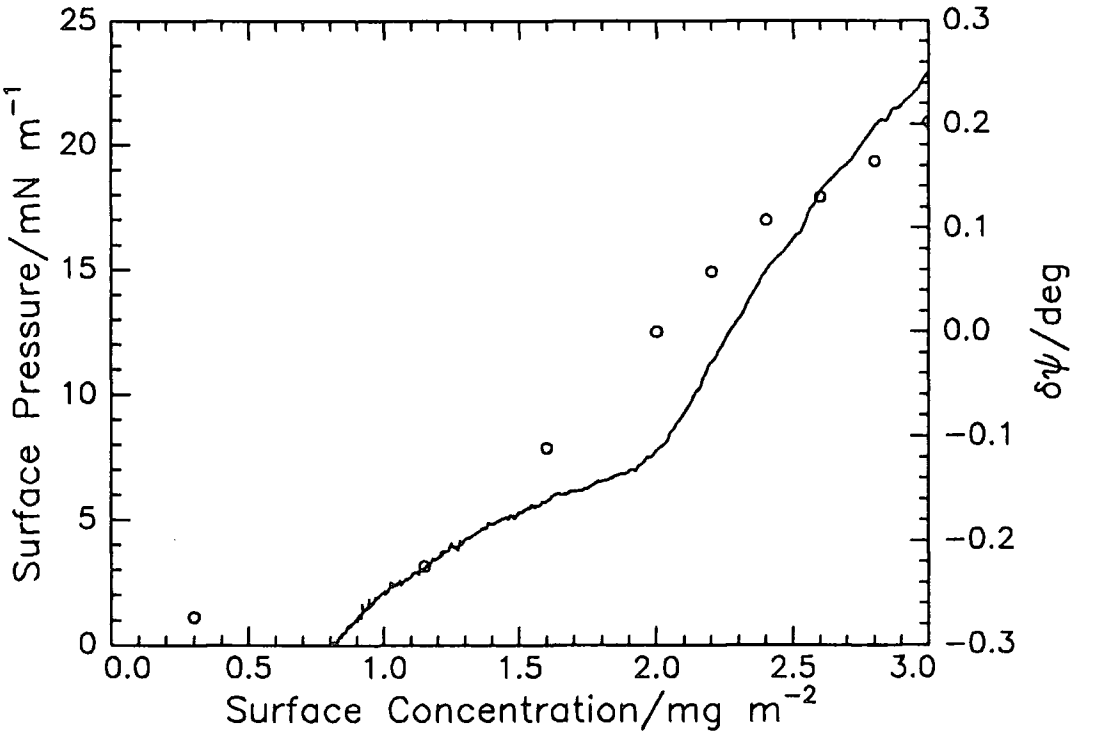

Figure 6.6 Surface pressure (-) and the change in amplitude attenuation $\delta\psi$ (o) versus surface concentration at 3.8eV (λ = 3265Å)

concentrations, inferring a constant refractive index, and the film thickness estimated at each surface concentration (figure 6.7). The layer thickness for some of the low concentration data are missing due to the scatter in the ellipsometry data caused by the associated higher signal to noise ratio. It can be seen that the layer thickness increased and then remained constant over the range of surface concentrations used in accordance with the observed changes in $\delta\Delta$.

6.1.2 Discussion

For monolayers on a liquid surface it is impossible to obtain an unambiguous ellipsometric characterisation because one ellipsometric measurement parameter is affected by both the layer thickness, d, and the refractive index, n. Since the observed increases in $\delta\Delta$ are directly proportional to the layer thickness then figures 6.3 and 6.4 suggest that the layer thickness increases rapidly before reaching a plateau at about 1.00mg/m^2. These observations agree with the neutron reflectometry results of Chapter 4 where a clear increase in the layer thickness occurs, rising from 14Å at 0.6mg/m^2 to 27Å at 1.2mg/m^2. This doubling of the total layer thickness is mirrored in the ellipsometry results over the same surface concentration range (figure 6.7) although the values are underestimated by about 50%. This under estimation is most likely due to a constant refractive index being used over the surface concentration range studied which was a weighted average of the indices of PMMA and water and did not take into account the presence of PEO in the surface layer. However, these layer thicknesses are comparable with those of Kawaguchi[1] and Sauer[2], who took full surface coverage as being the point where surface pressure becomes constant, and calculated layer thicknesses of 12 and 14Å respectively. In the same study Kawaguchi investigated binary mixed films of 0.64/0.36 and 0.78/0.22 mole ratios PMMA/PEO and calculated layer thicknesses of 15 and 13Å respectively. The small amount of PEO in both mixtures meant that it was not

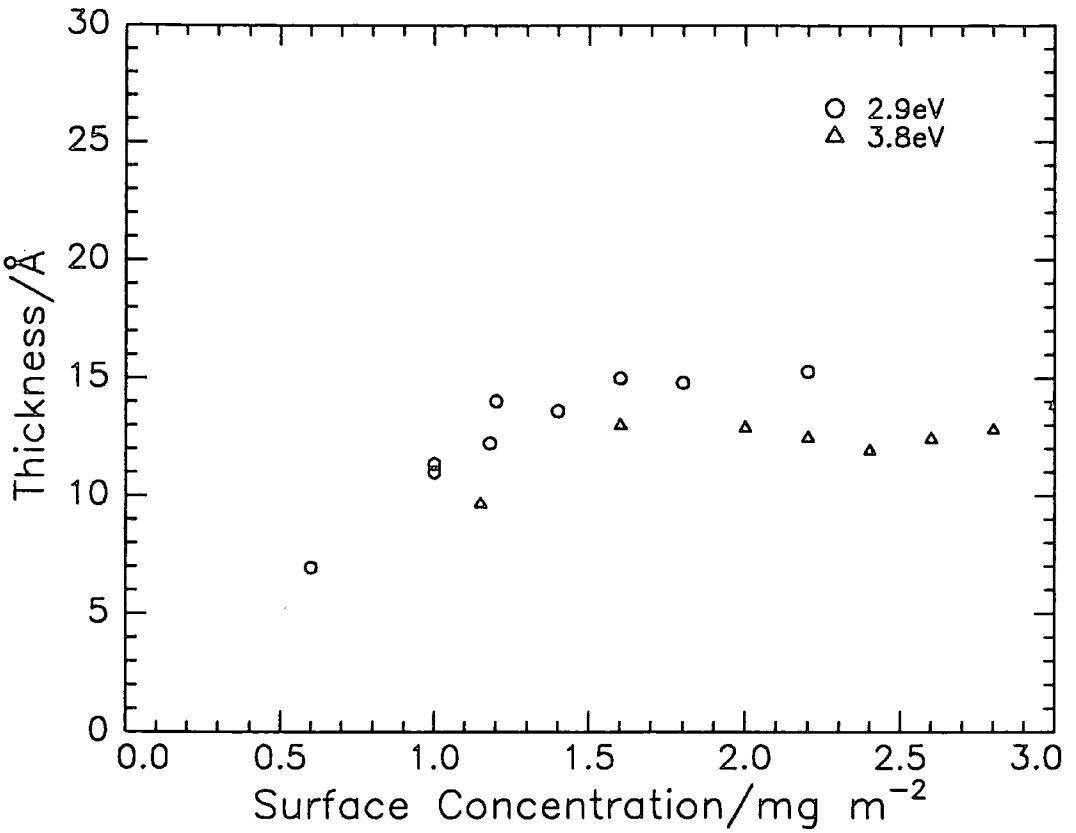

Figure 6.7 Layer thickness as a function of surface concentration

expected to desorb from the interface. The layer thicknesses of these PMMA/PEO binary mixed films are therefore comparable with the 0.50/0.50 mole ratio PMMA/PEO diblock copolymers studied having a layer thickness of about 13-15Å at full surface coverage.

6.2 MICELLIZATION IN SOLUTION

The micellization of an MMA/EO diblock copolymer in solution was investigated using light scattering, the main objective being an examination of the hydrodynamic dimensions of the copolymers in solution as a function of temperature. This work was important since it has been reported that surface micelles form when block polyelectrolytes are spread at the air/water interface[3-7] and aggregation of monolayers of polystyrene monomolecular particles have been noted[8]. Studies such as Transmission Electron Microscopy (TEM) of the corresponding Langmuir-Blodgett films are necessary to show the presence of surface micelles, neither of these techniques were available. However, an investigation of the copolymers in solution was thought to be an interesting prospect.

All the copolymers listed in Table 2.1 were insoluble in water although varying degrees of solubility existed when solutions of the copolymers were prepared from methanol. Light scattering studies were attempted on the 50:50 (BR20), 35:65 (BR22) and 30:70 (BR29) MMA:EO mole composition copolymer dispersions in methanol. The 50:50 molar composition copolymers (BR20 and BR27) formed hazy solutions, those having less than 50% PEO (BR26) were insoluble, while those having 65% or more PEO (BR22 and BR29) were soluble. Due to the temperature range accessible in the experiments, only the 50:50 (BR20) copolymer was used. This copolymer was used to investigate both the thermodynamics of micellization and the variation of the hydrodynamic radius with temperature.

6.2.1 Results

6.2.1.1 Thermodynamics of Micellization

It has been shown that for investigations of the thermodynamics of micellization that the best experimental protocol is to measure scattered light as a function of temperature at a fixed solution concentration[9]. The critical micelle temperature (cmt) is defined as the point where the presence of micelles can just be detected. A typical plot of the dependence of the scattered intensity on temperature is shown in figure 6.8. The low end of the temperature range has a high scattering intensity due to the presence of micelles, which falls off sharply as the temperature is increased until T=40°C where the copolymer exists in its unassociated state. The temperature where the scattered light intensity is constant is taken as the cmt of the solution. Changes in scattered light intensity reflect the reduction in intermolecular interactions with increasing temperature. The sudden decrease in intensity with increasing temperature is due to a decrease of the micelle concentration which occurs until a temperature is reached where the copolymer is in its unassociated state.

The cmt was determined for several other solution concentrations of the same copolymer. For the concentration range studied, 0.075 to 0.25mg/mL, the same trends in the data were noted. It was not possible to obtain cmt value for solution concentrations below 0.075mg/mL, which was thought to be due to these solutions being below the critical micelle concentration (cmc), while solution concentrations above 0.25mg/mL scattered light to a high magnitude which flooded the photomultiplier tube.

Figure 6.9 shows a plot of ln c versus $(cmt)^{-1}$ which is linear within experimental error over the solution range studied. The thermodynamic data for the micelle formation were calculated by linear least squares fitting the data and using equations (1.6.3 to 1.6.5) with T=40°C, the parameters ΔG°, ΔH° and $-T\Delta S^\circ$ are shown in Table 6.1 as per mole of

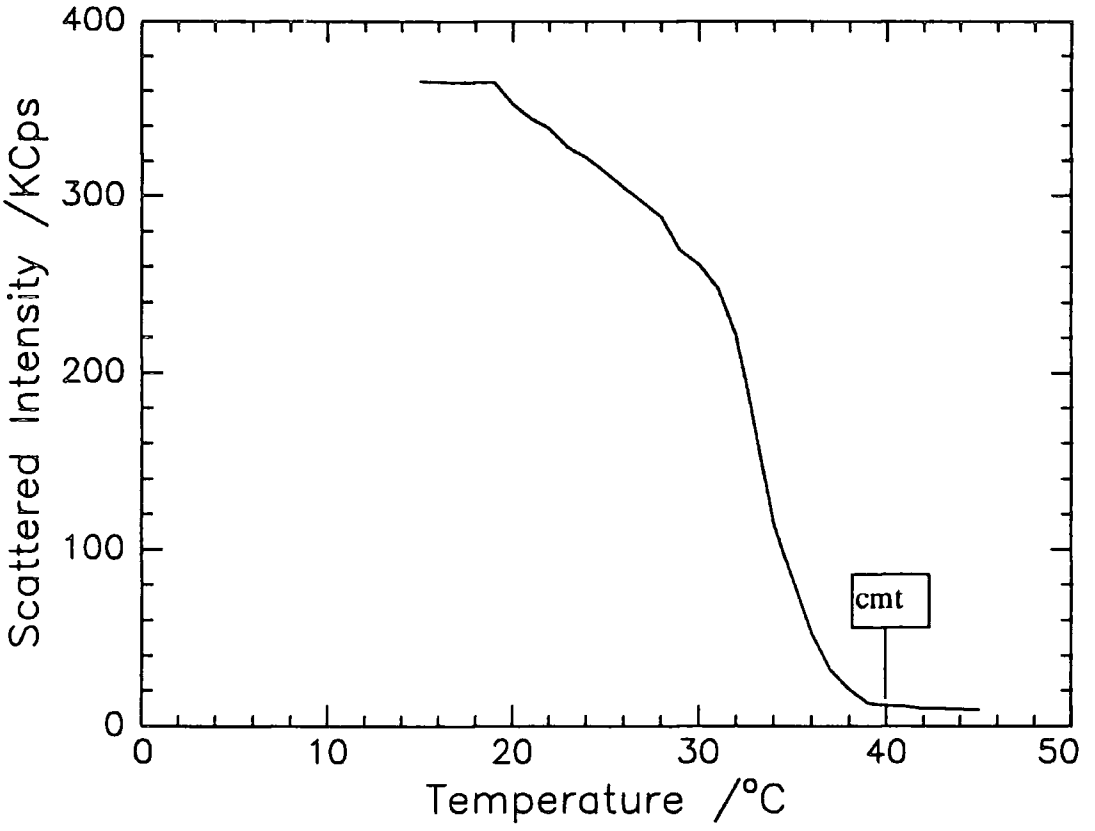

Figure 6.8 Scattered Intensity versus temperature at 0.10mg/mL solution concentraton

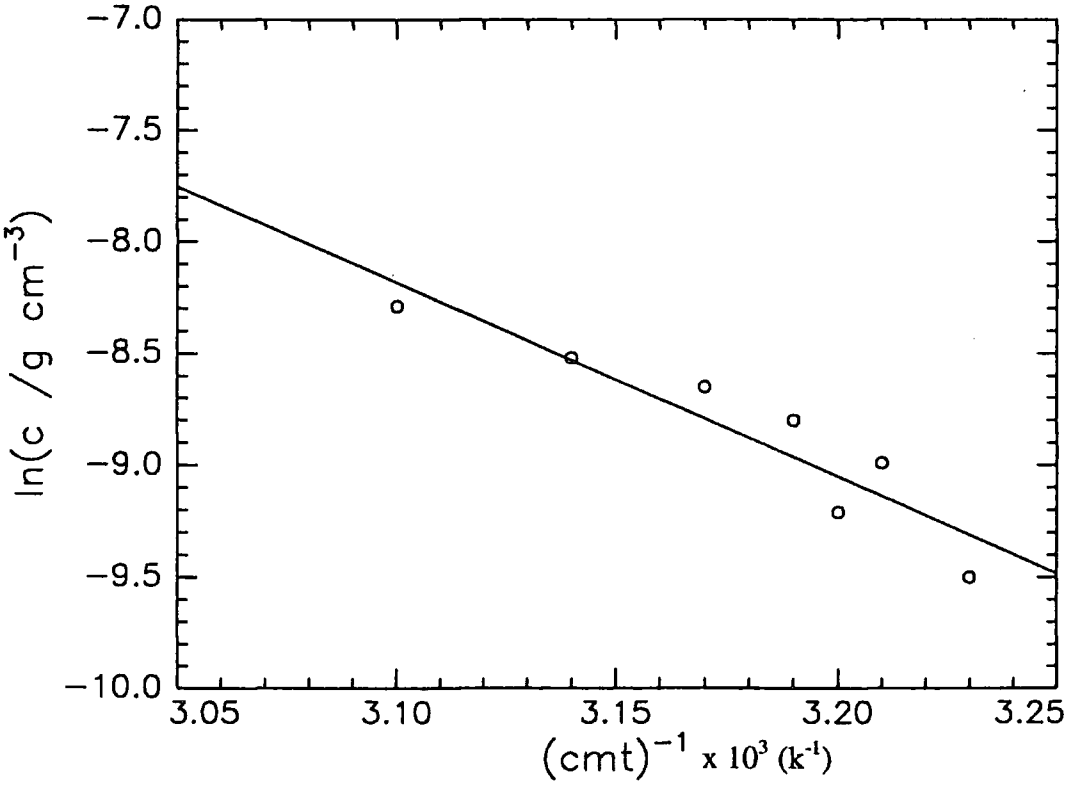

Figure 6.9 Plot of the logarithm of the solution concentration against the reciprocal of the critical micelle temperature. Line (-) shows linear least squares fit to the data.

Copolymer	ΔG° = RT ln(cmt) (kJ mol^{-1})(1)	ΔH° = $\Delta H \approx R d\ln(cmt)/dT^{-1}$ (kJ mol^{-1})(2)	$-T\Delta S^\circ$ = $(\Delta G^0 - \Delta H^0)$ (kJ mol^{-1})
BR20	-48.61KJ mol^{-1}	-72.05KJ mol^{-1}	23.44KJ mol^{-1}

(1) intercept = ln (cmt) = -8.66 (2) slope = $d\ln(cmt)/dT^{-1}$ = 18.66

Table 6.1 Thermodynamic data for the block copolymer

copolymer chain. The standard states for micelles and chains are states with ideally dilute solution behaviour and a concentration of 1mol dm^{-3}.

6.2.1.2 Variation of hydrodynamic radius with temperature

The diffusion coefficients (D) of the copolymer solutions in the range 0.075 to 0.25mg/mL were measured over the temperature range 15 to 40°C. Plots of D as a function of temperature are shown in figure 6.10, the larger values of D at high temperature being due to the effect of temperature on the equilibrium between micelles and free chains. These curves provided the basis for the plots of D as a function of solution concentration (figure 6.11) which were linear. By extrapolating the data to infinite dilution it was possible to obtain D_0, where D_0 is the z-average diffusion coefficient, for all the temperatures studied. It can be seen that at 35 and 40°C the slope becomes more negative as the micelles dissociate to unimers, the solvent changing from good to poor as PEO-methanol interactions are replaced by PMMA-methanol interactions. The values of D_0 were used to calculate the corresponding hydrodynamic radii (R_h) of the micelles at each temperature value using the Stokes-Einstein equation (equation 1.6.9). Both D_0 and R_h are listed in Table 6.2 over the experimental temperature range, while figure 6.12 shows a plot of R_h as a function of temperature.

6.2.2 Discussion

6.2.2.1 Thermodynamics of Micellization

Table 6.1 shows that the standard enthalpy of micellization, ΔH°, is large and negative, the standard entropy contribution, $-T\Delta S$, to the standard Gibbs energy of micellization is positive and therefore unfavourable to micelle formation. These thermodynamic values are comparable with literature values for block copolymers of similar molecular weight[10-12]. This thermodynamic behaviour of the micelle formation is in contrast to that observed for amphiphilic molecules in aqueous media[13,14]. A large proportion of $-T\Delta S^\circ$ in the

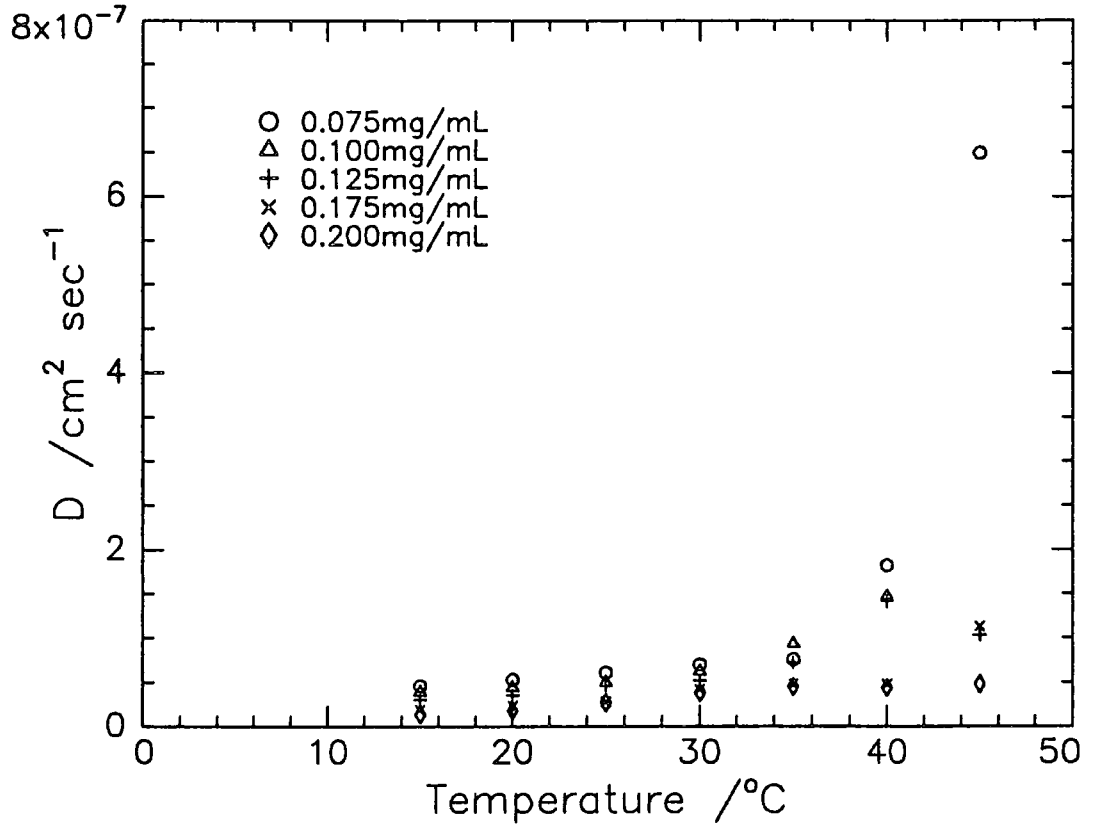

Figure 6.10 Diffusion coefficient as a function of temperature

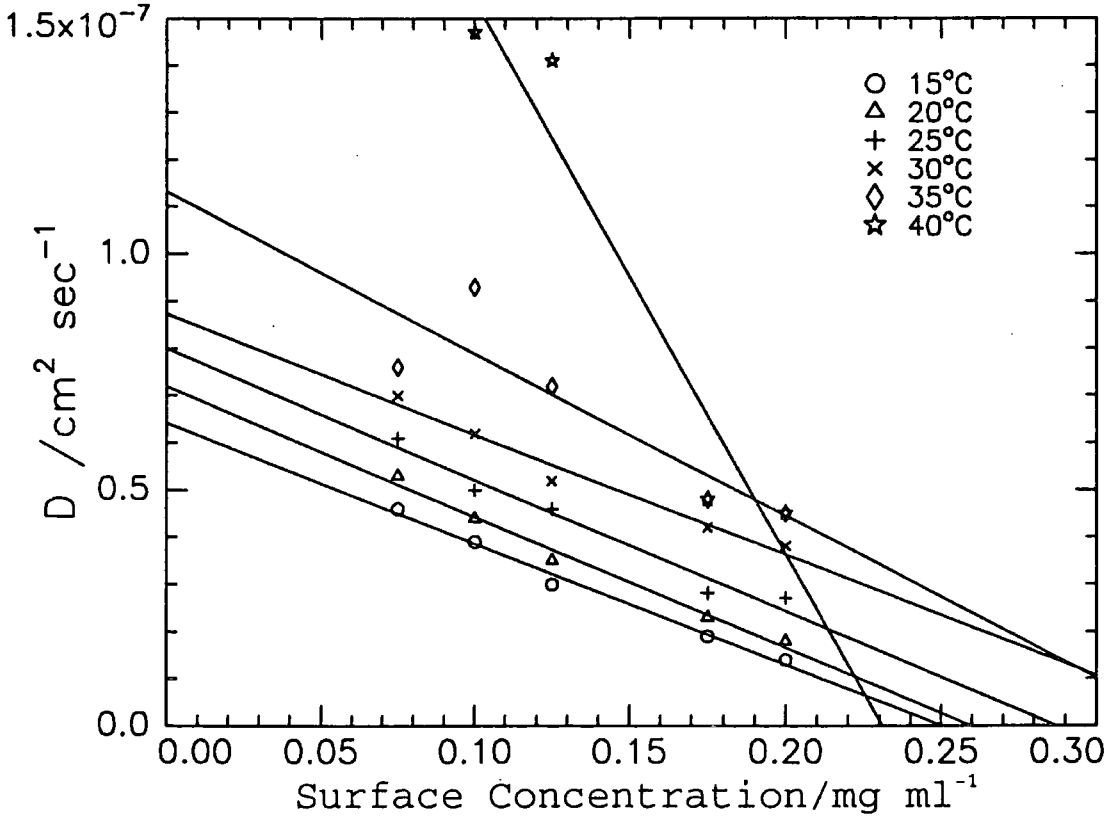

Figure 6.11 Diffusion coefficient as a function of solution concentration. Lines (-) show linear least squares fits to the data.

T/°C	$D_0/cm^2\ s^{-1}$	R_h/Å
15	6.42e-8	528
20	7.20e-8	500
25	8.00e-8	496
30	8.72e-8	499
35	1.36e-7	346
40	2.71e-7	197
45	1.01e-6	56

Table 6.2 Temperature dependence of the diffusion coefficient D_0 and hydrodynamic radius

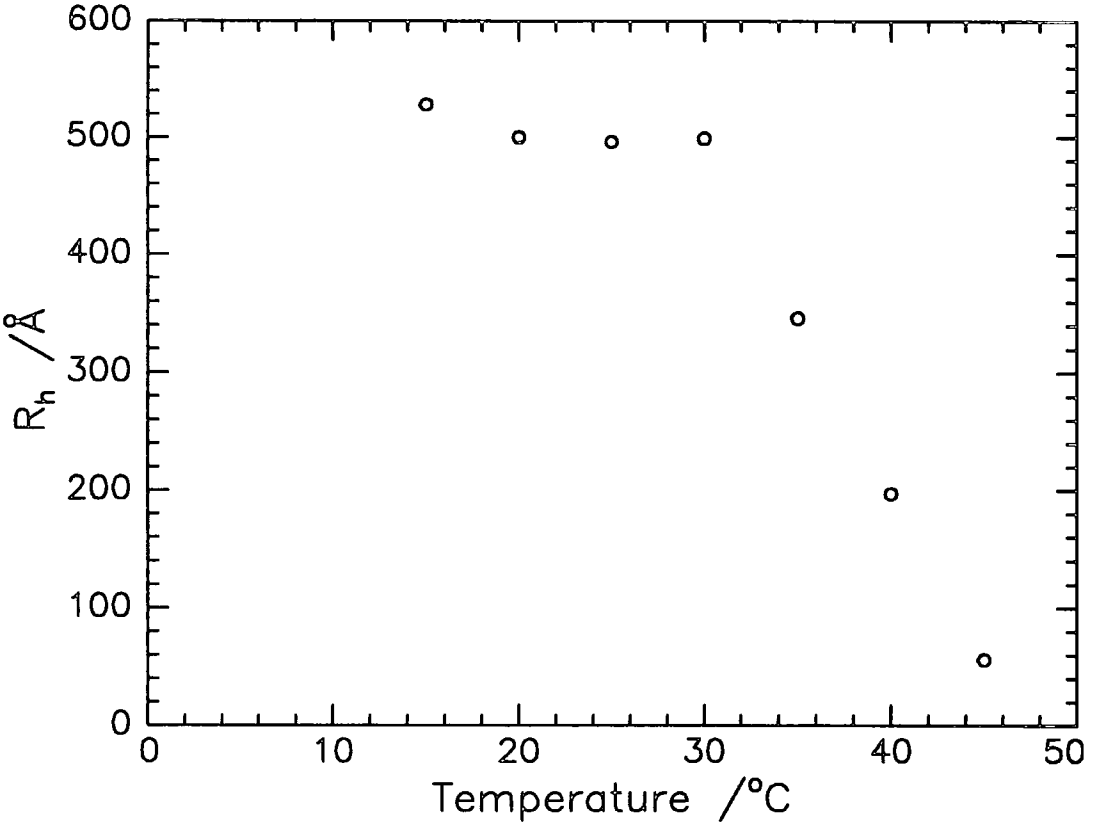

Figure 6.12 Plot of hydrodynamic radius as a function of temperature

block copolymer micellization occurs due to the loss in combinatorial entropy which happens due to the chains being significantly less swollen in the micelles than in the unassociated state. The large negative standard enthalpy of micellization of the PMMA-b-PEO block copolymers in methanol is due mainly to the high exothermic interchange energy occurring due to replacement of PMMA/methanol segmental interactions by PMMA/PMMA and methanol/methanol segmental interactions on formation of the micellar cores.

6.2.2.2 Variation of hydrodynamic radius with temperature

If the micellization process was an open association then a uniform distribution of molecular species would exist over the temperature range studied. Figure 6.12 shows that the hydrodynamic radii of the molecular species are approximately constant upto about 30°C but thereafter these values fall off rapidly as the micelles break up into unassociated species characteristic of a mainly closed association process. By assuming a spherical volume for all species present then

$$V = \frac{4}{3}\pi r^3 \qquad (6.2)$$

The upper and lower R_h values therefore suggest an association number of about 500. This number is only an approximation and could much different since the all species present do not actually exist as spheres in the system, and since the temperature region where both extremes of association occur have not been fully explored.

References

1. Sauer, B.B., Yu, H., Yazdanian, M., Zografi, G., Kim, M.W., *Macromolecules*, 1989, 22, 2332.

2. Katsutoshi, N., Kawaguchi, M., *Macromolecules*, 1990, 23, 3957.

3. Zhu, J., Eisenberg, A., Lennox, R.B., *J. Am. Chem. Soc.*, 1991, 113, 5583.

4. Zhu, J., Lennox, R.B., Eisenberg, A., *Langmuir*, 1991, 7, 1579.

5. Zhu, J., Lennox, R.B., Eisenberg, A., *J. Phys. Chem.*, 1992, 96, 4727.

6. Zhu, J., Eisenberg, A., Lennox, R.B., *Macromolecules*, 1992, 25, 6547.

7. Zhu, J., Eisenberg, A., Lennox, R.B., *Macromolecules*, 1992, 25, 6556.

8. Kumaki, J., *Macromolecules*, 1988, 21, 749.

9. Price, C., Stubbersfield, R.B., El-Kafrawy, S., Kendall, K.D., *British Polymer Journal*, 1989, 21, 391.

10. Price, C., Chan, E.K.M., Stubbersfield, R.B., *Eur. Polym. J.*, 1987, 23, 649.

11. Quintana, J.R., Villacampa, M., Muñoz, M., Andrio, A., Katime, I.A., *Macromolecules*, 1992, 25, 3125.

12. Quintana, J.R., Villacampa, M., Katime, I.A., *Polymer*, 1993, 34, 2380.

13. King, T.A., Knox, A., Lee, W.I., McAdam, J.D.G., *Polymer*, 1973, 14, 151.

14. Han, C.C., McCrackin, F.L., *Polymer*, 1979, 20, 427.

CHAPTER 7 - CONCLUSIONS

The main objectives of this work were to investigate the structure and dynamics of a spread PMMA/PEO diblock copolymer at the air/water interface.

The relationship between the behaviour of the classical surface pressure isotherm and the surface organisation of the PMMA and PEO blocks has been investigated using neutron reflectometry. Initial investigations showed some difference in structure between 2,5, and 10mN/m surface pressure. The results showed that a model incorporating two uniform layers could give an estimate of the composition of the interfacial region. Two layer fits to the experimental data suggested an upper layer of PMMA containing a small fraction of PEO and water, while the lower layer contained most of the PEO which was highly diluted by the subphase. It was possible to apply a more direct approach to the analysis of the reflectivity data using partial structure factors and solving the kinematic approximation equations. Deuterium labelling of one or both blocks allowed the six simultaneous equations of the kinematic approximation to be solved allowing the thickness and spatial organisation of the interfacial species to be obtained. Surface concentrations calculated by describing the partial structure factors as Gaussian distributions had better agreement than those from uniform layer models. These distributions were used in diagrams of the surface organisation of the PMMA and PEO blocks. The dimensions of the layers were approximately constant over the surface pressure range studied and no correlation with scaling laws was possible.

The description of the surface organisation was improved dramatically by the use of a constant area method, synthesis of an HMDE copolymer having a longer DEO chain, and extension of the Q range down to 0.0267Å. Increasing the surface concentration from 0.6mg/m^2 to 1.2mg/m^2 had the effect of separating the uniformly mixed PMMA and PEO blocks, i.e. a surface phase separation, with the PMMA block being confined essentially

at the surface while the PEO block dangled in solution. This increase in surface concentration also squeezed water out of the layer as the distance between PEO blocks decreased and they became more extended into the subphase.

The fact that neutron reflectivity showed that the total layer thickness doubled over the range 0.6 to 1.2mg/m^2 was confirmed by the ellipsometry measurements. In addition, these measurements also showed that above 1.2mg/m^2 the layer thickness remained constant. At 0.6mg/m^2 there was a high degree of mixing between the two blocks at the interface and the PEO block did not extend far into the subphase, the PEO density distribution resembling a 'squashed mushroom'. The PEO density distribution at 1.2mg/m^2 had more 'brushlike' characteristics than at 0.6mg/m^2, with loops of the PEO chains extending into the subphase, accounting for the segments 'lost' the technique

Surface quasi-elastic light scattering showed that by applying a Maxwell model to the viscoelastic data then much faster relaxation times occurred for the copolymer at about 1.3mg/m^2. Since only the PEO block contributes to the frequency dependence of the surface tension and transverse shear viscosity then the change in relaxation times may be attributed to it. The faster relaxation times at 1.3mg/m^2 must indicate a higher mobility of the EO segments due to their increased solubility in the water subphase. The relaxation times are then seen to decrease with surface concentration as the PEO segments become less mobile due to increased crowding and further extension into the subphase.

In the context of the work discussed in this thesis it is worth mentioning several areas where further work would be relevant. By investigating more surface concentrations in the 0 to 3.00mg/m^2 range then neutron reflectometry would show more clearly the surface concentration where phase separation occurs. This would allow a direct comparison with the more detailed SQELS surface concentration data and more detailed conclusions to be drawn.

A more detailed study of the effect of composition of the copolymers in the 5 to 95% PEO mole fraction range using surface pressure measurements would show the effect of temperature dependence on the isotherms. Neutron reflectometry could also be used to investigate the degree of mixing of the PMMA and PEO blocks at the surface for these varying compositions and compare the results with the surface pressure isotherms.

It may be useful to collect the ellipsometry data over longer periods of time, especially at low surface concentrations, which could improve the signal to noise ratio. By improving the quality of the data then the parameters of the fits to the data should be more accurate. Since thin films are not easily characterised by Ellipsometry, then it may be useful to investigate the possibility of forming Langmuir-Blodgett films on a solid substrate. It is uncertain whether or not these thicker films would be ordered or mixed, but subjecting them to ellipsometric measurements may produce interesting results.

It would be interesting to collect SQELS data for the copolymers synthesised in the range 5 to 95% mole fraction PEO. These copolymers have transitions in their surface pressure isotherms dependent upon the size of the PEO blocks and thus the transitions could be compared directly to changes occurring for the various SQELS viscoelastic parameters. Since the PEO blocks have frequency dependent surface tensions and transverse shear viscosities then these variations could be used in the direct comparison.

Overall perturbation of the air/water interface by air currents could be minimised by enclosing the trough in an air-tight perspex box.

The light scattering studies on methanol solutions of a diblock copolymer did not allow calculation of the molecular weight of the various micellar species. The main reason was that the refractive index increment dn/dc of the copolymer solutions was not available due to instrument failure. A combination of dn/dc and multiple angle scans would give a far better idea of the association number mechanism of micelle formation.

The spread monolayer at the air/water interface system described in this thesis involved spreading a diblock copolymer on the surface of water. It would be interesting to alter this system by spreading the diblock copolymers on an organic solvent such as methanol instead. Since light scattering has shown that methanol solutions of the copolymers form micelles then this micellization could be investigated further using the Wilhelmy surface pressure method since micelles in solution affect the surface tension. For a PMMA-b-PEO/methanol solution the PMMA forms the 'core' of the micelles while the PEO forms the outer 'corona'. By using an oppositely selective solvent from methanol, i.e. where PMMA is soluble and PEO insoluble, then reverse micelles would be formed and could be observed in the same way as described previously.

Quantitative External Reflection Infrared Spectroscopy is a technique which could be applied to the diblock copolymers at the air/water interface. This technique has a very low resolution and usually the FTIR spectrometer requires a Mercury Cadmium Telluride detector. The technique measures, in situ, the infrared spectrum of a monolayer at the air/water interface. In principle, it should be possible to distinguish between PMMA homopolymer and PMMA-b-PEO due mainly to the presence of C-O-C stretching at about 1100 cm^{-1}. Since the PMMA block has a single C=O carbonyl peak at 1730 cm^{-1} then a quantitative comparison of this peak and the C-O-C peak should give an indication of the proportion of each block in the surface layer.

APPENDIX A

Calculation of scattering length density prefactors for copolymers

Term	$b_m^2h_m$ (h_{mm})	$b_e^2h_e$ (h_{ee})	$b_w^2h_w$ (h_{ww})	$2b_mb_eh_{me}$ (h_{me})	$2b_mb_wh_{mw}$ (h_{mw})	$2b_eb_wh_{ew}$ (h_{ew})
HMHE/ D_2O	2.22e-8	1.71e-9	3.69e-8	1.23e-8	5.72e-8	1.59e-8
DMHE/ D_2O	9.64e-7	1.71e-9	3.69e-8	8.13e-8	3.77e-7	1.59e-8
HMDE/ D_2O	2.22e-8	2.10e-7	3.69e-8	1.36e-7	5.72e-8	1.76e-7
DMDE/ nrw	9.64e-7	2.10e-7	0	9.00e-7	0	0
DMHE/ nrw	9.64e-7	1.71e-9	0	8.13e-8	0	0
HMDE/ nrw	2.22e-8	2.10e-7	0	1.36e-7	0	0
DMDE/ D_2O	9.64e-7	2.10e-7	3.69e-8	9.00e-7	3.77e-7	1.76e-7

Table of coherent scattering densities for partial structure factors

Degrees of polymerisation used

	MMA block	EO block
DMHE (BR20)	352	352
HMHE (BR22)	328	609
HMDE (BR26)	243	68
DMDE (BR27)	196	204
HMDE (BR29)	207	483

Scattering length density prefactors calculated by multiplying each value in the above table by the square of the degree of polymerisation, i.e.

Term	Polymer	h_{11}	h_{22}	h_{33}	h_{12}	h_{13}	h_{23}
HMHE/ D_2O	BR22	2.39e-3	6.34e-4	3.69e-8	2.46e-3	1.88e-5	3.48e-5
DMHE/ D_2O	BR20	1.19e-1	2.12e-4	3.69e-8	1.01e-2	1.33e-4	5.60e-6
HMDE/ D_2O	BR29	9.51e-4	4.90e-2	3.69e-8	1.36e-2	1.18e-5	6.57e-5
DMDE/ nrw	BR27	3.70e-2	8.40e-3	0	3.60e-2	0	0
DMHE/ nrw	BR20	1.19e-1	2.12e-4	0	1.01e-2	0	0
HMDE/ nrw	BR29	9.51e-4	4.90e-2	0	1.36e-2	0	0

the input file for PARTIAL3 must take the following format

2.39e-3	1.19e-1	9.51e-4	3.70e-2	1.19e-1	9.51e-4
6.34e-4	2.12e-4	4.90e-2	8.40e-3	2.12e-4	4.90e-2
3.69e-8	3.69e-8	3.69e-8	0	0	0
2.46e-3	1.01e-2	1.36e-2	3.60e-2	1.01e-2	1.36e-2
1.88e-5	1.33e-4	1.18e-5	0	0	0
3.48e-5	5.60e-6	6.57e-5	0	0	0

APPENDIX B: LECTURES, CONFERENCES AND COURSES ATTENDED

UNIVERSITY OF DURHAM
Board of Studies in Chemistry

COLLOQUIA, LECTURES AND SEMINARS FROM INVITED SPEAKERS

1992

October 15 Dr M. Glazer & Dr. S. Tarling, Oxford University & Birbeck College, London
It Pays to be British! - The Chemist's Role as an Expert Witness in Patent Litigation

October 20 Dr. H. E. Bryndza, Du Pont Central Research
Synthesis, Reactions and Thermochemistry of Metal (Alkyl) Cyanide Complexes and Their Impact on Olefin Hydrocyanation Catalysis

October 22 Prof. A. Davies, University College London
The Ingold-Albert Lecture The Behaviour of Hydrogen as a Pseudometal

October 28 Dr. J. K . Cockcroft, University of Durham
Recent Developments in Powder Diffraction

October 29 Dr. J. Emsley, Imperial College, London
The Shocking History of Phosphorus

November 4 Dr. T. P. Kee, University of Leeds
Synthesis and Co-ordination Chemistry of Silylated Phosphites

November 5 Dr. C. J. Ludman, University of Durham
Explosions, A Demonstration Lecture

November 11 Prof. D. Robins†, Glasgow University
Pyrrolizidine Alkaloids : Biological Activity, Biosynthesis and Benefits

November 12 Prof. M. R. Truter, University College, London
Luck and Logic in Host - Guest Chemistry

November 18 Dr. R. Nix†, Queen Mary College, London
Characterisation of Heterogeneous Catalysts

November 25 Prof. Y. Vallee. University of Caen
Reactive Thiocarbonyl Compounds

November 25 Prof. L. D. Quin†, University of Massachusetts, Amherst
Fragmentation of Phosphorous Heterocycles as a Route to Phosphoryl Species with Uncommon Bonding

November 26 Dr. D. Humber, Glaxo, Greenford
AIDS - The Development of a Novel Series of Inhibitors of HIV

December 2 Prof. A. F. Hegarty, University College, Dublin
Highly Reactive Enols Stabilised by Steric Protection

December 2 Dr. R. A. Aitken†, University of St. Andrews
The Versatile Cycloaddition Chemistry of $Bu_3P.CS_2$

December 3 Prof. P. Edwards, Birmingham University
The SCI Lecture - What is Metal?

December 9 Dr. A. N. Burgess†, ICI Runcorn
The Structure of Perfluorinated Ionomer Membranes

1993

January 20 Dr. D. C. Clary†, University of Cambridge
Energy Flow in Chemical Reactions

January 21 Prof. L. Hall, Cambridge
NMR - Window to the Human Body

January 27 Dr. W. Kerr, University of Strathclyde
Development of the Pauson-Khand Annulation Reaction : Organocobalt Mediated Synthesis of Natural and Unnatural Products

January 28 Prof. J. Mann, University of Reading
Murder, Magic and Medicine

February 3 Prof. S. M. Roberts, University of Exeter
Enzymes in Organic Synthesis

February 10 Dr. D. Gillies†, University of Surrey
NMR and Molecular Motion in Solution

February 11 Prof. S. Knox, Bristol University
The Tilden Lecture Organic Chemistry at Polynuclear Metal Centres

February 17 Dr. R. W. Kemmitt†, University of Leicester
Oxatrimethylenemethane Metal Complexes

February 18 Dr. I. Fraser, ICI Wilton
Reactive Processing of Composite Materials

February 22 Prof. D. M. Grant, University of Utah
Single Crystals, Molecular Structure, and Chemical-Shift Anisotropy

February 24 Prof. C. J. M. Stirling†, University of Sheffield
Chemistry on the Flat-Reactivity of Ordered Systems

March 10 Dr. P. K. Baker, University College of North Wales, Bangor
'Chemistry of Highly Versatile 7-Coordinate Complexes'

March 11 Dr. R. A. Y. Jones, University of East Anglia
The Chemistry of Wine Making

March 17 Dr. R. J. K. Taylor†, University of East Anglia
Adventures in Natural Product Synthesis

March 24 Prof. I. O. Sutherland†, University of Liverpool
Chromogenic Reagents for Cations

May 13 Prof. J. A. Pople, Carnegie-Mellon University, Pittsburgh, USA
The Boys-Rahman Lecture Applications of Molecular Orbital Theory

May 21 Prof. L. Weber, University of Bielefeld
Metallo-phospha Alkenes as Synthons in Organometallic Chemistry

June 1 Prof. J. P. Konopelski, University of California, Santa Cruz
Synthetic Adventures with Enantiomerically Pure Acetals

June 2 Prof. F. Ciardelli, University of Pisa
Chiral Discrimination in the Stereospecific Polymerisation of Alpha Olefins

June 7 Prof. R. S. Stein, University of Massachusetts
Scattering Studies of Crystalline and Liquid Crystalline Polymers

June 16 Prof. A. K. Covington, University of Newcastle
Use of Ion Selective Electrodes as Detectors in Ion Chromatography

June 17 Prof. O. F. Nielsen, H. C. _rsted Institute, University of Copenhagen
Low-Frequency IR - and Raman Studies of Hydrogen Bonded Liquids

September 13 Prof. Dr. A.D. Schlüter, Freie Universität Berlin, Germany
Synthesis and Characterisation of Molecular Rods and Ribbons

September 13 Dr. K.J. Wynne, Office of Naval Research, Washington, USA
Polymer Surface Design for Minimal Adhesion

September 14 Prof. J.M. DeSimone, University of North Carolina, Chapel Hill, USA
Homogeneous and Heterogeneous Polymerisations in Environmentally Responsible Carbon Dioxide

September 28 Prof. H. Ila, North Eastern Hill University, India
Synthetic Strategies for Cyclopentanoids via Oxoketene Dithioacetals

October 4 Prof. F.J. Feher†, University of California, Irvine, USA
Bridging the Gap between Surfaces and Solution with Sessilquioxanes

February 23 Prof. P.M. Maitlis†, University of Sheffield
Across the Border : From Homogeneous to Heterogeneous Catalysis

March 2 Dr. C. Hunter†, University of Sheffield
Noncovalent Interactions between Aromatic Molecules

March 9 Prof. F. Wilkinson, Loughborough University of Technology
Nanosecond and Picosecond Laser Flash Photolysis

March 10 Prof. S.V. Ley, University of Cambridge
New Methods for Organic Synthesis

March 25 Dr. J. Dilworth, University of Essex
Technetium and Rhenium Compounds with Applications as Imaging Agents

April 28 Prof. R. J. Gillespie, McMaster University, Canada
The Molecular Structure of some Metal Fluorides and Oxofluorides: Apparent Exceptions to the VSEPR Model.

May 12 Prof. D. A. Humphreys, McMaster University, Canada
Bringing Knowledge to Life

October 5 Prof. N. L. Owen, Brigham Young University, Utah, USA
Determining Molecular Structure - the INADEQUATE NMR way

October 19 Prof. N. Bartlett, University of California
Some Aspects of Ag(II) and Ag(III) Chemistry

November 2 Dr P. G. Edwards, University of Wales, Cardiff
The Manipulation of Electronic and Structural Diversity in Metal Complexes - New Ligands

November 3 Prof. B. F. G. Johnson, Edinburgh University
Arene - Metal Clusters - DUCS Lecture

November 9 Dr J. P. S. Badyal, University of Durham
Chemistry at Surfaces, A Demonstration Lecture

November 9 Dr G. Hogarth, University College, London
New Vistas in Metal Imido Chemistry

November 10 Dr M. Block, Zeneca Pharmaceuticals, Macclesfield
Large Scale Manufacture of the Thromboxane Antagonist Synthase Inhibitor ZD 1542

November 16 Prof. M. Page, University of Huddersfield
Four Membered Rings and b-Lactamase

November 23 Dr J. M. J. Williams, University of Loughborough
New Approaches to Asymmetric Catalysis

December 7 Prof. D. Briggs, ICI and University of Durham
Surface Mass Spectrometry

1995

January 11 Prof. P. Parsons, University of Reading
Applications of Tandem Reactions in Organic Synthesis

January 18 Dr G. Rumbles, Imperial College, London
Real or Imaginary 3rd Order non-Linear Optical Materials

January 25 Dr D. A. Roberts, Zeneca Pharmaceuticals
The Design and Synthesis of Inhibitors of the Renin-Angiotensin System

February 1 Dr T. Cosgrove, Bristol University
Polymers do it at Interfaces

February 8 Dr D. O'Hare, Oxford University
Synthesis and Solid State Properties of Poly-, Oligo- and Multidecker Metallocenes

February 22 Prof. E. Schaumann, University of Clausthal
Silicon and Sulphur Mediated Ring-opening Reactions of Epoxide

March 1 Dr M. Rosseinsky, Oxford University
Fullerene Intercalation Chemistry

March 8 Nikki Chesters, Wayne Devonport & Penelope Herbertson, University of Durham
1995 Graduate Seminar Series

March 15 Janet Hopkins, Brian Rochford & Graham Rivers, University of Durham
1995 Graduate Seminar Series

March 22 Dr M. Taylor, University of Auckland, New Zealand
Structural Methods in Main Group Chemistry

April 26 Dr M. Schroder, University of Edinburgh
Redox Active Macrocyclic Complexes : Rings, Stacks and Liquid Crystals

May 3 Prof. E. W. Randall, Queen Mary and Westfield College
New Perspectives in NMR Imaging

May 4 Prof. A. J. Kresge, University of Toronto
The Ingold Lecture - Reactive Intermediates : Carboxylic Acid Enols and Other Unstable Species

May 10 George Bates, Steve Carss, Martyn Coles, University of Durham
1995 Graduate Seminar Series

May 17	Graham McKelvey, Richard Towns & Tim Thompson, University of Durham Graduate Seminar Series
May 31	Rob Spink, Ian Reynolds & Nick Haylett, University of Durham 1995 Graduate Seminar Series
June 7	Abdulla Ahmed, Mike Chan & Alex Eberlin, University of Durham 1995 Graduate Seminar Series
June 14	Iain May, Leela Sequeira & Gareth Williams, University of Durham 1995 Graduate Seminar Series
June 21	Oliver Greenwood, Mike Chalton & Alex Roche, University of Durham 1995 Graduate Seminar Series
July 5	Alan Gilbert, Emma Rivers & Simon Lord, Univeristy of Durham 1995 Graduate Seminar Series
July 12	Martin Ryan, Steven Dunn & R Samadi, Univeristy of Durham 1995 Graduate Seminar Series

† Invited specially for the graduate training programme.

The author has also attended the following lectures in the IRC in Polymer Science and Technology International Seminar Series.

1993

March 16	Prof. J.M.G. Cowie (Heriot-Watt University), at Bradford University. High Technology in Chains: The Role of Polymers in Electronic Applications and Data Processing
April 1	Prof. H.W. Speiss (Max-Planck Institut for Polymerforschung, Mainz), at Durham University. Multidimensional NMR Studies of Structure and Dynamics of Polymers.
June 2	Prof. F. Ciardelli (University of Pisa), at Durham University. Chiral Discrimination in the Stereospecific Polymerisation of α-olefins.
June 8	Prof. B.E. Eichinger (BIOSYM Technologies Inc., San Diego), at Leeds University. Recent Polymer Modeling Results and a Look into the Future.
July 6	Prof. C.W. Macosko (University of Minnesota, Minneapolis), at Bradford University. Morphology Development in Immiscible Polymer-Polymer Blending.

Conferences, Meetings and Courses attended by the author

January 1993	IRC Polymer Engineering Course, Bradford University.
March 1993	IRC Polymer Physics Course, Leeds University.
April 1993	Macro Group (UK) Family Meeting, Lancaster University.
September 1993	Neutron Beam User's Meeting†, Sheffield.
September 1993	Polymers at Interfaces Conference, Bristol.
December 1993	RSC - Faraday Division (Colloid and Interface Science Group) Dynamics of Surfactant Monolayers, London.
April 1994	Macro Group (UK) Family Meeting, Birmingham University†.
September 1994	Faraday Discussion†, Bristol University
September 1994	IRC Club Meeting†, Leeds University.
December 1994	ICI Poster Competition†, Durham University.
April 1995	Neutron Beam User's Meeting†*, Manchester University.
April 1995	Macro Group (UK) Family Meeting†, Loughborough University.

† Poster presentation by the author
* Presentation by the author

Publications

1. Gissing, S.K., Richards, R.W., Rochford, B.R., *Colloids and Surfaces A: Physiochemical and Engineering Aspects*, 1994, **86**, 171.

2. Richards, R.W., Rochford, B.R., Webster, J.R.P., *Faraday Discuss.*, 1994, **98**, 263.

3. Richards, R.W., Rochford, B.R., Taylor, M.R., submitted for publishing.